AD-A263 503

AGARD-CP-530

AGARD

ADVISORY GROUP FOR AEROSPACE RESEARCH & DEVELOPMENT

7 RUE ANCELLE 92200 NEUILLY SUR SEINE FRANCE

AGARD CONFERENCE PROCEEDINGS 530

Debonding/Delamination of Composites

(Le Décollement et le Délaminage
des Matériaux Composites)

DTIC
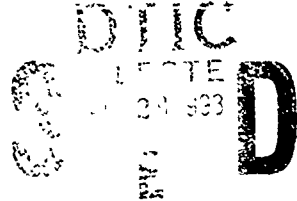
*Papers presented at the 74th Meeting of the AGARD Structures and Materials Panel,
held in Patras, Greece 24th—29th May 1992.*
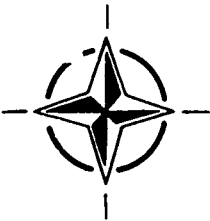
NORTH ATLANTIC TREATY ORGANIZATION

Published December 1992

Distribution and Availability on Back Cover

40th Anniversary Year

AGARD

ADVISORY GROUP FOR AEROSPACE RESEARCH & DEVELOPMENT

7 RUE ANCELLE 92200 NEUILLY SUR SEINE FRANCE

Accesion For		
NTIS CRA&I		☒
DTIC TAB		☒
Unannounced		☐
Justification		
By		
Distribution /		
Availability Codes		
Dist	Avail and / or Special	
A-1		

AGARD CONFERENCE PROCEEDINGS 530

Debonding/Delamination of Composites

(Le Décollement et le Délaminage
des Matériaux Composites)

Papers presented at the 74th Meeting of the AGARD Structures and Materials Panel,
held in Patras, Greece 24th—29th May 1992.

North Atlantic Treaty Organization
Organisation du Traité de l'Atlantique Nord

The Mission of AGARD

According to its Charter, the mission of AGARD is to bring together the leading personalities of the NATO nations in the fields of science and technology relating to aerospace for the following purposes:

— Recommending effective ways for the member nations to use their research and development capabilities for the common benefit of the NATO community;

— Providing scientific and technical advice and assistance to the Military Committee in the field of aerospace research and development (with particular regard to its military application);

— Continuously stimulating advances in the aerospace sciences relevant to strengthening the common defence posture;

— Improving the co-operation among member nations in aerospace research and development;

— Exchange of scientific and technical information;

— Providing assistance to member nations for the purpose of increasing their scientific and technical potential;

— Rendering scientific and technical assistance, as requested, to other NATO bodies and to member nations in connection with research and development problems in the aerospace field.

The highest authority within AGARD is the National Delegates Board consisting of officially appointed senior representatives from each member nation. The mission of AGARD is carried out through the Panels which are composed of experts appointed by the National Delegates, the Consultant and Exchange Programme and the Aerospace Applications Studies Programme. The results of AGARD work are reported to the member nations and the NATO Authorities through the AGARD series of publications of which this is one.

Participation in AGARD activities is by invitation only and is normally limited to citizens of the NATO nations.

Preface

Composite laminate components are prone to debonding/delamination when subjected to high interlaminar stress or when under impact. While delamination failure in itself is not usually catastrophic, its weakening influence on a component may lead to subsequent failure modes. Hence debonding or delamination may significantly reduce the strength of an aircraft or its fatigue life.

The objective of the Specialists' Meeting, organised by the Structures and Materials Panel in the Spring of 1992, was to review the present state-of-the-art in the analysis, detection and repair of delamination. Twenty-nine excellent papers were presented to an audience of over 100 leading specialists from NATO countries. Discussion of the papers presented and the final summary session revealed some common concerns and issues and gave rise to several recommendations.

In bringing together the various experiences of air forces, governments, industry and universities, the Specialists' Meeting has helped in identifying the key issues related to the debonding/delamination problem

Préface

Les éléments stratifies composites sont sujets au décollement et au délaminage lorsqu'ils sont soumis à des contraintes interlaminaires élevées ou à un choc. Bien que le délaminage ne soit généralement pas catastrophique en lui-même, l'affaiblissement de l'élément qui en découle peut causer d'autres modes de défaillance. Par consequent, le décollement ou le délaminage peut considérablement réduire la résistance d'un aéronef, notamment sa durée de vie en fatigue.

L'objectif de la Réunion des specialistes, organisée au printemps 1992 par le Groupe de travail sur les structures et les matériaux, était de faire le point sur l'etat actuel des techniques d'analyse, de detection et de correction du délaminage. Vingt-neuf excellents documents ont ete présentes à un auditoire de plus de 100 specialistes de pointe représentant les pays de l'OTAN. Les discussions sur les documents présentés et la séance de clôture ont permis d'identifier certains intérêts communs et d'énoncer plusieurs recommendations.

En permettant aux armées de l'air, aux gouvernements, à l'industrie et aux universités de mettre en commun leurs expériences, la Réunion des specialistes a contribue à l'identification des principaux aspects du problème de décollement ou de délaminage.

JJ Kacprzynski
Chairman
Sub-committee on
Debonding/Delamination of Composites

Structures and Materials Panel

Chairman: Mr Samuel L. Venneri
  Director, Materials & Structures
    Division (Code RM)
  Office of Aeronautics & Space Technology
  NASA Hq
  Washington DC 20546
  United States

Deputy Chairman: Mr Roger Labourdette
  Directeur Scientifique des Structures
  ONERA
  29 ave de la Division Leclerc
  92322 Châtillon
  France

SUB-COMMITTEE ON
DEBONDING/DELAMINATION OF COMPOSITES

Chairman: Dr J.J. Kacprzynski
  Senior Research Officer
  Structures & Materials Laboratory
  Institute for Aerospace Research
  National Research Council of Canada
  Ottawa, Ont K1A 0R6 Canada

Members

D. Chaumette	FR	S. Paipetis	GR
L. Chesta	FR	D.B. Paul	US
P. Costa	FR	R.J. Pax	SP
R. Dechaene	BE	B.F. Peters	CA
M. Doruk	TU	R. Potter	UK
G. Duvaut	FR	M. Rother	GE
C.N. Economidis	GR	A. Salvetti	IT
W. Elber	US	N. Sandsmark	NO
H. Försching	GE	M. Scolaris	IT
V. Giavotto	IT	O. Sensburg	GE
H. Goncalo	PO	A.F. Tovar de Lemos	PO
L. Grabowski	UK	D. Tzimis	GR
L. Kompotiatis	GR	S.L. Venneri	US
R. Labourdette	FR	J. Waldman	US
M.L. Minges	US	W. Wallace	CA
G. Oddone	IT	A.P. Ward	UK
J. Odorico	FR	H. Zocher	GE
H.H. Ottens	NL		

PANEL EXECUTIVE

Contents

SESSION IV

SESSION V

SESSION VI

SESSION VII

FREE EDGE DELAMINATION PREVENTION IN COMPOSITE LAMINATES

N. J. Pagano
WL/MLBM
Wright Patterson Air Force Base
Dayton, Ohio 45433-6533 USA

and

S. R. Soni
AdTech Systems Research, Inc.
1342 North Fairfield Road
Dayton, Ohio 45432-2698 USA

1. SUMMARY

The key to success in the prevention of free edge delamination is the understanding of stress components and contributing factors responsible for the onset of delamination. The contributing factors may be fiber/matrix properties, ply orientations and stacking sequence. In the past two decades the authors have done extensive theoretical and experimental investigations on this topic. As a result of their continuous work in this area a unique software package, "Automated System for Composite Analysis" has been developed. This paper demonstrates the effectiveness of the Automated System for Composite Analysis (ASCA) for identifying the contributions of the influencing factors responsible for the onset of delamination and help select safer configurations. For this purpose two material systems (one polymer matrix composite AS4/3501 and one metal matrix composite SCS6/Ti) have been considered. These two composites represent highly orthotropic and near quasi-isotropic material properties. The ASCA code has been used to obtain the effective ply properties by utilizing NDSANDS module. These ply properties are automatically transmitted into the free edge stress analysis (FESAP) module. The FESAP module calculates all the six stress components at different locations of the laminate for given applied in-plane strain. These stresses are automatically transferred to the NDSANDS module to predict stresses in the constituents. This sequence provides the user the detailed information to identify the influencing factor for controlling the onset of delamination. The same cycle can be used for point stress analysis in the lamination theory (CLAP) module and the analysis of laminate with transverse crack (ALTRAC) module. The investigation of a few important aspects for the above mentioned two material systems has revealed the following messages:

The interlaminar normal stress σ_z at the mid surface reduces with increased number of (0/90) stacks in the $(0/90)_{ns}$ laminates of polymer matrix material. The free edge region diminishes with increasing value of n. This also reduces the stress concentration factor. The free edge out-of-plane normal stress component σ_z at the midsurface for a delamination prone laminate $(\pm 30/90)_s$ is higher for the metal matrix composite than that for the polymer matrix composite. The same observation is made for the $(0/90/\pm 45)_s$ laminate. Because of the near quasi-isotropic nature of the metal matrix composites it is believed that the free edge delamination is not a point of concern. The abovementioned fact shows contrary to this belief. These are extremely important observations to develop methods for avoiding free edge delamination in composite laminates.

2. INTRODUCTION

Various models to calculate the nature of the interlaminar stress field in the neighborhood of the free edge of a composite laminate under axial extension are presented [1]. The first model [2] is a primitive one that can be used to determine exact results for the interlaminar stress and moment resultants. This model serves the purpose of defining the detailed stacking sequence required to either promote or resist delamination. The method involves the use of classical lamination theory in conjunction with force and moment equilibrium on a ply-by-ply basis.

The second model [3, 4] provides a detailed solution for the stresses in a particular laminate once the stacking sequence has been selected. This model is based on the representation of individual layer response by in-plane forces and moments per unit length plus interlaminar tractions. The field equations are then derived from an extension of Reissner's variational principle for laminated bodies. While this model can be shown to approach exact theory of elasticity in the limit of vanishing layer thickness, solution of practical problems can be limited to 10 to 20 layers because of the complexity of the model.

The Global-Local Model [5] removes the restriction on number of layers and provides tractable solutions for laminates of arbitrary thickness. The key to the new approach lies in the precise modeling of local geometry in predetermined region for which accurate stress predictions are needed (Local) while the remaining region is represented by its overall response in terms of forces and moments over the entire region (Global). Mathematically, different variational functionals provide the mechanism for such dual representation. Numerous practical solutions have demonstrated the efficacy of Global-Local modeling in predicting the steep interlaminar stress gradients characteristic of laminate free-edge regions. Furthermore, application of the new model in defining a realistic criterion for the onset of delamination has also been demonstrated.

The three models were utilized and correlated with extensive experimental data reporting onset of delamination to deduce a so-called average stress failure criterion [6,7]. The effects of residual curing stresses are included in the analyses. A convenient summary of the above work can be found in chapters by R. Y. Kim and the present authors in reference [1].

This paper comprises a number of investigations including micromechanics, free edge stress analysis and the effect of constituent properties on the response characteristics of different laminates. All the computations are done using the ASCA computer code. This code is designed for personal computers and is a result of a cooperative R&D agreement between the organizations of the authors of this paper. This code incorporates various models, including micromechanics and lamination theory, failure analysis, free edge stress analysis [3] and computation of stresses in the vicinity of transverse crack (s) [9], in a convenient package[8]

3. PROBLEM DESCRIPTION

Figure 1 shows the laminate geometry, co-ordinate axis, and the direction of applied strain. The magnitude of the resulting stress components in the laminate is dependent upon the properties and geometric parameters of the constituents (i.e. fiber, matrix and/or coating properties, fiber volume fraction) stacking sequence and applied load. Any one of these stress components or a combination thereof may be responsible for onset of delamination in the laminate. Because of 'ow interface strength in certain composites (ceramics or metal matrix) the fiber matrix interface may develop damage. In this study the following investigations are conducted by using the ASCA code:

3.1. Determination of effective ply properties for two material systems, namely AS4/3501 and SCS6/Ti. The material properties of the fiber and matrix materials for each composite are given in Table I The fiber volume fraction for AS4/3501 is considered to be 67% and that for SCS6/Ti is considered to be 30%.

3 2. Investigate the free edge region in (0/90)ns laminates. Five values of n (=1,2,3,4 and 5) for AS4/3501 material and one value of n (=1) for SCS6/Ti material are considered. This provides a qualitative and quantitative understanding for reducing stress concentration at the free edge thereby revealing a method to prevent delamination

Study the convergence of calculated stress σ_z based upon different subdivisions of the ply thickness.

3 3 Study two commonly used delamination prone quasi-isotropic laminates ($\pm 30/90$)s and (0/90/± 45)s to compare the response between two distinctly different material systems AS4/3501 and SCS6/Ti.

3.4. Study the stress distribution, in fiber and matrix materials, stimulated by the applied inplane strain at the free edge and away from the free edge. This will provide details of impending fiber/ matrix interface failure.

4. BRIEF DESCRIPTION OF ASCA

Figure 2 shows the steps ASCA undertakes for investigating different strength and stiffness aspects of composite laminates. After the initial material design screening phase, optimum materials can then be subjected to experimental characterization Fiber and matrix properties (and coatings, if present), as well as simulated interface conditions can be used to compute composite layer moduli in a micromechanics module These moduli are then automatically transmitted to either of the following:

4.1) a laminate module (CLAP) to define effective laminate properties, point stress analysis and failure analysis.

4.2) a module (FESAP) to define the stress field in the presence of free edges, so that one may understand the behavior of the laminate in a subsequent experiment under applied in-plane loading, including the influence of residual thermal stresses.

4 3) a module (ALTRAC) to determine the stress field in the neighborhood of a transverse crack in one or several layers

4.4) a module (NDSANDS) to analyze an N-directional composite (one in which fibers are oriented in N oblique directions in space).

Afterwards, the behavior of the laminates (for which the precise stacking sequence can be determined theoretically) is recycled to the micromechanics module to compute the stress fields in the fiber and the matrix (and the coating if present). Thus the in-situ response of the constituent materials in the laboratory test specimen can be determined theoretically, at

which point new decisions regarding constituent material and/ or interface selection can be made.

TABLE I
Fiber and matrix material properties for two composite material systems

	AS4/3501		SCS6/Ti	
	Fiber	Matrix	Fiber	Matrix
E_A (MSI)	34.0	0 62	60	12
F_T (MSI)	2.0	0 62	60	12
υ_A	.20	0.34	.22	.3
υ_T	25	0 34	22	.3
G_A (MSI)	4.1	0.23	25	4.7

5. RESULTS AND DISCUSSION

Effective ply properties for the two material systems considered here are given in Table II These properties are calculated by using the NDSANDS module of the ASCA code Figures 3-8 show the interlaminar stress component acting at the midsurface of each laminate of the properties of table II transmitted in to the free edge stress analysis module FESAP from NDSANDS. The applied inplane strain was $\varepsilon_x = 00001$. Figures 9-14 give the micro-mechanics stress components in the vicinity of the fiber under the influence of applied load at two locations (free edge and 069" away from the free edge) for AS4/3501 material

Table II

Ply Properties for AS4/3501 and SCS6/Ti Composites

Property	AS4/3501	SCS6/Ti
E_{11} (MSI)	22 9	26.6
E_{22} (MSI)	1 4	18 3
E_{33}(MSI)	1.4	18.3
G_{12}(MSI)	0.9	7.03
G_{13}(MSI)	0.9	7.03
G_{23}(MSI)	0 51	6.98
v_{12}	0.24	0.3
v_{13}	0 24	0 3
v_{23}	0 35	0 31

Figure 3 contains σ_z at the midsurface of the (0/90)s laminate with four different mathematical subdivisions of the half laminate thickness i e. {(0/90)s, (0/0/90/90)s, (0/90/90/90)s and (0/0/0/90/90/90)s}. In the laminate notation the underline orientations are subdivisions of a ply with that angle i e. (0/0/90/90)s represents a (0/90)s laminate with two subdivisions of each ply It has been observed, as expected, that the stress component σ_z in the vicinity of the free edge for different configurations is different where as at location more than a ply thickness away from the free edge the magnitude is almost the same for each configuration. Figure 3 shows that the results for the latter three configurations provide a convergent result at the free edge Similar observations were made for two cases (0/90/0/90)s and (0/90/0/90/90)s configurations Based upon the results in the (0/90)s case studies, the curve with (0/90/0/0/90/90)s configuration (not shown in figures) is the convergent result

Table III

Effective In plane Properties for Laminates Considered

	AS4/3501			SCS6-T		
	(0/90)$_s$	(±30/90)	(0/90/±45)$_s$	(0/90)$_s$	(±30/90)	(0/90/±45)$_s$
E_x	12 2	8.85	8 85	22.5	20 9	20 9
E_y	12 2	8 85	8.85	22 5	20 9	20 9
v_{xy}	03	29	29	0 24	0 3	0 3
G_{xy}	0 9	3 4	3 4	7 03	8 03	8 03

Figure 4 shows the stress component σ_z at the midsurface of the following configurations of (0/90/0/90/0/90)$_s$ laminate:

(0/90/0/90/0/90)$_s$
(0/90/0/90/0/0/90/90)$_s$
(0/90/0/90/0/0/0/90/90/90)$_s$
(0/90/0/90/0/0/90/90/90/90)$_s$

The results for all the four cases are close beyond the distance .001" away from the free edge. Near the free edge the latter two cases give close results and the first two cases give considerably different results. figure 4b shows results near the free edge, with finer subdivisions of the width region. The computational experiment on the results of σ_z at midsurfaces of (0/90/0/90/0/90/0/90)$_s$, (0/90/0/90/0/90/0/0/90/90)$_s$ and (0/90/0/90/0/90/0/90/90)$_s$ laminates again show the similar trend in convergence of results in the free edge region.

Figure 5 shows the stress component σ_z at the midsurface of (0/90)$_s$, (0/90/0/90)$_s$, (0/90/0/90/0/90)$_s$, (0/90/0/90/0/90/0/90)$_s$ and (0/90/0/90/0/90/0/90/0/90)$_s$ laminates. The stress at the free edge for various laminates are different than the actual stresses. That is because of inadequate subdivision of the layers. Away from the free edge, the stresses are within acceptable range of accuracy. The key element of this figure is the variation of σ_z trend as we go away from the free edge. Figure 5a shows the stress distribution for these laminates within the vicinity of the free edge (for distance 0 to 01" of the Figure 5) with refined subdivisions. It is seen from figure 5a that the stress concentration at the free edge is monotonically decreasing with the increase of repeated (0/90) ply stacks. The application of an average stress failure criterion will give lower effective σ_z for laminates with increasing number of 0/90 stacks.

Figure 5 also gives as dotted lines the extrapolated results near the free edge by considering a straight line between the first two points away from the free edge. The values of σ_z at the free edge computed by this process are close to the values computed by subdividing the layer thickness as shown in Figures 3 to 5. These extrapolated and thickness subdivided computational values are given in Table IV.

Table IV

Comparison of σ_z at the free edge between extrapolated values and refined model values

Laminate	Extrapolated	Refined
(0/90)$_s$	2.03	2.1
(0/90/0/90)$_s$	1.2	1.27
(0/90/0/90/0/90)$_s$	0.95	1.05
(0/90/0/90/0/90/0/90)$_s$	0.85	.96
(0/90/0/90/0/90/0/90/0/90)$_s$	0.8	-

In the past the authors have demonstrated that the average stress over a region equal to a ply thickness from the free edge is considered the effective free edge stress. For finding the average (or effective) stress under this criterion the area under the curve is divided by the width. The area can be approximated as half of the stress at free edge times the ply thickness. The mathematical simplification of area divided by the ply thickness provides that the crude approximation of the effective stress σ_z acting at the free edge in (0/90)$_{ns}$ laminates is about a half of the maximum stress at the free edge.

Figures 6-8 show comparisons of σ_z between two material systems for (±30/90)$_s$ and (0/90/±45)$_s$ laminates. To compare the response between two distinctly different material systems, AS4/3501 and SCS6/Ti were considered. It has been observed that σ_z for SCS6/Ti is higher than that for AS4/3501 for both the laminates (±30/90)$_s$ and (0/90/±45)$_s$. Both these AS4/3501 laminates are delamination prone. The figures 7 and 8 suggest that SCS6/Ti laminates will also be delamination prone.

Figures 9-14 shows the micromechanics stress components computed for (0/90) laminate in the vicinity of the interface for one material system. The applied stress components for the micromechanics model come from the FESAP module. Two locations are used for the computations, one at the free edge and the other at a distance .069" away from the free edge. Only σ_1 and σ_2 at one radius of the fiber or matrix in the representative volume element of the material are computed. The computations are done for two combinations of radial and circumferential directions. Figure 9 shows the stress component σ_1 in the ply coordinate system using micromechanics module. Thus σ_1 is stress component acting in fiber direction in the 90 degree ply. This is based upon the stress distribution computed in FESAP module and used in the micromechanics module. This study provides the required information to understand the mode of failure. The key observations in micromechanics stress results are the stress discontinuities at the fiber matrix interface. Based upon the loading and the material properties these discontinuities can be responsible for the onset of delamination or transverse crack. The code provides a very useful tool to design laminates not prone to delamination

6. FUTURE PLANS

The ASCA computer code is modified to incorporate nonlinear matrix properties. The work is in progress to include the probabilistic aspects of composite materials. New modules are also developed to investigate the joining of composites. The present capability for joining aspects consists of bolted joint and double lap joints. For that purpose the code is available immediately. New modules will be developed for other joints. With the ever increasing developments in composite material science and technology, the capabilities of the ASCA computer code is constantly growing.

8. REFERENCES

1. N. J. Pagano (ed.), *Interlaminar Response of Composite Materials*, Elsevier (1989).

2. N. J. Pagano and R.B. Pipes, *The Influence of Stacking Sequence on Laminate Strength*, J. Comp. Mat., 5 (1971).

3. N. J. Pagano, *Stress Fields in Composite Laminates*, Int. J. Solids & Struct. 14 (1978).

4. N. J. Pagano, *Free Edge Stress Fields in Composite Laminates*, Int. J. Solids & Struct. 14 (1978).

5. N. J. Pagano and S. R. Soni, *Global-Local Luminate Variational Model*, Int. J. Solids & Struct. 19 (1983).

6. J. M. Whitney and R. J. Nuismer, *Stress Fracture Criteria for Laminated Composites Containing Stress Concentrations*, J. Comp. Mat. 8 (1974).

7. R. Y. Kim, *Matrix Damage in Composite Laminates*, 11th Southeastern Conference on Theoretical and Applied Mechanics, Huntsville AL (1982).

8. "Automated System for Composite Analysis", A leading edge software package for composite material design by theoretical analysis, Technomic publishing Co., 1992.

9. "Analysis of a laminate with transverse cracks", AdTech Technical Report .
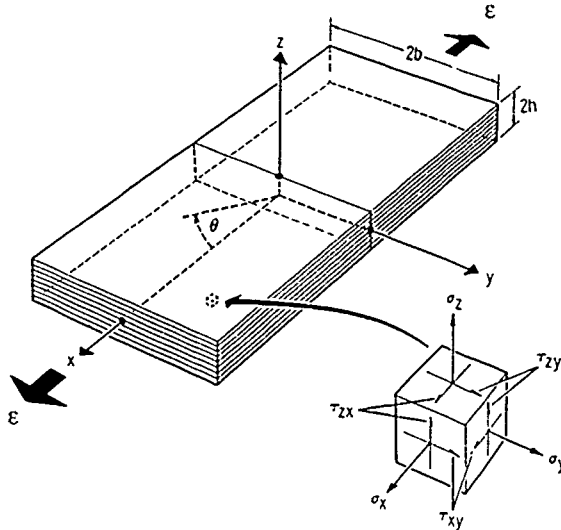
LAMINATE GEOMETRY

Figure 1: Laminate geometry with coordinate axis
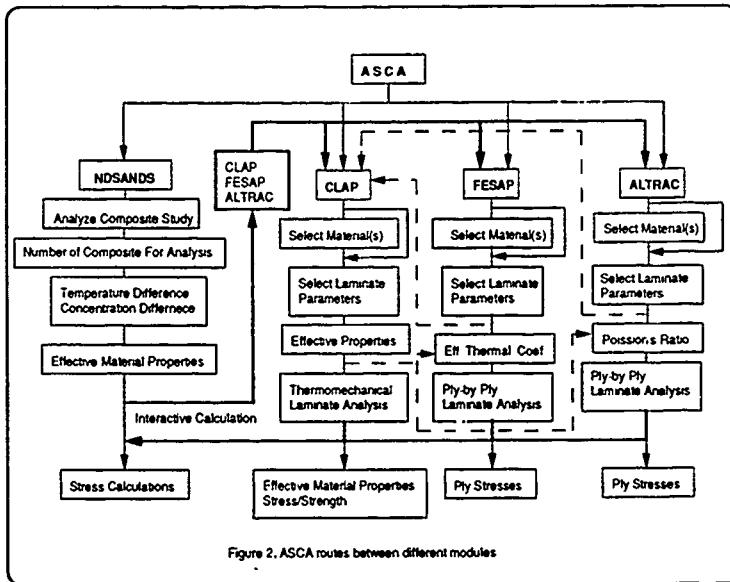
Figure 2. ASCA routes between different modules

σ_z   Mid Surface AS4/3501
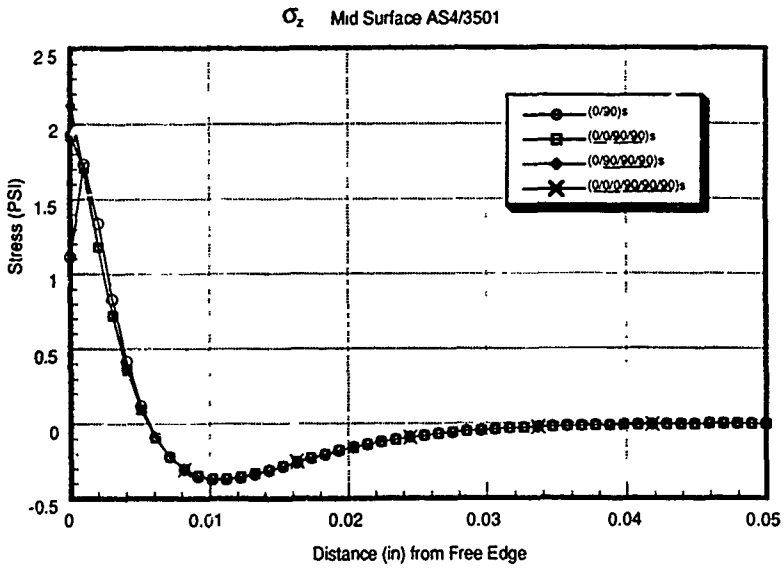
Figure 3: Comparison of σ_z at the laminate midsurface near free edge
(for finer subdivision of width) amongst four cases of ply representation.

σ_z   Mid Surface AS4/3501
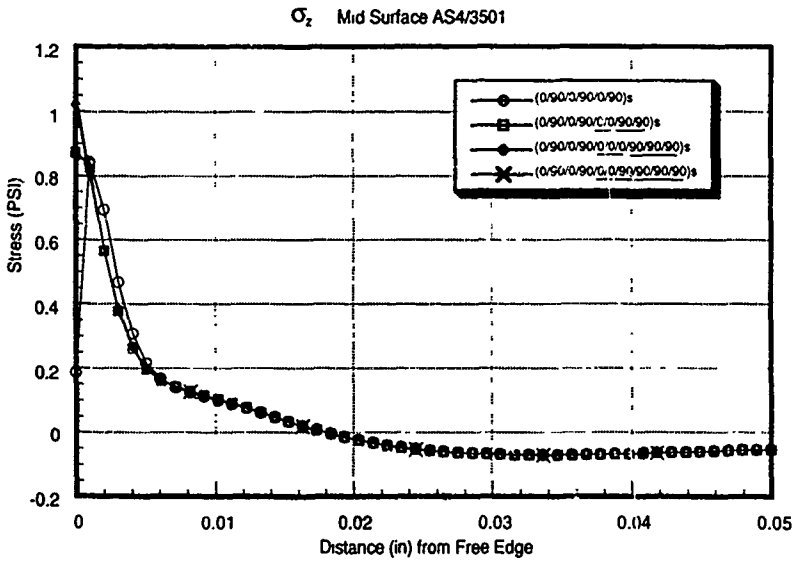
Figure 4: Comparison of σ_z at the laminate midsurface near free edge
amongst fourcases of ply representations.

σ_z Mid Surface AS4/3501
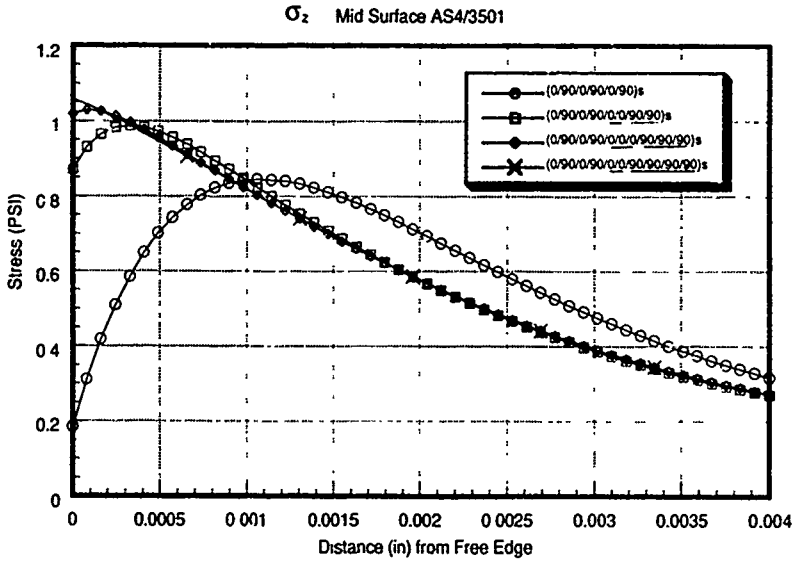
Figure 4a: Comparison of σ_z at the laminate midsurface near free edge (for finer subdivision of width) amongst four cases of ply representation

σ_z Mid Surface AS4/3501
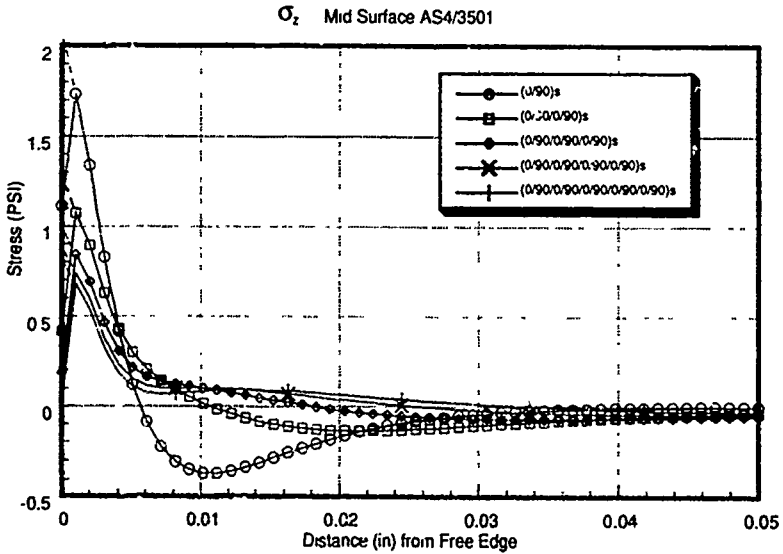
Figure 5: Comparison of σ_z at midsurface of five cases of $(0/90)_{ns}$ laminate (n=1,2...,5). --- line represents extrapolated value.
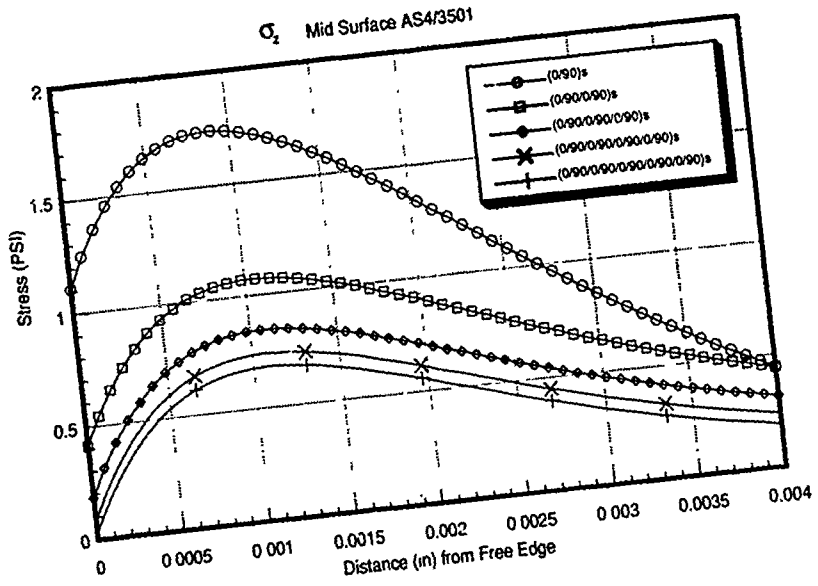
Figure 5a: Results of figure 5 in the vicinity of the free edge with finer sub-divisions of the width.
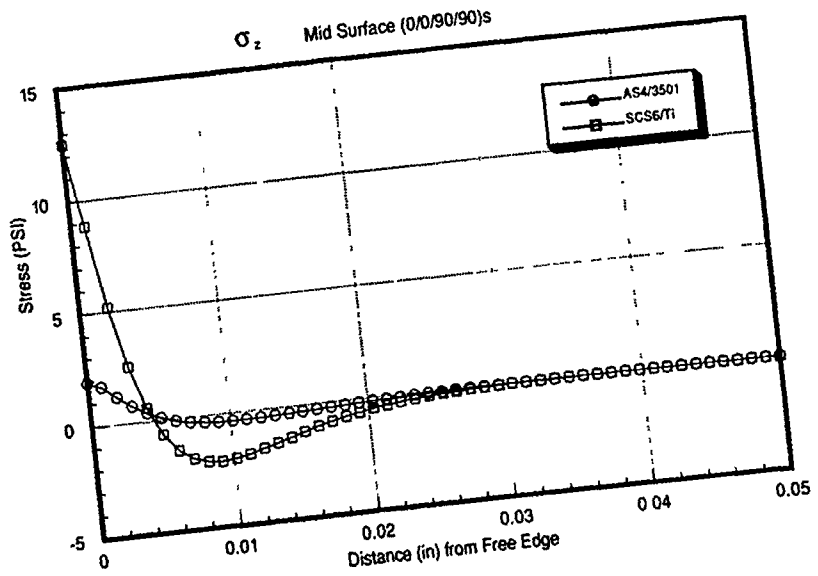
Figure 6: Comparison of σ_z at the midsurface of $(0/90)_s$ laminate between AS4/3501 and SCS6/Ti materials.

σ_z Mid Surface (30/-30/90/90)s
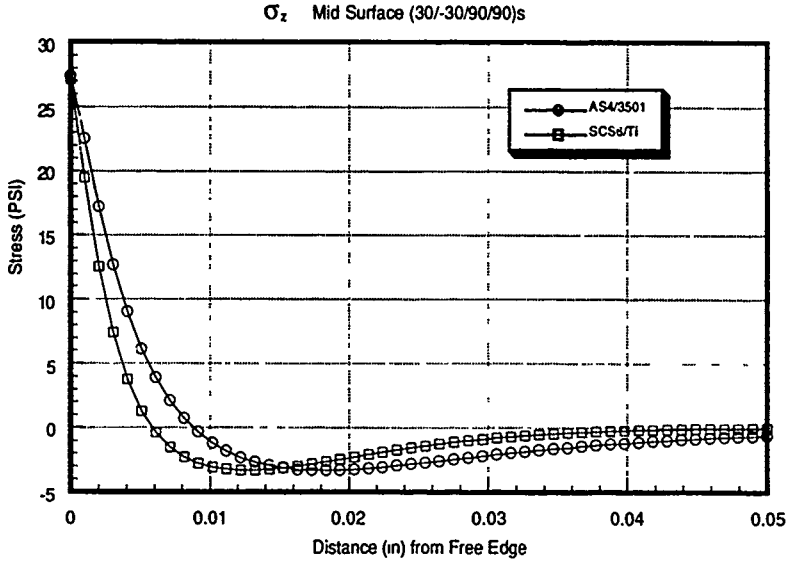
Figure 7: Comparison of σ_z at the midsurface of $(\pm30/90)_s$ laminate between AS4/3501 and SCS6/Ti materials.

σ_z Mid Surface (0/90/45/-45)s
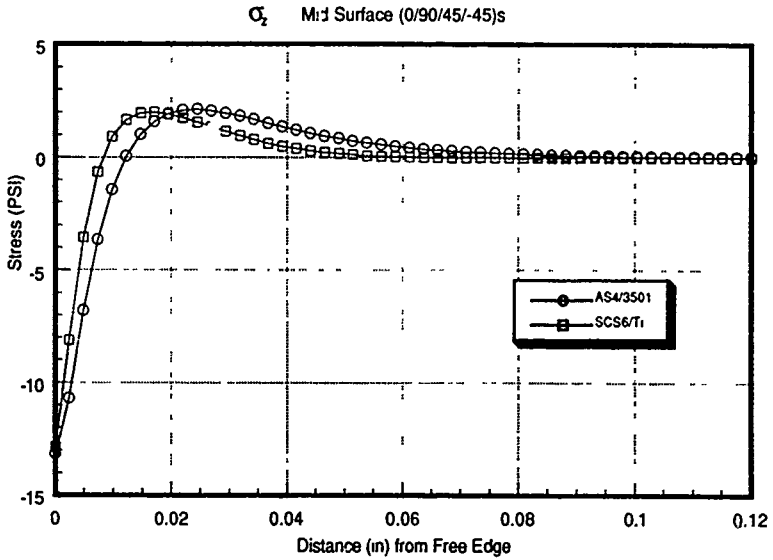
Figure 8: Comparison of σ_z at the midsurface of $(0/90/\pm45)_s$ laminate between AS4/3501 and SCS6/Ti materials.
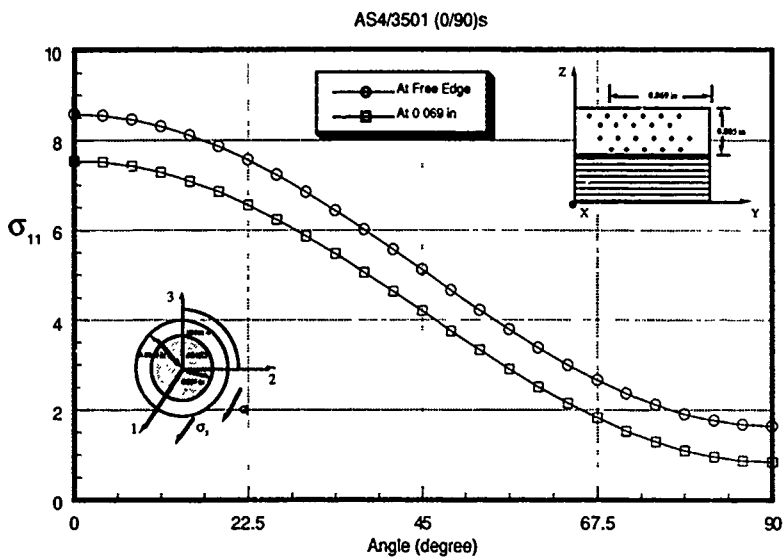
Figure 9: Comparison of micromechanics stress component σ_{11} at different circumferential locations of the representative volume element pertaining to the stresses active at the free edge and .069" away from the free edge.
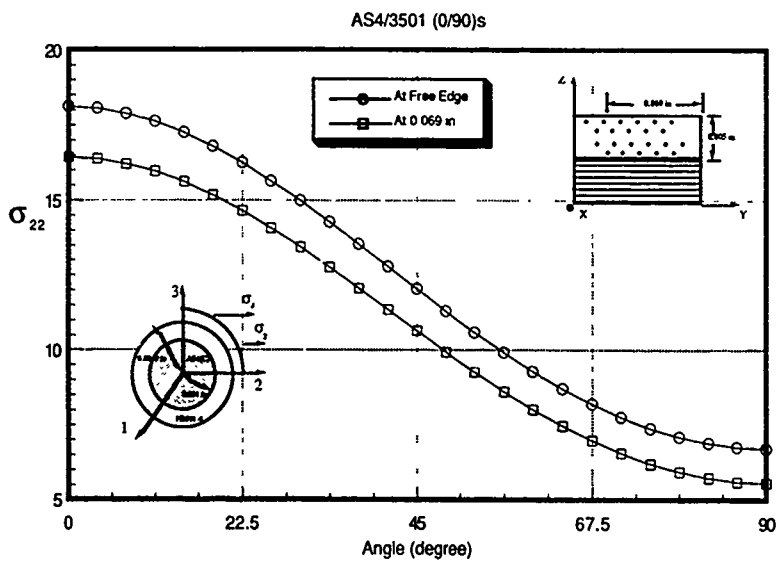
Figure 10: Micromechanics stress component σ_{22} at different circumferential locations of the representative volume element pertaining to the stresses active at the free edge and .069" away from the free edge.
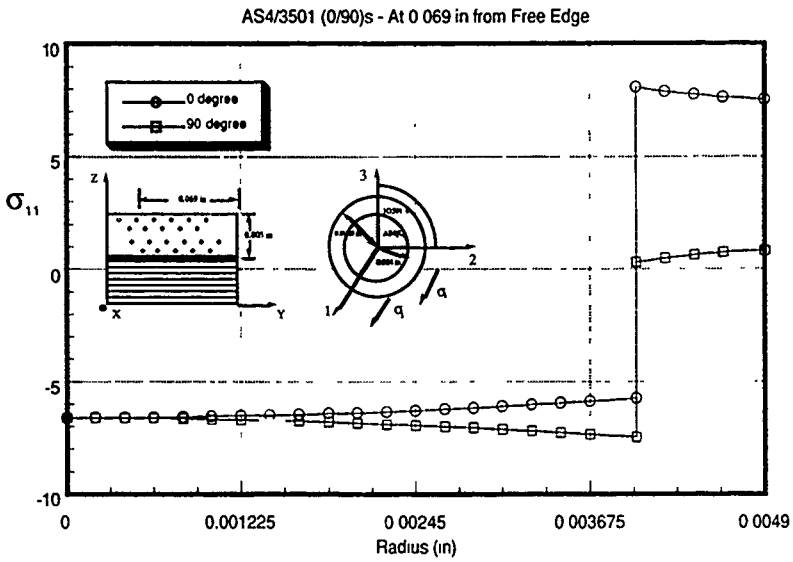
Figure 11: Micromechanics stress component σ_{11} at two values of circumferential parameter along radial direction at free edge.
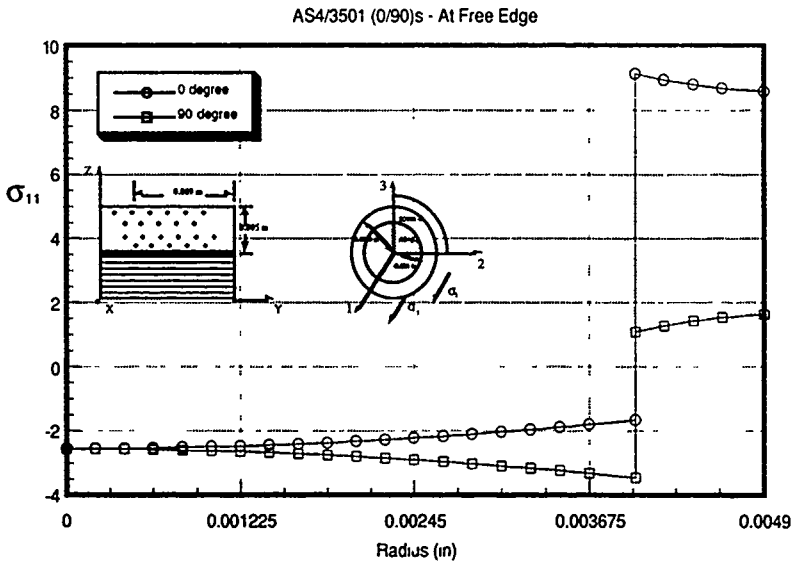
Figure 12. Micromechanics stress component σ_{11} at two values of circumferential parameter along radial direction at distance .069" away from the free edge.

AS4/3501 (0/90)s - At Free Edge
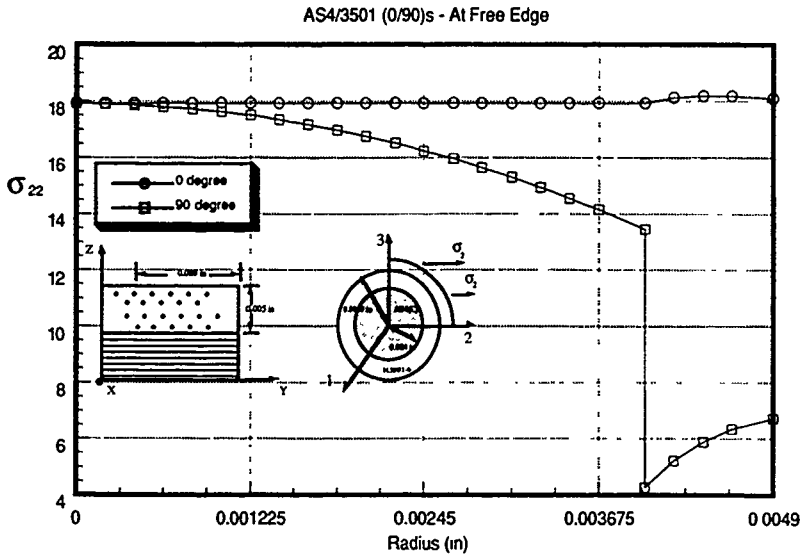
Figure 13.   Micromechanics stress component σ_{22} at two values of circumferential parameter along radial direction at free edge.

AS4/3501 (0/90)s - At 0 069 in
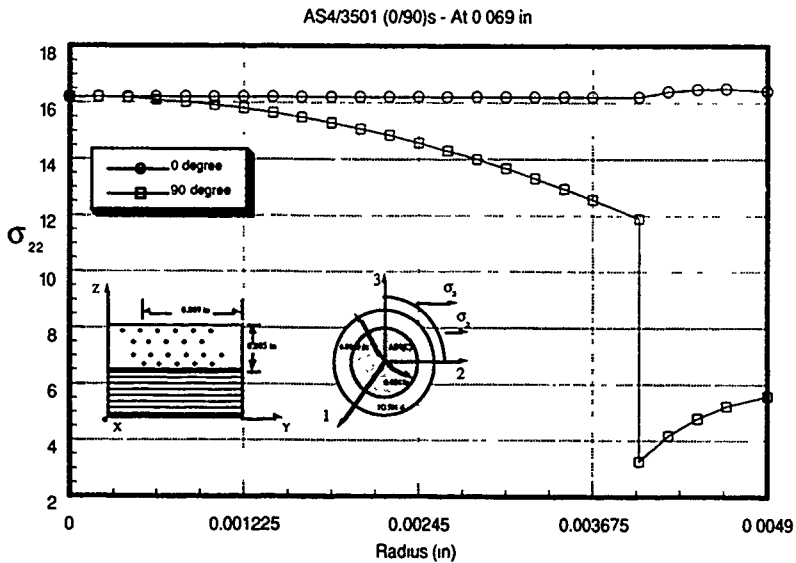
Figure 14:   Micromechanics stress component σ_{22} at two values of circumferential parameter along radial direction at distance .069" away from the free edge.

Delamination and Fatigue of Composite Materials: A Review

T. K. O'Brien
W. Elber
U.S. Army Aerostructures Directorate
Mail Stop 266
Langley Research Center
Hampton, Virginia 23665
USA

SUMMARY
Research exploring the role of delamination on the durability and damage tolerance of advanced composite materials is reviewed. Recent studies on the characterization of composite delamination are summarized. Recent analytical solutions for interlaminar stresses and strain energy release rates associated with common sources of delamination are also reviewed. The role of delamination in (1) low velocity impact, (2) residual compression strength, and (3) fatigue is highlighted. Delamination is shown to be the common damage mode observed in all of these problems. A Damage Threshold/Fail-safety concept for addressing composite damage tolerance is discussed

1. INTRODUCTION
As high strength, fiber reinforced polymer matrix composites are considered for highly strained primary aircraft structures, increased attention is being devoted to the understanding and characterization of composite delamination Delamination may result from low velocity impact, from eccentricities in structural load paths that induce out-of-plane loads, or from discontinuities in the structure that create local interlaminar stress singularities. The purpose of this review paper is to highlight some recent research studies on composite delamination. Work by the authors and others are highlighted along with some significant results in the literature.

2. DELAMINATION CHARACTERIZATION

2.1 Monotonic loading
Composite delamination is most commonly characterized using fracture mechanics test methods. Critical values of strain energy release rate are measured to quantify the interlaminar fracture toughness Because composite

delamination may arise as a result of a combination of interlaminar normal tensile stresses and interlaminar shear stresses, the delamination may be a mixture of the three classical fracture modes. These include an opening mode I, a sliding shear mode II, and a scissoring shear mode III.

The mode I interlaminar fracture toughness is typically measured using the Double Cantilever Beam (DCB) test [1] In the DCB test, delaminations start at the insert and grow in a stable manner along the beam. However, because the beams are unidirectional, the fiber nesting that is typically present results in fiber bridging across the delamination plane between the two beams as the delamination grows [2,3]. This fiber bridging causes the apparent toughness to increase with delamination length (fig 1) [4]. However, because fiber bridging is not present initially, the onset value of G_{Ic} measured from the insert may be representative of a naturally occurring delamination, assuming the insert is sufficiently thin (fig.2) [4].

The mode II interlaminar fracture toughness is typically measured using the End Notched Flexure (ENF) test. The ENF test involves loading a unidirectional beam, with a thin insert at the midplane of one end, in three point bending Delaminations start at the insert and grow in an unstable manner along the beam [5]. Therefore, only the onset of mode II delamination is measured. Recently, a stabilized version was proposed whereby the test is controlled to a constant shear displacement at the delamination front [6]. However, any value measured after the onset will have shear damage at the delamination front that may influence G_{IIc} measurements [7,8]

Presently, there are no commonly accepted test methods for measuring mode III scissoring delamination A Split Cantilever Beam (SCB) was proposed for this purpose [9], however, it was demonstrated to contain a significant mode II contribution [10] Delaminations that occur naturally are mixed-mode, resulting from both interlaminar tension and shear stresses To date, all the mixed-mode tests that have been prescribed are combinations of mode I and mode II [11-14] Recently, a Mixed-Mode Bending (MMB) test was developed that utilizes the same unidirectional beam tested in the DCB and ENF tests [13,14]. The MMB test provides toughness measurements over a wide ratio of mode I and mode II that may be used with the DCB and ENF measurements to develop mixed mode delamination failure criteria.

2.2 Cyclic Loading   The same tests that are commonly used to measure interlaminar fracture toughness have been used to characterize delamination in fatigue. Early work attempted to simulate crack growth laws by correlating the rate of delamination growth with cycles, da/dN, with the maximum cyclic strain energy release rate, G_{max}, or the cyclic range of G [15,16] However, retardation occurs in the DCB test due to the fiber bridging that develops once the delamination forms [17] Figure 3 shows da/dN data generated on unidirectional DCB AS4/PEEK specimens As the delamination grows, G_{max} decreases and fiber bridging develops. Hence, the generic value of the slope of the log-log plot, and the apparent threshold value, are questionable. Furthermore, even with fiber bridging present these power law curves are much steeper, i.e., they have much larger slopes on a log-log plot of da/dN versus G, than similar curves for most metals Hence, a very small error in estimated load, and hence G, will result in a large error in delamination growth rate. Therefore, the classical damage tolerance approach of tracking crack growth may not be practical for composite delamination.

Another approach to characterize delamination onset under cyclic loads using the DCB and ENF tests by plotting the maximum cyclic G as a function of cycles to delamination onset has been proposed [17] Figure 4 shows a plot of G_{Imax} as a function of the number of cycles to delamination onset. The curve fit to the data reaches an asymptote, or threshold G value, near 10^6 cycles

3. DELAMINATION ANALYSIS

Many solutions have been generated for the strain energy release rate, G, associated with delamination growth Typically, these G solutions are generated using a finite element analysis and the virtual crack closure technique (VCCT) [18] This technique yields mode I, mode II and mode III strain energy release rate components The total G is obtained by summing these three modal components, and may be verified using a global energy balance analysis

3.1 Edge Delamination Early solutions in the literature showed that the strain energy release rate for edge delamination was independent of delamination size and varied with the ply thickness and the square of the applied strain [19]. Finite element analyses showed that the individual fracture modes were also independent of delamination length [20] These edge delamination solutions have been extended to the case of a laminate with an open hole using the rotated straight edge technique [21] A higher order plate theory (HPT) technique for calculating the various modal components was later developed and tested by comparing to finite element (FEM) analyses of the numerous edge delamination cases that result from the rotated straight edge analogy for the open hole [22] Figure 5 shows the variation in G_I and G_{III} with angular position around the hole for a delamination in a particular interface Similar plots may be generated for each unique interface in the laminate. These G calculations may be used to identify the most likely location for delamination to appear around the hole boundary.

3.2 Delaminations from Matrix Ply Cracks Early studies contrasted the difference in edge delaminations with the more localized delaminations that form at the intersection of the matrix crack and the stress free edge [23] This localized delamination commonly occurs in fatigue, and is the primary reason that fatigue failures occur in tension [24] Recent 3D finite element models of delaminations originating at the intersection of matrix cracks with free edges have demonstrated that very large tensile interlaminar normal stresses may develop at these locations [25,26]. Also, G components have the greatest magnitude near the intersection of the matrix crack and the free edge (fig 6)

3.3 Ply Drops in Tapered Laminates   In many structural applications, composite laminates are tapered to reduce thickness This tapering is typically achieved by dropping internal plies These terminated plies create discontinuities that result in local stress singularities. Several investigators have studied the interlaminar stresses that develop in tapered laminates [27,28] Recently, a study was completed where the strain energy release rate associated with delamination growth from a discontinuity in a tapered laminate was developed [29]. As shown in fig.7, strain energy release rate solutions were generated for delaminations growing from the juncture between the thin and tapered regions. The analysis was performed using the virtual crack closure technique (VCCT) as well as an energy balance technique that yielded similar results.

3.4 Delamination from buckled sublaminates One source of composite delamination growth is the local instability that arises from the buckling of a delaminated region under compression loading. The most commonly analyzed problem consists of a laminate with a through-width delamination near one surface Both the load at which the sublaminate will buckle and the strain energy release rate, G, for further delamination growth have been calculated [30]. Several authors have extended this analysis to an embedded circular or elliptical delamination [31,32].   G solutions have been generated and used with G_{Ic} values to predict delamination growth. Figure 8 shows that the predicted strain for the onset of sublaminate buckling varies with the depth of the initial delamination, which locates the delaminated interface and determines the sublaminate that will buckle [31]

4. DELAMINATION IN LOW VELOCITY IMPACT

Composite laminates subjected to   w velocity impacts often experience extreme damage that may not be visible on the impacted surface. This damage may lead to significant reductions in the ability of the laminate to carry the desired compression load

4.1 Impact Damage   Several studies have been conducted to characterize the nature of impact damage in composite laminates [33-34]. Typically, the high transverse shear stresses induced during the impact create a conical pattern of matrix cracks in each layer that initiate local delaminations between the

layers. Recently. several researchers have developed a rationale called the "K" rule for anticipating the damage pattern based on the laminate layup and stacking sequence [35-36]. This rule allows the analyst to anticipate the kind of "spiral staircase" pattern of matrix cracks and delaminations that develop during a low velocity impact on a laminate with arbitrary layup. Figure 9 shows the pattern that develops through the thickness of a quasi-isotropic laminate [36].

Recently, a finite element analysis was performed for delamination in laminates initiating from impact induced matrix cracking [37]. A three point bending load was applied to a   cross-ply laminate containing matrix cracks that were oriented in the 45 degree direction through the thickness of the central 90 degree ply to simulate a matrix crack resulting from transverse shear loads (fig.10). The analysis indicated that large tensile interlaminar normal stresses were created at the tip of the matrix crack in the 0/90 interfaces (fig 11), and that a mode I component is present with subsequent delamination growth from the matrix cracks (fig.12). Hence, delaminations that form due to low velocity impacts do not result from interlaminar shear stresses alone.

4.2 Compression After Impact   A model for predicting the residual compression strength for quasi-isotropic laminates having impact damage simulated by the "K" rule has been developed [38,39]. Impact damage was simulated by a spiral array of transverse cracks and delaminations forming 4-ply thick circular sublaminates. The analysis steps to predict the effects of this damage included a model of sublaminate stability, an equivalent reduced stiffness calculation for the buckled damage zone, and a finite element analysis of stress redistribution that included finite width effects. Sublaminate properties affecting damage tolerance were found to be the reduced bending stiffness, sublaminate thickness, and diameter The critical material properties affecting damage tolerance included moduli and undamaged compression strength.

5. DELAMINATION IN FATIGUE

Delamination is commonly observed in fatigue. Composite laminates that do not delaminate before final failure under monotonic loads will often exhibit stable delamination formation and growth in fatigue.

5.1 Unnotched Laminates Delaminations typically form at straight edges in unnotched laminates due to the Poisson mismatch created by the particular layup or stacking sequence [19,20]. Furthermore, delaminations also form at the straight edge as a result of matrix cracking [23,26] Recently, a tension fatigue life prediction methodology was proposed based on predicting the accumulation of delaminations through the laminate thickness [24] Unnotched laminates subjected to compression fatigue also fail in this way [40] For stitched laminates, the rate of delamination growth appears to be retarded [41] However, the ultimate compression failure also results from an accumulation of delaminations through the laminate thickness.

5.2 Tapered Laminates Finite element models of delamination in tapered laminates showed that the initial delamination growing from the juncture between the thin and tapered region consisted primarily of an opening (mode I) component [29]. Calculated G values have been compared to cyclic DCB data to predict the cycles to delamination onset in unidirectional and multi-ply tapered laminates [42,43].

5.3 Notched Laminates Open hole fatigue data is often used to compare one damage tolerance concept to another. For example, fig 13a shows the open hole compression (OHC) fatigue S-N data for a stitched AS4/3501-6 laminate and an unstitched IM7/8551-7 tape laminate, both containing a 1/4 inch diameter hole [44]. Both materials exhibit similar fatigue behavior, with the degradation in compression strength with cycles resulting from the formation, growth, and accumulation through the thickness of delaminations that begin either at the straight edge, or at the hole boundary.

Figure 13b shows fatigue results for the same two types of laminates that were first subjected to low velocity impacts Although the compression failure strain after impact (CAI) is 0 6%, or greater, for the toughened matrix and stitched composites, their fatigue strength continuously decreases, just as was observed for the open hole laminate. However, brittle matrix composites, like the unstitched AS4/3501-6 laminates, tend to have relatively flat S-N curves following low velocity impacts [45] The difference in the shape of the S-N curves following low velocity impact may be attributed to the type and severity of loading required to create the same accumulation of delaminations through the laminate thickness

For brittle matrix composites, delaminations form in nearly every interface during the impact Hence further cyclic loading creates little new damage. However, in the toughened matrix and stitched composites, only a few interfaces are delaminated during the impact However, subsequent cyclic loading will cause delaminations to form at the matrix cracks created by the impact, at the intersection of angle plies and free edges, or at the stitches, until nearly all the interfaces are delaminated. When the damage becomes extensive through the thickness, after 10^6 cycles or greater, the compression strengths become similar to those measured for the brittle matrix composites subjected to impact alone (fig 13b).

6. DAMAGE THRESHOLD/ FAIL-SAFETY CONCEPT

A Damage Threshold/Fail Safety philosophy has been proposed for ensuring that composite structures are both sufficiently durable for economy of operation, and adequately damage tolerant for safety of flight [46]. In this approach, matrix cracks are assumed to exist throughout the off-axis plies. Delamination onset is predicted using a strain energy release rate analysis Delamination growth is accounted for in one of three ways: either analytically, using delamination growth laws in conjunction with strain energy release rate analyses; experimentally, using measured stiffness loss; or conservatively, assuming catastrophic delamination growth. Fail safety is assessed by accounting for the accumulation of delaminations through the thickness. This concept was demonstrated for predicting tension fatigue life. Furthermore, techniques were also outlined for compression fatigue, tension/compression fatigue, and compression strength following low velocity impact.

7. SUMMARY

Research on delamination, durability and damage tolerance of composite materials was reviewed. Delamination characterization studies were summarized. Recent analytical solutions for interlaminar stresses and strain energy release rates associated with common sources of delamination were also reviewed. The role of delamination in low velocity impact, in residual compression strength, and in fatigue were highlighted. Delamination was shown to be the common damage mode observed in all of these problems A Damage

Threshold/Fail-safety concept for addressing composite damage tolerance was summarized.

6. REFERENCES

1   Whitney,J.M , et al , J. Rein. Plas. and Composites, 1. 1982, p 297.
2. deCharentenay,F.X , et al , ASTM STP 836, 1984, p.84 .
3   Johnson, W.S., and Mangalgiri,P.D., J Comp. Tech. and Res., 9.(1), 1987, p.3
4   Martin,R.H., 3rd ASC Conference on Composite Materials, Seattle, Proceedings, Sept.,1988, p 688.
5   Russell,A J., DREP Materials Report 82-O, Dec.,1982.
6. Kageyama,K., ASTM STP 1110, 1991, p.210.
7. Corleto,C.R., and Bradley,W.L., ASTM STP 972, 1988, p.201.
8. O'Brien,T.K., et al., ASTM STP 1012, 1989, p.222.
9. Donaldson,S.L., Composites Sci. and Tech., 32, (3), 1988, p 91.
10. Martin,R H., ASTM STP 1110, 1991, p.243.
11. Hashemi,S., et al , ASTM STP 1110, 1991, p.143.
12. O'Brien,T K., et al., ASTM STP 937, 1987, p 199.
13. Reeder,J R., and Crews,J H ,Jr., 30th AIAA Structures, Dynamics, and Materials Conference, Mobile, Proceedings, 1989, p.1640.
14 Reeder,J R , and Crews,J.H.,Jr , ICCM VIII, Honolulu, Proceedings, 1991, Paper No 36-B
15 Bathias,C., and Laksimi,A., ASTM STP 876, 1985, p 217.
16 Gustafson,C G , and Hojo,M., J. Rein. Plas and Comp., 6, (1), 1987, p.36
17 Martin,R.H., and Murri,G.B , ASTM STP 1059, 1990, p 251.
18. Rybicki,E F , and Kanninen,M.F., Eng. Frac. Mech , 9, (4), 1977, p 931.
19 O'Brien,T K , ASTM STP 775,1982, p.140.
20 O'Brien,T K , ASTM STP 836,1984, p.125.
21. O'Brien,T.K., and Raju,I.S , 25th AIAA Structures, Dynamics, and Materials Conference, Palm Springs, Proceedings, May,1984.
22. Armanios,E.A , et al , J. Comp. Tech. and Res. 11, (4), 1989, p.147.
23. O'Brien,T.K., ASTM STP 876,1985, p.242.
24 O'Brien,T K., et al., Int. J. of Fatigue, 11, (6), 1989, p 379.
25. Fish,J C., and O'Brien,T.K., ASTM STP 1120, 1992, p 348.
26. Salpekar,S A , and O'Brien,T.K., ASTM STP 1110, 1991, p 287.
27. Ochoa,O.O , and Chan,W.S , 3rd ASC Conference on Composite Materials, Seattle, Proceedings, Sept. 1988, p 633.
28 Kemp,B.L , and Johnson,E.R., 26th AIAA SDM Conference, Orlando, Proceedings,1985, p.13.
29. Salpekar,S.A., et al., 3rd ASC Conference on Composite Materials. Seattle, Proceedings, Sept.,1988, p 642.
30. Chai,H., et.al , Int. J. Solids and Structures, 17, (11), p 1069.
31. Flanagan,G., ASTM STP 972, 1988, p.180.
32. Whitcomb,J.D , ASTM STP 1059, 1990, p 215.
33 Byers,B.A., NASA CR 159293, August,1980.
34. Starnes,J.H., et.al , ASTM STP 696, 1979, p.145.
35. Gosse,J.H., et al., 20th Int. SAMPE Technical Conference, Proceedings, Sept.,1988.
36. Gosse,J H , and Mori,P.B Y., 3rd ASC Conference on Composite Materials, Seattle, Proceedings, Sept.,1988, p.344.
37. Salpekar, S.A., NASA CR 187594, Nov. 1991
38 Dost,E F., et al , 3rd ASC Conference on Composite Materials, Seattle, Proceedings, Sept.,1988, p 363
39. Dost,E.F , et al., ASTM STP 1110, 1991, p 476.
40 Harris,C E., and Morris,D H., ASTM STP 864, 1985, p.153.
41. Lubowinski,S J , and Poe,C.C., FIBER-TEX 87 Conference, Greenville, SC, Proceedings, Nov ,1987.
42. Murri,G.B , et al , ASTM STP 1110, 1991, p.312
43. Murri,G.B., et al., NASA TM 102628, April,1990.
44. Portanova,M., Whitcomb,J.D., and Poe, C.C , ASTM STP 1120, 1992, p.37.
45. Demuts,E., et.al , Composite Structures, 4, 1985, p. 45.
46. O'Brien,T K , ASTM STP 1059, 1990, p.7.
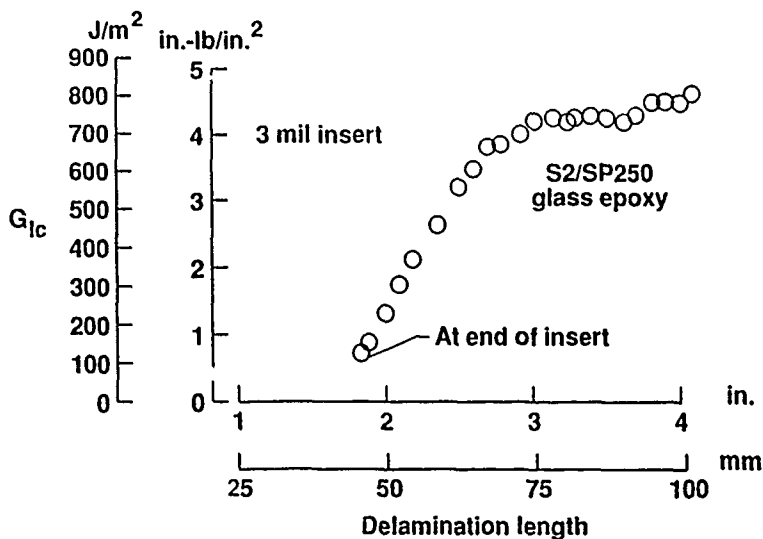
Fig. 1. Increase in G_{Ic} with delamination length due to fiber bridging in a DCB test [4].
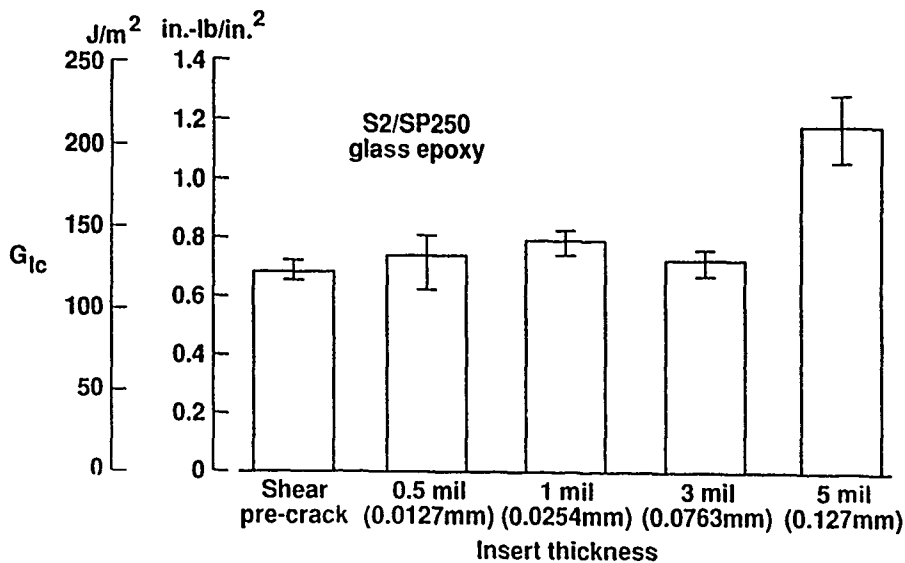
Fig 2. Effect of insert thickness on G_{Ic} [4]
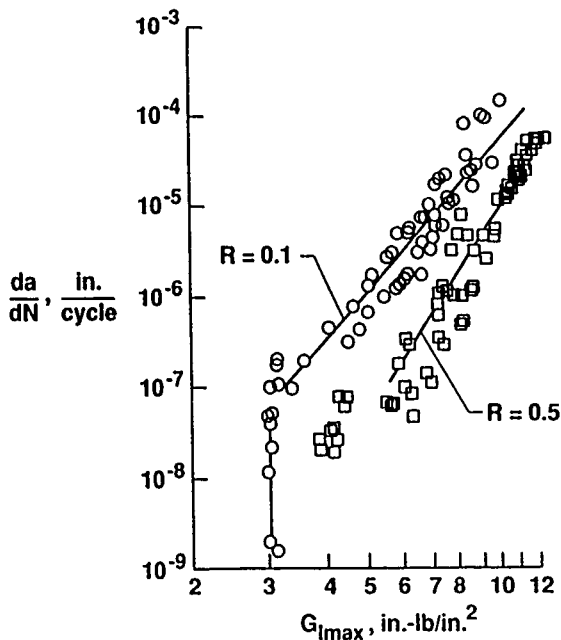
Fig. 3. Mode I fatigue delamination growth rates [17].
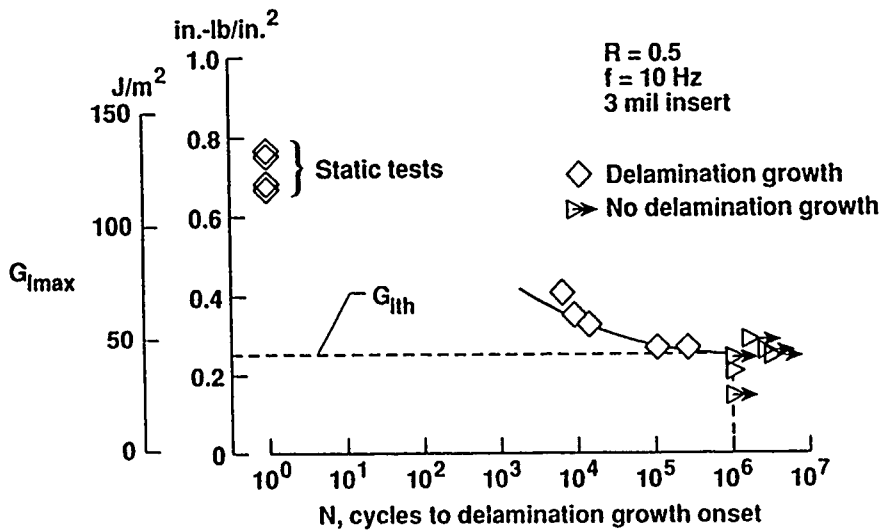
Fig. 4. G_{Imax} as a function of cycles to delamination onset [17]
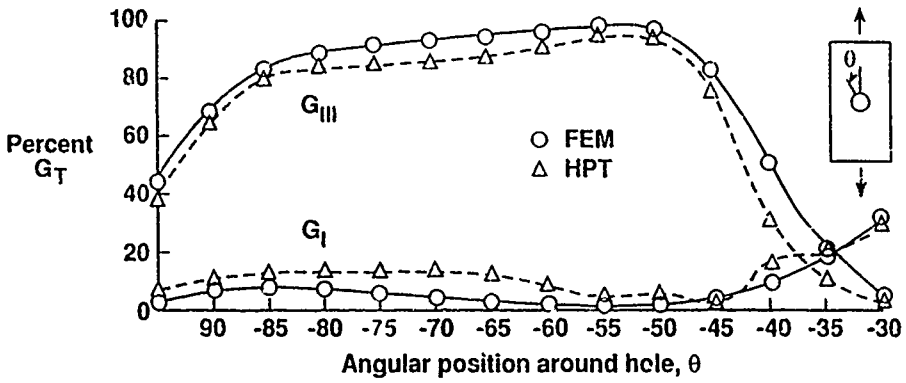
Fig. 5. Comparison of finite element (FEM) and Higher-order Plate Theory (HPT) analyses of G components for delamination at an open hole boundary [22].
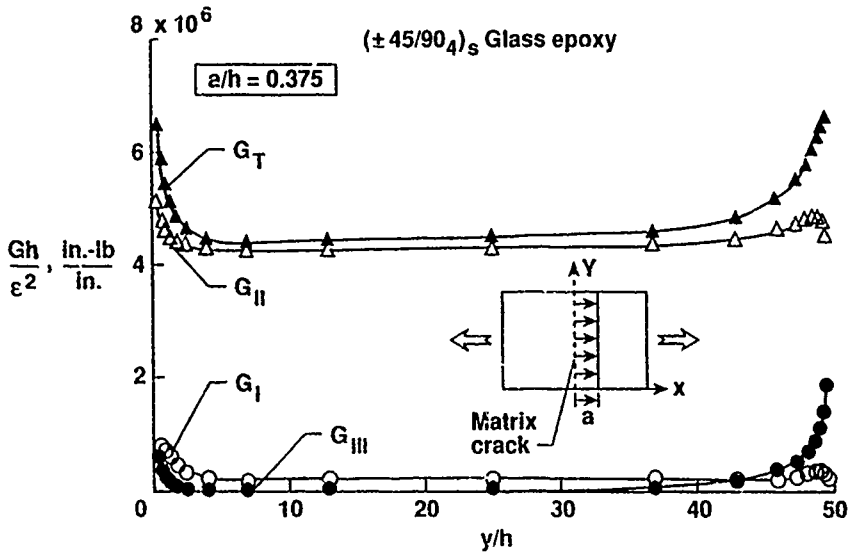
Fig. 6. Variation of normalized G and G components along a uniform delamination front originating at a 90 degree matrix ply crack (h = ply thickness) [26]
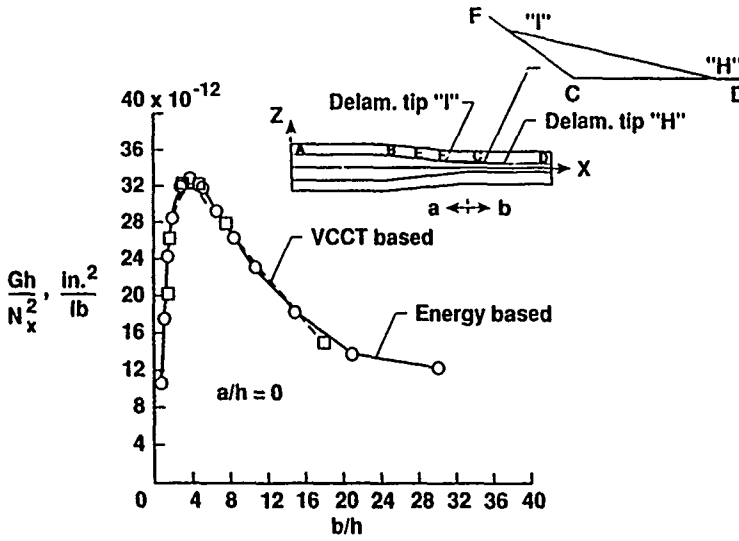
Fig 7. Normalized strain energy release rate for delamination originating in a tapered laminate (h = ply thickness) [29].
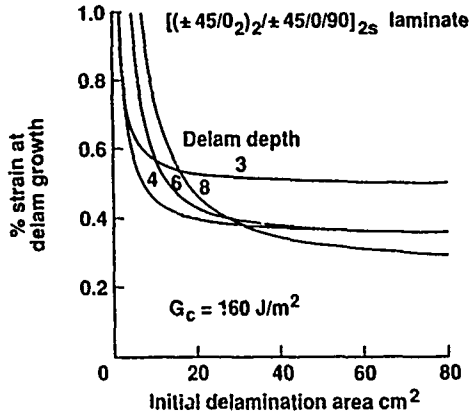
Fig 8 Predicted delamination onset strains as c function of initial delamination area for different delaminations (indicated by ply number from the top surface) in a compression loaded laminate [31]
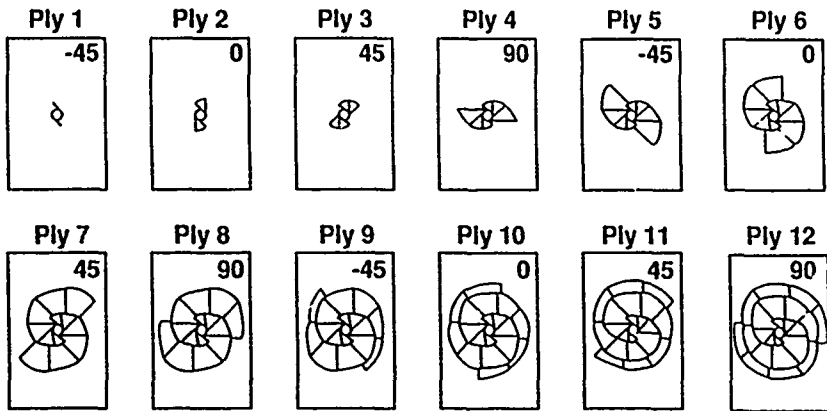
Fig. 9. Schematic of impact damage accumulation through the thickness of a (-45/0/45/90)$_{3s}$ laminate [36].
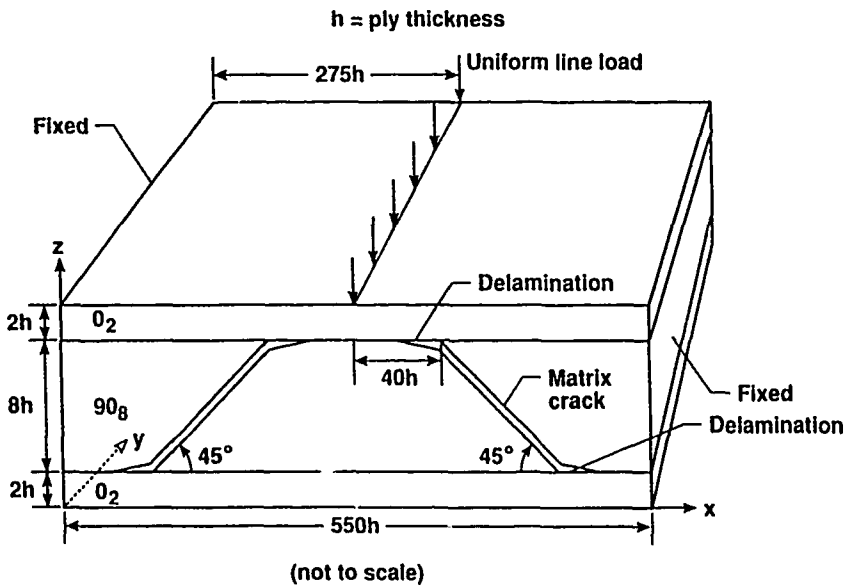
Fig. 10. Configuration and loading of a laminate containing impact induced induced matrix cracks [37]
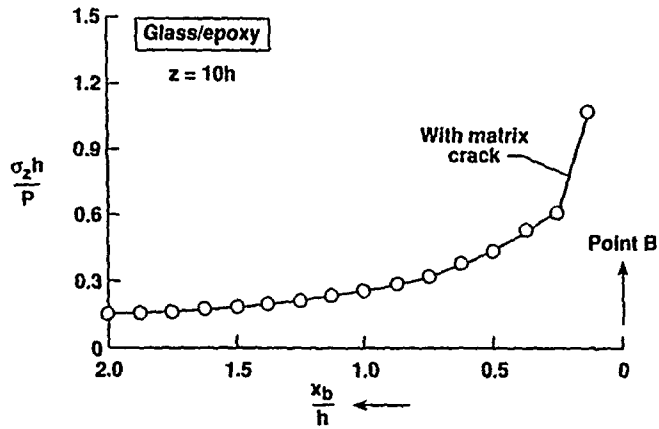
Fig. 11. Interlaminar normal stress with a 45° matrix crack [37].
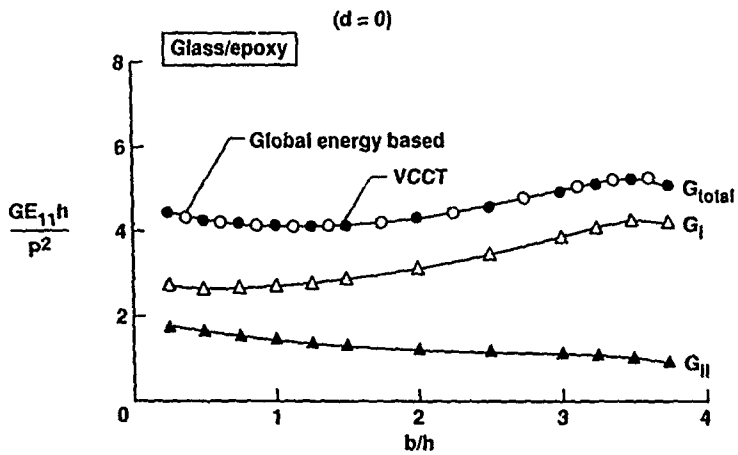
Fig. 12. Variation of G due to delamination growth from matrix crack [37].
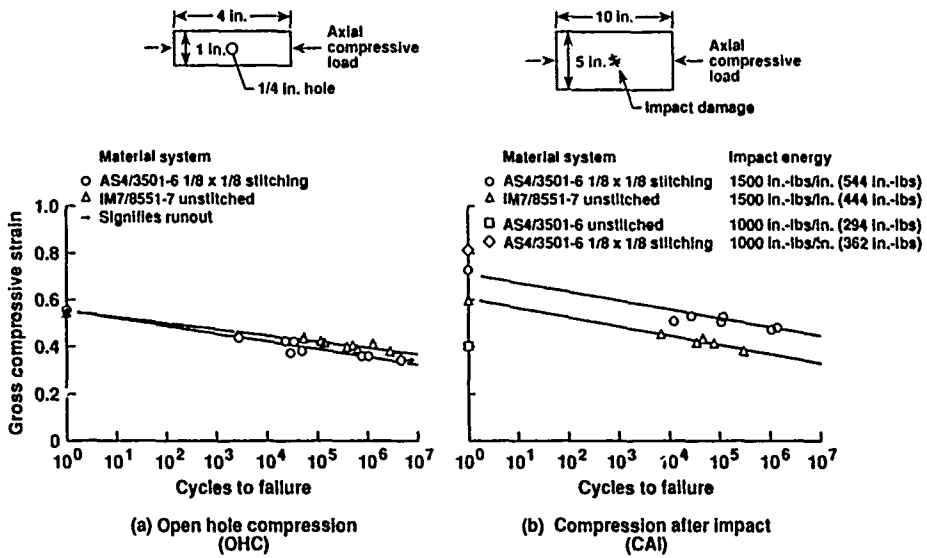
Fig. 13. Open hole compression and compression after impact as a function of fatigue cycles to failure in stitched and unstitched graphite epoxy coupons [44].

INITIATION AND PREVENTION OF EDGE DELAMINATION
WITH AND WITHOUT RESIDUAL STRESSES

R. S. Sandhu, G. P. Sendeckyj, G. A. Schoeppner and J. E. Pappas
Structures Division, Flight Dynamics Directorate, Wright Laboratory,
Wright-Patterson Air Force Base, Ohio 45433, USA

SUMMARY

The total delamination moment (DM) is shown to be a quantitative criterion for predicting delamination initiation in composite laminates near free edges. To determine the initiation of delamination near free edges, DM of the laminate is compared to the critical delamination moment obtained experimentally. Specially designed specimens incorporating variable radius geometries are used to determine the critical DM. The analytical technique coupled with the experimental data is used to minimize the tendency of the laminates to delaminate without increasing the designed thickness of the laminates. In addition, residual curing stresses are included in the analytical technique to determine their effect on the initiation of edge delamination.

1. INTRODUCTION

Composite laminates have a tendency to delaminate near free edges when subjected to in-plane loads. The tendency to delaminate and the resulting free edge stresses have been studied extensively using analytical and numerical techniques. These studies have provided insight into the nature of the stresses and the influencing factors. However, efforts [Ref. 1 thru 19] to experimentally determine the onset of edge delamination have met with varying degrees of success. Reference 18 provides an excellent review of various methods for real time delamination detection. These methods fall into five categories, namely, (a) quasi-static loading with inspection, (b) visual observation, (c) acoustic emission monitoring, (d) ultrasonic transmission scans, and (e) stiffness changes in laminates. Of all the reviewed techniques, the use of the in-situ ultrasonic transmission scan [Ref. 18,19] provides the most accurate assessment of the onset of edge delamination. However, the results could be improved if a shorter specimen were interrogated.

The standard approach for predicting the onset of delamination is to estimate the interlaminar tensile stress, σ_z, near the free edge and to assume that delamination occurs when this σ_z reaches a critical value. These computations are performed either by the finite element method or by various approximate techniques. The approximate techniques sometimes lead to erroneous results. For example, a study conducted to determine interlaminar normal stresses at delamination initiation in $(\pm 40^\circ_n/90^\circ)_s$ laminates indicated that both the interlaminar normal stresses calculated by the F.E. method and the delamination tendency quantified by delamination moment coefficient, DMC_σ, of the laminates increased with increasing number of $\pm 40^\circ$ plies. However, the use of an approximate method (Ref. 1, eq. 7) yielded interlaminar normal stresses that decreased with increasing number of $\pm 40^\circ$ plies (Fig. 1). In addition, these approaches are too tedious for use in a laminate stacking sequence optimization procedure for selecting laminates with a minimum tendency to delaminate. In previous work (Ref. 13 and 17), we suggested a much simpler approach based on the delamination moment concept for selecting stacking sequences minimizing the tendency for delamination. The total delamination moments can be easily calculated for all possible stacking sequences for a laminate with a given number of plies and used as a delamination initiation criterion. The total delamination moment is given by

$$DM = DMC_\sigma \, \sigma_0 + DMC_T \, \Delta T \qquad (1)$$

where DMC_T, ΔT, DMC_σ and σ_0 are the delamination moment contribution due to one degree change in temperature, the temperature change from the stress-free temperature to the test temperature, the stress-based delamination moment coefficient, and the axial stress at delamination onset, respectively. Both DMC_T and DMD_σ depend on the stacking sequence in a simple manner. Since DM is expected to be constant at delamination onset, the stress for delamination initiation can be easily calculated provided that ΔT is known.

The present research was performed to further investigate the use of the total delamination moment as a delamination criterion. The research consisted of analytical and experimental studies. In the experimental part of the study reported herein, we designed the specimen to have a reduced width in the central region so that delamination occurs in the area of reduced width. This specimen design was used to determine experimentally the onset of delamination. In addition, the effect of residual thermal stresses on the initiation of edge delamination in specimens was examined.

2. SPECIMEN DESIGN STUDY

The candidate specimen with bonded fiber glass tabs is shown in Fig 2. The specimen is 22.86 cm (9.0 inch) long and 3.81 cm (1.5 inch) wide except for a middle straight segment of 1.02 cm (0.4 inch) where the width is reduced to 2.54 cm (1.0 inch). The width reduction occurs over 2.54 cm (1.0 inch) fillet segments on both sides of the central straight segment. The usual method of reducing the width of the specimens is by using circular fillets. This method has a serious shortcoming, i e , at points where the straight edges are tangent to the circular arcs, there is a mismatch of the radii of curvature resulting in regions of high stress concentration. To resolve the problem, we tried the following two simple transition curves with variable radii

$$Y = K \, X^3 \qquad (2)$$
$$Y = K \, X^4 \qquad (3)$$

subject to the conditions Y=0 for X=0 and Y=0 635 cm (0 25 inch) for X=2.54 cm (1.0 inch). The radii of curvature for both curves are infinite at the points where they intersect the straight segments. A two-part feasibility study consisting of analytical and experimental efforts was conducted to finalize the design of the specimen.

For the analytical investigation, a two-dimensional linear finite element program developed at the Wright Laboratory was used. Based on the results of Ref. 13 and 17, the $(\pm 40_2/90)_s$ stacking sequence, which has a very high tendency to delaminate, was selected for this study. Since specimens have two axes of symmetry, one quarter of the specimen was modelled. Finite element models A, B and C (shown in Fig. 3) corresponding to specimens with (a) a circular fillet of radius equal to 5.4 cm (2 125 inch), (b) a variable radius fillet using Eq. 2, and (c) a variable radius fillet using Eq. 3, respectively, were generated. Each model had 918 nodes and 2544 elements with X and Y axes being directed along the length and width of the specimens, respectively. A uniform extensional displacement equal to 0.1524 mm (0 006 inches) was applied at the narrow end of the models (Fig 3). To compute stresses and strains in the specimens, the following material elastic constants were assumed.

$$E_{11} = 132.80 \text{ GPa (19.26 Msi)}$$
$$E_{22} = 9.10 \text{ GPa (1.32 Msi)}$$
$$G_{12} = 5.72 \text{ GPa (0 83 Msi)}$$
$$v_{12} = 0.35$$

Axial and transverse strains obtained from the finite element analysis were used to plot strain contours for the boxed portions (Fig 3) of the three models. The contour plots shown in Figure 4 and the plot of axial strains in elements near the edges of the specimens (Fig 5) indicate that a considerable improvement in the axial strain distribution in the test section resulted from the use of fillets with variable radii. To select the appropriate curve (Eq 2 or Eq. 3), a small experimental investigation was conducted

An AS4/3501-6 graphite/epoxy panel with a $(\pm 40_2/90)_s$ stacking sequence was fabricated Using a programmable water jet cutting system, the panel was cut into two sets of five specimens each with the two variable radius transition curves. The geometry of these specimens is shown in Figure 2. The specimens were strain gaged using eight CEA-03-125UW-350 gages as shown in Figure 6(a). The strain gages were bonded with their longitudinal axes transverse to the specimen axes to record transverse strains. The specimens were tested at ambient conditions in an Instron Test Machine, Floor Model TT-1115. They were loaded at a crosshead speed of 1.27 mm (0.05 inch) per minute. Data obtained consisted of axial stress and transverse strains for all specimens

On the basis of this feasibility study, it was determined that (a) edge delamination occurred in the reduced cross-sections of the specimens, (b) delamination initiation was indicated by a sudden increase in the transverse strains observed in the axial stress vs transverse strain plots, and (c) there was no marked difference between the two sets of specimens using the two variable radius cross-section transition curves Since the data was inconclusive, the transition curve corresponding to Eq.2 was selected for the rest of the studies

To determine whether the uniformity of the strain state observed in $(\pm 40_2/90)_s$ laminates is valid for angles other than 40°, finite element analyses were conducted. In these analyses model B, with the angles varying between 10 to 35°, was used. Axial strains in elements near the edges of the specimens were determined and plotted (Fig.7). The plot indicates a decrease in the uniformity of the strain state for decreasing angle α, while the location of maximum strain tends to move closer to the test section with decreasing angle α.

3. DELAMINATION INITIATION STUDY

It was shown in Ref 13 and 17 that the delamination moment coefficient (DMC) was a valid quantitative measure of the delamination tendency of laminates. Within the scope of the investigation in the references, only delamination tendencies of different laminates were compared. However, to determine when a particular laminate would delaminate, a critical value of DM, defined as the DM below which the laminate would not delaminate, must to be determined This critical DM (DM_{cr}) is expected to depend upon properties of the material system used in fabricating the laminates, but not on the stacking sequence.

In the feasibility studies, $(\pm 40_2/90)_s$ laminates were found to delaminate. Using the assumed elastic properties, the corresponding DMC of these laminates is 183 49 x 10^{-5} cm^3 (11.197×10^{-5} inch^3) For the same elastic properties, DMCs for $(\pm \alpha_2/90)_s$ laminates were determined for $\alpha = 10^\circ$ to 35° A plot of these DMCs is shown in Figure 8. It can be observed from the plot that DMC decreases to 19.632x10^{-5} cm^3 (1.198×10^{-5} inch^3) with decreasing angle α. This

observation suggests the possibility of determining the critical DM by testing $(\pm \alpha_2/90)_s$ specimens. To verify the observation, the following program was performed.

3.1 Fabrication of Panels

Using the manufacturer's recommended cure cycle, eleven AS4/3501-6 graphite/epoxy panels were fabricated in the Composites Facility of the Wright Laboratory The stacking sequences and sizes of the panels are given in Table 1. All panels were c-scanned and found to be free of defects before being trimmed and cut into specimens

3.2 Basic Mechanical Properties

To determine 0° and 90° tension and compression response under simple loading, the required specimens were cut from panel A. The geometry of the 0° and 90° tension specimens and 0° and 90° Sendeckyj-Rolfes compression specimens (Ref. 20 and 21) are shown in Figure 9(a) and 9(b), respectively. For determination of shear properties, specimens with geometry shown in Figure 9(a) were cut from panel B Each of the specimens had two CEA-03-062UR-350 strain gage rosettes bonded, back to back, in their central midsection. To determine compressive properties, the Rolfes fixture (Ref.20) was used The tensile and compression specimens were tested at a crosshead speed of 1.27 mm (0.05 inch) per minute. The data from these tests are summarized in Table 2.

3.3 Thermal Properties

The influence of stresses in laminates induced by means other than mechanical loading have been extensively investigated (Ref. 22 thru 54) However, in this study only the effect of curing stresses on initiation of edge delamination is considered For this purpose, two thermal properties, namely, (a) linear coefficients of thermal expansion along the fiber direction (α_0) and the transverse direction (α_{90}) and (b) the temperature corresponding to the stress free state are required.

3.3.1 *Coefficients of Linear Thermal Expansion* (α_0 and α_{90})

To determine coefficients of linear thermal expansion, ten specimens (TM1) of size 6 35mm (0 25 inch) x 6 35mm (0 25 inch) and ten specimens (TM2) with the dimensions given in Figure 9(c) were cut from panel A (Table 1). Three techniques were used to obtain the required coefficients.

Specimens TM1 were tested at the Materials Directorate of Wright Laboratory using a TMA 800 operated in accordance with ASTM Standard D696-79. The specimens were heated at a rate of 2.0 °C (3.6°F) per minute from room temperature to 100°C (212°F) and the coefficients of linear thermal expansion were determined The average values of five tests each for α_0 and α_{90} are included and designated ASTM in Table 2.

Five TM2 specimens were tested at the Flight Dynamics Directorate of Wright Laboratory using the procedures of References 55 and 56 One strain gage rosette CEA-03-250UR-350 and two thermocouples ETG-50B/W were bonded to each of the specimens as shown in Figure 9(c). Each of the five specimens was placed on a rack fabricated at the Composites Facility of Wright Laboratory This rack had small diameter rods supported at their ends by instrument ball bearings as shown in Figure 10 This arrangement not only provided nearly frictionless support to the specimen but also exposed the underside of the specimen for transfer of heat. The specimens were placed in a small oven and heated. The output data from the strain gage rosettes and the thermocouples were recorded. When a maximum temperature of about 100°C (212°F) was reached, the

specimens were gradually cooled and data obtained. A composite plot of strain data, parallel and transverse to the fiber direction, versus temperature for the five specimens is shown in Figure 11. The apparent coefficients α^a_0 and α^a_{90} of linear thermal expansion obtained from Figure 11 are -7.3773 μm/m/^{o}C (-4.0985 μin/in/^{o}F) and 27.481 μm/m/^{o}C (15.267 μin/in/^{o}F), respectively. Using the self temperature compensation (STC) number of 5.4 μm/m/^{o}C (3.0 μin/in/^{o}F) of the strain gage rosettes, the coefficients of linear thermal expansion α_0 and α_{90} are given by

$$\alpha_0 = \alpha^a_0 + \text{STC Number} \quad (4)$$

$$\alpha_{90} = \alpha^a_{90} + \text{STC Number} \quad (5)$$

The average values of α_0 and α_{90} are included in Table 2 and designated as Tuttle.

Five TM2 specimens were tested by the North Carolina Agricultural & Technical State University using the procedure described in Reference 57. The values of α_0 and α_{90} are included in Table 2 and designated NCA&TU.

There is good agreement between the values of α_0 and α_{90} obtained by NCA&TU and the Flight Dynamics Directorate of Wright Laboratory. However, both differ considerably from the values of α_0 and α_{90} generated by the Materials Directorate of Wright Laboratory. The difference is due to the techniques used to determine α_0 and α_{90}. In tests conducted at the Materials Directorate, the coefficients of linear thermal expansion, α_0 and α_{90}, correspond to the initial slope of the strain vs temperature curves whereas in the other two methods the values of α_0 and α_{90} represent the average over the temperature range used in the tests.

3.3.2 Stress Free Temperature

To determine the temperature that corresponds to the stress-free state of the laminates, each of two unsymmetric panels C2 (0/90) and C4 (0$_2$/90$_2$) were cut into 2.54 cm (1.0 inch) wide and 27.94 cm (11.0 inch) long specimens. Radii of curvature, R, of each of two sets of five specimens were measured. The average radii values of the (0/90) and (0$_2$/90$_2$) curved specimens were 16.335 cm (6.341 inch) and 43.49 cm (17.122 inch), respectively. Using Timoshenko's analysis of bimetal thermostats (Ref 58), the temperature difference, ΔT, to produce the measured radius of curvature is given by

$$\Delta T = (h/R)(B/A) \quad (6)$$

where

h = thickness of the specimen
R = radius of curvature
A = 24.0 ($\alpha_0 - \alpha_{90}$)
B = 14.0 + $E^t_1/E^t_2 + E^t_2/E^t_1$

E^t_1 = tensile Young's modulus in fiber direction
E^t_2 = tensile Young's modulus transverse to fiber direction
Using the elastic constants from Table 2, we get

$$\Delta T = 54.4^oC (98.0^oF) \quad \text{for (0/90) specimen}$$

and

$$\Delta T = 40.3^oC (72.6^oF) \quad \text{for (0}_2\text{/90}_2\text{) specimen}$$

The two values of ΔT differ substantially and are much lower than expected. This discrepancy can be attributed to the assumptions made in the derivation of Eq 6, namely, small displacements and temperature independent elastic properties. As pointed out by Naim and Zoller (Ref. 45), one must use temperature dependent moduli to obtain results that are more accurate. Since the required data are not available for AS4/3501-6 graphite-epoxy, we measured the stress-free temperature experimentally.

To determine ΔT experimentally, one J-type thermocouple was bonded to each of the specimens of the two sets. Each specimen was placed in a fixture fabricated at the Composites Facility of Wright Laboratory. The fixture and specimen (without a thermocouple) are shown in Figure 12. The specimen was gripped between the movable and fixed center pins and supported on two semi-circular rods attached to a metal block. The whole assembly was placed in an oven. An additional thermocouple was placed in the oven to measure the temperature of the air surrounding the assembly. The assembly was heated and temperatures of the air and specimen were recorded at 15-minute intervals until the two outer segments of the specimen came to rest against the outer fixed pins indicating that the specimen had completely straightened. The measured values of ΔT relative to the room temperature of 26.7^{o}C (80°F) were 127.8^{o}C (230°F) and 97.8^{o}C (176°F) for (0/90) and (0$_2$/90$_2$) specimens, respectively. The measured values of ΔT are much closer to expected values. Nevertheless, there still is a large discrepancy between the ΔT values for the two unsymmetric laminates.

The discrepancy observed between values of ΔT for (0/90) and (0$_2$/90$_2$) specimens may be due to cross curvature. To evaluate the cross curvature effect, (0/90) and (0$_2$/90$_2$) specimens were modeled using QUAD4 finite elements. The finite element models were 12.7 cm (5.0 inch) long and 2.54 cm (1.0 inch) wide. They were assume clamped at one of the shorter sides and free at the other sides. No mechanical load was applied. They were subjected to a temperature change of 127.8^{o}C (230°F). The elastic constants and coefficients of thermal expansion were assumed to be temperature independent. Displacements, stresses and strains for the two specimens were obtained using Cosmic NASTRAN. Computed out-of-plane displacement contours are shown in Figure 13. As can be seen from the figure, the cross curvature is more pronounced in the (0/90) specimens than in the (0$_2$/90$_2$) specimens. This implies that ΔT for the (0/90) specimens should be lower than for the (0$_2$/90$_2$) ones, contradicting the experimental data. Thus, the cross curvature effect does not explain the experimental results. The most likely explanation for the observed dependence of stress-free temperature on ply thickness is subtle differences in the resin cross-linking rate in the two laminates during curing. Other possible explanations are differences in fiber volume content and temperature dependence of the thermomechanical properties of the two unsymmetric laminates.

The maximum temperature experienced by (0/90) specimens was larger than the temperature used to determine coefficients of linear thermal expansion α_0 and α_{90}. The specimens, used previously to determine α_0 and α_{90}, were subjected to a heating and cooling cycle of approximately 26.7^{o}C (80°F) to 160°C (320°F). During the thermal cycle, temperature and strain values were measured. The temperature and strain data are shown in Figure 14. Unlike the data in Figure 11, heating and cooling data shown in Figure 14 diverge. Further investigations into the causes of the discrepancy were discontinued for the time being. To determine the effects of residual stresses caused by temperature change on stress states of delamination specimens, ΔT was assumed to be 97.8^{o}C (176°F)

3.4 Experimental Delamination Initiation Data

Ten specimens, with the dimensions shown in Figure 2 and using the transition curve represented by Eq 2, were cut from each of the seven panels D10 thru D40 (Table 1). All specimens were instrumented using two SK-03-045PG-350 strip gages and one CEA-03-062UR-350 strain gage rosette. The strip gages were used to detect the onset of delamination in the specimens. The strain gage rosette was used to

determine axial and transverse strains at the onset of delamination. The locations of the gages are shown in Figure 6(b). Two views of the edge delamination specimens with lead wires cut off are shown in Figure 15. In addition to the strain gages, two cameras were used to simultaneously video tape the reduced width section edges of the specimens and a voltmeter. The voltmeter was used to obtain the load level at which some significant event took place. Edges of the specimens were coated with white chalk to aid in detection of edge delamination. When a specimen delaminated suddenly, puffs of chalk were observed. In some cases, the test was terminated when this occurred. In other cases, loading was continued until the delamination became clearly visible.

The specimens were tested in an Instron Test Machine, Floor Model TT-115. The specimens were loaded at a crosshead speed of 1.27 cm (0 05 inch). The data consisted of the axial stress and 23 strain channels. The strain gage data was analyzed as follows to determine the onset of delamination. The raw axial stress data were plotted against the raw transverse strain data from the strip gages. The resulting plots were searched for sudden jumps in transverse strain, which correspond to delamination initiation. The location of the delamination initiation was determined on the basis of which transverse gage showed the earliest strain jump. Figures 16 and 17 show typical stress-strain plots with sudden changes in strain gage readings indicating the onset of delamination. The corresponding axial and transverse strains were corrected to ensure zero strains at zero axial stress. The corrected transverse strains, axial strains, and axial stresses at delamination initiation are summarized in the columns with headings ε_{90}, ε_0, and σ_{m0} in Table 3. The video tapes of the tests were reviewed for the first indications of chalk puffs, which were known to correspond to delamination. The voltmeter readings, corresponding to the first chalk puffs, were converted to axial stresses. These stresses are summarized in the σ_{v0} column in Table 3. As can be seen from Table 3, the σ_{v0} values are typically higher than the σ_{m0} values. This discrepancy is due to the fact that it takes an energetic delamination event to produce a chalk puff. Moreover, the camera coverage in some of the tests was such that chalk puffs from the cross-section transition regions could be missed. It should be noted that in most cases delamination initiation occurred in the width transition region, where small stress concentrations were present. As a result, the true delamination initiation stresses are slightly higher than those given in Table 3. This was disregarded in the subsequent analyses. Table 3 does not include the data for the $(\pm 10_2/90)_s$ specimens because the laminates failed in non-delamination modes. The average failure stress for the $(\pm 10_2/90)_s$ specimens was 84.29 ksi.

3.5 Analysis of Delamination Data

To determine free edge stresses in delamination specimens, initially we considered two approaches both utilizing the finite element (F.E.) method. In the first approach, Pagano's stress based theory (Ref 59) that had been reformulated (Ref. 60 and 61) was implemented into a finite element program. This theory provides an accurate measure of the three dimensional stress field near the free edges of the specimen. However, the analysis is computationally expensive. In the second approach, the analysis was performed using an axisymmetric F.E. computer program which allows for both isotropic and anisotropic materials. Wright Laboratory's version of the program, enhanced by Dandan (Ref. 62), uses an axisymmetric solid formulation capable of predicting the three dimensional stress field in delamination specimens. The specimen is modelled as a segment of a large radius axisymmetric ring under low uniform radial pressure resulting in a uniform circumferential strain.

Both the stress based and axisymmetric formulations use linear elastic material behavior, giving rise to stress singularities at the free edges of the coupon. Therefore, the

magnitude of the predicted free edge interlaminar normal stresses in both formulations depends on the refinement of the finite element mesh at the free edge. However, the average stress over a small δy (of the order a lamina thickness) near the free edge should remain constant and independent of mesh refinement. To compare the two formulations, the two finite element models for the axisymmetric and stress based formulations were used to compare free edge stresses. The specimens were 2 54 cm (1 0 inch) wide by 0.13335 cm (0 0525 inch) thick. Models of one half of the specimen width are shown in Figure 18(a) and 18(c). Details of the models' refined meshes near the free edge are shown in Figures 18(b) and 18(d) with elements nearest the free edge being one half of a ply thick.

Analyses were performed using the material properties from Table 2, and the results are presented in Table 4, where the average σ_z between the 90° plies over δy near the free edge divided by the average applied axial stress σ_0 at the center of the specimen is defined as the free edge stress scale factor σ_{sz}. The table shows that over a distance equal to one half of a ply thickness from the free edge and over a distance equal to a ply thickness from the free edge the two formulations yield very close free edge stress scale factors. Consequently, Dandan's formulation (Ref 62) was used for subsequent F E analyses because it incorporates temperature effects and is computationally less expensive.

To determine the residual free edge stresses, a thermal analysis using the model shown in Figures 18(a) and 18(b) and the material properties of Table 2 with α_0 equal to 1.977 $\mu m/m/^\circ C$ (-1 098 $\mu in/in/^\circ F$) and α_{90} equal to 32 881 $\mu m/m/^\circ C$ (18 267 $\mu in/in/^\circ F$) was performed. The calculated average σ^T_{dz} stress between the 90° plies for δy equal to half the ply thickness per degree temperature drop are shown in Table 5. Also, the calculated average σ^T_z for ΔT equal to -98.7°C (-176°F) for the laminates in the experimental program are presented in the table. It can be seen from the table that the average residual thermal stress σ^T_z between the 90° plies near the free edge decreases with increasing angle α for $(\pm \alpha_2/90)_s$ laminates.

The total interlaminar normal free edge average stress σ_{nz} due to combined mechanical and residual thermal loading is given by

$$\sigma_{nz} = \sigma^T_{dz} \, \Delta T + \sigma_{sz} \, \sigma_0 \qquad (7)$$

where σ^T_{dz} is average normal thermal stress per degree change of temperature, and σ_{sz} is average normal stress per unit applied axial stress (σ_0). A measure of the average mechanical stress σ_z between the 90° plies near the free edge at the onset of delamination can be obtained by multiplying σ_{sz} from Table 4 by the experimentally obtained axial stress σ_0 corresponding to the onset of delamination. The stress-based delamination moment coefficients DMC_σ and DM^T due to temperature change ΔT of -97 8°C (-176°F) were calculated using a Wright Laboratory modified point stress analysis program. The values of σ_{sz}, σ^T_{dz}, σ_0, DMC_σ, DM^T, σ^T_z, DM and σ_{nz} are given in Table 6. It can be seen from Table 6 that for $(\pm \alpha_2/90)_s$ laminates DM^T decrease whereas DM_σ increases with increasing angle α.

3.6 Discussion of Delamination Initiation Results

The results of the delamination initiation study are presented in graphical form in Figure 19. In the figure, the delamination moment contribution due to curing residual stresses and average axial stresses are shown as solid and

open squares. The average and individual total delamination moments are shown as open circles and solid triangles, respectively. As can be seen from the figure, the average delamination moment for all specimens that exhibited edge delamination falls within the range of the individual delamination moments at delamination initiation. This implies that the total delamination moment is a valid criterion for predicting delamination initiation. Nevertheless, the average and individual delamination moments for each angle show a trend that implies a slight dependence of the total delamination moment on stacking sequence angle α.

As was pointed out in Section 3.4, delamination initiation occurred in the cross-section transition region in most of the specimens, especially those with low α. As a result, the delamination moments of specimens with low α are actually higher than shown in Figure 19. If the data were corrected for the stress concentration effect, the agreement between the experimental data and total total delamination moment based delamination initiation criterion would have been better

Moreover, a ΔT of -97 8 °C (-176 °F) was used to estimate the curing residual stress contribution to the total DM. If a larger ΔT were used, the total DM for the specimens with lower α would be higher. This would also improve the agreement between the experimental data and the total delamination moment based delamination initiation criterion

Upon examining the results in Table 6, we see that the scatter in the σ_{nz} data is larger than in the DM data. This implies that the DM delamination initiation criterion does a better job of correlating the experimental data than the σ_{nz} based delamination criterion. Another reason for the superiority of the DM criterion over the σ_{nz} criterion is that DM includes the effect of shear stresses. Moreover, computation of DM is much simpler than computation of σ_{nz}.

4. PREVENTION OF EDGE DELAMINATION

Over the years many approaches (Ref 63 thru 76) have been proposed to prevent edge delamination. These include, (a) bonding fiberglass cloth at edges, (b) stitching along edges, (c) use of fibrous mat or cloth or tough adhesive at the crack plane, (d) use of adhesive layers selectively placed in laminates, (e) use of U-shaped caps, (f) termination of critical plies near edges, (g) altering the ply layup near edges, and (h) creation of narrow and shallow notches along edges of specimens All the above techniques tend to change the design characteristics of the laminates. In this study, a new method to prevent edge delamination of laminates without modifying materials and manufacturing processes is presented.

Analytical procedures used in designing composite laminates yield information relative to total thicknesses of the laminates and percentages of various groups of plies (L % of 0°, M % of 90° and N % of ±45° plies). The plies of these groups can be arranged in a variety of stacking sequences to satisfy design constraints. The delamination moment criterion provides a valid technique to determine the stacking sequences that are less likely to delaminate at the free edge. Laminates having DM > DM_{cr} will delaminate and those having DM < DM_{cr} will not delaminate. To illustrate the application of the criterion, we examined the family of quasi-isotropic (±45/0/90) laminates of Reference 63 and 77. The stacking sequence that yielded compressive maximum σ_z values were excluded from the study.

The stacking sequences considered from Ref. 63 (Q1 thru Q8) are shown in Table 7. All of these stacking sequences were analyzed using Wright Laboratory point stress analysis program to determine the stress-based delamination moment coefficients DMC_σ and DM^T due to temperature change ΔT

of -97.8°C (-176°F) The DMC_σ and DM^T at all of the four interfaces between plies for all the stacking sequences are given in Table 7. To determine the delamination moments DM_σ due to mechanical loads, the failure stress σ_0 was assumed to be equal to 584.87 MPa (84.825 ksi) and the calculated DM_σ and DM^T were combined to obtain the delamination moment DM. The σ_z values were taken from Reference 63. It can be observed from the table that the delamination tendency increases progressively from stacking sequence Q1 to stacking sequence Q8. Moreover, the ranking of the stacking sequences based on DM differs from that based on σ_z. This is due to the fact that the effect of curing residual stresses was neglected in Reference 63. Stacking sequences Q1 thru Q4 are not likely to delaminate. The final selection depends upon other design constraints.

Eight ply thick stacking sequences Q1 thru Q8 were analyzed to determine their relative delamination tendencies, but for these laminates no experimental data were available to verify the conclusions However, Reference 77 has extensive experimental data and includes tests results for sixteen ply thick quasi-isotropic laminates with two stacking sequences L1 and L2. Both of the laminates were analyzed and data similar to that of Table 7 were computed. The results of the analysis are given in Table 8 It can be observed from the table that stacking sequence L1 has far higher tendency to delaminate than stacking sequence L2. The experimental data indicate that specimens L1 and L2 failed at 64 93 ksi (447 69MPa) and 86 12 ksi (662 74MPa), respectively Failed specimens L2 showed no indication of delamination, whereas in specimens L1 delamination was extensive and was marked by large jumps in transverse strains recorded by strain gage rosettes

5. CONCLUDING REMARKS

The results presented herein show that there exists a critical value of total delamination moment, DM_{cr}, below which delaminations do not initiate. As a result, DM_{cr} can be used as a criterion for designing composite structures that will not delaminate at the free edges The criterion was verified using (±α_2/90)$_s$ laminates, with α varying from 15° to 40°. The specimens with α = 10° exhibited matrix cracking in the 90° plies prior to delamination and, hence, were not included in the analysis.

To use the DM_{cr} initiation criterion, the total delamination moment DM must be calculated for the laminate DM consists of two terms, a curing residual stress contribution and a contribution due to mechanical stresses Calculation of DM^T requires knowledge of the stress-free temperature. Our attempts to measure the stress-free temperature gave inconsistent results This is an area requiring additional research Calculations of DM_σ is straightforward and very easy The fact that the effect of curing residual stresses was neglected in most of the published papers on delamination initiation helps to explain the inconsistencies in the literature and delay in formulation of a valid delamination criterion

Finally the total delamination moment criterion for predicting delamination initiation is computationally simple. It can be easily implemented in a laminate optimization code. Addition research is required to thoroughly evaluate the new and simple criterion

6. REFERENCES

1. Pagano, N. J., and Pipes, R B., "Some Observations on the Interlaminar Strength of Composite Materials," International Journal of Mechanical Sciences, Vol 15, 1973, pp. 679-688.

2. Rybicki, E. F., Schmueser, D. W. and Fox, J., "An Energy Release Rate Approach for Stable Crack Growth

in the Free-Edge Delamination Problems," Journal of Composite Materials. Vol.11,1977, pp.470-487

3. Harris, A. and Orringer, O., "Investigation of Angle-ply Delamination Specimen for interlaminar Strength Test," Journal of Composite Materials, Vol. 12, 1978, pp 285-299

4. Crossman, F. W, Warren, W. J., Wang, A S. D. and Law, G. E , Jr , "Initiation and Growth of Transverse Cracks and Edge Delamination in Composite Laminates, Part 2. Experimental Correlation," Journal of Composite Materials Supplement, Vol. 14, 1980, pp.88-108.

5. Chou, S. C., "Delamination of T300/5208 Graphite/Epoxy Laminates," in Fracture of Composite Materials, G. C. Sih and V. P[. Tamuzs, eds, Martinus Nijhoff Publications, 1981, pp. 247-263.

6. O'Brien, T K , "Characterization of Delamination Onset in a Composite Laminate," Damage in Composite Materials, ASTM STP 775, 1982, pp 140-167.

7 Crossman, F. W. and Wang, A. S. D., "The Dependence of Transverse Cracking and Delamination on Ply Thickness in Graphite/Epoxy Laminates," in Damage in Composite Materials, ASTM STP 775, 1982, pp.118-139.

8. Kim, R. Y. and Soni, S. R., "Experimental and Analytical Studies on the Onset of Delamination in Laminated Composites," Journal of Composite Materials, Vol. 18, 1984, pp. 70-80

9. Conti, P. and DePaulis, A , "A Simple Model to Simulate the Interlaminar Stresses Generated Near the Free Edge of a Composite Laminate," in Delamination and Debonding of Materials, ASTM STP 876, 1985, pp. 35-51

10. Whitney, J. M. and Knight, M., "A Modified Free-Edge Delamination Specimen," in Delamination and Debonding of Materials, ASTM STP 876, 1985, pp.298-314.

11. Henneke, E. G., II, "Destructive and Nondestructive Tests," Engineered Materials Handbook, Volume 1: Composites, C. A Dostal, Ed. 1987.

12. Lagace, P. A. and Brewer, J. C., "Studies of Delamination Growth and Final Failure under Tensile Loading," Proceedings of the Sixth International Conference on Composite Materials, Vol. 5, July 1987, pp 5 262-5.273.

13. Sandhu, R. S. and Sendeckyj, G. P., "On Delamination of $(\pm\theta_m / 90_{n/2})_s$ Laminates Subjected to Tensile Loading," Air Force Wright Aeronautical Laboratories Technical Report, AFWAL-TR-79-3058, July 1987

14. Ono, K., "Acoustic Emission Behavior of Flawed Unidirectional Carbon Fiber-Epoxy Composites," Journal of Reinforced Plastics and Composites, Vol. 7, 1988, pp 90-105.

15. Sun, C. T. and Zhou, S. G., "Failure of Quasi-Isotropic Composite Laminates with Free Edges," Journal of Reinforced Plastics and Composites, Vol. 7, 1988, pp. 515-557.

16 Shalve, D. and Reifsnider, K. L , "Study of the Onset of Delamination at Holes in Composite Laminates," Journal of Composite Materials, Vol. 24, 1990 , pp 42-71.

17. Sandhu R. S. and Sendeckyj, G. P., "Edge Delamination of $(\pm\theta_m / 90_{n/2})_s$ Laminates Subjected to Tensile Loading," ASTM Journal of Composites Technology and Research, Vol. 13, No. 2, Summer 1991, pp.78-90.

18. Pawlikowski, K., "Experimental Development of Delamination Onset in Composite Tensile Coupons," M S Thesis, Department of Civil Engineering, the Ohio State University, Columbus, Ohio, Spring 1991.

19. Pawlikowski, K., and Wolfe, W. E., "Exprimental Determination of Delamination On-set in Composite Tensile Coupons," Presented at ASTM 11th Symposium on Composite Materials: Testing and Design, Pittsburgh, PA, 4-5 May 1992.

20. Rolfes, R L., "Compression Test Fixture Evaluation of Oriented Fiber Composites with the Prototype Compression Fixture (1983)," Air Force Wright Aeronautical LaboratoriesTechnical Memorandum,AFWAL-TM-87-172-FIBC, January 1987.

21. Daniels, J. A and Sandhu, R. S., "Evaluation of Compression Specimens and Fixtures for Testing Unidirectional Composite Laminates," Presented at ASTM 11th Symposium on Composite Materials: Testing and Design, Pittsburgh, PA, 4-5 May 1992.

22 Chamis, C C , "Lamination Residual Stresses in Cross-plied Fiber Composites," Proceedings 26th Annual Conference of SPI 'Reinforced Plastics/Composites Come of Age', 9-12 February 1971, Shoreham Hotel, Washington D.C.

23. Chamis, C C , "Lamination Residual Stresses in Mululayered Fiber Composites," NASA TN-D-6148 (AD-D401 061), February 1971.

24 Hahn, H. T and Pagano, N J "Curing Stresses in Composite Laminates," Journal of Composite Materials, Vol.9, No. 1, pp. 91-106, January 1975.

25 Daniel, I. M and Liber, T. "Lamination Residual Stresses in F.ber Composites," Interim Report, NASA-CR-134826, March 1975

26. Daniel, I M. and Liber, T , "Lamination Residual Stresses in Fiber Composites," Final Report, NASA-CR-135085, June 1976.

27. Hahn, H T., "Residual Stresses in Polymer Matrix Composite Laminates," Proceedings 'Advances in Engineering Science ' 13th Annual Meeting, Society of Engineering Science, 1-3 November 1976, Hampton, VA, also Journal of Composite Materials Vol. 10, No. 4, pp. 266-278, October 1976

28. Herakovich, C. T. and Wong, D M "Influence of Residual Stresses on the Tensile Strength of Composite-Metal Sandwich Laminates," Experimental Mechanics, Voi 17, No 11, November 1977, pp. 409-414

29 Hahn, H. T. and Kim, R Y. "Swelling of Composite Laminates," in Advanced Composite Materials: Environmental Effects, ASTM STP 658, 1978, pp. 98-120

30. Crossman, F. W., Mauri, R. E. and Warren, W. J. "Moisture -Altered Viscoelastic Response of Graphite/Epoxy Composites," Advanced Composite Materials-Environmental Effects, ASTM STP 658, 1978, pp. 205-220.

31. Kim, R. Y., "Effect of Curing Stresses on the First ply-failure in Composite Laminates," Journal of Composite Materials, Vol. 13, January 1979, pp. 1-16

32. Hyer, M. W , "Some Observations on the Cured Shapes of Thin Unsymmetric Laminates," Journal of Composite Materials, Vol. 15, March 1981, pp.175-194.

33. Hyer, M. W , "Calculations of the Room Temperature Shapes of Unsymmetric Laminates," Journal of Composite Materials, Vol. 15, July 1981, pp.296-310.

34. Hahn, H. T., "Warping of Unsymmetric Cross-Ply Graphite/Epoxy Laminates," ASTM Journal of Composites Technology Review, 1981, pp.114-117.

35. Hahn, H. T. and Hwang, D. G., "Residual Stresses and Their Effects in Composite Laminates," Proceedings of the International Symposium, part 2, 29-31 December 1981, Tainan, Republic of China, pp 1199-1214.

36. Hyer, M. W., "The Room-Temperature Shapes of Four-Layer Unsymmetric Cross-Ply Laminates," Journal of Composite Materials, Vol 16, July 1982, pp 319-340.

37. Hyer, M W , "Nonlinear Effects of Elastic Coupling in Unsymmetric Laminates," in Mechanics of Composite Materials Recent Advances, Ed. Hashin and Herakovich, Pegamon Press, 1982, pp. 243-258.

38 Kriz, R. D , and Stinchcomb, W. W. "Effect of Moisture, Residual Thermal Curing Stresses, and Mechanical Load on the Damage Development in Quasi-Isotropic Laminates," Damage in Composite Materials, ASTM STP 775,1982, pp 63-80

39 Hyer, M W , Herakovich,C T , Milkovich S M. and Short, J. S , Jr , "Temperature Dependence of Mechanical and Thermal expansion Properties of T300/5208 Graphite/Epoxy," Composites, Vol 14, No 3, July 1983, pp.276-280.

40. Dennis, Scott Thomas, "Unsymmetric Laminated Graphite/Epoxy Composite Plate and Beam Analysis for Determining Coefficients of Thermal Expansion," Master's Thesis, AFIT / CI / NR-83-5T, February 1983.

41. Stango, R. J. and Wang, S. S. "Process-Induced Residual Thermal Stresses in Advanced Fiber-Reinforced Composite Laminates," Journal of Engineering for Industry, Transactions ASME Vol 106, No 1, February 1984 pp 48-54.

42 Zewi, I G , Daniel, I M and Gotro, J. T., "Residual Stresses and Warpage in Circuit Board Composite Laminates," Proceedings of the Society for Experimental Mechanics Fall Conference, 17-20 November 1985, Grenelefe, Florida,

43. Russell, A J and Street, K. N., "Moisture and Temperature Effects on the Mixed-Mode Delamination Fracture of Unidirectional Graphite/Epoxy," Delamination and Debonding of Materials, ASTM STP 876, 1985,pp. 349-370.

44 Nairn, J. A and Zoller, P., "Matrix Solidification and the Resulting Residual Thermal Stresses in Composites," Journal of Materials Science, Vol 20, 1985 pp. 355-367.

45. Nairn, J. A. and Zoller, P.,"The Development of Residual Thermal Stresses in Amorphous and Semicrystalline Thermoplastic Matrix Composites," Toughened Composites, ASTM STP 937, 1987, pp.328-341.

46. Griffen, O. Hayden Jr., "Three Dimensional Thermal Stresses in Angle-Ply Composite Laminates," Journal of Composite Materials, Vol 22, No 1, January 1988, pp 53-70.

47. Armanios, E A. and Mahler, M. A. "Residual Thermal and Moisture Influences on the Free-Edge Delamination of Laminated Composites," 29th AIAA / ASME / ASCE / AHS / ASC Structures, Structural Dynamics and Materials Conference, 1988, pp. 371-381.

48. Whitney, J. M., Knight, M , "Effect of Residual Stresses on Edge Delamination in Composite Materials," 29th AIAA / ASME / ASCE / AHS / ASC Structures, Structural

Dynamics and Materials Conference, 1989, pp 1666-1670.

49. Hong C. S. and Kim, D. M., "Stacking Method of Thick Composite Laminates Considering Interlaminar Normal Stress," 34th International SAMPE Symposium and Exhibition, Vol. 34, May 1989, pp. 1010-1018.

50. Roy, Ajit K.,"Response of Thick Laminated Composite Rings due to Thermal Stresses," 34th International SAMPE Symposium and Exhibition, Vol. 34, May 1989, pp 549-558.

51. Penn, L S., Chou, R. C. T., Wang, A. S D and Binienda, W. K , " The Effect of Matrix Shrinkage on Damage Accumulation in Composites," Journal of Composites Materials, Vol 23, June 1989, pp. 570-586.

52. Sun, L. X., Hsu, T. R , "Thermal Stress Analysis of Laminated Composite Solids of Axisymmetric Geometry," AIAA Journal Vol 28, No 8, August 1990, pp. 1527-1529.

53. White, S. R and Hahn , H. T., "On Reduction of Processing-Induced Residual Stresses in Composite Materials by Cure Cycle Optimization," Pennsylvania State University Report No. CMTC-9015 Prepared for Air Force Office of Scientific Research under AFSOR Grant 87-0242 , August 1990.

54 Bogetti,Travis A and Gillespie, John W., "Process Induced Stress and Deformation in Thick Section Thermoset Composite Laminates," Army Ballistic Research Laboratory Technical Report BRL-TR-90-3182, AD-D443 456, Aberdeen Proving Ground, MD, December 1990

55 Measurements GroupTechnical Note TN-513, "Measurements of Thermal Coefficient Using Strain Gages," 1986.

56. Tuttle, M E , "Errors in Strain Measurements Obtained Using Strain Gages on Composites," Proceedings of the 1985 Fall SEM Conference in Experimental Mechanics (Transducer Technology for Physical Measurements), held at Grenelefe, Florida, on 17-20 November, 1985, pp 170-179.

57 Goforth, Eric, "Automated Thermal Strain and Data Acquisition System," M S Thesis, Department of Mechanical Engineering, North Carolina Agricultural & Technical State University, Greensboro, NC, 1992.

58. Timoshenko, S , "Analysis of Bimetal Thermostats," Journal of Optical Society of America, Vol 11, 1925, pp 233-256.

59 Pagano, N. J., "Stress Fields in Composite Laminates," International Journal of Solids and Structures, Vol 14, 1978, pp.385-400.

60. Chyou, H., A., "Variational Formulation and Implementation of Pagano's Theory of Laminated Plates," Ph D. Dissertation, Department of Civil Engineering, the Ohio State University, Columbus, Ohio, 1989

61. Schoeppner, G. A. "A Stress Based Theory Describing the Dynamic Behavior of Laminated Plates," Ph D. Dissertation, Department of Civil Engineering, the Ohio State University,, Columbus, Ohio, 1991.

62. Dandan, Razan A., "Finite Element Analysis of Laminated Composite Axisymmetric Solids," M S Thesis, Department of Civil Engineering, the Ohio State University, Columbus, Ohio, 1988.

63. Herakovich, C T , "On the Relationship Between Engineering Properties and Delamination of Composite Materials," Journal of Composite Materials, Vol 15, 1981, pp 336-348.

64 Kim, R. Y., "Prevention of Free -edge Delamination,"
28th National SAMPE Symposium , April 12-14, 1983,
pp.200-209

65. Mignery, L. A., Tan , T. M. and Sun, C. T., "The Use
of Stitching to Suppress Delamination in Laminated
Composites," Delamination and Debonding, ASTM STP
876, 1985, pp.371-385

66. Chan S. W., "Delamination Arrester-an Adhesive Inner
Layer in Laminated Composites," Composite Materials,
Fatigue and Fracture, ASTM STP 907, 1986, pp.176-196

67. Browning, C. E. and Schwartz, H S , "Delamination
Resistant Composite Concepts," Composite Materials:
Testing and Design (Seventh Conference), ASTM STP 893,
1986, pp.256-265.

68. Chan, W. S., Rogers, C and Aker, S , "Improvement
of Edge Delamination Stresngth of Composite Laminates
Using Adhesive Layers,"Composite Materials, Testing and
Design (Seventh Conference), ASTM STP 893, 1986,
pp.266-285.

69. Howard, W. E., Gossard, T and June , R. M.,
"Reinforcement of Composite Laminate Free Edges with U-
Shaped Caps," 27th AIAA/ASME/ASCE/AHS/ASC
Structures, Structural Dynamics and Materials Conference,
1986, pp. 472-485.

70. Chan, W. S. and Ochoa, O. O., "Suppression of Edge
Delamination in Composite Laminates by Terminating a
Critical Ply near the Edges," 29th AIAA / ASME / ASCE /
AHS / ASC Structures, Structural Dynamics and Materials
Conference, 1988, pp.359-364

71. Johnson, W. S. and Mangalgiri, P. D., "Influence of the
Resin on Interlaminar Mixed-Mode Fracture," Toughened
Composites, ASTM STP 937, 1987, pp.295-315.

72. Vizzini, A. J , "Prevention of Free-Edge Delamination
via Edge Alteration," 29th AIAA / ASME / ASCE / AHS /
ASC Structures, Structural Dynamics and Materials
Conference, 1988, pp 365-370.

73 Pogue, W. R and Vizzini, A. J., "Structural Tailoring
Techniques to Prevent Delamination in Composite
Laminates," Journal of the American Helicopter Society,
Vol.35, No 4, October 1990, pp 38-45.

74 Sun, C. T. and Dhu, G. D., "Reducing Free Edge Effect
on Laminate Strength by Edge Modification," Journal of
Composite Materials, Vol. 25, February 1991, pp.142-161.

75. Chan S. W , "Design Approaches for Edge Delamination
Resistance in Laminated Composites," Journal of Composites
Technology & Research, Vol 14, No. 2, Summer 1991,
pp 91-96.

76 Jones, R. M , "Delamination-Sppression Concepts for
Composite Laminates Free Edges," Proceedings of the Eighth
International Conference on Composite Materials
(ICCM/VIII), Honolulu, July 15-19, 1991, published by
Society for the Advancement of Materials and Process
Engineering (SAMPE), pp 28-M-1 to 10.

77. Sandhu R S , " Analytical-Experimental Correlation of
the Behavior of 0o,±45o, 90o Family of AS/3501-5 Graphite
Epoxy Composite Laminates under Uniaxial Tensile
Loading," The Air Force Flight Dynamics Laboratory
Technical Report, AFFDL-TR-79-3064, May 1979, Wright-
Patterson Air Force Base, Ohio

Table 1. Panels fabricated using graphite/epoxy (AS4/3501-6) material system

Panel	Stacking sequence	plies	Size before trimming	Size after trimming
A	$(0^o)_{15}$	16	12.0 (30.48) x 30 0 (76 20)[*]	11.0 (27.94) x 29.0 (73.66)[*]
B	$(\pm 45^o)_{2s}$	8	11.0 (27.94) x 8.0 (20 32)	10.0 (25.40) x 7.0 (17.78)
C2	$(0^o/90^o)$	2	12.0 (30.48) x 12.0 (30.48)	11.0 (27.94) x 11.0 (27.94)
C4	$(0^o{}_2/90^o{}_2)$	4	12.0 (30.48) x 12.0 (30.48)	11.0 (27 94) x 11.0 (27.94)
D10	$(\pm 10^o{}_2/90^o)_s$	10	12.0 (30.48) x 21.0 (55.88)	11.0 (27 94) x 21.0 (53.34)
D15	$(\pm 15^o{}_2/90^o)_s$	10	12.0 (30 48) x 21.0 (55 88)	11.0 (27.94) x 21.0 (53.34)
D20	$(\pm 20^o{}_2/90^o)_s$	10	12.0 (30.48) x 21.0 (55.88)	11.0 (27.94) x 21.0 (53.34)
D25	$(\pm 25^o{}_2/90^o)_s$	10	12 0 (30.48) x 21.0 (55.88)	11 0 (27.94) x 21.0 (53.34)
D30	$(\pm 30^o{}_2/90^o)_s$	10	12 0 (30.48) x 21.0 (55.88)	11 0 (27.94) x 21 0 (53.34)
D35	$(\pm 35^o{}_2/90^o)_s$	10	12 0 (30.48) x 21.0 (55.88)	11.0 (27.94) x 21.0 (53.34)
D40	$(\pm 40^o{}_2/90^o)_s$	10	12.0 (30.48) x 21.0 (55.88)	11.0 (27.94) x 21.0 (53.34)

NOTE: [*] inch (cm)

Table 2. Basic Material Properties of AS4/3501-6 Graphite Epoxy at Room Temperature

Elastic Modulus along the fibers in tension	E_1^t	134.59 GPa (19.52 Msi)
Elastic Modulus along the fibers in compression	E_1^c	135.87 GPa (19.70 Msi)
Elastic Modulus transverse to the fibers in tension	E_2^t	10 02 GPa (1.453 Msi)
Elastic Modulus transverse to the fibers in compression	E_2^c	10 89 GPa (1.579 Msi)
Major Poisson's ratio in tension	μ_{12}^t	0.317
Major Poisson's ratio in compression	μ_{12}^c	0.276
Elastic Modulus in shear	G_{12}	6.38 GPa (0.925 Msi)
Coefficient of linear expansion in fiber direction (Tuttle)	α_0	-1.977 μm/m/ ^oC (-1.098 μin/in/ ^oF)
Coefficient of linear expansion in fiber direction (ASTM)	α_0	-0.508 μm/m/ ^oC (-0.282 μin/in/ ^oF)
Coefficient of linear expansion in fiber direction (NCA&TU)	α_0	-2.028 μm/m/ ^oC (-1.127 μin/in/ ^oF)
Coefficient of linear expansion in direction transverse to fibers (Tuttle)	α_{90}	32.881 μm/m/ ^oC (18.267 μin/in/ ^oF)
Coefficient of linear expansion in direction transverse to fibers (ASTM)	α_{90}	26.886 μ m/m/ ^oC (14.937 μin/in/ ^oF)
Coefficient of linear expansion in direction transverse to fibers (NCA&TU)	α_{90}	34 194 μm/m/ ^oC (18.997 μin/in/ ^oF)

Table 4. Comparison of Stress Based and Axisymmetric Formulations

	σ_{sz} for $\delta y = 0$ 5t from free edge		σ_{sz} for $\delta y = 1$ 0t from free edge	
Laminate	Stress Based	Axisymmetric	Stress Based	Axisymmetric
$(\pm 10_2/90)_s$	0.08615	0 08713	0 06780	0 07345
$(\pm 15_2/90)_s$	0.14152	0 14293	0.11114	0.12102
$(\pm 20_2/90)_s$	0.21739	0 21602	0.17098	0.18349
$(\pm 25_2/90)_s$	0.31072	0.29995	0.24464	0 25530
$(\pm 30_2/90)_s$	0.41669	0 39209	0.32848	0 33396
$(\pm 35_2/90)_s$	0 53245	0 51822	0 41957	0.43799
$(\pm 40_2/90)_s$	0 64721	0 57005	0 50967	0 48586

Table 5. Average thermal free edge stress σ_z^T for $\delta y = 0.5t$, $\Delta T = -97.8^oC$ (-176^oF)

Laminate	σ_{dz}^T	$\sigma_z^T = \sigma_{dz}^T \cdot \Delta T$
$(\pm 10_2/90)_s$	-0 4891 (39.41)[*]	47.8 (6937 3)[**]
$(\pm 15_2/90)_s$	-0 4529 (36 49)	44.3 (6422 0)
$(\pm 20_2/90)_s$	-0.4011 (32 32)	39.2 (5663 8)
$(\pm 25_2/90)_s$	-0.3342 (26 93)	32 7 (4740 8)
$(\pm 30_2/90)_s$	-0 2586 (20 84)	25.3 (3668.0)
$(\pm 35_2/90)_s$	-0.1782 (14.36)	17.4 (2528 0)
$(\pm 40_2/90)_s$	-0 0972 (07.83)	09.5 (1379 2)

[*] MPa/^oC (psi /^oF)
[**] MPa (psi)

Table 3. Experimentally obtained stresses and strains of delaminating specimens

Specimen No	Specimen D40				Specimen D35			
	Strain Gages		Axial Stress		Strain Gages		Axial Stress	
	ε_{90} μ in/in	ε_0 μ in/in	σ_{m0}, ksi	σ_{v0}, ksi	ε_{90} μ in/in	ε_0 μ in/in	σ_{m0}, ksi	σ_{v0}, ksi
1	-2640	4360	20 44	a	-2660	3460	21 56	27 73[b]
2	-2750	4120	19 16	a	-2470	3450	22 32	41 26[b]
3	-2830	3810	18 05	18 65[b]	-2520	3500	22.86	27.86[b]
4	-2950	3760	18 23	18 88[b]	-2210	3250	21 23	24 51[b]
5	-3570	3850	18 23	19 10[b]	-3000	3220	21 49	25 56[b]
6	-2960	4000	18 41	21 30[b]	-2840	3570	22.76	3? 77[b]
7	-2620	4140	20 25	24 29[b]	-2890	3330	19.90	27 69[b]
8	-2870	3790	18 25	22 95[b]	-2710	3740	23.45	28 08[b]
9	-3250	5380	24 77	25.58[b]	-2430	3660	24.10	27 31[b]
10	-3400	4820	22 15	22 12[b]	-2650	3700	20 22	23 21[b]
Average	2980	4200	19 79		-2640	3490	21.99	

Specimen No	Specimen D30				Specimen D25			
	Strain Gages		Axial Stress		Strain Gages		Axial Stress	
	ε_{90} μ in/in	ε_0 μ in/in	σ_{m0}, ksi	σ_{v0}, ksi	ε_{90} μ in/in	ε_0 μ in/in	σ_{m0}, ksi	σ_{v0}, ksi
1	-2130	2350	20 35	20.33[b]	-1780	2530	26.51	53 58[b]
2	-2090	2420	21.10	35 62[b]-	-1740	2770	29 69	40 96[b]
3	-2140	2590	22 59	29 42[b]	-1700	3030	31 35	52 67[b]
4	-2350	3070	26 59	37.23[b]	-1760	3000	32 54	32 83[b]
5	-1980	3000	22 32	28.71[b]	-1570	2350	25 84	30 62[b]
6	-2060	2690	22 77	26 98[b]	-1640	3100	34 51	40 58[b]
7	-2090	2810	24 62	32 78[b]	-1930	2260	24.44	32 38[b]
8	-2370	3400	30 21	34.23[b]	-1920	3140	32 30	34.95[b]
9	-2290	2460	21 24	24 02[b]	-1450	2660	27.84	44 16[b]
10	-2300	2510	23 09	24.93[b]	-1750	2800	29.77	30 10[b]
Average	-2180	2730	23 49		-1720	2760	29 48	

Specimen No	Specimen D20				Specimen D15			
	Strain Gages		Axial Stress		Strain Gages		Axial Stress	
	ε_{90} μ in/in	ε_0 μ in/in	σ_{m0}, ksi	σ_{v0}, ksi	ε_{90} μ in/in	ε_0 μ in/in	σ_{m0}, ksi	σ_{v0}, ksi[e]
1	-1300	3140	40 95	41 16[b]	-1050	3390	53 08	84 64[b]
2	c	c	c	38 47[b]	-1520	5200	77 22	81 92[b]
3	-1360	2290	30 50	46 18[b]	-1430	4130	61 35	90 99[b]
4	-1420	2610	34 34	49 04[b]	-1080	3930	60 54	66 32[b]
5	-1340	2370	33 62	d	-1230	3460	53 19	80 26[b]
6	-1200	2530	29 94	d	-1400	2040	52 72	79 72[b]
7		3780	47 82	d	-1240	4050	59 26	85 52[b]
8		3630	47 29	48 80[b]	-1610	4180	60 61	77 39[b]
9		3400	46 34	69.40[b]	-1250	4350	63 42	d
10	-1800	3020	41 27	59 09[b]	-2150	4490	70 52	d
Average	-1510	2970	39 10		-1400	3920	61 19	

a Load not recorded on video tape
b Corresponds to damage event and not damage (delamination) initiation
c Data missing, technician error
d Video taping error
e 1.0 ksi = 6 895 MPa

Table 6. Mechanical, thermal and total normal delamination stresses and moments in laminates

Laminate	σ_{sz}	Mechanical				Thermal		Total	
		$DMC_\sigma 10^{-5}$ inch³	σ_0 ksi	σ_z ksi	$DM_\sigma 10^{-5}$ kip-inch	$DM_T 10^{-5}$ kip-inch	σ^T_z ksi	$DM 10^{-5}$ kip[-inch	σ_{nz} ksi
$(\pm 10_2/90)_S$*	0 08713	1.153	84 29	7.34	97.19	88.71	6.94	185.90**	14.23**
$(\pm 15_2/90)_S$	0.14293	1.960	61 19	8 75	119.93	84.02	6 42	203 95	15 17
$(\pm 20_2/90)_S$	0 21602	3.108	39.10	8.45	121.52	76 22	5 69	197.74	14.14
$(\pm 25_2/90)_S$	0.29995	4.601	29.48	8.83	135 64	64.67	4.74	200.31	13.57
$(\pm 30_2/90)_S$	0.39209	6 414	23.49	9.21	150 67	53.54	3 67	204.21	12 88
$(\pm 35_2/90)_S$	0.51822	8.464	21.99	11.40	186 12	37.59	2.53	223.71	13.93
$(\pm 40_2/90)_S$	0.57005	10.558	19.79	11.28	208 94	19.21	1.387	228 15	12.66
Average								209.68	13 73

* This laminate did not delaminate, σ_0 correspond to the stress level when odd behavior of outside gages was observed.
** This result not included in the average.

1 kip = 454 kg; 1 inch = 2.54 cm; 1ksi = 6 895 MPa

Table 7. Application of DM to ($\pm 45/0/90$) family of laminates-I

Laminate	Interface	$DMC_\sigma 10^{-5}$ inch³	$DM_\sigma^a 10^{-5}$ kip-inch	$DM^T 10^{-5}$ kip-inch	$DM^b 10^{-5}$ kip-inch	σ_z^c ksi
$(45/90/0/-45)_S$	1	0 4315	36 60	0.	36 60	6 6
	2	0 4268	36.20	-4.57	31.63	
Q1	3	-0 4409	-37 40	-9.14	-46 54	
	4	-0.8724	-74 00	-9.14	-83.14	
$(45/90/-45/0)_S$	1	0 4315	36 60	0.	36 60	6 9
	2	0 4268	36 20	-4.57	31 63	
Q2	3	-0.0140	-1.19	-13.71	-14.90	
	4	-0 0187	-1.59	-18.28	-19.87	
$(0/-45/90/45)_S$	1	0 0047	0 40	4.57	4 97	6 2
	2	0.4455	37.79	13 71	51.50	
Q3	3	0.4502	38.19	18 28	56.47	
	4	0 0187	1.59	18.28	19 87	
$(45/0/90/-45)_S$	1	0 4315	36 60	0	36 60	7 6
	2	1 2992	110.20	4.57	114.77	
Q4	3	1.3039	110 60	9.14	119 74	
	4	0 8724	74 00	9.14	83.14	
$(45/-45/90/0)_S$	1	0 4315	36 60	0	36 60	9 0
	2	1.7260	146 41	0.	146 41	
Q5	3	2 5844	219 22	-4.57	214 65	
	4	2.5797	218 82	-9 14	209 68	
$(0/45/-45/90)_S$	1	0 0047	0 40	4 57	4.97	10 0
	2	0 4455	37.79	13.71	51 50	
Q6	3	1.7494	148 39	22.85	171 24	
	4	2 6171	222 00	27 41	249 41	
$(45/0/-45/90)_S$	1	0 4315	36.60	0.	36 60	10 4
	2	1.2992	110 20	4 57	114 77	
Q7	3	2 6031	220 81	13 71	234 52	
	4	3.4708	294.41	18 28	312.69	
$(45/-45/0/90)_S$	1	0 4315	36 60	0.	36 60	10 9
	2	1.7260	146 41	0.	146 41	
Q8	3	3 4567	293.21	4 57	297 88	
	4	4 3244	366 82	9.14	375 96	

a. $DM_\sigma = 84.825 \times DMC_\sigma$ b. $DM = DM_\sigma + DM^T$ c. Reference 63 values, interface not indicated in the reference

1 kip = 454 kg, 1 inch = 2 54 cm, 1 ksi = 6 895 MPa

Table 8. Application of DM to (±45/0/90) family of laminates-II

Laminate	Interface	$DMC_\sigma 10^{-5}$ inch^3	$DM_\sigma^a 10^{-5}$ kip-inch	$DM^T 10^{-5}$ kip inch	$DM^b 10^{-5}$ kip-inch
(±45/0₂/±45/90₂)s	1	0 4315	36 60	0	36 60
	2	1.7260	146 41	0	146.41
L1	3	3.4567	293 21	4 57	297.78
	4	5.1968	440 82	18.27	459 09
	5	7.3730	625 41	26.55	661.96
	6	10 4123	883.22	54 83	938 05
	7	13 0154	1104 03	68 54	1172 57
	8	13 8831	1177 63	73 11	1250 74
(±45/90₂/±45/0₂)s	1	0 4315	36 60	0	36 60
	2	1.7260	146 41	0	146 41
L2	3	2 5843	219 21	-4.57	214 64
	4	1.7073	144 82	-18 27	126 55
	5	0.3941	33 43	-36 55	-3.12
	6	-0 0561	-4.76	-54 83	-59 59
	7	-0 0701	-5 95	-68 54	-74 49
	8	-0 0748	-6 34	-73 11	-79.45

a $DM_\sigma = 84\,825 \times DMC_\sigma$ b $DM = DM_\sigma + DM^T$
1 kip = 454 kg, 1 inch = 2 54 cm, 1 ksi = 6 895 MPa
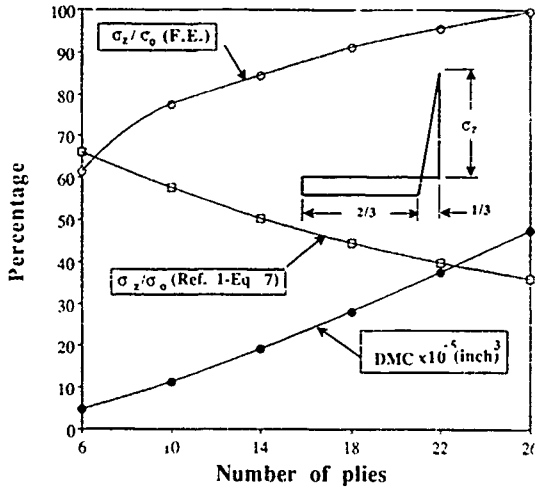
Figure 1. DMC and interlaminar normal stress vs number of plies
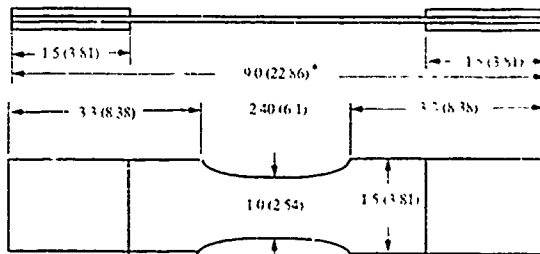
All dimensions in inches(cm)

Figure 2. Delamination Specimen
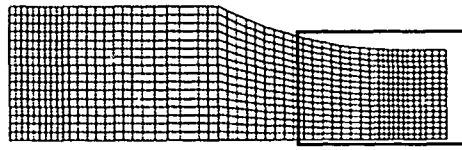
(a) Model A
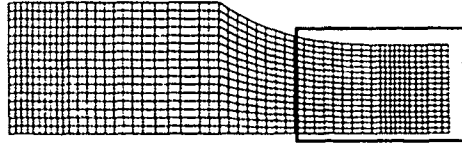
(b) Model B
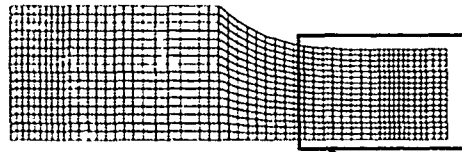
(c) Model C

Contours shown for
this part in Fig. 4

Figure 3. Finite element models

Axial strains

Transverse
strains

(a) Model A

(b) Model B

(c) Model C
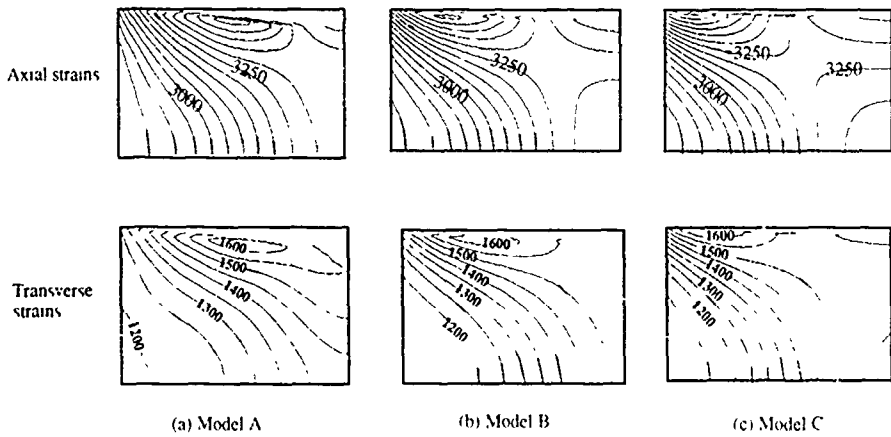
Figure 4. Contours of strains (micro m/m) for three F.E. models
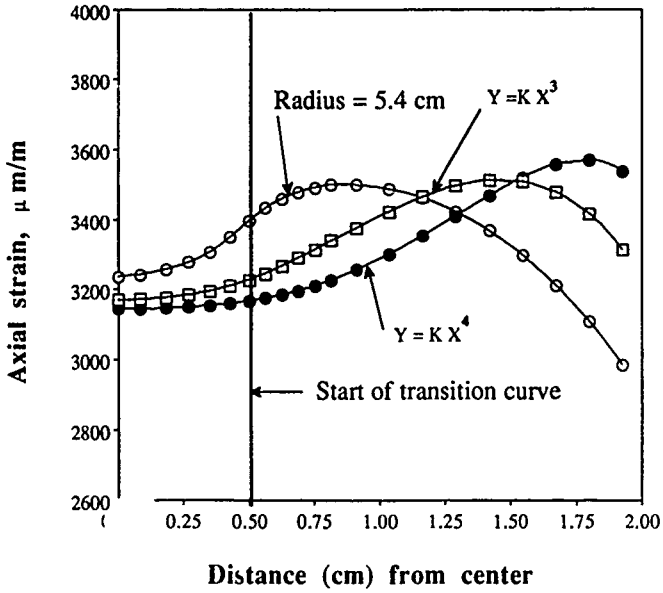
Figure 5. Axial strain near free edge for three F.E. models
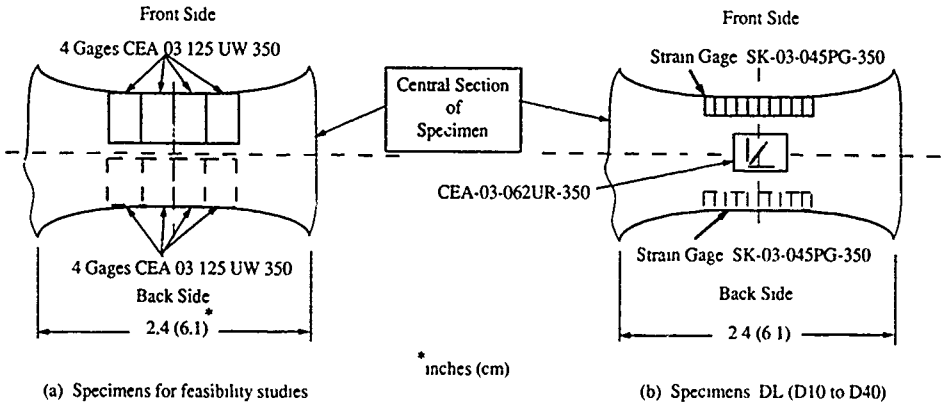
Figure 6. Location of gages on specimens with reduced section
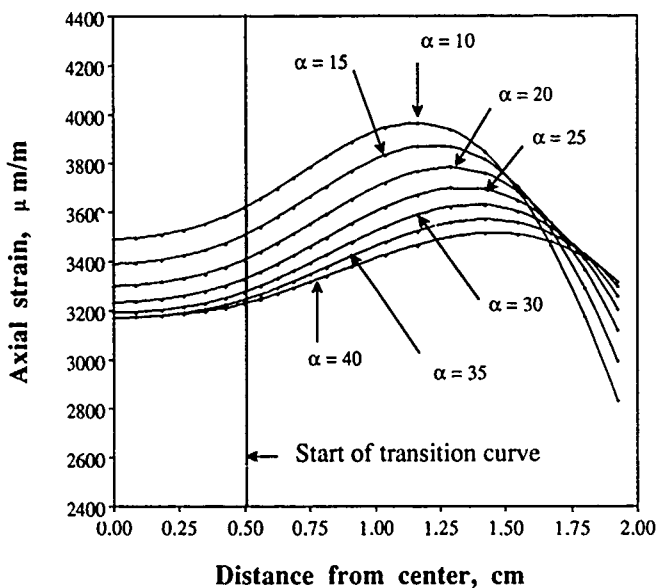
Figure 7. Axial strain near free edge for $(\pm\alpha_2/90)_s$ laminates

$^*1.0 \text{ inch}^3 = 16.387 \text{ cm}^3$
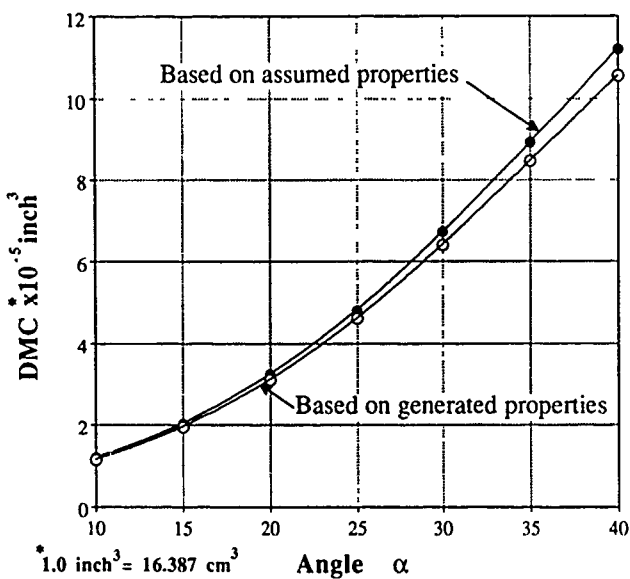
Figure 8. Variation of delamination moment coefficient vs angle
for $(\pm\alpha_2/90)_s$ laminates

(a) Tension specimens

(b) Compression specimens

(c) Specimens for measuring α
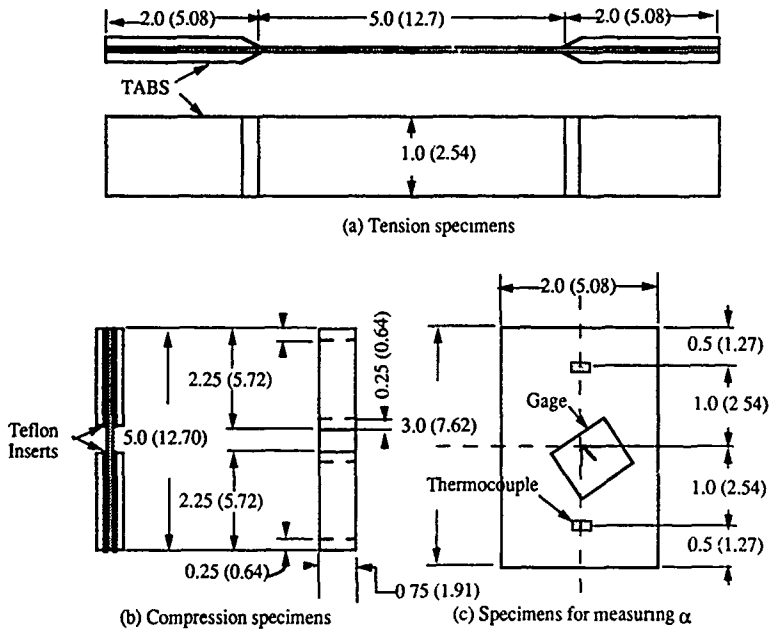
NOTE: All dimensions in inches (cm)

Figure 9. Specimens for basic property data
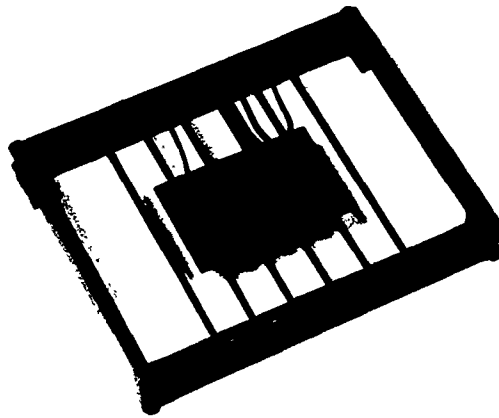
Figure 10 Support fixture for specimen to determine α
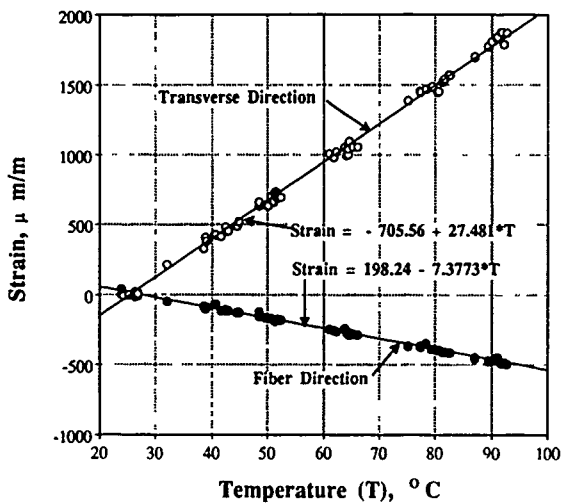
Figure 11. Plot of strain vs temperature (20 to 100 °C)
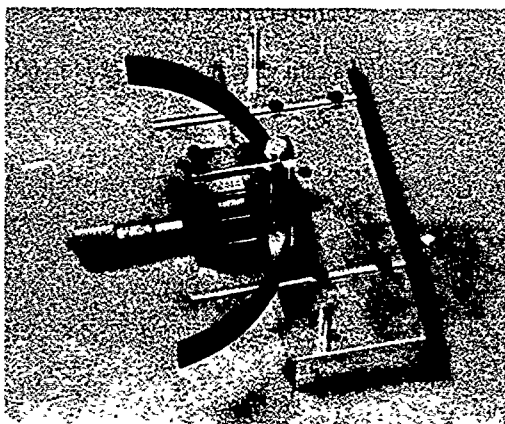
Figure 12. Fixture for determining thermal stress-free state
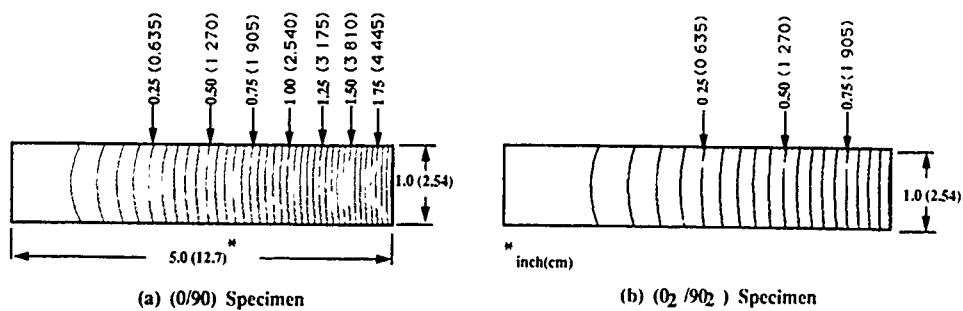
Figure 13. Out of plane displacement contours
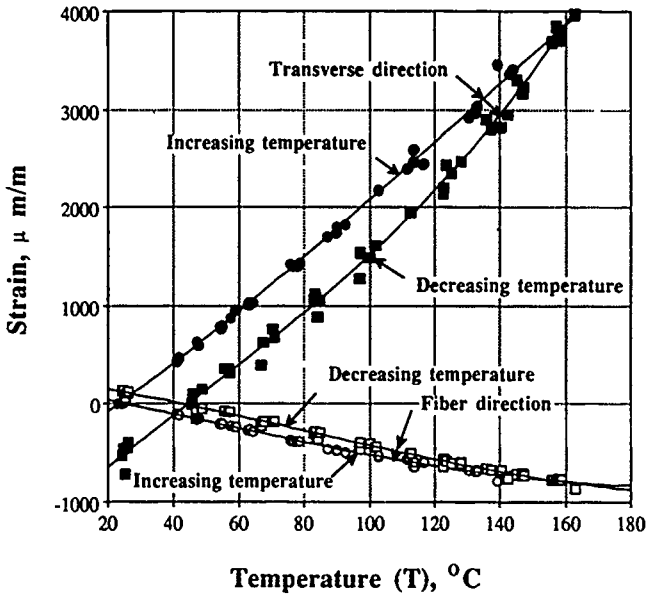
Figure 14. Plot of strain vs temperature (20 to 160 ^{O}C)
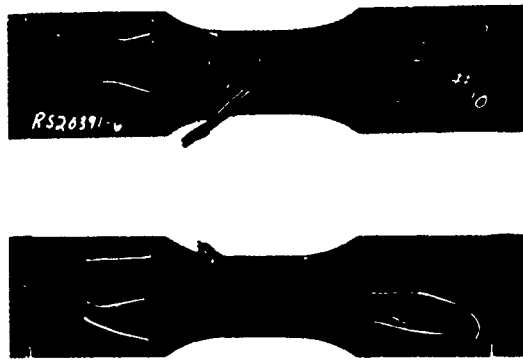
Figure 15. Instrumented delamination specimen
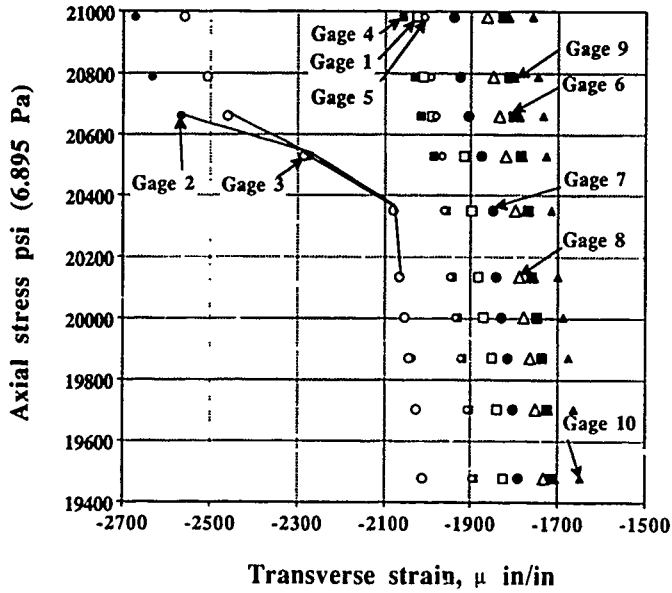
Figure 16. Experimental stress-strain plot for specimen D30-1
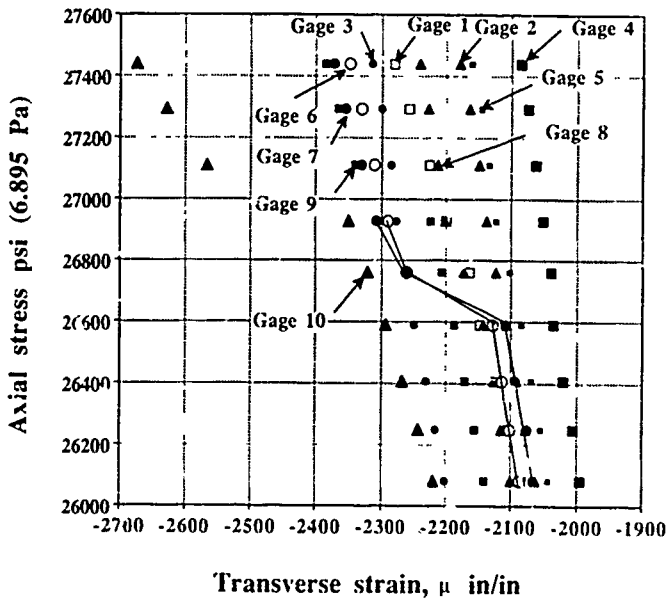
Figure 17. Experimental stress-strain plot for specimen D30-4

(a) Axisymmetric model

(c) Stress based model

(b) Enlarged view of boxed section

(d) Enlarged view of boxed section
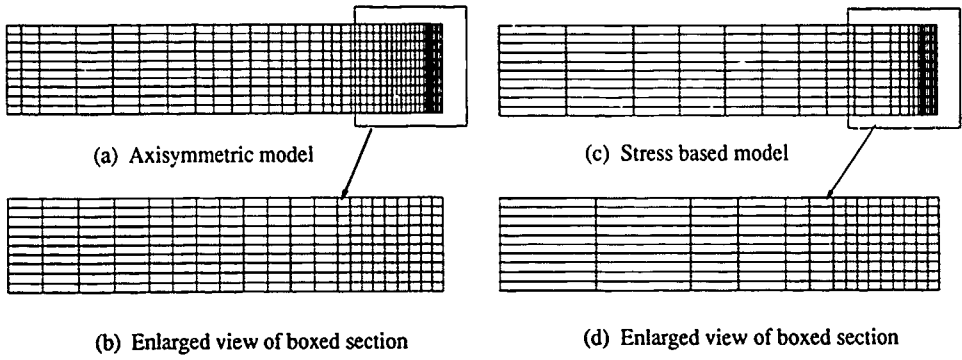
Figure 18. F. E. models for axisymmetric and stress based formulation
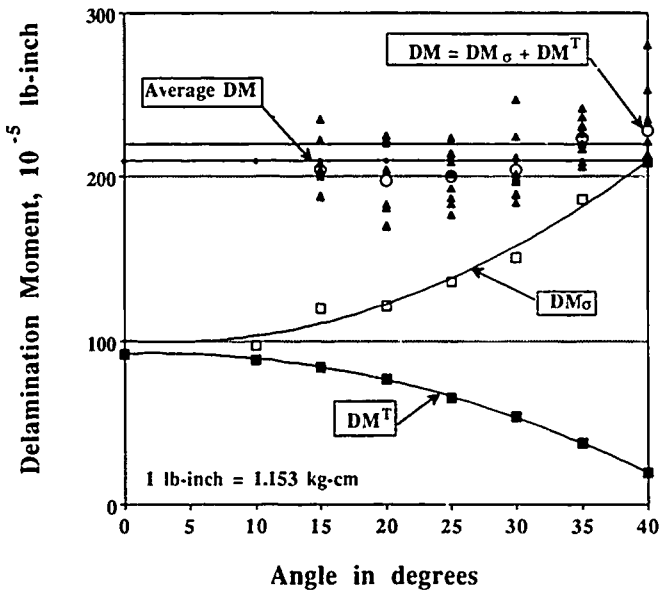
Figure 19. Mechanical, thermal and average DM vs angle

NUMERICAL ANALYSIS OF THE THERMOELASTIC EFFECTS IN LAMINATED STRUCTURES AND ITS USE IN THE IDENTIFICATION OF DEFECTS.

D. Van Hemelrijck, L. Schillemans, P. De Wilde, A. Cardon
Composite Systems and Adhesion Research Group of the Free University of Brussels
COSARGUB - VUB - TW - Kb - Pleinlaan 2 - 1050 Brussels - Belgium

M. Kyriakopoulos, G. Roupaklas
University of Patras Applied Mecnanics Laboratory
PO Box 1134 Patras 26110-GREECE

1. SUMMARY

The thermoelastic effect first analysed by Lord Kelvin is governed by a simple relation between amplitude of temperature and amplitude of sum of principle stress change as long as adiabatic conditions are maintained. Although valid for isotropic materials it is shown that this simple relation leads to very poor results for anisotropic materials. A non-adiabatic theory taken into account the inter-laminar heat transfer shows a better agreement between theory and experiment. Experimental data were obtained on a Fibredux 914C-TS-5_34% carbon epoxy laminate using single point measurements.

2. INTRODUCTION

Although the theoretical treatment of the thermoelasic effect was first published in 1853 by Lord Kelvin, it took over a century before its potential as a device for stress analysis was realised. This was mainly due to the low sensitivity of the available instrumentation. Recent developments in electro-optical and signal processing techniques were necessary before a practical device, referred to as SPATE (Stress Pattern Analysis by Thermal Emission), became available. Though relatively young, the use of SPATE as a remote infrared sensing technique to produce full-field stress maps, became increasingly widespread, particularly for metallic structures. A selected number of papers [1,2] confirmed the validity of the theoretical basis of the technique and demonstrated its scope and potential.
However, on composite structures the thermoelastic analysis has thus far been limited primarily to simple studies or to qualitative NDT-type applications (e.g. [3,4]). The reason is due largely to a general lack of a thorough understanding of the thermoelastic behaviour of composite materials.

3. ADIABATIC THEORY

Based on the thermodynamics of irreversible processes the thermoelastic equation, relating deformation and temperature, for a perfectly elastic isotropic body under adiabatic conditions may be calculated as:

$$\frac{\Delta T}{T_0} = -\frac{\alpha}{\rho c_\varepsilon}\left[\Delta\sigma_{11} + \Delta\sigma_{22}\right] \qquad (1)$$

where ΔT is the local cyclic temperature change, T_0 is the local absolute temperature, α is the coefficient of thermal expansion, ρ is the density, c_ε is the specific heat at constant strain and $\Delta\sigma_{ij}$ is the sum of the cyclic principal stress amplitudes.
This expression was validated several times by different authors, especially P. Stanley [1,2] used SPATE to study the stress distribution in beams, "Brazilian" discs, rectangular plates and circular rings. The agreement between the experimental results and the numerical solution was very good. H. Wölfel [5] showed an excellent agreement between stress results obtained by thermoelastic stress analysis and Finite Elements. The differences found are overall less than 1 N/mm^2.

To ensure adiabatic conditions the cyclic load has to be applied at a frequency high enough so that the stress-induced temperature fluctuation has insufficient time to diffuse within the material. It was found that a frequency greater than approximately 8 Hz is sufficient for most applications. The thermoelastic effect is further, for higher frequencies independent of the frequency.

Based on the same assumptions the thermoelastic relation for a perfectly elastic but anisotropic body under adiabatic conditions is:

$$\frac{\Delta T}{T_0} = -\frac{1}{\rho c_\varepsilon}\left[\alpha_{11}\Delta\sigma_{11} + \alpha_{22}\Delta\sigma_{22}\right] \qquad (2.)$$

In the case of fibre reinforced composites the stresses involved can either be the local ply-stresses or the integrated stresses over the total thickness of the laminate.

As an example we consider an Fibredux 914C-TS carbon epoxy laminate with the following stacking sequence $[0°,90°_2,0°_5]_s$.
Assuming an applied uniaxial sinusoidal stress $\sigma = \Delta\sigma$ sinωt in the x-direction where $\Delta\sigma$ is an arbitrary constant equal to 1N/mm^2. It may be shown from the classical lamination theory that the global laminate stresses are given by:
σ_x=1.0 E06 N/m^2 and the linear expansion coefficient in the x-direction α_x= 1.386E-06 /°C and in the y-direction α_y=5.85E-06 /°C. The values ρ=1610 kg/m^3 and c_ε=921 J/kg °C were taken from reference [6].

The corresponding stress-induced relative temperature change e.g. eqn. (2.) is equal for this case to:
$\Delta T / T_0 = 9E-07$.

Figure 1 gives the measured SPATE response for a frequency of 1 to 20 Hz. As in Dunn *et al.* all amplitude data are normalised by the 20 Hz signal.
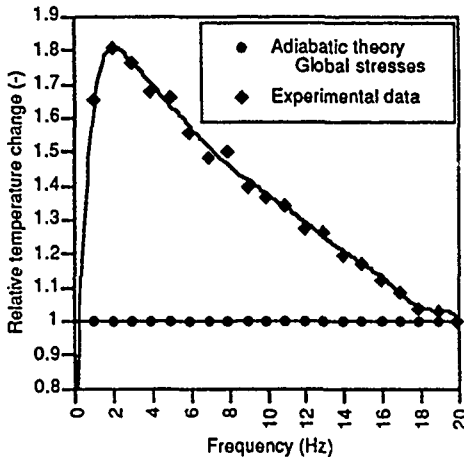

Fig. 1 Normalised amplitude data.

Figure 1. shows clearly a very poor agreement between theory and experiment.

Knowing that homogenisation of all the layer data leads to bad results and since SPATE is a surface measuring device, the measured data could only reflect the stresses in the surface layer (e.g. [7]).
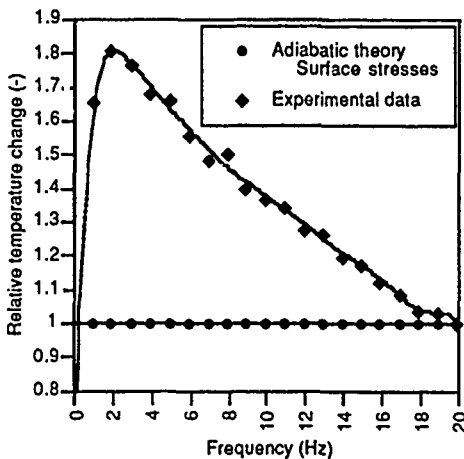
Fig. 2 Normalised amplitude data.

For the same lay-up and loading conditions the classical lamination theory gives for the local surface (0°) layer stresses: $\sigma_x = 1.30E06$ N/m^2 and $\sigma_y = 2.25E04$ N/m^2 and the linear expansion coefficient in the x-direction $\alpha_x = 0.29E-06$ /°C and in the y-direction $\alpha_y = 29.0E-06$ /°C

The corresponding relative temperature change (e.g. eqn. (2.)) is this time equal to: $\Delta T / T_0 = 7E-07$.
Figure 2. compares theory and experiment and shows again a very poor agreement.

4. NON-ADIABATIC THEORY

While analysing the thermoelastic response of fibre reinforced composites a rather interesting question raises: do, as a consequence of cyclic loading, fibre and matrix experience the same temperature fluctuation. This question is even more under discussion since in the case of polymeric matrix reinforced material systems there exist large stress gradients in the form of stress discontinuities between the stiff fibre and the weak matrix.
To resolve this question, consider a single fibre which is subjected to a sudden change in its surface temperature. The single fibre is idealised as an infinite long circular cylinder of radius r=R. Initially the fibre is in thermal equilibrium with the surrounding such that at t < o we have T(r,T)=T$_0$. At t=0, the boundary condition T=T$_a$ for r=R is imposed. The problem to solve is described by the one-dimensional heat diffusion equation in cylindrical co-ordinates:

$$\frac{1}{\gamma}\frac{\partial T}{\partial t} - \frac{\partial^2 T}{\partial r^2} - \frac{1}{r}\frac{\partial T}{\partial r} = 0 \qquad (3.)$$

where $\gamma = \dfrac{k}{\rho c}$ is the diffusion coefficient, and in which k is the conduction coefficient, ρ is the density and c is the specific heat capacity.

The solution of eq. (3.) may be expressed as a series of Bessel functions:

$$\theta = \sum_{i=1}^{\infty} a_i J_0\left(\mu_i \frac{r}{R}\right) \exp\left(-\mu_i^2 F_0\right) \qquad (4.)$$

where $\theta = \dfrac{T - T_a}{T_0 - T_a}$ and $a_i = \dfrac{2}{\mu_i J_1(\mu_i)}$

J_0 and J_1 are respectively the zero-th. and first order Bessel functions of the first kind, μ_i are the roots of J_0 and $F_0 = \dfrac{\gamma t}{R^2}$ is known as the Fourrier number.

Figure 3. shows the temperature profiles across the radius of the cylinder. It is seen that the process of heat transfer is essentially completed for a Fourrier number equal to 0.8 This means that for a typical carbon fibre for which $\gamma = 1.5 \ 10^{-3}$ m^2/s, a uniform temperature is attained after 4.6 10^{-7} s. As this time is much smaller that a quarter of a period of a 20Hz loading cycle it is concluded that the fibre and his surrounding matrix experience the same temperature fluctuations. In other words, for the thermoelastic stress analysis of fibre reinforced composites we don't need to go down to the micro-scale of analysing fibre and matrix separately. Indeed, a single layer of carbon fiber reinforced composite, can be treated as a homogeneous orthotropic material.
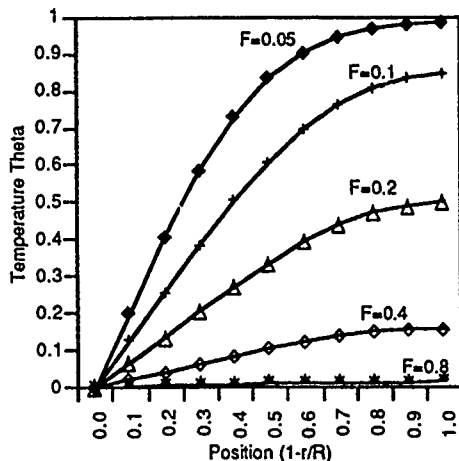
Fig. 3 Temperatures profiles of infinite cylinder.

From Fig. 4, it is seen that the diffusion process is finished when $F_0=0.5$. For a carbon epoxy lamina, with $\gamma=6\ 10-7\ m2/s$ and L=0.125 mm, this is after 0.013 s. As this is of the same order as a quarter period of a 20Hz cycle it is concluded that a complete homogenisation of the temperature between different layers will not occur. For the thermoelastic analysis of carbon fibre reinforced composite a single orthotropic lamina will be the basic building bloc to consider.

From the previous section we can conclude that the simple relation eqn. (2.) is not valid. For a more accurate representation of the problem each ply of the laminate will be considered separately. Since each ply can be treated as a homogeneous orthotropic plate, it may be shown from principles of mechanics and thermodynamics of irreversible processes [8] that, for quasi-static conditions and small temperature changes:

$$\sum_{i=1}^{3}\frac{\partial Q_i}{\partial X_i} = -\rho c_\varepsilon \frac{\partial T}{\partial t} - T_0[\alpha_{11}\Delta\sigma_{11} + \alpha_{22}\Delta\sigma_{22}] \qquad (6.)$$

where Q_i is the heat flux passing through the point under consideration, ρ is the density, C_ε the specific heat under constant strain, T_0 is the absolute temperature, α_{11}, α_{22} are the coefficient of thermal expansion and σ_{11}, σ_{22} are the stress components in the respective inplane orthotropic directions.

In general, a laminate consists of many plies of different orientations. Each ply can experience different stresses which may be computed by use of the classical lamination theory. At the interface between two layers high stress discontinuities may arise. Similar to the previous analysis, the process of heat transfer between plies may be assessed by considering an infinite plate initially at a uniform temperature being subjected to a sudden change in temperature at both its surfaces. The solution to this problem is given in eq.(5.):

$$\theta = \sum_{n=1}^{\infty}\frac{4}{\omega_n}\exp^{-\omega_n^2 F_0}\sin\omega_n x \qquad (5.)$$

with $\omega_n = n\pi$ and n=1,3,5,....

The fourier number in this case is: $F_0 = \frac{\gamma t}{L^2}$ in which L is the ply thickness.

As the in-plane stress gradients are much less than the stress gradients between plies, we can assume that the heat transfer during thermoelastic cycling is dominated by diffusion in the through-thickness direction. The heat conduction equation of Fourier gives:

$$\sum_{i=1}^{3}\frac{\partial Q_i}{\partial X_i} = -K\cdot\frac{\partial^2 T}{\partial Z^2} \qquad (7.)$$

where Z is the co-ordinate in the through-thickness direction and K is the corresponding heat conduction coefficient.

Defining the non-dimensional temperature $\theta = (T-T_0)/T_0$ and substituting eqn (7.) into eqn (6.) yields the classical one-dimensional diffusion equation:

$$\frac{\partial\theta}{\partial t} - D\frac{\partial^2\theta}{\partial Z^2} = S \qquad (8.)$$

where $D=K/\rho C_\varepsilon$ is the coefficient of thermal diffusivity and

$$S = -\frac{1}{\rho c_\varepsilon}[\alpha_{11}\dot\sigma_{11} + \alpha_{22}\dot\sigma_{22}] \qquad (9.)$$

represents an internal heat source.

Due to the complexity of this partial differential equation the solution is best sought by numerical methods. The recommended method for this type of problem is a Crank Nicolson finite difference scheme. We discretised each ply by 30 nodes and a typical time step of 0.02 π/ω seconds was used for all frequencies studied. Computation was done using double precision arithmetic. The full temperature

Fig.4 Temperature profiles of infinite plate.

field was solved every time step and the surface temperature was monitored.

Figure 5 shows both the computed and measured specimen surface temperature response when subjected to cyclic loading. Maintaining the convention of *Dunn et al.* all the amplitude data have been normalised by the corresponding result at 20 Hz.
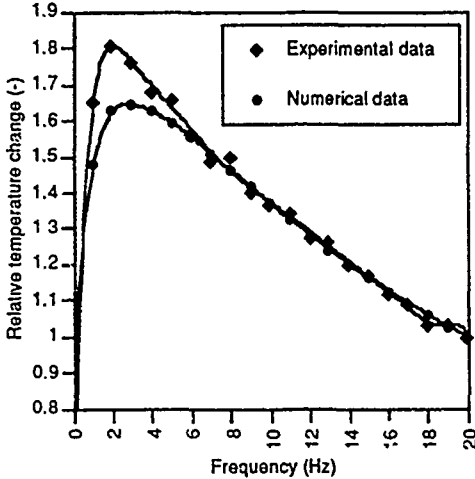
Fig. 5 Normalised amplitude data for [0°,90°2,0°5] laminate.

Despite the fact that a large number of material parameters, some taken from literature, were involved in the computation the agreement between numerical and experimental results is relatively good. It may be seen clearly from the computed results that there exists a maximum which corresponds to the transition from the domination of the surface temperature by the 90° plies to that of the 0° ply. As the frequency goes higher the heat conduction process becomes more adiabatic and the importance of the 0° ply increases. In fact the homogenisation of all the layers gives for this type of laminate an upper-bound and considering the surface layer alone gives for the thermoelastic effect a lower-bound.

5. Spate as NDT-device.

To acquire Spate results, it is essential to load dynamically the structure and correlate the signal coming from the infrared sensor with a reference signal. This way, any signal component with a frequency or phase different from the reference signal will be rejected. This is the main reason why Spate is so sensitive for small temperature changes. The implication of this is that it is impossible to measure any static temperature. During investigation of the motion problem, it was found to be interesting to be able to visualize the static temperature distribution on the surface of the specimen under consideration. By hardware modification of the Spate equipment, it is possible to monitor static temperature components. By adding an optical chopper to the system (see figure 6), the DC component of the infrared sensor signal is converted to a block function with frequency 2 determined by the rotation speed of the DC motor driving the chopper blade. It is essential that the chopper blade is made from exactly the same material as the specimen and that it has the same surface preparation. The chopper blade is on the same ambient temperature as the specimen is. However, it is not dynamically loaded. Under these conditions the peak to peak value of the resulting block function is proportional to the static change in surface temperature of the specimen and will be seen by the computer at the output of the correlator. By knowing a temperature at one point of the surface (i e. by thermocouple), it is possible to calibrate Spate equipment for static temperature measurements.
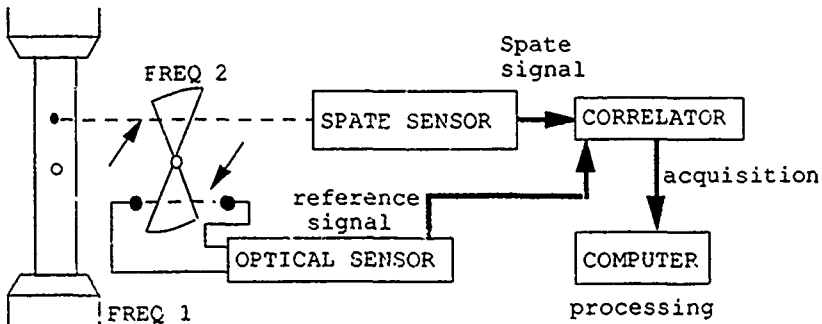
Figure 6. Basic principle of optical chopper

6. DAMAGE ASSESSMENT

Under cyclic loading conditions, fibre reinforced composite systems show an internal heating which can be used to monitor the damage initiation and evolution [11]

By modification of the SPATE-system, explained in previous paragraph, it is possible to measure in a very accurate way, the generated heat within the specimen. This internal heat generation is a consequence of viscoelastic effects and inter-laminar fretting due to damage growth. Figure 7 shows the SPATE scans of a specimen loaded in fatigue at 0.3 $\sigma_{failure}$ and a frequency of 10 Hz The material used was of a 914C-TS type carbon fibre composite and the lay-up considered was $(90°_3, 0°_4, 90°)_s$.

Figure 7. Static temperature field at 78, 387, 509, 597, and 688 10^3 cycles.

Cross reference with ultrasonic c-scans suggests that growing delaminations, and thus a growing damage state, is correlated with an increasing static temperature component.

CONCLUSIONS

It has been demonstrated that the thermoelastic relation as developed by Lord Kelvin is inadequate for fibre reinforced composite systems. A non-adiabatic model for the thermoelastic effect for laminated composite plates has shown relatively good agreement between computed and experimentally measured surface temperature response. It is concluded that, at lower loading frequency the process of inter-laminar heat transfer makes the direct interpretation of SPATE results very difficult The thermoelastic response is strongly dependent on the loading frequencies in the range of say 1-20 Hz. On the other hand, at very high frequencies only the surface ply is to be consider for the thermoelastic response.
By modification of Spate hardware, it was possible to monitor the static temperature distributions, whom are related to interior damage phenomenon.

REFERENCES

[1]   Stanley P., Chan W.K 'Quantitative stress analysis by means of the thermoelastic effect', Proc. Int. congress on exp mech SEM, June 1984, 547-554

[2]   Stanley P., Chan W.K., ' 'SPATE' stress studies of plates and rings unde. in-plane loading', experimental mechanics, dec 1986, volume 26, num 4

[3]   Owens R.H., 'Application of the thermoelastic effect to typical aerospace composite materials', Proc. SPIE Conf., Stress Analysis by

Thermoelastic Techniques, London, V731, 74-85 (1987)

[4]   Sandor B.I., Lohr D.T. and Schmid K.C., 'Nondestructive testing using differential infrared thermography', Materials Evaluation, V45, 392-395 (1987)

[5]   Wölfel H., Feickert W., 'Comparison of thermoelastic stress analysis and finite-element results', Proc. of the 9th Int. conference on exp. mechanics,Copenhagen Denmark, Aug. 1990

[6]   Henneke E. G., Jones T.S., 'Detection of damage in composite materials by vibrothermography', Nondestructive evaluation and flaw criticality of composite materials, ASTM STP 696, 83-95

[7]   Potter R.T., 'Stress analysis in laminated fibre composites by thermoelastic emission',Proc. SPIE conf., Stress analysis by thermoelastic techniques, London 731, 110 (1987)

[8]   Wong A.K., 'A non-adiabatic thermoelastic theory for composite laminates', J. Phys. Chem. Solids Vol. 52, No 3., 483-494 (1991)

[9]   Van Hemelrijck, D., Schillemans, L., et al, 'Comparative study between ultrasonic inspection and vibrothermography for the assessment of damage in Carbon Fibre Reinforced Plastics', Science and engineering of composite materials, Vol. 1. No. 4 1989, pp 109-116

[10]   D. Van Hemelrijck, L Schillemans et al., 'The use of thermoelastic emission techniques (SPATE) for damage analysis of graphite epoxy composites', International Colloquium on Durability of Polymer Based Composite Systems for Structural Applications, 27-31 august '90, Brussels, Belgium

[11]   K. Schulte, 'The continuous monitoring of fatigue damage in composite materials', International Colloquium on Durability of Polymer Based Composite Systems for Structural Applications, 27-31 august '90, Brussels, Belgium

PREDICTING FAILURE BY DEBONDING/DELAMINATION

by

G.A.O. Davies and P. Robinson
Department of Aeronautics
Imperial College of Science, Technology and Medicine
Prince Consort Road
London SW7 2BY
United Kingdom

SUMMARY

This paper highlights the need for predicting delamination or debonding in carbon fibre composite structures in two situations where the effect is crucial. Firstly interior barely visible damage due to low velocity impact, and secondly the debonded joint between panel and stiffener in a post-buckled compression panel. It is shown that for impact damage a stress-based failure criteria might work for thin plates less than 2mm thick but as the thickness increases a fracture model becomes necessary. A strategy for bridging this gap and also avoiding the need for a hypothetical flaw is advocated. An improved method for finding mode III fracture toughness is shown.

INTRODUCTION

Debonding and delamination are still the Achilles heel of high performance laminated composite materials in structures, and much effort has been expended in trying to understand the occurrence and preventing it by detailed design. The type of structure most under threat is the compression panel where delamination is much more debilitating than for the tension structure. The failure of stiffened compression panels of carbon fibre reinforced composites, particularly in the post-buckling regime, is almost certainly going to involve debonding at a stiffener/spar/rib support if these joints are co-cured or co-bonded rather than mechanically fastened. The other threat is that of internal delamination due to low velocity impact (BVID) and the current limitation of allowable strains to 0.3% – 0.4%, due to the combined threat of BVID in hot/wet environments, illustrates dramatically the sacrifice of more than 100% in strength which should not be tolerated. Both of these forms of degradation are discussed in this paper. Interim results are quoted from two ongoing projects sponsored by the EEC Brite-Euram programme. These two projects are respectively "Design methodology for improved damage tolerance in carbon composite structures, BE 3159," and "The post-buckling behaviour of CFC structures, BE 3160." Both of these projects involve consortia of industrial and research establishments, in particular British Aerospace, MBB, Fokker, Dornier, CASA, SAAB, Dassault, NLR, the Katholieke University of Leuven, and Imperial College.

DELAMINATION BY LOW VELOCITY IMPACT DAMAGE

Although the theme of this workshop is not impact damage, the main results of low velocity impact can be barely or totally invisible internal delamination. A hidden menace. The term "low velocity" should be defined since high velocity produces local ballistic types of damage, far from invisible, and extremely local. Simple coupon tests suffice to demonstrate the behaviour of a full scale structure. The term low velocity is defined as that lower bound which does not excite through thickness stress waves but allows the structure to respond dynamically so that the thin plates deform as in classical thin plate theory rather than local 3-D stress fields. It may be shown [2] that this velocity is of order the speed of sound in the matrix x the failure strain threshold. This turns out to be about 20m/sec in carbon fibre composites, so we are considering tool drop and similar accidents.

The current philosophy is to conduct drop tests and then test for residual "compression after impact" strength. The coupons mostly used are 125mm x 75mm (attributed to Boeing) and 200mm x 200mm (attributed to MBB). However the low velocity dynamic response of real structures may be far from the response of a coupon compared with which it may be stiffer or more flexible, and in the typically 3 to 6m/sec impact event, much energy can be absorbed elastically by a surrounding structure. To test all likely and different impact sites on an aircraft wing or fuselage is not feasible, so some sort of reliable theoretical/experimental predictor is invaluable.

Even to use two different sets of "standard coupons" with possibly two boundary conditions (simply supported and clamped) is to confuse comparisons between tests. It is conventional to map damage and residual strength variations against incident energy since this is how the threat is usually defined yet clearly variations in specimen stiffness will result in different elastic energy absorption. This paper therefore addresses several topics

- How to relate damage to the incident energy and allow for test specimens of different dynamic responses

- How to translate coupon damage to real components and assess the compression after impact strength

- How to predict damage theoretically without conducting coupon tests at all.

This latter task has been approached in two ways. Firstly, by SAAB using DYNA 3-D, a very detailed finite element model reconstructs the impact event. The model deploys tiny eight-node bricks per lamina and is very computer intensive, but it should reveal the limitations on numerical simulation which are due to incorrect modelling of the physics rather than the strain field. Recognising that 3-D simulation of realistic structural details will involve many supercomputer hours, a second approach by Imperial College has used simpler composite plate elements and another finite element code FINEL 77. This has been used to test the limits on simulating the failure process, but also to use a fall back strategy if all else fails. This strategy postulates that the low velocity impact damage depends primarily on the impactor contact force signature for a given plates' local layup. This force history can be readily simulated by a crude finite element model and therefore enables

as to embed a coupon calibration test in any structure and predict the nature of the damage from the force history. There could also be near surface damage due to bending strains alone and these are separately modelled and monitored

All these strategies have been validated by tests on plates made from HTA T800 6376 prepreg using a basic quasi-isotropic layup [±45, 90, 0]$_{ns}$ with n = 1,2 and 4 The 1mm 8-ply plates are thinner than most primary structures but have been chosen to contain the DYNA 3-D computing time to one or two hours during this modelling validation stage

Test Results and Conclusions

The tests have used a drop test rig capable of monitoring impact force, plate strains, and velocity during the event The damage areas have been diagnosed by C-scan to get the envelope, and by using high frequency scanners and image processing at KUL. Figure 1 shows the C-scan image with increasing incident energy. Initially the interior delamination is invisible and almost circular, but this is deceptive Figures 2 and 3 show the several layers of delamination of a characteristic "peanut" shape extending in the direction of the local fibres. At higher incident energies the plates' response is a bending mode and matrix cracking normal to the surface fibres starts to propagate for the top one or two laminas The elongation shown in Figure 1(d) depicts this. The results of mapping damage against force history are dramatic and confirm that we can indeed allow for the different dynamic responses Using two sets of plate sizes with both simply supported and clamped boundary conditions allows four sets of results to be compared Figure 4(a) shows that the use of force makes the variations between specimens indistinguishable. Surface fibre splitting started at about 800N and the sudden rise at 1100N coincided with this back-face splitting The more conventional use of incident energy in Figure 4(b) does separate the stiff and flexible plates, and in Figures 5(a) and 5(b) this becomes much more acute for the 2mm plates The changing damage mode is also not obvious in the energy maps The 4mm and 6mm plates are being evaluated but a preview from some early Fokker tests is shown in Figure 6 Here only three energy levels have been selected, but the force map is still more convincing We now briefly describe the numerical models needed to predict force history as well as give a possible insight into the failure process

Prediction of dynamic response and damage

The 3-D model using the DYNA 3 D simulation is shown in Figure 7 This is a crude model using three element through the thickness with smeared properties, a total of 1500 8-node bricks for a quarter of the plate The impactor needs to be modelled geometrically accurate at the contact point to avoid singular loading which would precipitate hour-glassing After a dynamic simulation is completed to the end of the half period, a finer substructure of 225 elements can be extracted using lamina size bricks, and the interface of this substructure is then excited by the displacement and velocity histories saved from the first analysis This global-local strategy reduces the computing time enormously which nevertheless still takes up 1 2 hours on a CRAY XMP48 A detailed output of strain history revealed strain rates up to 85 per second but for less than 10microsecs, they then fall almost immediately to about 10 per second for the rest of the event Tests conducted by KUL show that there is no strain rate effect on 0° fibre dominated properties and even for 90° tests the strength enhancement and modulus softening do not come in until rates of 20 or more per second Strain rate effects therefore seem of no consequence for the carbon composites discussed here

A much less expensive finite element model will suffice if only the force history and bending strains are needed, plus a mean estimate of the interlaminar shears Our finite element code,

using an explicit mode for integrating the equations of motion, has deployed only sixteen 9 noded Mindlin plate bending elements, which include shear deformation (see Figure 8) Figure 9 shows the predictions of force and the test results before and after a modest filter to remove noise. The experimental force is measured directly by a load cell at the impactor tip The response is almost sinusoidal with no higher frequency ringing suggesting that the peak force can be predicted by simply equating maximum strain energy to incident kinetic energy. This turns out to be true in this case, but not so for stiffer plates Notice that the predicted deflection of 1.5mm is less than the 2mm plate thickness in this example, but for larger plates this is not so and it is necessary to allow for the non-linear stiffening which can occur even for modest strain levels Figure 10 shows the response for the larger 200mm x 200mm x 2mm thick plate where the maximum deflection predicted by a linear model would exceed 5mm The non linear deflection shown agrees well with the impactor test right up to bouncing, and with the plate thereafter The higher force predicted shows the effect of non-linear stiffening, and now there is some higher frequency response. The 4% critical damping used in this model could be tuned to remove the slight phase change (but hasn't) Figure 10b shows results for another nonlinear impact on 1mm plates with displacements exceeding 5mm The agreement with the full 3-D model is excellent, but of course no damage degradation has been incorporated This is also reasonable for modest interlaminar delamination but less so for large amounts of near surface failure when the flexural response could start to change The finite element predictions for surface strains turned out also to be reliable. Strain gauges were placed along the surface 45° fibre directions where it was observed that surface fibre splitting developed. Figure 11 shows the experimental and theoretical histories for strains at 6mm and 17mm from the impact zone The surface splitting at 1 3msec destroyed the gauges at a strain normal to the fibres of about 0 9% which compares with the KUL prediction of 1% at these strain rates of 10 per second Although we have no direct way of measuring the interlaminar shear strains we can compare the mean (Mindlin) shear strains to the value of the shear we would expect in a statically loaded axi-symmetrical plate, i e load + 2πrtG. In fact the shears in this quasi-isotropic layup are not quite axi-symmetrical but the quasi static approximation is valid (For a maximum impactor load of 2000N the net inertia force in a plate radius of 20mm was less than 1N) Figure 12 shows the finite element and test deduced shear strains

Having some confidence in the numerical predictions, the next stage is to test the assertion that a coupon test may be embedded in a stiffened panel via finite element predictions of force history But before this it is tempting to try and predict the delamination and surface fracture using the theoretical strain histories, and thus avoid coupon testing altogether It is the intention to use 3-D models to test various strategies for predicting damage thresholds and growth such as

- Some permissible equivalent stress or strain level

- Some equivalent fracture toughness and energy release rate

- A damage mechanics model

The finite shell element will not deliver through thickness peeling stress so damage mechanics is out, and in any case a special resin-rich layer would be needed to predict delamination We therefore turn to the first two criteria to assess their success in predicting delamination thresholds and extent. Our analysis models are highly idealised at this stage but serve to illustrate which criteria are likely to be productive in a full 3-D model with multiple delaminations. Simplified models not only target the physics specifically, if only

moderately successful they can isolate the important parameters which enable us to produce better designs by changing the influential material properties

The first criteria is tempting. The two most common methods for defining interlaminar shear strength are the Iosipescu test and the short beam in three or four point bending. The four point bending tests avoid the likelihood of damage at a single central load and agree well with the Iosipescu tests. Moreover similar strengths are obtained with specimens either 8 ply or 16-ply thick so a stress based criteria seems to work. There is some theoretical basis for this if we examine the energy release rate for a central delamination in the three point bend tests. Details are given in the annexe where it is shown that the mode II energy release rate is

$$G_{II} = \frac{9}{64} \frac{P^2 a^2}{B^2 E h^3}$$

so the failure load

$$P = \frac{8}{3} \frac{B}{a} [E h^3 G_{IIC}]^{\frac{1}{2}}$$

If a stress-based criterion is used,

$$P = 2\bar{\tau} \, B2h$$

where $\bar{\tau}$ is the mean shear, or $\frac{2}{3}$ x the interlaminar strength τ for a parabolic variation in a uni-directional specimen. Thus we expect fracture to take over from stress based criterion when the two are equal, i.e.

$$a = \sqrt{E h G_{IIC}/\tau}$$

For uni-directional CFC we use E = 140GPa, G is 0 8N/mm, τ = 90MPa, and we take a beam depth of 2mm to agree with the depth of 16-ply recommended by CRAG (2) We therefore find a half crack length a = 3 7mm. This is far in excess of both observed flaws and assumed "effective" crack lengths of order 2mm [4], so we expect a stress based criteria to predict initiation of the delamination and thereafter the crack to be unstable when it exceeds 3 or 4mm

We now look at a simplified axi-symmetrical interlaminar shear strength model for our quasi isotropic plate We could actually dispense with the axi-symmetric model and use our 2-D finite element model to extract the interlaminar shear stresses by integrating the equations of equilibrium through the thickness This has been done [5] and does indeed reveal the peanut profiles mentioned earlier Our simplified model for the quasi isotropic axi-symmetric plate simply uses the maximum shear stress

$$\bar{\tau} = P/2\pi rt,$$

where t = 2h, and putting $\bar{\tau} = \frac{2}{3}\tau$, and the area inside the delamination front A = πr^2, we find

$$A = \frac{9}{16\pi^2} \left(\frac{P}{\tau}\right)^2 \qquad (1)$$

This criterion has the advantage that it should not be too sensitive to the number of delamination layers since the shear stress distribution does not change much in the middle two thirds of the plate depth It should cease to be valid close to the impact point where the stress field is no longer 2 D, so equation (1) should be curtailed at r = t or 2t say, or A πt^2 or

$4\pi t^2$ It will also cease to be valid when the surface bending strain takes over as the failure mode In our tests the delamination planes were invariably and obviously between dissimilar orientations 0/90 and 0/±45 (for which the strength is somewhat smaller) The curve (1) for τ = 50MPa is superposed on the test results in Figure 4 and the agreement appears to be encouraging up to a force 1100N when the failure mode definitely switches However if we impose equation (1) for t = 2mm on Figure 5 we find the agreement is now poor, even as a lower bound, and for Figure 6 it fails completely. Whenever a stress-based criterion fails to scale with structure volume, we usually turn to fracture mechanics to explain

In the annexe we show the axi-symmetrical solution for an internal delamination in the mid-plane, and the consequent energy release rate when the circular patch grows This solution is a very simplified approximation since the material is assumed isotropic This is only approximately true for quasi-isotropic layups and only for laminas in excess of 16 ply will the effective moduli in tension and in flexure be nearly the same The presence of multiple delamination is also ignored here, which will tend to diminish slightly the ratio of energy release rate per unit area However the analysis does show rather surprisingly that for this case, the mode II energy release is constant and does not depend on delamination radius or plate dimension This at least relieves us of the need to invent a hypothetical initial flaw The critical value (equation iii) is given by

$$G = \frac{9 P^2 (1-v^2)}{64 \pi^2 E h^3}$$

or the critical applied load by

$$P_c^2 = \frac{8\pi^2 E(2h)^3 G_c}{9(1-v^2)} \qquad (2)$$

(This closed form solution is a very convenient benchmark for testing the degree of refinement needed in a numerical finite element model for energy release.)

For the quasi isotropic layup and using ENF tests for propagation (not initiation) we use E = 60GPa, G_c = 0 8N/mm, v = 0 3 Then

$$P_c = 680t^{3/2} \qquad (3)$$

We thus expect no internal delamination at values below equation (3) and then a growth without further load increase until another (surface) failure mode takes over Figure 13 shows the three critical loads given by equation (3) for t = 1,2, and 4.3mm compared with test values for rapid increase in area Considering the crudity of the model the trend certainly seems to be captured, and much more successfully than the interlaminar shear strength-based criteria It explains why there is a threshold for delamination rather than using the arbitrary lower band r = 2t in equation (1) If anything the trend to a fracture model increases with plate thickness as shown in the annexe It remained now to simulate the energy release in a finite element model, relaxing the axi symmetric assumptions, and attempt to predict the change in fracture mode from internal delamination to surface fracture.

Without turning immediately to the general finite element solution, the trend can again be captured by the axi symmetric analytical solution We concentrate on the delamination front radii corresponding to the three critical loads given by (3) and in Figure 13 The critical loads increase as $t^{1/2}$ whereas the bending strains depend on P/t^2 and the position which

decreases like $ln\,(a/R)$ If we use these with the critical loads of 680, 1923, and 6060, we find the bending strains actually decrease. The crucial strains at right angles to the ±45 fibres turn out to be 1.9%, 0 7% and 0 4% Only the middle values get close to the expected failure threshold, but more importantly they decrease with position and cannot be used as an independent criteria It looks therefore that a fracture criteria needs to be used for surface in interfibre splitting and this is going to be difficult to model It is not through thickness fracture, although a fairly definite radial splitting between fibres is accompanied by a circumferential delamination below the split lamina surfaces

These results are at variance with earlier work at NASA Langley [21] where a transition from initiation to propagation was detected and modelled, and as the plate thicknesses were increased the failure was governed by the shear strength and not in a fracture mode

Numerical evaluation of energy release rate G

The above simplified treatment was only to illustrate the trend and to try to identify the delamination driver To predict even statically the delamination front and its growth in complex geometric situations, we need to use a suitable finite element model. 2-D plate elements are preferable if they mimic the real life problem, but 3 D bricks may be needed. However it looks as if quite crude algorithms for G are adequate This is a little surprising when one considers the effort devoted to modelling fracture in the elasto-plastic metal community There are a wealth of virtual crack tension methods, J integrals, and hybrid mixtures usually justifying a crack tip singular element to capture the $r^{-1/2}$ strain field near the crack front It looks now as if this is not necessary for delamination fracture A modified crack closure method [6] has been shown to work using nodal forces ahead of the crack x the corresponding nodal crack-opening displacements just behind the crack front [7]. By selecting all three nodal components it is possible to extract all three modes I, II and III values of G. That this works equally well for 3 D bricks and 2 D plate elements indicates that it is not necessary to simulate the singular field at all Providing that the crack tip strain fields are self-similar, then the energy release rate effectively determines the release due to the basic non-singular strains and stresses The crack tip field is not simulated precisely and if the composite material is ductile enough to flow, or if there is significant fibre breaking or bridging, we assume these effects are encapsulated into the experimental values for G_c These issues turn out to be important again in the compression panel stiffener debonding problem.

THE POST-BUCKLED COMPRESSION PANEL

There is no shortage of evidence from industrial sources that the ultimate strength of stiffened carbon composite compression panels is determined by the strength of the bond between panel and stiffener [7], particularly if the ultimate design load is close to or in excess of the initial buckling load The nature of the stress field between stiffener and panel can be complex, and what to do with the solved stresses is still not clear, but to build confidence in our predictive capability we should not just rely on the experimental failure load and a post mortem on the observed failure mode. One can always tune failure criteria to match a given test and then discover that a different configuration requires different curve fitting. If the problem is internal fracture by delamination, one needs to locate the source of failure with some certainty

Some years back [9] we decided to investigate the onset of post buckling failure in a series of long simply supported panels whose width/thickness (b/t) ratios gave a range of

failure/initial buckling loads from 1 to 3 A series of stacking sequences were also chosen

$$(0/90/\pm45)2s,\quad (0/\pm45/90)2s,\quad (45/0/-45/90)s3$$

A small hyperstiff displacement-controlled panel buckling machine was available and the onset of delamination was captured using acoustic emission sensors as early warning devices, followed by C-scanning We found that edge delamination started as late as 95% of the failure load and the delamination spread rapidly across the panel The sources were all at the node lines of the buckled mode and occurred in all layups at ±45 interfaces in a regular patten along the panel alternating above and below the panel centre surface and on opposite edges. (C-scans are shown in Figure 14) It had been anticipated that edge delamination was likely but might have been expected at the buckled crests where the longitudinal stress resultants N_{xx} were a maximum (see Figure 15). In common with Starnes and Rouse [8] we found that failure occurred at the node lines It transpired that the through-thickness stresses responsible were partly due to the usual edge effect associated with N_{xx} but also – and in equal measure – due to the twisting moment M_{xy} whose shear stresses σ_{xy} have to decay to zero at the simply supported edge A detailed finite element model was constructed using three brick elements per lamina in a zone 8mm (4t) from the edge In order to contain the size of the model it was argued that stress variations along the panel direction (x) varied with a half wave length of order of panel width b, which was large compared with the boundary layer edge effect Thus a 2-D analysis is reasonable The results are shown in Figure 16 and indicate just how complex edge effects can be However we were able to locate precisely the stress component (τ_{xz}) and the level at which delamination was occurring in the alternating pattern observed and due to M_{xy} A fractograph post mortem of the failure surface confirmed the direction of shearing The theoretical magnitude of 80MPa was not too dissimilar for the current interlaminar shear strength for XAS/914 The prediction of failure for a whole series of b/t ratios and stacking sequences was on average exact, to within a standard deviation of 12% compared with predictions based on maximum fibre strains which were more than 40% to conservative

However the agreement was to a certain extent fortuitous, since if we refine the finite element mesh then the peeling stresses would undoubtedly appear singular at the free edge, and a case for fracture by delamination was clear Unfortunately the significance of the twist induced longitudinal stress σ_{xz} meant we needed to know the mode III toughness, which highlighted the need to design a pure mode III test and described later. Another feature of this study was that an analytical boundary layer solution was possible for both N_{xx} and M_{xy} (Reference [9] and Figure 17) where it was shown that the edge effect would extend to a distance of order $t\sqrt{\dfrac{G_{xy}}{G_{xz}}}$ This is important in constructing finite element models In isotropic materials the boundary layer is of order t whereas for a typical composite ratio $G_{xy}/G_{xz} = 10$, and a boundary layer of order 4t or more As part of the current Brite Euram project mentioned we will use a new hyperstiff 250 tonne testing machine with platens 0 5m x 1 5m and panel length up to 1 5m We thus expect to be able to monitor panel and stiffener debonding failure as soon as it initiates, so it is worth summarising the analytical predictive techniques we expect to be able to validate

Prediction of stiffener debonding in post-buckled compression panels

The prediction of internal stress resultants and their behaviour well into the post buckling regime does not appear to be a

problem. For a proposed I-stiffened compression panel, having post-buckling strength in excess of twice the initial buckling load, identical behaviour has been predicted by several finite element codes NASTRAN, ELFINI, ABAQUS, PANDA, and FINEL 77. The big question is what to do with the answers, and can we use stress-based criteria, fracture mechanics, or is something else needed?

We might expect the debonding stresses to depend on whether the stiffener is carrying a net resultant or whether it is simply accumulating stress by diffusion. The stiffener may resist panel normal loading (due to fuel pressure for example) or experience "lift-off" forces due to post-buckling curvature, or it may provide a torsional resistance at points along its length. Such loading (Figure 18(a)) involves a net resultant force between panel and stiffener. On the other hand (Figure 18(b)) the internal stress resultants N_y, M_x, M_{xy} etc will equilibrate across the stiffener but still allow stress to diffuse into the stiffener flange and hence cause debonding shears and peeling stresses. As a matter of fact the stress concentrations at the stiffener edges depend on a local boundary layer in both types of loading, although the consequent propagation of delamination might be different for type (a) and (b). The length of the boundary layer in the vicinity of the stiffener edge is now roughly of order

$$\frac{1}{[th\,E_{yy}/G_{yz}]^{\frac{1}{2}}}$$

where t is the stiffener flange thickness and E_{yy} the equivalent modulus in the y direction h is the equivalent thickness of the resin-rich bond layer and G_{yz} the bond shear modulus. The modulus ratio can be in excess of thirty but this is counteracted by the usually small thickness h, hence the boundary layer can be only of order t. In fact there is a secondary layer due to the bond transverse modulus E_{zz} and this can be very small leading to high gradients and peel stresses near the stiffener edge. Once again a linear elastic solution is likely to lead to a near singular stress field, and suggests a fracture approach would be more realistic. However stress-based criteria have been quoted as leading to reasonable predictions. One method uses a structural mechanics approach replacing the bond by an elastic foundation having shear and tensional stiffness (the interfacial stress field model) and uses the Hill-Tsai criteria to couple the consequent shear and peel stresses. In Reference [7] the prediction of stiffener debonding for a buckled panel under shear and compression is compared with test and the agreement is impressive although no attempt is made to simulate delamination by fracture.

Another stress-based simulation in Reference [10] tackles the normal pressure (0 05MPa) case with direct stiffener loading. After global post-buckling analysis the skin-stiffener stresses were solved using a very refined 8-noded brick model in a substructure having a length of 6 elements in the x direction (a 2-D slice is possible providing the bricks have warping freedoms). Stresses were evaluated for a realistic case but no experimental confirmation of failure was available.

A recent report uses a more economical model deploying high order (56 degrees of freedom) plate elements for skin and stiffener with an interface element to return the bond strains all three strain components are combined in a quadratic interactive failure criterion. As an alternative it was assumed also that peeling would initiate at a threshold bending strain due to M_x at the stiffener edge. This threshold was found experimentally using a 4-point bending test. No attempt was made to evaluate the effects of N_y or M_{xy} (as in Figure 18). Post buckling tests in a shear rig showed that stiffener

debonding occurred quite closely to the predicted strain level, but other loading cases needed to be verified.

In the present BE 3160 programme it is intended to compare stiffener debonding predictions with test as mentioned earlier, but a fracture delamination model should be fully assessed since no stress-based criteria can be 100% reliable when the magnitude of the interface stresses depends on the degree of refinement of the finite element model - assuming no material or non linear softening of course. Currently we only have one first-hand evaluation to date, in a series of tests conducted by partner Dassault in 1988 [12]. A series of fundamental tests was carried out whereby a blade stiffener was subjected to a resultant pull off load, as shown in Figure 19(a) and 19(b), and an indirect diffusion loading Figure 19(c). In case b the degree of flexure in the skin panel was controlled by varying the span between the supports. This type of loading causes unrealistic stress concentrations but the objectives were to test the validity of stress based or fracture-based criteria. Two resin-fibre systems were tested. The finite element model was a 2 D assembly of bricks with the linear bending and twisting strains as background and the generalised warping field $u(y,z)$ to be solved. The number of elements exceeded 7,000, and Figures 20 and 21 illustrate the extremely fine assembly used to obtain accurate energy release rates for central delamination (19(b)) and for edge delamination (case 19(c))

The stress-based criterion used was the familiar quadratic

$$\left(\frac{\sigma_z}{\sigma_r}\right)^2 + \left(\frac{\tau_{yz}}{\tau_r}\right)^2 = 1$$

where the rupture stresses were $\sigma_r = 16MPa$ and $\tau_r = 50MPa$. In all cases when the failure load was applied numerically the criterion was exceeded handsomely (particularly since σ_z was greater than 16MPa alone in most cases) and the singular nature of the field at the flange tip clearly cast doubts on the stress-based criterion for case 19c - see Figure 22. The energy release rates for cases 19a and 19b were dominated by mode I and were unstable, so have the problem of choosing the initial flaw (The size of the Bermuda Triangle?) Disbonds of 3mm were incorporated in the specimen and values of G_{1c} were then deduced to be 330 and 200J/m² for the two materials. Case 19c was then simulated for flaws at the edge and found to result in an almost constant energy release rate after a flaw length of 1mm. Mode II dominated. Two interactive criterion relating G_I/G_{IC} and G_{II}/G_{IIC} were then tested (linear and quadratic) to see if a constant value of G_{IIC} emerged. For one material T300/914 the values were quite inconsistent but for G803/914 the values were in the range 300 to 325J/m² for the quadratic criteria. These seem a little low, and clearly more basic tests are needed.

The picture so far seems uncertain, but the daunting problem of modelling in 2-D's the detail skin-stiffener junction now seems no longer to be daunting. The use of energy release therefore does seem to offer the best scope for realistic criteria, even though the problem of initial flaw size remains to be chosen for those cases where $\partial G/\partial a$ is positive. However there are encouraging signs that an alternative approach may be cheaper and more convenient to use. The idea is developed in Reference 13 to use an interface element for the finite stiffness up to a stress level limit and then a non linear softening such that the total energy to failure corresponds to the known value of G_{IC}, G_{IIC}, or G_{IIIC}. Initial tests seem promising and no more artificial than damage mechanics.

MODE III FRACTURE TOUGHNESS

The difficulties of validating a fracture approach to delamination and debonding have been highlighted and a suitable interaction formula forms part of that validation process. As mentioned when discussing the need to include warping elements in 2-D models, and the possibility of energy release due to twisting moments, there is considerable uncertainty in knowing what value to use for mode III toughness. The measurement of mode III delamination toughness has received relatively little attention, in comparison with modes I and II because it has proved difficult to devise a satisfactory test for this mode of fracture. Indeed a recent review [14] concluded that no satisfactory test exists for mode III. A number of mode III test techniques have been proposed in the literature. These include the Crack Rail Shear test (CRS) [15, 16] and the Split Cantilever Beam (SCB) [17,18,19,20] and these are shown diagramatically in Figure 23. Unfortunately neither of these test methods has proved satisfactory.

In the CRS test the crack growth was reported to be non-uniform as indicated in Figure 24 and often crack jumping was observed. Also because of the high loads required to cause delamination, slippage between rails and the specimen occurred in some cases. The SCB specimen suffers from the considerable disadvantage that the delamination growth is not pure mode III but is in fact mixed mode II and III. This is due to the existence of a bending moment in the crack front in addition to the shear force which is required to drive the crack in mode III. The bending moment in one arm causes, say, tensile stresses at the upper face while in the adjacent arm the flexural stresses are compressive at the upper surface. Thus at the two surfaces the predominant modes are mode II leaving only the centre of the crack front in the desired mode III. Figure 25 shows a finite element prediction of the distribution of both energy release rates at the crack front from the centre to a surface.

Supported by the UK Defence Research Agency (Aerospace) we have overcome this problem by redesigning a modified SCB test rig so that the applied forces align themselves with the current position of the crack front. The U-shaped rig is shown in Figure 26 together with the finite element model used to predict the success of this arrangement. The mode II opening is virtually zero and the mode III release rate almost constant. The success of this test method can be judged by the scanning electron microscope photographs of the fracture surfaces shown in Figure 27 for carbon epoxy XAS-913C uni-directional laminates. The pure mode II specimen (which is easier to achieve) shows characteristic hackles as the crack front shears across the fibres. These are present again in a standard SCB specimen (b) except on the centre line but in the new rig (c) are virtually absent. We are now finding pure mode III toughness values for this composite to be approximately 1,000J/m² compared to half this value for mode II. These values are not yet as repeatable as we would like and the rig is now being modified so that the loads in Figure 26 are more precisely in line with the crack front rather than offset by half a bar thickness.

CONCLUSIONS

The work reported upon in this paper forms part of three separate research projects, but they all have one thing in common. Is the onset of debonding and delamination a brittle fracture process and can it be predicted using current or future analysis methods? The ability to predict energy release rates numerically is here with us now and the use of friendly and rapid finite element pre-processors to create models in a global/local strategy, plus the dramatic decrease in cost of powerful workstations, puts us in a strong position to simulate delamination energy releases. However there remains the problem of identifying the source – possibly multiple sources – of delamination in the first instance. A strong bond is no consolation if the failure starts in the adjacent adherent due to the through thickness stress field caused by the loading and by discontinuous geometry.

REFERENCES

1. Williams J G. "On the calculation of energy release rates for cracked laminates". Int Jnl Fracture. 36, pp101-119, 1988.

2. Godwin E W & Davies G A O. "Impact Behaviour of Thermoplastic Composites". "CAD in Comp Mat.Tech.". Ed. Brebbia, de Wilde & Blain Pub Springer-Verlag. April 1988.

3. Curtis P T (Ed.) "CRAG test methods for the measurement of the engineering properties of fibre reinforced plastics". RAE TR88012 (Farnborough) February 1988.

4. Davies G A O & Cui de Yu "Three dimensional edge effects in composite plates". Computers & Structures 31, no. 1, pp11-16, 1989.

5. Wang H & Vu-Khanh T. "Low Velocity Impact Damage of Carbon/Peel cross-ply laminates" ICCMVI, paper 32-E-2, Hawaii, 1991

6. Rybicki E F & Kanninen M F "A finite element calculation of stress intensity factors by a modified crack closure integral". Engng Fracture Mech. 9, pp431-738, 1977

7. Paul P C, Saff C R, Sanger K B, Mapler M A, Kan H P and Keutz E F "Out of plane analysis for composite structures" Eight DOD/NASA/FAA Conference on Fibrous Composites in Structural Design. Norfolk Virginia, November 1989

8. Starnes J H & Rouse M "Post-buckling and failure characteristics of flat rectangular graphite epoxy plates loaded in compression" Proc. AIAA/ASME/AMS 22nd Street, Struct Dyn. & Maths Conf 1, pp423. April 1981.

9. Davies G A O, Buskell N and Stevens K A "Edge effects in failure of compression panels" EUROMECH. 214, Symp. on Composites. Elsevier, 1986

10. WiggenRadd J F M & Bauld N R "Interlaminar stress anlysis at the skin/stiffener interface of a grid-stiffened composite panel" Composite Structures 6, Paisley, Pub Elsevier, 1991

11. Hachenberg D & Kossira H 'Theoretical and experimental investigation of stringer peeling effects at stiffened shear loaded composite panels in the postbuckling range ICAS-90-4 3.1

12. Criteres Locaux de rupture de panneaux raidis en composites carbone/epoxy et tenue au dephage de rayon. Ref. MD-BA N.S 26322, 1988

13. Schellekens J C J & de Borst R "Numerical Simulation of free edge delamination in graphite-epoxy laminates under uni-axial tension" Composite Structures 6, Paisley, Pub. Elsevier, 1991

14. Martin R H. "Interlaminar Fracture characterisation a current review" NASA CR-187573. July 1991

15. Becht G & Gillespie J W Jr "Design and Analysis of the Crack Rail Shear specimen for Mode III interlaminar fracture' Composits Science & Technology. 31, pp143 157, 1988

16. Becht G & Gillespie J W Jr "Numerical and experimental evaluation of the Mode III interlaminar fracture toughness of composite materials" Polymer Comp. V10, No.5, October 1989

17. Donaldson S L "Mode III interlaminar fracture characterization of composite materials". Composites Science and Technology. 32, pp225-249, 1988

18. Lingg C L "Characterization of delamination in advanced composite materials under Mode III loading" Master's Thesis, Air Force Inst of Tech, Wright-Patterson AFB OH, Dec 88.

19. Chai H. "Shear Fracture", Int Journal of Fracture. 37, pp. 137-157, 1988

20. Martin R H. "Evauluation of the split cantilever beam for Mode III delamination testing" NASA Technical Memorandum 101562, March 1989

21. Bostaph G M & Elber W. "A fracture mechanics analysis for delamination growth during impact on composite plates" ASME Winter Conference, 1982

ANNEXE
Energy-Release Rates for internal delamination

The energy release rates for edge delaminations are well known indeed the Edge Notched Flexure test for beams is the most common method for determining mode II critical rate G_{IIC}. For a beam of width B and depth 2h, with a crack length a, it is known that a tip load P produces a rate

$$G = \frac{9\,P^2a^2}{4\,B^2\,Eh^2}. \qquad (i)$$

The corresponding rate for the centre notch in Figure A1 needs a little explanation
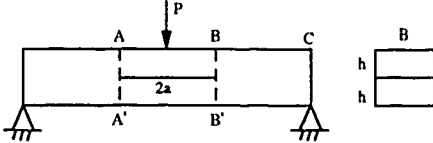
Figure A1

The outer portion of the beam BC is statically determinate and the rotation of BB' imparted to the central portion AB is exactly the same for the unotched or notched beam. This rotation produces bending moments in each split half, and equal and opposite forces These latter will be constant from A to B assuming no friction between the halves, so the applied load P is resisted by the gradients of moment in AB and A'B' and shared equally since the two halves move together. The difference in the internal strain energy U in the centre portion A-B can therefore be found in terms of the additional deflection of a centrally loaded beam clamped with respect to the two faces AA' and BB'.

For the undelaminated beam we have

$$\delta_u = Pa^3/2EB(2h)^3,$$

and for the notched version where the load is shared,

$$\delta_n = \frac{P}{2}a^3/2EBh^3$$

so the net gain in strain energy

$$U = \frac{1}{2}P\,\delta_n - \frac{1}{2}P.\delta_u = \frac{3}{32}\frac{P^2a^3}{.EBh^3}$$

In an incremental delamination therefore we have

$$G.B\ 2\delta a = \frac{\partial U}{\partial a}.\delta a,$$

$$\text{or } G = \frac{9\,P^2}{64EB^2h^3} \qquad (ii)$$

Notice that the critical load, for a given crack length, varies as $h^{3/2}$ For a given beam length, if flexural compressive or tensile stress were the failure criterion, the load would vary as h^2, so as the beam depth is increased any tendency to failure in conventional flexure mode could be overtaken by delamination fracture. This phenomenon is known, and reappears again in different form for the plate problem.

The general composite plate problem is formidable, so we use a simplified model, to try to capture the trend, by assuming axial symmetry. It is possible to use quasi-isotropic layups like [0, 90, ±45]sn having 'n' layers, and if n is sufficiently large the effective moduli in extension and flexure will be the same, and the following analysis a good approximation.

The corresponding central deflections for a clamped plate of radius 'a', and for the notched plate with a central delamination, can be found to be

$$\delta_u = 3Pa^2(1-v^2)/4\pi(2h)^3 \text{ and } \delta_n = 3\frac{P}{2}a^2(1-v^2)/4\pi h^3$$

Thus net energy gain $U = \frac{1}{2}P\,(\delta_n - \delta_u) = \frac{9\,Pa^2(1-v^2)}{64\pi Eh^3}$

and equating $\qquad G\ 2\pi a.\delta a. = \frac{\partial U}{\partial a}.\delta a,$

we find $\qquad G = \frac{9\,P^2(1-v^2)}{64\pi^2 Eh^3} \qquad (iii)$

Note once more that this is independent of the plate size or boundary conditions

(a) F_{max}=1770N

(b) F_{max}=2050N

(c) F_{max}=2290N

(d) F_{max}=2325N
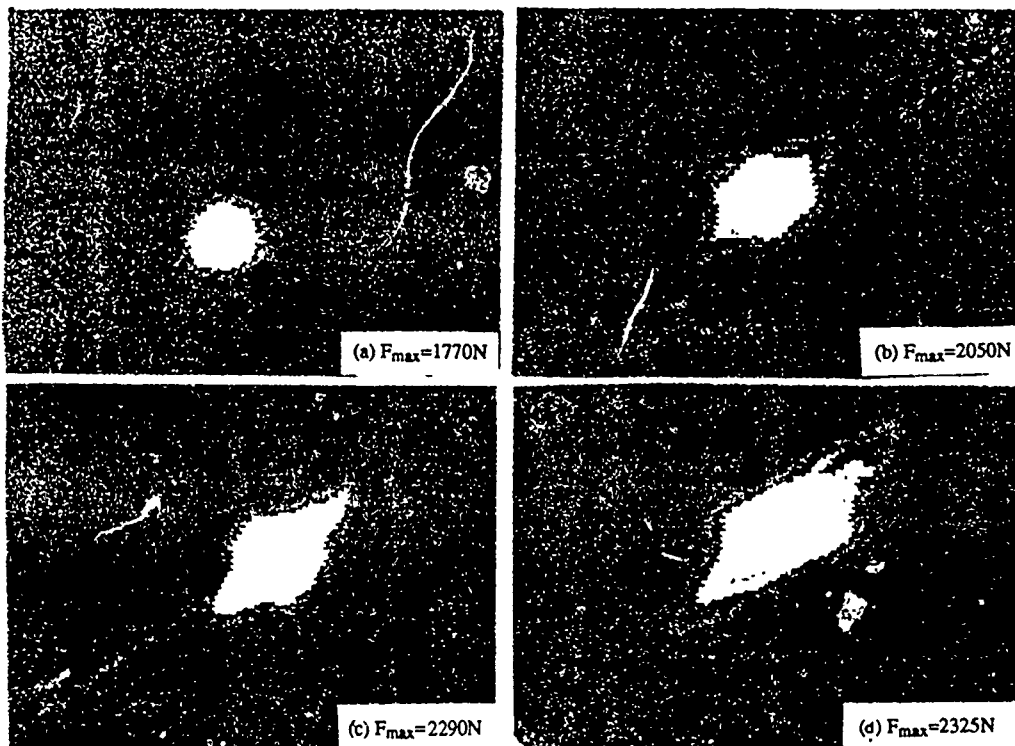
Figure 1   Progressive delamination with force.
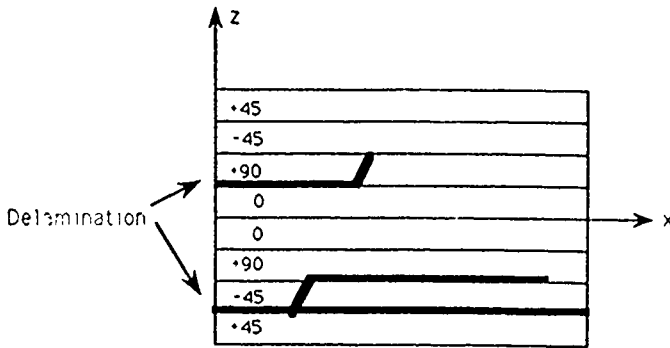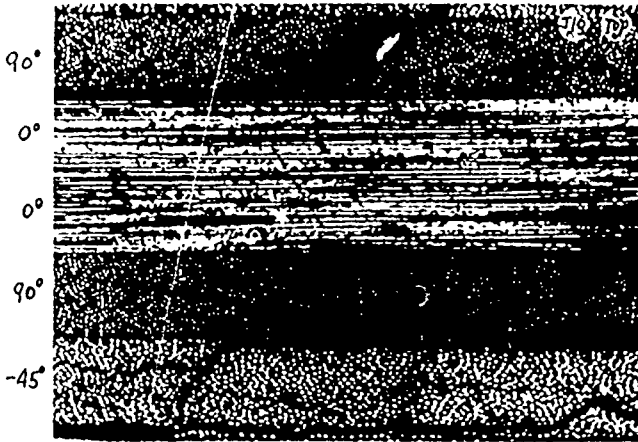
Figure 2   Multiple delamination levels.
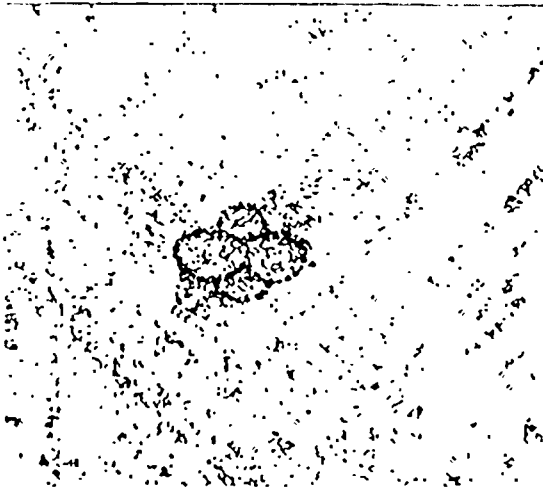
Figure 3   Overlapping 'peanut' delaminations.
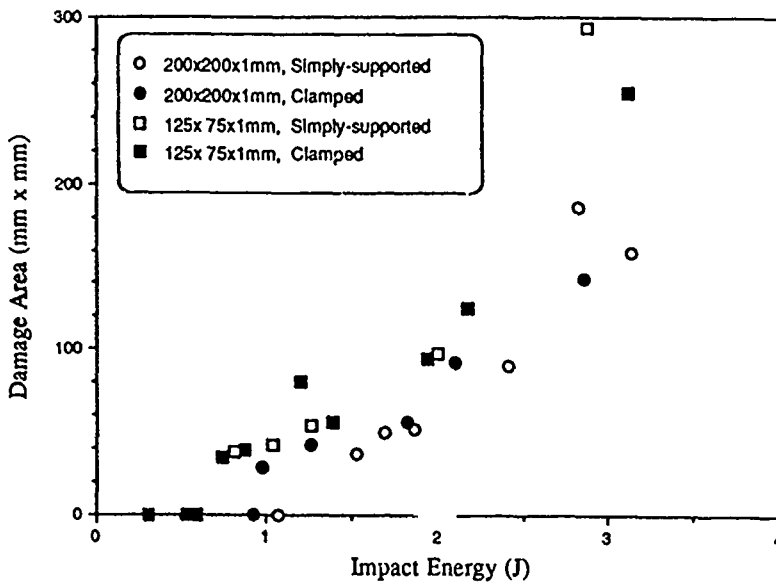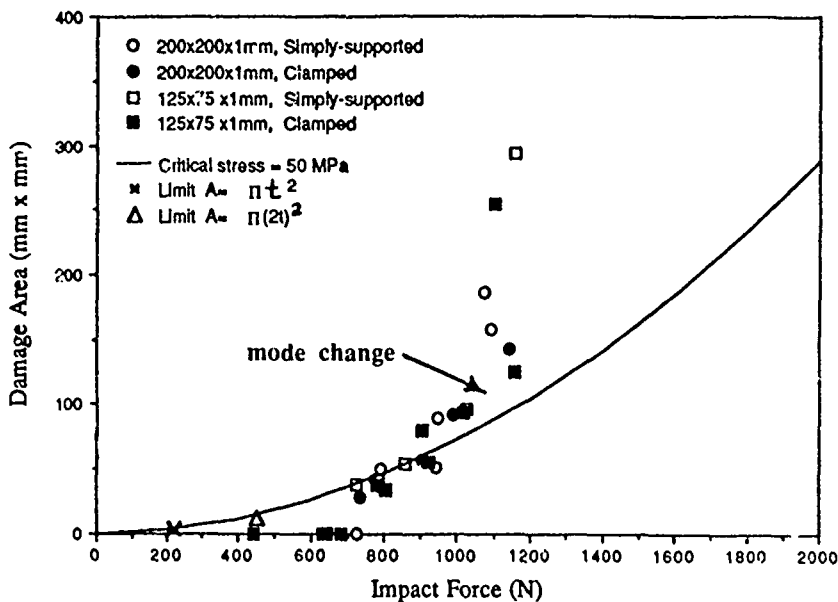
Figure 4   Damage mapped against force and incident energy for 1mm plates.
Stress-based predictions.
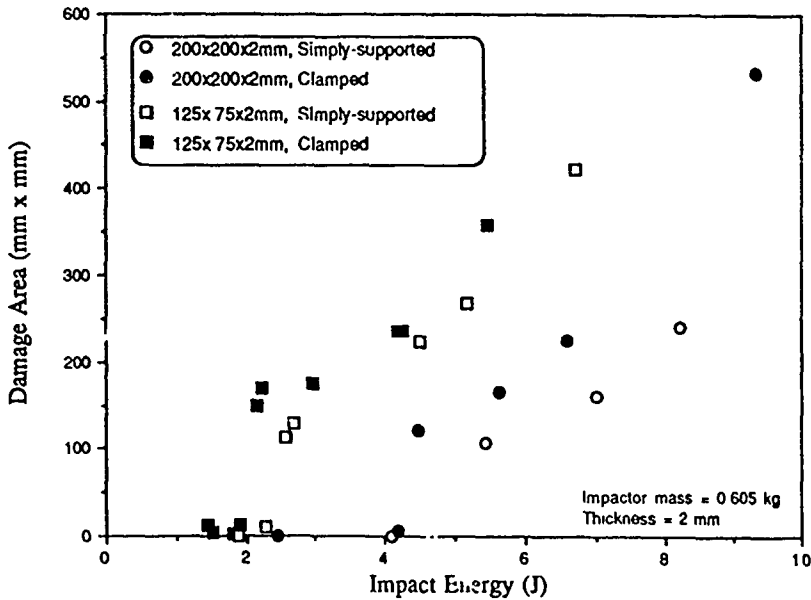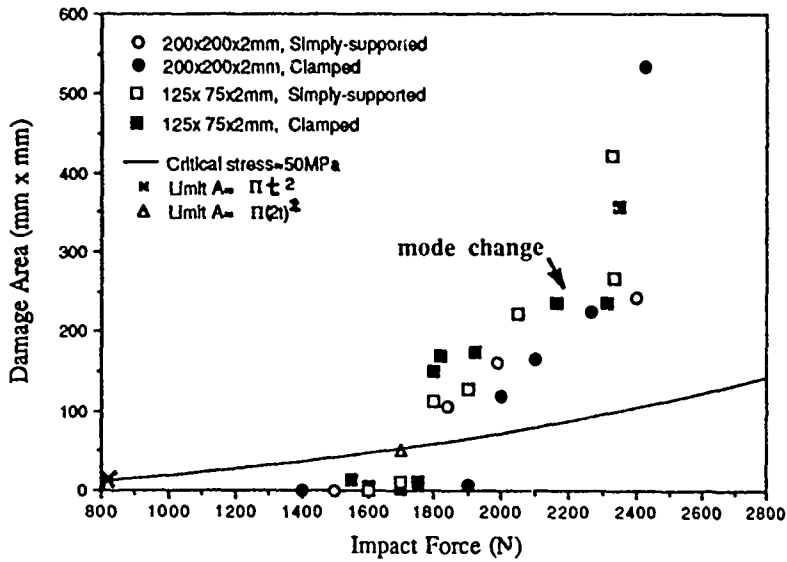
Figure 5   Damage mapped against force and incident energy for 2mm plates. Stress-based predictions.
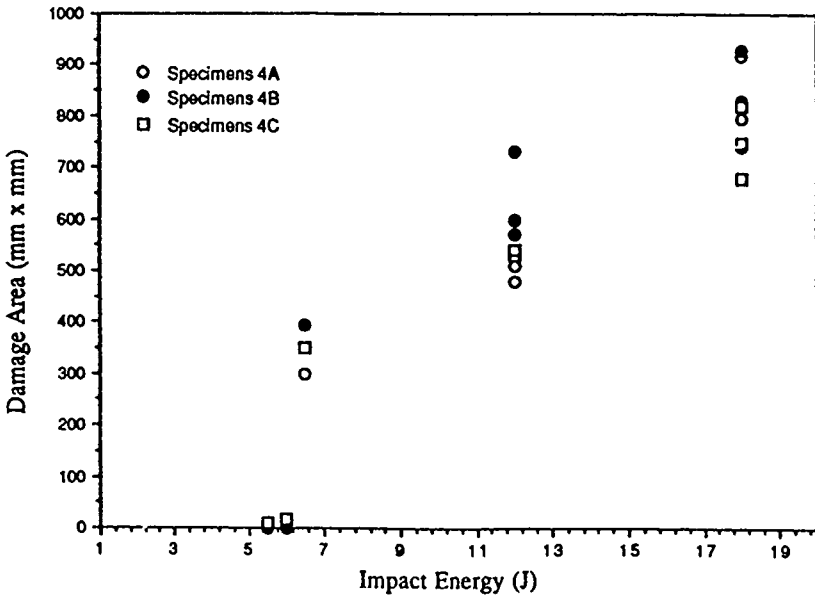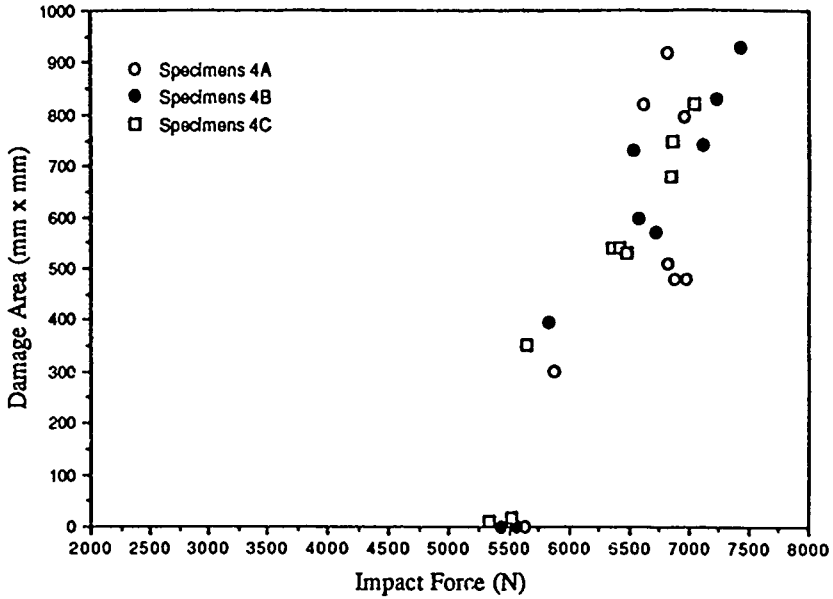
Figure 6   (Courtesy Fokker) Damage mapped against force and
energy for 4.3mm plates.

Imperial College test SC12a

IC Test SC12a
m=0.42Kg
v=1.70 m/s
E=0.61 J
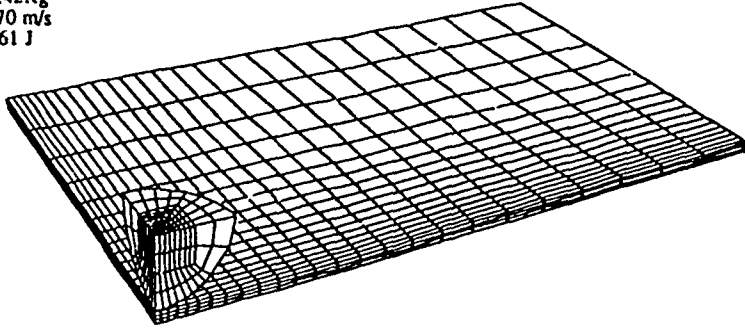
time • 0.25000E-02
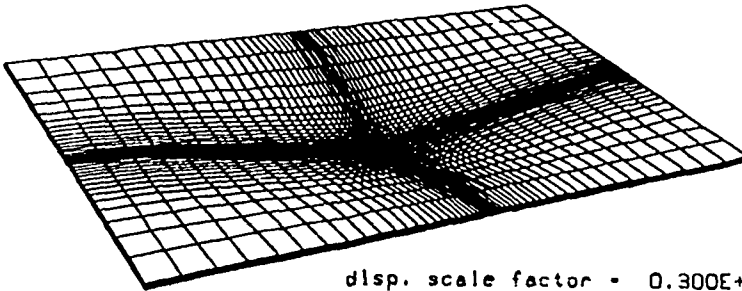
disp. scale factor • 0.300E+01

Figure 7   DYNA 3-D model for plate and impactor.
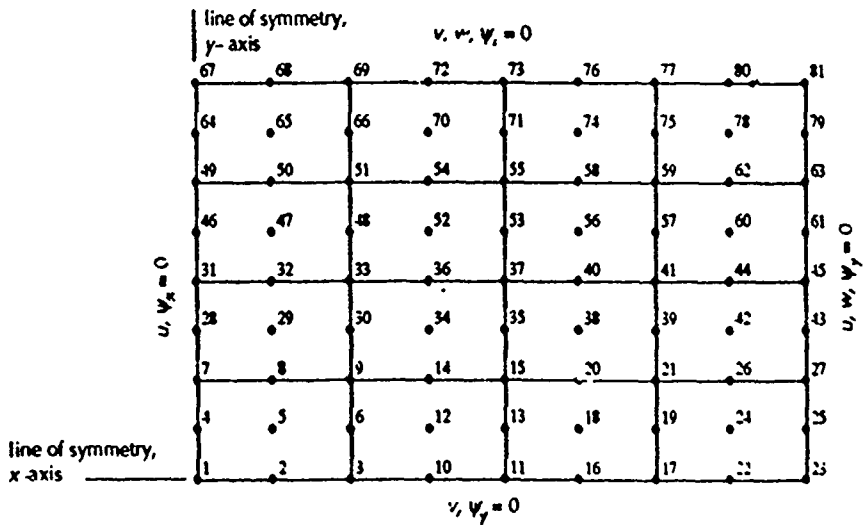
Figure 8   Coarse finite element model.
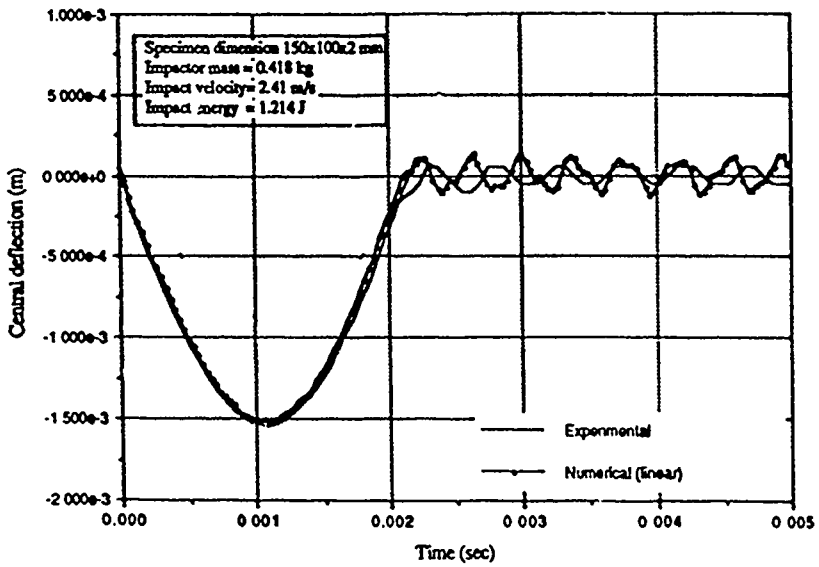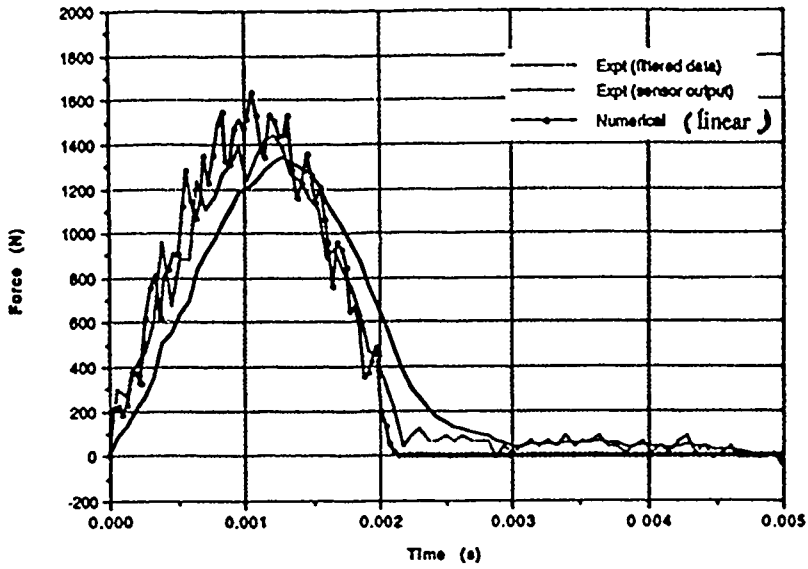
Figure 9   Comparison of finite element predictions with test – small deflections, linear response.
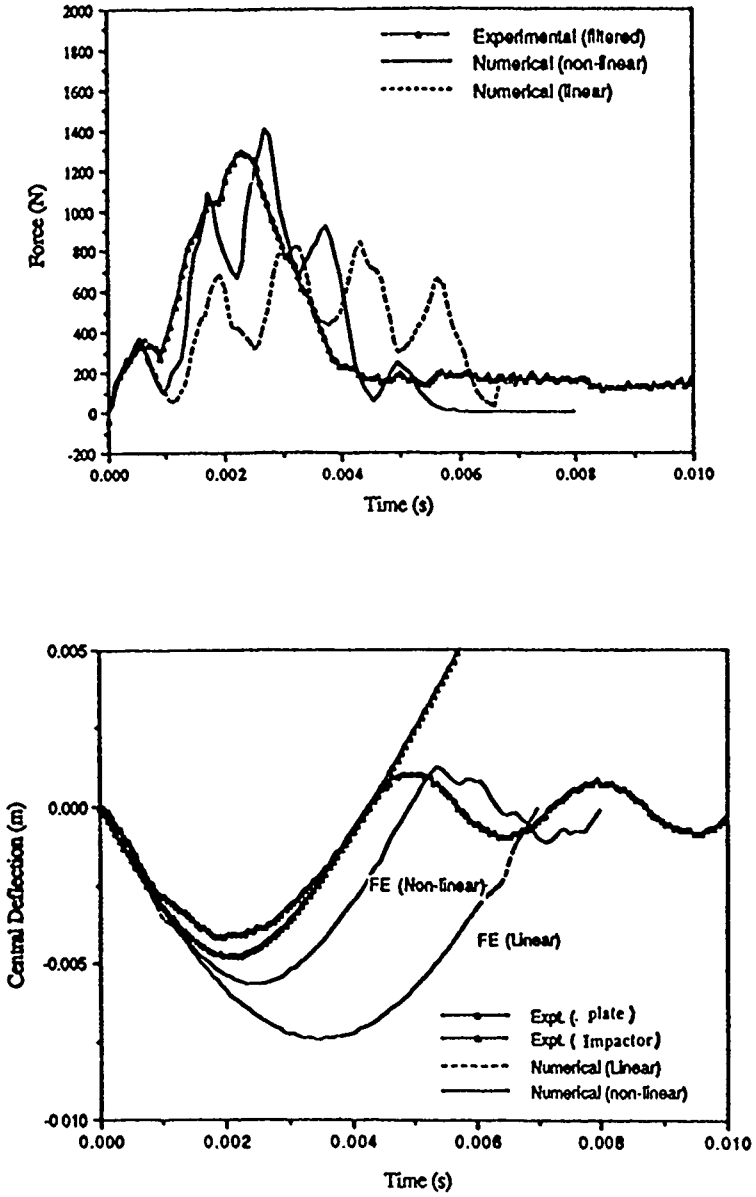
Figure 10   Finite element predictions and test results.   Gross deformation in excess of plate thickness: non-linear stiffening.

Test SC1-2a (Mass=0.42kg, v=1.71m/s, E=0.61J, Specimen 125x75x1mm, Clamped)
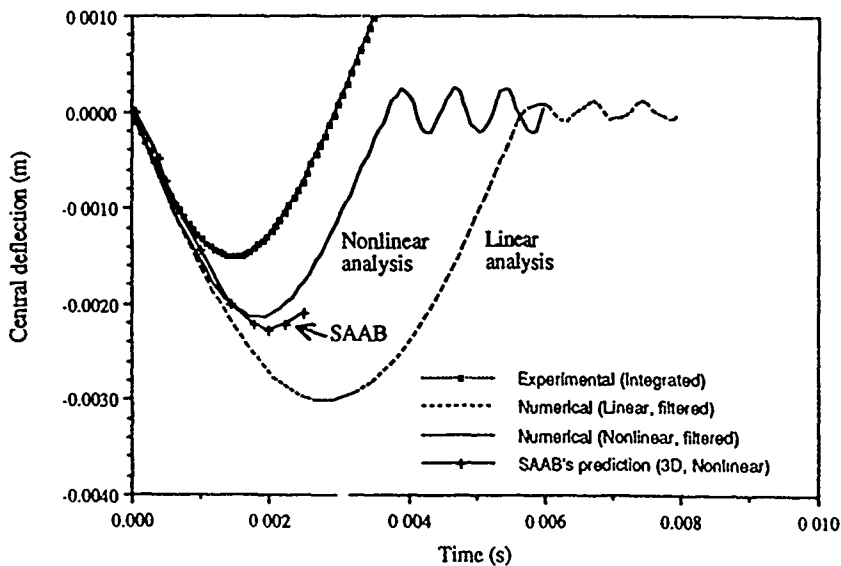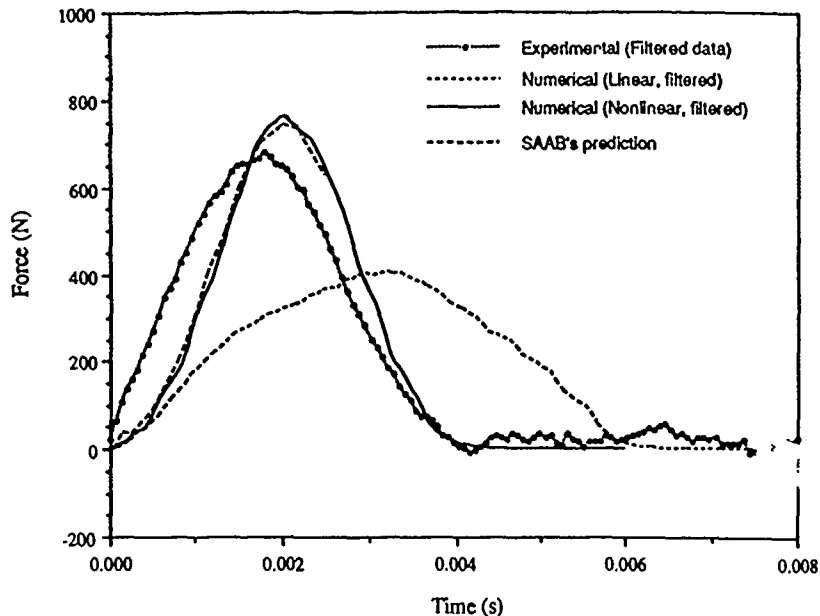
Figure 10b Nonlinear force and deflection predictions using F.E. plates or DYNA-3-D bricks.
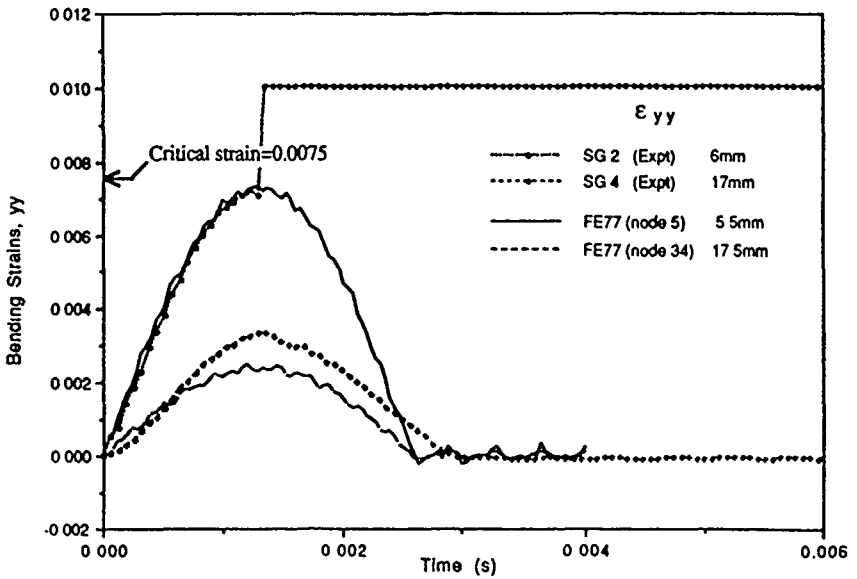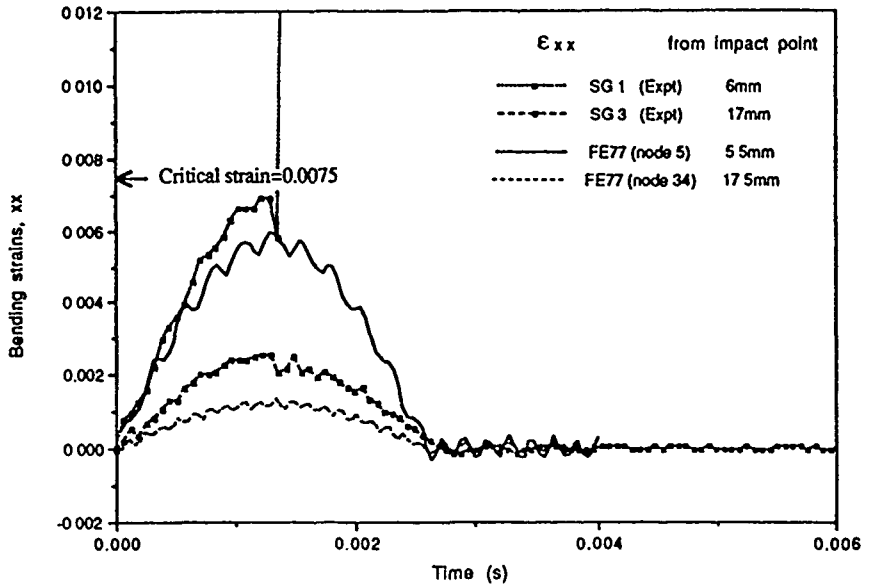
Figure 11   Prediction and test results for surface strains.
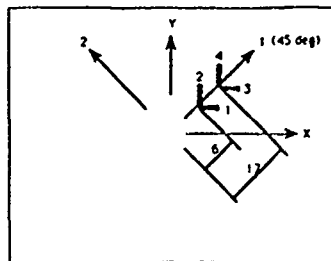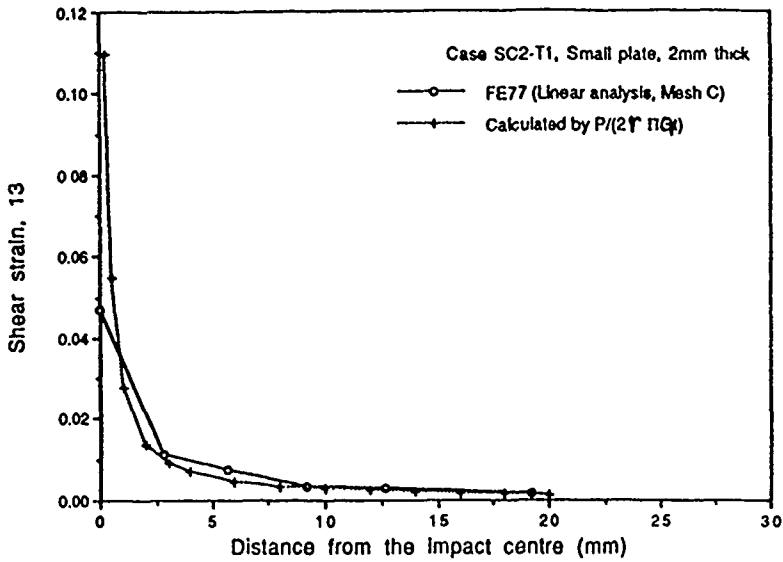
Figure 12   Distribution of radial shear strain.
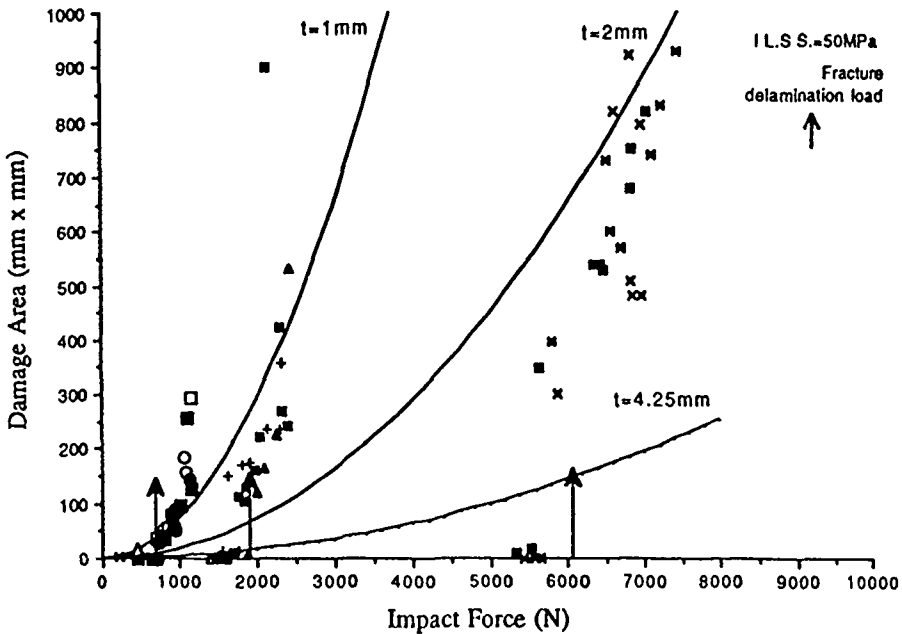
Figure 13   Stress-based and fracture-based predictions for delamination in a variety of plate thicknesses.
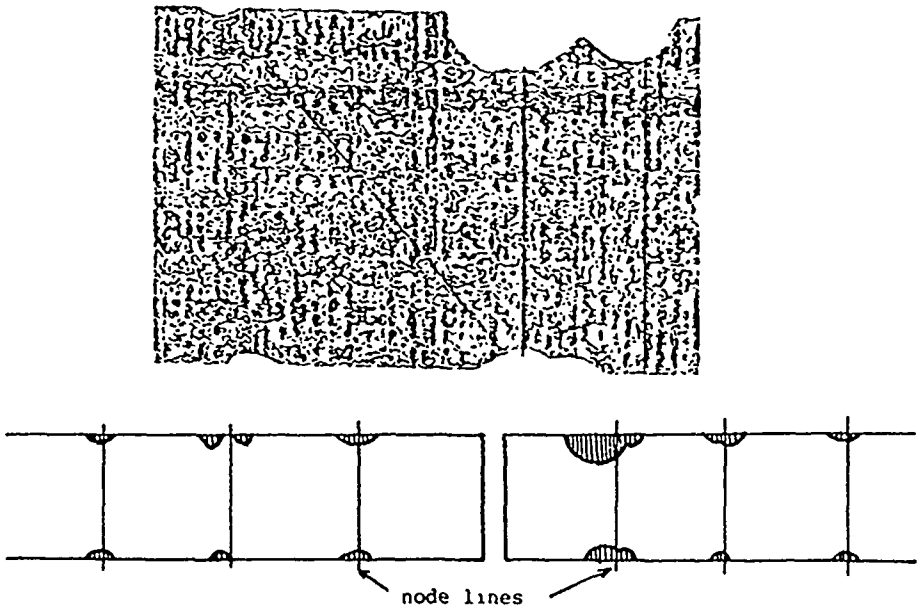
Figure 14   Delamination sites from C-scans.
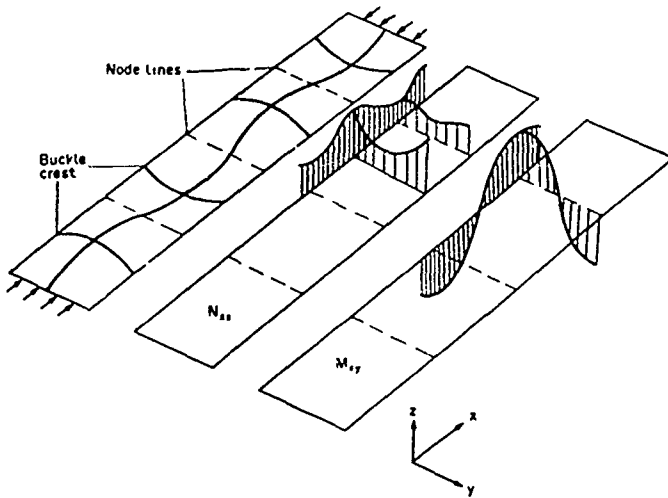
Figure 15   Post-buckling stress fields.
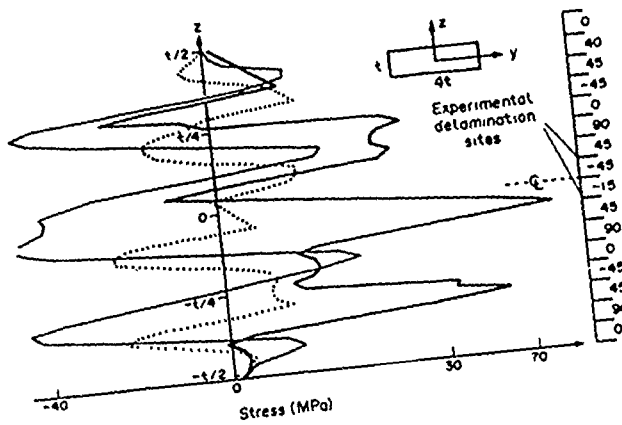
Figure 16   Three interlaminar stress components near simply supported edge due to N_{xx} and M_{xy}.

(a) Due to M_{xy}

(b) Due to N_{xx}
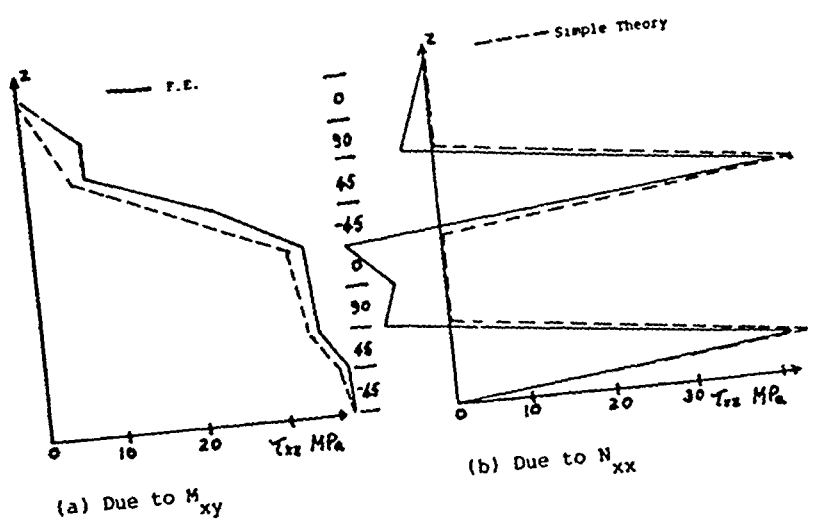
Figure 17   Boundary layer analysis (of edge effect) predictions for τ_{xz}.
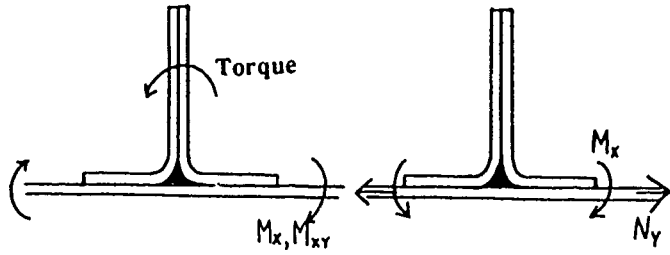
Figure 18　　**Resultant Loading**　　　　　**Diffusion Loading**

　　　　　　　　　　　　(a)　　　　　　　　　　　　　　　(b)

　　　　(a)　　　　　　　　(b)　　　　　　　(c)
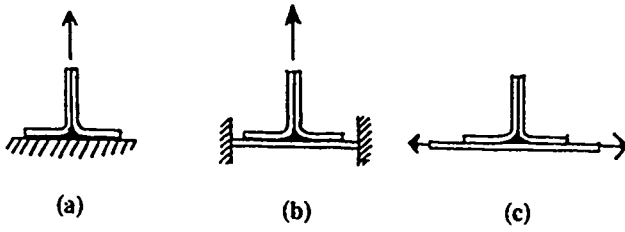
Figure 19　　Three types of loading
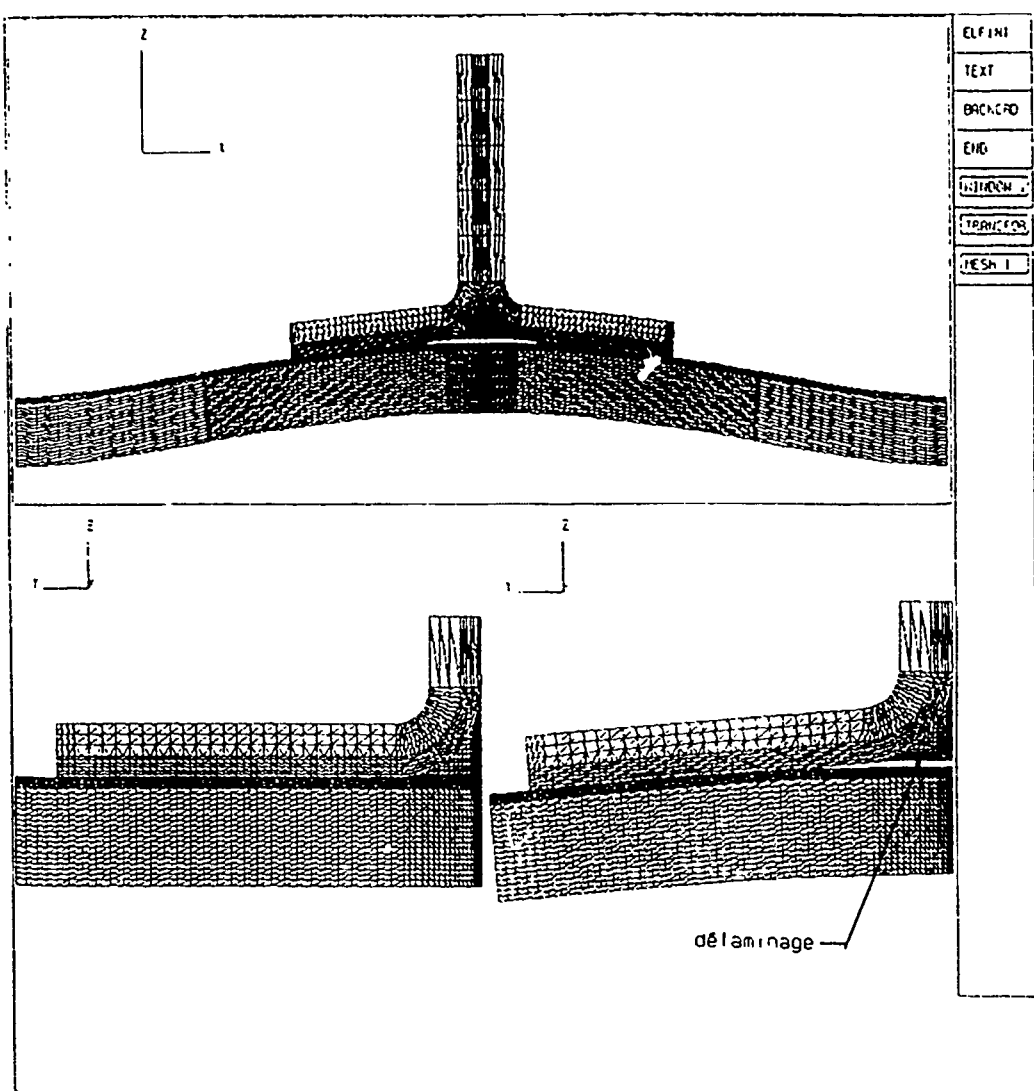
Figure 20   F.E. model for Figure 19(b) loading.
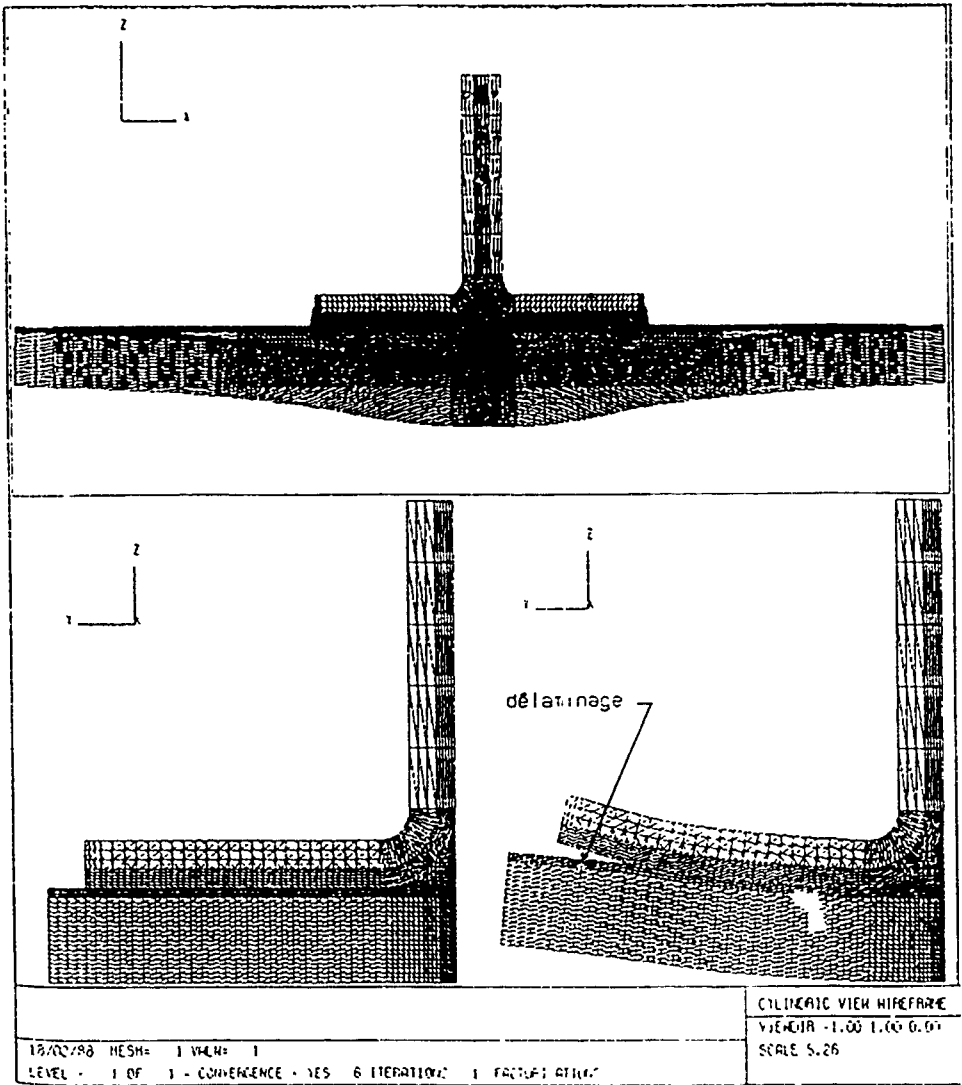
Figure 21   F.E. model for Figure 19(c) loading.
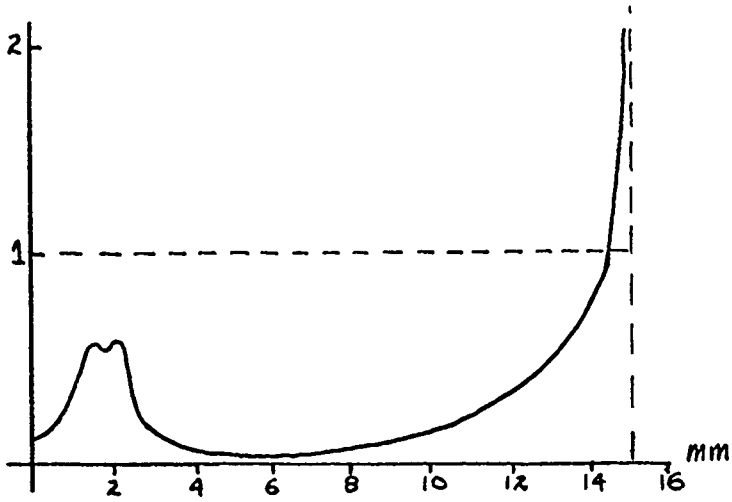
Flange bond position.

Figure 22   Quadratic stress-based failure criteria.
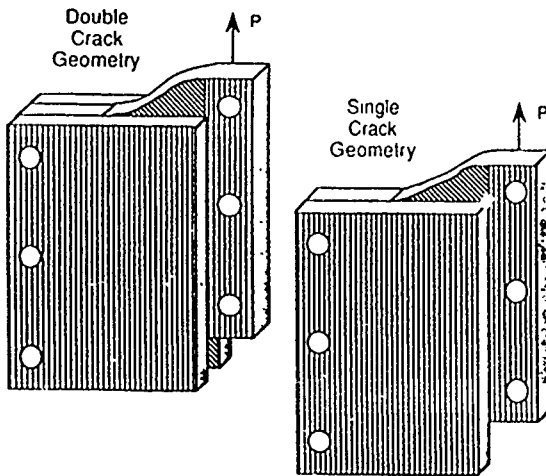
a) Crack rail shear specimen geometries
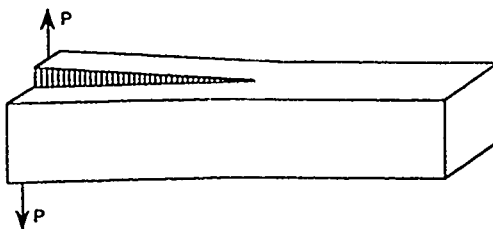
Figure 23   CRS and SCB test configurations.
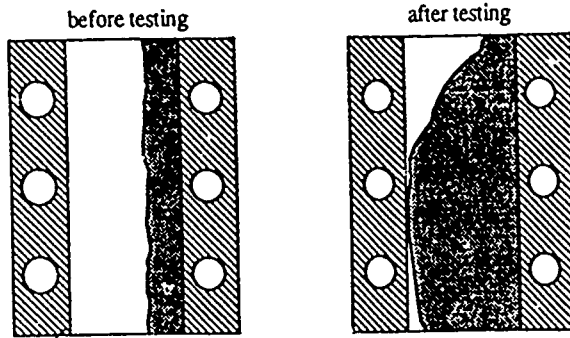
Figure 24   CRS non-uniform crack front profile.
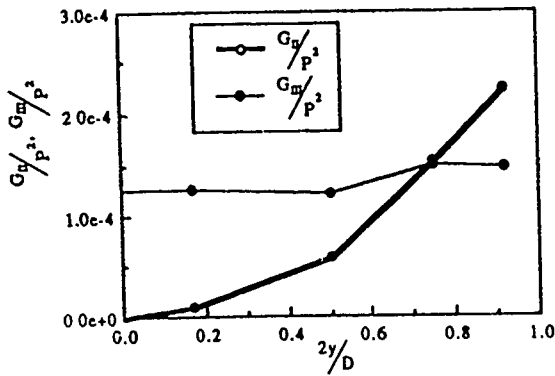
Figure 25   Mixed m. d.: energy release rate across the SCB crack front.
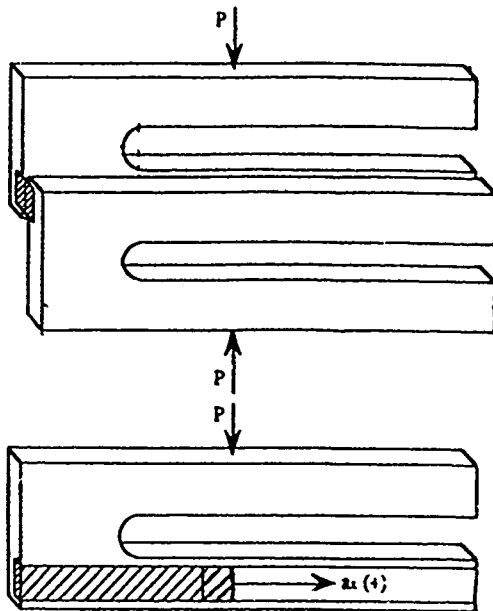
Schematic of modified SCB specimen
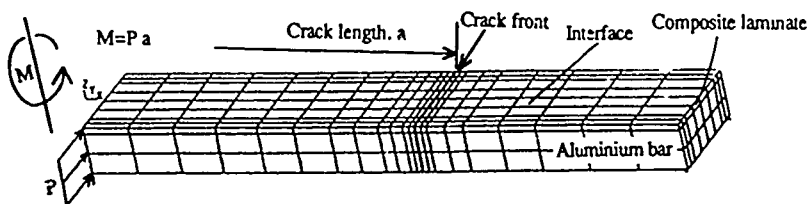
(a) Undeformed mesh
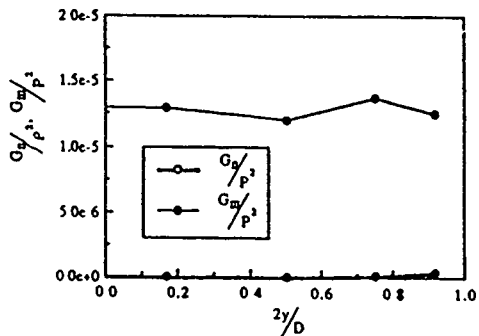
Figure 26 Modified SCB test using U-shaped bars and aligned loads.

(a) Pure mode II test specimen
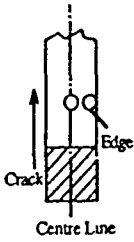
(b) Standard SCB test specimen
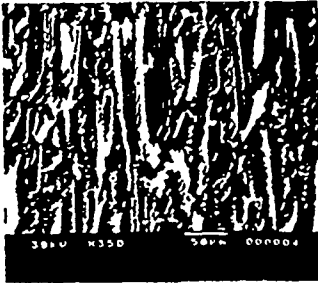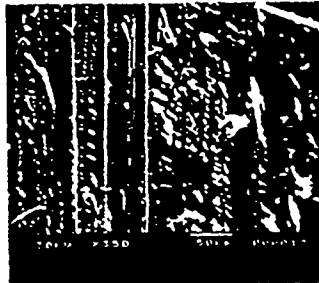
At the centre line   Around the edge

(c) Modified SCB test specimen
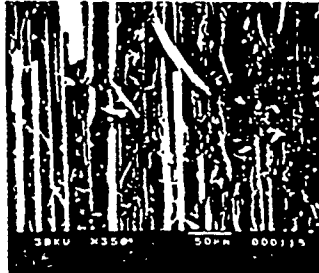
At the centre line   Around the edge

Figure 27   Fracture surfaces for the modified mode III test.

GARTEUR Damage Mechanics for Composite Materials
Analytical / Experimental Research on Delaminations

M. Gä?\e,DLR (pres.); D.J. Allman,RAE; C. Czékajski,Aérospatiale;
H. Eggers,DLR: D. Giletta, R. Girard,ONERA; R. Hillgert,MBB;
J. Laméris,NLR; R.F. Mosley, R.T. Potter,RAE

DLR - Institute for Structural Mechanics
D - 3300 Braunschweig / Flughafen
Germany

1. Summary

Currently used carbonfiber-reinforced plastics (CFRP) - mainly with epoxy matrices - show a sensitive reaction to impact damage which stimulated the establishment of a cooperation programme within GARTEUR [1]) Group of Responsables for Structures and Materials Studies in this field had shown that *DELAMINATION* is a critical damage in this area for airframe structures with principal points of concern *tendency of buckling of delaminated areas* and *potential growth of delaminations*.

It should be stated that damage in composite materials and the criticality of damaged areas to the materials response are much more complicated than with metallic materials, due to the presence of local defects which cannot be avoided in practice and to damages originating under service conditions Nevertheless, based on the knowledge from previous studies, it appears that delamination - arising from whatever kind of origin - is the governing failure mode in airframe or aerospace structures. This research therefore was mainly focussed on the buckling and growth of artificially delaminated areas of different geometrical sizes in narrow and wide CFRE - coupon specimens while one experimental contribution dealt with impacted stringer-stiffened panels The main experimental results were achieved by quasi-static loading, but in addition there was one contribution on the delamination behaviour of multidirectional CFRE specimens with artificially introduced delaminations under compression-compression and tension-compression fatigue loading

By concentrating on the compression and on the combined compression-shear load regime - for the coupon and the panel testing respectively - the investigations during the cooperation have fully covered the buckling and growth of delaminated areas to gain a substantial degree of insight and understanding of delamination growth mechanisms. The experiment work was performed with advanced composites, i e high strain carbon fibers in toughened epoxy (high temperature curing), and it was attempted to correlate the results of the experimental part of the investigation with corresponding analytical studies The results of the investigations on delamination growth under quasi-static loading show the influence of the delamination size, the stacking sequence, the thickness and the stiffness of the separated sublaminates. In all cases buckling of the delaminated areas occured prior to failure depending on the level of compression loading and has been the major contributor to strength of the test coupons As far as fatigue loading is concerned, a new test procedure enables the observation of t!e relevant damage mechanisms during the last cycles prior to failure without destroying the test specimens The influence of the depth as well as of the diameter of delaminations could be made evident with special reference to failure critical damage.

2. Introduction

The work done at O. ' E R.A. concerning the mechanical behaviour of locally delaminated composite plates, subjected to compressive loading was led with particular attention for two features

- Determination of the damage state inside plies at the vicinity of delamination front Damage state means the transverse microcracks development in the matrix. A damage model is introduced in the constitutive law of each layer Internal damage variables are defined by the relative stiffness reduction of the material.

- On the other hand, computation of energy release rate along the crack front This quantity is determined by the explicit calculation, at the front, of total potential derivative with respect to nodal coordinates

With the theoretical tools implemented in the finite element DAMSTRAT programme, a numerical simulation of a DLR (Braunschweig) test was detailed The main characteristics of the specimen behaviour were predicted, especially the influence of local buckling on damage development and crack appearance

From AEROSPATIALE (Toulouse) a contribution was made for an analytical calculation of the critical buckling load for the local buckling around a defect in a laminated plate made of multidirectional laminae Based on the principle of equilibrium the problem was narrowed with an energy method by the expression of total potential energy With a parametric study as a function of external loads and the mechanical characteristic material values the influence of the plate on the delamination-zone was determined, i. e. the apparent Poisson s moduli The computational work was verified on experimental studies carried out by AEROSPATIALE Suresnes (Laboratoire Central des Suresnes) on artificially delaminated laminate plates under compressive loading

The computational work done at NLR dealt with the prediction of the local buckling and the subsequently delamination growth of an artificially delaminated composite specimen under compressive loading Use was made of the non-linear finite element programme STAGS Modelling and calculations followed closely the experiments conducted in parallel

The UK contribution to damage mechanics of composites consisted of an experimental programme carried out at RAE and analytical studies carried out by Cambridge Consultants Ltd (CCL) under RAF funding The experimental programme was to evaluate the effects of delamination size and location on growth under quasi-static loading The analytical studies have been reported in [1 3]

The FRG contribution consisted of an experimental

research by MBB on impacted stringer-stiffened panels, which was designed to show how the combined effects of environment and barely visible impacts do reduce the failure strain achieved with unimpacted panels, and a threefold contribution by DLR's Institute of Structural Mechanics (Braunschweig):

- a first experimental one was designed for the elastic and strength properties determination under different environmental conditions for reason of the sensitivity of matrix systems to temperature and moisture which can reduce the compressive stiffness and strength of undamaged laminates, in addition the thermal and moisture expansion coefficients were determined for that CFRE material, which was used in the delamination test programme under static compression loading to examine the parameters governing the delamination growth and failure. A major aim in this context was to set up a basis for the development of analytical models, which are descriptive of the fracture processes and can serve as predictive tools [4].

- the second experimental one was carried out for the investigation and understanding of delamination behaviour under cyclic loading because these are essential for the application of composite materials to high performance structures. In particular under service loading spectra containing compressive loads the buckling of delaminated sublaminates can lead to catastrophic failure by unstable delamination growth [5].

- the third was an analytical one which was designed for reason that the evaluation of the post-buckling behaviour of a compressed specimen by finite volume elements is quite expensive and difficult to conduct. Therefore an approximation method named Beam-Lattice-Model (BLM) was generated, guided by the measured forms of the delaminations [6]. The model consists of two layers of beam lattices, coupled around the delamination, see Figure 1. According to the delamination growth, the coupling points at the crack tip will be shifted to the actual delamination front. The level of stressing at this front is determined by ERRs. The delamination growths when the ERRs, induced by the buckling of the blister, over-step critical values for the material
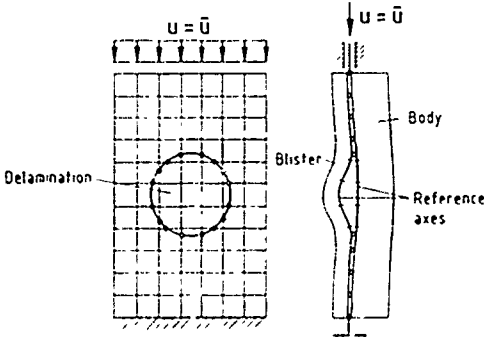
Figure 1. Beam Lattice Model (BLM)

3. Experimental Research

The entire experimental programme was carried out using the carbonfiber-reinforced epoxy materials mentioned in Table 1

Partner	Material	Test Component
AS	914C/T300	100/300 mm^2
NLR	6376/T400H	100/250 mm^2
RAE	914C/XAS	70/230 mm^2 100/230 mm^2
	6376/T800H 6376/T800H	75/230 mm^2 300/430 mm^2 stiffened
MBB	913C - 35 913C - 40	790/2254 mm^2 stiffened
DLR	914C/T300	12/135 mm^2 properties 40/380 mm^2 delamination

Table 1. Test Materials

The used different stacking sequences can be depicted from Table 2.

Partner	Laminate type I/III	Laminate type II
AS	$[(0°/ - 45°/90°/45°)_4]_s$	see fn
NLR	$[0°/90°/45°/ - 45°]_{3S}$	$[90°/0°/ - 45°/45°]_{3S}$
RAE	$[(\pm 45°/0°/0°)_3]_S$	$[(\pm 45°/90°/0°)_3]_S$
	Panels $[(\pm 45°/0°/90°)_2]_S$	
MBB	Stringers $[\pm 45°F/0°_4/ \pm 45°_4F]$ Skins $[0°_4/ \pm 45°_3F]$	$[\pm 45°F/0°_5/ \pm 45°_6F]$ $[0°_6/ \pm 45°_3F/0°_2]$
DLR	$[0°_2/45°/0°_2/$ $45°/0°/90°]_S$ $[\pm 2°/45°/ \pm 2°/ - 45°/0°/90°]_S$ $[0°_2/90°/0°_2/45°/0°/$ $45°]_S$	

Table 2 Laminate Stacking Sequences

In the *Laboratoire Central de Surenes* of AEROSPATIALE (AS) the experimental investigations were carried out with laminated panels. The test pieces were built-up as 32-ply symmetric laminates. Four different types of deliberated delaminations were used

- rectangular area of 25 by 25 mm
- circular area of 25 mm in diameter
- elliptical area of a = 30 mm (oriented in 0°), b = 15 mm
- elliptical area of a = 30 mm (oriented in 90°), b = 15 mm

These artificial delaminations were located at two positions in the panels, between the 4th and 5th ply and between the 8th and 9th ply, respectively.

The panels were tested under compression loading and displacements were measured by LVDTs (Linear Variable Displacement Transducers) at the panel center on both sides for delaminations at position 1 and with strain gages on both sides of the panels for delaminations at position 2.

At NLR experimental investigations were carried out with wide test specimens, which were built up as a 24-ply symmetric laminate. The resulting area of the crossection is 300 mm². Artificial delaminations were introduced by locally precuring the delaminating plies at 177 °C for 5 minutes in a rectangular area of 20 by 25 mm, located in

fn [0°/45°/0°/   45°/90°/45°/90°/   45°/0°/45°/90°/   45°/0°/   45°/90°/45°]$_S$

the center of the test piece, followed by a brush application of two layers of a release agent, ROCOL. This technique came out as the most optimal one in a preliminary comparative study using specimens with NARMCO and Hexel F-593 fibres.

The experimental programme was done in two phases. In phase I a laminate with the stacking sequence Laminate I (Table 2) was used. The purpose of this phase was to study the best way to determine local buckling and delamination growth under compressive loading. In combination with the use of C-scans, several methods were used in this phase. These methods consisted of the use of SPATE-8000, a method based upon thermo-elastic measurements during cyclic loads, of a grid projection method and of out-of-plane measurement with a LVDT, mounted on a moveable frame. Based upon these results and the calculations the laminate used for the phase-II programme was changed into the Laminate II in Table 2. Ten specimens were manufactured, five with an artificial delamination between the 4th and 5th ply, and five with an artificial delamination between the 2nd and 3rd layer. Back-to-back strain gauges were applied to determine the overall strain, which was also determined by measuring the end-shortening. In addition, the grid projection method was used to determine the out-of-plane deformation of the delaminated areas.

Basic material tests were conducted to determine the ultimate compression strength and Young's modulus of the new laminate. Using a standard test configuration, the longitudinal and transverse moduli were determined at 0 4 % strain.

Initial calculations indicated that the laminate stacking sequence no. I, used in the Phase I experimental programme led to local buckling (= blister) of the delaminated plies inwards, e.g. in the direction of the sublaminate

In a first phase at RAE, Courtaulds XAS fibres in Ciba-Geigy 914 resin were used to validate the specimen configuration and to evaluate the effect of delamination

Material 914 C / T 300
Stacking sequence [0³]ₛ ≃ 2mm
Numerical values Average of 5 specimens with standard deviation
Dotted plane Surface of regression

Figure 2   Longitudinal Compressive Strength of UD CFRE Laminates as Function of Temperature and Moisture Content

location in two different ply lay-ups A second phase at RAE, using the advanced Toray T800H fibres in Ciba-Geigy 6376 resin, was designed primarily to examine the effect of initial size of the delamination on growth and failure.

In the stringer-stiffened-panel tests, strain was measured using foil strain gauges to ensure reasonable uniformity of loading across the panel width and to allow delamination growth data to be plotted against end strain One of the coupon specimens was strain gauged to allow data from these specimens to be presented in similar manner

Out-of-plane movement of the delaminated material was monitored using a shadow moire technique. Each moire fringe is effectively a contour of constant displacement normal to the plane of the fringe plate (which is arranged to be parallel to the laminate) Changes in the fringe pattern with increasing load were recorded on video tape. For the stringer panels, stil photographs were also taken at frequent intervals during the loading Comparison of the final moire fringe pattern with ultrasonic measurements of delamination size in unfailed panels confirmed that this technique gave an accurate measurement of delamination width

The tests on stringer panels with implanted delaminations were stopped when the delaminations started to grow rapidly with only minor increases in end strain. The cessation of the test at this point ensured that the fractographic evidence related to stable delamination growth was not destroyed or masked by the final fracture process

Stringer-stiffened panels were manufactured from Material 913C-35 and 913C-40 and tested under compression and combined compression, shear loading by MBB For reason to show that the combined effects of environment and barely visible impacts do not reduce the failure strain achieved with unimpacted panels at RT by more than 20 %, four impacted panels were tested under service conditions (70 °C wet structure).

At DLR's Institute of Structural Mechanics (IfSM) unidirectional laminates out of 914C,T300 were tested to establish four elastic constants and six strength components in dependence on temperature and moisture contents; in addition the thermal and moisture expansion coefficients were determined for that CFRE material, which was used in the delamination test programme in order to take into account the prestress state in multidirectional laminates With these characteristic values predictions of first-ply failures, ultimate strength and stiffness properties were executed and were checked against test results from laminates with six different stacking orders (not mentioned in Table 2). A short presentation of these results are given here in form of general diagrams (carpet plots) as a generalization for balanced and symmetrical laminates built-up of 0° , ± 45° and 90° plies for discrete values of test temperature and and saturation moisture contents (Figures 2, 3 and 4) More detailed informations are contained in [7]

In a comprehensive test programme at DLR's IfSM - supported by an ESA/ESTEC-contracts [8, 9] - the behaviour of artificially introduced delaminations with four different configurations of size, five depth of location under quasi-static compression and under compression-compression as well as under tension-compression fatigue loading was studied. From former investigations with undamaged CFRP-laminates [10, 11, 12] it is well known that tension-compression loading represents the *worst case* of loading conditions because of the influence of tension
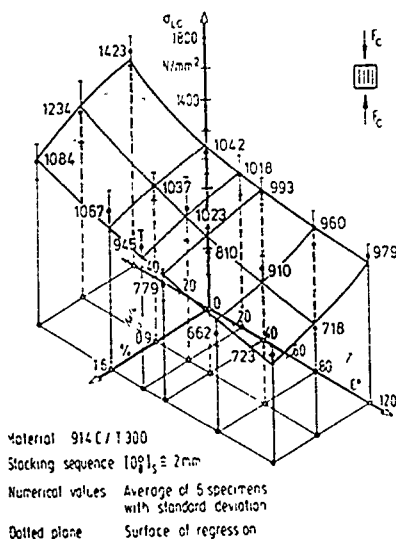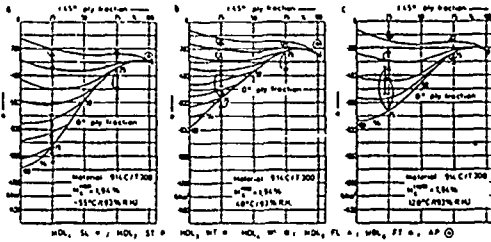
Figure 3. Failure Limits of $[0°_i/\pm 45°_m/90°_n]_s$ - CFRE Laminate
Family In Depend of Ply Fraction and Temperature
Constant Saturation Moisture Content at 93 % R H
Compressive Loading

Figure 4. Failure Limits of $[0°_i/\pm 45°_m/90°_n]_s$ - CFRE Laminate
Family in Dep of Ply Fraction and Moisture Content
Test Temperature 23 °C
Compressive Loading

4. Analytical Research

The entire analytical programme was carried out using different computer programmes, developed by or existing at the different partners. More details of these computer programmes can be taken from the literature at the end of this paper.

At ONERA main tools were developed in the DAM-STRAT programme. This program is essentially devoted to the non-linear computation of composite structures. The principal functions are:

- Non-linear constitutive law: Damage model;

- Energy release rate computation in linear and non-linear cases.

- Composite structures computation with large displacements.

A total Lagrangian formulation is used in this context. In the isoparametric finite element coordinates and displacements for any point of an element are written in terms of the nodal coordinates and displacements with linear shape functions in the thickness and in plane shape functions. The use of such a kinematic enables to take into account average transverse shear strains, see Figure 5.

The solution is reached owing to an iterative process (Newton-Raphson method) In the problem bifurcation point and buckling mode (secondary path) of the specimen delaminated area have to be determined This is realised by the use of an imperfection (very little force).

load induced damage onto the other damage mechanisms. Thus, the damage development like matrix crack formation in off-axis plies under tension-compression loading was of special interest
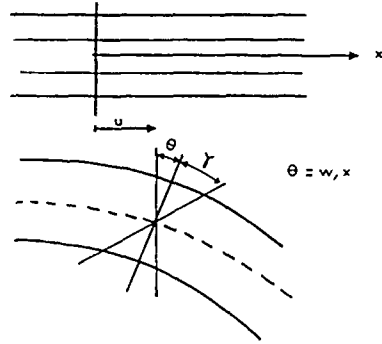
Figure 5 Average Transverse Shear
ONERA

The meaning of damage is the stiffness reduction of material due to the development of microcracks. For composite materials, the damage growth is anisotropic, because it is guided by reinforcement directions Identification of the model parameters is achieved by mechanical tests in which the loading phase is interrupted by a load decrease up to free stress state, in order to measure the specimen stiffness reduction.

Because of the very different kind of layer failure occuring in fiber direction and other ones, a multi-failure criterion was developed Failure in fiber direction is brittle and a maximum strain criterion is quite accurate For the layer matrix mode of failure, a criterion is derived from an instability condition. The derivate of strain energy is computed for nodes belonging to the delamination front

Perturbation is made only in the normal direction to the front line

The energy release rate computational method used, requires the crack tip finite element representation, shown in Figure 6 However to avoid too important degrees of freedom, the two layers of elements are connected with a ngle layer, by the mean of a penalty method This connection has to be applied at some distance from the crack front, because of the resulting perturbation in kinematic field
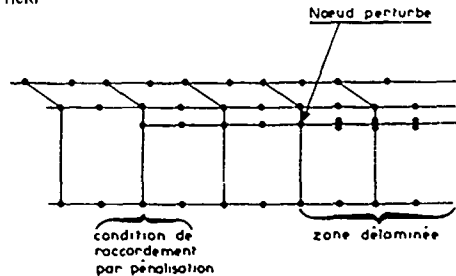
Figure 6. Crack Tip Representation
ONERA

AEROSPATIALE used the total potential energy which is the difference between the distortional energy and the potential energy of the external loads The configuration of stable equilibrium corresponds to a minimum of energy To determine the critical buckling load the total potential energy was developed in a Taylor serie around the equilibrium position before buckling The variational method of Rayleigh-Ritz was used to solve the equatio In Figure 7 the principle and details of the model are shown

ETUDE D'UN CAS

SCHEMATISATION
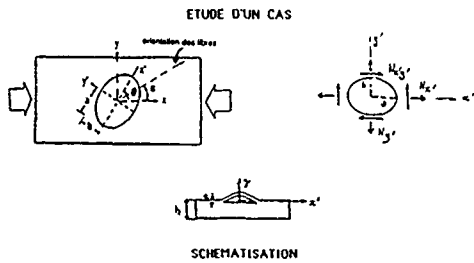
Figure 7. Analytical Model for Calculation
     AEROSPATIALE

In the second part of the study at NLR, computational work was conducted with the Phase II laminate stacking sequence no. II (in Table 2) by adaption of special purpose software for the calculation of energy release rate distributions along the boundary of embedded cracks (by the virtual crack extension method) to the MARC general purpose programme package and the modelling of layered plates for linear buckling analysis and for non-linear pre- and postbuckling analysis using the STAGS-code. Delamination growth is controlled, presumably by the magnitude of stresses and strains around the delamination boundary. These, theoretically singular, field quantities are related, however, to a finite total potential energy value. This energy value and its gradient associated with delamination growth can be computed by numerical methods.

Two separate non-linear runs have to be executed with the same loading and boundary conditions but with different delamination extension sizes (one node realeased at each time) At a certain load level the runs are stopped and the solutions of the last step of the two runs are used to determine the energy release rate In order to obtain accurate results, different values of the end tolerance used in the iteration procedure must be evaluated.

For symmetry reasons only a quarter model of the specimen was used. Several models were investigated to study the effect of element size and constraint conditions

Use is made of transition elements and of additional elements to be used for delamination extension All models were discretised with '410 STAGS elements

The analytical resea 1 work from RAE, carried out by Cambridge Consult . Ltd (CCL) under RAE funding, demonstrated conclusively that linear models were not adequate and that a non-linear large displacement solution incorporating local buckling effects was essential New finite element models were developed to include the phenomenon. The early models used 3-D solid elements, but the use of such elements in a non-linear analysis is prohibitively expensive and CCL concentrated on using 2-D plate bending elements. PACEF includes such an element with the capability to model multiple plies and large displacements. The results have been checked for some items by a parallel set of analyses on the ANSYS finite element system, which gave very similar results.

Additional extensions to the PACEF programme were implemented to allow direct calculations of stress intensity factors and strain energy release rate for orthotropic materials.

The beam lattice model (BLM) developed by DLR [6] allows a direct coupling of different lattices to each other

due the fixing of the reference axes to the upper or lower beam surface In the solution routine the principle of virtual displacement is used to equilibrate the nodal forces in a beam lattice

Initially the specimen is planar Only the tangential displacements exist. Even though the loading of the specimen oversteps the buckling load F_{cr}^B of the blister, only the quasi-linear solution Z_0, Figure 8, can be derived by the equation for the linearized system using the global stiffness matrix and the nonlinear solution- and load-vectors
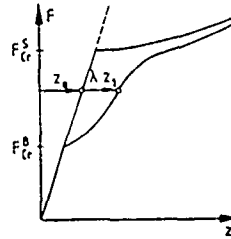
Figure 8   Buckling of a Delaminated Specimen
     DLR - IfSM

In order to introduce the local buckling mode, the solution Z_0 is augmented by the first eigenmode Z_1, magnified by a scale factor λ . In the algebraic system the eigenmode correlates to a certain Pivot-element, which changes its sign during loading, Figure 9.

Pivot < 0

Figure 9   Solution Scheme for BLM
     DLR - IfSM

The Energy Release Rates (ERRs) were defined by crack closure method Generally, the crack front intersects the cross section of the beam by an angle Therefore the ERRs were transformed to crack tip coordinates, where axes are normal and tangential to the crack front, respectively, and where the third axe, distinguished by the normality to the crack surface, remains unchanged By the transformation of beam- to crack-tip coordinates the G values related to stresses are invariant.

For isotropic materials the stresses close to the crack tip can be approximated by a plane strain state Similarly, a modified plane strain state was chosen for a multilayered laminate, Figure 10.

5. Performance

Experiments

Due to the huge amount of test results worked out during the existence of this GARTEUR Action Group, only a few results can be shown here.

The test results of AEROSPATIALE are laid down in the Technical Report no. 50440/F of AEROSPATIALE LCdS

6-6
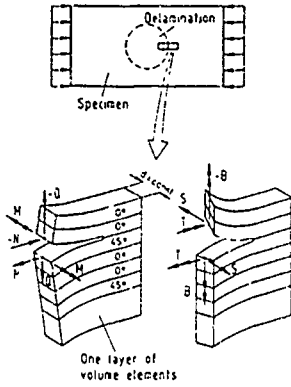
Figure 10. Evaluation of ERRs in Layered Structures
DLR - IISM

At NLR the specimens were quasi-statically loaded under uni-axial compression in a step by step fashion, in which the load was controlled. At least once each test was temporarily stopped in order to take the specimen out the machine for C-scanning.

Three specimens of type I were tested under compression and only one specimen exhibited local buckling of the delaminated area and, subsequently, delamination growth. The two other specimens failed without experiencing local buckling This type of laminate has the property that the 4-ply blister will move inwards against the 20-ply sublaminate. Laminate type II showed that an initially outward deformation of the blister would occur.

One results of the phase I' programme was, that local buckling for specimens with the deeper located delaminations did not occur in a consistent way.

Figure 11 shows the C-scan of a specimen's superimposed contour lines of the delamination at the highest load achieved - 75 kN. At high loads the global deformation of the specimen interfered with the local buckling mode of the delamination. The out-of-plane deformation of the center of the blister in relation to the backplane of the sublaminate was measured by two LVDTs normal to the specimen for the different specimens.
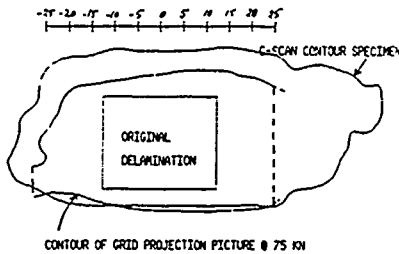
Figure 11. Comparison of Delamination Size
C-Scans vs Grid Projection Method
NLR

At RAE laminate type I and II (Table 2), which are generically representative of military aircraft wing skins were used. Artificial delaminations were made from folded patches of teflon and were placed either between the 2nd and 3rd plies or between the 4th and 5th plies

The primary objective of the Phase II programme was to make detailed measurements of delamination growth, to study the effect of initial size of the delamination and to acquire information on the growth mechanism by fractographic examination of the tested specimens. In order to evaluate larger delaminations, 300 mm wide panels stabilised by foam-filled stringers were produced, see Figure 12, which is not typical of aircraft structure, due to a design for stability of the face sheet to high strain levels The artificial delaminations in these panels were 25 mm, 50 mm or 100 mm square. In order to compare the effects of single, artificial delaminations with multiple, impact-induced delaminations, one further stringer panel was manufactured. An impact on the front face producing damage of a conical form through the panel thickness would be most representative of service conditions. The panel was subjected to an 8 Joule impact on the rear face whilst supported on ring support of 44 mm diameter. This impact caused multiple delaminations as shown in Figure 13.
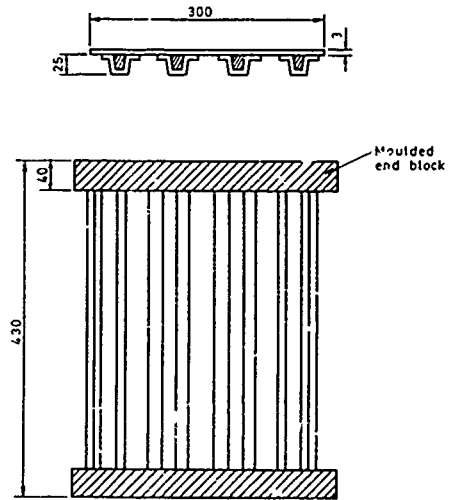
Figure 12. Foam-filled Stringer Panel
RAE
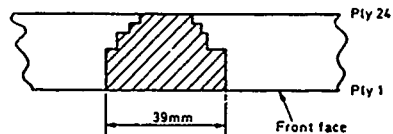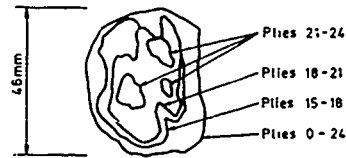
Figure 13 Impact Damage In Stringer Panel
RAE

For all but the largest delamination in coupon testing a single buckle formed in the delaminated plies resulting in

lateral growth with increasing end strain For the largest delamination (100 mm square), a single buckle formed at low load but this changed to a double buckle at an end strain of about 0 15 %. Each of the buckles then gave rise to lateral growth as indicated in Figure 14.
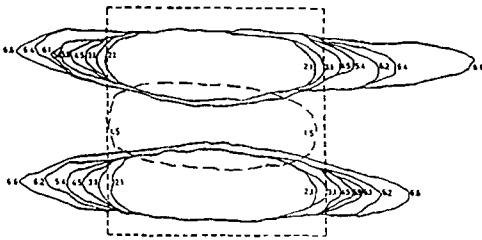
Figure 14. **100 mm Delamination, Growth vs End Strain (x 10³)**
RAE

MBB used for the research on stringer-stiffened panels large scale structural elements, the dimension of which can be taken from Figure 15 The four impacted ones were the following:
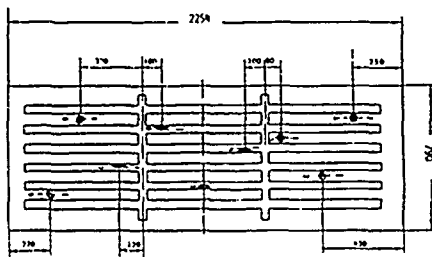
Figure 15 **Typical Impact Panel (Stringer-Stiffened)**
MBB

- Test panel 19.02 was impacted at six positions (3x stringer 3x midbay) with a delamination range of 140 – 1040 mm². Material. 913C-35

- Test panel 19 06 was impacted at nine positions (4x stringer 5x midbay) with a delamination range of 495 – 1105 mm² Material. 913C-35

- Test panel 19.14 was impacted at seven positions (3x stringer 4x midbay) with a delamination range of 170 – 1484 mm². Material 913C-40

- Test panel 19.16 was impacted at one zone several times up to a delamination area of 6500 mm² Material: 913C-40

Only test panel 19.16 showed a delamination growth under loading and rupture due to the impacts

For the investigation at DLR s IfSM of the material response of undamaged laminates under quasi-static compression loading, and in the presence of different temperatures and saturation-moisture contents, nine different laminate configurations were tested [4]

For the understanding of the delamination behaviour a doubled A 4000 stretch release foil was used from a halogen release film for high temperature and high pressure applications with a thickness of 40 μm The delaminations of 5.7 to 21 mm in diameter were placed mainly between the second and third and the third and fourth plies In some tests they were placed between the 5ᵗʰ and 6ᵗʰ,

6ᵗʰ and 7ᵗʰ and 7ᵗʰ and 8ᵗʰ plies An anti-buckling guide was located at the coupon to remove gross out-of-plane deformation. Two central windows of 26 by 35 mm in both sides of the guide allowed local out-of-plane deflection near the delamination The delaminations near the surface first popped out into a blister, then they grow as a whole and finally cracks appear disconnecting the blister from the specimen at both sides of the delamination, which change the buckling mode from a two-dimensional form to a more one-dimensional form. The change in the buckling mode is combined by an unstable growth of the delamination. More details are presented in [11].

Results depicted from Figure 16 shows the comparison of reflected gratings at the same load levels for the laminate types I and II (Table 2 for DLR) for a more tolerant delamination growth behaviour with well defined "misalignment" of surface layers A detailed analysis for DLR IfSM's Laminate type II with an 11 mm delamination between plies 2 and 3 is shown in [9].

Material	1350 914C			
Stacking sequence	[0,/45,/0,/ −45/0/90]ₛ		[±2/45/±2/ −45/0/90]ₛ	
Interface no	2/3	3/4	2/3	3/4
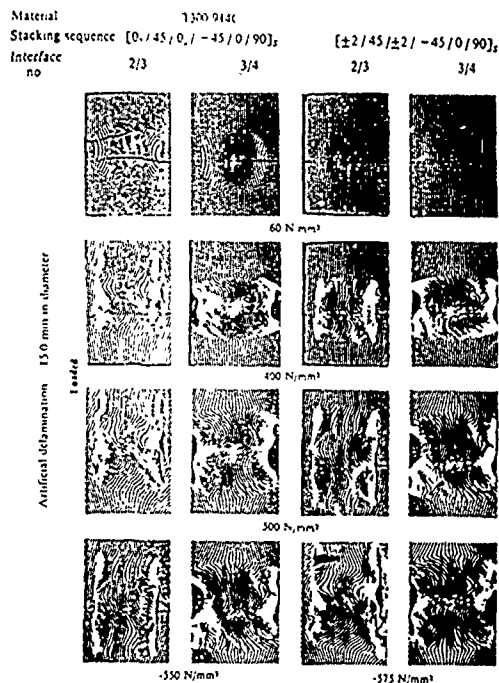
Figure 16 **Photographs of Reflected Gratings Under Different Compressive Stress States (Specs under Load)**
DLR - IfSM

The tests under fatigue loading were oriented towards the static tests The two multidirectional 16 plies thick laminate types I and III (Table 2 for DLR) were selected, which were sufficiently studied in former investigations [13] A third multidirectional laminate was modified in ± 2° plies in order to confirm the more tolerant crack and delamination growth of such a laminate noticed during the static tests under fatigue loading, see laminate type II in Table 2.

From former fatigue tests on specimens without artificial delaminations it is well known that the S-N-curves under compression-compression and tension-compression exhibit characteristic differences in the slope as depicted in Figure 17.
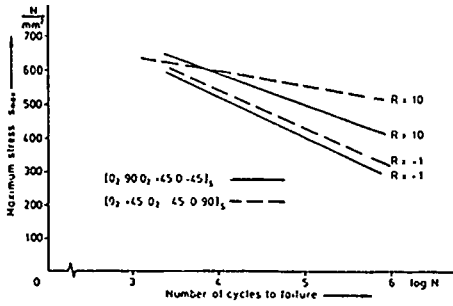
Figure 17. S-N - Curves with R = 10 and R = -1
DLR - IfSM

In the case of Laminate type I the onset of delamination growth was characterized by the clearly audible tearing of the two 0°-plies on the left and right border of the delamination. The optical grating reflection method [14] enabled the determination of time of onset as well as the observation of growth rate with sufficient accuracy. In all investigations the beginning of growth in specimens under R = −1 was found to depend on the intensity of the stress amplitude and takes place, therefore, at very different numbers of load cycles. Figure 18 shows this dependency for delaminations of 11 mm diameter in the 2/3 laminate type I.
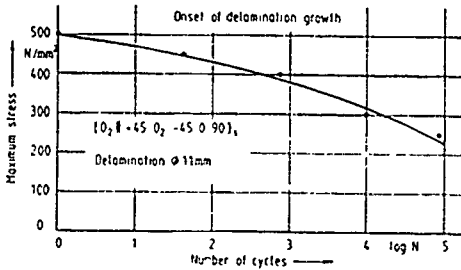
Figure 18. Onset of Delamination Growth, Laminate Type I
DLR - IfSM

The investigation of the influence of large delamination diameters on fatigue failure was of special interest with respect to damage tolerant behaviour. Figure 19 shows a plot of the Weibull distributions for comparison of 11 and 15 mm delaminations at the 5/6 interface of laminate type I under maximum stress of ± 450N/mm².

Laminates of type III containing 15 mm delaminations at the 6/7 interface show no growth of the artificial delaminations, but unstable growth of "natural" delaminations at the 2/3 interfaces. With types I and III no degradation of the fatigue lives by at 6/7 interface introduced 15 mm delaminations was found, but similar to type I laminates the 5/6 interfaces are much more critical as can be seen in Figure 20.

Computation

At ONERA the O'Brien specimen [± 35°/0°/90°]$_s$ was used as an example to calculate the influence of damage development inside plies on the energy release rate value, see Figure 21.

The second computation was done by modelling the laminate type II from Table 2 for DLR's specimen. The initial delamination, penny-shaped in real test, was modelled as a square shape area in the FEM analysis. Quadratic shape functions were chosen, except for elements having
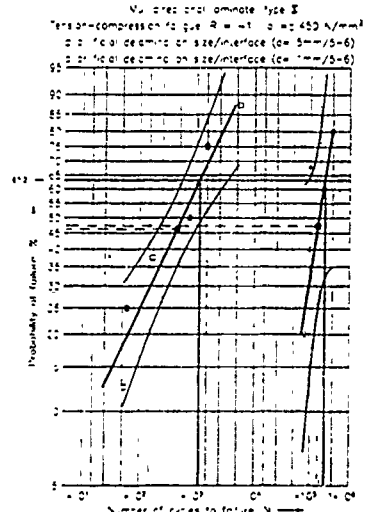
Figure 19. Comparison of Different Delamination Sizes
DLR - IfSM
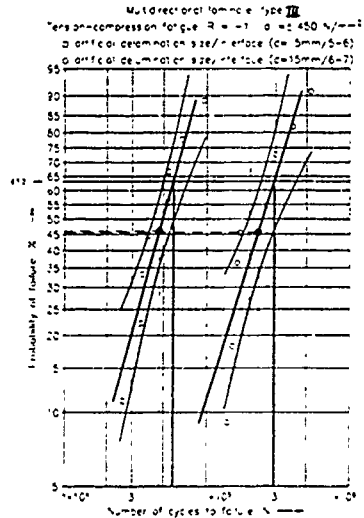
Figure 20 Comparison of Delamination Position, Laminate Type III
DLR - IfSM

one side on the crack front. On this side linear shape function were used. Special limit conditions are imposed inside the anti-buckling guide region. By the use of a little imperfection, the post-buckling behaviour of the blister was got. The result was not far from experimental observation, even so finite element specimen idealization had been quite simplified

Bifurcation and non-linear analysis runs were conducted at NLR to determine onset of local buckling of delaminated plies and to analyse the deformation of the different components in the specimens in the longitudinal and in the transverse directions. Figure 22 shows one of the displacement curves.

The computational work done by CCL for RAE and by AEROSPATIALE will be shown in Chapter 6 Corre-

lation.
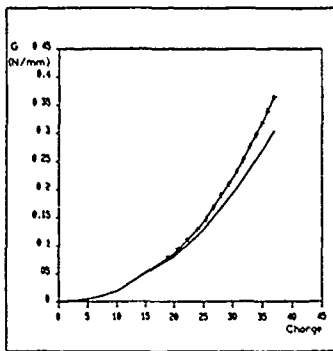
Figure 21 Influence of Damage, Stacking Sequence
[± 35°/0°//90°₂/0°/ ± 35°], (K. O'Brien Specimen)
ONERA
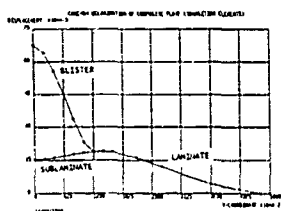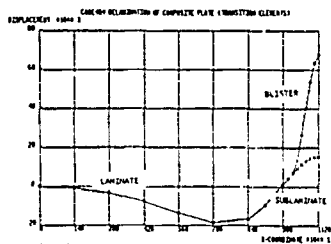
Figure 22. Results of Non-Linear Analysis
NLR

6. Correlation of Analytical and Experimental Research

The computational simulation done by ONERA for the DLR specimen with laminate type II configuration take into account that the main mode for delamination growth is rotation mode. Due to the fact that the critical energy release rate G_f^r is a function of the angle Θ between the two layers fiber direction, the interface of which is delaminated, gave insight that a variation of the critical G value versus $\Theta/2$ had to be established. In Figure 23 the value of f (f − criterion) is plotted for different reduction factors, at a load level of $\sigma = -430 N/mm^2$

The experimental and analytical results for AEROSPA-TIALE's research is shown in Figure 24 for laminate type
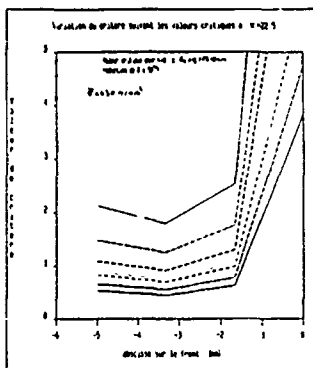
Figure 23 Values of Criterion
ONERA
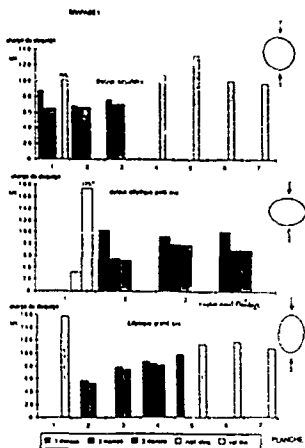
Figure 24 Experimental and Computational Results for CFRE-Panels
Laminate Type I
AEROSPATIALE

I (Table 2 for AS) and in Figure 25 for laminate type II. The numerical calculated values are higher than the experimental ones, except in the case of a circular deliberate delamination

In Figure 26 results of RAE experimental research is demonstrated The variation in lateral width of the fringe pattern is shown as a function of end strain for each of the specimens containing artificial delaminations For some of the specimens the initial buckle did not extend the full width of the delamination (the final points do not represent complete failure) The stringer panel tests were stopped prior to failure to prevent post failure damage

Figure 27 shows the buckle amplitude versus end strain for each of the specimens The perturbation in the curve for the 100 mm delamination corresponds to the change from a single to a double buckle.

Figure 28 shows the experimental results obtained by MBB on stringer-stiffened panels together with the failure criteria which can be used It can be concluded by this this research - including impact tests - that the combined effects of environment and barely visible impacts do not reduce the failure strain achieved with unimpacted panels at RT more than 20 % (70 °C wet structure)

6-10

AEROSPATIALE
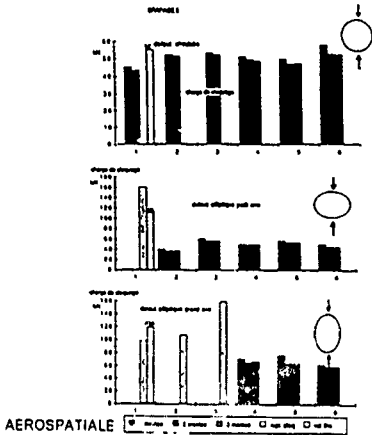
Figure 25. Experimental and Computational Results for CFRE-Panels Laminate Type II

RAE
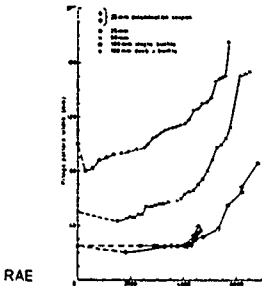
Figure 26. Fringe Pattern Width vs End Strain

RAE
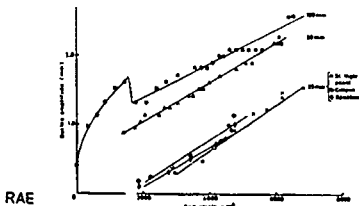
Figure 27. Buckle Amplitude vs End Strain

MBB
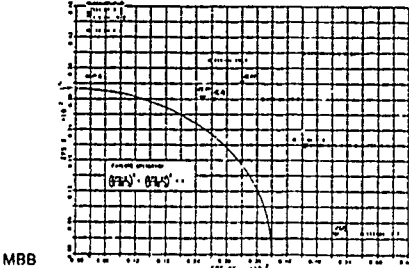
Figure 28 Test Results of Impacted Stringer-Stiffened Panels and Derived Failure Criterion

7. Conclusions

Having studied the compressive buckling and the subse-

quent growth of defects and damages in detail it is now possible to predict the buckling and growth of single-plane delaminations with reasonable accuracy. Very large amounts of computer time were required by such detailed analysis if it was extended to include multiple delaminations and other damage forms in order to model impact damage. In addition the coupon tests showed that single-plane delamination growth was accelerated by the damage mechanism *matrix cracking* in the adjacent plies under quasi-static and fatigue loading This is particular true with tension-compression fatigue where in some cases the matrix crack formation in off-axis plies, rather than the artificial delamination, seems to induce the compressive failure. With respect to damage tolerance considerations some configurations of delamination states proved to be non-critical. Experimental results on large integrally stiffened panels seemed to show that delamination growth might not be the primary cause of failure in impact damaged full-scale structures Single-plane delaminations close to the surface grow and may cause early failure in material coupons but in large panels they will precipitate failure only, if at all, at very high strain levels It appears that other damages in the sublaminate can precipitate the failure of wide panels whereby the buckling of surface plies only causes some load redistribution

Only small insight in and therefore lack of complete understanding and modelling of the interaction of the damage mechanisms *single* and *multiple delamination* with *matrix cracking* and *impact damage* exists.

8. Outlook

Since DAMAGE TOLERANCE BEHAVIOUR of CFRP is important for Composite Designs the governing failure mechanisms should be determined in relation to structural elements or structures and from the first objectives (including fracture analysis by SEM [?]) methods as existing, see for example Figure 29) - as listed below - sig-
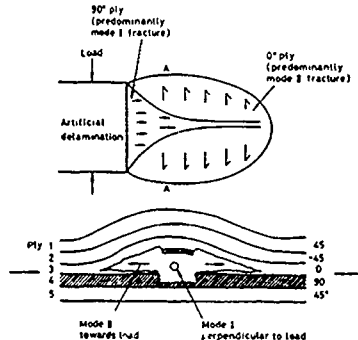
Figure 29. Fractographic Results for Delamination Growth in CFRE Test Coupon
upper part Top View
lower part Cross Section AA
RAE

nificant effort can be put into the development of analytical models for a research on the damage propagation in composite structural elements and real structures, may be in a follower GARTEUR activity:

1. Tests on structural panels (typical aircraft stuctural panels) with experimental modelling of defects to investigate the damage mechanisms *single* and *multi-*

[?] SEM = Scanning Electron Microscop,BEM = Boundery Element Method FEM = Finite Element Method

ple delaminations and *low energy impact.*

2. Tests and analysis with impact damage together with failure analysis under dynamic loading for static and fatigue aspects by using 2D and 3D failure criteria and application of BEM [2]) to create special elements for FEM [2]).

3. Failure analysis (incl failure criteria) of crack growth in notched specimens (holes and sharp notches)

The ultimate aim must be to formulate acceptance criteria based on experimental research with the goal to establish a damage classification on theoretical foundations

9. Bibliography

[1] W. T. Chester and M H Pavier. *Predictive Modelling of Damage in CFRP Delamination in PEEK APC 2* CCL-C2448-R01 a (Cambridge Consultant Ltd Final Report to RAE, Farnborough, Hampshire, UK) 1987

[2] W. T. Chester and M. J Pavier *Mixed mode fracture criterion for carbon fibre reinforced epoxy resin* CCL Report C2448-R02 (April 1987)

[3] W. T Chester and M. H. Pavier *Predictive Modelling of Damage in CFRP Delamination in Carbon-Epoxy* CCL-C2448-R 03 b (Cambridge Consultant Ltd Final Report to RAE, Farnborough, Hampshire, UK) 1987.

[4] M Gädke. *Delamination Tests under Static Compression Loading.* Proc. Intern Conf.. Spacecraft Structures and Mechanical Testing, ESA SP-289, 1989, pp 579 - 585

[5] H C. Goetting. *Delamination Tests under Compression-Compression and Tension-Compression Loading* Proc Intern. Conf Spacecraft Structures and Mechanical Testing, ESA SP-289, 1989, pp 587 - 592

[6] H Eggers *Analysis of Delamination Growth* Proc Intern Conf.. Spacecraft Structures and Mechanical Testing, ESA SP-289, 1989, pp 377 - 381.

[7] M. Gädke *Hygrothermomechanical Behaviour of Carbonfibre Reinforced Epoxies* VDI-Fortschrittsberichte, R 5, No 136 (1988)

[8] H. W Bergmann et al. *Development of Fracture Mechanics Maps for Composite Materials* ESTEC 4825/81/NL/PB(SC) (DFVLR Final Report Vol 1,2,3,4 to ESA) 1985

[9] H W. Bergmann et al. *Development of Fracture Mechanics Maps for Composite Materials (Compression Loading)* LSILC 6400/85/NL/PB(SC) (DFVLR Final Report Vol 1,2 to ESA) 1988

[10] H W Bergmann et al.: *Mechanical Properties and Damage Mechanisms of Carbonfibre-Reinforced Composites - Tension Loading.* DFVLR-FB 85-45 (1985)

[11] H W Bergmann et al *Mechanical Properties and Damage Mechanisms of Carbonfibre-Reinforced Composites - Compression Loading* DFVLR-FB 88-41 (1988)

[12] H. C. Goetting and M. Gädke, H Eggers *Response of Laminates Containing Delaminations. In Development of Fracture Mechanics Maps for Composite Materials (Compression Loading)* Final Report ESA/LSILC Contract No 6400/85/NL/PB(SC), Vol. 2, pp 212-261, April 1988

[13] R. Schütze and W Hillger, H Bäuml. *Schadenuntersuchungen an multidirektionalen CFK-Laminaten nach Schwingbelastungen mit R = -1* Z Werkstofftechnik 18, S 124-130, 1987.

[14] R Schütze and H C Goetting *On-Line Measurement of Onset and Growth of Edge-Delaminations in CFRP-Laminates by an Optical Grating Reflection Method* Z Werkstofftechnik 16, 9(1985), pp 306 - 310

[15] E Riks *Some computational aspects of the stability of non-linear structures* NLR-MP-82034U (1982)

[16] D Giletta de Saint Joseph *Composites 2D Modelisation mécanique et identification de la couche élémentaire* Thèse Docteur-Ingénieur, Univ. Paris VI- ENS Cachan LMT (1985).

[17] O Allix and P. Ladeveze, E le Dantec, E Vittecoq *Damage mechanics for composite laminates under complex loading* Proceedings IUTAM/ICM Symposium Yielding, Damage, and Failure of anisotropic solids Grenoble (1987)

[18] L. M Kachanov: *Time on the rupture process under creep conditions.* TVZ AKAD, Nauk SSR, OID Techno Nauk, Vol 8 (1958)

[19] P Ladeveze. *Sur une théorie d'endommagement anisotrope* Rapport interne n° 34 LMT-ENS Cachan (1983)

[20] K J. Bathe and T. Sussman. *The gradient of the finite element variational indicator with respect to nodal point coordinates an explicit calculation and applications in fracture mechanics and mesh optimization* Int Journal for Num Meth. in Eng, Vol. 21 (1985), pp 763-774

[21] JP. Favre and C Marais - Laizet - Rapport ONERA (1988)

[22] D J Wilkins. *The Engineering Significance of Defects in Composite Structures* Characterization, Analysis and Significance of Defects in Composite Materials London 12-14 April 1983, AGARD-CP-355

[23] R. I Potter and G Dorey *The Effects and Structural Significance of Defects and Damage in Composite Materials* RAE-Report 1984

[24] R Prinz, and H C. Goetting, K Schmidt *Experimental and Analytical Study of Strength Degradation During Fatigue of Graphite/Epoxy Laminates* Proc of 12th ICAF Symposium, Toulouse, May 1983, pp 2 3/1 - 2 3/33

[25] H C Goetting *Einfluß verschiedener Parameter auf die Schadensentwicklung.* In. Schadensmechanik kohlenstoffaserverstärkter Kunststoffe bei Schwingbelastung DFVLR-Mitt. 87-08, S. 29-61, Juli 1987

[26] R Prinz. *Schädigungsmechanismen und Abschätzung der Lebensdauer von CFK-Laminaten* DFVLR Mitt 87-08 1987

[27] S M Bishop and G D Howard, C J Wood *The Notch Sensitivity and Impact Performance of [0° / + 45° / - 45°] Carbon Fibre Reinforced PEEK.* RAE TR 84066 1984.

[28] H P Spanier *Sechs Meß- und Prüfprogramme mit und ohne Ausgabe eines Sollwerts für das universelle Funktionsgerät UNFUG* DFVLR-Interner Bericht IB 131-86/23, 1986.

[29] K Marguerre *Zur Theorie der gekrümmten Platte großer Formänderungen.* Proc 5 Int Congress of Appl Mech (1983), pp 93-101

[30] I. Szabo *Höhere Technische Mechanik.* Berlin, Springer Verlag (1960), S. 284-289.

[31] F G Buchholz. *Improved formulae for the II-calculation of the strain energy release rate by modified crack closure method* Proc 3. World Congress on Finite Elements, Interlaken 1984, pp 650-659

[32] J G Williams. *On the calculation of energy release rates of cracked laminates* Int J Fracture 36 (1988), pp 101-119

[33] K Rohwer. *Stress and deformation in laminated test specimens of carbonfiber reinforced composites* DFVLR-FB 82-15

BUCKLING AND POST-BUCKLING BEHAVIOR OF A DELAMINATION IN A CARBON-EPOXY LAMINATED STRUCTURE : EXPERIMENTS AND MODELLING

D.GUEDRA-DEGEORGES, S.MAISON, D.TRALLERO
Aérospatiale. Louis Blériot Joint Research Center
92152 Suresnes Cédex, France

J.L.PETITNIOT
Institut de Mécanique des Fluides de Lille (ONERA)
59045 Lille Cédex, France

1. SUMMARY

This paper presents results of a study aiming the following objectives :
- experimental identification of sensitivity to local buckling and characterization of post buckling behavior of a delamination in a plate under compression.
- to perform non linear three dimensionnal finite element computations in order to establish local buckling loads, shape of the blister, load levels and direction related to the propagation of the delamination.
Two shapes of defect (circle and elliptic) and one stacking sequence of a 24 plies quasi-isotropic laminate in T300/914 material have been investigated.
Artificial delaminations have been located in the thickness of sample between 3rd and 4th ply.
An experimental device to assess accurately buckling loads and shape of the blister during propagation has been developped.
Fracture mechanics was used for computing by finite element method the strain energy release rate G and partition G_I, G_{II}, G_{III} all around the delamination during post-buckling.
A propagation criterion based on G_{Ic}, G_{IIc} of the material set up in Aérospatiale has been used for the assessment of load levels and direction related to the propagation of the delamination.
Comparisons between tests and computations are also performed and it is shown that computations are able to predict accurately load levels and direction related to the propagation of the delamination.

2. INTRODUCTION

Many researches into buckling-compression behavior of composite with a delamination are running at the moment because of the compression design of aeronautical structural parts. This work has therefore been achieved in relationship with the aircraft division of Aérospatiale.
Delaminations can occur during the material processing or under external loading of the structure during service : impact of foreign bodies or mechanical loading of the structure.
Many works dealing with local buckling have been achieved but at the moment there is only a few work describing the behavior after buckling of such delaminations.
The aim of this study is to set up a numerical methodology based on finite element analysis and fracture mechanics able to predict load level related to propagation of a delamination using a propagation criterion established in Aérospatiale.
Special test apparatus has been developed in order to follow up the propagation of the delamination and geometry of the blister (without contact laser diode transducer, acoustic emission) during compression loading.
Comparisons between tests and computations have been achieved and show that the numerical strategy proposed is able to predict accurately load level related to propagation of delamination and also its direction.

3. EXPERIMENTAL

3.1 Materials

The laminate of this study is made of the following pre-preg:
- Fibre TORAY T300B 6k / Resin CIBA-GEIGY 914

3.2 Stacking sequence

One stacking sequence of a quasi-isotropic 24 plies is studied : $[(45/135/0/90)_3]_{sym}$
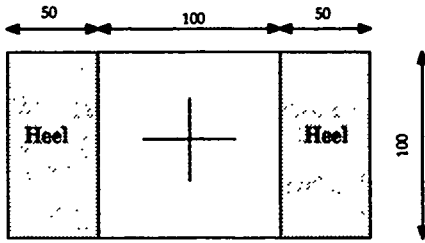
Fig 1: Sample dimensions

Nota : the heels are made of 3 (±45°) glass plies

3.3 Defect simulation

We consider 2 defect shapes :
• circle (∅ 30 mm)
• elliptic (main axis 45 mm, minus axis 20 mm)
    - elliptic main axis oriented O° (axis effort)
    - elliptic main axis oriented 90°(⊥ effort)

The area of all defects is 707 mm².

Defects are located between 3rd and 4th ply (interface 0°/90°) at the middle plane of the sample and were created with two superposed thin polyethylen films (25 μm thick each).

3.4 Test equipment and description

Tests were performed at I.M.F.L. at room temperature with a 100 kN INSTRON machine. Loading speed was 0.1 or 0.2 mm per minute.
A special anti-buckling device was developped reducing dimension of window from 100 mm x 100 mm to 92 mm x 74 mm (see figure 2).
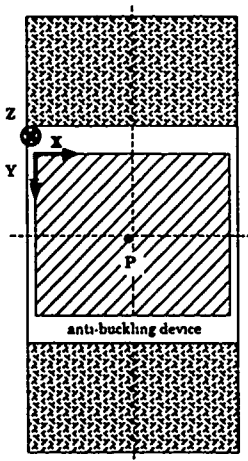
Fig 2 : Anti-buckling device and axis

One without contact laser diode transducer is located on each face of the sample. Displacement of these transducers are controlled by computer allowing the measurement of out of plane deflection of the whole plate (see figure 3). Data acquisition is stored at some chosen load levels.
This instrumentation allows an accurate determination of the blister geometry and also of the propagation load.
A camera is also used to follow the test and acoustic emission is used for selected samples.
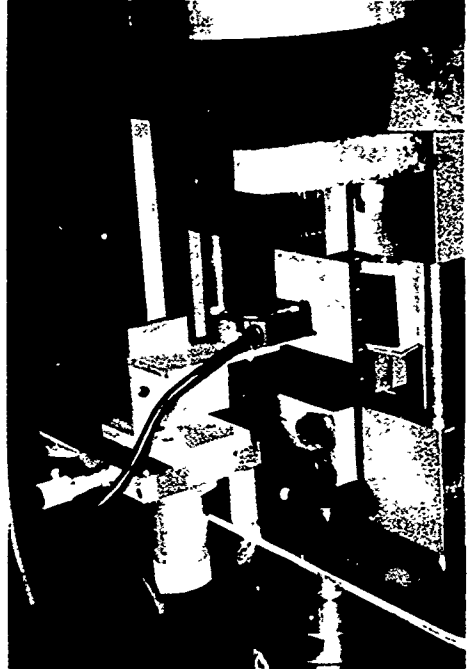
Fig 3 : View of test fixture and laser diode transducer

Remarks concerning local buckling of artificial defect

Preliminary tests showed that local buckling (with instantaneous propagation) occured at the same time than global buckling for a load level greater than expected by computations as if the defect was bonded.
The assumption made is that vacuum performed during material processing induces vacuum between both films of polyethylen result being an additional effort needed when loading the sample to balance the difference of pressure.
It is the reason why a small hole was drilled in the without defect side of the sample which allowed for all following tests expected behavior.

Nota : This method is acceptable because in a real structure even if vacuum is performed a delamination is never made of two superposed films. In our case contact polyethylen-polyethylen is obviously very dependant of the pressure difference.

3.5 Test results

In order to be as clear as possible the only circular defects will be described in this part. Behavior of other defects (elliptic) is almost identical and main results are given in table 1.

3.5.1 Deflection versus load

Transducers are in this part located at point P on each side of the sample (see figure 2). Out of plane deflection are measured on each side of the specimen. Difference between both measures gives the height of the blister (figure 4).
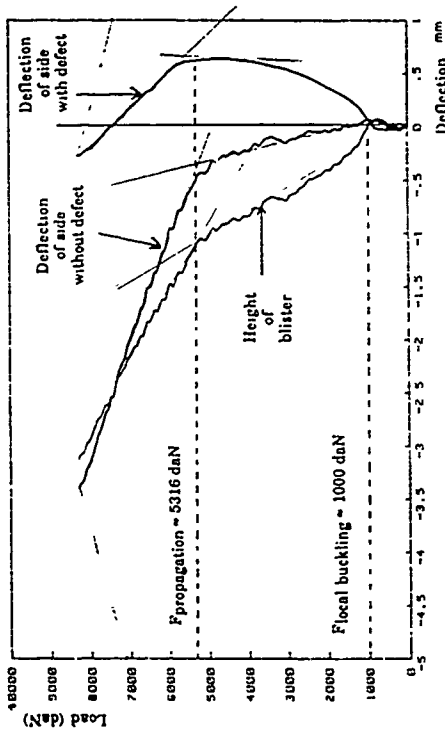
Fig 4 : Out of plane deflections versus load

Local buckling load is about 1000 daN, first propagation about 5468 daN. Rupture load is 8685 daN (determination of the loads is made by using the change of curve slopes).

3.5.2 Mapping of out of plane displacements of both sides of the whole sample

In this part the test is stopped at some load levels in order to measure by displacement of both transducers (step is 0.1 mm on X and Y axis) the out of plane deflections of the sample.

The interest of these mappings is to give an estimation of the propagation load of the defect, to follow up direction of propagation and to provide data directly comparable to the computations.

As an example mappings (figure 5 and 6) are given at load 4500 daN and 6000 daN for the circular delamination.
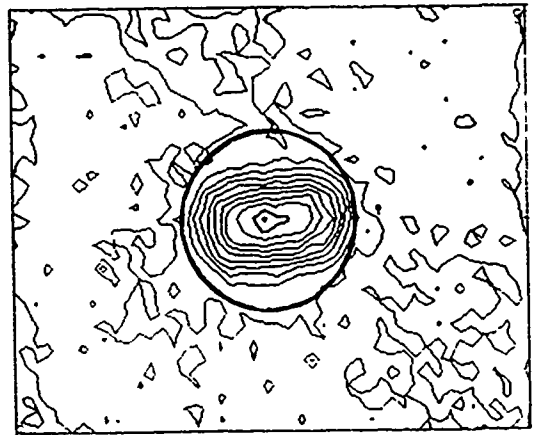
Fig 5 : Mapping at 4500 daN (no propagation)
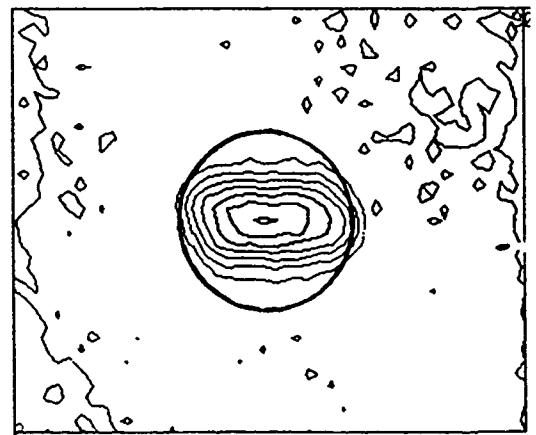
Fig 6 : Mapping at 6000 daN (propagation)

These mappings confirm that propagation is between 4500 daN and 6000 daN (good agreement with results given by figure 4).

3.5.3 Acoustic emission

Acoustic emission has also been perfomed on some samples using two transducers located on both side of the specimen.
It has been found that acoustic emission was very important at propagation of the delamination.
This technique seems to be a good indicator to determine load related to local buckling and also load of first delamination propagation.
An example of acoustic activity of the sample related to the propagation of an elliptic delamination is given figure 7.
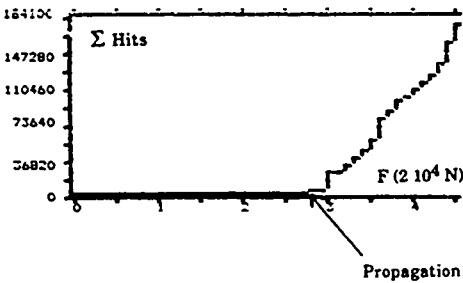
Fig 7 : Acoustic activity related to propagation of an elliptic delamination

3.5.4 Synthesis of test results - discussion

In table 1 loads related to local buckling and to propagation for all defect shapes are reported.

Identification of sample	Local buckling load	Propagation load
65 EC 3	2000 daN	5772 daN
65 EC 4	1000 daN	5316 daN
66 EG 2	835 daN	5468 daN
66 EG 3	-	4500 daN< <6000 daN
66 EG 4	1220 daN	4500 daN< <6000 daN
67 EP 2	1215 daN	5316 daN
67 EP 3	-	4500daN< <6000daN
67 EP 4	2582 daN	4500daN< <6000daN

Table 1 : Main quantitative experimental data

Nota :EC means circular defect
EG means elliptical defect, main axis 0°
EP means elliptical defect, main axis $\perp$ 0°

One can remark scattering concerning local buckling loads.

Some cross sections of the geometry of the blister (Ox and Oy cross sections) always show the same geometries and a dissymetry between Ox and Oy cross sections.

Concerning the propagation load it is not easy to determine it accurately. However curves load - out of plane displacement added to acoustic emission and camera follow up allow determination of good assessment.

There is a good coherence between all results and there is no significative sensibility to the defect shape when looking at it's propagation : all defects have quite the same propagation load and related direction is always near perpendicular to the loading direction.

It also must be noted that propagation of the defect is always associated to an increase of the bending of the plies located under the defect.

4. COMPUTATIONS

The only circular configuration of defect is described in this part.

4.1 Fracture mechanics

Fracture mechanics deals with behavior of structure containing cracks. Its main objective is to predict condition of propagation of a defect (load related to propagation, stability or instability of the propagation).
The elastic linear behavior of the material studied (carbon fibres + epoxy resin) and small displacements assumption when computing strain energy release rate allows the use of Linear Elastic Fracture Mechanics.

The stress fields can be separated in three simple modes near the delamination edge : in plane stresses gives opening mode called mode I (fig 8), in plane
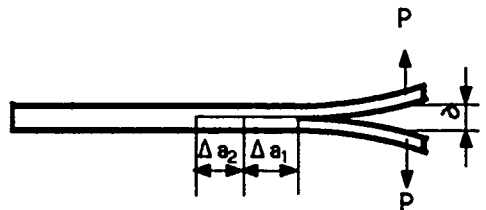
shear gives shear mode called mode II (fig 9) and out of plane shear gives mode III (fig 10).

Fig 8 : Mode I (opening mode)
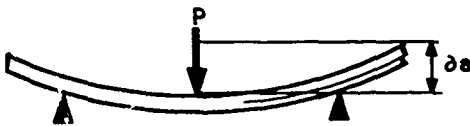
Fig 9 : Mode II (in plane shear)
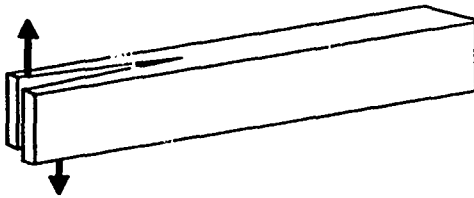
Fig 10 : Mode III (out of plane shear)

4.1.1 Strain energy release rate

A parameter which can characterize crack propagation is the strain energy release rate G.

G is defined as follows:

$$G = -\delta E_p / \delta S \quad (1)$$

where δE_p is the variation of the potential energy of the structure and δS is the variation of the crack area for an infinitesimal propagation.
It can be showed that G can be written :

$$G = \delta U / \delta S \quad (2)$$

where δU is the variation of elastic energy of the structure.
G is a computed value related to a virtual crack propagation. The quantity that characterizes the propagation is the critical strain energy release rate called G_c which has to be determined experimentally.

Comparison of G and G_c can allow the prediction of the crack propagation :
• if $G > G_c$ there is propagation
    • if $\delta G / \delta S < 0$, propagation is stable
    • if $\delta G / \delta S > 0$, propagation is unstable
• if $G < G_c$ there is no propagation

The use of this simple concept is not so easy for laminated composite structures. Indeed G_c depends on material, loads, defect geometry and can also change along the delamination edge. It is therefore necessary to express G_c as a function of intrinsic values of the material to avoid characterization of each defect configuration.

The solution to this problem is to separate G in its three basic modes: $G = G_I + G_{II} + G_{III}$
and to apply a material criterion based on intrinsic G_{Ic}, G_{IIc} and G_{IIIc}.

4.1.2 Propagation criterion

G_{Ic}, G_{IIc} and G_{IIIc} being considered as intrinsic values of the material, the aim of this part is to establish a relationship as :

$$G_c = f(\text{partition}, G_{Ic}, G_{IIc}, G_{IIIc}) \quad (3)$$

Nota :
    • Partition is the amount per cent of mode 1, mode 2 and mode 3.
    • Experience (ref 1) showed that for carbon-epoxy materials G_{IIIc} is much higher than G_{Ic} and G_{IIc}. This fracture mode will be therefore neglected in the following parts

A complete set of tests has been achieved with varying values of partition in order to establish the prior relationship. Tests performed were Double Cantilever Beam for mode 1, End Notched Flexure for mode 2, Mixed Mode Flexure and Crack Lap Shear for mixed mode.

Different partitions are obtained for the two last samples by changing the location of the delamination in the thickness of the sample. The partition is determined by Finite Element Computations.

As an example different rates studied and respective configurations are showed in figure 11.

Sample configuration	Mode 1 %	Mode 2 %
8 plis CLS 8	4	95
16 plis CLS 16	21	78
24 plis CLS 24	42	58
8 plis MMF 8	51,5	48,5
16 plis MMF 16	58	42
24 plis MMF 24	61	39
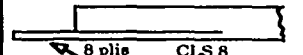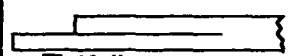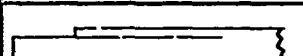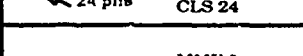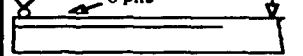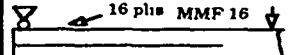
Fig 11 : Computed partitions for tested configurations

When we plot $G_I / G_{Ic} + G_{II} / G_{IIc}$ as a function of mode 1 percentage we obtain as a first approach :

$$G_I/G_{Ic}+G_{II}/G_{IIc}=1 \quad (4)$$

One can express differently this propagation criterion:

Let $tg\alpha=G_I/G_{II}$ and $G=G_I+G_{II}$

It comes:

$$Gc=(1+tg\alpha)G_{Ic}G_{IIc}/(G_{Ic}+tg\alpha G_{IIc}) \quad (fig\ 12)$$
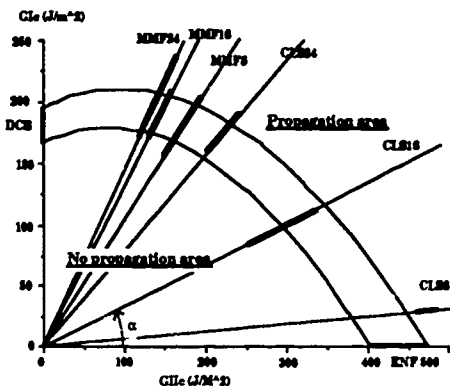
Fig 12 : G_c as a function of α (related to mode partition)

This expression of the criterion shows that the only knowledge of G_{Ic} and G_{IIc} allows the determination of G_c related to the propagation of a delamination once mode partition is determined.

Prior study has shown that the criterion proposed gave good results (ref 2).

4.2 Finite element computations

In case of complex structures (geometry, loads, non-linear behavior) it is necessary to use finite element method to determine G and its partition. This is the aim of this part.

4.2.1 Description of the problem

The part of the specimen modelized is limited to 100mm x 100mm (tabs not modelized). A circular delamination (Ø 30 mm) is located under 3 plies. The three-dimensionnal multi-layers elements of SAMCEF code are used. Problem is considered geometrically non linear (Riks algorithm is used for resolution). Computer is a VAX 6510.

4.2.2 Mechanical properties of the unidirectionnal tape

E_{11}=140000 MPa v_{12}=0,31
G_{12}=5700 MPa
E_{22}=10000 MPa v_{23}=0,48
G_{13}=5700 MPa
E_{33}=10000 MPa v_{13}=0,31
G_{23}=3600 MPa

11 : fibre direction
22 : transverse direction
33 : thickness direction

Ply thickness : 125 µm

4.2.3 Defect modelling

Two three-dimensionnal multi-layers elements (8 nodes) are disposed in the thickness of the sample : one for the upper skin (3 plies) and the other for the outer skin (21 plies). Lower nodes of upper element are the same as upper nodes of lower element in the "no defect" region.

Lower nodes are different from upper nodes in the defect region. They have the same co-ordinates but there is no link between the respective degrees of freedom which allow the defect to buckle :
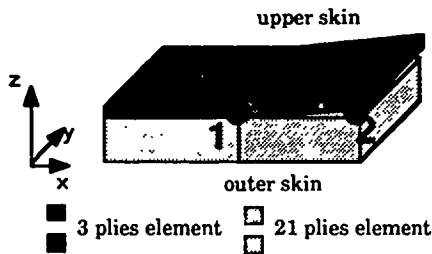
Fig 13 : Mesh strategy for modelling the defect

4.2.4 Mesh and boundary conditions

Mesh is made of 348 elements with refinement near delamination edge.
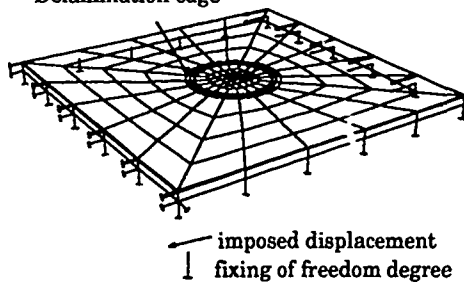
Fig 14 : Mesh and boundary conditions

4.2.5 Non linear computation on global structure

Non linear computation is perfomed on the whole structure (16 increments of load - about half an hour CPU time, VAX 6510). Out of plane displacement of point P on each side of the sample versus load is

presented in figure 15.

Load (daN)
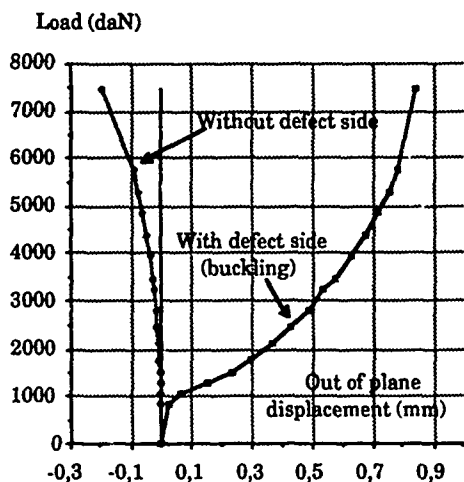
Fig 15 : Out of plane displacement versus load

Computed local buckling load is about 950 daN.
As an example it is shown at figure 16 shape of
structure at 5761 daN (fifteenth increment).

Fig 16 : Deformed mesh at 5761 daN (x10)
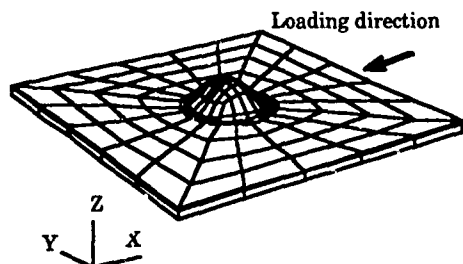
4.2.6 Computation of strain energy release rate G

It has been shown that G could be written :
$$G=\delta U/\delta S$$
In the frame of finite element analysis and for a
"small" crack propagation G can also be
approximated :
$$G=Ep(a+\Delta a)-Ep(a))/\Delta a \quad (5)$$
where :   a is the crack length
        Δa is the propagation length
        Ep is the potential energy of the
        structure
This method needs two computations :
● one for a crack which length is a
● a another for a crack which length is a + Δa

In order to decrease CPU amount of such a

computation, simplification can be made by
considering that only stiffness of elements in the
vicinity of the delamination edge is affected by the
crack propagation. This hypothesis verified in prior
studies (ref 2) allows very important reduction of
the size of the problem when computing G by working
only for this step on a reduced structure delimited
by the delamination edge.

Taking account of this hypothesis G can be written :
$$G=-1/2(Ep_{reduced}(a+\Delta a)-Ep_{reduced}(a)) \quad (6)$$

In our case the problem is geometrically non linear.
This means that extraction of reduced structure
must be achieved with special care. The cut struc-
ture must be as far as possible of non linear behavior
imposing a mesh refinment near the edge
delamination (fig 17).

Location of cut

A: high non linear part
B: "nearly linear" part
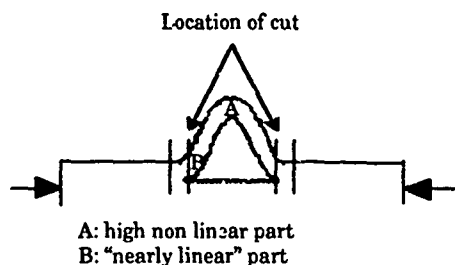
Fig 17: Location of cut imposed by non linear behavior

*Implementation of the previous method with finite
element code SAMCEF*

● Step 1
Non linear computation of the whole structure
including initial delamination as described
previously.
● Step 2
For each load level computed in step1 :
        - extraction of reduced structure (fig 18)
        - linear computations on reduced structure
Displacements extracted from non linear
computations are applied on the reduced structure
external skin.
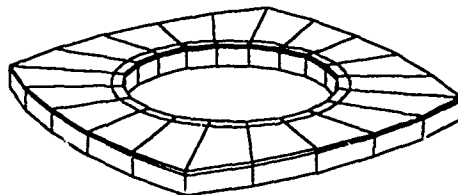
Fig 18 : Reduced mesh used for G computation

This step provides $Ep_{reduced}(a)$

● Step 3
Pertubation of each delamination edge node loca-
tion (one by one) of Δa. (Virtual Crack Extension
method)
● Step 4
Linear computation of the perturbed reduced struc-
ture.
This step provides $Ep_{reduced}(a+\Delta a)$
● Step 5
Computation of G for each node (equation 6).

Nota : a special program has been developped in
Aérospatiale in order to automatize step 2, 3, 4 and
5. This program only requires as input nodes of
delamination edge, perturbation Δa and its direc-
tion.

Remarks on Δa choice

● previous studies showed that direction of pertur-
bation has a very slight effect on G calculation (ref
3).
● A convergence study has been performed on Δa
length and it's influence on G (fig 19).

Fig 19 : Local G as a function of Δa

G (J/m2)

Delta a (mm)
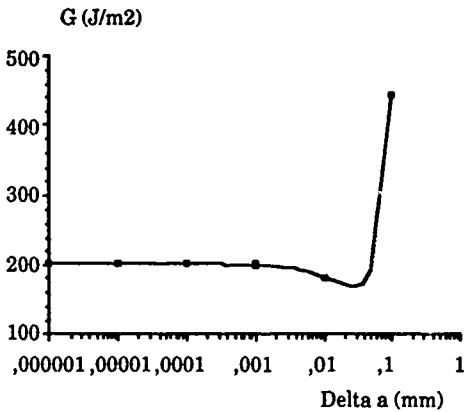
Δa equals 10⁻⁴ mm for all G calculations.

G computation results

Local G values around the edge delamination are
presented at figure 20 for 3 load levels. These
results conduct to assume that propagation direc-
tion will be near the perpendicular to the loading
one.
G can also give some information on propagation or
no propagation of delamination by comparing its
value to the smallest of G_{Ic}, G_{IIc}, G_{IIIc} (here GIc equals
180 J/m2). This conservative prediction is
nevertheless not able to provide accurate estima-
tion of load related to propagation of the
delamination.
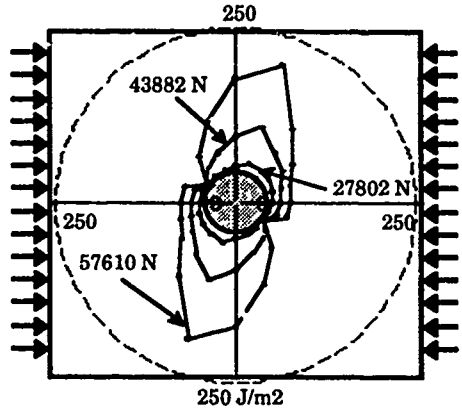
Fig 20 : Local G values around the edge delamination

We now need partition of mode to get more accurate
information on direction of propagation and to be
able to apply the propagation criterion proposed.

4.2.7 Computation of mode partition

Let see the differences with computing G.
● step 1
Non linear computation of the whole structure is of
course always the same start point.
● step 2
For each load level computed in step 1 :
         - extraction of reduced structure
         - linear computation on reduced structure.
Displacements extracted from non linear
computations are still applied on reduced struc-
ture.
The difference in this step is the reduced structure
for the following reason : for G calculation the
Virtual Crack Extension method was used. This
method doesn't allow the partition determination.
At this time the delamination propagation is
obtained by detaching superposed nodes located
ahead the delamination edge (the propagation length
is therefore imposed by first element ahead
delamination edge length).
This means that we need one more finite element in
the reduced structure. The reduced mesh used for
partition computation is presented at figure 21.
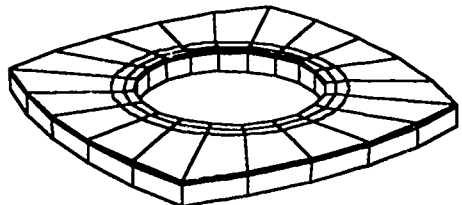
Fig 21 : Reduced mesh used for partition computation

At this step superposed nodes ahead delamination are detached.

This step provides displacements u, v and w (respectively u', v' and w' for superposed nodes) of each node near ahead delamination edge.

● step 3

Superposed nodes are attached. A linear computation is performed.

This step provides reaction R_x, R_y, R_z of each node near ahead delamination edge.

● step 4

Calculation of mode partition:

where at this time 1, 2 and 3 are local axis depending of the node (see figure 22).

$$GI(a) = 1/2b\Delta \ a \ F1 \ (u_1 \ -u_1')$$

$$GII(a) = 1/2b\Delta \ a \ F2 \ (v_2 \ -v_2')$$

$$GIII(a) = 1/2b\Delta \ a \ F3 \ (w_3 \ -w_3')$$
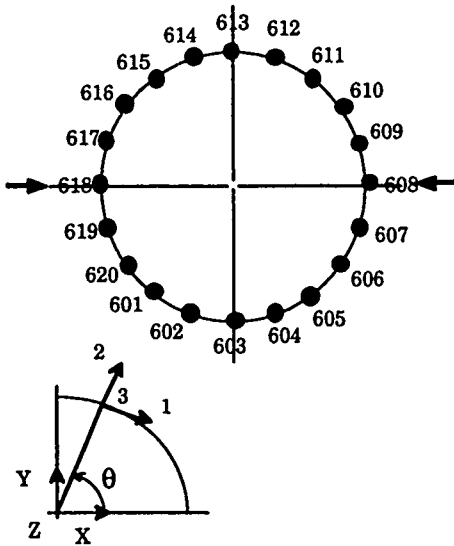
Fig 22 : Local coordinates around delamination edge

Partition results

Computed partition is given for three load levels at figures 23, 24 and 25.

G_{III} value is not reported but its contribution is always below 10%. This confirms that the contribution of this term can be neglected in the criterion (considering furthermore that G_{IIIc} value is very high).

We can notice an evolution of the repartition G_I, G_{II} when increasing the load level.

Nota : G increases especially when global bending of the sample appears in the computation. This tends to prove that bending brings propagation (see remark § 3.5.4).
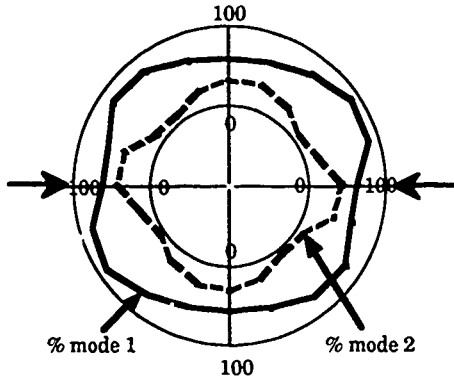
Fig 23 : Mode partition around delamination (F=2780 daN)
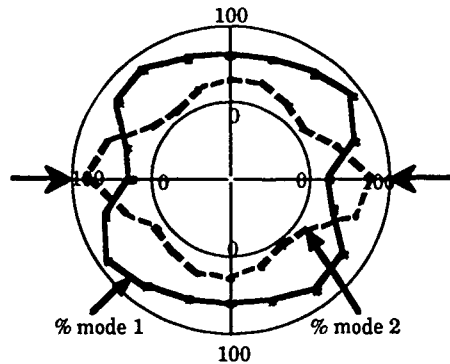
Fig 24 : Mode partition around delamination (F= 4388 daN)
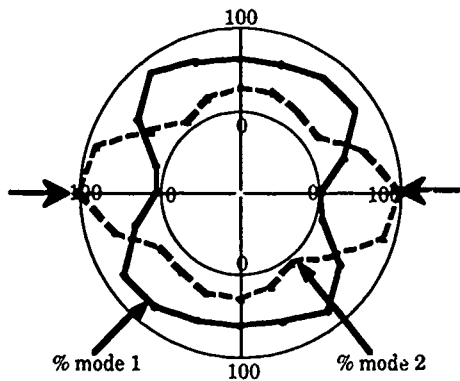
Fig 25 : Mode partition around delamination (F=5761 daN)

4.3 Prediction of propagation

Let's now apply the propagation criterion previoulsy described at the different load levels. Criterion equals 1 at 5761 daN (figure 26). This means that propagation of the delamination should occur at about 5800 daN.
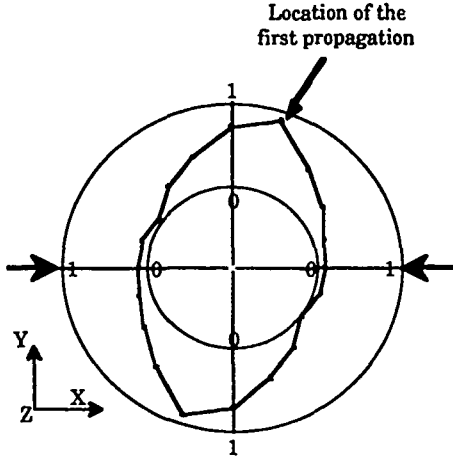
Fig 26 : Criterion around delamination
(F=5761daN)

When looking at the shape of the criterion one can also predict that propagation will occur at a direction near the perpendicular (about 70°) to the loading direction.

5. COMPARISONS BETWEEN TESTS AND COMPUTATIONS

Because computation doesn't take into account the propagation of the delamination the only part of the curves to be compared is below propagation load.

● *Curves out of plane displacements - loads (figures 4 and 15)*

There is a good agreement between experiments and computations especially when comparing the buckling skin of the sample.
Nota :More global bending of the specimen is observed during tests than predicted by computation (probably due to boundary conditions).

● *Blister shape*

A comparison between Ox and Oy cuts of the blister has been achieved both for tests and computations. These investigations showed that there is a good agreement between tests and experiments for loads below propagation of the delamination (same shapes, same displacements and same dissymetry).

● *Propagation of the delamination*

Predicted propagation load is 5800 daN.
When looking at experimental curves displacements as function of loads, propagation loads are 5316 daN or 5772 daN depending of the sample. Out of plane displacements mappings confirm that propagation load is between 4500 daN and 6000 daN and acoustic emission reveals propagation for loads about 6000 daN.
We can therefore consider that numeric strategy used and propagation criterion proposed are able to provide a good prediction of the propagation of the delamination.
Let's now compare criterion values around delamination edge (fig 26) and experimental out of plane mappings at 6000 daN and 7450 daN (fig 27):
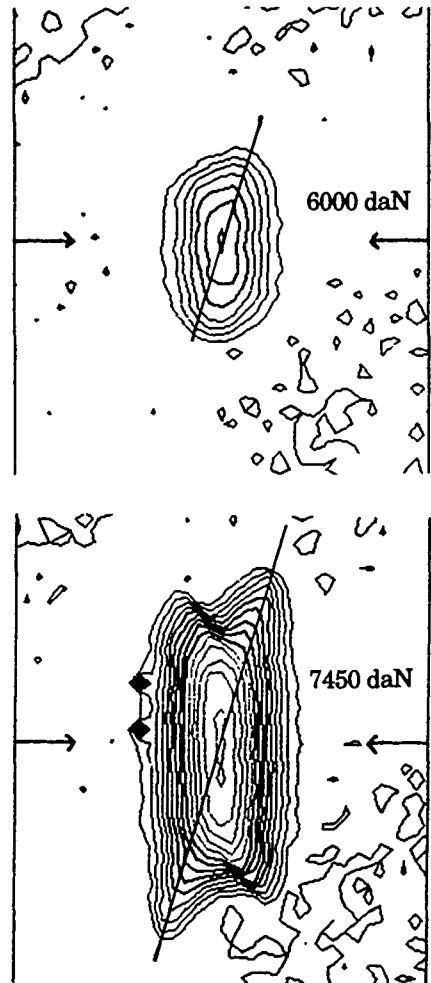
Fig 27 : Mappings after propagation

This comparison reveals that computation is also able to predict direction of the propagation

CONCLUSION

The objective of the study was to set up a numerical methodology based on finite element analysis and fracture mechanics able to predict load level related to propagation of a delamination under compression using a mat rial criterion established in Aérospatiale.
One quasi-isotropic stacking sequence (24 plies) of a carbon-epoxy material was studied. Two shapes of defect (circle and elliptic) located under 3 plies were considered.
Tests were performed with special instrumentation (I.M.F.L.) allowing to follow up the propagation of the delamination and the geometry of the blister (without contact laser diode transducers).
Geometrically non linear fully three-dimensionnal composite finite element analysis has been achieved and special programs developped in Aérospatiale used in order to establish the strain energy release rate G and its partition (G_I, G_{II}, G_{III}) all around the delamination edge. Criterion developped in Aérospatiale was also applied.
Comparisons between experiments and computations show a good agreement. In particular it shows that numerical methodology used is able to establish a good prediction of the propagation load and also its direction.
Such a methodology should be very useful in case of delamination in a real aeronautical structure when quantitative and also qualitative information are needed to analyse detected delamination defects.

References

[1]   D.LANG, D.TRALLERO, J.E.BRUNEL
"A criterion of mixed mode delamination propagation in composite materials"
EUROMECH 269, St-Etienne, France, 1990

[2]   D.TRALLERO
"Experimental study and numerical modelling of damage fracture of holed composite laminates"
ECCM 5,Bordeaux, France, 1992

[3]   J.E.BRUNEL
"Méthodologie de calcul du taux de restitution d'énergie - application au mat rotor X380"
Aérospatiale, PV n° 60069/F, 1991

[4]   S.MAISON, D.GUEDRA-DEGEORGES
"Behavior of a local delamination under compressive load"
ICCAS 17, Suède, 1990

[5]   J.D.WHITCOMB
"Mechanics of instability-related delamination growth"
Composite Materials, Testing and Design, Vol 9, 1988

[6]   B.COCHELIN, M.POTTIER-FERRY
"Un modèle de flambage pour les plaques stratifiées délaminées"
JNC 7, Lyon, France, 1990

PROGRESSIVE DELAMINATION IN POLYMER MATRIX COMPOSITE LAMINATES
A NEW APPROACH

by

C.C. Chamis and P.L.N. Murthy
NASA Lewis Research Center
21000 Brookpark Road
Cleveland OH 44135
United States

L. Minnetyan
Department of Civil Engineering
Clarkson University
Potsdam, New York
United States

ABSTRACT

A new approach independent of stress intensity factors and fracture toughness parameters has been developed and is described for the computational simulation of progressive delamination in Polymer Matrix composite laminates. The damage stages are quantified based on physics via composite mechanics while the degradation of the laminate behavior is quantified via the finite element method. The approach accounts for all types of composite behavior, laminate configuration, load conditions, and delamination processes starting from damage initiation, to unstable propagation and to laminate fracture. Results of laminate fracture in composite beams, panels, plates, and shells are presented to demonstrate the effectiveness and versatility of this new approach.

1. INTRODUCTION

It is generally accepted that composite structures with delaminations fail when local delaminations grow or coalesce to a critical dimension such that (1) the laminate cannot safely perform as designed and qualified, or (2) catastrophic laminate fracture is imminent. Any predictive approach for simulating delamination fracture in fiber composite laminates needs to formally quantify: (1) types of local delaminations, (2) the types of stresses which initiates them, and (3) the coalescing and propagation of local delaminations to critical dimensions for imminent laminate fracture.

One of the ongoing research activities at NASA Lewis Research Center is directed toward the development of a methodology for the "Computational Simulation of Delamination Fracture in Fiber Composites Laminates". A part of this methodology consists of step-by-step procedures to simulate individual and mixed mode delamination fracture in a variety of generic composite components (Refs. 1, 2, and 3). Another part has been to incorporate these methodologies into an integrated computer code identified as CODSTRAN for composite durability structural analysis (Refs. 4 and 5). The

objective of this report is to describe the fundamental aspects of this new approach and to illustrate its application to a variety of generic composite laminate and structures.

The generic types of composite laminate delaminations illustrated in this report are those that would occur in: (1) single and combined mode fracture in beams, (2) laminate free-edge delamination fracture, (3) laminate center flaw progressive fracture and (4) plate and shell structural fractures. Structural fracture is assessed by one or all of the following indicators: (1) the displacements increase very rapidly, (2) the frequencies decrease very rapidly, (3) the buckling loads decrease very rapidly, or (4) the strain energy release rates increases very rapidly. These rapid changes are herein assumed to denote sufficient delaminations for imminent global structural fracture.

In the present approach computational simulation is defined in a specific way. Also general remarks are included with respect to (1) application of this new approach to large structures and/or structural systems, and 2) lessons learned about conducting such a long duration research activity, with regard to increasing computational efficiency, gaining confidence, and expediting its application.

2. FUNDAMENTALS

This new approach to structural fracture is based on the following concepts.

1. Any laminate or structural component made from this laminate can sustain a certain amount of delamination prior to structural fracture (collapse).

2. During delamination propagation, the laminate exhibits progressive degradation of laminate integrity as measured by global structural behavior variables such as loss in frequency, loss in buckling resistance or excessive displacements.

3. The critical delamination can be characterized as the amount of damage beyond which the laminate integrity degradation is very rapid, induced by either (1) small additional damage or (2) small loading increase.

4. Laminate delamination damage is characterized by the following sequential stages: (1) initiation (2) growth, (3) accumulation, (4) stable or slow propagation (up to critical amount), and (5) unstable or very rapid propagation (beyond the critical amount) to collapse.

These concepts are fundamental to developing formal procedures to (1) identify the five different stages of delamination (2) quantify the amount of damage at each stage and (3) relate the degradation of global laminate behavior to the amount of damage at each stage. The formal procedures included in this new approach are as follows:

1. **Delamination Stages Identification:** (1) Delamination initiates when the local stress state exceeds the corresponding material resistance (2) Delamination grows when the stress exceeds the corresponding material resistance on the delamination periphery for every possible failure mode. (3) Delamination accumulates when multiple cites of delamination coalesce. (4) Delamination propagation is stable or slow when small increases, in either the delamination propagation or loading condition, produce insignificant or relatively small degradation in the structural behavior (frequencies, buckling resistance, and displacements). (5) Delamination propagation is unstable or very rapid when small increases in the delamination propagation or in loading conditions produce significant or very large changes in the global structural behavior variables (frequencies, buckling resistance, and displacements).

2. **Delamination Quantification:** The amount of delamination is formally quantified by suitable modeling of the physics in the periphery of the delaminated region in order to keep the laminate/structure in equilibrium for the specified loading conditions, structural configuration and boundary conditions. This part of the procedure is most conveniently handled by using computational simulation in conjunction with incremental/iterative methods as will be described later.

3. **Laminate Structural Behavior Degradation:** This part of the procedure is quantified by using composite mechanics in conjunction with the finite element analysis. The delamination stages are quantified by the use of composite mechanics while degradation of the structural behavior is quantified by the finite element method where the delaminated part of the structure does not contribute to the resistance but is carried along as a parasitic material. It is very important to note that nowhere in this approach was there any mention of either stress intensity factors or fracture toughness parameters This new approach by-passes both of them. However, use is made of the structural fracture toughness in terms of global Strain Energy Release Rate (SERR) because it is a convenient parameter to identify the "critical delamination amount". The critical global SERR in the context of present approach is described subsequently.

The fundamental concepts described previously are concisely summarized in Figure 1. The steps are few and simple and the parameters for "critical delamination" are readily identifiable.

The combination of composite mechanics with the finite element method to permit formal description of local conditions to global structural behavior is normally handled through an integrated computer code as shown schematically in Figure 2. The bottom of this figure describes the conditions of the material (microstress versus resistance) and where the criteria for delamination initiation, growth, accumulation and propagation are examined. The left part integrates (synthesizes) local delamination conditions to global structural behavior (response). The right part of the figure tracks (decomposes) the effects of global changes (loading conditions for example) on the local (micro) material stress/resistance. Increases in delamination are induced at the micro level while increases in the load conditions are applied at the global structural model. Overall structural equilibrium is maintained by iterations around the "cart-wheel" until a specified convergence is reached. Implementation of the new approach to track the various stages of delamination is illustrated schematically in Figure 3. The final result in terms of load versus global displacement is shown in Figure 4. The schematics in Figures 1 to 4, collectively summarize the fundamentals and implementation of this new approach to composite delamination fracture and also to composite structural fracture in general. Applications to specific structures/components are described in subsequent sections.

3. BEAMS

The new approach has been applied to three different types of beams: (1) Double cantilever for opening mode delamination, (2) end-notch-shear for shear mode delamination and (3) mixed mode delamination. Typical results obtained are summarized below. The details are described in the references cited for each specific application.

1. **Double Cantilever** - A typical result from applying this new approach to a double cantilever for opening mode delamination is shown in Figure 5 (Ref. 1). For this simulation, a pre-existing delamination (one inch long) was assumed across the beam width. A small amount of delamination growth/accumulation (about 0.05 inch) had severe effect on the strain energy release rate (SERR-G). Rapid delamination occurred to about 1.12 inch beyond which the SERR increased very rapidly indicating unstable delamination propagation to complete delamination. Referring to Figure 1, the critical delamination for this beam is less than 1.0 inch length (a) and less than 1.0 psi-in structural fracture toughness (G) These values are in the range of those experimentally measured by using the double cantilever test method (about 0.8 psi-in at 1-inch crack length).

2. **End-Notch-Shear** - Typical results for shear-mode delamination in a beam, as can be measured by end-notch-flexure, are shown in Figure 6 (Ref. 1). A pre-existing delamination of one inch across the width was assumed for the simulation. A rapid delamination growth/accumulation took place to about 1.1 inches followed by a stable delamination propagation to about 1.18 inches. Beyond this point, the delamination propagation became unstable. Note that the range of measured data is indicated by the horizontal dashed lines. Note also that the local crack closure technique, which is commonly used in fracture mechanics studies, is also shown with the dashed curve. Applying the criteria in Figure 1, the critical fracture toughness parameters are from the global curve about 1.18 inches for "a" and about 3.5 psi-in for "G". Those from the local curve are about 1.2 inches and for "a" and 2.5 psi-in for "G". This example illustrates the difference between local and global quantities. It is worth noting that the local method requires about three times the computer time compared to the global.

3. **Mixed Mode Delamination** - Two types can be simulated: Shear (Mode II) combined with opening (Mode I) and opening (Mode I combined with shear (Mode II) and with tearing (Mode III). A typical result for the first type is shown in Figure 7 (Ref. 1). This figure illustrates that the global method does not distinguish how much each mode contributes. It is necessary to use the local closure technique to quantify the simultaneous contribution of each mode. An interesting observation is that the opening mode drives the delamination to beam splitting while the shear mode reaches a stable propagation state. Referring to Figure 1, the critical structural fracture parameters are about 1.15 inch for "a" and about 3.3 psi-in for "G". These are about five and eight percent smaller, respectively, compared to shear Mode (Mode II) delamination.

A typical result for the second type of mixed mode delamination is shown in Figure 8 (Ref. 2). The curves plotted in this figure are for critical values obtained from Figure 1, that is, when the damage propagation state becomes unstable. The individual mode contributions were obtained by the local "crack closure" technique. A few interesting observations are: (1) The tearing mode (III) is insignificant compared to the other two; (2) Mode I contributes the most and; (3) superposition of the three modes does not equal that of the total. This again indicates that the global fracture parameters appear to be more representative indicators of laminate/structural fracture. The other important observation is that the unsymmetric laminate configuration can be used in the end-notch mixed mode beam to measure the tearing mode. This is a simple test method indeed. The authors are not aware of any measured results obtained by using this test method. Collectively, the results from the different beams demonstrate that the new approach is readily applicable to these types of composite structures.

4. PANELS

The new approach has been applied to computationally simulate structural delamination of composite panels subjected to in-plane loads. Typical results for three types of delamination are described to demonstrate application of the procedure (Ref. 3).

1. **Edge Delamination** - The physics and stress state of edge delamination in composite laminates are schematically illustrated in Figure 9. The delamination processes and their quantification using global parameters is shown in the schematic in Figure 10. Typical results obtained for laminates from three different composite systems are shown in Figure 11. This type of delamination grows/accumulates rapidly to about six percent of the area and then reaches a stable state. This stable state implies: (1) That a specific composite laminate will have a unique critical delamination parameter and (2) edge delamination, induced by predominately tensile in-plane stress, will not lead to panel collapse or disintegration.

Referring to Figure 1, the parameters for stable damage state are about seven percent area delamination for all composite systems and about 35, 50 and 70 psi-in for S-G/IMHS, AS/HMHS, and AS/IMHS composites, respectively. Additional observations from Figure 11 are that the structure fracture toughness depends on fiber type (difference in S-G and AS for the same matrix IMHS) and matrix (HMHS and IMHS for the same fiber AS). An important conclusion is that this new approach provides a relatively simple formal procedure to evaluate and/or identify fiber/matrix combinations for specified structural fracture toughness.

2. **Edge-Pocket-Delamination** - Edge delamination is usually preceded by transply cracks which can occur in several locations simultaneously thus forming pocket-type delaminations along the edge. These types of delaminations can be simulated the same way as described previously except that they represent a form of multisite delamination initiation, growth, accumulation and propagation. Typical results for structural fracture toughness are shown in Figure 12 for three different composite systems. Several interesting aspects of fracture progression can be observed in this figure. (1) Pocket delaminations grow rapidly inward to about five percent in delaminated area. (2) Stable delamination occurs inward to about twenty percent in delaminated area. (3) The pocket delaminations coalesce as indicated by the jump in "G". (4) The accumulated delamination grows with a decreasing rate to a stable level of about forty-five percent in delaminated area, and (5) the propagation exhibits stable behavior beyond this delaminated area. The structural fracture toughness value after stabilization is the same as that for stable edge delamination. The important conclusions are: (1) this new approach provides sufficient information to identify/quantify the delamination fracture process from initiation to structure/component collapse and (2) it is readily adaptable to multiple site delamination initiation.

3. **Internal or Embedded Delamination** - This type of delamination is a result of the fabrication process or damage sustained by inadvertent normal impact. In either case the delamination growth, accumulation, and propagation can be simulated by using this new approach. Typical results are shown in Figure 13 for the three different composite systems. An important observation is that substantial internal damage (up to fifty-five percent in delaminated area) occurs with negligible increase in the global SERR. Keep in mind that this panel and delamination results are for tensile in-plane load which does not cause local buckling.

The results from the panel clearly demonstrate that the new approach for structural fracture is readily adaptable to these types of delamination fractures including those initiated at internal hidden sites.

5. EFFECTS OF DELAMINATION ON LAMINATE STRUCTURAL INTEGRITY

The effects of delamination on laminate structural integrity (structural integrity degradation) are evaluated by plotting changes in the structural integrity variables such as: (1) increases in displacement, (2) loss in stiffness, (3) loss in vibration frequency, and (4) loss in buckling load versus percent of delaminated area. Plots for all of these are available in Reference 3 for different laminates, for each of the delamination types (center and off-set), and for each of the three composite systems (AS/IMHS, AS/HMHS and S-G/IMHS). One typical plot is shown in Figure 14 for buckling load. This plot is similar to those for axial stiffness and vibration frequency and complementary to that for end displacement. Collectively, the results indicate the following general trends: (1) practically linear decrease in the structural integrity variables with increasing percent in delaminated area, (2) the rate of structural integrity degradation (dx) with respect to delaminated area (dA), (dx/dA) is less that 20 percent, (3) the higher the fiber modulus in the composite the lower the degradation rate, and (5) the vibration frequency exhibits the lowest degradation rate while the axial stiffness is the greatest. One important conclusion from the above discussion is that the computational simulation procedure described herein is effective in evaluating the structural integrity degradation of laminates with various types of delaminations. Furthermore, since the method is not restricted to the cases studied it should also be equally as effective for composite structures in general.

6. PLATES

This case is selected to illustrate the effects of damage propagation on vibration frequencies and buckling resistance as well as the effects of hygrothermal environments. Typical results obtained by using CODSTRAN (Fig. 2) are shown in Figures 15 (Refs. 6, 7, and 8) where the schematics of the plate and the various hygrothermal environments are also shown. The important observations are: (1) The reference case, at room temperature and without moisture, exhibits the least amount of damage accumulation compared to the other cases; (2) moisture alone has a negligible effect on fracture load but increases the damage extent to fracture; (3) combined temperature and moisture (hygrothermal) decrease the load to fracture but permit substantial damage accumulation to fracture; (4) both the vibration

frequency and the buckling resistance decrease very rapidly as the fracture load (structural collapse) is approached; (5) the hygrothermal environments degrade the structural behavior of the plate; and (6) the buckling resistance is the most discriminating structural behavior for hygrothermal degradation.

The important conclusion is that this new approach provides the formalism to simulate complex environmental effects from the micromechanics to structural behavior. That is, the temperature and moisture affect the matrix locally while the composite mechanics and the finite element method integrate these local effects to structural behavior (buckling resistance in this case).

7. PLATES UNDER NORMAL IMPACT

A composite square plate (3- by 3-in.), supported along its four edges is loaded by a concentrated normal dynamic load at the center (Fig. 16(a)). Large deformations are included in the computational simulation. The laminate configuration is +45/-45/-45+45/, with a total composite plate thickness of 0.02 in. All edges have been restrained against displacement in the z direction in all cases. Within this constraint, two types of support conditions are considered. In the first type, support nodes are allowed to move in the x-y plane (the plane of the undeformed composite plate). In the second type of support, boundary nodes are restrained against displacement in all directions. The first and second types of support conditions will be referenced to as released and restrained supports, respectively (Ref.8).

The concentrated transient load is assumed to increase linearly with time until global fracture of the composite plate occurs. Three loading rates are considered. These loading rates are 0.1, 2.0 and 3.5 lb/ sec. Figure 16(b) shows the dynamic load-deflection histories at these three rates for the first type (released) boundary support conditions. The displacements are very small for the first load increment because of the large inertial load imparted when the structure is initially set in motion. Also, the higher the loading rate, the smaller the displacement because of the higher inertial force. After the first load increment, there is a dramatic increase in displacement, especially for the 0.1 lb/μsec loading rate. In this case, the time is sufficiently long for the entire plate to be set in motion. After a center deflection of approximately 0.3 in. membrane forces become significant and the incremental deflections are reduced. It may be noted that even though the support nodes are free to move in the x-y plane, membrane effects are developed due to the restraint of boundary nodes in the z direction and the square geometry of the plate. If the

support nodes were not restrained in the z direction, the corners of the plate would lift up and fold along the diagonals to allow for a truly unrestrained deflection of the plate without membrane forces. The load corresponding to 0.3 in. center deflection is 60 lb. This loading level also causes initial local damage in the composite laminate (ply 1 - the first ply on the tension side of the plate). The initial damage is caused by the ply transverse tensile stresses reaching their limits.

Next, the same loading at the same rates is applied to the composite plate with the second type support where all boundary nodes are restrained from translation in all directions. Figure 16(c) shows the load-deflection relations for the three loading rates applied to the plate with the restrained support. For the 0.1 lb/μsec loading rate, membrane action becomes much more important compared to the case of released supports and the displacements are significantly reduced as the restrained boundaries do not allow the majority of the plate to participate in transverse motion. Soon after the initial setting of the plate in motion, inertial forces become negligible because the loading rate is relatively slow. CODSTRAN analysis shows at 0.07 in. center deflection at the end of the first load increment, under 30 lb load. During the next load increment, damage is initiated at the center node in ply 1 by reaching the stress limit in the transverse tensile stress. The 60 lb load that initiates damage is the same as what was required to initiate damage under the released type support condition. However, the displacement under the load is only two-thirds of the displacement under the released support case. A summary of the failure modes caused by the loads in the two different plates is in the table on the lower part of Figure 16. The important observation is that the damage is primarily by transverse ply cracking.

8. SHELLS

CODSTRAN is used to simulate the damage initiation, growth accumulation, and propagation to fracture in a composite shell with through-the-thickness as well as partial initial defects and subjected to internal pressure with hygrothermal environment.

Through-the-Thickness Defect - Typical results for a through-the-thickness initial defect are shown in Figure 17 (Ref. 9). The results in this figure show that: (1) Shells subjected to internal pressure sustain relatively low damage accumulation to fracture compared to other structural components; (2) shells are less tolerant to hygrothermal effects compared to other structural components; (3) the vibration frequencies of the shell do not degrade rapidly as the fracture pressure is approached and (4) hygrothermal environments have a

significant effect on the vibration frequencies of the shell. An important observation is that composite shells with through-the-thickness defects subjected to internal pressure, exhibit a brittle type behavior to fracture with relatively negligible delamination. This explains, in part, the successful application of Linear Elastic Fracture Mechanics to internal pressure type structures.

9. CONCLUDING REMARKS

The salient results of an investigation of the fracture toughness of general delaminations in fiber composites are as follows:

1. A new approach has been developed to computationally simulate the fracture toughness (strain energy release rate (SERR)) in fiber composites with various delaminations.

2. Free-edge delaminations do not lead to laminate catastrophic fracture under tensile loadings.

3. Multiple free-edge delaminations are possible in thick laminates. The SERR for single and multiple delaminations is about the same.

4. Pocket free-edge delaminations are unstable. They rapidly coalesce into continuous delaminations along the free-edge.

5. Interior delaminations have no effect on laminate fracture toughness in tensile stress fields until they extend to the free edges. Then, their effects are the same as those of free-edge delaminations.

6. Laminate structural integrity in terms of: axial stiffness, buckling load and vibration frequency, degrades linearly with increasing delamination area. The rate of degradation is less than 20 percent. It is the highest for axial stiffness and the lowest for vibration frequency.

7. Increasing the fiber modulus increase the degradation rate of the laminates structural integrity while increasing the matrix modulus has the opposite effect.

8. Hygrothermal environment affects the delamination initiation in plates with through cracks. However, these delaminations have negligible effect on the plate's structural integrity up to about 70 percent of the fracture load.

9. Hygrothermal environments severely affects the delamination propagation in shells with through cracks.

REFERENCES

1. P. L. N. Murthy and C.C. Chamis: "Interlaminar Fracture Toughness: Three-Dimensional Finite-Element Modeling for End-Notch and Mixed-Mode Flexure". NASA TM 87138, 1985.

2. P. L. N. Murthy and C.C. Chamis: "Composite Interlaminar Fracture Toughness: 3-D Finite Element Modeling for Mixed Mode I, II, and III Fracture". NASA TM 88872, 1986.

3. T. A. Wilt, P. L. N. Murthy, and C. C. Chamis: "Fracture Toughness, Computational Simulation of General Delamination in Fiber Composites". NASA TM 101415, 1988.

4. C. C. Chamis and G. T. Smith: "Composite Durability Structural Analysis". NASA TM 79070, 1978.

5. C. C. Chamis: "Computational Simulation of Progressive Fracture in Fiber Composites. NASA TM 87341, 1986.

6. L. Minnetyan, C. C. Chamis and P. L. N. Murthy: "Structural Behavior of Composites with Progressive Fracture". NASA TM 102370, January 1990, 18 pp.

7. L. Minnetyan, P. L. N. Murthy and C. C. Chamis: "Composite Structure Global Fracture Toughness via Computational Simulation". Computers - Structures, Vol. 37, No. 2, pp. 175-180, 1990.

8. L. Minnetyan, P. L. N. Murthy and C. C. Chamis: "Progressive Damage and Fracture in Composites Under Dynamic Loading". NASA TM 103118, 1990.

9. L. Minnetyan, P. L. N. Murthy and C. C. Chamis: "Progressive Fracture in Composites Subjected to Hygrothermal Environment". Proceedings of the 32nd SDM Conference (Part 1), Baltimore, Maryland, April 8-10, 1991, pp. 867-877.

GENERAL PROCEDURE FOR PREDICTING FRACTURE TOUGHNESS IN COMPOSITE STRUCTURES WITH DEFECTS

o Determine requisite properties at desired conditions using composite mechanics

o Run 3-D finite element analysis for an arbitrary loading condition.

o Scale loading condition to match ply stress (or microstresses) at the maximum stress element(s) adjacent to defect(s).

o With scaled loading condition extend defect(s) and plot strain energy release rate vs extended defects(s).

o Select critical "G" and critical "A"
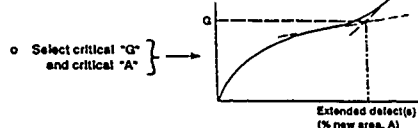
o Method is versatile/general.

FIGURE 1

OVERALL CODSTRAN SIMULATION
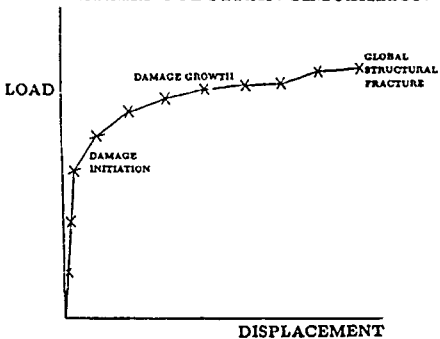
FIGURE 4

CODSTRAN ANALYSIS CYCLE
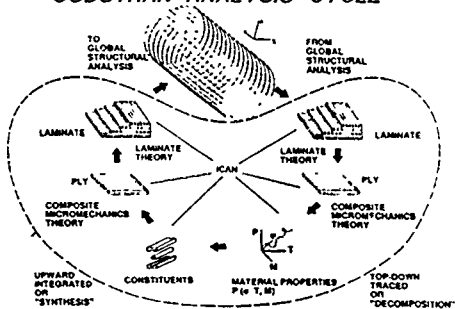
FIGURE 2
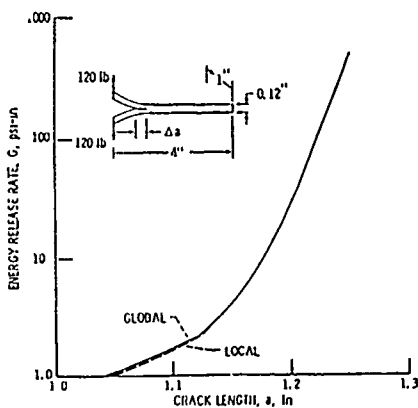
Double-cantilever energy release rate-comparisons

FIGURE 5

CODSTRAN LOAD INCREMENTATION

1 EQUILIBRIUM

2. INCREMENTAL DAMAGE DEGRADE PROPERTIES

3 ADDITIONAL DAMAGE MORE DEGRADATION

4 EQUILIBRIUM: NO ADDITIONAL DAMAGE

5 NEXT LOAD INCREMENT
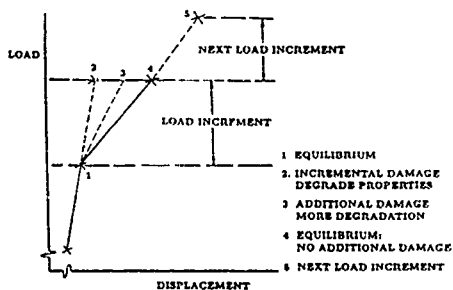
FIGURE 3

END NOTCH FLEXURE ENERGY RELEASE RATE-COMPARISONS
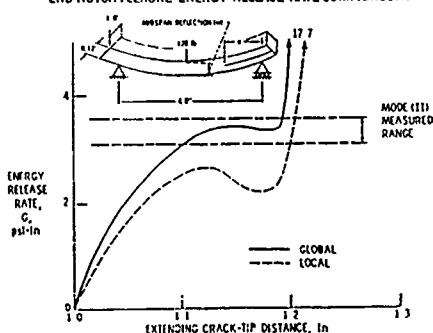
FIGURE 6

MIXED-MODE-FLEXURE ENERGY RELEASE RATE AND COMPONENTS (AS/E)
SINGLE POINT CONSTRAINED (LEVIS) METHOD

FIGURE 7
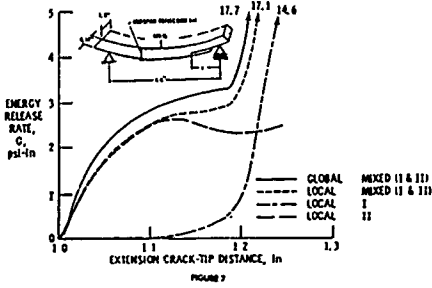
STRAIN ENERGY RELEASE RATE FOR A "TYPICAL" LAB SPECIMEN

(AS/E [±30/90]ₛ 0.6 FVR COMPOSITE)

FIGURE 10
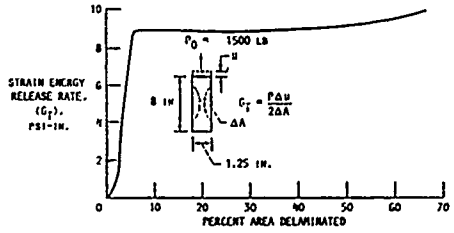
PLY ORIENTATION EFFECTS ON MAXIMUM STRAIN ENERGY RELEASE RATES (in lb/in²) FOR CONSTANT LOAD [-θ₃₆/+θ₁₂]

FIGURE 8
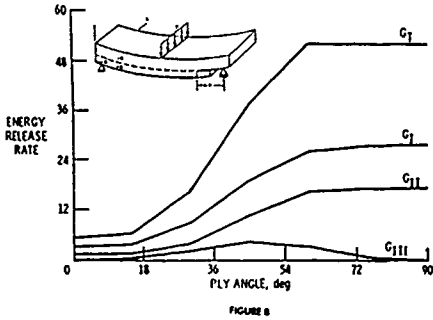
STRAIN ENERGY RELEASE RATE
6-PLY CENTER DELAMINATION
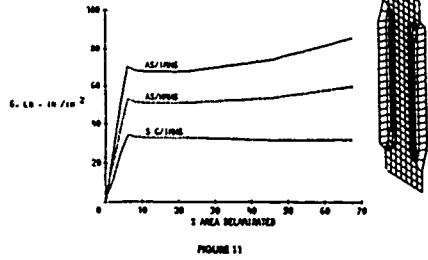
FIGURE 11

LAMINATION DECOMPOSITION FOR FREE EDGE INTERLAMINAR STRESSES
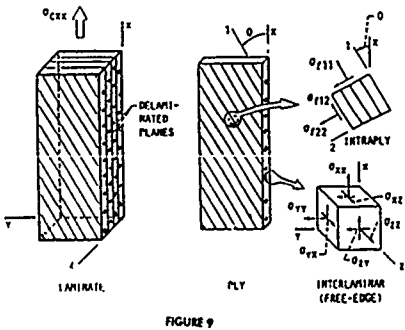
FIGURE 9

STRAIN ENERGY RELEASE RATE
6-PLY CENTER/POCKET DELAMINATION
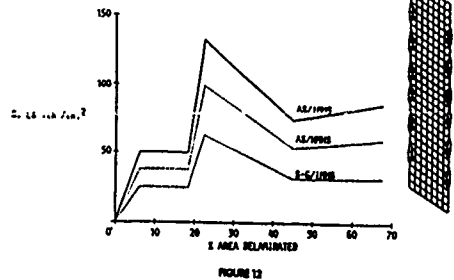
FIGURE 12

STRAIN ENERGY RELEASE RATE
6-PLY INTERIOR/CENTER DELAMINATION
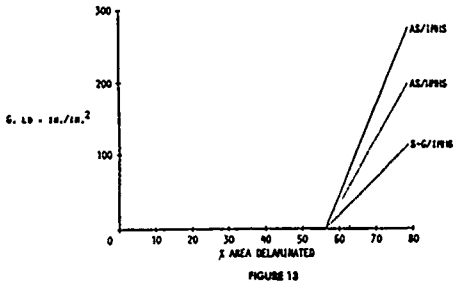
FIGURE 13
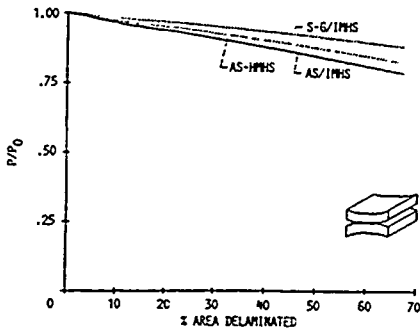
BUCKLING LOAD 6-PLY CENTER DELAMINATION
(SIMILAR BEHAVIOR FOR AXIAL STIFFNESS AND VIBRATION
FREQUENCY AND COMPLEMENTARY BEHAVIOR FOR END DIS-
PLACEMENT).

FIGURE 14

PROGRESSIVE DAMAGE IN COMPOSITE PLATES
UNDER NORMAL IMPACT ([1±45]; T300/EP)

(a) PLATE GEOMETRY (3 in. x 3 in.)

(b) UNRESTRAINED

(c) RESTRAINED
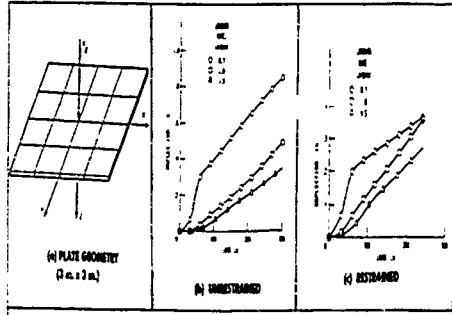
SUMMARY OF FAILURE MODES

Notation: σ_{122}^T - Tensile failure at transverse stress limit for ply.
σ_{311}^T - Tensile failure at longitudinal stress limit for ply.
MDE - Failure according to modified distortion energy criterion.
RR - Failure according to relative rotation limit.

FIGURE 16

LOAD INDUCED PROGRESSIVE DAMAGE AND EFFECTS ON COMPOSITE (T300/EP [±15]s)
PLATE STRUCTURAL RESPONSE INCLUDING HYGROTHERMAL ENVIRONMENT
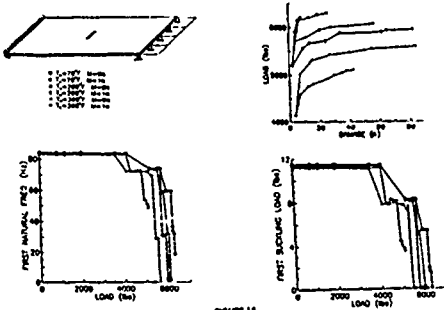
FIGURE 15

LOAD INDUCED PROGRESSIVE DAMAGE AND EFFECTS ON COMPOSITE SHELL
(T300/EP [90/±15/90/±15/90/±15/90]) STRUCTURAL BEHAVIOR
INCLUDING HYGROTHERMAL ENVIRONMENT
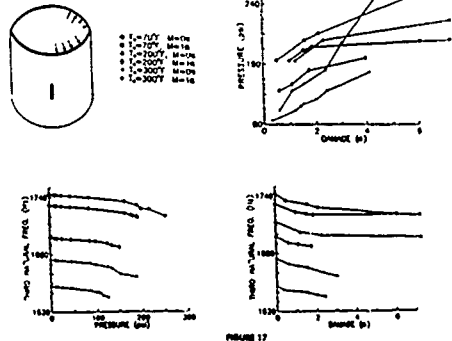
FIGURE 17

Delamination Damage and Its Effect on Buckling of Laminated Cylindrical Shells

R. C. Tennyson and S. Krishna Kumar

University of Toronto Institute for Aerospace Studies
4925 Dufferin Street
Downsview, Ontario, Canada
M3H 5T6

SUMMARY
The development of delamination damage in thin GFRP circular cylindrical shells subjected to lateral impact was investigated experimentally. Two distinct modes of delamination response were observed. The threshold energy for transition from one mode to another was identified and its relation to shell geometry and ply orientation studied. Axial compression tests were conducted on impacted cylinders to determine the degradation in their buckling strength. Comparisons were made between the effects of real and simulated damage (using embedded Teflon® inserts). Image Enhanced Backlighting and Structurally Embedded Fiber Optic Sensors were employed to detect and map out the internal delamination damage zones.

1 . INTRODUCTION
During recent years it has been recognized that a major weakness of light-weight fiber-reinforced laminate construction is its susceptibility to impact damage.

Delamination, or inter-laminar fracture, is one of the major modes of failure characterizing fiber reinforced laminate composites. Inter-laminar debonding primarily reduces the stiffness of the laminate, which significantly reduces the performance of the structure under bending and compressive loading. In addition, the presence of delamination in laminates loaded in compression also makes them susceptible to delamination buckling, i e , the separation and local buckling of the delaminated layer [1-4] This phenomenon can precipitate catastrophic failure, since the buckling induces delamination growth, which in turn promotes further buckling and global weakening of the laminate.

A major source of delamination in composites is low velocity impact damage, especially that caused by blunt-headed projectiles. The damage induced may be barely visible, but can produce as much as a 40% reduction in static and fatigue strength of laminates [5, 6]. The majority of investigations in this area have been conducted on plane laminates and the effect of impact damage and delaminations in curved panels and shells, particularly on their buckling performance, has only received scant attention. Recent analyses have indicated that delamination buckling can occur in cylindrical shells subjected to axial compression [7, 8] or external pressure [9] at loads far below their pristine strengths, depending upon the transverse location and size of the initial delamination. Experimental studies using Teflon® and Mylar® inserts in curved cylindrical panels showed 20 to 35% reduction in axial buckling loads, although no delamination growth was reported [10]. An analytical investigation on delamination buckling in axially loaded cylindrical shells [8] has yielded results similar to those obtained for plane laminates, predicting the onset of instability at loads as low as 25% of that of the undamaged specimen. However, the occurrence of local buckling in cylinders with delaminations has yet to be observed experimentally.

This paper presents a study on the effect of delamination damage, in particular that arising from low velocity impact, on the load carrying capacity of thin composite cylindrical shells under axial compression Experimentally the work involved four phases: (i) creation and assessment of delamination due to lateral impact on circular cylinders; (ii) manufacture of cylinders with implanted Teflon® inserts simulating various delamination sizes and shapes; (iii) evaluation of cylinder buckling strength as a function of damage state (real and simulated); and (iv) evaluating the influence of delamination size on buckling strength and correlating real/simulated damage effects.

2 . EXPERIMENTAL SETUP AND TEST SPECIMENS

2.1 Test Specimens
The test specimens were manufactured with glass fiber reinforced epoxy (3M SP-1003) unidirectional prepreg, using a belt wrapping machine to facilitate rolling of the material onto an aluminum cylindrical mandrel Each she. was then bagged and cured at 175°C with a vacuum and external pressure of 500 kPa for two hours. The cylindrical specimens had a mean radius (R) of 100 mm, average thickness of 0.19 mm per ply with an average length (L) of 150 mm (see Table 1). Each cylinder consisted of 8 plies, in a symmetric, balanced layup $(+45_2, -45_2)_s$. To provide a clamped end constraint, each shell was mounted into 25 mm thick aluminum end-rings, using a Hysol TE6175/HD3561 epoxy system

2.2 Impact Test Facility
A pendulum impactor, designed for low velocity impacts (less than 5 m/s) and capable of delivering impact energies of up to 150 Joules, was used for the impact tests. The impactor was designed to accommodate different hemispherical heads with radii of curvature ranging from 12.7 to 102 mm (1/2 to 4 inches). The input and rebound velocities of the impactor were measured using a reflective-type Object Sensor (TRW OPB 125A) mounted at the location of maximum velocity of the pendulum and connected to an Apple Computer whose internal clock

Table 1
Specifications and Impact Data for Buckling Test Specimens

Shell No.	Thickness (mm)	Shell Length (mm)	Impact Energy (Joules)	Delamination Area (sq.mm)	Buckling Load (KN)	Remarks
S102	1.600	265			103.6	Control specimen
S103	1.600	127			104.7	Control specimen
S108	1.575	149	39.5	4203	90.3	Impact test
S109	1.575	149			100.1	Control specimen
S110	1.575	149	39.7	3964	90.1	Impact test
S111	1.575	152		4925	94.3	Diamond-shaped implant
S112	1.575	138			100.1	Control specimen
S113	1.575	140		22080	79.7	Full-length implant
S114	1.575	140		3087	91.7	Diamond-shaped implant
S115	1.600	140		88316	78.1	Axisymmetric implant
S116	1.600	145		45735	77.9	Full-length implant
S117	1.600	145			104.6	Control specimen
S118	1.549	140	40.3	3618	83.3	Impact test
S120	1.549	147		69480	72.3	Full-length implant
S121	1.549	145		34270	74.1	Full-length implant
S122	1.549	65			96.9	Control specimen
S124	1.549	143	39.9	3157	88.1	Impact test
S125	1.549	144		68060	72.3	Axisymmetric implant
S126	1.549	146		11500	82.8	Full-length implant
S127	1.524	145		13710	76.5	Axisymmetric implant
S128	1.524	145		27420	70.7	Axisymmetric implant
S129	1.524	145		45690	71.6	Axisymmetric implant
S131	1.524	120			93.7	Control specimen
S139	1.524	155			93.9	Control specimen
S140	1.524	160	41.3	7069	81.4	Impact test
S141	1.524	156	41.0	7555	77.4	Impact test

Radius = 100 mm. Lamination sequence: 8 ply $(45,45,-45,-45)_s$ for all shells.

(with a frequency 1.0 MHz) was used for the time measurement. Calibration tests showed that the measured input velocity and the estimated impact energy were within 1% of the theoretical values computed from energy considerations of the compound pendulum. Table 1 presents a summary of the tests conducted, including the measured delamination areas for various impact energies.

2.3 Cylinder Models with Implanted Delaminations

Internal delamination damage was simulated by embedding thin sheets of Teflon® (thickness less than 0.025 mm) between the second and third innermost plies of the cylinders. This interface was chosen to conform with the location of the delaminations created in the impact tests. In two of the shells, diamond-shaped implants were placed at the mid-section. These were approximately the same size in area as the real delaminations produced by impact.

In all the remaining specimens the inserts covered either the full length or the entire circumference of the shell. Table 1 provides a summary of the implanted delaminations used in this investigation.

2.4 Delamination Mapping Techniques

Two optical damage assessment techniques were employed to map the delaminations generated in the shells, both prior and subsequent to compression buckling tests.

2.4.1 Damage Detection with Image Enhanced Backlighting

Delaminations were mapped using a simple but highly effective optical damage assessment system, known as the Image Enhanced Backlighting Technique [11] The technique is specifically suited to mapping of delaminations, but is applicable only to translucent materials. It basically involves illuminating the specimen

from behind (prior to impact), and capturing the image created by the transmitted light with a CCD camera. The information pertaining to the delamination is extracted from changes caused by its presence in the transmitted intensity. Briefly, the process consists of recording the images of the specimen taken before and after the impact, subtracting them digitally and then selectively enhancing the grey scale values to provide the desired definition and sharpness in the image of the delamination. Although the backlighting method does not provide data regarding the depth at which delaminations occur, its sensitivity makes it possible to distinguish between delaminations at different interfaces. The use of this technique permitted multiple impact tests to be performed on a cylinder, by ensuring that each delamination zone was confined to a local area in the shell wall.

2.4.2 Damage Assessment Using Fiber Optic Sensors

In many of the shells, the Structurally Embedded Fiber Optic Damage Assessment System [12] was employed to map the delaminations. The cylinders were bonded into specially designed mounting rings, which facilitated the optical fibers emerging from the cylinder ends to be connected to a coherent light source, while permitting axial loading of the cylinder without stressing the fibers. The optical fibers were embedded between the first and the second innermost plies, perpendicular to the fiber orientation in these plies. They were subjected to an etching treatment developed at UTIAS [12] to tailor their strengths to match the damage threshold level of the composite. The fracture locations of the optical fibers were pin-pointed by the profuse bleeding of light upon interrogation of the fibers using a laser source after the impact event and were marked to obtain a discrete mapping of the delaminated area.

3. EXPERIMENTAL RESULTS

3.1 Impact Test Damage

Preliminary tests performed on shells with different thicknesses and ply orientations, employing impactor heads with different radii of curvature, established that the curvature of the projectile head played a critical role in determining the extent of delamination. It was found that there is a limiting value for the radius of curvature of the hemispherical head, when this was exceeded, no delamination was produced, even when energies were high enough to cause severe transverse cracking and fiber failure in the cylinder. The limiting radius was determined to be 25 mm and 51 mm for 6 and 8 ply shells, respectively. Although all impactors with smaller radii induced delaminations, the least amount of transverse cracking on the front and rear surfaces of the shell occurred when the curvature was the least, hence the impactor with the limiting radius of curvature was employed in the majority of the tests.

The particular lay-up employed for the 8 ply shells had only two distinct interfaces between plies of dissimilar orientations, where delaminations could occur: one between the second and the third plies, and the other between the sixth and the seventh plies. The response of the shells being predominantly in the flexural mode, the damage was primarily induced at the innermost interface, while the delamination at the outer interface, when present, was restricted to a very small area. The geometry of the delaminations generated belonged to two distinct categories depending upon the magnitude of the impact energy. At energy levels below a threshold value, the induced delamination had the classical "peanut" shape usually observed in impact tests on flat plates [13], whereas at energies above the threshold level, it had an extended "Zee" shape, as seen in Figs. 1a and 1b, respectively. The latter shape, not mentioned hitherto in the literature, was generated repeatedly and consistently in a number of cylinders, and hence identified as a characteristic response specific to cylindrical laminates subjected to impact energies above the threshold level. The straight edges of this delamination, which are typical of this mode, are caused by the presence of transverse cracks in the two innermost plies of the shell wall, which restrain the inter-laminar crack from propagating sideways. It may be noted that the limbs of the "Zee" shape as well as the major axis of the "peanut" delamination, are oriented at 45° to the shell axis, i.e., parallel to the fibers in the lamina immediately below the interface, as predicted by the Bending Stiffness Mismatch [13] and Peel Separation [14] models for delamination. The extended shape in Fig. 1b is clearly due to the action of peel forces described in the latter model, its peculiar asymmetry appears to be caused by the difference in stiffnesses in the axial and circumferential directions of the shell.

Apart from geometry, the major difference between the two modes of damage is in the size of the delamination area. The peanut-shaped ones are much smaller by comparison. In Fig. 2 impact energy is plotted against delamination area for a number of 8-ply shells having a length of about 150 mm. It can be seen that the two modes are separated by a large gap. The peanut-shaped delaminations are all below 1000 sq mm in size while the Zee shaped ones exceed 2600 sq mm. The threshold energy is seen to be just under 40 Joules. The direct relationship between impact energy and damage size established earlier for peanut-shaped delaminations [13] appears to hold good, even in the present case, until the threshold level is reached. At this point there is a drastic increase in the delamination growth, indicating a sudden instability in crack propagation. This instability is associated with the change in delamination mode. Above the threshold level the delamination size once again appears to be proportional to the magnitude of energy as indicated by the rising curve in Fig 2. However, in this region, the shells suffered a considerable amount of extraneous damage in the form of intra-laminar cracks, which also increased in proportion to the energy. This limited the possibility of creating 'clean' delaminations of larger size by increasing the impact energy.

(a)   (b)

|—50 mm—|

|————109 mm————|
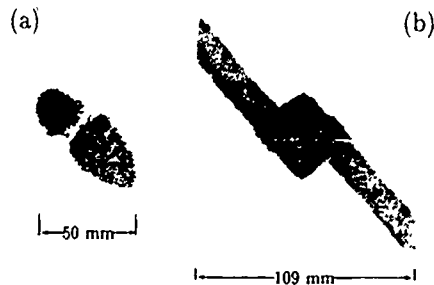
Fig. 1. (a) "Peanut and (b) extended delaminations.

The results plotted in Fig. 2 were obtained from tests performed on different shells. Subsequently, results were also obtained by conducting a series of impacts at different locations on the same shell, which are plotted in Fig. 3. This shell had a length of 145 mm. Again, the sharp transition from one mode to another can be observed at a threshold level of about 38 Joules. The similarity between the lower and upper portions of the curve suggests that the rates of growth of the Peanut and Zee delaminations are about the same, although at higher energies there is additional intra-laminar damage.

The threshold level for transition between the modes was observed to be related to the shell geometry as well as ply configuration. In Fig. 4, the delamination area is plotted against impact energy for shells of three different length-to-radius ratios. At $L/R = 0.6$, the shell was too short to develop the extended delaminations. The threshold level is seen to have risen from about 38 to 48 Joules, between $L/R = 1.5$ and $L/R = 2.7$. The relationship between delamination area and impact energy for shells of the $(+45_2, -45_2)$, lay-up used in the buckling tests are compared with those of shells with $(0,0,90,90)_s$ and $(90,90,0,0)_s$ lay-ups in Fig. 5. The zero-ninety shells are seen to require impacts of much higher energies to develop extended delaminations, while the ninety-zero lay-up requires lower energies. Also the transition from one mode to another is not well defined in these cases. Moreover, the

extended delaminations in these two cases were not Zee-shaped, but merely elongated in the axial direction of the shell.

The results obtained with fiber optic sensors in one of the shells (S30) are shown along with the image of the delamination mapped by the backlighting technique in Fig. 6. The two results appear to agree quite well although some of the optical fibers have been fractured outside the delamination area, perhaps due to their over-sensitivity. The test was conducted with a 51 mm dia. impactor using 41 Joules of energy.

3.2   Compression Buckling Tests
The buckling tests were undertaken in a four-screw Tinius Olsen loading machine with a load capacity of 250 KN. A summary of the buckling results is given in Table 1 for cylinders after they had been subjected to lateral impact as well as for those containing implanted delaminations. The experimental results are presented in graph form in terms of a "knockdown" factor which is the ratio of the buckling load for cylinders with delaminations to those of control shells of the same geometry without any delamination

It was observed that in shells with the peanut-shaped delaminations, no appreciable reduction in buckling strength occurred However, the shells with the Zee-shaped delaminations showed 10 to 15% degradation in strength,
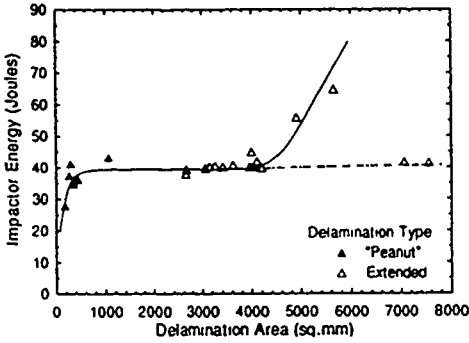
Fig. 2. Variation of delamination area with impact energy in tests conducted on fourteen different shells.
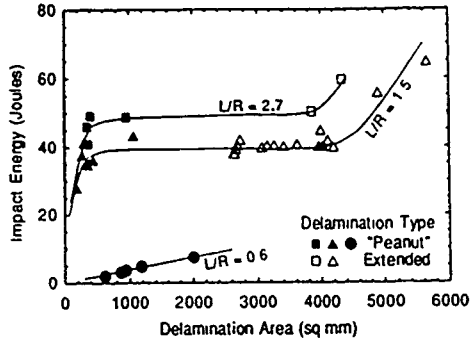
Fig. 4 Effect of shell length on impact damage
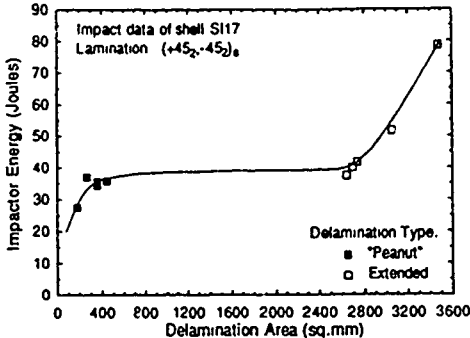
Fig. 3 Variation of delamination area with impact energy in tests conducted on a single shell (S117).
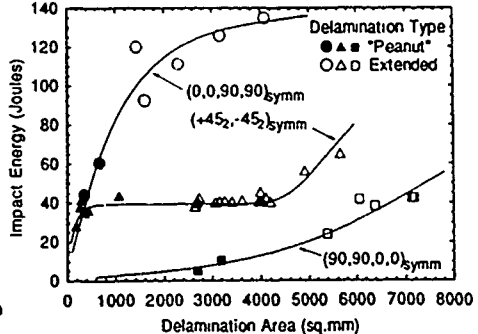
Fig. 5 Effect of ply orientation on impact damage

as can be seen in the plot of knockdown factor versus "percentage delamination area" in Fig. 7.

Buckling tests were also conducted on several shells with simulated delaminations, created by embedding thin sheets of Teflon® (thickness less than 0.025 mm) between the second and the third inner plies during the manufacturing stage. Two groups of specimens were tested: one having delaminations along the full length of the cylinder, and the other with inserts going around the entire circumference of the shell. The benchmark was established by testing control specimens without any delaminations. The specifications, delamination size, impact as well as buckling data for all the specimens are listed in Table 1. The knockdown factors recorded for all shells with implanted Teflon® sheets are plotted in Fig. 8. The abscissa is the ratio of the delamination area to the surface area of the shell. The buckling load drops steeply in the initial stage, but soon levels off and asymptotes to a value of about 75% of the pristine load. Data belonging to both groups of shells follow the same trend, indicating that the reduction in load is independent of the orientation of the delamination. Also plotted in the figure are the values obtained for two shells which had diamond-shaped Teflon® inserts, providing a closer approximation of the actual delamination created by impact. These had approximately sensors.the same area as the Zee-shaped delaminations observed in the impact tests.
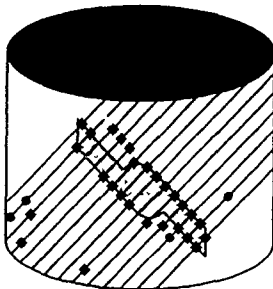
Shell : S30 (45,45,-45,-45)s   Impact energy = 41 J
◆ fracture point of optical fibers   ● partial bleeding
▢ image from backlighting

Fig. 6. Delamination mapping with fiber optic
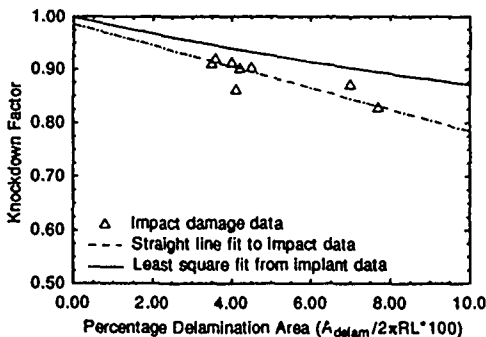
In every test with implanted delaminations, the two debonded layers invariably buckled together, developing, in all but one case, the classic asymmetric diamond buckling pattern normally observed in thin cylinders under axial compression. Only the shell with the narrowest axisymmetric Teflon® insert (22 mm wide), buckled into an axisymmetric mode. (The half-wavelength predicted by theory for axisymmetric buckling in this shell is 24 mm.) Even in this case, the layers on either side of the implant appeared to deform together, bulging outward forming an axisymmetric ripple with the same half-wavelength as the width of the delamination. Thus no evidence of delamination buckling was observed in any of these tests, nor was there any indication of propagation of the delamination before the onset of buckling. It appears that the occurrence of delamination buckling in cylindrical shells is restricted by geometry, at least where the thinner layer is on the inside of the shell, as in the present case. The curvature of the cylinder prevents inward axisymmetric deformation of the inner layer, while its buckling into an asymmetric pattern would require radially outward movement which is restricted by the outer layer. In either case, the thinner layer is constrained, and its buckling delayed to match that of the thicker segment The suppression of delamination buckling in this manner is significant, for it allows the cylinder to carry a much higher load.

These buckling results are also plotted in Fig. 7 over the range of delamination area observed in the impact tests. The shells having impact-induced delaminations are seen to have consistently lower buckling values than those predicted by the curve for the same delamination area This is probably due to the presence of additional damage caused by the impact, such as the minor delaminations at the upper interface, and the inter-laminar matrix cracks in the two innermost plies. Since the occurrence of such additional damage accompanies any inter-laminar fracture caused by impact damage, it is recommended that the buckling data of shells with simulated delaminations be used with a reduction factor to yield realistic estimates of buckling strength for shells with impact-induced delaminations.

4 . CONCLUSIONS

The development of delaminations due to low velocity lateral impact on thin laminated cylindrical shells has been investigated as a function of impact energy, ply orientation and cylinder L/R ratio. The shape of the delamination produced was mapped accurately using two

Fig. 7. Buckling strength reduction due to impact damage.
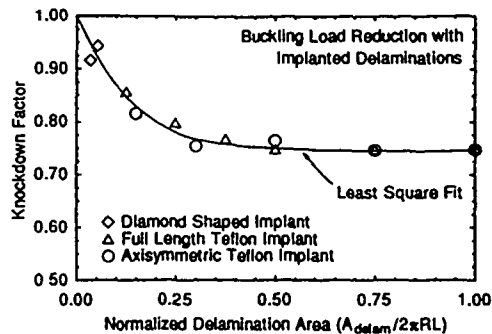
Fig. 8. Reduction in buckling strength due to implanted delaminations.

different optical techniques. Two distinct modes of delamination have been identified, and a threshold energy level for changing from one mode to another was determined experimentally for a specific shell geometry. In addition, the effect of inter-ply debonding on the buckling strength of axially loaded cylindrical shells was determined by a series of tests on shells with implanted Teflon® inserts and an empirical load reduction curve obtained. The tests reveal that as the area of delamination approaches the total shell area the buckling strength asymptotes to about 75% of that of the undamaged shell. No delamination buckling was observed in these tests. The results of buckling tests conducted on shells with actual impact damage were also compared with those obtained with simulated delaminations. It was found that the specimens damaged by impact have lower buckling loads probably due to the presence of additional matrix damage generated by the impact.

REFERENCES

1. Starnes, J. H., Jr., Rhodes, M. D., and Williams, J. G., "The Effect of Impact Damage and Circular Holes on the Compressive Strength of a Graphite Epoxy Laminate", NASA TM 78796, 1978

2. Cantwell, W. J., and Morton, J., "Comparison of Low and High Velocity Impact Response of CFRP", Composites, 20, 6, 1989, pp. 545-551.

3. Kachanov, L. M., "Delamination Buckling of Composite Materials", Kluwer Academic Publishers, 1988.

4. Chai, H., and Babcock, C D, "Two Dimensional Modelling of Compressive Failure in Delaminated Laminates", J. Composite Materials, 19, 1985, pp. 67-96.

5. Christoforou, A. P., and Swanson, S R., "Strength Loss in Composite Cylinders Under Impact", Trans. ASME, 110, 2, 1988, pp. 180-184.

6. Poe, C. C., Jr., and Illg, W., "Strength of a Thick Graphite/Epoxy Rocket Motor Case after Impact by a Blunt Object", NASA TM 89099, 1987.

7. Vizzini, A. J., and Lagace, P. A., "The Role of Pl, Buckling in the Compression Failure of Graphite Epoxy Tubes", 25th Structures, Structural Dynamics and Materials Conference, Proc. AIAA, 1984, pp 342-350.

8. Sallam, S., and Simitses, G. J., "Delamination Buckling of Cylindrical Shells Under Axial Compression", Comp. Struct, 7, 1987, pp. 83-101.

9. Chen, Z, and Simitses, G. J., "Delamination Buckling of Pressure-Loaded Cross-Ply Laminated Cylindrical Shells", Z. Angew. Math. Mech, 68, 10, 1988, pp. 491-501.

10 Horban, B, Palazotto, A., and Maddux, G., "The Use of Stereo X-Ray and De-Ply Techniques for Evaluating Instability of Composite Cylindrical Panels with Delaminations", SEM Spring Conference on Exp. Mechanics, Houston, Texas, June 1987, pp. 341-352

11. Glossop, N. D. W., Tsaw, W., Measures, R. M, and Tennyson, R. C., "Image-Enhanced Backlighting A New Method of NDE for Translucent Composites", J. of Nondestructive Evaluation 8, 3, 1989, pp 181-193.

12 Measures, R. M., Glossop, N. D W, Lymer, J, LeBlanc, M, West, J., Dubois, S., Tsaw, W., and Tennyson, R C., "Structurally Integrated Fiber Optic Impact Damage Assessment System for Composite Materials", Applied Optics, 28, 13, July 1989, pp. 2626-2633.

13 Liu, D, "Impact-Induced Delamination — A View of Bending Stiffness Mismatching", J. Composite Materials, 22, 1988, pp. 674-692.

14. Clark, G., "Modelling of Impact Damage in Composite Laminates", Composites, 20, 3, 1989, pp. 209-214.

FRACTURE ANALYSIS OF BMI SYSTEM IN PRESENCE OF MOISTURE

by

G. Barbiso and M.R. Boccuti
Alenia Aeronautica, GAD
Materials Technology Department
Corso Marche 41— C.P. 437
10146 Torino
Italy

ABSTRACT

Working with today's composite materials not predicted phenomena mainly related to the matrix chemical behaviour can occurr. Delaminations on solid laminate and honeycomb structure using a BMI resin have been detected. Analysis of the delaminated parts have been carried out to understand the nature of the defect. Correlation of the chemical behaviour affecting the mechanical properties and the solution to overcame the delamination problems are described in this paper.

LIST OF ABBREVIATIONS

Bismaleimide Resin System	BMI
Carbon Fibre Composite	CFC
Delaminations	DEL.
Differential Scanning Calorimetry	DSC
Fiberglass Honeycomb core	HRP
Flatwise Test	FTW
Fourier Tranformate Infrared	FTIR
Glass Transition Temperature	Tg
Honeycomb core	H/C
Identification	ID
Intermediate Modulus	I M.
Non Destructive Inspections	N.D I.
Nomex honeycomb core	HRH
Nuclear Magnetic Resonance	NMR
Scanning Electron Microscopy	SEM
Short Beam Flexure	SBF
Solid Laminate	SL
Thermogravimetric Analysis	TGA

1. INTRODUCTION

During the manufacturing process definition for monolithic and sandwich structures manufactured in Alenia using Intermediate Modulus (I.M.) graphite fibers with BMI matrix, some delaminations have been observed after the post-cure cycle. The delaminations in the solid laminate parts looked like surface blisters while the sandwich parts showed disbonding between the plies. To explain the defects several considerations have been done (eg. presence of moisture, stacking sequence, prepreg resin content etc.). In the mean time all small solid laminates manufactured to reproduce the phenomenon were completely free of defects. The only difference between these and the defected ones was the shorter out time of the prepreg in the shop and shorter time between cure and post-cure cycle. This led to the hypothesis that one of the major cause could be attributed to the moisture up take during lay-up phase or during the time between cure and post cure cycle. The effect was still present in small sandwich panels using HRH core whereas it was not occurred using metallic H/C so that another moisture source has been located in the HRH core. The degradation due to the moisture that occurrs on chemical bond of polymeric matrix may be investigated performing not only the Tg test, as suggested by Patherick and al. [1], but also by physical-chemical tests like FTIR, SEM, NMR, DSC, TGA and so on. In particular, the purpose of this work is to establish some correlations between thermogravimetric analysis, mechanical and microscopic test results obtained on delaminated graphite BMI parts, with the aim to establish the quality of the CFC part by means of the TGA test only. This could be the only possible test to be performed on the suspected parts (some defects cannot be detected by traditional N.D.I.) without destroy them.

2. DEFECTS SURVEY

The aspect of the defect looks different for the two configurations of panels.

2.1 Solid Laminate Parts

The delaminations were found through visual and N.D.I. inspection on the tool face after the post-cure cycle. The defects had the appearance of blisters as described in figure 1.

2.2 Sandwich Parts

Delaminations were in some cases observed as complete disbonding between the plies. In other cases the delaminations have been observed between the 1st and 2nd plies of CFC against the honeycomb core (see figure 2). This second location of defect was discovered after sectioning sampled panels declared acceptable by visual and N.D.I. inspections.

3. SAMPLE DESCRIPTION

Panels have been produced using different H/C and different manufacturing procedure. In particular only six of them (A, B, C, D, E, F) have been selected and fully characterized for this work. The only difference among these panels was the moisture content.

4. EXPERIMENTAL PROCEDURE

To produce test evidence in understanding the nature of the defect a Test Plan to correlate Physio-Chemical and mechanical analysis has been pursued as described below:

4.1 Physio-Chemical Inspections

4.1.1 *Thermogravimetric Analysis*
TGA tests were carried out using a thermogravimetric analyzer mod. TGA-7 (Perkin Elmer) in the following experimental conditions:

temperature range:	50° C / 450° C ±2° C
heating rate:	10° C / min
sample weigth:	12.00 / 15.00 mg ± 0.01 mg
atmosphere (air)	50 ml / min
temperature calibration.	Curie-point method

The samples were obtained from mechanically tested specimens or by peeling the defected plies.

4.1.2 *Micrographic Inspections*
Defected surfaces were observed at higher magnifications using a scanning electron microscope (SEM) JEOL 840A. Specimens to be analyzed were previously metalized with JEE-43/4C metalizer.

4.2 Mechanical Tests

4.2.1 *Solid Laminate Flatwise (FTW)*
This test was carried out by bonding each specimen, coming from solid laminate or skin of sandwich to aluminum alloy end blocks, with room temperature curing adhesive. Load was then applied at a displacement rate of 1.27 mm/min.

4.2.2 *Honeycomb Flatwise (FTW)*
The test was performed in according to ASTM C297 by bonding each specimen to aluminum alloy end blocks with room temperature curing adhesive. Load was then applied at a displacement rate of 1.27 mm/min

4.2.3 *Short Beam Flexure (SBF)*
The tests were performed on specimens obtained from the skin of the same panels used for FTW tests. The test was carried out at two loading points on a 13 mm distance support bars on 38 mm centers. Properly designed specimens were choosen due to the thickness of the skins (70mm x 20mm x 1.25mm).

4.4 N.D.I.
Each panel was submitted to Ultra Sonic (US) inspection, using the Alenia designed F2 system (ν = 5 MHz), in order to detect possible defects and to select the location for micrographic inspections. For these panels the delamination phenomena were found through visual and N.D.I. inspections on the tool fare, after the post curing procedure.

5. MECHANICAL TEST RESULTS

5.1 Solid Laminate FTW
In table I are reported the flatwise test results for defected and defect free panels. The average values were calculated from five specimens.

Table I. Solid Laminate Flatwise test results

PANEL ID.	DEFECTED PANELS Average Results [MPa]	DEFECT FREE PANELS Average Results [MPa]
A	4 9	/
B	5.2	/
C	7.4	/
D	9.5	/
E	/	16.2
F	/	15.2
G	/	18.0
H	/	19 2
I	/	14.5

5.2 Honeycomb Flatwise FTW
In table II the FTW test results, using different kinds of H/C core and the relevant failure modes, are reported.

Table II Honeycomb Flatwise Results

KIND OF H/C CORE	PANEL ID.	AVERAGE RESULTS [MPa]	FAILURE MODE
HRH 1/8" GRADE 3	A	/	UNABLE TO TEST
	B	1.40	DEL 1st, 2nd PLIES
	C	1.85	DEL. 1st, 2nd PLIES
	D	1 95	50% H/C FAILURE, 50% DEL.
	E	2 10	H/C FAILURE
	F	2.17	H/C FAILURE
HRH 1/8" GRADE 4	G	2.89	H/C FAILURE
	H	3.00	H/C FAILURE
	I	2 60	DEL 1st, 2nd PLIES
HRP 3/16" GRADE 8	L	6 06	ADHESIVE FAILURE
	M	5 80	ADHESIVE FAILURE
	N	4 64	DEL. 1st, 2nd PLIES
	O	5 90	ADHESIVE FAILURE
ALUMINUM CORE 1/8" 5056-32	P	6 30	H/C FAILURE
	Q	6 08	H/C FAILURE

5.3 Short Beam Flexure SBF
In table III are reported the Short Beam Flexure results on specimens obtained from the same panels used for FTW tests (see table II). The specimens were produced using HRH 1/8" Grade 3 core.

Table III. Short Beam Flexure Results

PANEL ID.	AVERAGE RESULTS [N]	FAILURE MODE
A	/	UNABLE TO TEST
B	550	MULTIPLE PLIES DEL.
C	800	MULTIPLE PLIES DEL.
D	1163	1st, 2nd PLIES ON THE COMPRESSION SIDE
E	1903	1st, 2nd PLIES ON THE COMPRESSION SIDE
F	1758	1st, 2nd PLIES ON THE COMPRESSION SIDE

Table IV. Comparison between H/C FTW, Solid Laminate FTW, SBF and TGA for six panels

PANEL ID.	H/C FTW AVERAGE RESULTS [MPa]	SL FTW AVERAGE RESULTS [MPa]	SBF AVERAGE RESULTS [N]	TGA AVERAGE RESULTS [° C]
A	/	4.9	/	/
B	1.40	5.2	550	185/290
C	1.85	7.4	800	187/295
D	1.95	9.5	1163	188/310
E	2.10	16.2	1903	214/345
F	2.17	15.2	1758	215/335

6. PHYSIO/CHEMICAL RESULTS

6.1 Thermogravimetrical Analysis
Samples for analysis have been obtained from flat-wise specimens after testing or from some areas of the panels picking up the interested CFC plies. Two values have been selected: the first one is the decomposition temperature onset (Tstart), graphically determined (see figure 3); the second one is the temperature associated to the 2.5 % of weight loss (T2.5 %) (see figure 3). Results for all the panels are reported in figure 4 and figure 4a.

6.2 Microscopic Analysis (SEM)
Surface matrix morphology was checked by Scanning Electron Microscope on defected and defect free panels. Typical pictures at two different magnifications of defected parts are reported in figure 5 and showing granular fracture. On the contrary, figure 6 reports the state of not defected surfaces at two magnifications. In this second case a typical flake fracture is showed.

7. DISCUSSION
In order to have a general overview of the results, allowing the comparison among different kinds of properties, six panels of the same configuration, representing the real structure has been selected. Three of them were manufactured in the normal shop conditions and two have been strictly controlled to avoid as far as possible, the moisture up take (e.g. H/C drying, short out time, quick lay-up operations after H/C drying etc). Comparison of the test results is reported in Table IV

The values have been also plotted in three an axial diagram (see fig. 7) representing the three mechanical properties as a function of the TGA. Each triangle is relevant to a single panel with its own TGA values. The mechanical behaviour improves proportionally to the triangle surfaces with the associated TGA values. The dashed triangle shows the boundary between acceptable and not acceptable panel qualities.The morphology of the fracture surface has been also correlated to the TGA and was observed that when the morphology aspect of the surface changes from globular to flake aspect the TGA value is in the region of 208° C / 320° C and the mechanical properties increase drastically. This behaviour was confirmed by these six panels.

8. CONCLUSIONS
The modifications occurred in the matrix system, as shown by TGA and micrographic analysis, seems to be related to the moisture absorption. The presence of this and mainly affects significantly the mechanical properties. This lead to the conclusion that, with some BMI system special care has to be taken to strictly control the moisture absorption during the manufacturing steps. The TGA test only looks a profitable approach to establish the good quality of the parts On the bases of our experience, the most reliable temperature value to be taken into account is the temperature recorded at 2.5 % of the weight loss. Tests are still running in Alenia to better define the TGA acceptable value on a statistical basis and to investigate the defect behaviour under fatigue loading.

REFERENCES

[1] EPOXY RESINS - Chemistry and Technology Second Edition, revised and expanded, edited by Clayton A. May. 1988 (ISBN 0 8247 7690 9) pp 615-648.

Figure 1. Section of defects on solid laminate
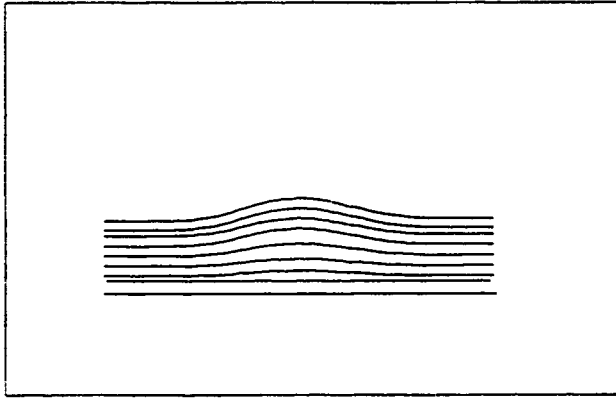
Figure 2. Delamination between 1st, 2nd plies on H/C parts
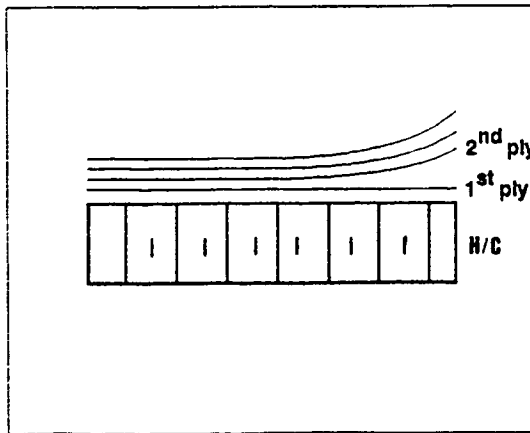
Figure 3. Typical TGA Thermogram
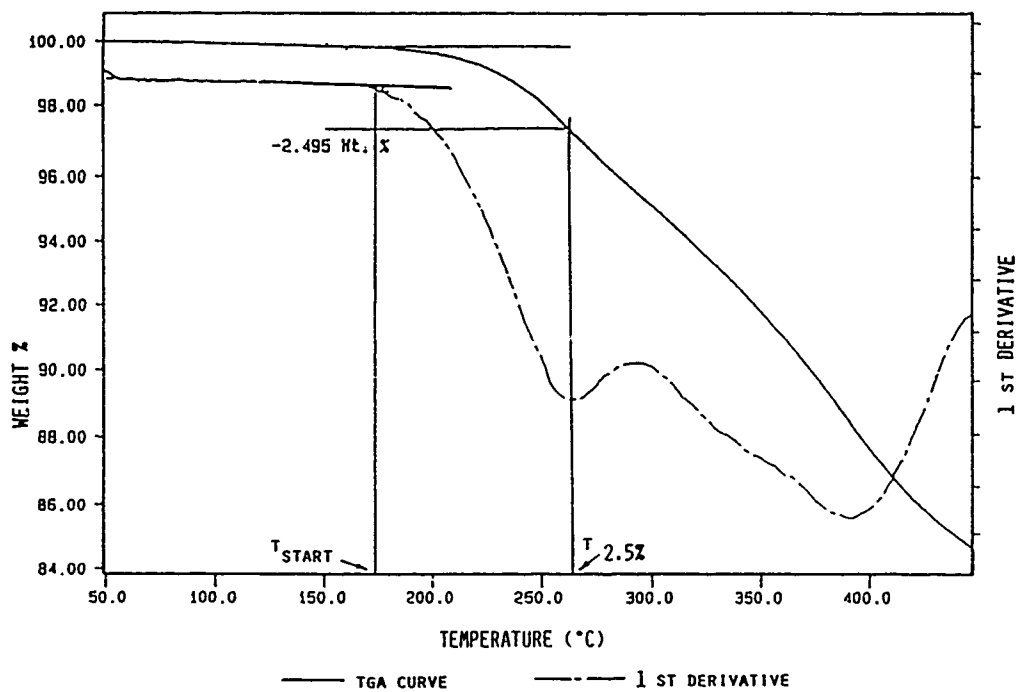
Figure 4. Histogram of Tstart and T2.5% for B, C, D, E, F panels
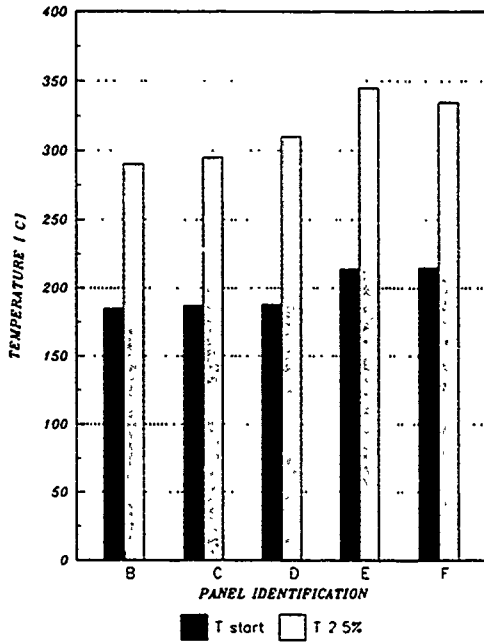
Figure 4a. Histogram of tstart and T2.5% for G, H, I etc. panels
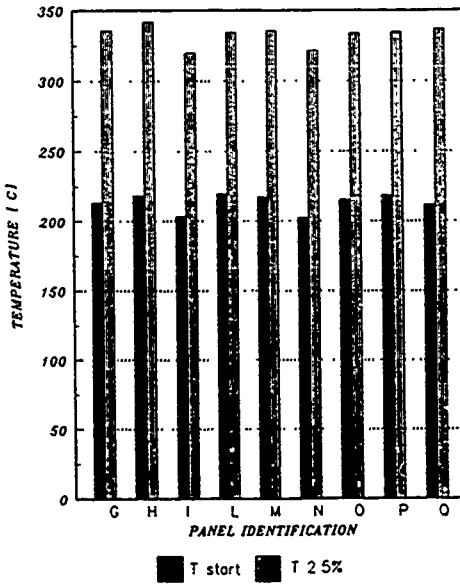
Figure 5. Typical scanning electron micrograph of defected surface parts.
(A) magnification x 500, (B) magnification x 1000
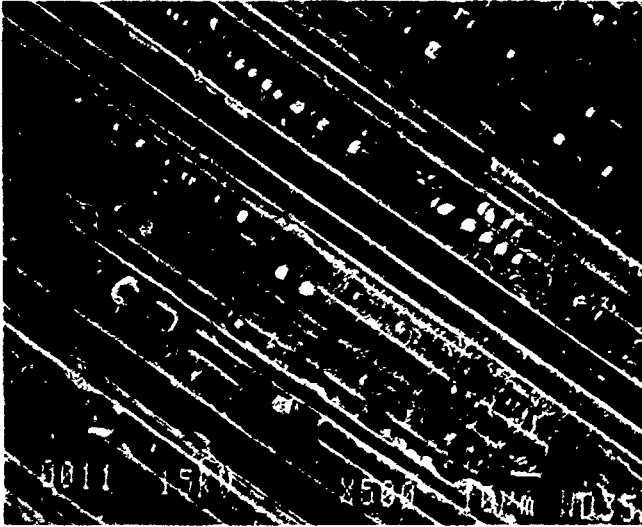
(A)

(B)

Figure 6. Typical scanning electron micrograph of no defected surface parts. (C) magnification x 500, (D) magnification x 3000
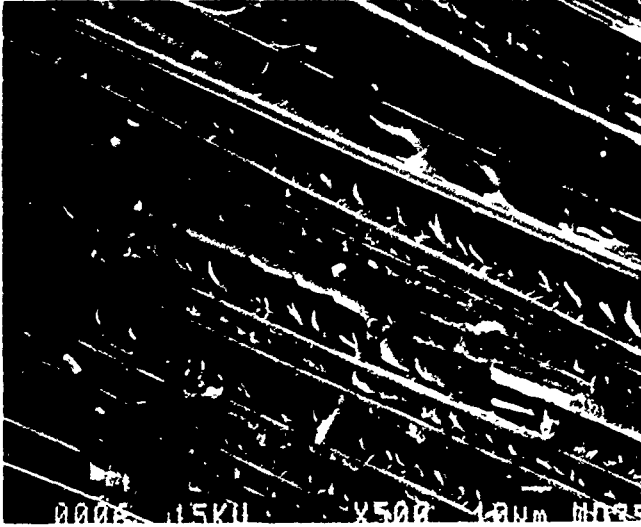
(C)

(D)

Figure 7. Three axial diagram
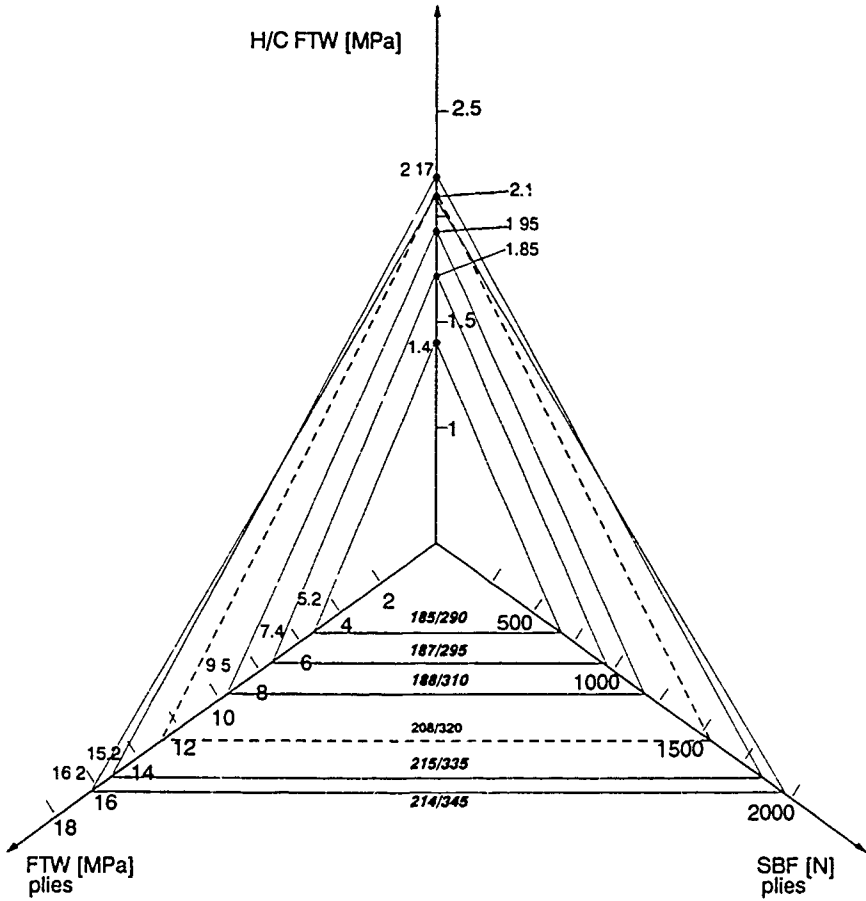
MODELISATION AND COMPUTATION OF COMPOSITE MATERIALS

by Georges DUVAUT

Office National d'Etudes et de Recherches Aérospatiales – BP 72 – F 92322 Châtillon CEDEX,
and Université Pierre et Marie Curie – Paris

1. INTRODUCTION

Composite materials are more and more widely used in aeronautical and spacial engineering and industry. Their main advantage is the gain in weight but it is not the only one : non corrosion and their ability to assume complex functions without bearings are also very valuable in some cases.

The drawback is the difficulty to predict their behaviour and write valuable constitutive relations to perform structure computations. This is due to the microscopic heterogeneities and the various phases and interfaces whose behaviour is not well-known.

In this paper, we propose an homogenization method which allows, when the microscopic structure can be assumed periodic at some intermediate scale, to build a constitutive relation from the assumed knowledge of the behaviour of the various phases and interfaces.

The method can also be used as an inverse method to identify some parameters involved in these constitutive relations.

In the cases where the structure is stratifed, the method leads to explicit calculations as we shall see in the second part of the paper.

2. THE GENERAL HOMOGENIZATION RESULT
([1], [3], [5], [6])

Let us take an elastic composite material, which occupies an open region $\Omega \subset R^3$, whose microscopic structure is periodic and let ε be the diameter of the period with respect to the diameter of the whole structure. Now, we enlarge one period to the scale $1/\varepsilon$ and get what we will call the reference (or basic period) (Y) that we assume here to be a rectangular parallelepiped.
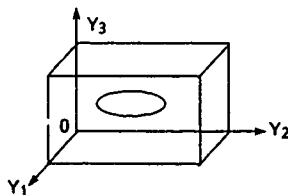
The actual composite material is made of a great number of εY periods.

Let us call a_{ijkh} (y) the elastic coefficients in the Y-period and extend it by Y-periodicity to the whole R^3 space. In the actual composite material, the elastic coefficients are given by

$$a^\varepsilon_{ijkh}(x) = a_{ijkh}\left(\frac{x}{\varepsilon}\right)$$

An elastic boundary value problem of equilibrium in Ω will be the following :

Problem 1. *Find the displacement field* $\vec{u} = (u_1, u_2, u_3)$ *and the stress field* $\bar{\sigma} = \{\sigma_{ij}\}$ *such that*

$$(2.1) \qquad \frac{\partial \sigma_{ij}}{\partial x_j} + f_i = 0 \ in \ \Omega$$

$$(2.2) \qquad \sigma_{ij} = a^\varepsilon_{ijkh}(x)\,\epsilon_{kh}(u)$$

$$(2.3) \qquad \vec{u} = \vec{U} \quad on \quad \Gamma_U \subset \partial\Omega$$

$$(2.4) \qquad \sigma\vec{n} = \vec{F} \quad on \quad \Gamma_F \subset \partial\Omega$$

where $\quad f = \{f_i\}, \quad F = \{F_i\}, \quad u = \{U_i\} \quad$ are given

and $\quad \Gamma_u \cap F_F = \varnothing, \quad \Gamma_U \cup F_F = \partial\Omega$

Under classical hypothesis on the elastic coefficients a_{ijkh} (y),

$$(H) \quad \begin{cases} a_{ijkh} = a_{jikh} = a_{khij} \ , \\ \exists \, a_0 > 0, \ a_{ijkh}(y)\epsilon_{kh}\epsilon_{ij} \geq a_0 \epsilon_{ij}\epsilon_{ij} \ , for \ any \ e_{ij} = e_{ij} \end{cases}$$

we know that the problem (1) - (4) possesses a unique solution

$$\vec{u} = u^\varepsilon(x), \quad \bar{\sigma} = \bar{\sigma}^\varepsilon(x)$$

which depends on ε.

The basic problem of homogenization is then the following.

Problem 2. *What is the limit of* $u^\varepsilon(x)$ *and* $\bar{\sigma}^\varepsilon(x)$ *when* ε *tends to zero ?*
The answer to a similar thermic problem has been given by L. Tartar ([5], [6]). Several authors have extended the result to elastic problem ([1], [3]), and the result is :

Theorem 1.
When ε *tends to zero*

$$u^\varepsilon \to u^o, \quad \bar{\sigma}^\varepsilon \to \Sigma$$

where u^o *and* Σ *are solution of the following elastic problem*

$$(2.5) \qquad \frac{\partial \sigma_{ij}}{\partial x_j}\Sigma_{ij} + f_i = 0 \quad in \ \Omega$$

(2.6) $\qquad \Sigma_{ij} = q_{ijkh} \epsilon_{kh}(u^o)$

(2.7) $\qquad \vec{u}^o = \vec{U} \quad on \quad \Gamma_U$

(2.8) $\qquad \Sigma(\vec{n}) = \vec{F} \quad on \; \Gamma_F$

The elastic coefficients q_{ijkh} are constant and can be computed from the knowledge of the basic period (Y) only. It means that, at the limit $\epsilon \to 0$, the composite material behaves as an homogeneous elastic medium : we call it the homogenized material and the relation (2.6) is called the homogenized constitutive relation.

Computation of the homogenized coefficients $\{q_{ijkh}\}$
We shall introduce the mean value of a function on Y

$$< f(y) > = \frac{1}{(Y)} \int_Y f(y)\, dy$$

Let us now consider the following problem on the basic period (Y) :

Problem 3. _Find u (y) and $\bar{o}$ (y) such that_

(2.9) $\qquad \dfrac{\partial o_{ij}}{\partial y_j} = 0 \quad on \; Y$

(2.10) $\quad o_{ij} = a_{ijkh}(y)\, e_{kh}(u). \quad e_{kh}(u) = \dfrac{1}{2}\left(\dfrac{\partial u_k}{\partial y_h} + \dfrac{\partial u_h}{\partial y_k} \right)$

(2.11) $\qquad < e_{kh}(u) > = E_{kh}$

(2.12) $\qquad u_i - E_{ij} y_j \; is \; Y-periodic \; (i = 1, 2, 3)$

(2.13) $\quad o_{ij} n_j \; takes\; opposite\; values\; on\; opposite\; faces\; of\; Y$

$$where\, E = \{E_{kh}\}$$

is a given symmetric matrix.

We can show that this problem has a solution which is unique up to an additive constant. This involves that the strain field e (u) and the stress field $\bar{o}$ are unique. From the fact that the problem is linear, the solution u, $\bar{o}$ depends linearly on the given symmetric matrix E. We have in particular,

(2.14) $\qquad o_{ij}(y) = B_{ijkh}(y) E_{kh}.$

which implies

(2.15) $\qquad < o_{ij}(y) > = < B_{ijkh}(y) > E_{kh}$

The homogenized coefficients $\{q_{ijkh}\}$ are given by

(2.16) $\qquad q_{ijkh} = < B_{ijkh}(y) >$

Practically we compute $q_{i_oj_ok_oh_o}$ by solving the elastic problem (2.9)-(2.13) for

(2.17) $\qquad E_{kh} = \dfrac{1}{2}(\delta_{kk_o}\delta_{hh_o} + \delta_{hk_o}\delta_{kh_o})$

and, $\left\{ o_{ij}^{k_oh_o}(y) \right\}$ being the solution, we have

(2.18) $\qquad q_{i_oj_ok_oh_o} = < o_{i_oj_o}^{k_oh_o}(y) >$

Remark 1.
(2.17) implies that $E_{kh} = 0$ except for $E_{k_oh_o} = E_{h_ok_o}$ $= 0.5$ if $k_o \neq h_o$ and $E_{k_oh_o} = 1$ if $k_o = h_o$.

An important fact is that the result can be interpreted by the following : the homogenized constitutive relation is the relation between the mean value of the strain field and the mean value of the stress field where the displacement field and the stress field are linked in problem 3. This result has been proved for linear elastic material (see references before) and for several cases of non linear material (G. Duvaut and M. Artola..., P. Suquet....). As it has a strong physical meaning, it seems that it is true for any type of constitutive relation in problem 3.

Asymptotic expansion
It results also, from the homogenization theory, that we have an asymptotic expansion of the displacement field and stress field in problem 1 :

(2.19) $\qquad u^\epsilon(x) = u^o(x) + \epsilon\, u^1(x,y)\Big|_{y = \frac{x}{\epsilon}} + O(\epsilon^2)$

(2.20) $\qquad o_{ij}^\epsilon = B_{ijkh}(y)\Big|_{y = \frac{x}{\epsilon}} \epsilon_{kh}(u^o) + O(\epsilon)$

where $u^o(x)$ is the displacement field solution of problem 2 and $u^1(x, y)$ a vector field depending on $x \in \Omega$ and Y-periodic with respect to y. The relation (2.20) shows that the first term of the asymptotic expansion of o_{ij}^ϵ is the stress field solution of problem 3 when we choose $E_{kh} = \epsilon_{kh}(u_o)$. The mean value on (Y) of this first term is the macroscopic stress field $\Sigma(x)$ since

$$< B_{ijkh}(y) > \epsilon_{kh}(u^o) = q_{ijkh}\, \epsilon_{kh}(u^o) = \Sigma_{ij}(x)$$

This shows that, at a point x in the homogenized structure, the macroscopic stress $\Sigma(x)$ is the mean value of a microscopic stress field on an ϵY period located at point $x \in \Omega$. It means that, if we know the macroscopic stress $\Sigma(x)$ at a point $x \in \Omega$, we are able to calculate the field of microstresses on an ϵY period at that point : we calculate the macroscopic strain field $\epsilon(u_o)$ at that point by inverting the relation,

$$\Sigma_{ij}(x) = q_{ijkh}\, \epsilon_{kh}(u_o)$$

and then, solving problem 3 with

$$E_{kh} = \epsilon_{kh}(u_o)$$

we get the stress field solution of problem 3

$$o_{ij} = B_{ijkh}\, \epsilon_{kh}(u_o)$$

which is the microstress field that we were looking for.

Remark 2.
In all the previous developments, we have assumed that we have a perfect junction (without slip or deboundage) between the various components of the composite material. If this is not the case, we must specify the interphase relations, but the general results given remain valid provided that we compute correctly the strain field taking into account the possible slip between the various phases. This will occur and will be illustrated in the rest of this paper.

3. PERIODIC STRATIFIED MATERIAL WITH INTERFACE-SLIP

3.1 Description and notations
The composite material considered here is stratified and periodic which means that the same sequence of

layers reproduces periodically. Suppose that the period is made of N layers parallel to the plane $y_3 = 0$ with interfaces at $y_3 = 0, \xi_1, ...\xi_N, \xi_{N+1}...$.

We choose the basic period (Y) defined by

$$Y = \left\{ y \,\middle|\, \frac{\xi_1}{2} < y_3 < \frac{\xi_N + \xi_{N+1}}{2} \right\}$$
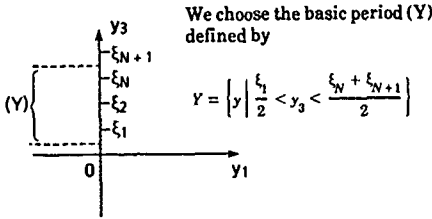
The spreading of the period in directions y_1 and y_2 is not determined since the constitutive relations do not depend on y_1 and y_2. This implies that a periodic function in y will be a function which is periodic with respect to y_3 and does not depend on y_1 and y_2.

The displacement field $u = (u_1, u_2, u_3)$ may be discontinuous at the interfaces ξ_i, $i = 0,1,...$, and we shall write $[\![\vec{u}]\!]_i$ for the jump according to the relation

$$[\![\vec{u}]\!]_i = \vec{u}(\xi_i^+) - \vec{u}(\xi_i^-)$$

We shall assume that

$$[\![u_3]\!] = 0$$

which means that the layers may slip but do not separate, but this assumption is not necessary for the mathematical treatment.

If we introduce

(3.1) $$\tilde{u} = \vec{u} - \sum_{n=1}^{N} [\![\vec{u}]\!]_n H(z - \xi_n),$$

where $H(\xi)$ is the Heaviside function (equal to zero if $\xi < 0$ and equal to one if $\xi > 0$) the vector $\tilde{u}$ is continuous at the interfaces ξ_i, $i = 1....N$.

3.2 Homogenization

The homogenized constitutive relation comes from the solution of problem 3. Here we can see that we have major simplifications. First of all, the stress field which has to be periodic will only depend on the variable y_3 (or $z = y_3$) which implies, from the equilibrium relations, that

(3.2) σ_{i3} is constant in y for $i = 1, 2, 3$

We can also prove, from compatibility equations that

(3.3) $\varepsilon_{\alpha\beta}(u)$ is constant in y for $\alpha, \beta = 1, 2$

We can always write the elastic constitutive relation of each layer in the form

(3.4) $$\begin{cases} \sigma_{\alpha\beta} = a_{\alpha\beta\gamma} \sigma_{j3} + a_{\alpha\beta\gamma\delta} e_{\gamma\delta}(\tilde{u}) \\ e_{i3}(\tilde{u}) = b_{ij} \sigma_{j3} + b_{i\gamma\delta} e_{\gamma\delta}(\tilde{u}), \end{cases}$$

where the greek indices take value 1 and 2, and latin ones take values 1, 2 and 3. We notice that in relations (3.4) the components of $\{\sigma_{ij}\}$ and $\{e_{ij}\}$ which are in the right members are constant, according to (3.2) and (3.3), while the coefficients may depend on the layers.

This allows to take the mean value of both members of relations 3.4.

Before we must compute $<e_{ij}(u)>$, taking into account the discontinuities of u, in order to express the conditions

(3.5) $$< e_{ij}(u) > = E_{ij}$$

of problem 3. As a consequence of (3.1) we have

(3.6) $$\frac{\partial u_i}{\partial x_j} = \frac{\partial \tilde{u}_i}{\partial x_j} + \sum_{n=1}^{N} [\![u_i]\!]_n \delta(z - \xi_n) \delta_{j3}$$

where $\delta(\ )$ is the Dirac function and δ_{j3} the Kronecker symbol. It comes from (3.6) that

(3.7) $$E_{ij} = < e_{ij}(u) > = < e_{ij}(\tilde{u}) > + \frac{1}{2e} \sum_{n=1}^{N} \left([\![u_i]\!]_n \delta_{j3} + [\![u_j]\!]_n \delta_{j3} \right)$$

which, if we assume $[\![u_3]\!]_n = 0$, gives

(3.8) $$\begin{cases} < \varepsilon_{\alpha\beta}(u) > = E_{\alpha\beta} = < \varepsilon_{\alpha\beta}(\tilde{u}) >, (\alpha = 1, 2, \beta = 1, 2) \\ < \varepsilon_{\beta3}(u) > = E_{\beta3} = < \varepsilon_{\beta3}(\tilde{u}) > + \frac{1}{2e} \sum_{n=1}^{N} [\![u_\beta]\!]_n, (\beta = 1, 2) \\ < \varepsilon_{33}(u) > = E_{33} = < \varepsilon_{33}(\tilde{u}) >, \end{cases}$$

where e stands for the thickness of the periodic layer Y in direction $y_3 = z$.

We can now take the mean values in (3.4) ; writing Σ_{ij} for $< \sigma_{ij} >$, it leads to

(3.9) $$\begin{cases} \Sigma_{\alpha\beta} = < a_{\alpha\beta j} > \Sigma_{j3} + < a_{\alpha\beta\gamma\delta} > E_{\gamma\delta} \\ E_{\beta3} = \frac{1}{2e} \sum_{n=1}^{N} [\![u_\beta]\!]_n + < b_{\beta j} > \Sigma_{j3} + < b_{\beta\gamma\delta} > E_{\gamma\delta} \\ E_{33} = < b_{3j} > \Sigma_{j3} + < b_{3\gamma\delta} > E_{\gamma\delta} \end{cases}$$

When the various layers are perfectly linked, there is no jump of displacement at the interphases and writing $[\![u]\!] = 0$ in (3.9) we get explicitly the homogenized constitutive relation for the composite.

When this is not the case, we must specify the constitutive laws of the junction between the various layers. Assuming $[\![u_3]\!] = 0$, these will take the form of a relation between the shear vector $\vec{T}$

$$\vec{T} = (\sigma_{13}, \sigma_{23}) = (\Sigma_{13}, \Sigma_{23})$$

since σ_{13} and σ_{23} are constant according to (3.2), and the displacement jump (tangential) $\vec{W}$,

$$W = \left([\![u_1]\!]_n, [\![u_2]\!]_n \right)$$

Assuming that all interfaces behave in the same way, $\vec{W}$ will be independent of n since $\vec{T}$ is.

We are now able to get the desired homogenized constitutive relation of the stratified composite.

Extracting $\vec{W} = ([\![u_1]\!], [\![u_2]\!])$ from the second relation

(3.9), we get two scalar relations between E and Σ, which joined to the first and third relation (3.9) provide the desired result.

4. EXAMPLES

1°) *Perfect interlayer bond* [2] :

In this case $[\![\vec{u}]\!] = 0$ and the homogenized constitutive relation (HCR) is obtained from (3.9) where the displacement jump is put equal to zero.

If each layer is isotropic, with "Lamé" coefficients λ, μ, the HCR is given by

$$(3.10) \begin{cases} \Sigma_{\alpha\beta} = \left(< \dfrac{\lambda}{\lambda + 2\mu} > \Sigma_{33} + < \dfrac{2\lambda\mu}{\lambda + 2\mu} > E_{\gamma\gamma} \right)\delta_{\alpha\beta} \\ \qquad + 2 <\mu> E_{\alpha\beta}, \\ E_{\beta3} = < \dfrac{1}{2\mu} > \Sigma_{\beta3}. \\ E_{33} = < \dfrac{1}{\lambda + 2\mu} > \Sigma_{33} - < \dfrac{\lambda}{\lambda + 2\mu} > E_{\beta\beta} \end{cases}$$

The homogenized material is elastic non isotropic.

2°) *Elastic slip*
The displacement jump is proportional to the shear force

$$\vec{T} = k \vec{W}$$

which allows us to replace $[\![\vec{u}]\!]$ in (3.9) to get the HCR

$$(3.12) \begin{cases} \Sigma_{\alpha\beta} = < a_{\alpha\beta j} > \Sigma_{j3} + < a_{\alpha\beta\gamma\delta} > E_{\gamma\delta} \\ E_{\beta3} = \dfrac{N}{2ke} \Sigma_{\beta3} + < b_{\beta j} > \Sigma_{j3} + < b_{\beta\gamma\delta} > E_{\gamma\delta} \\ E_{33} = < b_{3j} > \Sigma_{j3} + < b_{3\gamma\delta} > E_{\gamma\delta} \end{cases}$$

In the case of isotropic layers, these relations become

$$(3.13) \begin{cases} \Sigma_{\alpha\beta} = \left(< \dfrac{\lambda}{\lambda + 2\mu} > \Sigma_{\wedge} + < \dfrac{2\lambda\mu}{\lambda + 2\mu} > E_{\gamma\gamma} \right)\delta_{\alpha\beta} \\ \qquad + 2 <\mu> E_{\alpha\beta}, \\ E_{\beta3} = \left(\dfrac{N}{2ke} + < \dfrac{1}{2\mu} > \right) \Sigma_{\beta3}. \\ E_{33} = < \dfrac{1}{\lambda + 2\mu} > \Sigma_{33} - < \dfrac{\lambda}{\lambda + 2\mu} > E_{\beta\beta} \end{cases}$$

which correspond to an anisotropic elastic behaviour.

3°) *Linear or non-linear viscous slip* ([4])
The displacement jump is governed by

$$(3.14) \qquad \frac{\partial W}{\partial t} = \phi(\vec{T})\, \vec{T},$$

where $\phi(\vec{T})$ is a scalar function of $\vec{T}$ inverse of the viscosity. In the linear case $\phi(\vec{T})$ is a constant.

The resulting HCR is the following,

$$(3.14 bis) \begin{cases} \Sigma_{\alpha\beta} = < a_{\alpha\beta j} > \Sigma_{j3} + < a_{\alpha\beta\gamma\delta} > E_{\gamma\delta} \\ \dfrac{\partial}{\partial t} E_{\beta3} = \dfrac{N}{2e} \phi(\vec{T})\Sigma_{\beta3} + < b_{\beta j} > \dfrac{\partial}{\partial t} \Sigma_{j3} \\ \qquad + < b_{\beta\gamma\delta} > \dfrac{\partial}{\partial t} E_{\gamma\delta} \\ E_{33} = < b_{3j} > \Sigma_{j3} + < b_{3\gamma\delta} > E_{\gamma\delta} \end{cases}$$

which gives a viscoelastic behaviour.

In the case where the layers are isotropic, we get

$$(3.15) \begin{cases} \Sigma_{\alpha\beta} = \left(< \dfrac{\lambda}{\lambda + 2\mu} > \Sigma_{33} + < \dfrac{2\lambda\mu}{\lambda + 2\mu} > E_{\gamma\gamma} \right)\delta_{\alpha\beta} \\ \qquad + 2 <\mu> E_{\alpha\beta}, \\ \dfrac{\partial}{\partial t} E_{\beta3} = \dfrac{N}{2e} \phi(\vec{T})\Sigma_{\beta3} + < \dfrac{1}{2\mu} > \dfrac{\partial}{\partial t} \Sigma_{\beta3}. \\ E_{33} = < \dfrac{1}{\lambda + 2\mu} > \Sigma_{33} - < \dfrac{\lambda}{\lambda + 2\mu} > E_{\beta\beta}. \end{cases}$$

which gives a non isotropic viscoelastic behaviour.

4°) *Slip with Coulomb friction law*
Coulomb friction law can be written by

$$(3.16) \begin{cases} \vec{T} \leq f|\Sigma_{33}| \\ \vec{T} < f|\Sigma_{33}| \implies \dfrac{\partial}{\partial t}[\![\vec{u}]\!] = 0 \\ \vec{T} = f|\Sigma_{33}| \implies \exists \lambda \geq 0, \dfrac{\partial}{\partial t}[\![\vec{u}]\!] = \lambda \vec{T} \end{cases}$$

where f is a friction coefficient and

$$\vec{T} = (\Sigma_{13}, \Sigma_{23})$$

Relations (3.9) have to be joined to (3.16), $[\![u]\!]$ remaining in the relations as an internal variable. The constitutive relation obtained is of elasto-plastic type.

If the layers are isotropic, relations (3.9) have to be replaced by

$$(3.17) \begin{cases} \Sigma_{\alpha\beta} = \left(< \dfrac{\lambda}{\lambda + 2\mu} > \Sigma_{33} + < \dfrac{2\lambda\mu}{\lambda + 2\mu} > E_{\gamma\gamma} \right)\delta_{\alpha\beta} \\ \qquad + 2 <\mu> E_{\alpha\beta}, \\ \dfrac{\partial}{\partial t} E_{\beta3} = \dfrac{N}{2e}[\![u_\beta]\!] + < \dfrac{1}{2\mu} > \Sigma_{\beta3}. \\ E_{33} = < \dfrac{1}{\lambda + 2\mu} > \Sigma_{33} - < \dfrac{\lambda}{\lambda + 2\mu} > E_{\beta\beta} \end{cases}$$

Remark 3
Very often Σ_{33} is assumed to be known. If we introduce $g = f|\Sigma_{33}|$ the friction law (3.16) simply becomes

$$(3.18) \begin{cases} |\vec{T}| \leq g \\ |\vec{T}| < g \implies \dfrac{\partial}{\partial t}[\![\vec{u}]\!] = 0 \\ |\vec{T}| = g \implies \exists \lambda \geq 0, \dfrac{\partial}{\partial t}[\![\vec{u}]\!] = \lambda T \end{cases}$$

5° *More general case* ([7])

Usually, the slip law is not known and we have to imagine a law which is sufficiently general to fit a great number of behaviours. Such a law is

$$(3.19)\, C_1 |\vec{W}|^{n_1-1}\, \vec{W} + \frac{\partial}{\partial t}\, \vec{W} = (C_2 + C_3 |\vec{T}|^{n_2}) \frac{\partial \vec{T}}{\partial t} + \phi(\vec{T}, \frac{\partial}{\partial t}\, \vec{T}),$$

where C_1, C_2, C_3, n_1, n_2, are constant parameters which have to be determined through an experiment. The function $\phi\left(\vec{T}, \frac{\partial}{\partial t}\, \vec{T}\right)$ may depend on the increasing or decreasing loading.

Relation (3.19) may take into account various elastic and viscoelastic behaviour, linear or non-linear : if $\phi(\ ) = 0$ and $C_1 = 0$, the law is an elastic one, linear if $C_3 = 0$, non-linear if $C_3 \neq 0$. If $C_1 = C_2 = C_3 = 0$ and $\phi = \phi(\vec{T})$, we may simulate a plastic law or a non-linear viscous law. If $C_1 \neq 0$ the law is viscoelastic.

Remark 4

This type of procedure has been used to identify the behaviour of a stratified material provided by AS/Marignane, the experiment performed to determine the coefficients of (3.19) being a three-points-flexion.

5. REFERENCES

1. Bensoussan, A., Lions, J.L. and Papanicolaou, G., "Asymptotic Analysis for Periodic Structures", Nort Holland, Amsterdam, 1978.

2. Dumontet, H., "Homogénéisation de matériaux stratifiés de type élastique linéaire, non linéaire et viscoélastique", Thèse de Troisième Cycle, Université P. et M. Curie, Paris, 1983.

3. Duvaut, G., "Matériaux élastiques composites à structure périodique", Homogénéisation Proc. Congrès IUTAM, Delft, Nort Holland, 1976.

4. Léné, F., "Contribution à l'étude des milieux composites et de leur endommagement", Thèse d'Etat, Université P. et M. Curie, Paris, 1984.

5. Tartar, L., "Cours Peccot", Collège de France, Sept. 1977.

6. Tartar, L., "Homogénéisation et compacité par compensation", Séminaire Goulaonic-Schwartz, Exposé n° 9, 1978.

7. Tomasi, G., Thèse de l'Université P. et M. Curie en préparation.

EDGE DELAMINATION OF COMPOSITE LAMINATES

C. Poon
N.C. Bellinger
Y. Xiong
R.W. Gould

Institute for Aerospace Research
National Research Council Canada
Ottawa, Canada K1A-0R6

SUMMARY

A review of the literature and the research performed at the Institute for Aerospace Research on the subject of delamination in composite laminates are presented. Delamination is known to initiate at free edges where the influence of interlaminar stresses is significant. These interlaminar stresses are three dimensional and cannot be calculated by the laminated plate theory. State-of-the-art stress analysis methods for interlaminar stresses are reviewed with emphasis on the reliability of finite element methods. The strength of materials and fracture mechanics approaches for the prediction of delamination onset and growth are discussed. Results of edge delamination, double cantilever beam and end notch flexure tests for toughened resin composites are presented. The effects of delamination on structural integrity are investigated by conducting cyclic tests on bread board specimens representing the bolted joint interface between the ply build-up ends of the composite arm booms and the metallic flanges of a sophisticated robotic system for space application. The onset of delamination at the curved edge of an open hole under compressive loading is detected using acoustic emission techniques and penetrant-enhanced X-radiography. The effects of impact-induced delaminations on the residual compressive strength of composite laminates are predicted using a model based on sublaminate buckling. Preliminary verification of the model shows good agreement between experimental and predicted results.

LIST OF SYMBOLS

a	crack length
C	compliance
E	axial modulus
E_o	slope of load-deflection curve
E_1, E_2	moduli of sublaminates
E_*	reduced modulus
F_i, F_{ij}	strength tensors
G	strain energy release rate
G_c	total critical s⁻ ⁻rgy release rate
G_I, G_{II}, G_{III}	strain energy re. . tes for modes I, II and III
G_{Ic}, G_{IIc}	critical energ ⁻⁻⁻⁻ rates for modes I and II
h	ply thickness
L	half length of loading span in ENF test
m, n	curve-fitting constants
P	load
t	thickness
w	width
δ	displacement
ε_c	critical strain for delamination onset
ε_o	failure strain for undamaged laminate
$\eta_{xy,x}$	coefficient of mutual influence
ν_{xy}	Poisson's ratio
σ_1, σ_2	inplane stresses in the material axes
$\sigma_3, \sigma_{23}, \sigma_{13}$	interlaminar stresses in the material axes
σ_B	sublaminate buckling stress
σ_x, σ_y	inplane stresses in the global axes
$\sigma_z, \tau_{xz}, \tau_{yz}$	interlaminar stresses in the global axes

1. INTRODUCTION

An increased application of fibre reinforced polymer composites in a wide range of high performance aircraft and spacecraft has been observed in recent years. These advanced composites are replacing metals in the fabrication of primary structures. This situation has rejuvenated extensive interest in the fracture analysis of laminated composites Engineers working in this area are often challenged by the complexity of the failure modes which must be modelled in the fracture analysis.

The laminated construction of composite structures is responsible for the complex failure modes which are fundamentally different from those found in metallic materials The failure of metallic structures is usually precipit...ted by a dominant crack which propagates in a self-similar manner until a critical size is reached. However, the failure of laminated composites is dominated by three major modes, which are intralaminar matrix cracking, interlaminar matrix cracking or delamination, and fibre fracture. The propagation of matrix cracks, in general, is not self-similar and is strongly influenced by the orientation of the fibre reinforcement with respect to the loading direction and the stacking sequence. The fibre reinforcement influences the pattern of crack propagation by acting as crack stoppers. This crack-arresting capability of the fibre reinforcement not only prohibits the dominance of a single crack but also encourages similar matrix cracks to form throughout the laminate at increased load levels The intralaminar and interlaminar matrix cracks often interact to form a complex network of matrix damage which affects structural performance. Its effect on structural integrity is manifested in stiffness loss and in the development of local stress concentration in the load-carrying plies which leads to a redistribution of loads within the laminated structure. The load redistribution is often responsible for the failure of fibres in the major load-carrying plies which, in turn, precipitates premature structural failure.

A review of the literature and the research performed at the Institute for Aerospace Research (IAR) on the interlaminar response of laminated composites will be presented in this paper with emphasis on the physical characteristics of delamination and its effect on structural performance The experimental and analytical techniques utilized for the modelling of delamination behaviour and some of the measures adopted for improving the resistance against delamination will be discussed

2. CHARACTERISTICS OF DELAMINATION

The problem of delamination has been researched extensively [1-4] and a broad knowledge base [5] on the behaviour of delamination has been developed. It is well known that delamination is caused by interlaminar stresses that exist at

structural locations where there is a free edge A free edge can be external such as at the edge of a fastener hole or at the ply drop-off region where a tapering in thickness occurs. A free edge can also be internal such as at the boundary of a sublaminate caused by impact or at discontinuities within an adhesively-bonded region or a cocured region

The presence of interlaminar stresses near the free edge is attributed to a mismatch in engineering properties between adjacent plies within the laminate. Herakovich's analysis [6] has shown that a mismatch in Poisson's ratio, v_{xy}, gives rise to the interlaminar normal stress, σ_z, and the interlaminar shear stress, τ_{yz}. A mismatch in the coefficient of mutual influence, $\eta_{xy,x}$, induces the interlaminar shear stress, τ_{xz}. The coordinate system of the stress components is shown in Fig. 1
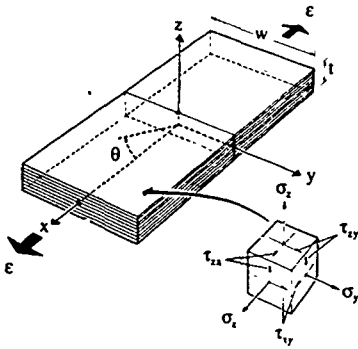
Figure 1: Coordinate system for the stress components in a laminated plate.

It is known that the interlaminar stresses occur at a boundary layer close to the free edge. However, the exact definition of the boundary layer size is arbitrary. The boundary layer is generally regarded as the region where the interlaminar stresses are appreciable. Based on equilibrium considerations which require σ_z to change sign as the distance from the free edge increases, Lagace et al. [7] define the boundary layer size as the distance from the free edge at which 99% of σ_z is counterbalanced. However, this definition does not work for certain laminates where σ_z is practically zero throughout the laminate. An alternative definition based on the point defined by 99% of the area under the interlaminar shear stress distribution was proposed [8] These two definitions do not, in general, yield the same boundary layer size for a laminate Wang and Choi [9] proposed that the boundary layer be defined as the region where strain energy density is greater than or equal to 1 03 times the far-field value This definition has the disadvantage that the boundary layer size is a function of the through-the-thickness location since it is well established that the magnitude of the interlaminar stress components vary through the thickness of the laminate It is apparent that a more universal definition should be developed It is generally agreed that the boundary layer size is of the order of one or more ply thicknesses, depending on the laminate layup and stacking sequence.

The magnitude and distribution of interlaminar stresses are known to be dependent upon laminate layup, ply stacking sequence and ply thickness. Therefore, these factors greatly influence the onset and growth of delamination Bjeletich et al [10] demonstrated experimentally that the uniaxial tensile

strength of the graphite/epoxy $[\pm45°/0°/90°]_s$ coupon was much lower than that of the $[0°/90°/\pm45°]_s$ coupon. Their results showed that the former coupon developed free-edge delamination, while the latter did not A stress analysis based on ply elasticity revealed that large interlaminar tensile stresses act along the free edges of the former coupon, while compressive interlaminar stresses of comparable magnitude exist at the free edges of the latter coupon Rodini et al [11] showed that interlaminar response also depends on ply thickness. They performed tensile tests on a special family of graphite/epoxy laminates with layups of $[\pm45°/0°_n/90°_n]_s$, where $n = 1$, 2 and 3, and found that the critical tensile strain for the onset of delamination decreases when n is increased This finding is consistent with the fact that grouping plies with the same fibre orientation increases the magnitude of interlaminar stresses at the free edge

3. DELAMINATION MODELLING APPROACHES

The understanding of the characteristics of delamination discussed in the previous section has provided a s und foundation for the analytical modelling of interlaminar response which is an essential prerequisite for performing a fracture analysis of structural laminates. Based on extensive research efforts, two main approaches have emerged for the predictive modelling of delamination behaviour

3.1 Strength of Materials Approach

This approach involves the calculation of interlaminar stresses and the application of appropriate failure criteria based on strength allowables for predicting delamination failure

The classical laminated plate theory is not adequate for the calculation of interlaminar stresses In Fig. 2, a $[0°/90°]_s$ laminate subjected to an uniaxial tensile load parallel to the $0°$ direction is considered as an example Due to the difference in Poisson's ratios, the $0°$ and $90°$ plies would deform differently in the y-direction However, the plate is bonded and the continuity of traction and displacement between adjacent plies
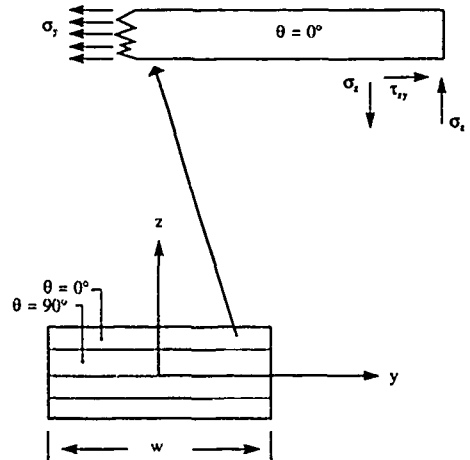
Figure 2   Development of σ_z at the $0°/90°$ interface

must be satisfied. In order to satisfy this condition σ_y must form in the plate according to laminated plate theory Also, σ_y must vanish at the free edge because of the boundary condition. As shown in Fig 2, σ_z is balanced by τ_{yz} and these two stresses form a couple. The moment formed by this couple is equilibrated by a σ_z distribution in a boundary layer region near the free edge. The laminated plate theory cannot determine these three dimensional stresses in the boundary layer.

Pipes and Pagano [1] determined the interlaminar stresses near the free edge of a four ply, symmetric laminate under uniaxial extension by using the theory of anisotropic elasticity without any simplifying assumptions. They derived a set of three elliptic, coupled partial differential equations for the free edge problem which were solved by the finite difference method. Subsequent to this classic work, Pagano [12] developed a self-consistent model based on Reissner's variational theorem [13] which became the foundation of a local model for laminate stress analysis. Pagano and Soni [14] incorporated this local model into a new concept called "global-local variational model" which was further enhanced by Soni and Chu [15]. The enhanced model can be used to determine the stress fields in practical laminates containing as many as 50 distinct local or global regions.

Besides the finite difference method and Reissner's variational theorem used by Pagano et al , the interlaminar stress problem has been solved by using the finite element method [16-19], the boundary layer theory [20], the Galerkin method [21], and the force balance method [22] It is worth mentioning that an efficient computer code based on the force balance method and the principle of minimum complementary energy has been developed by Kassapoglou and Lagace [23] for the calculation of interlaminar stresses of straight-edged laminates with a thickness of one hundred or more plies. Comprehensive reviews of the literature on the determination of interlaminar stresses can be found in References 24 and 25

Since the interlaminar stresses occur in a boundary layer near the free edge, the stress gradients are very steep and the stresses may be singular at the ply interface edge where delamination initiates. Indeed, Raju and Crews [26] showed that stress singularities exist for [θ°/(θ°-90°)]ₛ laminates, where 0≤θ≤90. It is well known that the stresses at a singular point cannot be determined exactly by numerical methods, including the displacement-formulated finite element method based on the total potential energy theorem and the finite difference method Whitcomb et al. [27] investigated the reliability of the finite element method for calculating free edge stresses in composite laminates Accurate interlaminar stress distributions were obtained within the region $(w/2 - y)/h \geq .08$, where w = specimen width, h = ply thickness, and y = distance along the y-axis. At the singular point where $y = w/2$, the interlaminar stress values are strongly dependent on the mesh size, with the finest mesh producing the largest value.

In light of the fact that the proximity of the free edge is characterized by very high interlaminar stresses which often exceed the tensile or shear strength of the matrix material, the maximum stress may not be suitable for the prediction of delamination failure In order to circumvent this difficulty, a similar approach based on the point stress or average stress criterion developed by Whitney and Nuismer [28] for the prediction of notched strength of composite laminates is required. Kim and Soni [29] adopted an average stress approach for the prediction of the onset of delamination In

this approach, the stresses used in the prediction model were averaged by integrating the interlaminar stress distributions over a characteristic distance of one ply thickness from the free edge The onset of delamination is predicted when the average interlaminar normal stress exceeds the transverse tensile strength of the composite material Predictions were also made using the in-plane shear strength as the failure parameter for comparing against the average interlaminar shear strength Kim [30] used a modified Tsai-Wu criterion to achieve accurate prediction of delamination onset under the combined influence of interlaminar normal and shear stresses. It is important to mention that the characteristic distance is a function of material, layup, stacking sequence, geometry, loading, etc , and must be determined based on experimental data

3.2 Fracture Mechanics Approach

Since the interlaminar stresses at the free edge are singular, it appears appropriate to adopt a fracture mechanics approach to characterize delamination fracture A popular methodology
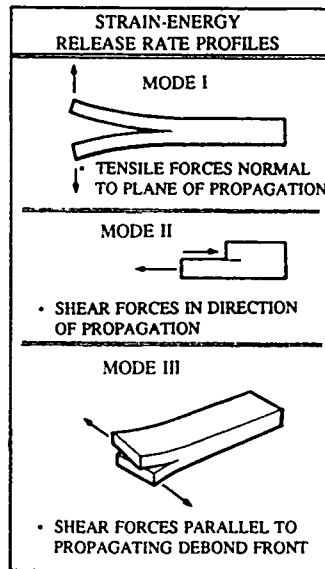
Figure 3: Interlaminar fracture modes.

employs the concept of strain energy release rate [31-33] This methodology generally involves a calculation of the strain energy release rate, G, for a delamination crack of assumed size which corresponds roughly to the size of the boundary layer at the free edge [31]. A crack-closure integral technique has been incorporated into the finite element method for the determination of G [32] This technique is very powerful because it can be used to determine the strain energy release rates, G_I, G_{II} and G_{III}, for all three basic modes of interlaminar fractures As indicated in Fig 3, modes I, II and III represent the peel, sliding shear and twisting shear mode respectively The characterization of delamination has been focused on mode I and mode II and combinations of these two modes For the prediction of delamination growth under mixed mode condition, the following criterion is often used

$$(G_I / G_{Ic})^m + (G_{II} / G_{IIc})^n = 1 \qquad (1)$$

where G_{Ic} and G_{IIc} are the critical energy release rates for modes I and II respectively, m and n are constants determined by curve-fitting of the experimental data.

Test methods for the determination of G_{Ic} and G_{IIc} using the double cantilever beam (DCB) specimen [34] and the end notch flexure (ENF) specimen [35], respectively, have been developed. It is worth mentioning that O'Brien [36] developed the edge delamination test (EDT) which can be used to determine the total critical strain energy release rate, G_c, under mixed-mode fracture. A detailed description of the test procedures and data reduction techniques of the above three methods and other experimental methods for the characterization of delamination fracture can be found in Reference 37.

4.0 ASSESSMENT OF DELAMINATION

The problem of delamination in laminated composites has been investigated at IAR Using the analytical and experimental methods discussed in the previous section, delamination of straight edge specimens subjected to uniaxial tensile extension was assessed Most of the tests were performed with constant thickness specimens and two tests were performed with specimens having tapered thickness caused by ply drop-off. In addition, rectangular laminates with an open hole or internal delaminations caused by dropweight impact were tested under compressive loading In this section, the effect of delamination on structural integrity is assessed with the aid of mechanical tests and nondestructive inspection results

4.1 Experimental Determination of Strain Energy Release Rates

The resistance of delamination in composite materials is often characterized by the strain energy release rates. In this work, the strain energy release rates for mixed-mode, mode I and mode II interlaminar fracture are determined using EDT, DCB and ENF test, respectively.

The edge delamination test was used to determine the G_c of three toughened resin composites [38] These composites are reinforced with the Hercules IM6 carbon fibre which has a tensile modulus of 280 GPa and a failure strain of 1.5% The resin materials are Narmco 5245C, Hexcel F584 and Cyanamid 1806 The first resin is a modified bismalimide and the remaining two resins are toughened epoxies. Rectangular specimens, 38 1 mm by 254 mm, were made from the three composite materials by an autoclave curing process [39] In addition, control specimens were made from Narmco T300/5208, a conventional graphite/epoxy material

The EDT specimens have a layup of $[\pm 35°/0°/90°]_s$ The selection of this layup is based on the optimization study [36] of the $[\pm \theta/0°/90°]$ family of layups which indicates th the lowest total critical strain, ε_c, occurs when $\theta \approx 35°$ According to O'Brien's finite element analysis [36], the contribution of G_I and G_{II} to G_c for the selected layup is 90% and 10% respectively. His results also indicate that changing θ from 45°, a commonly used fibre orientation, to 35 will result in higher total G at the same remote strain The inclusion of 90° plies at the centre is intended to create high interlaminar tensile stresses at the 0/90 interfaces The inclusion of 0 plies is intended to suppress material nonlinearity by having a fibre dominated layup

The EDT specimen was loaded in tension using a MTS machine under stroke control at a rate of 0.15 mm/min. An extensometer with a gauge length of 102 mm was mounted in the centre of the specimen. An X-Y recorder was used to provide a real-time analog display of deflection and load. The specimen was extended until edge delamination was detected. At this moment, a deviation in the load-deflection curve was observed, as illustrated in Fig. 4. The extensometer deflection at this point was divided by the gauge length to yield the critical strain for delamination onset, ε_c. An equation derived by O'Brien [36] is used for calculating G_c:

$$G_c = \varepsilon_c^2 \, t \, (E_o - E^*) / 2 \qquad (2)$$

where E_o = slope of the load-deflection curve, t = specimen thickness, and E^* is the stiffness after the 0°/90° interfaces are completely delaminated and is derived based on the rule of mixtures:

$$E^* = (6E_1 + 2E_2) / 8 \qquad (3)$$

where E_1 and E_2 = stiffness of sublaminate with a layup of $[\pm 35°/0°]$ and $[90°]$, respectively.
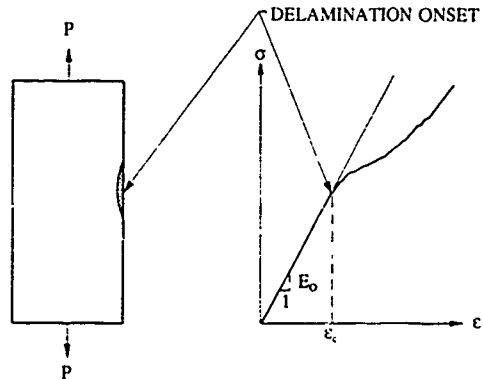
Figure 4   Detection of delamination onset from the stress-strain curve

The results of the calculations for G_c are summarized in Table 1. The G_c of the toughened resin composites are higher than that of the T300/5208 It was observed during the experiment that the delamination initiated at the edges of the specimens made with toughened resin composites and then progressed in a stable manner until it reached the entire length of the specimen. For the control specimens, the onset of delamination was immediately followed by a sudden extension to the entire length. For all specimens tested, the delamination onset and growth can only be considered as subcritical because the ultimate failure of the specimen is caused by the fracture of the fibres in the $[\pm 35°/]$ sublaminate

The DCB and ENF tests were also performed to determine the strain energy release rates under mode I and mode II fracture, respectively, of an advanced toughened resin composite, IM7/977-2 This thermoset material and a thermoplastic material, IM7/ACP-2, have been considered by FRE Composites Inc as candidate materials for the construction of the arm booms for a sophisticated robotic system for space application Tests on thermoplastic specimens are being planned

Table 1: Determination of G_c based on EDT results.

Material	Specimen ID	ε_c (µm/m)	G_c (kJ/m²)
IM6/5245C	147-1	4656	.159
	147-2	5016	.192
	147-3	5313	.211
	147-4	4750	.190
	147-5	4938	.229
Average		4935	.196
IM6/F584	82-2	5344	.207
	82-4	5297	215
	82-5	4641	.178
	82-6	4391	.174
	82-7	4578	.192
Average		4850	.193
IM6/1806	141-1		.209
	141-2	.1	.133
	141-3	4141	.156
	141-4	3781	110
	141-6	3969	125
Average		4188	.147
T300/5208	16-1	5156	180
	16-2	4406	135
	16-3	5194	.150
	16-4	4813	129
	16-5	5188	135
Average		4951	146

The DCB and ENF specimens were machined from a laminated plate with 26 unidirectional plies. The plate was consolidated using an autoclave curing procedure recommended by FRE Composites Inc The plate was subjected to an ultrasonic C-scan inspection after curing to ensure that no significant flaws were present. The dimensions for the DCB and ENF specimens are 38 mm by 280 mm and 13 mm by 330 mm, respectively. The fibre direction is parallel to the length of the specimen. A Teflon film with a thickness of 13 µm was inserted at the midplane of the laminate during layup to form an initiation site for delamination onset The DCB and ENF tests are illustrated in Fig 5

The DCB specimens were loaded in an Instron machine operated in a displacement control mode with a constant rate of 2 54 mm/min The tensile load was applied perpendicular to the plane of delamination growth via a pair of piano hinges adhesively bonded to one end of the specimen The load-displacement relationship was continuously monitored during each test on a chart recorder The specimen was loaded until the delamination crack reached a length of 51 mm
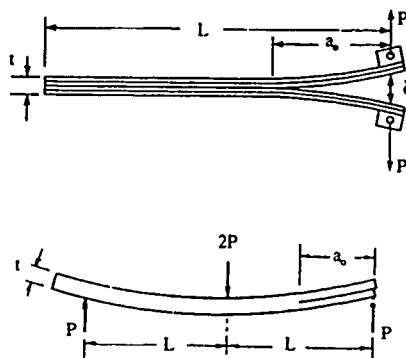
Figure 5: Double cantilever beam test and end notch flexure test for G_{Ic} and G_{IIc}, respectively.

approximately. The machine was stopped and the crack tip on both edges of the specimen was located using a magnifying glass and marked to allow accurate length measurement using a travelling microscope after the test The load versus displacement curve was also marked so that this point in the test could be identified The machine was then restarted and the procedure was repeated for crack lengths of approximately 76 mm, 102 mm, 127 mm, and 152 mm

The G_{Ic} was calculated by the compliance calibration method [40] The compliance C is defined as

$$C = \delta / P \qquad (4)$$

where δ = displacement of crosshead, and P = applied load Using a least squares technique, a straight line was fitted to the log-log plot of C versus the crack length, a The slope of the fitted line, n, is used in the following equation to calculate G_{Ic}.

$$G_{Ic} = (n P \delta) / (2 W a) \qquad (5)$$

where W is the width of the specimen The result of the calculation of G_{Ic} is presented in Table 2 During the DCB test, fibre bridging which was associated with fibres being pulled out from one side of the delamination plane to the other plane was observed. It is well known that fibre bridging can significantly elevate the fracture energy Therefore the values presented in Table 2 may be higher than the true G_{Ic} of the material.

The ENF specimen was loaded in a three-point loading fixture (see Fig. 5) at a crosshead displacement rate of 2.54 mm/min until the delamination crack propagated A chart recorder was used to continuously monitor load versus displacement. After the crack was arrested, the loading was stopped and the location of the crack tip was marked on both edges of the specimen. After precracking, the load was removed and the specimen was repositioned such that the new crack tip was 25 4 mm from the centre of the reaction point of the fixture. The specimen was reloaded until crack propagation took place This procedure was repeated three times for each specimen The critical load and compliance were determined from the load-displacement curve The load-displacement curve obtained from precracking was not used The G_{IIc} value for each crack propagation was calculated by.

$$G_{IIc} = (9\ a^2\ P^2\ C) / \{2\ W\ (2L^3 + 3a^3)\} \qquad (6)$$

where a = 25.4 mm and L = half length of the loading span, 50.8 mm. The G_{IIc} values are presented in Table 2. It is noted that the G_{IIc} is about 2 times higher than the G_{Ic} for this material.

Table 2: Strain Energy Release Rates for IM7/997-2 Material

Specimen ID	Strain Energy Release Rate
	G_I (kJ/m²)
632-I-1	.351
632-I-2	.412
632-I-3	.325
632-I-4	.430
Average	.381
	G_{II} (kJ/m²)
632-II-1	.692
632-II-2	762
632-II-3	1 041
632-II-4	.757
Average	813

4.2 Delamination in Ply Drop-Off Region

The arm booms of the robotic system are tubular structures made of an advanced composite material The ends of the arm boom are connected to metallic flanges by titanium fasteners In order to satisfy the high load transfer requirement at the bolted composite/metal interface, a ply build-up process is used to thicken the ends of the composite arm boom At the early stage of product development, bread board specimens designed to represent the detail features of the bolted interface were subjected to vigorous mechanical testing

The configuration of a typical specimen made of a thermoset composite, IM7/977-2, is shown in Fig 6. The results of the tensile tests on the thermoset specimens conducted by the technical staff of FRE Composites Inc. using the testing facilities at IAR indicates that the average failure load is 134.7 kN and the ultimate failure mode is shear-out failure of the fastener holes in the build-up section of the composite laminate. Another prominent failure mode observed during the test is the growth of delamination in the 90°/30° interface in the vicinity of the tapered end in the ply drop-off region, see Fig. 7. The delamination initiates at a free edge formed by a transverse crack of the 90° plies

In collaboration with FRE Composites Inc , the IAR conducted two constant amplitude cyclic tests on thermoset specimens with the objective of investigating the effect of delamination on the structural integrity of the bolted interface. The first test was conducted using a sinusoidal waveform with a frequency of 0.5 Hz and a R ratio of zero The maximum load amplitude was 120.1 kN which is about 90% of the average static failure load. The first cycle consisted of a manual load increase to the maximum and then a manual return to zero Major audible acoutic emissions were noticed when the load levels were 99.9

kN and 119.0 kN. At this moment, a transverse crack of the 90° plies and a delamination, which had initiated at the tip of the transverse crack and had extended along the 90°/30° interface, were observed in the vicinity of the tapered end of the ply drop-off region As shown in Fig 7, this delamination had extended across the entire width and into the bolted interface area. After the first cycle, the cyclic test was conducted and the specimen failed after 5001 cycles were elapsed.

The second test was conducted with a maximum load amplitude of 113.4 kN which is about 85% of the average static failure load. During the first cycle, the loading was halted when a major audible acoustic emission was noticed at 94.1 kN. At this moment, the 90° crack was observed. The delamination of the 90°/30° interface was found at one edge of the specimen The size of the delamination was determined by an ultrasonic time-of-flight C-scan method, see Fig 8 Using the C-scan method, the delamination was found to grow in a stable manner and after 10,000 cycles, it had propagated across the entire width and into the bolted interface area The specimen failed with a life of 18,459 cycles

The failed specimens were disassembled to examine the failure mode. The disassembled parts are shown in Fig. 9. It is noticed that the delamination causes the tapered laminate to separate into two sublaminates The load is redistributed to the flat sublaminate and as a result the tapered sublaminate carries no load. This phenomenon is supported by the shear-out failure at the fastener holes of the flat sublaminate and the absence of damage at the fastener holes of the tapered sublaminate This load redistribution accelerates the failure of the bolted interface. It is concluded that the delamination failure is subcritical which nullifies the structural benefit of the ply build-up and reduces the fatigue life of the bolted interface.

4.3 Prediction of Delamination in Tapered Laminate

A two dimensional finite element model of the tapered laminate was generated using a commercial code called NISA The purpose of the analysis is to predict the transverse cracking and the interlaminar response of the 90°/30° interface at the tapered end of the ply drop off region Orthotropic shell elements were concentrated at the transition from the tapered section to the flat section and also along the critical interface The finite element model is shown in Fig 10a It is important to mention that the fastener holes, fasteners and the metallic flange are not modelled As a result, the model is not capable of predicting the ultimate failure at the fastener holes However, it is important to simulate the boundary conditions created by the metallic flange which was used in the test. To accomplish this, nodes along the flat portion of the built-up area were constrained in the z-direction while nodes along the line x=0 were fixed in all directions A constant axial strain of 0.001 mm/mm was applied at the end of the flat section The material properties of IM7/977-2 used in the analysis are shown in Table 3

The stresses for each ply were used in conjunction with the maximum stress criterion to predict failure on a ply-by-ply basis The strength allowables given in Table 3 were compared with the calculated stresses to determine the critical location at which the failure of the first ply would occur It was determined that the axial stress in the 90° ply at the 30°/90° interface (see Fig 10b) exceeded the transverse tensile strength of the material when the applied axial strain was 0.00293 mm/mm Thus a matrix failure of the 90° ply in the form of
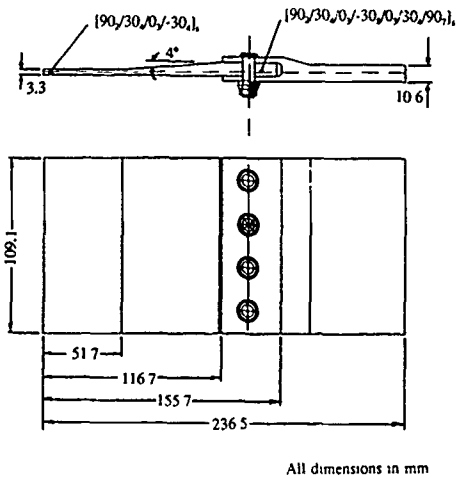
Figure 6. Configuration of the bread board specimen used to simulate the bolted composite/metal interface

$[90_2/30_4/0_2/-30_4]_s$ $[90_2/30_4/0_2/-30_4/0_2/30_4/90_2]_s$

3.3   10 6

109.1

51 7
116 7
155 7
236 5

All dimensions in mm
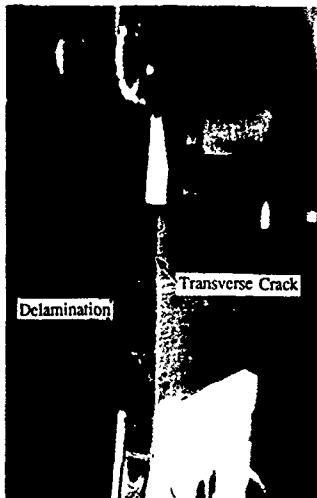
Figure 7: Transverse cracking and delamination at the tapered end of the ply drop-off region

Delamination

Transverse Crack
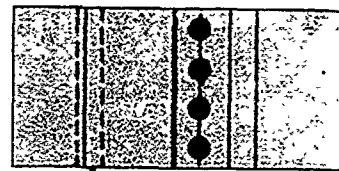
Scan area

100

75

50

25

0

Delamination

All dimensions in mm

Figure 8· Delamination at the tapered end of the ply drop-off region detected by ultrasonic time-of-flight C-scan

Figure 9   Delamination failure of the tapered laminate

IM6/5245C
[45₄/0₄/-45₄/90₆]ₛ
ε = -2510 μm/m

Delamination

0° Matrix
Cracks
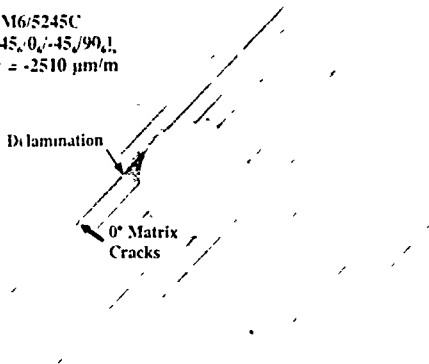
Figure 11   Penetrant enhanced X ray image of delamination initiated at hole edge under compressive loading

(a)   Overall model.

Matrix failure
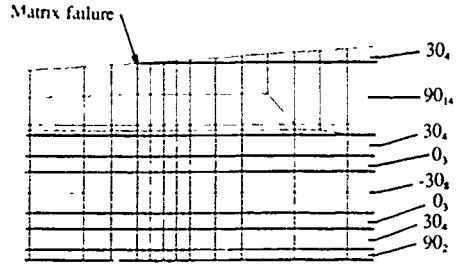
(b)   Mesh details at vicinity of transverse cracking location
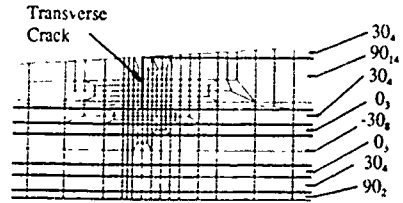
Transverse
Crack

(c)   Modified mesh for calculation of crack-tip interlaminar stresses at 90°/30° interface

Figure 10   Finite element models of the tapered laminate

Localized
Bulging

Figure 12   Localized bulging of laminate surface at hole edge

a transverse crack is predicted. This was in good agreement with the experimentally determined strain level of 0.003 mm/mm which corresponded to the detection of the transverse cracking in the specimen It is also noted that the predicted location of transverse cracking was in good agreement with the actual failure location.

Table 3: Properties of IM7/977-2*

Elastic Properties	
E_1=159.3 GPa	E_2=E_3=8 67 GPa
G_{12}=G_{13}=G_{23}=3.80 GPa	v_{12}=v_{13}=v_{23}=0.30
Strength Properties	
X_T=2482 MPa	Y_T=Z_T=72 9 MPa
S_{12}=S_{13}=S_{23}=109 MPa	X_C=1613 MPa
Y_C=Z_C=154 MPa	

* Properties supplied by FRE Composites Inc

The finite element mesh was then modified to include a transverse crack in the 90° ply which extended from the tapered edge to the 90°/30° interface, see Figure 10c The initial failure strain of 0 00293 mm/mm was applied to the modified model and the analysis was re-run The maximum stress failure criterion was applied to the 30° ply at the crack tip to determine if the crack would extend into that ply The analysis showed that although the stress was high enough to cause cracking in the matrix, the fibres in the 30° ply would not fail and thus the 90° transverse crack would not grow into the 30° ply.

In order to predict the delamination failure at the tip of the transverse crack which was arrested at the 90°/30° interface, a quadratic failure criterion based on the interlaminar stresses was used.

$$\sigma_3 F_3 + \sigma_3^2 F_{33} + \sigma_{13}^2 F_{44} + \sigma_{23}^2 F_{55} = 1 \qquad (7)$$

where F_3, F_{33}, F_{44}, F_{55} are identical to the terms used in the tensor polynomial failure criterion [41]

When the interlaminar stresses, σ_3 and σ_{13}, obtained from the finite element analysis were substituted into Equation 7, failure of the ply interface was predicted The σ_{23} was ignored because this stress was not calculated in the two dimensional analysis and was considered not important in the present case The prediction suggests that once the transverse crack initiates in the 90° ply, a delamination forms instantaneously at the 90°/30° interface This conclusion was verified by the experimental observation that a delamination was present at the tip of the transverse crack when the test was halted at the detection of the first audible acoustic emission.

To prevent transverse cracking and delamination failure from occurring in the tapered laminate of the bolted composite/metallic flange interface, either the composite material which the lamina is fabricated from must be changed or the layup has to be modified or both The results of the finite element analysis indicate that the tapered laminate is weakened by grouping fourteen 90° plies at the end of the ply drop-off region where a high stress concentration exists

Furthermore, grouping of 90° plies introduces high interlaminar stresses at the ply interface which makes it susceptible to delamination A new layup for the tapered laminate with a less severe grouping of 90° and a replacement of the thermoset material with a thermoplastic material, IM7/APC-2, are being investigated at IAR.

4.4   Delamination at the Edge of an Open Hole

The interlaminar response at the edge of an open hole in a laminated plate subjected to compressive loading was investigated at IAR [42,43] Using acoustic emission techniques and penetrant-enhanced X-radiography, the localized damage development at the curved edge of an open hole was studied. It was observed that the initial damage consisted of a delamination which formed at a critical ply interface. A penetrant-enhanced X-ray image of this initial delamination is shown in Fig 11. Acoustic signals emitted from the plate under compressive loading were collected by three piezoelectric sensors attached on the plate These acoustic emission signals were processed during the test and were used as a guide to halt the test in order to perform a nondestructive inspection of the hole edge using the X-ray procedure Detailed descriptions of the acoustic emission technique and the method of acoustic signal processing are described in Reference 44

Under increasing compressive load, localized buckling of the load-carrying 0° plies was observed almost immediately after the onset of delamination This buckling produced a localized bulging of the surface at the hole edge as shown in Fig 12. The X-ray image shown in Fig 13 indicates that the initial delamination was extended further after the buckling of the 0° plies increased the strain at the edge of the delamination to a level which exceeded the critical strain energy release rate of the material This series of X-ray images confirms the proposed mechanisms for damage initiation and growth at a curved free edge under compressive loading [43]

IM6/5245C
[45$_2$/0$_4$/-45$_2$/90$_6$]$_s$
ε = -2852 µm/m
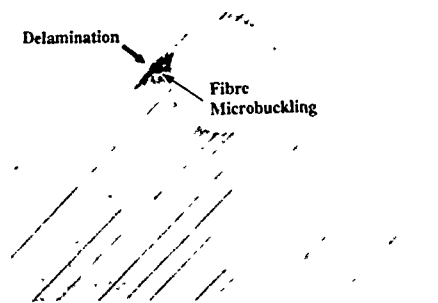
Figure 13: Penetrant-enhanced X-ray image of delamination growth promoted by localized fibre buckling

The onset of delamination at the curved edge was predicted by using the quadratic failure criterion given in Equation 7 [42] The interlaminar stresses were calculated using a 3-D finite element method. A good correlation between experimental and predicted results [43] indicates that the strength of materials approach is satisfactory in the prediction of delamination onset

4.5 Effect of Impact Damage

It is well known that dynamic impact loading applied perpendicular to a laminated plate (see Fig 14) will produce internal delaminations which have been demonstrated to degrade the compressive strength of the plate by as much as 70% [45] This strength reduction is believed to be caused by a buckling of the sublaminates formed by the internal delaminations under inplane compressive loads This buckling of the sublaminates will trigger unstable delamination growth which in turn will lead to the premature failure of the laminated plate.
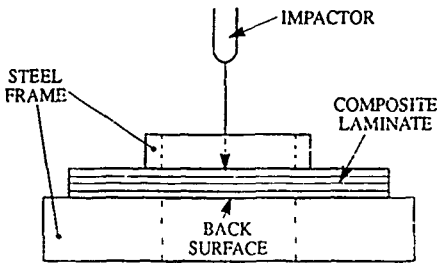
Figure 14: Impact loading of composite laminate.

A dropweight impact method was used to investigate the extent of the damage as a function of impact energy [46] The ultrasonic time-of-flight C-scan method was used to determine the extent of impact damage [47]. It was found that the damage area increases with impact energy up to a critical level and then remains constant Using a destructive sectioning method, the damage state was determined to be internal delaminations when the impact energy was below the critical level. When the impact energy was equal to or above the critical level, a punch-out region with extensive fibre breakage began to develop within the delaminated area

Based on the experimental characterization of the impact damage state, two approaches for the prediction of the degrading effect of impact damage on the compressive strength of composite materials have been proposed For the impact damage with a punch-out region, the predictive model can be based on a macroscopic, semi-empirical failure criterion such as the point stress or average stress criterion because of the resemblance of the impact damage state to an open hole. For the impact damage characterized by internal delaminations, the predictive model is based on a delamination buckling criterion The development of the latter model will be presented.

There are five major stages in the development of the predictive model for the residual compressive strength of composite laminates containing impact-induced delaminations The first stage involves the determination of the planar area, thickness and shape of the largest delamination which is usually located close to the back surface. The back surface is used here to denote the planar surface of a laminate which is not subjected to the impact loading. The second stage involves the determination of the critical stress for the largest delamination to buckle. A procedure based on the Rayleigh-Ritz method is developed for the calculation of the delamination buckling stress [48]

In the third stage, the damaged region is simulated as a soft inclusion. The procedure to determine the reduced axial modulus of the soft inclusion is illustrated in Fig. 15 The reduction in the axial modulus, E, depends on the stability of the largest delamination In the current analysis, the impact-damaged laminate is assumed to follow a linear-deflection path until the outermost sublaminate buckles The thickness of the outermost sublaminate, which is defined by the distance of the largest delamination to the back surface, and the shape of sublaminate are used in calculating the buckling stress, σ_B. After buckling, the load carried by the sublaminate becomes constant, as in Euler buckling. It is noted that the post-buckled modulus of the damaged region is decreased when the compressive strain is increased. As shown in Fig. 15, the most critical reduced axial modulus, E^*, is the one which coincides with the strain at failure, ε_o, of the undamaged laminate. The E^* is defined as:

$$E^* = \sigma_B / \varepsilon_o \qquad (8)$$

The modulus retention ratio, MRR, is equal to the ratio of E to E^* It is assumed that the transverse and shear moduli for the soft inclusion are reduced by the same ratio, while the Poisson's ratio remains unchanged
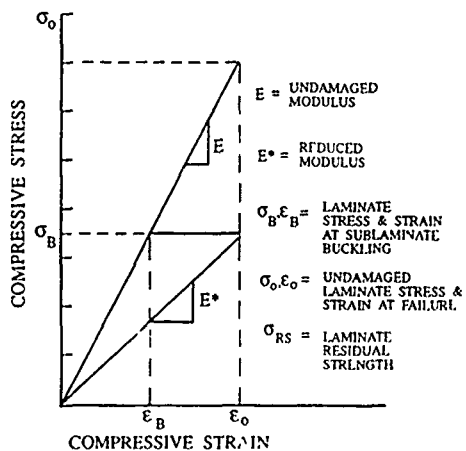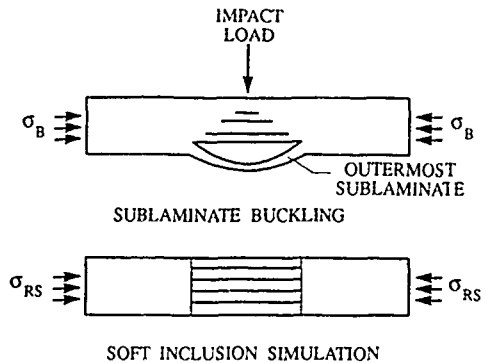
Figure 15. Calculation of reduced modulus using sublaminate buckling approach

In the fourth stage, the stress redistribution in an infinite width laminate containing an anisotropic inclusion with moduli defined earlier is determined using Lekhnitskii's complex variable approach [49] The stress distribution in a finite width laminate is obtained by using a finite width correction factor [50].

In the fifth stage, the strength retention ratio, which is defined as the ratio of the residual compressive strength to the compressive strength of the undamaged laminate, is determined by using appropriate failure criteria based on strength allowables in conjunction with the stress distribution in the vicinity of the soft inclusion.

The point stress criterion [28] was used in Reference 49 to predict the strength retention ratios of quasi-isotropic laminates fabricated from Hercules AS4/3501-6. The layup of these laminates was [45°/0°/-45°/90°]$_{6s}$ and the sublaminate was assumed to be 4 ply thick and circular in shape. The assumptions for sublaminate thickness and shape are in close agreement with the results of damage characterization reported in Reference 47. The prediction was carried out for a range of damage diameters As shown in Fig. 16, the predicted strength retention ratios are in good agreement with the experimental results [46] when a characteristic distance of 0 147 mm was used in the point stress criterion

AS4/3501-6
[45°/0°/-45°/90°]$_{6s}$
4 PLY SUBLAMINATE
$D_o = 0.147$ mm

■ EXPERIMENTAL RESULTS

···· PREDICTION WITHOUT FWC

— PREDICTION WITH FWC
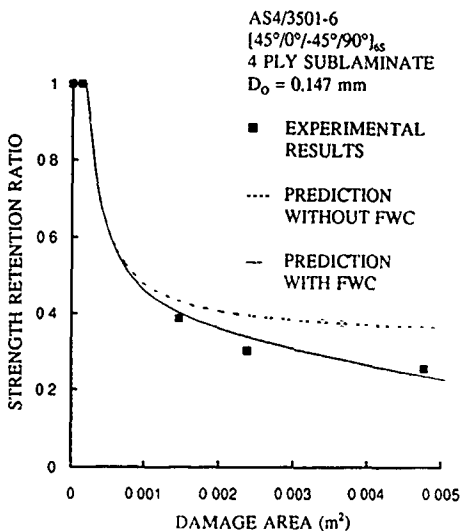
Figure 16 Comparison of predicted strength retention ratios with experimental results.

Subsequent to this preliminary verification of the predictive model, an extensive experimental program will be conducted in collaboration with de Havilland Inc and the Carleton University. This program will involve impact testing of over one hundred laminates with different stacking sequences and thicknesses The main composite material to be investigated is Toray T800/3900-2. This program is expected not only to provide complete verification of the proposed predictive model but also to provide a data base which is required for damage tolerance analysis of composite structures

5. CONCLUSIONS

Based on the research conducted at IAR, the following conclusions are reached

1 Using the edge delamination test, the G_c for three toughened resin composites were found to be higher than that of the control material, T300/5208 This means that the toughened resin composites can resist delamination better than T300/5208.

2. Under tensile static or cyclic loading, the effects of delamination on structural integrity were manifested in stiffness reduction and load redistribution which could lead to premature failure. In the case of the bread board specimens representing the bolted interface of the robotic arm boom, the growth of the delamination initiated at the tip of the transverse crack redistributed the cyclic load to a sublaminate which failed in a shearout mode at the fastener holes The delamination nullified the structural benefit of the ply build-up and shortened the fatigue life of the tapered laminates

3. Using acoustic emission techniques and penetrant-enhanced X-radiography, experimental evidence was found which confirmed that the onset of delamination at the curved edge of an open hole under compressive loading led to the localized buckling of the load-carrying plies This finding has validated the use of the quadratic failure criterion based on the interlaminar stresses in predicting delamination onset.

4. Under compressive loading, delamination was found to play a major role in affecting the stability of the load-carrying plies Based on this finding, a model based on the buckling of impact-induced sublaminates was developed to predict the residual compressive strength of composite laminates Preliminary verification of model showed good agreement between experimental and predicted results

6. ACKNOWLEDGEMENT

7. REFERENCES

1 Pipes, R B and Pagano, N J, Interlaminar Stresses in Composite Laminates under Uniform Axial Extension, Journal of Composite Materials, Vol 4, 1970, pp 538-548

2 O'Brien, T K, "Characterization of Delamination Onset and Growth in a Composite Laminate," Damage in Composite Materials, ASTM STP 775, Reifsnider, K L, Ed, American Society for Testing and Materials, Philadelphia, 1982, pp 140-167

3. Mohlin, T., Blom, A.F., Carlsson, L A., and Gustavsson, A I, "Delamination Growth in a Notched Graphite/Epoxy Laminate under Compression Fatigue Loading," Delamination and Debonding of Materials, ASTM STP 876, Johnson, S W, Ed, American Society for Testing and Materials, Philadelphia, 1985, pp. 168-188.

4. Kim, R.Y and Soni, S.R., "Failure of Composite Laminates due to Combined Interlaminar Normal and Shear Stresses," Composites '86: Recent Advances in Japan and the United States, Kawata, K.,Umekawa, S, and Kobayashi, A, Ed, Japan Society for Composite Materials, Tokyo, Japan, 1986, pp. 341-350.

5. Pagano, N.J., Ed., Interlaminar Response of Composite Materials, Composite Materials Series, Vol. 5, Pipes, R. B., Series Ed, Elsevier Science Publishers B V, Amsterdam, the Netherlands, 1989.

6. Herakovich, C T., "On the relationship between Engineering Properties and Delamination of Composite Materials," Journal of Composite Materials, Vol 15, July 1981, pp. 336-348.

7. Lagace, P, Brewer, J, and Kassapoglou, C, "The Effect of Thickness on Interlaminar Stresses and Delamination in Straight-Edged Laminates," Journal of Composite Technology and Research, Vol 9, No 3, Fall 1987, pp 81-87.

8. Kassapoglou, C and Lagace, P, "Closed Form Solutions for the Interlaminar Stress Field in Angle-Ply and Cross-Ply Laminates," Journal of Composite Materials, Vol 21, 1987, pp. 292-308

9. Wang, S.S. and Choi, I., "Boundary-Layer Effects in Composite Laminates. Part 1 -- Free-Edge Stress Singularities," Journal of Applied Mechanics, Vol 49, 1982, pp. 541-548.

10. Bjeletich, J G, Crossman, F.W., and Warren, W.J., "The Influence of Stacking Sequence on Failure Modes in Quasi-Isotropic Graphite-Epoxy Laminates," Failure Modes in Composites - IV, Cornie, J R and Crossman, F.W., Eds., American Institute of Mining, Metallurgical and Petroleum Engineers, New York, 1979, pp 118-139

11. Rodini, B.T. and Eisenmann, J R, "An Analytical and Experimental Investigation of Edge Delamination in Composite Laminates," Fibrous Composites in Structural Design, Lenoe, E M, Oplinger, D W and Burke, J.J, Eds., Plenum Press, New York, 1978, pp 441-457

12. Pagano, N J, "Free Edge Stress Fields in Composite Laminates," International Journal of Solids and Structures, Vol 14, 1978, pp 401-415.

13. Reissner, E, "On Variational Theorem in Elasticity," Journal of Mathematical Physics, Vol 29, 1950, pp 90-101

14. Pagano, N.J. and Soni, S R, "Global-Local Laminate Variational Model," International Journal of Solids and structures, Vol 19, 1983, pp. 207-228

15. Soni, S R. and Chu, D.K., "An Improved Procedure for Free Edge Stress Analysis in Composite Laminates," Proceedings of Third Technical Conference on Integrated Composite Technology, American Society for Composites, Stauffer Madison Hotel, Seattle, Washington, September 25-29, 1988, pp. 80-92.

16. Rybicki, E.F, "Approximate Three-Dimensional Solutions for Symmetric Laminates under Inplane Loading," Journal of Composite Materials, Vol. 5, 1971, pp. 354-360.

17. Wang, A.S.D. and Crossman, F.W, "Some New Results on Edge Effect in Symmetric Composite Laminates," Journal of Composite Materials, Vol 11, 1978, pp 92-106.

18. Herakovich, C.T., Nagarkar, A. and O'Brien, D A., "Failure Analysis of Composite Laminates with Free Edges," Modern Developments in Composite Materials and Structures, Vinson, J R, Ed., American Society of Mechanical Engineering, 1979, pp. 53-66.

19 Spilker, R.L and Chou, S C., "Edge Effects in Symmetric Composite Laminates: Importance of Satisfying the Traction-Free Edge Condition," Journal of Composite Materials, Vol. 14, 1980, pp. 2-20

20. Tang, S. and Levy, A., "A Boundary Layer Theory -- Part II: Extension of Laminated Finite Strip," Journal of Composite Materials, Vol 9, 1975, pp. 42-52

2 Wang, T S and Dickson, J N, "Interlaminar Stresses in Symmetric Composite Laminates," Journal of Composite Materials, Vol. 12, 1978, pp 390-402

22 Lagace, P A and Kassapoglou, C, "An Efficient Method for the Calculation of Interlaminar Stress in Composite Materials Part I -- The Force Balance Method," Technology Laboratory for Advanced Composites Report No. 85-5, Massachusetts Institute of Technology, Cambridge, MA, 1985

23 Kassapoglou, C and Lagace, P A, "An Efficient Method for the Calculation of Interlaminar stresses in Composite Materials," Transactions of the ASME, Vol 53, December 1986, pp 744-750

24 Salamon, N J, "An Assessment of the Interlaminar Stress Problem in Laminated Composites," Journal of Composite Materials Supplement, Vol 14, 1980, pp 177-194

25. Garg, A C, "Delamination -- A Damage Mode in Composite Structures," Engineering Fracture Mechanics, Vol 29, No 5, 1988, pp 557-584

26 Raju, I.S. and Crews, J H. Jr, "Interlaminar Stress Singularities at a Straight Free Edge in Composite Laminates," NASA TM-81876, 1980

27. Whitcomb, J D., Raju, I S. and Goree, J.G., "Reliability of the Finite Element Method for Calculating Free Edge Stresses in Composite Laminates," Computers and Structures, Vol 15, No 1, 1982, pp. 23-37

28 Whitney, J M and Nuismer, R J, "Stress Fracture Criteria for Laminated Composites Containing Stress Concentrations," Journal of Composite Materials, Vol 8, July 1974, pp 253-265

29. Kim, R.Y and Soni, S R , "Experimental and Analytical Studies on the Onset of Delamination in Laminated Composites," Journal of Composite Materials, Vol 18,1984.

30. Kim, R Y , "Experimental Observations of Free-Edge Delamination," Chapter Three, Interlaminar Response of Composite Materials, Composite Materials Series, Vol. 5, Pipes, R.B., Series Ed , Elsevier Science Publishers B V , Amsterdam, the Netherlands, 1989, pp 111-160

31. Wang, A.S D., "Fracture Analysis of Interlaminar Cracking," Chapter Two, Interlaminar Response of Composite Materials, Composite Materials Series, Vol 5, Pipes, R B., Series Ed , Elsevier Science Publishers B V., Amsterdam, the Netherlands, 1989, pp 69-109

32. Rybicki, E F and Kanninen, M F , "A Finite Element Calculation of Stress Intensity Factors by a Modified Crack Closure Integral," Engineering Fracture Mechanics, Vol. 9, 1977, pp 931-938.

33. O'Brien, T.K., "Interlaminar Fracture of Composites," NASA TM 85768, NASA Langley Research Center, Hampton, Virginia, 1984.

34. Wilkins, D J., Eisenmann, J.R , Camin, R A , Margolis, W.S and Benson, R A , "Characterizing Delamination Growth in Graphite-Epoxy," Damage in Composite Materials, ASTM STP 775, Reifsnider, K. L , Ed , American Society for Testing and Materials, 1982, pp 168-183

35. Russell, A J and Street, K N , "Factors Affecting the Interlaminar Fracture Energy of Graphite/Epoxy Laminates," Progress in Science and Engineering of Composites, ICCM-IV, Japan Society of Composite Materials, Tokyo, 1982, pp 279-286

36. O'Brien, T K , "Mixed-Mode Strain-Energy-Release Rate Effects on Edge Delamination of Composites," Effects of Defects in Composite Materials, ASTM STP 836, American Society for Testing and Materials, 1984, pp 125-142.

37. Whitney, J M , "Experimental Characterization of Delamination Fracture," Chapter Four, Interlaminar Response of Composite Materials, Composite Materials Series, Vol 5, Pipes, R B , Series Ed , Elsevier Science Publishers B V , Amsterdam, the Netherlands, 1989, pp 161-250

38. Poon, C., Scott, R F and Lee, S , Testing of New-Generation Carbon Fibre/Toughened Resin Epoxy Systems," Polymer Composites, Vol 9, No 5, October 1988, pp 318-329

39. Lee, S , Scott, R F. and Colton, J , "Methods for Processing Aerospace Composite Materials at NAE," LTR-ST-1558, Institute for Aerospace Research, National Research Council Canada, Ottawa, December 1985

40. Berry, J P , "Determination of Fracture Surface Energies by the Cleavage Technique, Journal of Applied Physics, Vol 34, 1983, pp 62-66

41. Tsai, S W. and Wu, E M , 'A General Theory of Strength for Anisotropic Materials,' Journal of Composite Materials, Vol. 5, 1971, pp 58-69

42. Poon, C., Bellinger, N C., Gould, R.W and Raizenne, M D., "Damage Progression under Compressive Loading in Composite Laminates Containing an Open Hole," Presented at the 73rd AGARD-SMP Workshop on the Utilization of Advanced Composites in Military Aircraft, San Diego, California, October 1991

43. Poon, C , Bellinger, N C , and Gould, R. W., "Localized Damage Development in Notched Composite Plates Subjected to Compressive Loading," to be presented in the Second International Conference on Computer Aided Assessment and Control Localized Damage '92, Wessex Institute of Technology, Southampton, U K , July 1-3, 1992.

44 Poon, C , Fahr, A., Bellinger, N C., and Vietinghoff, H., "Damage Initiation in Composite Plates with an Open Hole under Compressive Loading," to be presented at the 6th Canadian Symposium on Aerospace Structures and Materials, Ottawa, May 4-5, 1992

45 Poon, C , Benak, T and Gould, R W , "Assessment of Impact Damage in Toughened Resin Composites," Theoretical and Applied Fracture Mechanics, Vol 13, 1990, pp 81-97

46 Poon, C , Komorowski, J P , Gould, R W and Chapman, C E , "Quantitative Assessment of Impact Damage in Composites," Proceedings of the International Conference on Aircraft Damage Assessment and Repair, Melbourne, Australia, August 26-28, 1991, pp 54-58

47 Poon, C , Chapman, C E and Gould, R W , "Nondestructive Characterization of Impact Damage in Composites," CSNDT Journal, Vol 13, No 1, January 1992, pp. 14-30.

48 Xiong, Y and Poon, C , "Buckling of Delamination in Composite Laminates," LTR-ST-1870, Institute for Aerospace Research, National Research Council Canada, Ottawa, March 1992

49 Lekhnitskii, S G., Anisotropic Plates, Gordon and Breach Science Publishers, New York, 1968

50. Xiong, Y. and Poon, C., "Prediction of Residual Compressive Strength of Impact-Damaged Composite Laminates," to be published as an LTR report, Institute for Aerospace Research, National Research Council Canada, Ottawa

Synergism between Layer Cracking and Delaminations in MD-laminates of CFRE

H. Eggers, H.C. Goetting, H. Bäuml

DLR-Institut für Strukturmechanik
D-3300 Braunschweig / Flughafen
Germany

1. Summary

The synergism between successive layer cracking and delamination growth was studied for laminates fabricated out of T300/914C solely. Unidirectional (UD) and fiber dominated multidirectional (MD) laminates were tested after static or fatigue loading Typical examples for damage mechanisms were analysed numerically and used to develop damage conditions An increase of the damage resistance was observed for MD-laminates stacked by quasi-unidirectional [± 2]-double layers (QD-layers)

In crossply laminates of various stacking sequences the crack distances were measured on the inner 90°-layers after T-fatigue loading. Expressions for the mean crack distances and the residual layer stiffnesses were developed in dependence of layer thicknesses, mean layer strains $\varepsilon_\perp$ perpendicular to the fibers and number of load cycles For the Characteristic Damage State (CDS) an energy condition was established to evaluate the crack distances $A_{r\,DS}$ for brittle matrices.

In order to describe more properly the delamination growth interferred by layer cracking, a second order tensor was established for the released energy The mean values of this tensor are the common energy release rates (ERR) for the different crack modes and the first invariant is the total ERR. But the ERR-tensor has three invariants, which can be used to establish more complex damage conditions.

Keywords: Material T300/914C, damage mechanism, crossply laminate, Characteristic Damage State, residual layer stiffness, energy release rate, matrix crack condition

2. Introduction

Since several decades fiber reinforced composites are used in aerospace structures. Nevertheless, a consistent design philosophy for damage tolerant composites does not exist. For the design of structures the industry chooses conservative strain limits ($\varepsilon_{ULT} \approx 0\ 5\%$) and qualifies critical parts by extensive testing. A limited number of rather large structures is tested for proving accomplishment of the qualification requirements Unfortunately, these tests often do not allow more general testimonies to the damage behavior of stuctures.

In research institutes, numerous but small substructures or even specimens were tested in general for studying damage modes, their synergism and the damage progression . Detailed analyses of damaged zones give insights into the behavior of composites and yield clues to the design of more damage tolerant structures In order to achieve a definite damage, unrealistic stacking sequences and/or loading conditions were used occasionally.

Both concepts yield a maximum of information only, if the tested structures are also analyzed numerically But the principles of continuum and fracture mechanics are rather inadequate tools to calculate extreme heterogeneous, multiple cracked composites For a definite damage to be investigated, only specific models are available, which homogenizes most of the structure

In this work for a delaminated layered structure the sublayers are modelled separately in general, whereas the fiber-matrix system as well as the layer cracks were homogenized For this model, residual stiffnesses were gener-
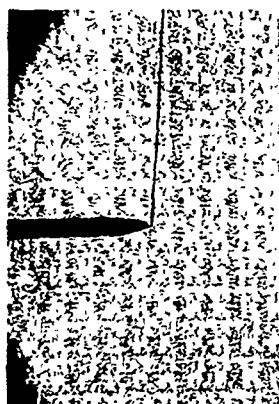
Figure 1   Crack initiation at the notch tip of a [5]₄-laminate

Tests L Kirschke
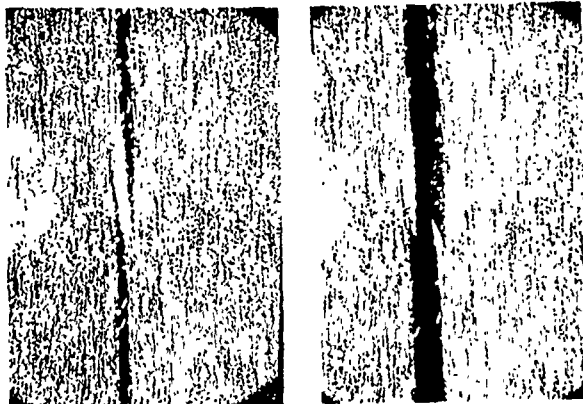
Figure 2   Misaligned fiber bundels bridging a crack in a UD-laminate before and after breakage

Tests L Kirschke
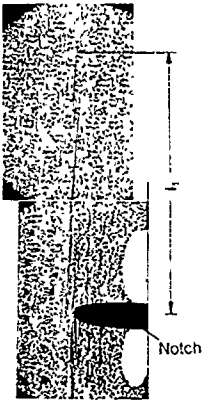
Figure 3

Crack pattern in side-notched
[± 2]₂ₛ-laminates

Tests L Kirschke

Figure 4 ERR's in notched [0]ₙ- and [± 2]₂ₛ-laminates

Tests L Kirschke

ated in dependence of geometry and straining of the layers Additionally, a generalised ERR concept is introduced for more sophisticated analyses of delamination growth

3. Damage behaviour of MD-laminates

In order to gain insight into the damage behavior of layered composites, typical damage modes will be depicted, which influence the analytical models Only matrix cracking will be considered well below the rupture strength of the T300/914C-material

In UD-laminates cracks propagate easily along the fibers, Fig 1 Occasionally misaligned fiber bundels bridge a crack and restrain the crack propagation significantly, Fig 2 In order to utilise this effect for more damage tolerant laminates consecutively stacked UD-layers were misaligned alternately by ±2° In quasi-unidirectional [± 2]ₙ-angleply laminates (QD-laminates) the residual stiffnesses and strengths remain unchanged except of the shear resistance, which increases significantly Instead of a single crack a narrow extended damage zone appears, where sequences of staggered opening cracks are seperated by fiber bundels bridging the damage, Fig 3 In both types of laminates the damage initiate at about the same stress level In UD-laminates the crack propagation accelerated rather soon, whereas in QD-laminates an unstable crack growth was not observed in the tests even for significantly higher load levels, Fig. 4a Probably, this

advantage will vanish for a damage caused by mode I-stresses solely

The cracklike damage in notched QD-laminates was modelled numerically by a single opening crack (mode I only) After a short crack initiation the critical ERR, where the crack just starts to propagate, is much higher for QD-laminates than for UD-laminates, Fig. 4b. After some distance from the crack tip the sequence of opening cracks must be followed by a total crack, where also the fibers are broken Unfortunately, the length of the total crack cannot be measured because of the brushlike overlapping of fibers. In reality, after a certain crack length both curves must become parallel to each other

In MD-laminates various types of cracks appear, which interfere in each other. In general, layer cracks in parallel to the fibers of the UD-layers will be generated first at rather low load levels and/or number of load cycles The layer cracks, formed side by side at narrow sequences damage the interface and steer the subsequent delamination progress

Matrix cracks were never observed in micrographs extending over a fraction of a UD-layer only Once, a microcrack starts to propagate, more and more energy is released at the crack tip, see Chapter 11 in [2] The crack speed increases until the crack tip hits upon the next off-axis layer The undamaged UD-cell between two layer cracks is strained at the interface by shear and peeling stresses The stresses with their maxima close to the layer crack

Source H J Seifert
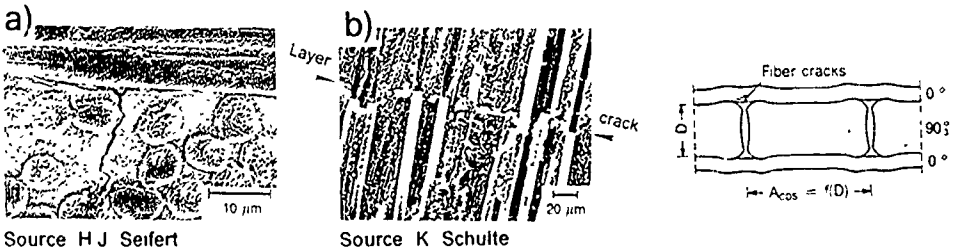
Source K Schulte

Figure 5 Microdelaminations induced by layer cracks

cause an extreme contraction of the layer at the crack surface. A short microdelamination releases peeling stresses significantly, whereas the magnitude of shear stresses remains unchanged.

Layer cracking seems to be a dynamic process. The sudden contraction of the layer at the crack causes not only microdelaminations but also fiber cracking and -debonding at the surface of adjacent layers. Microdelaminations, expected on account of the discussed stress- and displace-ment fields, are rarely found in micrographs, Fig 5a Nevertheless, there is a local damage at the interface equivalent to a microdelamination. [3] Fig 5b shows a photograph of the interface of the deplied upper layer The partly broken and debonded fibers are ordered along lines which relate exactly to the layer cracks

The local damage at the interface blunts the crack tip of a delamination Therefore, the delamination will grow preferably in the direction of the layer cracks rather than perpendicular to it, Fig 6a Fairly long parts of the delaminated front form rather straight lines in parallel to the layer cracks Under compression loading the delamination may jump to an interface which is located more closely to the surface of the structure, so that local buckling is enforced, Fig 6b

The jump of a delamination to adjacent interfaces is rather common in laminates fabricated out of UD-layers. An extreme example depicts Fig 7, which is a draft of the edge surface of a MD-specimen, delaminated by T-fatigue loading The draft was generated from a grating reflection photograph, which not only shows the curvature of the upper sublaminate but also the delamination front at the edge because of the inclined view at the specimen. [4]

a) Ultrasonic C-scan   b) X-ray radiograph

Hole 0	5 mm	Del 0	11 mm
σ_a	350 N/mm^2	σ_a	400 N/mm^2
N	96000 LC	N	260000 LC
Measured by W Hillger		Measured by H C Goetting	

Figure 6   Delaminations after T-fatigue loading

At the first glance it is surprising, that the delamination front jumps to the adjacent interface at **each** layer crack But the answer is rather simple The outher [0/45/0/−45/0]-sublimates are nearly balanced Under tension loading they contract und bend slightly to the inside. The stiff [90]-layers, connected alternately at both sublaminates, act like web-stiffeners, such that both sublaminates bend strongly to the outside

This mechanism can be avoided, when the [90]-layer is replaced by a [±88]-angle ply (90°-QD-layer) The QD-layer will not be separated completely by a layer crack, such that jumps of the delamination to adjacent interfaces are avoided The sublaminate connected with the 90° QD-layer will bend strongly to the outside as before But the other sublaminate will bend slightly to the inside, and the crack opening displacements caused by differences of curvature will be cut to halfes roughly Just by replacing UD-layers in a MD-laminate by QD-layers the damage tolerance may increase significantly. In order

$[0_2/-45/0_2/-45/0/[90_2]$ ...

Material T300 / 914C

Mirrored specimen   Crack

Figure 7
Grating reflection photograph and a compiled view at the specimen edge

a)   b)

[0 // +45/0, / −45/0 /90]$_s$ [±2 // +45/±2/−45/0/90]$_s$
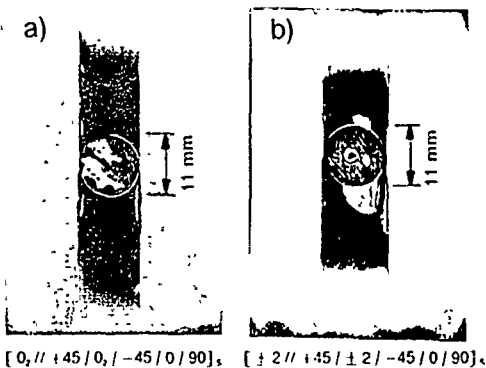
Figure 8   X-ray radiographs after T-C-fatigue loading

Stress ratio   1
Extreme stresses   +300 N/mm^2

to proof this assumption tension tests at laminates with the following stacking sequences are in preparation:

$$[0_2 // +45 / 0_2 / -45 / 0 / 90]_s$$

$$[\pm 2 // +45 / \pm 2 / -45 / 0 / \pm 88 / 0 / ..]$$

The buckling of UD-sublaminates, located at the surface of a MD-laminate, is accompanied by layer cracks at both sides of the delamination, Fig. 8a. These cracks coincide with the delamination length. Under compressive loading the UD-sublaminate buckles like a beam and this causes a mode I-crack at the delamination front

The size of the delamination zone will be reduced by ≈30%, when the UD-layers are replaced by QD-layers, Fig. 8b. The cracks, restrained by layer misalignments, are shorter than the length of the delamination. Therefore, a gliding-crack (mode II, III) in combination with compressive peeling stresses is generated at delamination front, Fig. 9

Material	T300 / 914C
σ_{BU}	1600 N/mm²
σ_{IU}	50 N/mm²
Stacking sequence	$[0_n / 90_m / 0_n]$
	n = 1, 2 4
	m = 1 , 4
Load F/F_U	0 5 , 0 9
Load frequency	5 Hz
Stress ratio	0 1
log (N)	3 .. 66

Figure 10   T fatigue tests at crossply laminates

Mean stress   -550 N/mm²
Material   T300 / 914C
Stack $[\pm 2 // 45 \ \pm 2 / -45 / 0 / 90]_s$
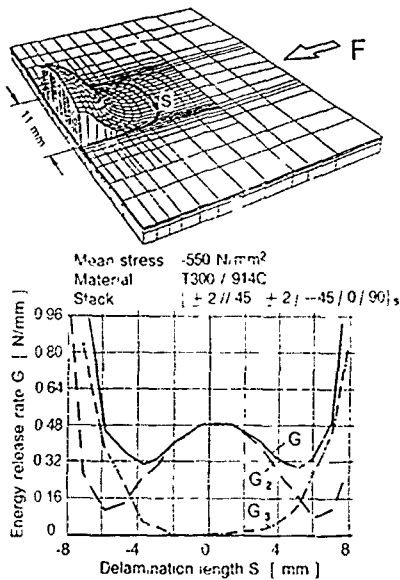
Figure 9.   ERR s at the delamination front

Calculation E Haug

MD-Laminates fabricated of QD- instead of UD-layers are more damage tolerant, because energyrich damage modes were suppressed. This advantage is accompanied by minor increase of fabrication costs. In order to support this statement, more tests are necessary on MD-laminates stacked of QD-layers.

4. Cracking of Embedded Layers

Tools for the analysis of various cracked MD-laminates are not available. Therefore, different models were developed to describe certain phenomena sufficiently accurate Generally, the material is homogenized and the embedded cracks are modelled directly by finite elements. Secondary effects of lower or higher order are taken into account by stiffness reductions and/or boundary and loading conditions

In the vicinity of the delamination front a tridimensional stress state must be analyzed for a crack growing along an interface damaged by layer cracking. For stress calculations often stiffness components perpendicular to the fibers are neglected, which change the results unpredictably. To overcome this shortcoming, formulas for reduced layer stiffnesses were generated for the material T300 914C. Probably, they are sufficiently accurate for any brittle resin system, if some characteristic parameters will be modified by guiding tests

Crossply laminates were tested under T-fatigue loading at ambient temperature. The specimen configurations, the variations of stacking sequences, load levels and number of load cycles are depicted in Fig 10. Each specimen was cycled with controlled load levels in a servohydraulic testing machine. After the proposed number of load cycles the specimens were dismounted, contrasted with dijodmethan and X rayed

In the X-ray photographs the cracks seemed to be concentrated at both edges. Therefore, one specimen was cut into halfs and contrasted and X-rayed again. The new X-ray photograph showed the same crack concentration at the specimen axis as at the edge. The check verified, that the visible crack concentration at the boundary is representative for the whole specimen. Therefore, in the X-ray photographs the coordinates of the cracks were measured only along both edges. For the measurements a light microscope was used combined with a stepper motor controlled manipulator, which generated and stored the coordinates automatically. For the chosen test configurations Tab I shows the measured mean values for crack distances

Unfortunately, the cracks did not appear in X-ray photographs of specimens with one 90°-layer only. In order to get at least a first estimation of the crack distances micrographs were taken after 100 000 load cycles on $[0_n / 90_1 / 0_n]$-laminates. Due to limited time and money the single layer could not be studied more thoroughly by a higher number of micrographs

Table 1 Measured mean crack distances in crossply laminates

Stack	Load f/Fu	5	10	20	50	100	200	500	1000	2000	4000
					Measured mean crack distances A mm						
$[0_1/90_1/0_1]$	0.90	0.73	0.58	0.47	0.49						
$[0_1/90_1/0_1]$		0.73	0.74	0.64		0.56					
$[0_1/90_1/0\ ]$		0.87	0.87	0.82	0.75						
$[0_1/90_1/0_1]$	0.60					0.22					
$[0_1/90_1/0_1]$		(2.49)	(1.16)	0.61	0.50	0.45					
$[0_1/90_1/0_1]$		0.85	0.84	0.69	0.66	0.57					
$[0_1/90_1/0_1]$		1.25	1.07	0.93	0.80	0.76					
$[0_1/90_1/0_1]$	0.70	(4.81)		(1.72)	0.71	0.56		0.48	0.41	0.39	
$[0_1/90_1/0_1]$		(2.60)	1.24	1.04	0.80	0.62		0.56	0.54		
$[0_1/90_1/0_1]$			1.37	1.10	0.92	0.65		0.72	0.72	0.69	0.67
$[0_1/90_1/0_2]$	0.84					0.19					
$[0_1/90_1/0_2]$			0.64		0.54	0.47	0.40				
$[0_1/90_1/0_2]$			0.76		0.57	0.63	0.57				
$[0_1/90_1/0_2]$			0.96		0.71	0.69	0.63				
$[0_1/90_1/0_3]$	0.75				0.65	0.47	0.43				
$[0_1/90_1/0_3]$				0.96	0.74	0.62	0.62				
$[0_1/90_1/0_3]$				1.04	0.82	0.79	0.72				
$[0_1/90_1/0_3]$	0.66				0.95	0.67	0.55				
$[0_1/90_1/0_3]$				1.62	1.01	0.79	0.72	0.55	0.51		
$[0_1/90_1/0_3]$				1.43	1.00	0.91	0.89	0.70	0.67	0.66	
$[0_4/90_4/0_4]$	0.70	0.89	0.63	0.61	0.60	0.50	0.46				
$[0_4/90_4/0_4]$	0.50				1.63	1.21	0.90	0.71	0.61	0.53	
$[0_4/90_4/0_4]$	0.70	0.97	0.85	0.83	0.79	0.78	0.77	0.76			
$[0_4/90_4/0_4]$	0.50			1.43	1.20	1.05	0.92	0.81	0.73	0.73	0.71

Material T300 / 914C   Outliers in brackets

Figure 11 plot — axes: Mean crack distance A [mm] vs No of load cycles log(N); labels: "Successive layer cracking", "Microdelamination growth", ○ 0.5 σ_u, ● 0.7 σ_u
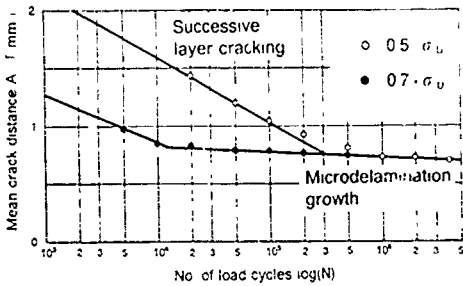
Figure 11 Crack distances in dependence of load cycles

Material   T300 / 914C
Stack   [0₄/90₄/0₄]
Stress ratio   0.1
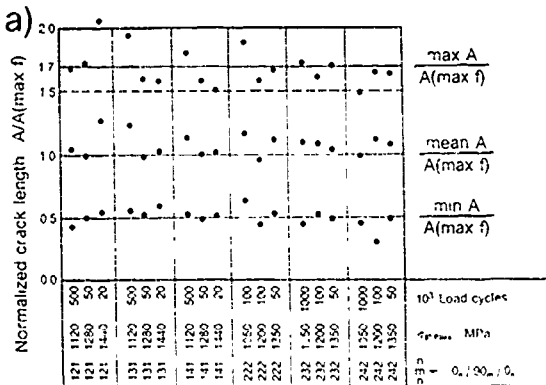
The measured mean crack distances, plotted for one configuration in Fig 11, decrease with the number of load cycles until a saturated state, the Characteristic Damage State (CDS), is achieved, [5] The CDS depends only on the thickness of the cracked layer but not on the load level This phenomenon is in contradiction to the elasticity theory and cannot be explained by material degradations solely. There are some indications, that the change of the slope might be accompanied by a change of the damage mode from successive layer cracking to microdelamination growth, [6] The transition point to the CDS is defined by a damage condition described in Chapter 5.

The relation of crack distances A_1 and A_2 between three successive cracks was studied Each couple of adjacent crack distances marks a point in a A_1-A_2-plane. The plane is subdivided into squares of 0.05 mm side length. Within each square the cluster of dots was counted and the cluster sum, plotted as a square column normal to the A_1-A_2-plane, forms a frequency surface The surface is smoothed and lines of equal frequencies were generated. Fig 12b With respect to the CDS, the frequency surface yields some remarkable results, Fig 12a.

- The mean crack distance marks the peak of the frequency surface.

$$A_{mean} \approx A(\max f) \tag{1}$$

- The extreme crack distances are limited by

$$0.5 \cdot A_{mean} \leq A \leq 1.5\ A_{mean} \tag{2}$$

- A Gauß-distribution can be used to describe the frequency of the crack distances at the CDS

In Tab 2 an approximation is given for the mean crack distances in crossply laminates. Except of some outliers, enclosed in brackets in Tab 1, the approximation is rather accurate (standard deviation 11%) For the CDS the formula yields the following mean crack distances for different stacking sequences (n ≤ 4):

Stack	A_{CDS} [mm]
$[0_n/90_1/0_n]$	0.24
$[0_n/90_2/0_n]$	0.38
$[0_n/90_3/0_n]$	0.53
$[0_n/90_4/0_n]$	0.67

a) plot — axis: Normalized crack length A/A(max f); reference lines: max A / A(max f), mean A / A(max f), min A / A(max f); x-axis 10³ Load cycles, σ_max MPa; Stack 0₁/90_m/0₁

b) Material T300 / 914C — plot with axes A_2 [mm] and A_1 [mm]; labels: max A, A(max f), min A, f/f_max = 5%, 100%

Figure 12 Characteristic crack lengths for the saturated state
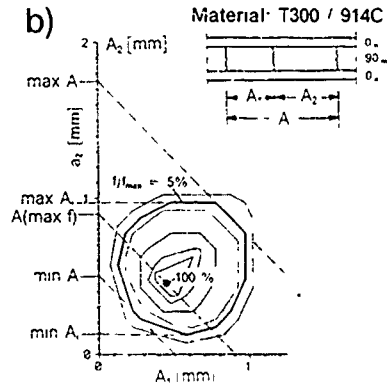
Table 2   Approximation for mean crack distances in crossply laminates

$$A_m = \frac{A_4^{CDS}}{D} + C_{1m} \cdot (m - 4) \qquad \text{for } 0 \leq D \leq 1$$

$$D = B_0 + B_1 \cdot \log (\varepsilon_\perp / \varepsilon_{\perp U}) + B_2 \cdot \log(N)$$

Standard deviation of the approximation error 11 %

A_4^{CDS} =	0 674 mm	B_0 =	-0 037
C_{1m} =	0 146 mm	B_1 =	1 637
$\varepsilon_{\perp U}$ =	1 2 %	B_2 =	0 225

A_m	Mean crack distance
m	No of 90°-layers (layer thickness 0 125 mm)
N	No of load cycles
$\varepsilon_\perp$	Mean strain in the 90°-layers
	(Design strain $\varepsilon_\perp \leq 0\,3\%$)

Material T300 / 914C

Fig. 13 depicts the mean crack distances in 90°-layers in dependence on the number of the load cycles and the mean strain $\varepsilon_\perp$ normal to the fibers The crack distances are plotted for four 90°-layers with a total thickness of 0 5 mm For each layer less the crack distances must be reduced by 0.146 mm.
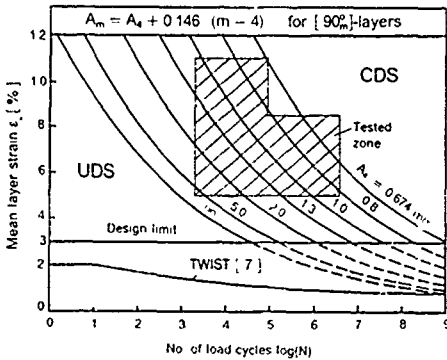
Figure 13   Mean crack distances in crossply laminates after T-fatigue loading

Stress ratio 0 1

The range of the undamaged state (UDS) is rather large For an aircraft component, designed for safe life, the design strain for static loading is often limited to $r \approx$ 0.3%. The actual service load is lower and is a function of the number of load cycles Relevant values for load sequences are plotted in Fig. 13, taken from the Transport Wing Standard (TWIST), [7] Both curves indicate, that for a design limit of about $r \leq 0.3$ % the structure remains undamaged during its service life, justifying the common practice in aircraft design to cover the strength degradation caused by dynamic service loadings by the choice of a conservative static design strain of $r \leq 0\,3\%$

Fig. 13 allows also an assessment of the effect, if the design strain for static loading increases If the strain limit is elevated to $\varepsilon = 0.5\%$ the first crack will be expected after 10^7 load cycles and after 10^9 load cycles a mean crack distance of ≈ 1.6 mm is achieved in a single 90°-layer approximately.

5. Residual stiffnesses of cracked UD-layers

In [8] a theory is developed for the analysis of residual stiffnesses of crossply laminates. Since the common laminate theory is not accurate enough to analyse local damage, the formulas given in [8] must be simplified in order to generate the constitutive equations for the tridimensional stress state of a multiple cracked UD-layer, see Appendix 11.8 in [2]

Displacement fields

$$u = u \, (x, z)$$
$$v = x \cdot \bar{\gamma}_{xy} + y \cdot \bar{\varepsilon}_y$$
$$w = x \cdot \bar{\gamma}_{xz} + y \cdot \gamma_{yz} + z \cdot \bar{\varepsilon}_z$$

Boundary conditions at the interfaces

$$u \, (z = h) = x \cdot \bar{\varepsilon}_x$$
$$v \, (z = h) = x \cdot \bar{\gamma}_{xy} + y \cdot \bar{\varepsilon}_y$$
$$w \, (z = h) = x \cdot \bar{\gamma}_{xz} + y \cdot \gamma_{yz} + h \cdot \bar{\varepsilon}_z$$

Approximation of shear strains

$$\tau_{xz} = a_1(x) + b_1(x) \cdot z$$
$$\tau_{yz} = a_2(x) + b_2(x) \cdot z$$
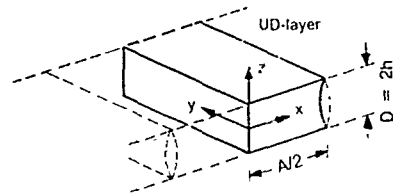
Figure 14   Presumptions for the analysis of cracked UD-layers

The UD-layer is constrained at the interfaces, which causes constant strains in the uncracked layer Fig 14 illustrates the presumptions of the analysis, where the prescribed constant strains at the interfaces are marked by overbars The final formulas for the constitutive equations of multiple cracked UD-layers are given by

$$
\begin{bmatrix} \sigma_x \\ \sigma_y \\ \sigma_z \\ \hline \tau_{yz} \\ \tau_{xz} \\ \tau_{xy} \end{bmatrix}
=
\left[C_{ij} + (\beta_k - 1) \frac{C_{ki} \cdot C_{kj}}{C_{kk}} \right]
\begin{bmatrix} \varepsilon_x - \alpha_x \cdot T \\ \varepsilon_y - \alpha_y \cdot T \\ \varepsilon_z - \alpha_z \cdot T \\ \hline \gamma_{yz} \\ \gamma_{xz} \\ \gamma_{xy} \end{bmatrix}
\tag{3}
$$

with the parameter for stiffness reduction

$$\beta_k - 1 = -\frac{\tanh(\gamma_k)}{\gamma_k}$$

$$\gamma_1 = \frac{A}{D} \cdot \frac{\sqrt{3 \cdot C_{55}}}{C_{11}}$$

$$\gamma_6 = \frac{A}{D} \cdot \frac{\sqrt{3 \cdot C_{44}}}{C_{66}} \qquad (4)$$

and where the indices

$$k = 1 \text{ and } i,j = 1,2,3,5$$
$$k = 6 \text{ and } i,j = 4,6$$

mark the inplane stress states for tension and shear load-ing, respectively Together with the formulas for the mean crack distances in Tab 2 the residual stiffnesses can be evaluated in dependence on the number of load cycles and the mean strain ε_1 of the layer

At the CDS the relative crack distance does not vary and the influence on the residual stiffnesses is even smaller The following values give an idea of the lowest possible residual stiffnesses normalized with the corresponding stiffnesses of the undamaged material

$$\frac{C_{ij}^{CDS}}{C_{ij}} = \begin{bmatrix} 0.33 & 0.33 & 0.33 & & & \\ 0.33 & 0.99 & 0.78 & & & \\ 0.33 & 0.78 & 0.93 & & & \\ & & & 1.0 & & \\ & & & & 1.0 & \\ & & & & & 0.59 \end{bmatrix} \qquad (5)$$

Even at the CDS the residual tensile stiffness perpendicular to the fibers is not close to zero as often assumed in numerical analyses

6. Generalized Crack Conditions

In MD-laminates layer cracking and delamination inter-feres and intensify each other. Despite of the synergism only delaminations were modelled accurately, whereas layer cracking is either neglected or considered by reduced stiffnesses only This process homogenize the material with the effect that layer cracking becomes insignificant for the delamination growth This is not true in reality and, therefore, some ideas will be discussed here to over-come this shortcoming

In order to describe the layer cracking a specific energy release rate $_t$ is defined by

$$g(A) = \frac{1}{A \cdot F_C} \cdot \int_{F_C} \frac{G(A)}{\frac{1}{2} \cdot \tilde{r}_i \cdot \tilde{H}^{ij} \cdot \tilde{r}_j} \cdot dF \qquad (6)$$

where G is the ERR at the tip of a growing layer crack and A, F_C are the crack spacing and the cross-section of the layer, respectively, Fig 15 The denominator of the integrand describes the specific energy referred to the normal of the crack surface
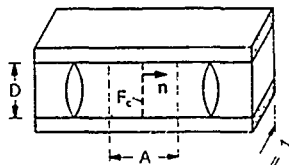
Figure 15   Notation for the specific ERR

$$\tilde{H}^{ij} = H^{ikjl} \cdot n_k \cdot n_l$$
$$\tilde{r}_i = r_{ik} \cdot n^k \qquad (7)$$

A tilde denotes the uncracked material and n_i are the components of the unit vector normal to the crack surface This definition is well known for the shear-lag model

In Fig. 16 the specific ERR is plotted versus the normalized crack spacing A / A_{CDS} For the saturated crack spacing at the CDS maximum values were achieved for the specific energy release rate independently of layer thickness and loading If this holds for different materials and mixed loading conditions max $g(A)$ can be used to define the crack spacing A_{CDS} independently of tests.
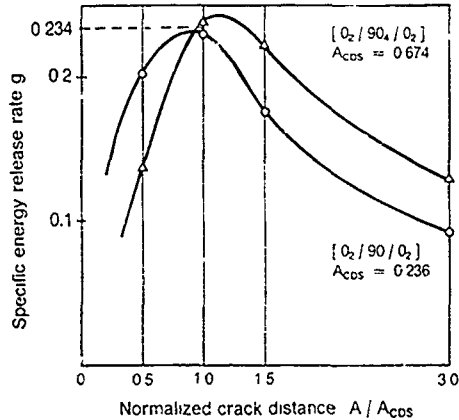
Figure 16   Specific ERR for embedded cracked UD-layers

In the next step the energy released at the delamination front will be observed more closely According to the fracture theory the ERR is defined by

$$G = \lim_{\Delta a \to 0} \frac{1}{2 \cdot \Delta a} \cdot \int_{\Delta a} \sigma^{ij} \cdot n_j \cdot \Delta u_i \cdot da \qquad (8)$$

where Δa and Δu_i are the fictitious crack extension and the corresponding crack opening displacements, respectively, and $\sigma^{ij} \cdot n_j$ are the tractions vanishing at the new crack surface. Numerically, the integration is difficult to conduct, because the stresses are singular at the crack tip Therefore, the crack closure method is used for finite ele-ment solutions, where the integral in Eq (8) is replaced by

$$G = \sum_{i=1}^{3} \frac{S_i \cdot \Delta U_i}{2 \cdot \Delta F_C} = G_1 + G_2 + G_3 \qquad (9)$$

S_i and U_i are the components for the forces and crack opening displacements at the element nodes, referred to the axes of the moving trihedral and ΔF_C is the area of the new crack surface generated by an elementwise crack extension In Eq. (9) each term of the sum describes the splitted ERR's G_i for the different crack modes These values are not invariant like G but depend on the chosen coordinate system Therefore, only mean values are used in damage conditions
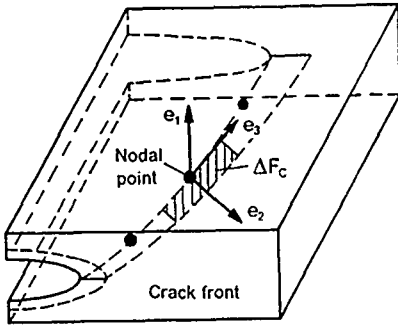
Figure 17   Moving trihedral at the crack front

$$D_1 (G , \text{extr } G_i : G_C , G_{iC}) \leq 1 \tag{10}$$

where the characteristic values G_c , G_{ic} depend on the material only. For homogeneous material the mean axes are spanned by the moving trihedral at the crack front, Fig. 17, and the evaluation of Eq. (9) is simple. Problems arise for composites, where the crack front is directed by the damage in adjacent layers, so that the moving trihedral declines from mean directions.

In order to generate the mean axes, nodal forces and -displacements are transformed to a rotated coordinate system. The basic vectors $\tilde{e}_i (\rho_k)$ depend on the rotational angles ρ_k, and the extrema of the ERR's

$$\frac{\partial \tilde{G}_i(\rho_k)}{\partial \rho_l} - 0 \tag{11}$$

define the mean directions. This scheme follows exactly the procedure for generating the mean stresses of a stress tensor, when the generalized ERR-tensor

$$G_{ik} = \lim_{\Delta f_c \to 0} \frac{S_i \cdot \Delta U_k + S_k \cdot \Delta U_i}{4 \cdot \Delta F_c} \tag{12}$$

is introduced with the invariants

$$I_1 = G_{ii}$$
$$I_2 = (- G_{ik} \cdot G_{ki} + G_{ii} \cdot G_{kk}) / 2 \tag{13}$$
$$I_3 = |G_{ij}|$$

Similar to the stress tensor a deviator may be defined by

$$G^D_{ij} = G_{ij} - \frac{1}{3} \cdot I_1 \cdot \delta_{ij} \tag{14}$$

with the invariants

$$I^D_1 = 0$$
$$I^D_2 = \frac{1}{2} \cdot G^D_{ij} \cdot G^D_{ji} \tag{15}$$
$$I^D_3 = \frac{1}{3} \cdot G^D_{ij} \cdot G^D_{jk} \cdot G^D_{ki}$$

Indices which appear twice in a product will be summed from 1 ... 3. The solution of the characteristic equation

$$\lambda^3 - I_1 \cdot \lambda^2 + I_2 \cdot \lambda - I_3 = 0 \tag{16}$$

defines the mean values λ_i for the splitted ERR s and

$$(G_{ij} - \lambda_k \cdot \delta_{ij}) \cdot \tilde{e}_{jk} = 0$$
$$|\tilde{e}_k| = 1 \tag{17}$$

the mean directions. The vector $\tilde{e}_1$ must coincide with the chosen direction of the crack extension. For a delamination in a layered composite the crack extends selfsimilar at the interface. Therefore, the axis $\tilde{e}_1 = e_1$ remains unchanged and the components $G_{1\alpha}$ ($\alpha = 1,2$) must be set to zero.

The ERR-tensor (12) is an extension to the common theory. The mean values λ_i coincide with the splitted ERR's G_i and the first invariant is identical to the total ERR G. However, Eq. (12) has the advantage, that two more invariants are available for generating more complex crack conditions

$$D_2 (I_1 , \lambda_i : I_{iC} , G_{iC}) \leq R \tag{18}$$

with the crack resistance

$$R = 1 \tag{19}$$

for homogeneous material. In Fig. 18 an example is given for a damage condition, which depends on the invariants I_1 and $\sqrt{I^D_2}$. I_{1C} is the minimum value for the critical ERR measured at notched UD-laminates stressed perpendicular to the fibers. The open holes refer to layer cracks in notched off-axes UD-laminates, [1] , and the dots mark
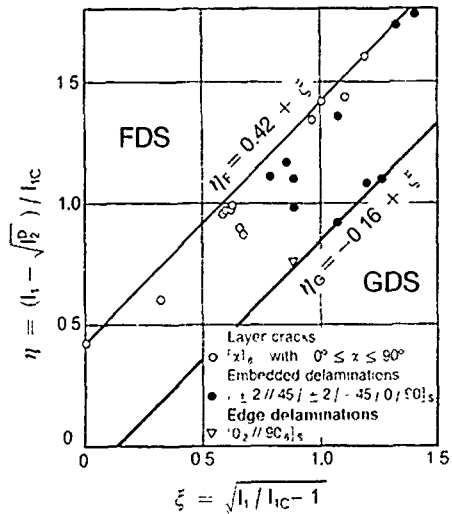
Figure 18   Interaction diagramme for matrix cracks

Material   T300/914C
Reference ERR I_{iC} 0.185 N/mm²

the values at the front of the embedded delamination described in Fig. 9. The value for the edge delamination is only a first rough estimation, because the subsequent change of the delamination front from one interface to the other was omitted, see Fig. 7.

The test results define a scatter band, which separates the frozen damage state FDS from the growing damage state GDS. The most accurate measurements and modeling were achieved for layer cracking in UD-layers. In Fig. 18 the generated values mark circles close to the η_f-line. They are accompanied by dots for the embedded delamination, where the crack front angle is close to +45° or -45°. Dots, which refer to more declined angles of the delamination front, are concentrated at the lower η_e-line. Apparently, the width of the scatter band is not a random variable,

but depends at least on the angles between the layer cracks and the delamination front and on the crack spacings.

In Eq (18) the left hand side depends solely on the material. Heterogeneous effects like layer cracking can be considered by a change of the resistance R. A first proposal migth be

$$R = 1 + \sum_{n-1,u} C_n \cdot \frac{A_{CDS}}{A_n} \cdot e^{-\left(\frac{\Delta\alpha_n}{\Delta\alpha}\right)^2} \quad (20)$$

C_i are constants determined by tests, the indices $n-1,u$ mark the lower and upper layer at the interface, respectively, and the angles are restricted to values between $\mp90°$. The parameters are depicted in Fig 19 In order to verify Eq (20) tests are necessary, in which not only the delamination front but also the crack spacing in the adjacent layers has to be measured
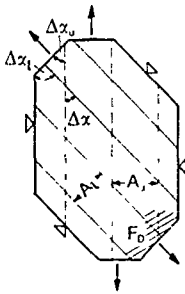
Figure 19   Notation for the crack resistance R

7. Conclusions

For multiple cracked UD-layers embedded in MD-laminates formulas for stiffness reduction were developed For service loading the reduction is rather small and influences barely the delamination process (in contradiction to interface damage, which inflicts the delamination growths significantly) Because of the still significant residual stiffnesses more complex damage patterns were prevented like jumps of the delamination to adjacent interfaces

In order to avoid delaminations spread over several interfaces, MD-laminates were stacked by QD-layers ([±2]-angleplies) solely These laminates are considerably more damage tolerant than those stacked by UD-layers only

The ERR is not a material constant and therefore insufficient to describe the crack growth In order to generate more complex crack conditions an ERR-tensor was introduced. The tensor defines not only the common ERR and its subdivision for different modes but also two more invariants describing ERR s of higher order A first proposal was made to take into account the texture at the surface of layers adjacent to the delamination

8. References

[1] H Eggers, L Kirschke, R Zick   Initiation and Propagation of Cracks in Notched UD-laminates of Carbon fiber Reinforced Epoxy under Static Tensile Load DLR-Report No DFVLR-FB86 30, 1986

[2] H W Bergmann et al   Fracture/Damage Mechanics of Composites Static and Fatigue Properties DLR-Report of the FSTFC-Contract No 8219/89/NL/PH(SC), 1991

[3] K Schulte, Ch Baron   Load and Failure Analyses of CFRP laminates by Means of Electrical Resistivity Measurements Comp Science and Technology 36(1989), 63-76

[4] R S. Atze, H C Goetting   Einfluß der Randdelaminationsbehinderung in multidirektionalen CFK-Laminaten unter Zugschwellbelastung ZFW 10 (1986) 267-272

[5] K L Reifsnider, A Talug   Analysis of Fatigue Damage in Composite Laminates Int J Fatigue, Jan 1980, 3-11

[6] H Eggers, H C Goetting   Damage Mechanisms and Constitutive Relations for Cracked UD-Layers in Crossply Laminates Proc Internat Conf Spacecraft Structures and Mechanical Testing, Noordwijk, The Netherlands, 24-26 April 1991 (ESA SP-321, October 1991)

[7] D Schutz, H Lowak, J B de Jonge, J Schijve   Standardisierter Einzelflugbelastungsablauf fur Schwingfestigkeitsversuche an Tragflachenbauteilen von Transportflugzeugen LBF-Report No FB-106 (1973)

[8] R J Nuismer, S C Tan   Constitutive Relations of a Cracked Composite Lamina J Comp Mat 22 (1988), 306-321

[9] H W Bergmann et al   Mechanical Properties and Damage Mechanisms of Carbonfiber-Reinforced Composites Compression Loading DFVLR-FB 88-41, 1988

DELAMINATION DEVELOPMENT UNDER FATIGUE LOADING

by

R.M. Aoki and J. Heyduck
German Aerospace Research Establishment—DLR
Institute for Structures and Design
Pfaffenwaldring 38-40
7000 Stuttgart 80
Germany

1 SUMMARY

Examples of delamination development in CFRP impact damaged specimens and structural parts under tensile and compressive fatigue loading investigated with help of the ultrasonic in-situ (USIS) method are presented The evaluation of the US-rear echo shows the manifold ways of delamination development depending on materials used, configuration of specimens, as well as loading conditions

2 INTRODUCTION

The investigation of the capability of composites to tolerate reasonable level of damage or defects that may be encountered during manufacture or in service is a very important topic that can influence the criteria for predicting the performance of a composite structural part. Even with impacts that show little indication of damage at the surface, the matrix and fibre damage in the interior of the laminate can be significant Delamination, matrix cracking and fiber breakage are three damage modes that may be present in composite structures Delamination is of primary concern, because it may reduce significantly the strength and stiffness of the material and consequently reduce the load-bearing capability of the structure

Thus, in the investigation of delamination development in composites under fatigue loading it is very important to try, on one side to localize the nuclei of the damage and on the other side to identify the nature of the occurring failure

The best way to monitore the damage development is with NDI-methods like ultrasonic (US) and X-ray

In this paper some phenomenological aspects of delamination are presented. The aim of the ongoing research is to correlate experimentally the US inspection with damage development and degree of degradation in CFRP flat specimens and small stringer stiffened structures.

3 EXPERIMENTAL PROCEDURE

The materials used in this investigation were HTA7 and HM45 carbon fibres in a Narmco 5245 resin for the flat specimens The laminate lay-up consisted of 47% 0° layers, 47% ±45° layers and 6% 90° layers, with a total of 17 layers The hybrid laminates had the ±45° layers from HM45 material For comparison purposes laminates with only HTA7 and only HM45 fibers having the same lay-up were fabricated by Dornier and also tested

Specimens of dimensions 170 mm by 50 mm were cut from the 2mm panels after impact damage and were fitted with GFRP tabs. The barely visible impact damage (BVID) was introduced in a drop weight test facility with the following parameters hemispherical steel impactor with a diameter of 10 mm, a mass of 300 g and a drop height of 1m The plates were clamped between two steel plates with a hole of 20 mm diameter

The materials used for the blade stiffened panels were T300 / Code 69 unidirectional tape prepreg, and A002 / Code 69, fabric prepreg, both graphite epoxy 180 °C cure systems The panels were cured after the one-shot method developed in our Institute [1] The specimens 120 mm by 85 mm, 2mm thick with 20 mm blade stiffeners, 44 mm apart, were cut from big panels using a diamond saw and the loading surfaces were ground flat and parallel to assure an uniform axial compressive load introduction. The configuration of the tested specimens are shown in Fig 1

3.1 Mechanical Tests

The fatigue tests were performed on a Schenk servo-controlled hydraulic test machine, load-controlled with sinusoidal axial loading at a frequency of 5 Hz The load level was chosen in such a way that an evident damage propagation was noticeable with the help of US-scanning

The blade stiffened panels tested under compression fatigue (R=10) were simply supported at the loaded ends, and the lateral edges were unsupported.

An extensometer from Schenk with a gage length of 10mm was used to measure the strain at the specimens All tests were done at room temperature and humidity.

3.2 Damage Monitoring Techniques

During fatigue loading the ultrasonic-in situ (USIS) method developed in our institute [2] was used to evaluate the degree of damage progression USIS allows the US inspection of specimens without removing them from the loading frame avoiding, firstly, the problem encountered with small

misalignments of the specimens which can cause a change in the direction of damage progression by clamping the specimen again after each US-inspection, and secondly the immersion in a water tank, a procedure which can lead to misinterpretation of US measurements [3] The ultrasonic equipment used was a Krautkrämer KB6000, a selfmade scanning mechanism and an IBM PC for data management The results of the US pulse echo measurement are the standard C-scan and the H-scan H-scan, which shows the isohypsi, lines connecting areas of equal rear-wall echo (RE) amplitude, offers the possibility to quantify the damage development in the specimen

To monitor the damage development penetrant- enhanced X-ray radiography (Seifert-Isovolt 60) was also used

4 TEST RESULTS AND DISCUSSION

4.1 Damage Development Under Fatigue Loading

Fig 2 shows USIS H-scan pictures of a HTA7 specimen after different number of tensile fatigue cycles The grey scale shows the degree of degradation of the laminate, i e white color no degradation, black color delamination

The quantification of the damage development in the specimens is possible by means of calculating the US-RE-mean value U_i for a specimen section related to the mean value U_1 of the virgin specimen, or the RE-mean value of the scanned section at the beginning of the test

The behaviour of U_i / U_1 for the 3 sections, see Fig 1, under fatigue loading can be seen in Fig 3 Comparing the damage progression in the first 2000 cycles we see that in section I it is larger than in section II, where the BVID damage was introduced The degradation of the laminate in section III started at a manufacturing defect, near the load introduction region, in direction to the free edge and impact delamination After 25900 cycles the delamination of the impact damage (section II) propagated to the one free edge and begun to grow in direction of the other free edge mainly in the 90°-layer The degradation in sections I and III have reached almost the same level, being the growth steeper in section III

For comparison purpose the change of slope of the load-strain curve E_i measured with the extensometer in section II related to the initial EI is also shown

Same investigations made with the HM laminates show a different delamination propagation Here is primarily the 0° layer delamination which grows in the first 21000 fatigue cycles, see Fig 4, combined with the beginning of delamination near the load introduction regions After 30000 cycles sections I and III of the specimen are almost completely delaminated The behaviour of U_i / U_1 can be seen in Fig 5 The BVID damaged region, i e section II shows less degradation than sections I and III

The behaviour of the load-strain curve E_i / E_1 measured again in section II is similar to the case of the HT- laminate, a gradual degradation

Fig 6 shows that the behaviour of the hybrid laminate is different to the preceding laminates Here, it can be clearly seen that the beginning of the primarily delamination initiates in the ±45° layers The U_i / U_1 development over fatigue cycles reveals again a steeper degradation of the laminate in the sections I and III, as shown in Fig 7

Subsequent local US in-situ investigations with the US-probe placed near the impact damage during fatigue loading of the specimens confirm the damage development observed previously Fig 8 depicts the curves obtained after the least square method of the US-RE-amplitude measurements done continuously over a period of 10000 cycles HT specimens show the least decrease of the RE-amplitude, meaning less deterioration than in case of HM and hybrid laminates

Confirmation of the observed US-behaviour of the different laminates demonstrates the X-ray picture of the penetrant enhaced specimens in Fig 9 HT laminates don't show any big change after a tensile fatigue loading of 10000 cycles In HM laminates a partial delamination of the outer 0° layers and the beginning of the edge delamination is visible The hybrid specimen exhibits clearly the edge delaminations and an enlargement of the delamination in the 0° layer near the impact region

The damage development in small blade stiffened panels made out of UD layers after different number of compressive fatigue loading cycles is shown in the H-scan picture in Fig 10 a. The change of U_i / U_1 over the number of cycles, again for the different sections, is shown in Fig 10 b Section II shows the steepest decrease in U_i / U_1 against the moderate decrease in sections I and III There is almost no slope change in the load-strain curve E measured at location RM of the panels

Fig. 11 a shows the H-scan pictures of the panel made out of fabric layers after different number of compressive load cycles The investigated fabric panel shows a difference in U_i / U_1 in sections I and III at the beginning of the tests, see Fig 11 b This difference can be attributed to small irregularities in the conjunction between stiffener and panel Section I degradates more than section III due to a premature buckling of the stiffeners The highest degradation and delamination development occurs in section II

The slope change in the load-strain curve measured in the location RM depicts a noticiable change between the last two measurements This can be attributed to stability effects which are influenced by the delamination propagation

5 CONCLUSIONS

The delamination development in HT, HM and hybrid laminates with BVID impact damage under tensile fatigue loading depends on the used fibres In all specimens a gradual degradation of the laminates before delamination enlargement was observed The evaluation of different sections of the specimens show that not only the impact damage but also fabrication defects as well as the load introduction regions play an important role in the delamination development in laminates

Small structural blade stiffened panels under compression fatigue loading show different behaviour depending on the material used A pronounced degradation of the laminate was concentrated in the impact damaged section of the panels

There is an essential difference in degradation development in laminates upon their loading condition. Under tensile fatigue loading the laminates degrade gradually over the whole specimen Under compression fatigue loading the degradation of the specimens is more pronounced in specific regions, e g

impacted damaged area, and they can influence the stability behaviour of the structure.

The quantification of US-RE opens a possibility for the prediction of degradation in composite laminates

6 REFERENCES

1 D. Wurzel, S. Dehm, in Proc. ICAS 86-4.6 2 (1986), London

2 R. M Aoki and J Heyduck, Developments in the Science and Technology of Composite Materials, ECCM 3, Elsevier Appl. Sci.: London, New York, 1989, pp 521 - 528.

3. G P. Sendeckyj, in AGARD-CP-35, 1983, 2
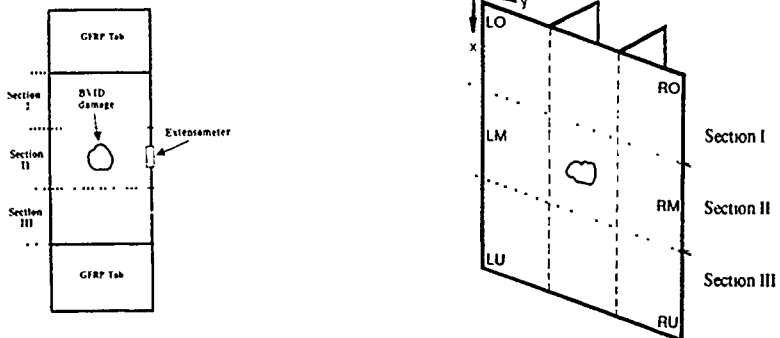
Fig 1   Specimen configuration
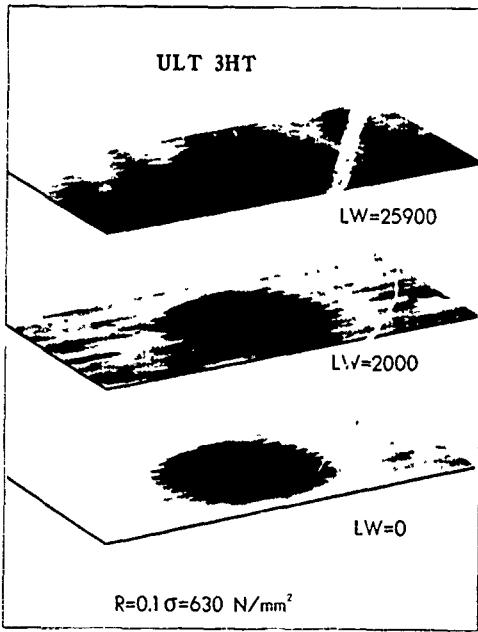
Fig 2   US-H-scan pictures of a HT specimen after different
number of load cycles Legend US-RE amplitude in %

Fig 3   Ui / U1 behaviour at different sections of a HT
specimen over tensile fatigue loading cycles
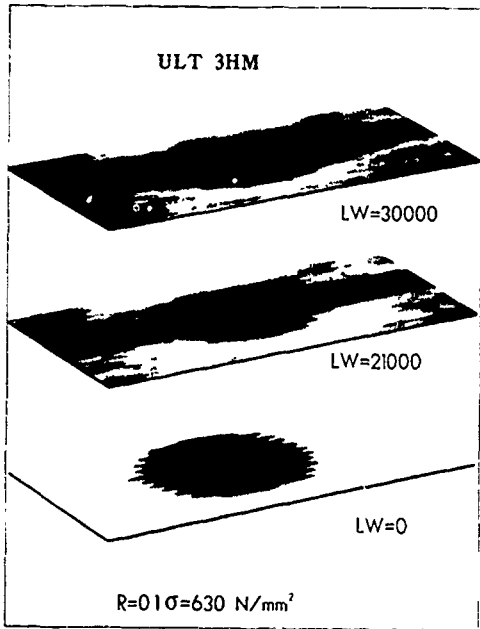
Fig 4   US-H-scan pictures of a HM specimen after tensile
fatigue loading (R = 0 1)
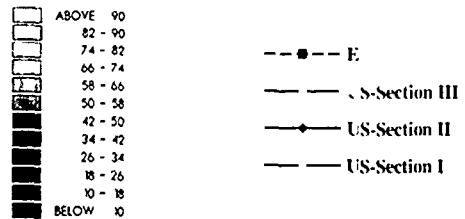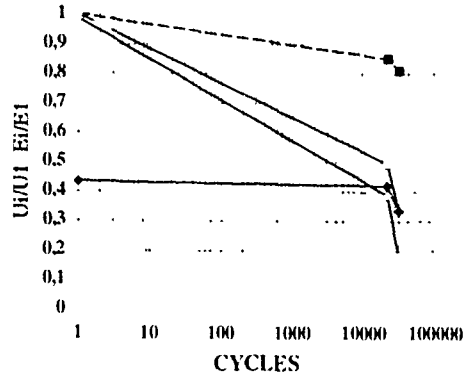
Fig 5   Development of U i / U1 in different sections of a HM
specimen Changes of the load-strain slope measured at
the right edge of the specimen
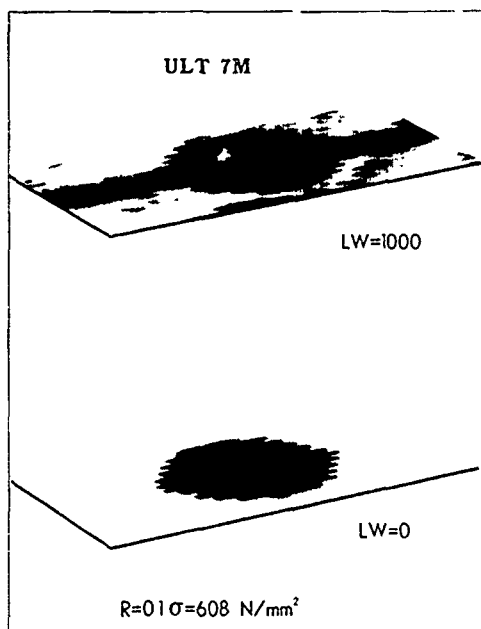
Fig 6 US-H- scan pictures of a hybrid specimen after tensile fatigue loading The beginning of the 45° layer degradation is visible
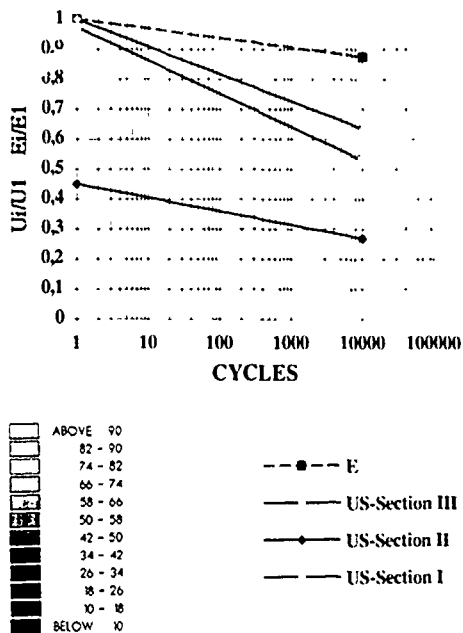
Fig 7 Quantification of the H-scans U_i / U_1 after different number of load cycles (R = 0 1)
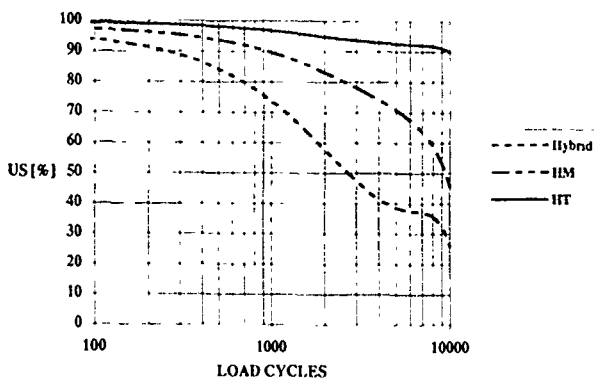
Fig. 8 Development of US-RE amplitude over fatigue loading cycles (R =0 1) near the impact damaged area

Fig 9   Penetrant enhanced (ZnI$_2$) X-ray pictures of impact
damaged specimens after 10000 load cycles (from left
H1, HM and hybrid)
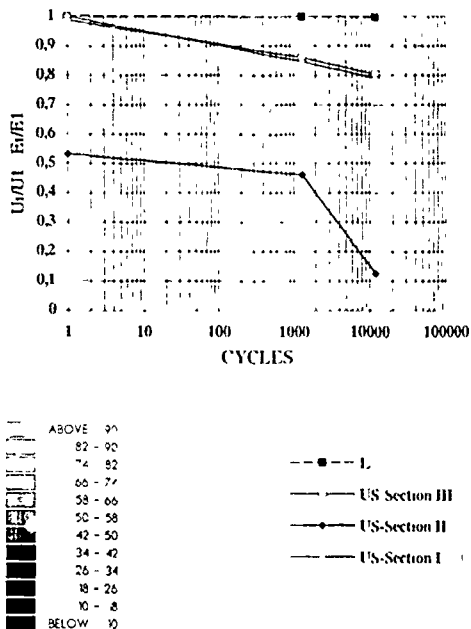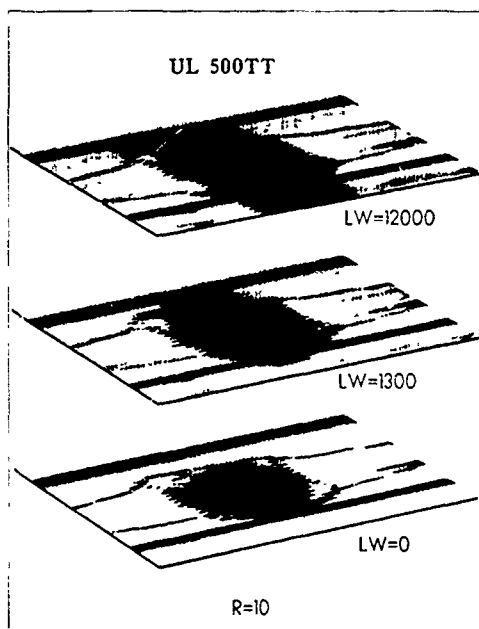
Fig 10 a) US-H-scan pictures after different fatigue load cycles
of an impact damaged blade stiffened panel made of
UD plies (0 / ±45 / 90)s
b) Ui /Ul development in the different sections of the
specimen and Ei / El behaviour at location RM
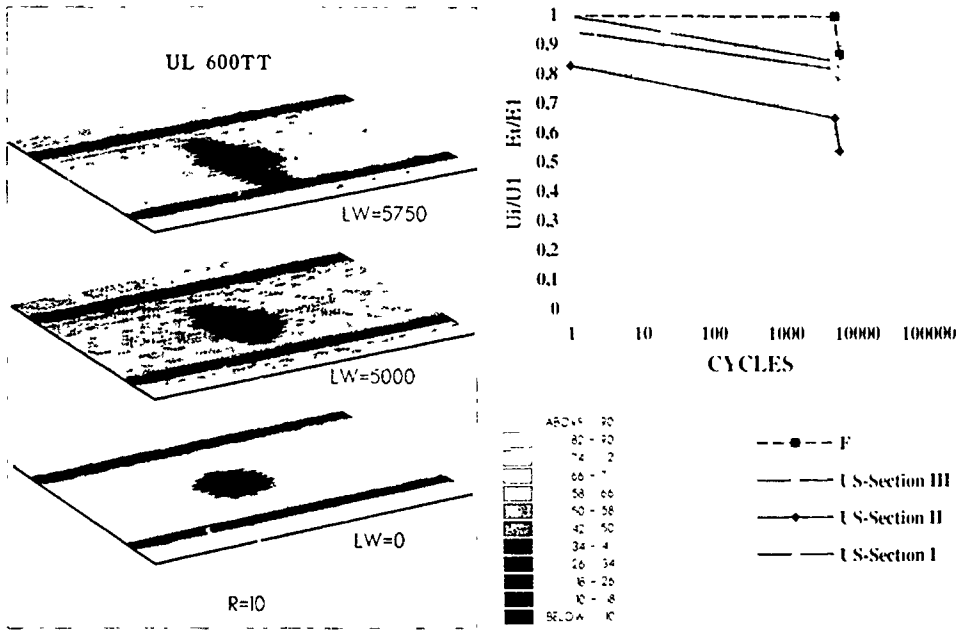
Fig 11 a) US-H-scan pictures after different fatigue load cycles
of an impact damaged blade stiffened panel made out of
fabric layers
b) Ui /Ui development in the different sections of the
specimen and Ei / E1 behaviour at location RM

Numerical finite element analysis of damage using Monte Carlo techniques

G. Van Vinckenroy, W.P. De Wilde
Analyse van Strukturen - Vrije Universiteit Brussel.
Pleinlaan, 2
1050 Brussel, Belgium

1. ABSTRACT

A method, based on the finite element technique, is proposed in order to study the behaviour of an adhesive single lap joint, together with stochastic material properties, taking into account the uncertainties of design parameters. The technique is applicable to linear and non linear problems, with more or less complicated structures. The needs are experimental determination of the components properties and numerical tools.

2. INTRODUCTION

When modeling structures in which the variability could be rather large, it is usually advantageous to use probabilistic models rather than deterministic models. An ideal random process model will capture the essential features of a complex random phenomenon with a minimum of parameters, which have to be experimentally accessible and physically meaningful. Whether or not formal treatment of uncertainty is warranted depends, among others things, on the quality and quantity of information data, the importance of the problem and the resources at hand.

The problems involving structural analysis under non deterministic loads and uncertain material properties are nowadays solved using safety coefficients. Recently developed methods, such as risk analysis and stochastic finite element methods (SFEM) can be used to estimate uncertainties of design parameters. In the SFEM, each material parameter is characterized by a statistical distribution, whereas in classical FEM, the approach is deterministic : a unique, defined value is used as design parameter. Coupled to Monte-Carlo simulation, SFEM allows to study the statistical distribution of the state variable under investigation.

3. EXPERIMENTAL TESTS

As explained before, the technique applied here relies on experimental determination of components of the structure. the necessary parameters for the finite element model are determined by extensive experimental testing.

Experimental tests are performed on the materials involved in the structure of the adhesively bonded joint. In this case, the adherend is aluminium, and the adhesive is a modified epoxy adhesive film. The tests are performed following the ASTM standards and yield the data needed as input for the finite element model, that is, the elastic and ultimate properties of materials.

Aluminium specimens are manufacturated following the B 557 M ASTM standard for rectangular tension test specimens. Adhesive is tested in accordance to the ASTM D 638 M. The tensile stress/strain curve is recorded on an Instron bench coupled to a data acquisition system, and the Young's modulus, Poisson's ratio and strength are determined for each specimen. The tests are performed for different specimens.

When performing experimental tests, there are different sources of uncertainties on results values. They can be classified in uncertainties due to measurement errors, and uncertainties due to the inherent variability of the material properties. The latter can not be reduced, but the former have to be reduced by performing more experiments and by improvement of the selected experimental techniques.

The first aspect in the development of statistical analysis is to choose a probability distribution to represent the parameters of the physical system, that fits the sample data and that could be used in prediction and design. The choice is often difficult, depending on operator judgment and prior experience. So, how to choose a model ? [1]

There are two possible ways:

- by understanding the nature of the underlying phenomenon under investigation and using then a statistical model that follows the same principles, verifying it with the available data.

- by selecting a model from a empirical distribution. sometimes, due to the complexity of the system or lack of understanding, a statistical model is selected for its ability to fit the given set of data rather then from its relationship to the phenomenon under study. Those models give no insight into the mechanism behind the data, they simply serve as a means to summarize the data.

In a first instance - and especially for problems stemming from the second type of approach - classical statistical distributions are used to fit the data: Normal, Log-Normal, Weibull and Extreme-values distributions. Once the model has been chosen, its parameters have to be estimated from the data. The data are considered as a random sample from an infinite population described by the probability distribution we selected. Because of the randomness of the data, the estimate of the parameters are random as well. General methods of parameter estimation do exist, the most common ones being the

following. the maximum likelihood method, the method of moments and probability plotting. Finally, a statistical test should be performed to determine whether the chosen distribution provides an adequate fit to the data. Among the available methods, the correlation coefficient and the Kolmogorov-Smirnov test are used.

The results obtained by the probability plotting method are summarized in the tables 1 and 2 for respectively the aluminium and the adhesive.

For the aluminium, the Weibull distribution is the one between the choosen distributions, that best fits the data for strength and Young's modulus, whereas the Poisson's ratio follows a Log-normal or a Normal distribution.

For the adhesive, the Log-normal distribution is the one between the choosen distributions, that best fits the data for strength, Young's modulus, and Poisson's ratio.

Some experiments are performed on bonded structures, in order to obtain experimental values to be compared with the numerical results and to check the validity of the procedure.

4. MACROSCOPICAL MODEL

The structure is modeled by means of the finite element method, to determine a approximation of the state variables of interest, usually stresses and strains. In a first instance, the model tests are performed with deterministic parameter values, to check the validity of the approximation geometry and boundary conditions as close as possible to the reality, element mesh fine enough to ensure acceptable accuracy

The second step consists in introducing stochastic parameters values. If the structure is complex, it is possible to apply the "zooming" technique to study only the most critical part of the structure before applying the stochastic treatment, in order to reduce computing time.

As a simple example, a three point bending test is studied. stochastic parameters are directly introduced in the full model. For the single lap, the "zooming" technique is applied, as the joint is submitted to a complex stress state, and this refined model will be referred to as the microscopical model.

For the three-point bending beam, we assume plane strain conditions, quadratic elements, the material used is aluminium. Material properties are considered deterministic in a first stage, stochastic treatment is applied in a second instance, on the same model geometry. The state variable is the displacement of the mid point on the lower surface of the beam.

A finite element model of the adhesive single lap joint is built up. We assume deterministic value for the material properties, that is, the mean values of the experimental results are used as model input, for the adherend as well as for the adhesive

The geometry of the model is based on real values obtained from test specimens. A two-dimensional model with plane strain conditions is assumed, elements are linear or quadratic, the applied boundary conditions are choosen to represent the real test conditions as close as possible (see Figure 1.). The materials are supposed to behave linearly or non linearly, depending on the complexity of the model.

5. MICROSCOPICAL MODEL

A finite element model of a restricted zone of the single lap is developed. we are interested in the interface region, so that the model zooms on adherend, adhesive and interface (see Figure 2.). The aim is to reduce computing time, and to construct a representative volume element of the interfacial region. Different stages are developed:

- zoom on the entire width of the bonded region;

- zoom on a local region at the end of the bonded surface, where the stresses are of paramount influence on the joint behaviour.

From the stress and strain patterns in the macroscopical model, the boundary conditions on the microscopical model can be determined by imposing forces (Neumann cond.tions) or displacements (Dirichlet conditions).

Neumann conditions.

In this approach, the forces to be applied at the boundary nodes of the microscopical model are calculated by the classical formula of finite element method [2].

$$[F]_e = \int_{ve} [B]_e^T [C] [\varepsilon^0]_e \, dV - \int_{ve} [B]_e^T [\sigma^0]^e \, dV + \int_{ve} [N]_e^T [f]_e \, dV + \int_{Se} [N]_e^T [p]_e \, dS$$

with initial strain $[\varepsilon^0]$ and initial stress $[\sigma^0]$, volume forces $[f]$ and surface forces $[p]$ applied to element e, $[N]_e$ is the interpolation function matrix (shape functions) for the displacement in element e ($[u]_e$) in function of nodal displacement ($[q]_e$).

In the case we are interested in, $[p]_e$ is the force vector applied by neighbouring elements on the boundaries of the microscopical model element. It is possible to determine those forces knowing the shape functions and the interpolation functions for the element, the constitutive stress/strain relationships and the nodal displacements. The integral to be evaluated can be expressed in the natural coordinates, and numerically calculated using Gauss-Legendre quadrature.

To reduce computing time required for evaluating this integral to determine the boundary conditions on the stresses, it is also possible to apply Dirichlet boundary conditions, that is by imposing the displacements

Dirichlet conditions.

In this case, we just take over the displacements at the nodes, determined by the macroscopical model. When refining the mesh, additional nodes appear on the boundary, whose displacements have to be calculated by interpolation from the original nodes. In this case, only the interpolation functions of the element have to be known, and the only mathematical operation to be performed is an evaluation of polynoms at given points.

6. PROBABILISTIC ASPECTS

When the finite element deterministic model has been set up, the stochastical aspects of materials properties are introduced in the model It can be performed on the macroscopical model or the microscopical model if the zooming technique is applied.

The properties are supposed to follow a given statistical distribution, and not to have a defined value. Given the distribution functions for the material properties, that is, their type and values of parameters, a random generator program using inversion or transformation technique is used to generate deviates from those distributions.The random values of the stochastic properties are then assigned to the elements of the microscopical model. With the FEM, state variables are calculated for this configuration of material properties.

The Monte Carlo simulation consists now in assigning other random values to each element, determine the state variable and repeat the procedure in order to obtain sufficient data to build up the statistical distribution of the state variable [3].

The procedure is illustrated by the flow chart in Figure 3.

In the example of the three-point bending test, the results are the following (as the results are obtained through calculation one takes more significant digits into consideration than would be the case with e.g. experimental results):

Deterministic case:

E-mod 72.087 GPa
Poisson's ratio 0.3282

Displacement of the mid-point. 4.1240 E-4 mm

Probabilistic case:

E-mod Weibull distribution with average 72 087 GPa and parameters $\eta = 58\ 8986$ and $\mu = 72.7797$

Poisson's ratio Normal distribution with average 0 3282 and parameters $\mu = 0\ 3282$ and $\sigma = 0\ 0032$

Displacement Normal distribut ... with average 4.1271E-4 mm (100 simulations) and parameters $\mu = 4.1271E-4$ and $\sigma = 0.0311E-4$

For the single-lap, we are interested in the stresses distribution on the corner of the joint.

7. INTERPHASE EFFECTS

The difference between the numerical and experimental results for the single lap strength can be attributed to interphase effects. It is well known that the contact in a joint does not arise through a straight interface, instead, the surface treatment, needed for bonding structures, affects the properties of the material at the surface. A surface layer appears, which has a different composition and morphology than the bulk material. The bonding process itself creates an intermediate layer between adherend and adhesive, with other properties than the bulk material properties. As this layer has a non zero thickness, it will be referred to as the interphase. The bonding phenomenon arises from mechanical and chemical effects on this layer.

The practical consequence is that the interphase can not be simply described, depending on the materials under investigation, the surface treatment applied, the conditions for the bonding process,.... It is quite difficult, even impossible to characterize the interphase layer in a bonded structure (mechanical properties, thickness, morphology,...) as it is in general experimentally unaccessible, and hypothesis have to be made to modelize it. Numerical simulation taking the presence of the interphase into account can only rely on information obtained on free treated surfaces.

In a first instance, the interphase is introduced into the microscopical model as a layer of uniform thickness, whose value is approximated by experimental measurements on oxydes layers of aluminium. Typically, the thickness of such oxydes layers is of the order of 0.5 mm to 5 mm, depending on the surface treatment. As the mechanical properties cannot be measured directly, they are assumed, in a first instance, to vary linearly on the thickness of the interphase between the properties of the two bonded materials. Again, deterministic and probabilistic finite element technique are used to study the state variable of the microscopical model.

8. CONCLUSIONS AND FURTHER DEVELOPMENTS

It has been shown that material properties can be modeled with statistical distributions as Weibull, Normal or Log-normal distributions. Those experimentally validated statistical distributions are used by means of a random number generator acting on them, as input for finite element models By repeating the calculation process, this procedure allows the determination of the statistical distribution of the state variable in a more or less complex problem. As an application, this procedure allows us to study the influence of the interphase on stresses in bonded joints In this case, simulation is necessary to compensate the lack of information of available data

The technique and results obtained in this first stage will be used for monitoring the progression of damage, based on the probability of failure calculated according to the found stress field in the single lap joint. Interphase influence will be investigated more deeply, according to the assumptions that could be made on the behaviour of the interphase, and related to joint strength. In further developments, Bayesian techniques will be applied to quantify the uncertainties due to model parameters and the model error, due to the choice of the model itself.

9. ACKNOWLEDGEMENTS

11. FIGURES AND TABLES

10. REFERENCES

[1]   M.G. KENDALL AND A. STUART
The advanced theory of statistics
vol 1, Hafner Publishing Company, New York
- 1958

[2]   J.F. IMBERT
Analyse des structures par éléments finis
Cepadues Editions - 1979

[3]   HAMMERSLEY J.M., HANDSCOMB D.C.
Monte Carlo methods
Methuen & co Ltd - 1964

[4]   KLEIJNEN J.P.C.
Statistical techniques in simulation (Statistics
Textbooks and Monographs,v 9 - parts I and II)
Marcel Dekker,Inc - 1974,1975
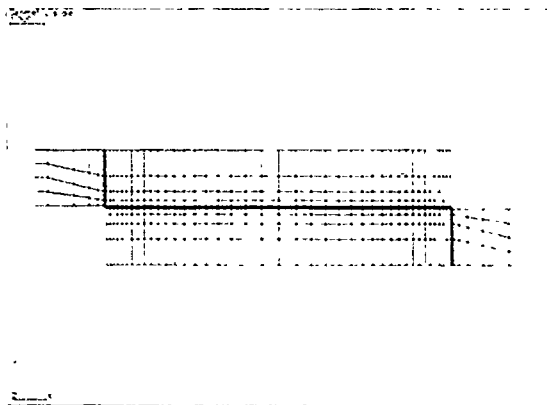
Figure 1. Macroscopical model of the single lap joint

Figure 2 Microscopical model of the single lap joint
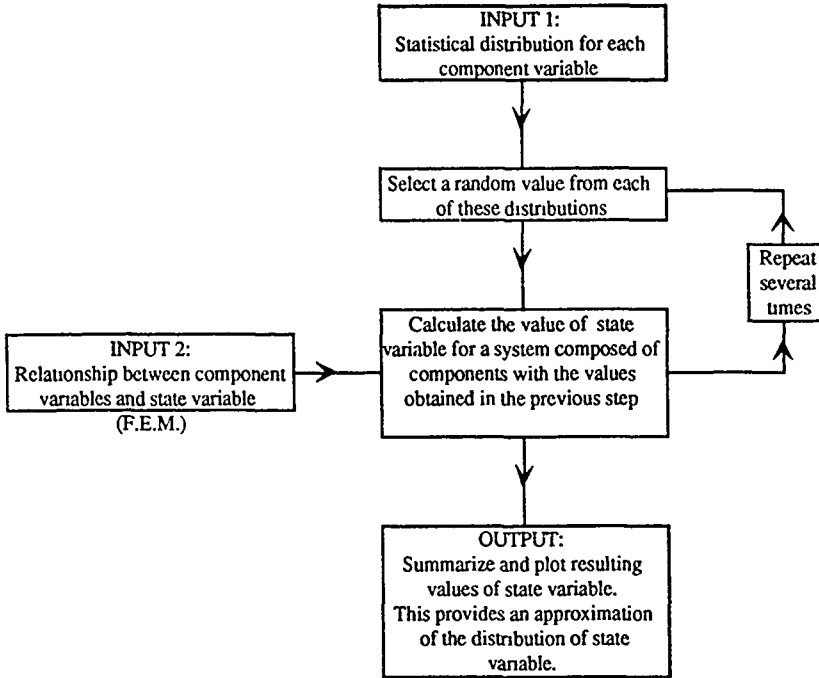
Figure 3. Flow chart of the applied procedure

TABLE 1
Statistical treatment for Aluminium data.

Property: Distribution:	strength	Young's modulus	Poisson's ratio
Normal μ σ	(corr. = 0.978) 481.9202 1.2329	(corr. = 0.900) 72.1426 1 5564	(corr. = 0.891) 0.3282 0.0032
Log-normal μ σ	(corr. = 0.978) 6.1778 0.0026	(corr. = 0.920) 4.2765 0 0204	(corr. = 0.893) -1.1143 0.0097
2-p. Weibull η σ	(corr. = 0.983) 481.6 482. 4	(corr. = 0.962) 58.8986 72.7797	(corr. = 0.783) 119.7088 0.3296
Extreme-value(sm.) η μ	(corr. = 0.983) 1.0003 482.4371	(corr. = 0.942) 1.2160 72.7829	(corr. = 0.780) 0.0028 0.3296

TABLE 2
Statistical treatment for Adhesive data.

Property: Distribution:	strength	Young's modulus	Poisson's ratio
Normal μ σ	(corr. = 0.965) 48 0022 0.5755	(corr. = 0.983) 2.5083 0.1352	(corr. = 0.889) 0 3905 0.0125
Log-normal μ σ	(corr. = 0.966) 3.8712 0.0120	(corr. = 0.985) 0.9187 0.0537	(corr. = 0.893) -0.9405 0.0319
2-p. Weibull η σ	(corr. = 0.905) 99.0449 48.2470	(corr. = 0.950) 22.3893 2 5636	(corr. = 0.839) 41.7007 0.3934
Extreme-value(sm.) η μ	(corr. = 0.903) 0.4863 48.2493	(corr. = 0.942) 0.1129 2 5657	(corr. = 0.834) 0.0094 0.3935

MODE II DAMAGE DEVELOPMENT IN CARBON FIBRE REINFORCED PLASTICS

by

M.J. Hiley and P.T. Curtis
DRA, RAE Farnborough
Hants GU14 6TD
United Kingdom

SUMMARY

A study of the mode II interlaminar fracture toughness of unidirectional carbon fibre reinforced plastics has been made using the End Notched Flexure (ENF) test A range of fibre reinforced thermosetting prepreg systems including a bismaleimide and four epoxy materials have been investigated, plus the thermoplastic PEEK A comparison between the materials showed the thermoplastic to be significantly tougher than any of the thermosetting systems. The two phase epoxy system 914 and the BMI V390 had the lowest toughness, with values of only 20% of those of the APC2 PEEK. The potential link between mode II fracture toughness and delamination growth and impact damage tolerance has been assessed

Measurements of delamination growth in mode II fatigue, for three of the materials, have also been made Potential links with the materials susceptibility to the growth of delaminations and more generally impact damage during fatigue loading have also been considered.

INTRODUCTION

The formation of delaminations within Carbon Fibre Reinforced Plastics (CFRP), particularly those induced by impacts, have imposed a limitation on the application of laminated CFRP structures Delaminations substantially reduce the bending stiffness of laminates with the result that buckling, under compressive loading, may occur at strains well below that of an equivalent undamaged laminate A need to have to take into account such defects has resulted in a conservative approach to design, with the effect that the potential weight savings offered by these materials have not yet been fully realised.

First generation CFRP systems were manufactured primarily with the aim of achieving high stiffness using epoxy resins with high cross link densities. However, these resins were quite brittle in nature and offered little resistance to delamination Tougher thermosets and thermoplastics such as PEEK have since superseded these early materials, and with their development there has been a need for a better understanding of delamination growth phenomena

In an attempt to assess the initiation and propagation behaviour of delaminations, a variety of testing techniques have evolved. Most have been concerned with the determination of quantitative fracture parameters such as fracture toughness and critical strain energy release rate G_c Commonly, in composite structures, delaminations are subjected to mixed mode loading, incorporating combinations of mode I (opening or peel) and mode II (sliding or forward shear). Test methods to evaluate toughness have been developed for both the pure modes and mixed mode situations (refs 1, 2, 3) In developing methods

suitable for mode II testing, interest has focused on the End Notched Flexure (ENF) test, demonstrated by Russell and Street (ref 4), as a convenient method for the determination of static values of G_{IIc}. Additionally the test may be easily adapted to study crack growth in fatigue (refs 5, 6) Figure 1 shows a schematic diagram of this simple test, which is based upon the growth of an artificial delamination located at the mid-plane of one end of a three point bend flexural specimen

The work outlined in this paper describes the evaluation of mode II fracture energies of a variety of carbon fibre resin systems using the ENF test Two forms of data reduction, that of beam theory and that of compliance calibration, have been examined and a comparison made between the two methods The assessment of crack growth rates under fatigue loading has also been made for three of the materials studied An analysis of the failed surfaces under the SEM is also reported

EXPERIMENTAL PROCEDURE

Specimen manufacture and materials

Six different carbon fibre reinforced matrix materials were studied including five thermosets, XAS/914, T800/5245, T400/6376, T300/V390, T800/924 and one thermoplastic system AS4/PEEK. Twenty-four ply unidirectional laminates 3mm thick were moulded from preimpregnated sheets with mid-plane teflon inserts 0 05mm thick, except for the PEEK panels for which kapton inserts 0.06mm thick were used Panels for fatigue specimens were moulded using 0.01mm thick inserts Thermosetting laminates were cured in an autoclave, according to the manufacturers recommended cure cycle, and post cured as neccessary Processing of the thermoplastic material was completed using a hot press at 380°C, and cooled at a rate of 4°C/min through the critical temperature range 380°C to 200°C Although this cooling rate was below the manufacturers recommended minimum cooling rate of 10°C/min, previous work on similarly cooled material suggested that the morphology and degree of crystalinity would be within normal limits (ref 7) The quality of all laminates was assessed using an ultrasonic C-scanning technique prior to being cut into specimens, approximately 150mm long by 25mm wide. All panels were of very good quality with the exception of the T800/924 material, which although considered suitable for testing, was noticeable inferior when compared against the other panels (this was a problem with fabrication at RAE and not due to any material deficiency) Once prepared, the edges of the specimens were painted white using a thin solution of typewriter correction fluid, to assist with visual crack length determination They were then stored in a dessicator to prevent any uptake in moisture. Specimens that were exposed to the environment for any period of time were dried in vacuum oven at 60°C and the

moisture content monitored until their was no further weight loss.

Precracking

Prior to ENF testing, it was necessary to precrack all specimens from the moulded inserts in order to produce a sharp crack front. Crack growth directly from the starter film requires the propagation of the crack through the resin pocket at the end of the insert, and can give rise to elevated values of G_{IIc} (ref.8)

Two types of precrack were considered, that of mode I (opening) or that of mode II (shear). Mode I had the advantage that the radically different fracture surface produced by peel failure facilitated easy identification of the forward shear surface produced in subsequent mode II testing. Mode II precracking had the advantage of producing deformation at the crack tip closely reflecting that of the loading conditions to be used during the ENF testing, and is similar to that commonly found around impact sites. For the purposes of these experiments it was decided to use the latter method.

It has been shown that delamination growth during the ENF test can be either stable or unstable, depending on the ratio of the initial delamination length a, to the half span length L, and that for the condition a/L>0 7 crack growth is stable (ref 9) Precracking was performed under stable conditions, using the three point bend fixture shown in figure 2, by controlled loading of the specimen until the crack had grown to the centre position. Loading was performed in position control at a rate of 1mm/min using a servohydraulic test machine. The tip of the crack was monitored visually using a travelling microscope, and the final position of the crack front marked on both sides of the specimen when crack growth had ceased. Since it was important to know the exact location of the crack tip before proceeding to the static and fatigue tests, some of the specimens were examined by C-scan to confirm the accuracy of the visual inspection. This was particularly useful for specimens having curved crack fronts. All specimen edges were sealed with a waterproof adhesive tape prior to C-scanning to prevent the ingress of water. As an additional precaution specimens were dried overnight in a vacuum oven prior to final testing

Static ENF testing

Once precracked, specimens were repositioned in the three point bend apparatus with the central roller located to give the required initial delamination length. In contrast to the precracking procedure, an a/L ratio of 0 5 (where a = 17 5mm and L = 35mm) giving unstable crack growth was used for this part of the experiment. Unstable crack growth was utilised since it produces a much more visible and well defined point of delamination onset on the load/displacement plot. Loading was again performed in position control at a rate of 1mm/min, and the centre point displacement measured using a linear variable differential transducer (lvdt), thus eliminating the necessity to have to allow for machine compliance. Figures 3 and 4 show typical load versus displacement plots for epoxy and thermoplastic materials respectively, from which Pc, the critical load for delamination onset, and the compliance C, were determined. Five specimens of each material were tested and a mean value of G_{IIc} evaluated using the data obtained

Compliance calibration

For static data reduction purposes, a compliance calibration was carried out for each material being investigated. With the exception of the T300/V390 and T800/924 materials, which were calibrated directly from the insert, precracked specimens were placed in the three-point bend fixture with the same span length L used for all previous tests. Each specimen was loaded at a variety of increasing crack lengths, a, by sliding the specimen along in the fixture. Loadings were performed at several points along the beam, over the range a = 0 to a = L. A limit of 50% of Pc, the critical load for delamination onset, was imposed since it was important not to extend the length of the delamination. For each new crack length a load versus displacement plot was obtained, enabling the change in compliance C, with crack length a, to be assessed. Ideally compliance calibrations should have been performed on every specimen tested statically. However, owing to the time consuming nature of the procedure, tests were undertaken on only two specimens of each type, and the results averaged

STATIC TEST DATA ANALYSIS

Two methods of data reduction were applied to the results from the static tests, these were beam theory and compliance calibration

Beam Theory

For an ENF specimen loaded in three point bending, a condition of almost pure shear exists at the delamination front. The strain energy release rate for this condition can be defined in terms of the Griffith-Irwin relationship

$$G = \frac{P^2}{2w} \times \frac{dC}{da} \qquad (1)$$

where P = load, w = width, C = compliance = δ/P, δ = displacement and a = crack length

From the relationship above, Russell and Street[4] have derived a closed form equation for compliance C and strain energy release rate G_{II}^{BT}, based on linear beam theory. Compliance can be defined as

$$C = \frac{2L^3 + 3a^3}{8E_{11}wh^3} \qquad (2)$$

where L = half span length, E_{11} = axial modulus and 2h = laminate thickness.

Substituting equation (2) into equation (1) gives the expression

$$G_{IIc}^{BT} = \frac{9a^2 P_c^2 C}{2w(2L^3 + 3a^3)} \qquad (3)$$

where P_c = critical load for delamination onset

Compliance calibration

An alternative approach to data reduction is that of compliance calibration. By measuring the compliance with a small load insufficient to cause any crack extension, an experimental curve of normalised compliance C/Co, where Co is the compliance of a beam with no crack, versus
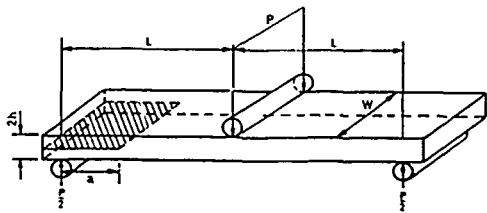
Fig 1 Schematic Diagram of ENF Specimen
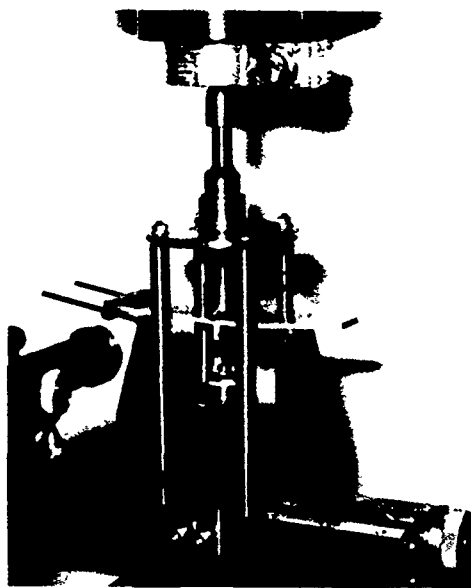
Fig 2 Three Point Bend Apparatus
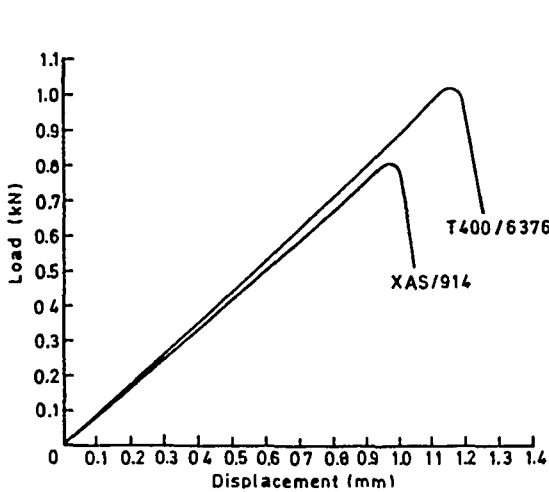
Fig 3 Load - Displacement curves for brittle & tough epoxy
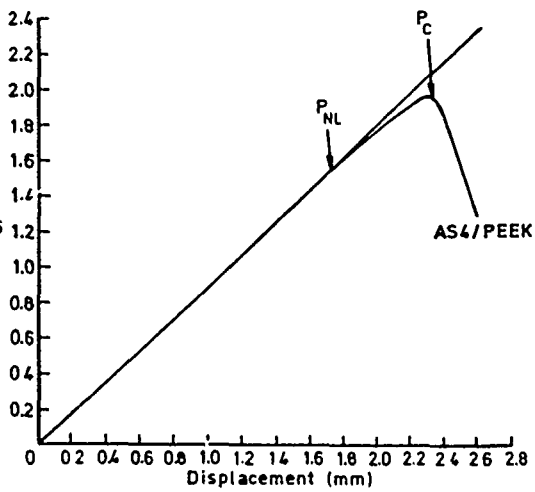
Fig 4 Load - Displacement curve for thermoplastic

normalised crack length cubed (a/L3), is constructed. A straight line fitted to the data yields:

$$\frac{C}{C_o} = A + B(a/L)^3 \qquad (4)$$

where B is the gradient and A the y-intercept, which under true beam theory would have values of 1.5 and 1 respectively. An expression for G_{IIc} is obtained by differentiation of C in equation (4) with respect to a, and multiplication with $P_c^2/2w$ to give

$$C = AC_o + \frac{BC_o}{L^3}(a^3)$$

$$\frac{dC}{da} = \frac{3BC_o}{L^3}a^2$$

$$G = \frac{P^2}{2w} \times \frac{dc}{da}$$

$$G_{IIc}^{cc} = \frac{3BP_c^2 a^2 C_o}{2wL^3} \qquad (5)$$

Fatigue Tests

In contrast to the static ENF tests, an lvdt was not used during the fatigue tests, displacement was measured directly from the the hydraulic ram movement As a result of this change several modifications were made to the experimental arrangement. Before commencing the fatigue tests the half span width L of the three point bend apparatus was increased from 70mm to 100mm This was done to allow slightly larger deflections for a given load, improving the signal/noise ratio of the ram measured displacement

Since no static load versus displacement data was available for the three point bend apparatus in the new wider configuration, static G_{IIc} tests were undertaken, as described previously, on three specimens of each material The values obtained, along with the critical displacements for delamination onset, were useful for setting up the subsequent fatigue tests. Values of G_{IIc} determined using the new configuration were found to be within 10% of the values obtained using the shorter half span width In the present study only the materials XAS/914, T800/924 and AS4/PEEK were examined in fatigue

Prior to undertaking the fatigue tests a compliance calibration was performed on each specimen This data would be used later for crack length determination during cycling. A relationship between the displacement measured using the lvdt, and the displacement measured by the hydraulic ram was also obtained, so that data could be corrected for machine compliance

Precracked specimens were placed in the three point bend apparatus with the initial delamination front positioned mid-way between the outer and centre loading rollers (a=25mm). The restraining fixture shown in figure 2 was adjusted so that it just touched the undelaminated end of the specimen A restraining fixture was added to the ENF apparatus during fatigue in order to prevent sideways movement of the specimen Sideways movement arises due to assymetric bending of the beam caused by one end of the specimen being delaminated Specimens of each material were fatigued under position control at a variety of fixed

displacements insufficient to cause static growth of the crack. Tests were conducted at a frequency of 5Hz using an R-ratio of 0.1. The maximum load (P), and displacement (d), were recorded against the corresponding number of cycles N, by using a computer as a data logger

Two methods for determining the fatigue crack length were utilised during the experiment The simplest involved briefly pausing the test, and visually monitoring of the crack front from both sides of the specimen using a travelling microscope. The second method utilised the compliance calibration data obtained earlier. Using the load versus displacement data recorded on the computer, corrected for machine compliance, the actual compliance of the specimen after a known number of cycles was determined From the compliance calibration data obtained for each specimen prior to fatigue testing, the crack length after a specified number of cycles could be determined from equation (4). The choice of method used was made according to the time period over which the test was expected to run. Where tests could be completed in a day, they were monitored visually, but if expected to run overnight, when visual observations could not be made, the compliance method was used When both methods were used simultaneously, good agreement was found to exist between measurements In the worst case, only a discrepancy of 7% was identified between the two methods.

FATIGUE DATA ANALYSIS

From the crack length versus cycles data obtained for each specimen, it is possible to describe the fatigue behaviour of a composite under mode II loading using the well known Paris equation.

$$\frac{da}{dN} = A(\Delta G_{II})^B$$

where A and B are constants dependent on the material, da/dN is the crack propagation rate per cycle and ΔG_{II} the cyclic strain energy release rate

The crack propagation rate per cycle da/dN was determined by plotting the crack length a as a function of cycles, as shown in figure 5 A polynomial curve was fitted to the data and the equation differentiated in order to find da/dN after a specified number of cycles In some cases polynomial functions as high as the order of six were required to get a satisfactory fit to the data

The strain energy release rate ΔG_{II} corresponding to each increase in crack length was calculated by differentiating equation (2) and rearrangement of equation (1), to give

$$\Delta G_{II} = \frac{9a^2(\Delta P)^2}{16E_{11}w^2h^3} \qquad (6)$$

where ΔP is the load amplitude Since ΔP is related to the displacement $\Delta \delta$ by $\Delta P = \Delta \delta/C$, Equation (6) can be rewritten in terms of δ and C as

$$\Delta G_{II} = \frac{9a^2(\Delta \delta)^2}{2w(2L^3 + 3a^3)C} \qquad (7)$$

$$y = -1.57E{-}26x^5 +1.76E{-}20x^4 -7.57E{-}15x^3 +1.39E{-}9x^2 -1.21E{-}5x^1 +20.9,$$
var.0.0141, max dev:0.172
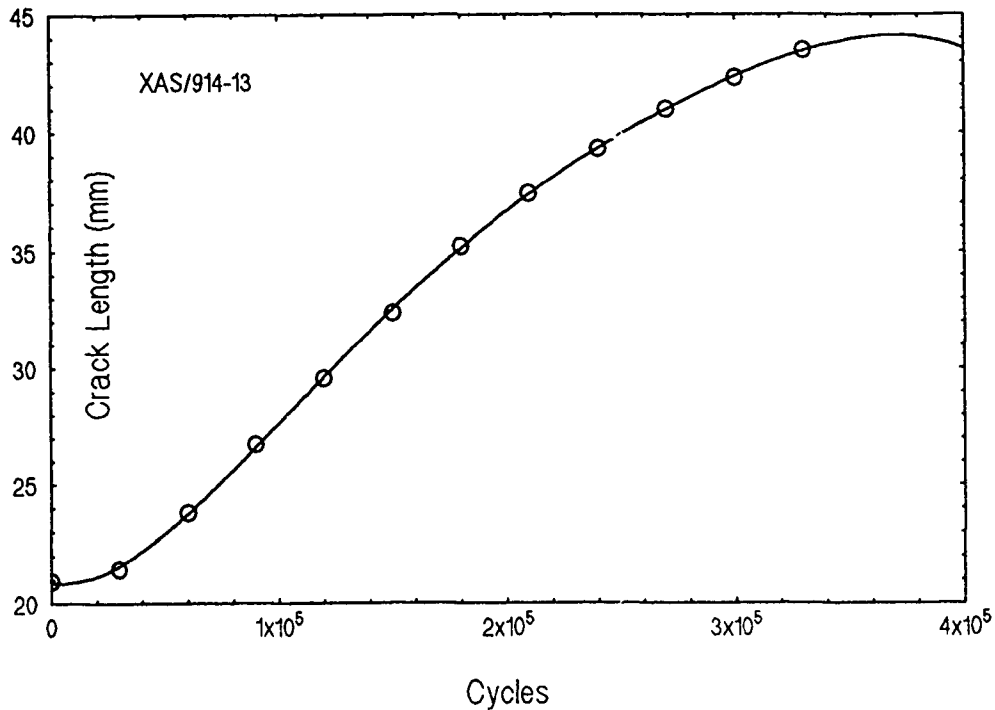
Fig 5 Crack Propogation Rate v. Cycles for XAS/914 - Polynomial fit to Experimental Values

Fig.6 T800/5245 resin fillet at end of insert

Fig.7 AS4/PEEK resin fillet at end of insert
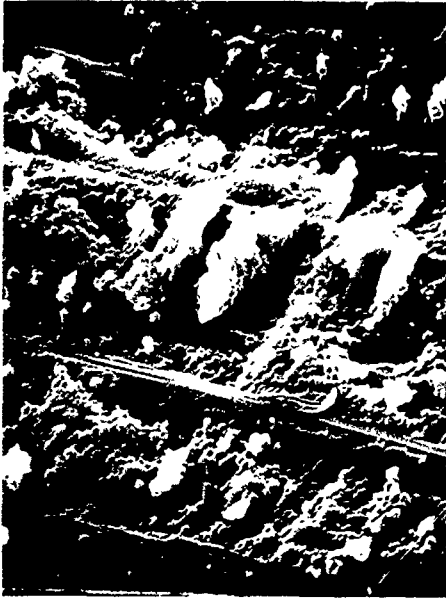
Fig 8 Shear Cusps in toughened epoxy, XAS 914

Fig 9 Shear Cusps in standard matrix T800/924

Fig 10 Shear Cusps in T800/5245

Fig 11 Shear Cusps in tough matrix, T800/924

It can be seen from equation (7) that for constant amplitude cycling, ΔG_{II} increases initially with crack length a, but at longer crack lengths the $(2L^3+3a^3)$ term becomes dominant, resulting in a reduction of ΔG_{II} past a maximum at a = 0 7L Thus for many values of ΔG, two measurements of da/dN, eitherside of the maxima can be obtained.

RESULTS

Compliance calibration

From the load versus displacement plots obtained, compliance values C for successive increments in crack length, were determined for each specimen tested Values of C were normalised by dividing by C_o, the compliance of the beam with no crack, and the resulting C/C_o value plotted against $(a/L)^3$ The intercept on the y axis, A, and slope, B, were then evaluated by applying a least squares fit to the data. Since only two specimens for each material were tested, averaged values of the coefficients A and B, were used in the final calculation of G_{IIc}^{CC}

Static ENF tests

The results of the static ENF tests, including the values of G_{IIc}^{BT} and G_{IIc}^{CC} are summarised in tables 1 & 2 An additional value of load, that of P^{NL}, has been incorporated into the table for the AS4/PEEK material As can be seen from figure 4, this material exhibited a marked degree of non-linearity during the latter portion of its 'oad/displacement plot. Since specimens showed an associated increase in compliance in this region, critical values of strain energy release rate would not seem to reflect accurately the true energy changes occurring during the test A value of G_{II}^{NL} was therefore evaluated by substitution of P^{NL} into equation (5), to yield a strain energy release rate at which the onset of subcritical crack growth is thought to occur

Fatigue ENF Tests

Using the crack growth data obtained from the three specimens of each material tested, log-log plots of da/dN versus ΔG_{II} were made, and the constants A and B evaluated Figures 14 to 16 show graphs for the XAS/914, T800/924 and AS4/PEEK respectively

DISCUSSION

Before examining the results of the static ENF tests, it is important to consider first the precracking procedure employed, since results suggested that the method adopted may have had a significant effect on the magnitude of the G_{IIc} values obtained.

In all instances where a shear precrack from the insert was required, it has been stated that the geometry of the ENF system was arranged so as to promote stable, controlled, crack growth to the centre roller, an a/l ratio greater than 0 7 being used to establish this condition (ref 6) It was interesting, therefore, to find that for a significant number of specimens, the observed crack growth was unstable in nature, even when a/l ratios in excess of 0 9 were used Tests performed on precracked specimens yielded stable

crack growth, as expected This latter point would suggest that the observed unstable behaviour was in some way attributable to the presence of the insert, in particular the resin pocket found at its end Figs 6 and 7 show micrographs, taken using a scanning electron microscope, of inserts found in the T800/5245 and AS4/PEEK material. Both show clearly the presence of a resin rich layer extending approximately 0.2 mm into the specimens. The presence of such resin pockets serve to blunt the crack tip, effectively enhancing the initial toughness of the system The energy required to propagate a crack through the resin pocket is substantially higher than that required to drive a sharp crack tip through the bulk composite material under stable conditions When the energy is sufficient for crack propagation from the insert, the extra energy is released by the rapid propagation of the crack front in an unstable manner Since the size of the resin pocket is related to the thickness of the insert, the only means of minimising this problem is to use as thin an insert as is available. Precracking in the fatigue specimens would appear to support this argument, since stable precrack growth was observed from the thinner 0 01mm inserts

An additional effect of precracking on the G_{IIc} values obtained is also illustrated by the data in Tables 1 and 2 For the 914, 5245 and V390 materials, toughness values were determined from specimens precracked in both tension and shear Although in each case only two specimens were tested from a mode I precrack, all tested in this manner yielded a lower value of G_{IIc} than equivalent laminates precracked in shear More tests are required, however, before any definite conclusions can be drawn

Both methods of data reduction were found to be suitable for the purpose of comparing materials for their relative toughness Beam theory was the most convenient, however, primarily because of its simplicity and the short time required to perform each test Where toughness values are required specifically for calculation, a more detailed approach to data reduction is possibly required (ref.7).

A comparison of the G_{IIc} values obtained using the two data reduction schemes showed the compliance calibration procedure to yield consistently lower values than those extracted by beam theory The extent of this difference is attributable to a certain degree to the size of the coefficients A and B, which in turn are related to the accuracy to which the compliance calibration was performed Initial attempts at compliance calibration rev ied the procedure to be very sensitive to errors in crack length determination This was complicated when the crack front was found to be curved It has been described how compliance calibration in the early stages of the programme was performed on precracked specimens, and at a later stage directly from the insert The latter offered several advantages, firstly the end of the insert was straight and easily visible, and thus reduced the error in crack length determination, and secondly the compliance calibration graph obtained could be used after precracking in order to reposition the specimen to the desired initial crack length required for static ENF testing The specimen should be lightly loaded several times in different positions until the compliance obtained corresponded to the crack length required This was particularly useful where visual and C-scan examination suggested the precrack front was curved.

(b) Sheared surface of thermoplastic matrix A5d/PEEK
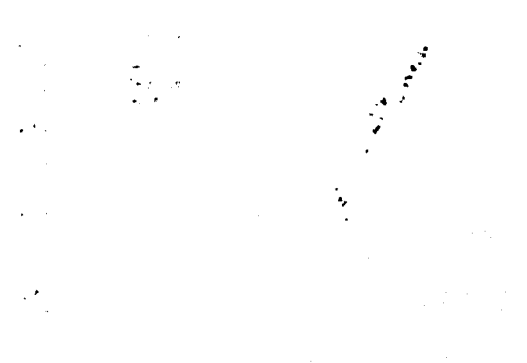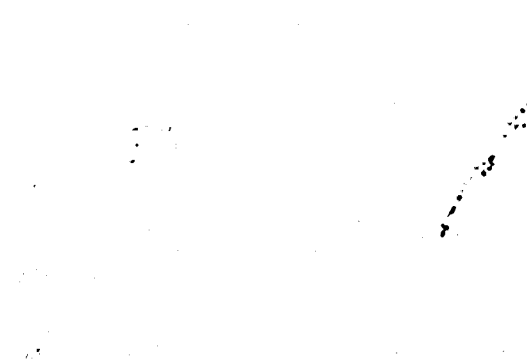
Fig 1c. Paris plot for A5d/PEEK material - fit to experiment

Whichever method of data reduction is used for comparison, it can be seen that the XAS/914 material exhibited the lowest value of toughness of the thermosetting systems, and the T400/6376 the highest. The thermoplastic AS4/PEEK material was considerably tougher than any of the thermosetting systems, with a G_{IIc} value approximately four times that of the toughest thermoset. Consistency between individual sets of results was good, with standard deviations for all of the epoxy systems being less that 10%.

Figs 8 to 12 show scanning electron micrographs of the sheared fracture surfaces of the five thermosetting systems. In all of the micrographs shown, characteristic S shaped cusps common to this mode of fracture can be seen (ref 11). These fractures develop initially in the matrix as 45o tensile cracks. As the surfaces move relative to each other, adjacent cracks coalesce, due to the constraining effect of the surrounding fibres. The cusp features produced are useful since they indicate the direction in which shear has occurred. In all of the pictures shown, the mating surface has moved in a right to left direction. It was interesting to note that, for the single phase thermosets, materials could be approximately ranked for toughness, purely by examination of the fracture surfaces. The T300/V390 showed a sharply defined brittle type fracture, which reflects the high cross link density and high glass transition temperature of this material. The failure surfaces of the T800/5245, T800/924 and T400/6376 materials showed increasingly more ductile behaviour, which possibly accounts for their additional energy absorbing capability. The XAS/914 material, shown in Fig 8, is complicated by the presence of a second phase and not easily compared with the fracture morphology of the single phase materials. Fig 13 illustrates the sheared fracture surface found in the AS4/PEEK thermoplastic. Significant ductile drawing of the matrix into fibrils has occurred, compared with the thermosets. Clearly this presents a mechanism by which the high toughness and non-linear behaviour of this material may be explained, and accounts to some extent for the 23% difference observed between the critical and non-linear values of G_{II}.

Examination of the fatigue data showed the crack growth rate for all specimens to be quite stable, even though the geometry of the system was unstable for the static condition. Figures 14 to 16 show graphs of the da dN versus ΔG_{II} data, for the XAS/914, T800/924 and AS4/PEEK, respectively. All three materials gave a good linear relation to the Paris crack growth law described by equation (7). Although the results presented in these graphs clearly show delamination growth, it must be noted that several specimens tested at low values of ΔG_{II} gave no apparent growth, even after a million cycles. Ther clearly exists a threshold value of ΔG_{II} below which growth does not occur. The presence of this threshold appears to be slightly visible in figure 16 for the PEEK material, where the data shows a small deviation from linearity at low values of ΔG_{II}. The general effect of increasing static toughness G_{IIc} on the fatigue results, appeared to be to shift the whole of the crack growth data to the right. This was in turn associated with a corresponding reduction in crack growth rate. Little difference was observed between the gradients obtained for the different materials.

The observation of reduced crack growth rates with increasing matrix toughness conflicts with previous work at DRA Farnborough, in which shear split growth in fatigue

was found to be more rapid in the tougher systems. This was used as a means of explaining the poorer fatigue behaviour observed in many toughened composites (ref 12). The reason for this may be that, in the current work, cracks have been grown in an interlaminar manner whereas the past work considered splits along the fibres, in an intralaminar fashion. Current work at DRA Farnborough is addressing this anomaly.

Fractographic examination of the shear fatigued specimens was not as useful as the examination of the static fractures, owing to the significant fretting that had occured between adjacent surfaces. Several interesting features were, however, observed. These included the identification of occasional striations, oriented perpendicular to the fibre direction, within the matrix of all three materials tested. Figures 17 and 18 show micrographs of striations in the AS4/PEEK and XAS 914 materials respectively. Close examination of the striation features failed to identify the mechanism by which they form, or to establish a relationship between their spacing and the cyclic load to which they were subjected. Extensive rolling of the matrix debris had occurred giving rise to an abundance of mini-matrix rollers (figs 19, 20). The size of these features appeared to vary according to the distance from the delamination front. In close proximity to the crack tip the rollers were only small, away from the crack tip the rollers appeared to increase in size. It may be possible that these roller features may actually serve to reduce the frictional forces between the surfaces, once they have formed.

The work described in this report has enabl_ _liable values for the mode II toughness to be determined for a range of composite materials. In these laminated materials the susceptibility to the initiation and growth of delaminations might be expected to be related to the mode II toughness. In impact, delaminations form mainly under the action of shear stresses and in subsequent loading undoubtedly grow due to the action of similar stresses. Thus the damage tolerance might be expected to be related to the materials mode II toughness. To some extent this is true, with the tougher thermosetting materials certainly showing greater resistance to impact and improved residual properties compared to standard materials. However, the initiation and growth of delaminations is more complicated than the simple scenario described above. Undoubtedly mode I toughness will also influence damage initiation and growth. In addition, thermoplastic materials exhibit behaviour very different from that of thermosetting materials, with different damage modes being observed. Thus a very large value of toughness does not necessarily confer very good delamination resistance, although the thermoplastic materials generally do show improvements over the thermosetting systems, but not in relation to their toughnesses. Clearly other factors are important, including the fibre type and the fibre/matrix interface. Certainly further work is required to help explain the relationship between damage tolerance and delamination resistance, and easily measurable materials properties.

CONCLUSIONS

The ENF test has been shown to be a useful tool for the characterisation of mode II toughness in carbon fibre reinforced plastics. Compliance calibration yielded slightly lower values of G_{IIc} than those from beam theory, however
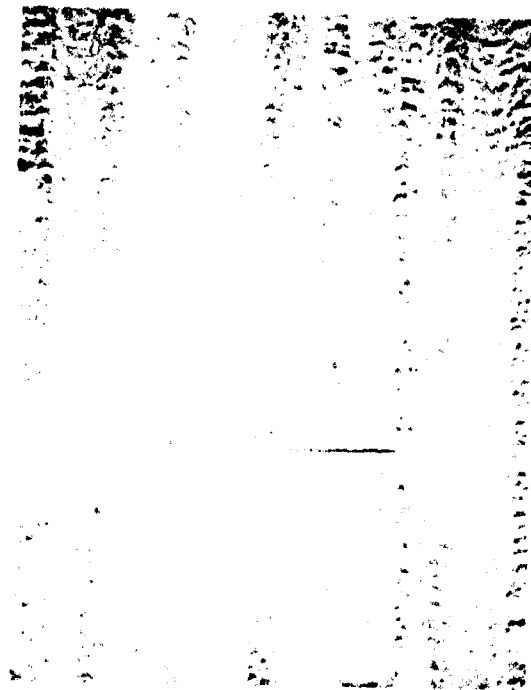
Fig 20. Matrix Robes in 1800/924

the difference is insignificant when testing is being undertaken for materials comparison purposes only Where values for accurate calculation are needed, a more rigorous approach to data reduction is probably required. Precracking procedure, in particular the mode used, had a noticeable effect on the G_{IIc} values obtained In the present study it was found that precracking in mode II gave rise to higher toughness values than precracking in mode I In the manufacturing of specimens it is recommended that an insert as thin as is available is used to avoid difficulties with the shear precracking procedure

Of the five fibre reinforced thermosets tested, XAS/914 and T300/V390 were found to have the lowest values of G_{IIc}, and T400/6376 the highest Fractography suggested that part of the energy absorbing capability of the tough thermosets may have been attributable to the increased ductility observed in the matrix Extra energy was apparently expended in deforming the tough matrices, in addition to breaking bonds to form new surface Plastic flow exhibited by the PEEK matrix appeared to account significantly for the high toughness found in APC2

The relevance of G_{IIc} with respect to design seems most significant when considering low energy impact damage, where the loading is essentially shear dominated It may therefore be possible to relate impact damage levels to the strain energy release rate of a known system In the case of compression after impact, however, peeling is probably also significant, requiring a mixed mode approach to impact damage growth predictions

In fatigue loading, the tougher materials exhibited slower mode 2 delamination crack growth rates than the standard XAS/914 material The sensitivity to fatigue, reflected in the slopes of the da/dN v G_{II} curves, was similar for the three materials tested Current work is considering crack growth thresholds from impact damage and will be related to this work in a future publication

TABLE 1 - SUMMARY OF ENF TEST RESULTS
Shear Precrack

Material	G_{IIc} Beam Theory	S D σ_{n-1}	G_{IIc} Compliance Calibratn	S D σ_{n-1}	Fibre Vf %
XAS 914	491	40 1	416	34	61
T300/V390	521	45	509	44	64 5
T800/5245	552	19	541	19	63 4
T800 924	582	54	549	51	60 8
T400/6276	655	36	602	33	61 8
AS4/PEEK (PXL)			1857	401	62 4
AS4/PEEK (P)	2418	302	2406	300	62 4

TABLE 2 - SUMMARY OF ENF TEST RESULTS
Tensile Precrack

Material	G_{IIc} Beam Theory	S D σ_{n-1}	G_{IIc} Compliance Calibratn	S D σ_{n-1}	Fibre Vf %
XAS/914	391	38	332	32	61
T800/5245	532	52	522	51	63.4
T300/V390	419	20	409	20	64 5

REFERENCES

1   N Sela   Interlaminar fracture toughness and
    O Isahi   toughening of laminated composite
                 materials a review, Composites, 20,
                 No 4, 423-435 (1989)
2. W S Johnson Influence of the resin on
    P Mangalgiri interlaminar mixed mode fracture
                 NASA TM 87571 (1985)
3   J R Reeder   Nonlinear analysis and redesign of
    J H.Crews   the mixed mode bending
                 delamination test NASA Technical
                 Memorandum 102777 (1991)
4   A J Russell Factors affecting the interlaminar
    K.N Street   fracture energy of graphite/epoxy
                 laminates ICCM-IV, Tokyo, (1982)
5   B.Trethewey Mode II cyclic delamination
    J.W Gillespie growth, J Composite Materials, 22,
    L A Carlsson 459-483 (1988)
6   R H.Martin   Characterisation of mode I and
    G.G Murri   mode II delamination growth
                 thresholds in graphite/PEEK
                 composites, NASA Technical
                 Memorandum 100577 (1988)

7   P T Curtis   An investigation of the mechanical
                 properties of improved carbon fibre
                 composites RAE Technical Report
                 86021 (1986)
8   L A Carlsson Mode II interlaminar fracture of
    J.W Gillespie graphite/epoxy and graphite/PEEK
    B.R Trethewey J Reinforced Plastics and
                 Composites, 5, 170-187, (1986)
9   L A Carlsson On the analysis and design of the
    J W.Gillespie ENF specimen for mode II testing.
    R B Pipes   J Composite Materials, 20, No.6,
                 594-604, (1986)
10 S Hashemi   The analysis of interlaminar fracture
    A J.Kinloch in uniaxial fibre-polymer
    J G Williams composites Proc R Soc. Lond.
                 A427, 173-199 (1990)
11 D Purslow   Matrix fractography of fibre epoxy
                 composites RAE Technical Report
                 86046 (1986)
12 P T Curtis   Tensile Fatigue Mechanisms in
                 Unidirectional Fibre Composites,
                 DRA Technical Report 91011
                 (1991)

BARELY VISIBLE DAMAGE THRESHOLD IN A BMI

Edvins Demuts and Raghbir S. Sandhu
Wright Laboratory, Flight Dynamics
Directorate, WL/FIBEC
Wright-Patterson Air Force Base,
Ohio 45433 USA

SUMMARY

This paper presents the test plan,
equipment and procedures employed and
results obtained in an experimental
investigation of IM7/5260 graphite
bismaleimide's resistance to low
velocity impact. The two velocities
used were approximately 15 ft/sec for
the four groups of thicker and approxi-
mately 10 ft/sec for the group of the
thinnest specimens. The planform
dimensions of the specimens were 7" x
10". The effect of two different layups
10/80/10 and 40/50/10 (percent of
$0^o/\pm45^o/90^o$ plies) on impact resistance
was investigated. There were five
thicknesses for the 10/80/10 layup - 9,
26, 48, 74, 96 plies and four thickness-
es for specimens of the 40/50/10 layup -
9, 27, 49, 73 plies. Four replicates
were used for each combination of layup
and thickness. Specimens were impacted
by a free-falling steel impactor of
1" diameter and with a hemispherical
end. During impact, specimens were
sandwiched between a 1" thick steel
bottom plate and a 0.25" thick aluminum
plate, clamped by four corner bolts.
Both plates had a central 5" x 5"
opening whose center was aligned with
those of the specimen and the impactor.
The impactor, upon rebound, was caught
thus avoiding subsequent impact. The
resulting dent depths were measured with
a dial gage and an ultrasonic through
transmission method determined the
damaged area extent. All testing was
performed at room temperature. Speci-
mens were not moisture preconditioned.

Results indicate that the post impact
dent depths and damaged areas of the
material investigated (IM7/5260 Gr/BMI)
are strong functions of the laminate
thickness. The effect of layup on both
the dent depth and the damaged area is
not uniformly consistent and, therefore,
a definite conclusion cannot be made at
this time. However, valid comparisons
of three material systems, AS4/3501-6,
IM6/CYCOM 3100 and IM7/5260, having the
same layup (10/90/10) reveal that both
the dent depths and the damaged areas of
IM7/5260 are smaller than those of the
other two materials except for IM6/CYCOM
3100 laminates thinner than 60 plies
whose dent depths are smaller than those
of IM7/5260. It can be concluded that,
based on dent depths and damaged areas,
the toughened bismaleimide (IM7/5260) is
more impact resistant than the graphite
epoxy (AS4/3501-6).

1 INTRODUCTION

The potential benefits to be derived
from the application of advanced
composites to airframes coupled with the
demand for safety has driven composites
researchers to develop technology
necessary for reliable exploitation of
the material. A logical approach has
been to provide a degree of static
strength, stiffness, durability, or
fatigue life, and damage tolerance to
the structure. These qualities comprise
structural integrity. Since fiber-
reinforced matrix composites have quite
different mechanical behavior and
properties than metals, the structural
integrity requirements for composites
are expected to be different and must be
developed specifically for such
materials.

One of the peculiar characteristics to
most matrix materials used in composites
is their relatively brittle nature. Due
to it, it is possible to impact a
composite laminate without leaving a
mark or other easily visible evidence of
an impact on the impact surface while
causing considerable interior damage.
Aircraft designers and operators are
concerned about this interior damage
because, as found in a USAF damage
tolerance program, an impact at the
barely visible threshold level, where
the impact evidence just barely starts
to show, may cause interior damage such
as to reduce the original undamaged
strength as much as 60%. Damage above
this level, although more severe, cannot
escape noticing. Examination and
appropriate corrective action would
follow. Using the structure containing
the undetected damage may lead to a
catastrophic failure. To avoid such
failure, the design attempts to account
for such barely visible damage (BVD) by
using an initial damage assumption
(IDA). IDA is arbitrary, even when
specified, but tends to be conservative.
The US Air Force, for example, currently
requires the designer to account for an
initial damage that has been caused by
either an impact resulting in 0.1 inch
deep dent or a 100 ft-lb impact,
whichever is less. Either damage is
caused by a 1" diameter hemispherical-
end steel impactor traveling at
16 ft/sec just before striking the
target. This requirement implicitly
defines the BVD as that due to 0.1 inch
deep dent. It governs the design of the
relatively thin laminates. As the

laminate thickness increases beyond a certain value (approximately 0.25 inch in AS4/3501-6 Gr/Ep), the impact energy to cause 0.1 inch deep dent may exceed 100 ft-lb. Whenever this is the case, the damage caused by a 100 ft-lb impact replaces the damage resulting from a 0.1 inch deep dent as the IDA in designing the primary components of an USAF airframe. In case of laminates thinner than 0.1 inch, to avoid penetration and the type of damage related more to high velocity impact, it has been suggested to use indentations equal to the laminate thickness (Ref 2). From the foregoing, it should be evident why BVD is critical in the design of composite structures.

2 OBJECTIVE

The main objective of the examination presented in this paper is to experimentally determine the damage extent in moisture nonpreconditioned IM7/5260 graphite bismaleimide when subjected to low velocity impact in accordance with the current US Air Force requirements and the suggestion outlined above in the INTRODUCTION. A secondary objective is to make valid pre- and post impact property comparisons of the current IM7/5260 with IM6/CYCOM3100 graphite bismaleimide and AS4/3501-6 graphite epoxy.

3 APPROACH

The rationale for selecting IM7/5260 graphite bismaleimide for this investigation was to verify its reportedly improved toughness as compared to earlier BMI systems and the popular AS4/3501-6 graphite epoxy. The two different layups of 10/80/10 and 40/50/10 (percent of 0^0, $\pm45^0$ and 90^0) and the five different thicknesses for each layup (nominally 9, 26, 48, 74 and 96 plies) were used to determine the effect, if any, of these two parameters on the impact resistance of the IM7/5260 Gr/BMI. The 10/80/10 layup due to its relatively large percentage of $\pm45^0$ plies (80%) and hence greater 0^0 strain to failure capability was to represent the "soft" end of the layup hardness or damage tolerance spectrum. The 40/50/10 layup, being "harder", hence less damage tolerant than the 10/80/10 layup, was to represent a point in the layup hardness spectrum where in comparison to the "software" some 0^0 stiffness and strength had been regained at the sacrifice of some damage tolerance. For the purpose of characterizing the material through the determination of basic mechanical properties, 16-ply thick unidirectional panels for tensile and compressive properties and 8-ply thick $\pm45^0$ panels for shear properties were prepared. All panels were cured in an autoclave according to the manufacturer's specifications. After curing, the panels were ultrasonically inspected for manufacturing flaws. Those panels passing the inspection were cut into specimens with a 1/8" thick 8" diameter diamond saw. Sizes of the

basic mechanical property specimens were 1" x 10" for 90^0 tension and shear, 3/4" x 10" for 0^0 tension and 3/4" x 5" for 0^0 and 90^0 compression. All basic mechanical property test specimens were tabbed. The impact specimen size was 7" x 10". Each of the six replicates of the basic mechanical property specimens was instrumented with two rosettes - one on each side of the specimen. The number of replicates used in the impact tests was four and the specimens were not instrumented. Neither the basic mechanical property nor the impact specimens were moisture preconditioned but they were allowed to absorb ambient moisture. All testing took place at room temperature.

An impact of predetermined magnitude was inflicted to each of the impact test specimens by a free-falling steel impactor of 1" diameter and a hemispherical end. The intended impactor velocity just before striking the specimen was 16 ft/sec. The specimens, during impact, were sandwiched between two metal plates having a central 5" square opening whose center was aligned with those of the specimen and the impactor. The plates supporting the specimen were rigidly supported in the vertical direction. During its rebound from the plate, the impactor was caught to prevent its falling back and impacting the specimen the second time. The raw data from the basic mechanical properties tests were acquired through the use of the VAX Data Acquisition System. Among the data recorded in the impact tests were the velocity and kinetic energy of the impactor. The history of load and energy absorbed by the specimen was automatically presented in a graphical form by the computer hooked up to the impact device. Dent depth due to the impact was measured with a dial gage and the impact damaged area was depicted by an ultrasonic through-transmission technique.

4 DISCUSSION OF RESULTS

During the cure of the 96-ply panel of 40/50/10 layup, faulty equipment caused the loss of the whole panel. Hence there are no data points associated with this panel's thickness and layup. It was determined that the average volume fraction of fibers for all panels was 62%. The basic mechanical properties of IM7/5260 graphite bismaleimide along with those of IM6/CYCOM 3100 Gr/BMI and AS4/3501-6 Gr/Ep obtained by the authors of this paper in similar tests (Ref 3), are presented in Table 1. IM7/5260 is superior in all ultimate strengths by an average of 29% in the matrix dominated strengths (F_{22}^{tu}, F_{12}^{su}, F_{22}^{cu}) and about 14% in fiber dominated tensile strength (F_{11}^{tu}). Also, the fiber dominated tensile modulus E_{11}^{t} and ultimate strain ϵ_{11}^{t} are superior to those of the two other material systems. It should be emphasized that the thicker laminates (48 to 96 plies) were impacted with a 100 ft-lb kinetic energy while the impact of the thinner laminates (9 to 27

plies) was governed by dent depths.
Kinetic energy for the 26 and 27-ply
laminates was such as to produce a
0.1 inch deep dent, and the target dent
depth for the 9-ply specimens was the
thickness of the specimen (0.0468").
Although the planned velocity of the
impactor for all impacts was 16 ft/sec
translating into a 3.98 foot height
($h = V^2/2g$) between the tip of the
impactor and top of the specimen, the
maximum
available height was only 3.55 ft.
Therefore, the velocities for all except
the 9-ply specimens were slightly lower
than the required 16 ft/sec and they
varied between 14.77 ft/sec and
15.13 ft/sec. In the case of the 9-ply
specimens, to achieve the desired dent
depths of 0.0468" with impactor's
velocity at about 15 ft/sec (max
available), the weight of the impactor
would have to be lower than the minimum
weight practically possible. This
condition compelled to lower the height
between the impactor and the specimen
resulting in 9.90 and 9.34 ft/sec
velocities and thus in a technical
violation of the 16 ft/sec impactor
velocity requirement. The actual
impactor velocities for each of the
specimen groups are shown in Table 2.
The dent depths and damaged areas
resulting from the impact tests are
given in Table 2 and are shown
graphically in Figures 1 and 2. As
expected, the impactor indentations are
greater in the thinner specimens under
the same impact energy. Except for the
49-ply specimens of layup #2 (.0/50/10),
the data indicate that damaged areas
tend to increase with increasing
thicknesses. It is suspected that the
recorded value of the 49-ply damaged
area is due to some, until now
undetermined, mistake. Hopefully,
investigation of the reasons for this
odd data point will confirm the
suspicion of mistake and will establish
a clear trend for the damaged areas of
layup #2. Examination of the "Time of
Maximum Load" values in Table 2 clearly
confirms the expected trend of such time
with respect to the laminate thickness.
One way to look at this phenomenon is
the following: as the laminate grows
thinner, the reduced bending stiffness
allows greater elastic deflections or
greater elastic strain energy stored in
the laminate until the maximum elastic
deflection is reached and consequently
the full impact load is felt by the
specimen. Also, the "Maximum Load"
values of Table 2, being greater for the
thicker laminates, fall among the
expected trends. The possession of
impact data of three material systems
(IM7/5260, IM6/CYCOM 3100 and AS4/3501-
6) with the same layup (10/80/10) and
identical impact infliction, i.e. same
shape, size and support/fixture of
specimen and same impactor (Ref 2 and
3), permitted valid "apple-to-apple"
comparisons. Such comparisons of
indentation depths and damaged areas are
graphically shown in Figures 3 and 4.
Obviously, IM7/5260 indentation depths
and damaged areas are smaller than those
of IM6/CYCOM 3100 and AS4/3501-6 when
subjected to a 100 ft-lb impact energy,
except for indentation depths of
IM6/CYCOM3100 Gr/BMI laminates thinner
than approximately 60 plies. In this
exceptional case, the indentation depths
of IM6/CYCOM 3100 are the smallest among
the three material systems under
comparison.

5 CONCLUSIONS

Experimental evidence of IM7/5260
graphite bismaleimide supports the
conclusion that both the time to develop
maximum load and the normalized dent per
thickness of laminate are decreasing
functions of the laminate thickness
while the maximum load felt by the
specimen and the energy absorbed by the
specimen at peak load are increasing
functions of the laminate thickness.
Also, the impact damaged area of the
10/80/10 layup is an increasing function
of laminate thickness. The same would
be true for the 40/50/10 layup if it
were not for a dubious data point,
currently under scrutiny. The 10/80/10
layup of IM7/5260 produces significantly
smaller dent depths and impact caused
damage areas than the same layup of
IM6/CYCOM 3100 and AS4/3501-6, except
for IM6/CYCOM 3100, 60 plies and
thinner, whose indentation depths due to
100 ft-lb impact are the smallest of the
three material systems being compared.

6 REFERENCES

1. NASA Reference Publication 1092,
1982.

2. Demuts, E., Sandhu, R. S. and
Maddux, G.E., "Barely Visible Damage
Threshold in Graphite Epoxy,"
Proceedings of the Eighth International
Conference on Composite Materials, July
1981, SAMPE, Vol 4, pp 32-N-1 to 32-N-
12.

3. Demuts, E., Sandhu, R. S. and
Daniels, J. A., "Post Impact Compressive
Strength in Composites," presented at
the 9th DOD/NASA/FAA Conference on
Fibrous Composites in Structural Design,
November 1991.

Table 1

Basic Mechanical Properties at Room Temperature

		IM7/5260 Gr/BMI	IM6/CYCOM 3100 Gr/BMI	AS4/3501-6 Gr/Ep
Elastic Modulus along the fibers in tension	E_1^t	24 00 msi	22 20 msi	22 00 msi
Elastic Modulus along the fibers in compression	E_1^c	20 20 msi	20 70 msi	20 20 msi
Elastic Modulus transverse to the fibers in tension	E_2^t	1 45 msi	1 54 msi	1 48 msi
Elastic Modulus transverse to the fibers in compression	E_2^c	1 59 msi	1 50 msi	1 55 msi
Elastic Modulus in shear	G_{12}	0 82 msi	0 85 msi	0 83 msi
Major Poisson's ratio in tension	μ_{12}^t	0 297	0 313	0 277
Major Poisson's ratio in compression	μ_{12}^c	0 355	0 379	0 ? 2
Ultimate strength along the fibers in tension	F_1^{tu}	332 00 ksi	280 00 ksi	289 3 ksi
Ultimate strain along the fibers in tension	ε_1^t %	1 40	1 18	1 30
Ultimate strength along the fibers in compression	F_1^{cu}	165.10 ksi	209 00 ksi	188 10 ksi
Ultimate strain along the fibers in compression	ε_1^c %	0 88	1 15	1 05
Ultimate strength transverse to the fibers in tension	F_2^{tu}	10 86 ksi	7 36 ksi	8.57 ksi
Ultimate strain transverse to the fibers in tension	ε_2^t %	0.78	0 55	0 57
Ultimate strength transverse to the fibers in compression	F_2^{cu}	37 70 ksi	33.00 ksi	34 20 ksi
Ultimate strain transverse to the fibers in compression	ε_2^c %	A	2 24	2 21
Ultimate in-plane shear strength	F_{12}^u	17 00 ksi	10 60 ksi	14 50 ksi
Ultimate in-plane shear strain	γ_{12}^u %	A	2.40	14 40

Notes.
1. Test environment: room temperature ambient relative humidity (TRA)
2. Specimen moisture, ambient, not moisture preconditioned
3. Tension — standard test
4. Compression: Rolfes fixture
5 Shear — ±45° specimen tested in tension

A Ultimate strains not available due to limits imposed on data recorder

Table 2   Low velocity impact results

No of plies	Layup	Kinetic energy (ft lb)	Velocity (ft/sec)	Time at Max load (msec)	Time at No load (msec)	Maximum load (lb)	Energy absorbed by specimen peak (ft lb)	Energy absorbed at no load (ft lb)	Dent depth (in)	Damaged area (in²)	Normalized dent depth/ lam thickness	Impact governer
96	1	103 50	14 78	0 74	3 54	12,695	103 2	76 7	0 00425	12 15	1 ··	A
96	2	---- --	--- ---	--.---	-- ---	-------	-- -	--- --	..... -	-- --	.	.
74	1	103 82	14 80	1 08	3 89	9 406	104 2	91 8	f 01175	8 12	1 65	A
73	2	103 94	14 81	1 23	3 73	8,583	104 5	99 7	0 01150	6 64	1 63	A
48	1	102 85	14 77	1 26	6 88	6,752	103 0	96 3	0 05325	4 42	11 5?	A
49	2	102 9?	14 77	1 28	6 70	6,797	103 2	94 0	0 04825	13 23	16 22	A
26	1	53 34	15 11	1 84	8 45	2,438	53 1	53 0	0 09275	3 97	37 02	B
27	2	59 98	15 13	1 65	8 67	2,566	60 6	60 6	0 10650	4 02	40 94	B
9	1	12 65	9 90	2 35	8 13	694	12 0	12 0	0 04575	1 51	52 76	B
9	2	11 26	9 34	2 88	8 76	936	11 4	11 4	0 05675	2 39	65 44	B

1. Values shown are the average of four
2 Material IM7/5260 Graphite/Bismaleimide
3 Layup: #1 (10/80/10)
4 Layup: #2 (40/50/10)
5. Environment room temperature and ambient relative humidity
6 Specimen moisture ambient, not moisture preconditioned

A. 100 ft-lb
B. Depth of indentation
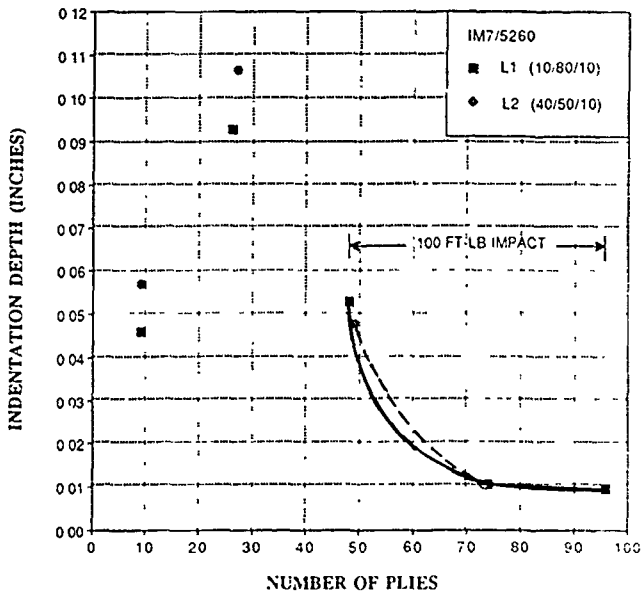
Figure 1. Indentation vs. Thickness for IM7/5260
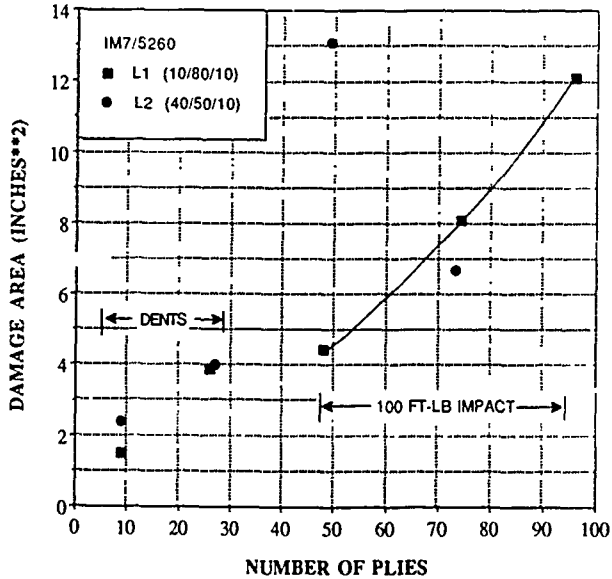

Figure 2. Damage Area vs. Thickness for IM7/5260
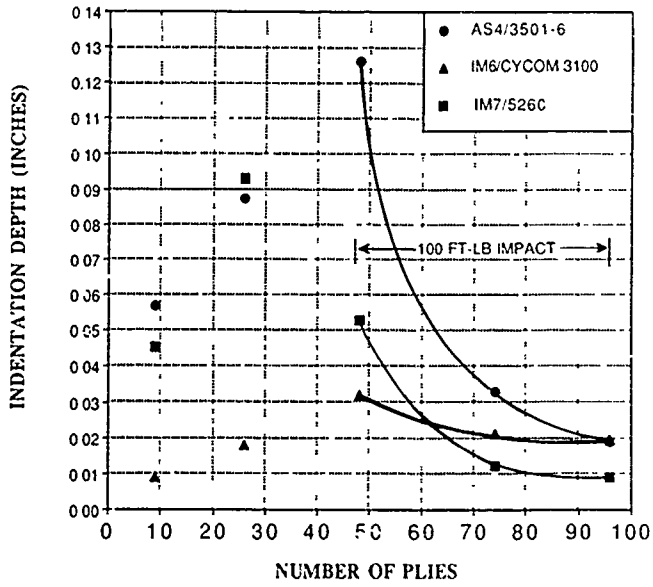
Figure 3. Indentation for Three Materials with Layups (10/80/10)
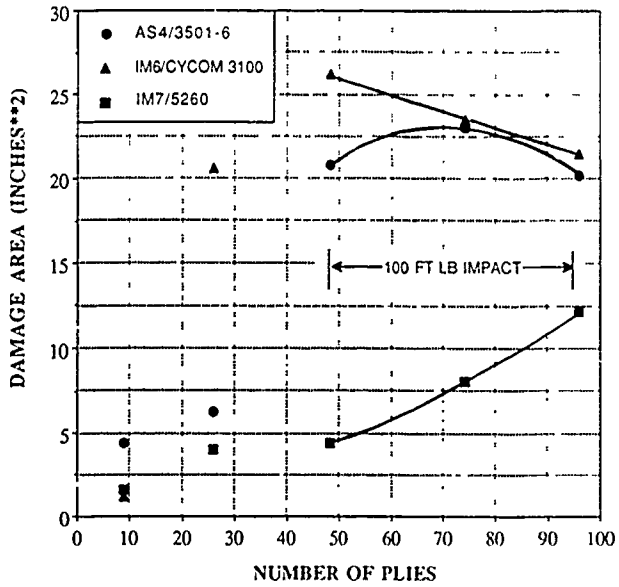

Figure 4. Damage Area for Three Materials for Layups (10/80/10)

THE INFLUENCE OF PARTICLE/MATRIX DEBONDING ON THE STRESS-STRAIN BEHAVIOR OF PARTICULATE COMPOSITES

E.E. Gdoutos

School of Engineering

Democritus University of Thrace

GR-671 00 Xanthi, Greece

ABSTRACT

A mathematical model to predict the nonlinear stress-strain behavior of particulate composites is proposed. The model consists of a rigid circular or square inclusion embedded in a matrix across part of its boundary, while the remaining part forms an interfacial crack. The stress field in the composite plate is determined by using the theory of complex potentials in conjunction with the conformal mapping technique. The local stress field in the vicinity of the crack tip is of mixed-mode and it is governed by the values of the opening-mode and sliding-mode stress intensity factors. Initiation of debonding along the inclusion/matrix interface and growth of the interfacial crack is studied by using the maximum circumferential stress criterion. It is shown that the nonlinear behavior of the stress-strain diagram of particulate composites can be explained by studying the stable growth of the interfacial crack along the inclusion boundary.

1. INTRODUCTION

Particulate composite materials consist of one or more particles of metallic or nonmetallic material embedded in a matrix of another material. A common example of a particulate composite made of a nonmetallic particle system in a nonmetallic matrix is concrete. It consists of a mixture of cement paste, sand particles and aggregates and sets and hardens uppon addition of water. It can be considered as a two-phase composite in which the aggregates are embedded into the mortar consisting of cement gel and sand particles. Mortar is regarded as a homogeneous and isotropic continuum functioning as the matrix binding the aggregates.

Nonlinear response between load and displacement of some particulate composites made of linear elastic constituents is a consequence of material damage by internal cracking In concrete, for example, microcracks are usually present even before loading at regions of high material porosity near the interface between the coarse aggregate and the mortar. They are caused by shrinking of the mortar during drying out of the concrete. Cracks are also present in the mortar matrix. Under an applied load both types of cracks start to increase and new cracks are formed. The interface cracks extend inside the mortar and are connected with the matrix cracks Aggregates act as crack arrestors. The process of crack growth is intimately related to the phenomenolocigal properties and the mechanical failure of concrete.

The objective of the present work is to present a mathematical model for the explanation of the nonlinear response of some particulate composite. The model is particularly suitable for modeling the nonlinear response of concrete. It has been observed that for concrete subjected to uniaxial compression and for applied stresses up to about 30 percent of the ultimate stress (f_c) the stress-strain response is linear For higher stresses nonlinearity starts to appear and a portion of the elastic strain energy is consumed for increasing bond failure. As the stress is increased above 70 percent f_c mortar cracks start to propagate and the deviation from nonlinearity of the stress-strain diagram becomes more pronounced For a description of the damage mechanism of concrete refer to reference [1]

Testa and Stubbs [2] proposed a model that considers the effect of bond failure for the explanation of the nonlinear stress-strain diagram of concrete . It consists of a circular rigid inclusion modeling the aggregate with two symmetrical interface cracks in a plate modeling the mortar. Propagation of the interface cracks is considered around the inclusion up to the point of branching into the mortar The nonlinear stress-strain response results from bond failure and depends on various parameters including the strength of bond and mortar and the size of the inclusion Along the same lines, Piva and Viola [3] considered a rigid elliptical inclusion partially bonded to the matrix For further details on the mechanical modeling of concrete refer to references [4] and [5].

In the present paper a model consisting of a circular or square rigid inclusion partially bonded to a matrix is considered for the study of the nonlinear behavior of the stress-strain diagram of concrete under biaxial loading. In Section 2 the stress and displacement fields for the case of a square inclusion are determined using the theory of complex potentials. The problem of the circular inclusion was not considered here as it was analyzed in reference [2] In Section 3 the local stress field in the neighborhood of the end of the interfacial crack along the inclusion/matrix boundary was analyzed Furthermore, linear fracture mechanics was used to study the growth of the crack along the interface or into the matrix. In Section 4 the proposed model was described and Castigliano theorem was used to determine strains The results of the present work are presented and discussed in Section 5.

2. A RIGID SQUARE INCLUSION PARTIALLY BONDED TO AN ELASTIC MATRIX

A typical element of the particulate composite is
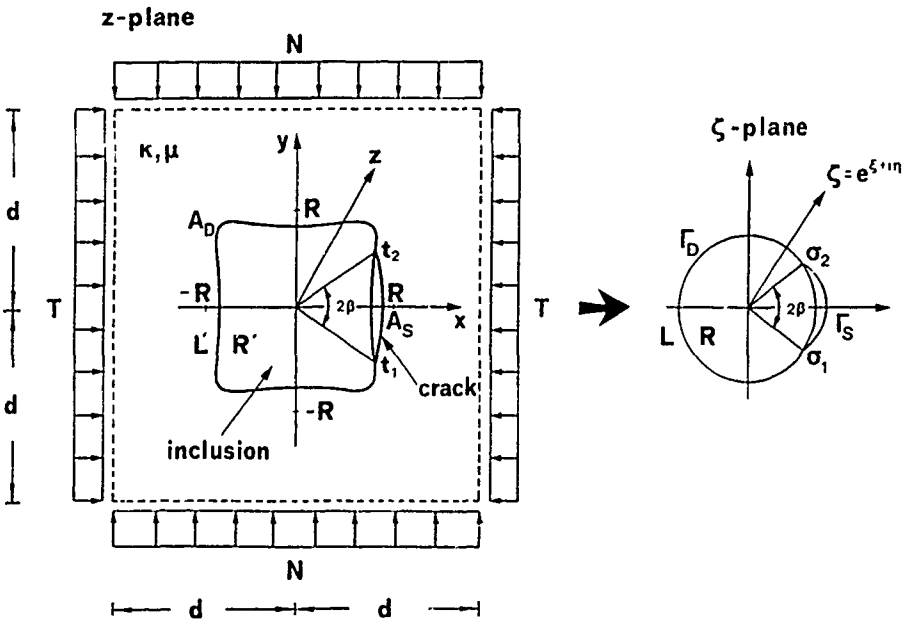
Fig. 1 Geometry and loading of proposed model and transformation of a square inclusion on to the unit circle.
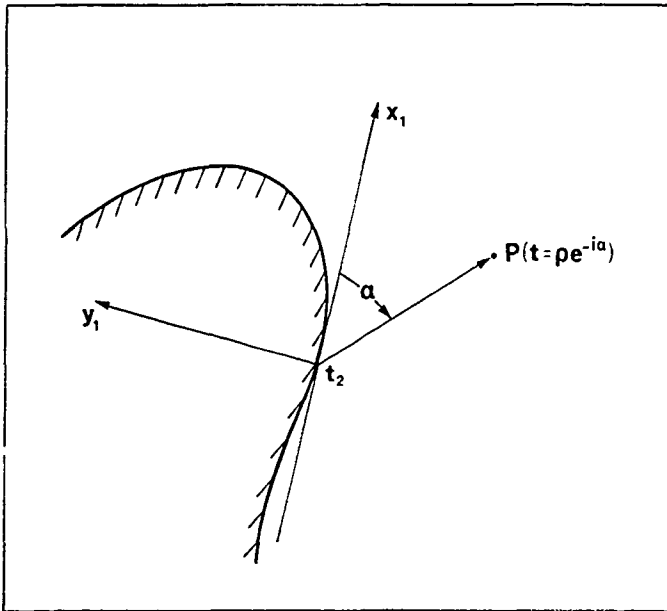
Fig. 2 Local coordinate system.

represented in Figure 1 by a square elastic solid of unit thickness and inplane dimensions 2dx2d containing a rigid curvilinear inclusion with length parameter R. It was taken $R=1$, so that d is indicative of the volume fraction of inclusion. The inclusion is perfectly bonded to the matrix except from a part of its boundary forming an interfacial crack symmetrically located with regard to the x-axis. The element is subjected to an uniform biaxial stress system N and T along the axes y and x at infinity. Let μ and v denote the modulus of rigidity and Poisson's ratio of the matrix which together with the inclusion occupy the z-plane. The inclusion boundary A is described in a clockwise sense so that the matrix is on the left when moving on A in the positive direction. Consider now the conformal mapping of the z-plane on the ζ-plane by the equation

$$z = m(\zeta) = R\left(\zeta + \frac{b}{\zeta^3}\right),$$

$$\zeta = \exp(\xi + i\eta)$$ (1)

which transforms the inclusion boundary on the unit circle $\Gamma(|\zeta| = 1)$ of the ζ-plane. The end points $t_1 = r\exp(-i\beta)$ and $t_2 = r\exp(i\beta)$ of the interfacial crack are mapped on the points $\sigma_1 = \exp(-i\beta)$ and $\sigma_2 = \exp(i\beta)$ of the circle Γ. Denote by A_D the bonded part of the inclusion and A_S the interfacial crack which are mapped on the parts Γ_D and Γ_S of Γ. It is easily seen from equation (1) that the matrix in the z-plane is mapped on the region L exterior of the circle Γ in the ζ-plane. For $b=0$ the inclusion is a circle, while for $b=1/6$ the inclusion is a square with rounded-off corners. Due to the mathematical difficulties for the solution of the problem of Figure 1 the case of an infinite plate is considered.

Equation (1) defines a system of orthogonal curvilinear coordinates in the z-plane. The stress components $\sigma_{\xi\xi}, \sigma_{\eta\eta}$ and $\sigma_{\xi\eta}$ in the system (ξ,η) and the displacement $D = u + iv$ in the system xy can be expressed in terms of the two complex potentials $W(\zeta)$ and $W(\zeta)$ by the following equations

$$2(\sigma_{\xi\xi} + i\sigma_{\xi\eta}) = W(\zeta) + \overline{W(\zeta)}$$
$$- \frac{\overline{\zeta} m(\zeta)}{\zeta m'(\zeta)} \overline{W'(\zeta)}$$
$$- \frac{\overline{\zeta} \overline{m'(\zeta)}}{\zeta m'(\zeta)} \overline{W(\zeta)}$$ (2a)

$$2(\sigma_{\eta\eta} - i\sigma_{\xi\eta}) = W(\zeta) + \overline{W(\zeta)}$$
$$- \frac{\overline{\zeta} m(\zeta)}{\zeta m'(\zeta)} \overline{W'(\zeta)}$$
$$- \frac{\overline{\zeta} \overline{m'(\zeta)}}{\zeta m'(\zeta)} \overline{W(\zeta)}$$ (2b)

$$4\mu \frac{\partial D}{\partial \eta} = [\kappa W(\zeta) - \overline{W(\zeta)}] i \zeta m'(\zeta)$$
$$+ [m(\zeta)\overline{W'(\zeta)} + \overline{m'(\zeta)} W(\zeta)] i \overline{\zeta}$$ (2c)

where $\kappa = 3-4v$ or $\kappa = (3-v)/(1+v)$ for plane strain or generalized plane stress conditions respectively

Furthermore, the following notation has been introduced

$$\overline{F}(z) = \overline{F(\overline{z})}$$ (3)

The boundary conditions of the problem may be stated follows

$$\sigma_{\xi\xi} + i\sigma_{\eta\eta} = 0, \quad \sigma \in A_S$$ (4a)

$$D = 0, \quad \sigma \in A_D$$ (4b)

The definition of the function $W(\zeta)$ from the L region outside the unit circle Γ in the ζ-plane is now extended to the region R inside the circle Γ by the equation

$$m'(\zeta) W(\zeta) = -m'(\zeta)\overline{W}\left(\frac{1}{\zeta}\right)$$
$$+ \frac{1}{\zeta^2} m(\zeta) \overline{W'}\left(\frac{1}{\zeta}\right)$$ (5)
$$+ \frac{1}{\zeta^2} \overline{m'}\left(\frac{1}{\zeta}\right) \overline{W}\left(\frac{1}{\zeta}\right), \quad \zeta \in R$$

From equation (4) we obtain

$$m'(\zeta) W(\zeta) = -\frac{d}{d\zeta}\left[\overline{m}\left(\frac{1}{\zeta}\right) W(\zeta)\right]$$
$$+ \frac{1}{\zeta^2} \overline{m'}\left(\frac{1}{\zeta}\right) \overline{W}\left(\frac{1}{\zeta}\right), \quad \zeta \in L$$ (6)

Introducing this value of $W(\zeta)$ into equation (2a) we obtain

$$2\zeta m'(\zeta)(\sigma_{\xi\xi} + i\sigma_{\xi\eta}) = \zeta m'(\zeta) W(\zeta)$$
$$- \frac{1}{\zeta} m'\left(\frac{1}{\zeta}\right) W\left(\frac{1}{\zeta}\right)$$
$$+ [\zeta m'(\zeta) - \frac{1}{\zeta} m'\left(\frac{1}{\zeta}\right)]\overline{W}(\overline{\zeta})$$
$$- [m(\zeta) - m\left(\frac{1}{\zeta}\right)]\overline{\zeta} \overline{W'}(\overline{\zeta})$$ (7)

which expresses the complex stress $\sigma_{\xi\xi} + i\sigma_{\xi\eta}$ in terms of $W(\zeta)$ defined in the region L and its analytical continuation into R

Equation (3) may now be expressed as

$$W_0^L(\sigma) - W_0^R(\sigma) = 0 \quad \sigma \in \Gamma_S$$ (8a)

$$\kappa W_0^L(\sigma) + W_0^R(\sigma) = 0 \quad \sigma \in \Gamma_D$$ (8b)

where it has been put

$$W_0(\zeta) = m'(\zeta) W(\zeta)$$ (9)

and $W^L(\sigma)$ and $W^R(\sigma)$ are the limiting values of $W(\zeta)$ as ζ tend to σ from L and R respectively.

Equations (8) constitute a Hilbert problem whose solution is [6]

$$W_0(\zeta) = X(\zeta) R(\zeta)$$ (10)

where

$$m(\zeta) = (\zeta - \sigma_1)^{-\tau}(\zeta - \sigma_2)^{-\bar{\tau}} \tag{11a}$$

$$R(\zeta) = A_1\zeta + A_0 + A_{-1}\zeta^{-1} + A_{-2}\zeta^{-2} + A_{-3}\zeta^{-3} + A_{-4}\zeta^{-4} \tag{11b}$$

$$\tau = 0.5 + i\lambda, \quad \lambda = (\ln\kappa)/2\pi \tag{11c}$$

Function $X(\zeta)$ is holomorphic in the ζ-plane cut along arc Γ_D on which it satisfies equation

$$\kappa X^L(\sigma) = -X^R(\sigma) \tag{12}$$

Only that branch of the function $X(\zeta)$ for which

$$\lim_{\zeta\to\infty} [\zeta X(\zeta)] = 1$$

will be used in the sequel.

For the determination of the coefficients A_j $(j = 1, 0, -1, -2, -3, -4)$ the condition that the complex potentials $W(\zeta)$ and $W(\zeta)$ should be holomorphic in the entire plane including the point at infinity is introduced. At infinity they take the form

$$W(\zeta) = \frac{N+T}{2} + 0\left(\frac{1}{R^2\zeta^2}\right) \tag{13a}$$

$$W(\zeta) = (N + T) - \frac{M + N'}{\pi R^2\zeta^2} + 0\left(\frac{1}{R^3\zeta^3}\right) \tag{13b}$$

From equations (13) it is obtained

$$A_1 = \frac{R(N + T)}{2} \tag{14a}$$

$$A_0 = -(\cos\beta + 2\lambda\sin\beta)A_1 \tag{14b}$$

For the remaining coefficients A_j it is obtained

$$\begin{bmatrix} d_0 & 0 & 0 & 0 \\ d_1 & d_0 & 0 & 0 \\ d_2 & d_1 & d_0 & -b \\ d_3 & d_2 & d_1 & d_0 \end{bmatrix} \begin{bmatrix} A_{-4} \\ A_{-3} \\ A_{-2} \\ A_{-1} \end{bmatrix} = \begin{bmatrix} 3bA_1 \\ 0 \\ bA_1(D_3-D_2^2)+R(N-T) \\ 0 \end{bmatrix} \tag{15}$$

where

$$d_0 = \exp[2\lambda(\pi - \beta)] \tag{16a}$$

$$d_1 = d_0(\cos\beta - 2\lambda\sin\beta) \tag{16b}$$

$$d_2 = \frac{1}{4}d_0[(3 - 4\lambda^2)\cos2\beta - 8\lambda\sin2\beta + (1 + 4\lambda^2)] \tag{16c}$$

$$d_3 = \frac{d_0}{24}[(15 - 36\lambda^2)\cos3\beta - \lambda(46 - 8\lambda^2)\sin3\beta + (1 + 4\lambda^2)(9\cos\beta - 6\lambda\sin\beta)] \tag{16d}$$

and

$$D_2 = \cos\beta + 2\lambda\sin\beta \tag{17a}$$

$$D_3 = \frac{1}{4}[(1 + 4\lambda^2) + (3 - 4\lambda^2)\cos2\beta + 8\lambda\sin2\beta] \tag{17b}$$

For a detailed analysis of the stress field in an infinite elastic solid containing a rigid square inclusion with rounded-off corners refer to reference [7].

3. LOCAL STRESS DISTRIBUTION AND CRACK GROWTH

A Cartesian coordinate system $t_2x_1y_1$ centered at the tip t_2 of the interfacial crack with the x_1-axis tangent to the inclusion boundary at t_2 is introduced (Figure 2). Let point P in the vicinity of t_2 be described by $t = \rho\exp(-\alpha)(\rho < < 1, 0 < \alpha < \pi)$. The complex potential W can then be put in the form

$$W(t) = \frac{R(\sigma_2)}{m'(\sigma_2)\sqrt{(\sigma_2 - \sigma_1)}ht} + 0(\sqrt{t}) \tag{18}$$

where

$$h = \frac{i\sigma_2}{|m'(\sigma_2)|} \tag{19}$$

We now define the complex stress intensity factor by

$$K = K_1 - iK_2 = \sqrt{2\pi}\lim_{t\to0}[\sqrt{t}\,W(t)] \tag{20}$$

Equation (18) renders

$$K_1 = \sqrt{\frac{\pi}{\sin\beta}}\left(-A\sin\frac{\beta}{2} + B\cos\frac{\beta}{2}\right) \tag{21a}$$

$$K_2 = \sqrt{\frac{\pi}{\sin\beta}}\left(A\cos\frac{\beta}{2} + B\sin\frac{\beta}{2}\right) \tag{21b}$$

quantities A and B are defined the following equations

$$A = \left[\text{Re}[m'(\sigma_2)]\text{Re}[R(\sigma_2)] + \text{Im}[m'(\sigma_2)]\text{Im}[R(\sigma_2)]\right]|m'(\sigma_2)|^{-3/2} \tag{22a}$$

$$B = \left[\text{Re}[m'(\sigma_2)]\text{Im}[R(\sigma_2)] - \text{Im}[m'(\sigma_2)]\text{Re}[R(\sigma_2)]\right]|m'(\sigma_2)|^{-3/2} \tag{22b}$$

In the above relations Re and Im express the real and the imaginary part of the complex quantity, respectively.

From equations (2), (18) and (21) the local stress field in the neighborhood of the crack tip is obtained as

$$\sigma_{\xi\xi} = \frac{1}{\sqrt{2\pi\rho}}\left[K_1\cos\frac{\alpha}{2}\left(1 + \sin\frac{\alpha}{2}\sin\frac{3\alpha}{2}\right) - K_2\sin\frac{\alpha}{2}\cos\frac{\alpha}{2}\cos\frac{3\alpha}{2}\right] \tag{23a}$$

From equations (23) the polar stress components $\sigma_{\alpha\alpha}, \sigma_{\rho\rho}$ and $\sigma_{\rho\alpha}$ can easily be obtained

$$\sigma_{\eta\eta} = \frac{1}{\sqrt{2\pi\varrho}} \left[K_1 \cos\frac{\alpha}{2} (1 - \sin\frac{\alpha}{2}\sin\frac{3\alpha}{2}) \right.$$
$$\left. + K_2 \sin\frac{\alpha}{2} (2 + \cos\frac{\alpha}{2}\cos\frac{3\alpha}{2}) \right] \tag{23b}$$

$$\sigma_{\xi\eta} = \frac{1}{\sqrt{2\pi\varrho}} \left[K_1 \sin\frac{\alpha}{2}\cos\frac{\alpha}{2}\cos\frac{3\alpha}{2} \right.$$
$$\left. - K_2 \cos\frac{\alpha}{2} (1 - \sin\frac{\alpha}{2}\sin\frac{3\alpha}{2}) \right] \tag{23c}$$

For monotonically increasing applied stresses N and T growth of the interfacial crack takes place either along the interface or into the matrix. The crack growth condition is expressed as follows

$$\sqrt{2\pi\varrho} \; \sigma_{\alpha\alpha}(0) = K_b \tag{24}$$

for growth along the interface, and

$$\sqrt{2\pi\varrho} \; \sigma_{\alpha\alpha}(\alpha_p) = K_m , \quad \sigma_{\alpha\alpha} > 0 \tag{25}$$

for growth into the matrix.
In equations (24) and (25) K_b and K_m are the critical stress intensity factors associated with crack growth along the interface or into the matrix. They are material constants. α_p is the angle that defines the direction along which the stress $\sigma_{\alpha\alpha}$ becomes maximum. Equations (24) and (25) are used for the determination of the critical applied stresses N and T for crack growth along the interface or into the matrix.

4. DETERMINATION OF STRAINS

Strain ε corresponding to applied stresses N and T (T = s N) is determined according to Castigliano's theorem as

$$\varepsilon = \frac{\partial U}{\partial N} \tag{26}$$

where U is the strain energy per unit volume of the element of Figure 1. U is calculated as

$$U = U_0 + U_c \tag{27a}$$

$$U_0 = \frac{1}{4d^2} \int_{V'} \left[\frac{\sigma_{\xi\xi,0}^2 + \sigma_{\eta\eta,0}^2}{2E} \right.$$
$$\left. + \frac{\sigma_{\xi\eta,0}^2}{2\mu} - \frac{\nu}{E}\sigma_{\xi\xi,0}\sigma_{\eta\eta,0} \right] dV' \tag{27b}$$

$$U_c = \frac{1-\nu^2}{4d^2 E} \int_0^{t_2} (K_1^2 + K_2^2)|dt_2| \tag{27c}$$

$$|dt_2| = R(1 + 9b^2 - 3b\cos 4\beta)^{1/2} d\beta \tag{27d}$$

where U_0 is the strain energy calculated from the uncracked specimen and U_c is the strain energy due to the presence of the interfacial crack.

From equations (26) and (27) it is obtained

$$\varepsilon = \frac{N}{E} \left(\frac{R}{2d}\right)^2 (1.5\pi I_c + I_0) \tag{28}$$

where

$$I_c = \int_0^\beta (\overline{K}_1^2 + \overline{K}_2^2)(1 + 9b^2 - 3b\cos 4\beta)^{1/2} d\beta \tag{29a}$$

$$I_0 = \frac{1}{R^2} \int_{V'} (\overline{\sigma}_{\xi\xi,0}^2 + \overline{\sigma}_{\eta\eta,0}^2$$
$$- \overline{\sigma}_{\xi\xi,0}\overline{\sigma}_{\eta\eta,0} + 3\overline{\sigma}_{\xi\eta,0}^2) dV' \tag{29b}$$

In the above equation it was put $\overline{K}_j = K_j/\sqrt{\pi R}$ (j = 1,2) and $\overline{\sigma}_{ij} = \sigma_{ij,0}/N$ (i,j = ξ,η).

5. RESULTS AND DISCUSSION

For the determination of the critical applied stress for crack initiation the case of an inclusion completely bonded to the matrix is considered. Crack initiates when the maximum radial stress along the inclusion boundary becomes equal to the bond strength N_b. The radial stress becomes maximum for both cases of circular and square inclusion at the point of the inclusion boundary along the x-axis Figure 3 presents the variation of the normalized critical compressive stress $\overline{N}_{cr,0} = N_{cr,0}/N_b$ for crack initiation versus the biaxiality coefficient s (T = s N) for the cases of circular (dotted line) and square (continuous line) inclusion. Note that the initiation stress is always larger for the square than for the circular inclusion.

When a crack has already initiated the critical stress for crack growth along the interface is determined from equation (24). Figure 4 presents the variation of the normalized critical stress for crack growth along the interface $\overline{N}_{cr} = N_{cr}\sqrt{\pi R}/K_b$ versus half crack angle β for the cases of the circular (a) and square (b) inclusions. The various curves of the figure correspond to different values of the biaxiality coefficient s. The stress N is always considered as compressive. Note that N_{cr} decreases as s also decreases. N_c becomes infinite at β = 0 and some other value of β depending on s and takes a minimum value at a critical half crack angle β_c between the above two values. This means that a decreasing applied stress is needed to grow the crack from β = 0 to β = β_c, that is crack growth up to the critical angle β_c is unstable. Beyond β_c crack growth is stable , that is higher stresses are required to increase the crack.

The critical stress for crack growth into the matrix is determined from equation (25). The variation of $\overline{N}_{cr} = N_{cr}\sqrt{\pi R}/K_b$ versus angle β for various values of the critical stress intensity factor K_m for a circular inclusion is shown in shown in figure 5. Figure 5a refers to uniaxial compression (s = 0), while figure 5b refers to biaxial loading with s = -0.5. Observe that N_{cr} decreases with β and increases as fracture toughness of matrix K_m increases. In the same figure the variation of N_{cr} versus β for crack growth along the interface is also shown by dotted line. The point of intersection of the solid and dotted lines denotes a value of angle β at
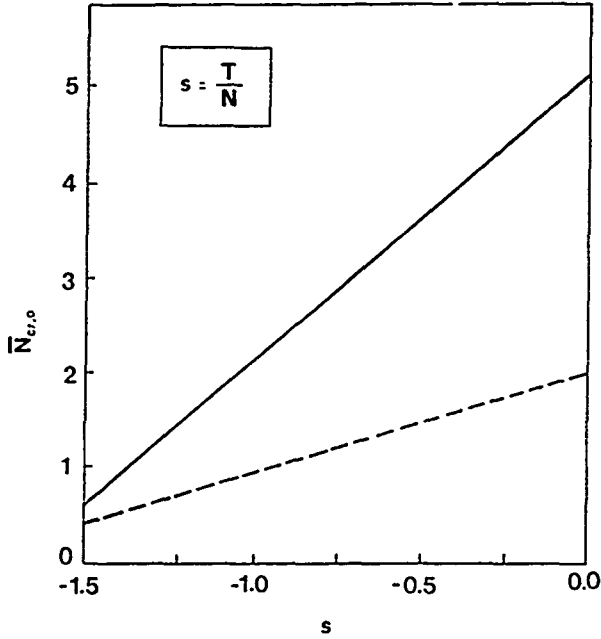
Fig. 3 Variation of normalized critical compressive stress $\overline{N}_{cr,0} = N_{cr,0}/N_b$ for crack initiation versus biaxiality coefficient s for a circular (dotted line) and a square (continuous line) inclusion.

(a)

(b)
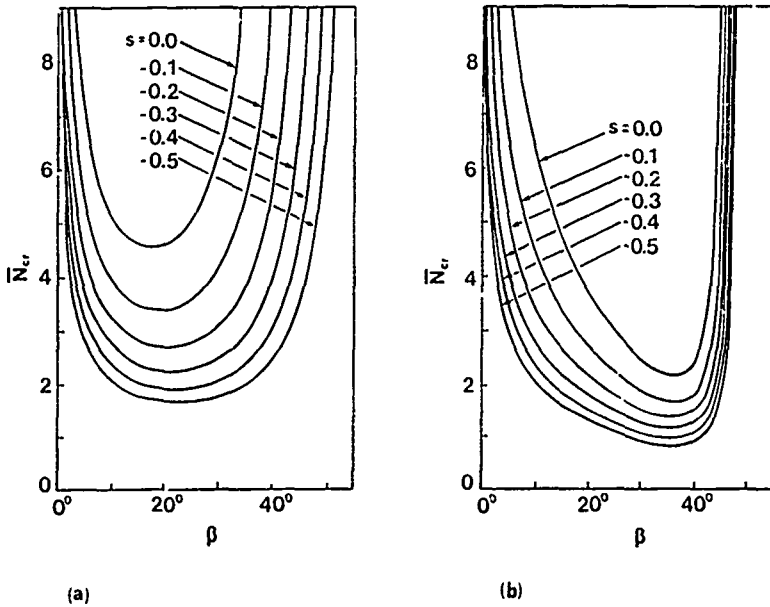
Fig. 4 Variation of normalized critical stress $\overline{N}_{cr} = N_{cr}\sqrt{nR}/K_b$ for crack growth along the interface versus half crack angle β for (a) circular and (b) a square inclusion. Biaxiality coefficient takes the values s = 0, -0.1, -0.2, -0.3, -0.4 and -0.5.

Fig. 5 Variation of normalized critical stress $\overline{N}_{cr} = N_{cr}\sqrt{nR}\,/K_b$ for crack growth into the matrix versus half crack angle β for a circular inclusion under (a) uniaxial compression and (b) biaxial loading with $s = -0.5$. The critical stress intensity factor K_m for crack growth into the matrix takes the values $K_m = K_b$, $= 2K_b$, $= 3K_b$, $= 4K_b$ and $= 5K_b$. The critical stress for crack growth along the interface is shown by dotted line.

(a)   (b)

Fig. 6 Variation of normalized critical stress $\overline{N}_{cr} = N_{cr}\sqrt{nR}\,/K_b$ for crack growth into the matrix versus half crack angle β for a square inclusion under (a) uniaxial compression and (b) biaxial loading with $s = -0.5$. The critical stress intensity factor K_m for crack growth into the matrix takes the values $K_m = K_b$, $= 2K_b$, $= 3K_b$, $= 4K_b$ and $= 5K_b$. The critical stress for crack growth along the interface is shown by dotted line.

Fig. 7 Stress-strain response for a circular inclusion under (a) uniaxial compression and (b) biaxial loading with s=-0.5. d takes the values 1.05 and 1.25.
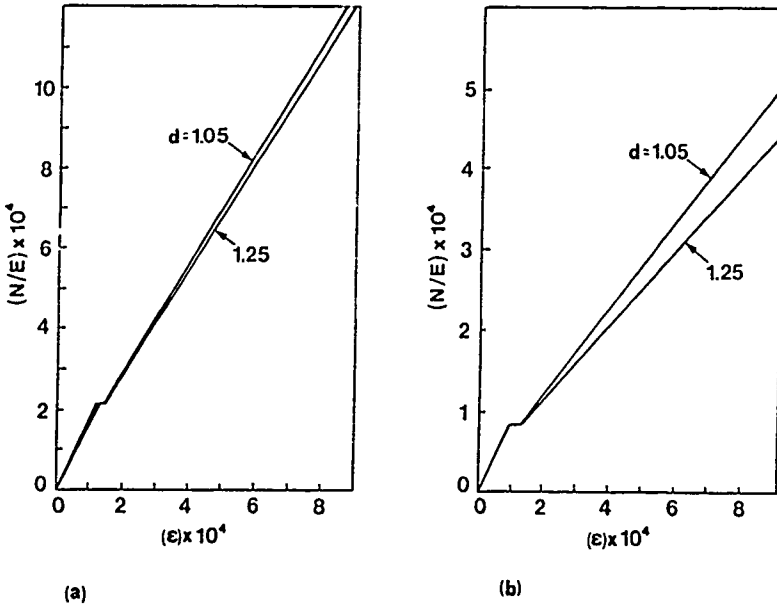
Fig. 8 Stress-strain response for a square inclusion under (a) uniaxial compression and (b) biaxial loading with s=-0.5. d takes the values 1.05 and 1.25.

which conditions of crack growth along the interface or into matrix are equally favorable. Results analogous to those of figure 5 for a square inclusion are shown in figure 6 Note in this case that N_{cr} does not decrease continuously with β, as in the case of circular inclusion, but presents a minimum in the internal $0 \leq \beta \leq 50^0$.

Based on equation (28) the overall stress-strain curve of the composite was determined. To obtain numerical results it was assumed that $K_b / (E\sqrt{\pi R}) = 10^{-4}$, which represents a typical bond strength in concrete. Furthermore, it was taken that the critical stress for crack initiation is equal to the minimum stress at which stable crack growth occurs (see figure 4). Figure 7 presents the stress-strain curve of the composite containing a circular inclusion with $d = 1.05$ and $d = 1.25$ subjected to uniaxial (s) and biaxial stresses with $s = -0.5$ (b). Analogous results for a square inclusion are shown in figure 8 There are three distinct segments of the stress-strain curves in figures 7 and 8 An initial linear part during which the inclusion is perfectly bonded to the matrix; a horizontal portion which refers to initiation and unstable growth of bond cracks up to a critical angle (see figure 4); and a nonlinear segment during which stable growth of the interfacial crack occurs.

6. CONCLUSIONS

A simple mathematical model to predict the nonlinear stress-strain response of particulate composites with particular relevance to concrete was proposed. The model consists of a rigid circular or square inclusion partially bonded to a matrix and considers the propagation of the interfacial crack along the inclusion boundary The boundary value problem in the composite plate was reduced to a Hilbert problem by using the theory of complex potentials in combination with the conformal mapping technique. The local stress field in the vicinity of the tip of the interfacial crack was expressed by the values of the opening-mode and sliding-mode stress intensity factors. The results of stress analysis were combined with the maximum circumferential stress criterion to study the growth of the crack. Strains were determined using Castigliano's theorem and results of stress analysis. The results of the study were presented in figures 7 and 8 and establish the dependence of observed nonlinearity of particulate composites on second-phase volume ratio and shape and other relevant mechanical parameters.

REFERENCES

[1] Meyers, B. L., Slate, F O. and Winter, G., Relationship between time dependent deformation and microcracking of plain concrete, *Journal of the American Institute Proceedings* 66, 60-80 (1969).

[2] Testa, R.B. and Stubbs, N., Bond failure and inelastic response of concrete, *ASCE Journal of the Engineering Mechanics Division* 103, 295-310 (1977).

[3] Piva, A. and Viola, E , Stress-strain response of a concrete mathematical model, Proc. of Fifth Congresso Nazionale Di Meccanica Teorica e Applicata, Palermo, 237-248 (1980).

[4] Ditommaso, A., Evaluation of concrete fracture, in *Fracture Mechanics of Concrete* (eds A. Carpinteri and A R. Ingraffea), Martinus Nijhoff Publ , pp. 31-65 (1984)

[5] Slate, F.O. and Hover, K.C., Microcracking of concrete, in *Fracture Mechanics of Concrete* (eds A. Carpinteri and A R Ingraffea), Martinus ijhoff Publ., pp. 137-159 (1984).

[6] Muskhelishvili, N I , Some Basic Problems of the Mathematical Theory of Elasticity, Third Ed , Noordhoff, Groningen (1953)

[7] Gdoutos, E.E., Kattis, M.A., Zacharopoulos, D.A and Kourounis, C G., A crack along the interface of a rigid curvilinear square inclusion embedded n an infinite solid, *Engineering Applications of New Composites,* edited by S A. Paipetis and G.C. Papanicolaou, Omega Scientific, pp 372-384 (1988).

IDENTIFICATION OF DELAMINATION BY EIGENFREQUENCY DEGRADATION- AN INVERSE PROBLEM.

B. STAMOS
V. KOSTOPOULOS
S. A. PAIPETIS
Mechanical Eng. Dept., University of Patras
260 01 Patras, Greece.

SUMMARY.
The free vibrations of a delaminated composite beam is investigated. The effect of interply delaminations on the eigenfrequencies of the beam is evaluated both analytically and numerically in the general case of an asymmetric laminate with a delamination of arbitrary size and location. Coupling between longitudinal and bending motion is considered, which affects the natural frequencies of the delaminated beam significantly. In general the delamination causes the even numbered vibration modes to degrade, e.g. to decrease, faster than the odd ones. An inversion method to determine position and size of the delamination is proposed, based on the degradation of the first two natural frequencies.

1. INTRODUCTION.
Delaminations in composite laminates, originating from a variety of reasons [1], have a detrimental effect on their structural performance and can be critical with vibrating laminated structures. The stiffness reduction thus produced causes the natural frequencies of the structure to decrease, while, since stress distribution in a vibrating structure is non-uniform and different for each mode, any localized damage, depending on its particular location and size, would affect each mode differently.

The influence of internal damage on modal parameters is important, both as a direct and as an inverse problem. The shifting of the eigenfrequencies has been used to identify internal damage due to various reasons, such as impact loading and matrix cracks [2,3] and in combination with the decrease of storage modulus and the increase of internal damping, to determine mechanical damage, such as sawcuts and local crashing [4,5].

Comparison of natural frequencies of the integral structure, analytically evaluated and/or experimentally confirmed, to those measured at certain life stages of a structure, offers a possibility to detect the development of damage and to identify its size and location. Results for a simply supported laminated beam have been recently reported [6]. The respective model allows for independent extensional and bending stiffnesses and includes the contact effect (no friction) between delaminated free surfaces.

In the present work, both symmetric and asymmetric vibration modes of a delaminated composite beam were investigated, while an inversion technique is proposed for the identification of delamination position and size. At this first stage it was assumed that the delamination was located on the middle surface of the beam and that material damping remained unchanged. In fact, it was attempted to determine an "equivalent" delamination located on the middle surface of the beam, causing the same frequency shifts as the real defects existing in the structure. This inversion procedure is in the sequence applied on a cantilever, e.g. a more flexible structural element as compared to the simply supported beam, permitting thus higher eigenfrequency shifting. The cantilever also secures uniqueness of inversion, as it exhibits no symmetrical vibration modes.

In the sequence, the general case of an asymmetric composite beam with an interply delamination is studied both analytically and numerically, and the effect of the particular location of the delamination (with respect to length and thickness of the beam) and its size, based on the first four natural frequencies is analyzed. Results are given for a symmetric beam as well, taken as a special case of the general problem, by which extensional/bending stiffness B_{ij} vanishes.

Furthermore, the inversion technique for the identification of location and size of the delamination, using the shifting of the first two natural frequencies and based on the above assumptions, is presented along with the respective numerical procedure. Results

for a delaminated cantilever are given and compared to the ones produced for a simply supported beam. Conclusions and hints on design are finally given.

2. FREE VIBRATION OF A DELAMINATED BEAM: ANALYTICAL FORMULATION.
The analysis is based on Euler beam theory. Consider the laminated beam of Figure 1 with unit width, thickness t and length L.
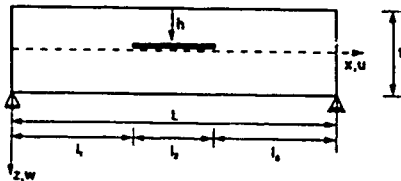
Figure 1: Geometry of the beam.

A delamination of length l_2 is located at a distance h from the upper surface and is extended parallel to the beam axis. The beam can be divided into four segments as shown in the free body diagram of Figure 2, each one characterized by an extensional stiffness A_i, an extensional/bending stiffness B_i, a bending stiffness D_i and a mass density per unit length m_i. When the beam is distorted from

Figure 2: Dynamic delamination model.

the undeflected position, self-equilibrating axial forces $P_{i(w)}$ in segments 2 and 3 develop. The governing differential equation for each segment is:

$$A_i u_{i,xx} - B_i w_{i,xxx} = 0 \tag{1}$$

$$D_i w_{i,xxxx} - B_i u_{i,xxx} = m_i \omega^2 w_i \tag{2}$$

The differential equations (1) and (2) form a coupled system. By differentiating equation (1) and substituting into equation (2), one obtains.

$$w_{i,xxxx} - m_i \frac{\omega^2}{\left[D_i - \frac{B_i^2}{A_i} \right]} w_i = 0 \tag{3}$$

Using the definitions:

$$k_i^4 = m_i \frac{\omega^2}{D_i^*} \qquad D_i^* = D_i - \frac{B_i^2}{A_i} \tag{4}$$

equation (3) yields:

$$w_{i,xxxx} - k_i^4 w_i = 0 \tag{5}$$

which has a general solution given by:

$$w_i(x) = \cosh(k_i x)C_{i1} + \sinh(k_i x)C_{i2}$$
$$+ \cosh(k_i x)C_{i3} + \sinh(k_i x)C_{i4} \qquad i = 1,....,4 \qquad (6)$$

where cosh, sinh, cos and sin, are the hyperbolic and circular trigonometric functions respectively. By substituting equation (6) into equation (1) and by solving the resulting nonhomogenous equation, the following complete solution is obtained:

$$u_i(x) = B_{i0} + B_{i1}x + \frac{B_i}{A_i}k_i \sinh(k_i x)C_{i1} + \frac{B_i}{A_i}k_i \cosh(k_i x)C_{i2}$$
$$- \frac{B_i}{A_i}k_i \sinh(k_i x)C_{i3} + \frac{B_i}{A_i}k_i \cosh(k_i x)C_{i4} \qquad i = 1, ..,4 \qquad (7)$$

Equations (6) and (7) possess twenty four unknown constants One can ignore rigid body motion with no loss of generality, and $B_{10} = B_{40} = 0$. The boundary conditions for a simply supported beam are:

For x=0

$$w_1 = 0 \qquad (8)$$

$$M_1 = 0 \qquad (9)$$

$$P_1 = 0 \qquad (10)$$

For x=l₁

$$w_1 = w_2 \qquad (11)$$

$$w_1 = w_3 \qquad (12)$$

$$\frac{dw_1}{dx} = \frac{dw_2}{dx} \qquad (13)$$

$$\frac{dw_1}{dx} = \frac{dw_3}{dx} \qquad (14)$$

$$V_1 = V_2 + V_3 \qquad (15)$$

$$M_1 = M_2 + M_3 + P_3\left(\frac{t}{2} - \frac{H}{2}\right) - P_2\left(\frac{t}{2} - \frac{h}{2}\right) \qquad (16)$$

$$u_2 = u_1 + \left(\frac{t}{2} - \frac{h}{2}\right)\frac{dw_1}{dx} \qquad (17)$$

$$u_3 = u_1 - \left(\frac{t}{2} - \frac{H}{2}\right)\frac{dw_1}{dx} \qquad (18)$$

$$P_2 + P_3 = 0 \qquad (19)$$

For x=l₁ +l₂

$$w_2 = w_4 \qquad (20)$$

$$w_3 = w_4 \qquad (21)$$

$$\frac{dw_2}{dx} = \frac{dw_4}{dx} \qquad (22)$$

$$\frac{dw_3}{dx} = \frac{dw_4}{dx} \qquad (23)$$

$$V_2 + V_3 = V_4 \qquad (24)$$

$$M_4 = M_2 + M_3 + P_3\left(\frac{t}{2} - \frac{H}{2}\right) - P_2\left(\frac{t}{2} - \frac{h}{2}\right) \qquad (25)$$

$$u_2 = u_3 + \frac{t}{2}\frac{dw_4}{dx} \qquad (26)$$

For x=L

$$w_4 = 0 \qquad (27)$$

$$M_4 = 0 \qquad (28)$$

$$P_4 = 0 \qquad (29)$$

By using the definitions of equivalent bending moment and of transverse and axial force:

$$M_i = -D_i \frac{d^2 w_i}{dx^2} + B_i \frac{du_i}{dx}$$

$$V_i = -\frac{d^3 w_i}{dx^3} \qquad (30)$$

$$P_i = A_i \frac{du_i}{dx} - B_i \frac{d^2 w_i}{dx^2}$$

the boundary conditions lead to a linear set of twenty two homogeneous equations with twenty two unknowns. In order to use dimensionless parameters, let m, t, L, D be mass per unit length, thickness, length and bending stiffness of the undelaminated beam respectively. By defining:

$$D_1 = D_4 = D, \quad m_1 = m_4 = m, \quad h + H = t$$
$$\overline{D}_2 = \frac{D_2}{D}, \quad \overline{D}_3 = \frac{D_3}{D}, \quad \overline{m}_2 = \frac{m_2}{m}$$
$$\overline{m}_3 = \frac{m_3}{m}, \quad \overline{h} = \frac{h}{t}, \quad \overline{H} = \frac{H}{t} \qquad (31)$$
$$\overline{A} = \frac{A_3}{A_2}, \quad \overline{R}_2 = \frac{A_2 s^2}{12D}, \quad \overline{R}_3 = \frac{A_3 s^2}{12D}$$
$$\overline{l}_2 = \frac{l_2}{L}, \quad \overline{s}_1 = \frac{l_1}{L}, \quad \overline{s}_2 = \frac{l_1 + l_2}{L}$$

$$s = \frac{x}{L}, \quad a_i^4 = \frac{\overline{m}_i}{\overline{D}_i}, \quad \overline{k} = \frac{m\omega^2 L^4}{D^*} \qquad (32)$$

and substituting into the boundary conditions, an equivalent homogeneous set of the twenty two equations results. The first three and the last of the boundary conditions yield $C_{11} = C_{13} = B_{11} = B_{14} = 0$ The final set of homogeneous equations is next given in matrix form:

$$[Q_{ij}(\overline{k})][V_j] = [0] \qquad (33)$$

where $[Q_{ij}]$ contains the coefficients of the eighteen unknowns, components of the vector $[V_j]$.

For a non trivial solution of the set, the determinant of the latter must vanish. When for two values of $\overline{k}$ the determinant changes sign, a solution lies within the respective interval. The exact solution is obtained by a bisection method.

Figure 3 shows the degradation of the first eigenfrequency for a $(90/0)_{10T}$ composite beam against delamination length for $s=0.5$ and for different distances of the delamination from the neutral axis of the beam. As this distance increases, the degradation increases too. These results are in good agreement with the relevant results by Wang et al. [7].

Figure 4 presents the degradation of the first eigenfrequency plotted against the delamination position along the x-axis, for
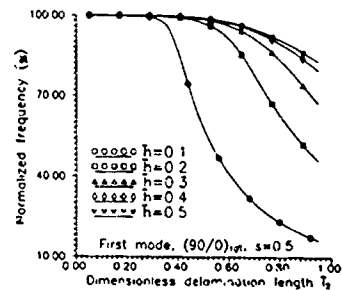
Figure 3: First frequency mode for various heights of delamination $\overline{h}$ versus its length $\overline{l}_2$

T_2=0.25 and for various distances from the neutral axis. As the latter decreases, the degradation of the natural frequency increases and this effect is more pronounced if the delamination is located closer to the neutral axis of the beam.

As it is evident from these two figures, the position of delamination "s" does not affect the eigenfrequencies as drastically as its length.

Figures 5 and 6 are analogous to the previous ones, but for a
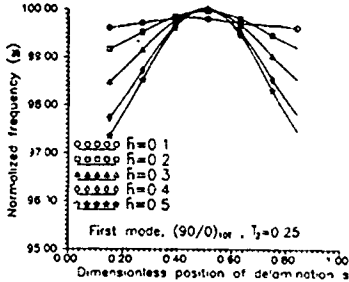
Figure 4: First frequency mode for various heights of delamination $\bar{h}$ versus its position s.

symmetric stacking sequence $(0/90_2/0)_{10T}$ The eigenfrequency for a symmetric laminate is not as sensitive towards delamination as the asymmetric one, since the degradation is probably less due to the absence of coupling.

Figures 7 and 8 show the degradation of natural frequencies for the first four modes of a $(90/0)_{10T}$ laminate as a function of length and position of a delamination located on the midplane of the beam. Obviously the influence of the delamination on the various
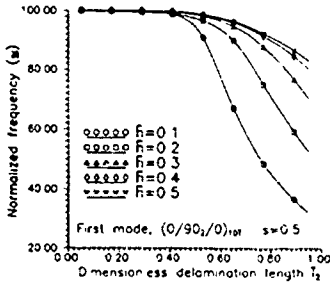
Figure 5: First frequency mode for various heights of delamination $\bar{h}$ versus its length T_2.
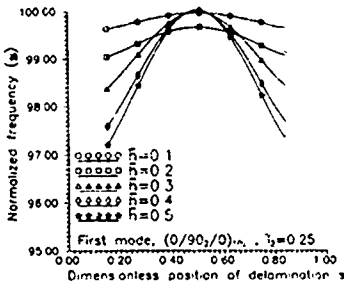
Figure 6: First frequency mode for various heights $\bar{h}$ versus delamination position s

vibrating modes is different. Furthermore, the diagram 8 is symmetric with respect to the middle point of the beam (s=0.5) and
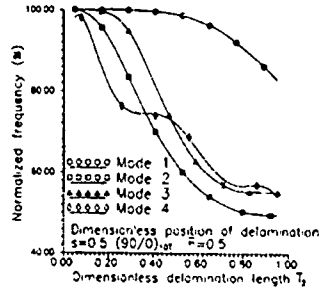
Figure 7: The first four modes for a $(90/0)_{10T}$ versus delamination length T_2 when it extends on the neutral beam axis.

this proves that the delamination with constant length T_2 has the same effect on the eigenfrequencies if located for example at s=0.2 or s=0.8.

3. FINITE ELEMENT APPROACH.

Consider a laminated composite beam situated just above the x-y plane [8-10] (Fig. 9). The in-plane and transverse displacements (shear deformation is also considered) are
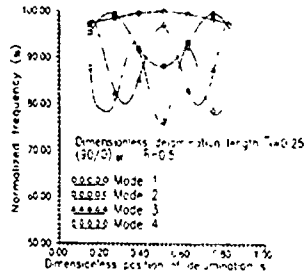
Figure 8 The first four modes for a $(90/0)_{10T}$ versus delamination position s when it extends on the neutral beam axis.

$$u(x,z) = u_o(x) + z \, \psi(x) \qquad (34)$$

$$w(x,z) = w(x) \qquad (35)$$

where $u_o(x)$ is the axial displacement of points in the plane and
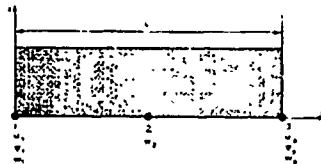
Figure 9 Beam finite element with nodes offset to the bottom side.

$\psi(x)$ is the rotation about the y-axis The transverse displacements $w(x)$ are assumed to be constant throughout the thickness of the laminate. The strains can be derived as

$$\varepsilon_{xx} = \frac{\partial u}{\partial x} = \varepsilon_1^o + z \, K_1^o$$

$$\gamma_{xz} = \frac{\partial u}{\partial z} + \frac{\partial w}{\partial x} = \varepsilon_5^o \qquad (36)$$

The force and moment resultants are defined as

$$[N, M, Q] = \int_0^h [\sigma_1, z\,\sigma_1, \sigma_5]\, dz \qquad (37)$$

Assuming no bending-twisting and extension-twisting coupling in the laminate and a state of plane strain parallel to the x-z plane, the stress-strain relations for a layer are of the form:

$$\sigma_{zz} = \sigma_1 = \bar{Q}_{11}\varepsilon_{zz}, \quad \tau_{zz} = \sigma_5 = \bar{Q}_{55}\gamma_{zz} \qquad (38)$$

The force and moment resultants are given by the relation:

$$\begin{bmatrix} N \\ M \\ Q \end{bmatrix} = \begin{bmatrix} A_{11} & B_{11} & 0 \\ B_{11} & D_{11} & 0 \\ 0 & 0 & A_{55} \end{bmatrix} \begin{bmatrix} \varepsilon_1^o \\ k_1^o \\ \varepsilon_5^o \end{bmatrix} \qquad (39)$$

where the stiffness coefficients of the laminate are defined as

$$[A_{11}, B_{11}, D_{11}, A_{55}] = \int_0^h [\bar{Q}_{11}, z\,\bar{Q}_{11}, z^2\bar{Q}_{11}, k\bar{Q}_{55}]\, dz \qquad (40)$$

In the above equations $k_1^o = \psi_{,x}$ is the beam curvature and the shear correction factor k may be assumed equal to 5/6. The above relations refer to a laminate lying above the x-y plane. For a laminate below the x-y plane, the lower and upper limits of integration in equations (37) through (40) are from -h to 0.

The differential equations of motion for a beam bending problem in terms of force and moment resultants are given as follows:

$$\frac{\partial N_1}{\partial x} = I_1 \ddot{u}_o + I_2 \ddot{\psi}_x$$

$$\frac{\partial M_1}{\partial x} - Q_1 = I_2 \ddot{u}_o + I_3 \ddot{\psi}_x \qquad (41)$$

$$\frac{\partial Q_1}{\partial x} = I_1 \ddot{w}_o$$

where N_1, Q_1 and M_1 are the resultant axial and shear forces and M_1 the resultant bending moment respectively. Also I_1, I_2, I_3 are defined:

$$I_1 = \int_0^h \rho\, dz, \quad I_2 = \int_0^h \rho z\, dz$$

$$I_3 = \int_0^h \rho z^2 dz \qquad (42)$$

Substituting the appropriate relations in equations (41) and applying the Rayleigh-Ritz method to the final equations, the finite element equations assume the form:

$$\left\{ \begin{bmatrix} [K_{11}] & [K_{12}] & [K_{13}] \\ & [K_{22}] & [K_{23}] \\ \text{sym.} & & [K_{33}] \end{bmatrix} - \omega^2 \begin{bmatrix} [M_{11}] & [M_{12}] & [M_{13}] \\ & [M_{22}] & [M_{23}] \\ \text{sym.} & & [M_{33}] \end{bmatrix} \right\} \begin{bmatrix} u \\ \psi \\ w \end{bmatrix} = \begin{bmatrix} 0 \\ 0 \\ 0 \end{bmatrix} \qquad (43)$$

The elements of the mass and stiffness matrices are given analytically in the Appendix.

The element used for the FEM analysis has seven degrees of freedom and its shape functions are given in the Appendix. It is interesting to note that if one combines stiffness and mass matrices of the top and bottom element, the corresponding matrices of a conventional beam element with nodes at midplane is recovered.

By using this type of approach, the laminated composite beam is assumed to consist of two layers of beam elements linked together by common nodes in the undelaminated region. No friction between the upper and the lower sublaminates exists. In the delaminated region the relative nodes of the upper and lower layers were linked by means of rod elements transmitting only compression between the double nodes only, to simulate the contact forces developing in the delaminated area. A comparison between the

results of the analytical and the numerical model for the first two vibrating modes of a (90/0)$_{10T}$ simply supported symmetric composite beam are presented in figures 10 and 11. Differences between these two diagrams are due to the additional shear corrections terms in the finite element analysis
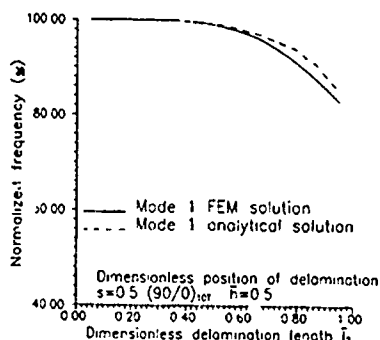
Figure 10. Comparison of analytical and numerical results for the first mode of a simply supported beam (90/0)$_{10T}$.
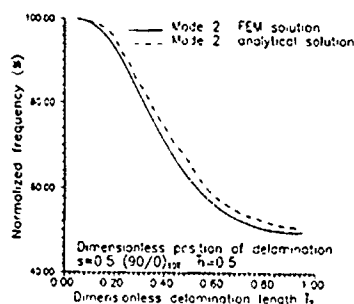
Figure 11. Comparison of analytical and numerical results for the second mode of a simply supported beam (90/0)$_{10T}$.

4. INVERSION OF THE PROBLEM.

This section aims at the identification of the delamination position and size using the eigenfrequency degradation. It is a typical inverse problem and as such is non-linear and intrinsically ill-posed. On the other hand, observing the respective figures of the simply supported delaminated beam, it is obvious that another reason to lose the uniqueness of solution of the inverse problem is the symmetry of these diagrams, due to the way that the vibrating beam is supported.

To overcome this difficulty and to increase the accuracy of the inversion, a cantilever beam is considered. This is a more flexible structure than the simply supported beam and possesses lower eigenfrequencies, while its vibrating modes are asymmetric. The geometry of the structure is given in Figure 12.

The formulation is identical as for the simply supported beam with the necessary modifications of the boundary conditions. In Figure 13 the first four normalized eigenfrequencies of a delaminated composite beam with stacking sequence (90,± 45,0)$_{2S}$ are given, with a midplane delamination centred at s=0.5, as a function of its dimensionless length $\bar{l}_2$ while Figure 14 shows the simply supported beam. It is worth noticing that the degradation of the first mode is higher for the cantilever beam.

Figure 15 shows the first four normalized eigenfrequencies of the previous beam with a delamination length $\bar{l}_2$=0.25 as a function of the dimensionless delamination position s. In Figure 16 the corre-
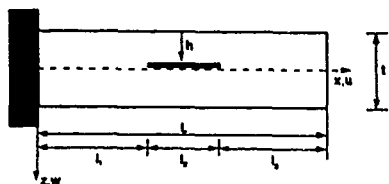
Figure 12: Geometry of the cantilever beam.
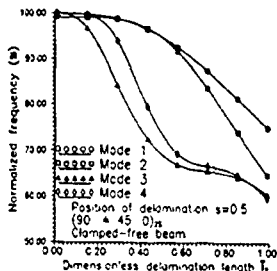
Figure 13: The first four modes for a cantilever $(90,\pm 45,0)_{2s}$ beam versus delamination length $\bar{l}_2$ when it extends on the neutral axis.
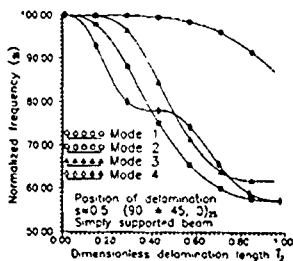
Figure 14: The first four modes for a simply supported $(90,\pm 45,0)_{2s}$ beam versus delamination length $\bar{l}_2$ when it extends on the neutral axis.

sponding diagram for the simply supported beam is presented. Comparing these two diagrams it is evident that the curves for the cantilever beam are asymmetric due to its asymmetric vibrating modes.

Going back to the inverse problem, a symmetric cantilever beam is considered and the shifting of two distinct eigenfrequencies is used to develop an algorithm for the identification of the delami-
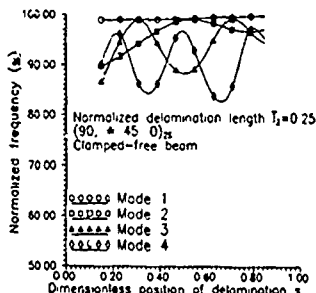
Figure 15: The first four modes for a cantilever $(90,\pm 45,0)_{2s}$ beam versus delamination position s when it extends on the neutral axis.
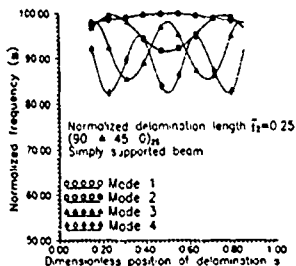
Figure 16: The first four modes for a simply supported $(90,\pm 45,0)_{2s}$ beam versus delamination position s when it extends on the neutral axis.

nation position and size. It is assumed that the eigenfrequency shifting measured is due to one delamination only and no other sources contribute to the shifts measured, therefore, the proposed technique can determine an "equivalent" delamination producing the same degradation of the natural frequencies as other possibly existing imperfections.

The proposed algorithm is based on the solution of the direct problem, where the eigenfrequency degradation depends on the delamination position and size as well as on the geometrical and physical characteristics of the beam. In the inversion step, again, the physical and geometrical characteristics of the beam are known, as well as the degradation of the eigenfrequencies of the first two or three modes which can be measured.

Accordingly, a non linear algebraic set thus formed is solved by a typical Newton-Raphson technique, for which initial values for the unknown delamination position and size are required. These values can be obtained from nomographs for a homogeneous and isotropic beam with identical geometrical characteristics of the beam considered. Such diagrams are presented in Figures 17 through 22 for the first, second and third vibrating modes. It is obvious that for small delaminations (shorter than 10% of the total length of the beam), no satisfactory accuracy can be obtained, as the initial values of delamination characteristics do not vary within this region. On the contrary, this method converges fast and
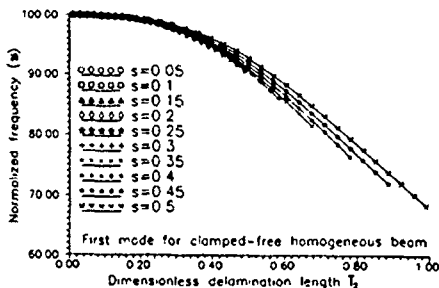
Figure 17: First mode for clamped-free homogenous beam for various positions of delamination (s–0.05 through s–0.5).

with remarkable accuracy for initial values not too close to the solution for delamination length over 15% of the total length of the beam.

Normally any couple of eigenfrequencies may be used for the solution of the inverse problem, but the first two eigenfrequencies are recommended, since their experimental determination can be obtained with good accuracy. A schematic presentation of the total procedure followed for the inversion of the problem is given in the following:
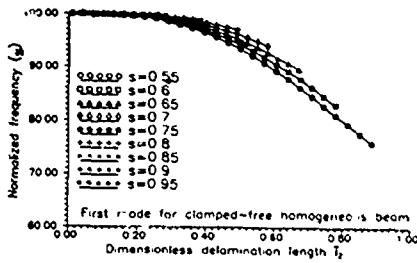
Figure 18: First mode for clamped-free homogeneous beam for various positions of delamination (s-0.55 through s-0.95).
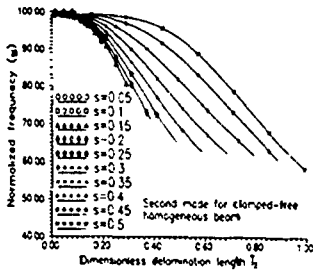
Figure 19: Second mode for clamped-free homogeneous beam for various positions of delamination (s-0.05 through s-0.5).
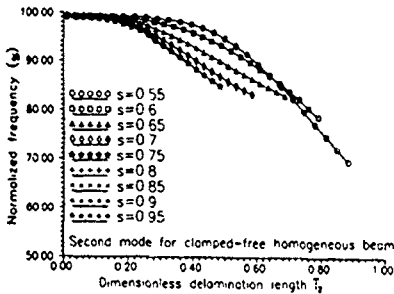
Figure 20: Second mode for clamped-free homogeneous beam for various positions of delamination (s-0.55 through s-0.95).
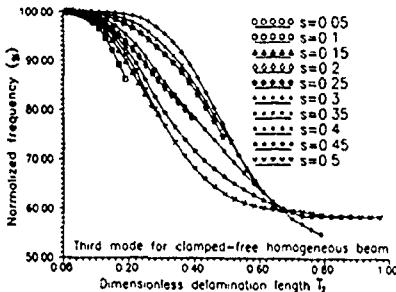
Figure 21: Third mode for clamped-free homogeneous beam for various positions of delamination (s-0.05 through s-0.5).
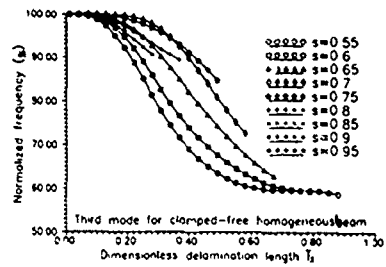
Figure 22 Third mode for clamped-free homogeneous beam for various positions of delamination (s-0.55 through s-0.95).

a. Experimental determination of the first two eigenfrequencies.

b. Charts of frequency shifting for a homogeneous beam.

c. Initial values.

d Start Newton-Rapshon procedure.

$$a_{ij} = \frac{\partial f_i}{\partial x_j}, \quad i,j = 1,2$$

e. Determination of inverse Jacobian matrix.

f. Multiplication of J^{-1} with matrix $[F_1, F_2]^T$.

g. Solution.

$$x_i(m) = x_i(m-1) - J^{-1}\begin{bmatrix} F_1 \\ F_2 \end{bmatrix}, \quad m = \text{iteration}$$

h. Results.

For example, if a degradation of 13% for the first mode and 36% for the second mode are measured for a symmetric cantilever beam with stacking sequence $(90, \pm 45, 0)_{2s}$, then by using Figures 17 and 19, initial values of the delamination position and size are obtained as $s=0.35$ and $l_2=0.58$. Using the above algorithm, results for $s=0.29$ and $l_2=0.61$ are obtained. The solution of the corresponding direct problem for this beam by introducing the same eigenfrequency degradation leads to delamination characteristics $s=0.3$ and $l_2=0.6$. A remarkably good accuracy achieved with three iterations only.

A necessary remark concerning the figures 20, 21 and 22 is that the intersection of the curves in the relative diagrams is due to numerical errors. The respective physical problem, as described by the equations (1) and (2) is well posed and exhibits unique solution.

5. CONCLUSIONS
It was shown, both analytically and numerically, that delaminations developing in a laminated composite beam, either symmetric or asymetric, undergoing flexural vibrations, may cause considerable degradation, i.e. decrease of its natural frequencies, depending on the delamination location and size. In fact, with increasing delamination length, increased degradation of the natural frequencies appears. On the other hand, if the delamination is located in areas where the mode shape displays high curvature, degradation is very low, while in the vicinity of areas with high shear force the degradation assumes maximum values. Finally the degradation increases with increasing distance of the delamination from the neutral axis.

Both the analytical and numerical formulations proposed are considering asymmetric, non balanced laminates, containing bending/extensional stiffness coupling terms B_{ij}. Results for symmetric laminates have been produced as a particular case of the

general problem. By comparison of analytical and numerical results, it is evident that the numerical model yields higher frequency degradation due to the presence of additional shear terms.

Finally an inverse method to identify an existing delamination, based on the solution of the direct problem, is proposed. The method evaluates the characteristics of an equivalent delamination located at the neutral axis of the beam, although the real damage may be different. By correlating this method with experimental values of internal damping of a structure may provide a powerful tool for the detrmination of the remaining life of a damaged composite structure.

REFERENCES

1. A.M. Garg, "Delamination-A damage mode in composite structures", Engineering Fracture Mechanics, Vol. 29, No 5, 1988, pp. 557-584.

2. K.L. Reifsnider, F.G. Henneke, W.W. Stinchcomb and J.L. Duke, Proceedings, IUTAM Conference, Blacksburg, Virginia, 1982, Pergamon Press, New York, 1983, pp. 339-390.

3. J.J. Tracy, D.J. Dimas and G.C Pardoen, "The effect of impact damage on the dynamic properties of laminated composite plates", Proceedings, 5th International Conference on Composite Materials, San Diego, CA (June 1985).

4. P. Cawley and R.D. Adams, " The location of the defects in structures from measurements of natural frequencies" Journal of Strain Analysis, vol. 14, No 2, 1979, p.49.

5. P. Cawley and R.D. Adams, "A vibration technique for non-destructive testing of fibre composite structures", Journal of Composite Materials, Vol. 13, 1979, p 161.

6. J.J. Tracy and G.C. Pardoen, "Effect of delamination on the natural frequencies of composite laminates", Journal of Composite Materials, Vol. 23, No. 4, 1989, pp 1200-1215

7. J.T.S Wang, Y.Y.Liu and J.A Gibby, "Vibrations of split beams", Journal of Sound and Vibration, Vol 84, No. 4, 1982, pp 491-502.

8. B.V. Sankar, "A finite element for modeling delaminations in composite beams", Computers and Structures, Vol. 28, No. 2, 1991, pp. 239-246.

9. S Hu, B.V. Sankar and C.T. Sun, "A finite element study of dynamic delamination growth in composite laminates", AIAA paper No. 89-1301-CP, Collection of Technical Papers presented at the 34th SDM Conference, Part 3, 1989, pp. 1250-1255.

10. B.V. Sankar and M A. Pinheiro, "An offset beam finite element for fracture analysis of delaminations", AIAA paper No 90-1024-CP 31st Structures, Structural Dynamics and Materials Conference, Long Beach, California, April 1990.

Appendix

The stiffness matrix is.

$$k_{ij}^{11} = \int_{x_1}^{x_2} \left[A_{11} \frac{\partial N_i}{\partial x} \frac{\partial N_j}{\partial x} dx \right],$$

$$k_{ij}^{12} = \int_{x_1}^{x_2} \left[B_{11} \frac{\partial N_i}{\partial x} \frac{\partial N_j}{\partial x} dx \right], \quad k_{ij}^{13} = 0$$

$$k_{ij}^{22} = \int_{x_1}^{x_2} \left[D_{11} \frac{\partial N_i}{\partial x} \frac{\partial N_j}{\partial x} dx \right] + \int_{x_1}^{x_2} [A_{55} N_i N_j dx]$$

$$k_{ij}^{23} = \int_{x_1}^{x_2} [A_{55} N_i \frac{\partial N_j}{\partial x} dx]$$

$$k_{ij}^{33} = \int_{x_1}^{x_2} [A_{55} \frac{\partial N_i}{\partial x} \frac{\partial N_j}{\partial x} dx]$$

The mass matrix is:

$$M_{ij}^{11} = \int_{x_1}^{x_2} [I_1 N_i N_j dx]$$

$$M_{ij}^{12} = \int_{x_1}^{x_2} [I_2 N_i N_j dx], \quad M_{ij}^{13} = 0$$

$$M_{ij}^{22} = \int_{x_1}^{x_2} [I_3 N_i N_j dx], \quad M_{ij}^{23} = 0$$

$$M_{ij}^{33} = \int_{x_1}^{x_2} [I_1 N_i N_j dx]$$

To avoid shear locking the shape functions for transverse displacement and axial displacement and rotation are different. So:

$$w(x) = w_1 N_1 + w_2 N_2 + w_3 N_3$$
$$u(x) = u_1 N_4 + u_3 N_5$$
$$\psi(x) = \psi_1 N_4 + \psi_2 N_5$$

where

$$N_1 = \left[1 - \frac{2x}{L} \right] \left[1 - \frac{x}{L} \right]$$

$$N_2 = \frac{4x}{L} \left[1 - \frac{x}{L} \right]$$

$$N_3 = \frac{x}{L} \left[\frac{2x}{L} - 1 \right]$$

$$N_4 = \left[1 - \frac{x}{L} \right]$$

$$N_5 = \frac{x}{L}$$

The final stiffnesses are 7x7 and are for the above the x-y plane. For the below the x-y plane the integrating limits are from -h to 0.

The laminate's material for the graphs was $AS_4/3501-6$ graphite epoxy.

INVESTIGATION OF THE BOND STRENGTH OF A DISCRETE
SKIN-STIFFENER INTERFACE

by
H.G.S.J. Thuis and J.F.M. Wiggenraad
National Aerospace Laboratory
P.O. Box 90502
1006 BM Amsterdam
The Netherlands

SUMMARY
This paper presents the results of an experimental study on the effects of several design parameters on the strength of a skin-stiffener interface. Desing parameters which are considered are skin and stiffener laminate properties and the .'idth of the bond layer. Test specimens consisting of a blade type stiffener secondarily bonded to skin laminate were fabricated. The specimens were tested by lateral tension tests, four-point bending tests and pull off tests. Calculation: were made with the numerical program BONDST. The test results are compared with each other and with the calculated results. Conclusions are drawn and design guidelines are provided.

LIST OF SYMBOLS

EA_{skin}	: Inplane stiffness of the skin laminate
D_{skin}	: Bending stiffness of the skin laminate.
t_{skin}	: Thickness of the skin laminate.
$EA_{stiffener}$	: Inplane stiffness of the stiffener laminate.
$D_{stiffener}$	: Bending .tiffness of the stiffener laminate.
$t_{stiffener}$	. Thickness of the stiffener flange.
t_{blade}	: Thickness of the stiffener blade.
E_c	: Modulus of the bond layer.
G_c	: Shear modulus of the bond layer
t_c	: Thickness of the bond layer.
L	: Width of the stiffener flange.
H	: Height of the stiffener
t	: Ply thickness.
E_x	' Longitudinal modulus.
E_y	: Lateral modulus.
G_{xy}	. Shear modulus
ν_{12}, ν_{21}	: Poisson's ratio.
F	: Lateral tension force.
M	: Bending moment.
P	: Pull off load.
Sk	: Skin configuration
St	: Stiffener configuration.

1. INTRODUCTION
Stiffened skin panels of composite materials can be configured either as integral cocured concepts, where the stiffener attachements intermingle with the skin plies, or as separate, often precured skin and stiffeners which are connected by a discreet bond layer In the latter case failure of a stiffenend panel may well be governed by the strength of the skin-stiffener interface
When designing a stiffened panel one can choose several design parameters which determine the strength and stiffness of that panel (Refs. 1 to 6). The strength of the skin- stiffener interface, however, is influenced by the chosen design parameters and the loading conditions.
In this paper the results of a test programme are presented. The tests were carried out on specimens which consist of a blade type stiffener secondarily

bonded to a skin laminate
In the specimens the following parameters were varied. skin and stiffener laminate properties and the stiffener flange width. The specimens were tested in three different ways.

1) Lateral tension tests.
2) Four - Point bending tests.
3) Pull Off tests.

The test results are compared to each other, and with results obtained from the computer program BONDST. This program models a skin - stiffener combination into a two dimensional model The program can determine (with numerical methods) the peel stress and the transverse shearing stress in the bond layer
The purpose of this investigation is to give a designer a database from which he can choose an optimal skin-stiffener combination for a given loading case.

2. TEST PROGRAMME

2 1 Test specimens
The test specimens consisted of a blade-type stiffener secondarily bonded to a skin laminate (see Fig. 1). The dimensions of the specimens were 250 * 50 mm.
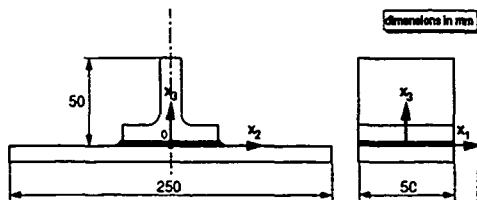
Fig 1 Dimensions of the test specimens and the definitions of the axis

The test specimens were made of Fibredux 6376/T400H with the following properties:

1) Ply thickness. $t - 0$ 181 mm
2) $E_x - 137000$ MPa (tension)
3) $E_x - 124000$ MPa (compression).
4) $E_y - 9500$ MPa (tension).
5) $E_y - 9000$ MPa (compression).
6) $G_{xy} - 5100$ MPa
7) $\nu_{12} - 0.3$.

2.2 Design parameters considered
'n a skin-stiffener combination the following design parameters can be distinguised (see Fig 2)

1) The inplane stiffness of the skin EA_{skin}
2) The bending stiffness of the skin D_{skin}

3) The thickness of the skin: t_{skin}.
4) The inplane stiffness of the stiffener. $EA_{stiffener}$.
5) The bending stiffness of the stiffener: $D_{stiffener}$.
6) The thickness of the stiffener flange: t_{flange}.
7) The thickness of the stiffener blade t_{blade}.
8) The modulus of the bond layer: E_c.
9) The shear modulus of the bond layer: G_c.
10) The thickness of the bond layer: t_c.
11) The width of the stiffener flange L
12) The height of the stiffener: H.

To limit the number of design parameters the stiffeners were bonded to the skin laminates with the same adhesive while the thickness of the bond layer was equal for all the specimens and all the stiffeners had the same height.
With the afore mentioned design parameters, different skin laminates and stiffener laminates can be defined. With these skin and stiffener laminates different skin-stiffener combinations can be made

2.3 Skin laminates selected
For this investigation the following skin laminates were defined which differed from each other by laminate structure and thickness.

Skin 1a
Skin Laminate [-45,45,-45 45,-45 45,45,-45 45 -45]
Skin thickness 1 61 mm
Skin 1b
Skin Laminate [-45,0,45,0,-45,45 0,45 0 -45]
Skin Thickness 1 81 mm
Skin 2a
Skin Laminate [-45,45,-45,45,-45,45,-45,45 -45,45]s
Skin Thickness 3 62 mm
Skin 2b
Skin Laminate [45,0,-45,0,45,0,-45,0,45 0 0,-45,0, -45,0,45,0,-45 0,45]
Skin Thickness 3 62 mm

flange,thickness of the stiffener blade and width of the stiffener flange (see Fig. 2). The thickness of the blade of a stiffener was varied by adding a 'core laminate' in the blade (see Fig. 3).

Stiffener 1a
Stiffener laminate [0,45,0,-45,0,90,0,-45,0,45,0]
Thickness of the flange 1 991 mm
Thickness of the blade 3 982 mm
Width of the blade 44 0 mm
Stiffener 1b
Stiffener laminate [0,45,0,-45,0,90,0,-45,0,45,0]
Core laminate [0₅]
Thickness of the flange 1 991 mm
Thickness of the blade 4 887 mm
Width of the blade 44 905 mm
Stiffener 1c
Stiffener laminate [0,45,0,-45,0,90,0,-45,0,45,0]
Core laminate [0,-45,0,45,0]₂
Thickness of the flange 1 991 mm
Thickness of the blade 5 792 mm
Width of the blade 45 81 mm
Stiffener 2a
Stiffener laminate [0 0,45,0,-45,0,90,0,-45,0,45,0,0]
Thickness of the flange 2 353 mm
Thickness of the blade 4 706 mm
Width of the blade 50 0 mm
Stiffener 2b
Stiffener laminate [0,0,45 0 -45 0,90,0,-45,0,45,0,0]
Core laminate [0,-45,0,45,0]₂
Thickness of the flange 2 353 mm
Thickness of the blade 6 516 mm
Width of the blade 51 81 mm
Stiffener 3a
Stiffener laminate [0,45,-45,45 0,-45,0,90 0,-45,0,45, -45 45 0]
Thickness of the flange 2 715 mm
Thickness of the blade 5 43 mm
Width of the blade 44 0 mm
Stiffener 3b
stiffener laminate [0,45,-45,45,0,-45,0,90,0,-45,0,45 -45 45 0]
Thickness of the flange 2 715 mm
Thickness of the blade 5 43 mm
Width of the blade 56 0 mm

2.4 Stiffeners selected
For this investigation the following stiffeners were defined, which differed from each other by laminate structure, thickness of the stiffener laminate structure.
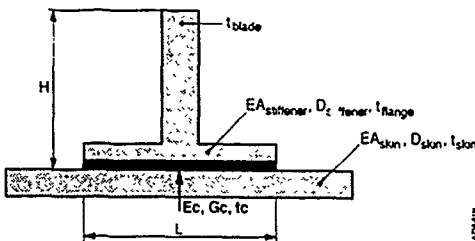
Fig 2 Design parameters in a skin - stiffener combination
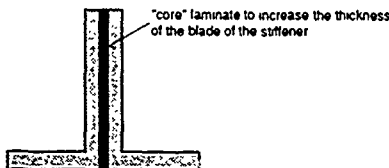
Fig 3 Increasing the thickness of the stiffener blade by adding a "core" laminate

2.5 Specimen configurations tested
With the different skin and stiffener types mentioned above the following skin-stiffener combinations were made (Sk means skin, St means stiffener):

	Sk1a	Sk1b	Sk2a	Sk2b
St1a				
St1b				
St1c				
St2a				
St2b				
St3a				
St3b				

3. FABRICATION OF THE TEST SPECIMENS

The skins and stiffeners were fabricated seperately and cured in an autoclave at a temperature of 177 °C and a pressure of 7 bar
The stiffeners were fabricated on steel molds The molds were build up from two form blocks and a caul plate (see Fig. 4). The stiffeners were fabricated from two angle shaped laminates which were laminated on the two form blocks. The two form blocks were then assembled and a filler made of 0° prepreg was placed. Two rubber strips were positioned along the flanges of the stiffeners and the caul plate was positioned. The rubber strips prevented the matrix to flow into the vacuum bag during the cure in the autoclave and at the same
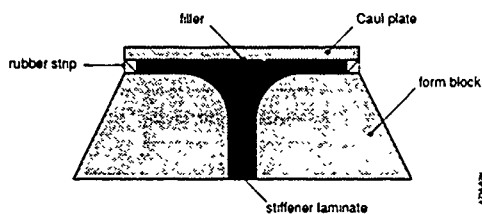
Fig 4 Assembled steel mould

Fig 6 Failure in a specimen during the lateral tension tests

time allow the caul plate to provide the necessary pressure on the stiffener laminate After curing the stiffeners were milled to the desired dimensions.
The stiffeners and skin laminates were then bonded together with the adhesive FM 300 K, a modified epoxy film adhesive The thickness of the bond film was 0 2 mm The skin stiffener combinations were then cut into test specimens (see Fig 1)

4. TESTING OF THE SPECIMENS

4.1 Introduction
Three different tests were performed
1) Lateral tension tests (see Fig 5)
2) Four-Point bending tests (see Fig 8)
3) Pull off tests (see Fig 11)

The strength of the different skin-stiffener combinations was determined by loading the specimens to failure For each skin-stiffener combination nine specimens were made Each skin-stiffener combination could be tested three times for each load case, to establish the scatter

4.2 1 Lateral tension tests
In the lateral tension test the load is applied to the skin laminate (see Fig. 5) The tests were performed with a with a velocity of 1mm/min During the tests the applied load and the displacement of the grips of the bench were measured
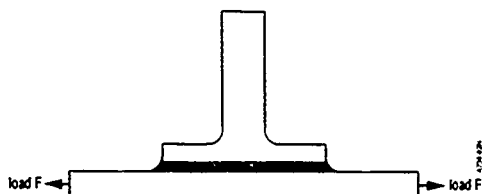
Fig 5 Loading condition during the lateral tension test

All the test specimens showed the following failure behaviour Because of the exentricity caused by the stiffener the specimens show an increasing curvature as the 'oad increases At a certain load level a crack starts to grow at the end of the stiffener flange This crack initiates in the fillet and then propagates in the bond layer or in the top layers of the skin laminate (see Fig 6) The crack propagates while the applied load still increases. At a certain load level the stress in the skin laminate reaches the failure stress of the skin laminate and the specimen fails
Failure initiation (when the crack propagates in the bond layer or in the top layers of the skin laminate) of the specimens may be caused by the
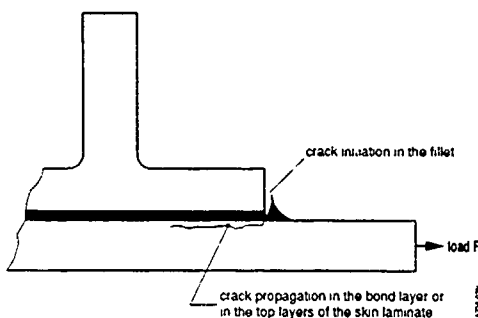
following stress situations

1) Shear stress caused by a lateral tension force

The skin is loaded in tension. The stiffener will be loaded by shear of the bond layer The shear stresses will be maximum at the edge of the stiffener flange (see Fig 7) These maximum shear stresses will increase with increasing stiffness ratio of stiffener flange and skin
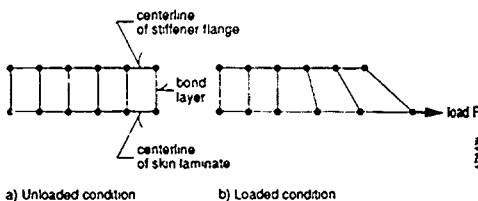
Fig 7 Shear stresses caused by a tensile force F

2) Peel stresses caused by out of plane bending

The exentric position of the stiffener causes secondary bending while loading the skin laminate in tension This bending causes negative (compressive) peel stresse in the bond layer.

3) Shear stresses caused by a mismatch between the Poisson's ratios of the skin and stiffener laminates

The skin and stiffener laminates can have different Poisson's ratios Because of these different Poisson's ratios different transverse strains occur in the skin and stiffener laminates The bond layer has to bridge these different strains which causes shear stresses in the bond layer The influence of these shear stresses on the strength of the skin-stiffener interface will increase as the ratio between the Poisson's ratios of the skin and stiffener laminates increases.

4 2 2 Lateral tension test results
In the following table the test results of the lateral tension tests can be seen During the tests the applied load increased while the crack propagated. However, the specimens were considered to be failed when the crack propagated from the fillet into the bond layer or into the top layers of the skin laminate Therefore in the table the load is the tensile load at which the crack propagates into the bond layer or into the top layers of the skin laminate

	E_{2skin}/E_{2stiff}	$\nu_{21skin}/\nu_{21stiff}$	Width of flange (mm)	$D_{22skin}/D_{22stiff}$	Load F (kN)
Sk1aSt1a	0.52	5 07	44 0	1.48	11 8
Sk1aSt1b	0 52	5 07	44 095	1 48	12 0
Sk1aSt2a	0 48	6 22	50 0	1 16	12 5
Sk1aSt2b	0 48	6 22	51 81	1 16	10 7
Sk1bSt1a	0 71	1 72	44 0	1 08	15 7
Sk1bSt1b	0 71	1 72	44 095	1 08	17 3
Sk1bSk2a	0 66	2 1	50 0	0 84	15 3
Sk1bSt2b	0.66	2 1	51 81	0 64	13.9
Sk2aSt1a	1 04	5 07	44 0	11 9	25 0
Sk2aSt1c	1 04	5 07	45 81	11 9	23 3
Sk2aSt3a	0 76	3 17	44 0	3 5	24 3
Sk2aSt3b	0 76	3 17	56 0	3 5	24 2
Sk2bSt1a	1 33	1 32	44 0	7 9	28 8
Sk2bSt1c	1 33	1 32	45 81	7 9	28 0
Sk2bSt3a	0 97	0 83	44 0	2 4	31 0
Sk2bSt3b	0 97	0 83	56 0	2 4	31 7

From these test results the following conclusions can be drawn

The width of the stiffener flange has no influence on the strength of a specimen (compare Sk2aSt3a with Sk2aSt3b and Sk2bSt3a with Sk2bSt3b)

The ratio between the bending stiffness of the skin and the bending stiffness of the stiffener flange and the mismatch between the Poisson's ratios of the skin and stiffener laminates have hardly any influence on the strength (see for instance Sk2aSt1a and Sk2aSt3a).

Specimens with skin laminates Sk1b and Sk2b can carry more load than their count parts with skin laminates Sk1a and Sk2a The reason for this is that the specimens with skin laminates Sk1b and Sk2b have a larger skin-stiffener stiffness ratio than their counter parts with skin laminates Sk1a and Sk2a.
The thickness of the blade of the stiffener has no noticible influence on the strength of the specimens (compare Sk2bSt1a with Sk2bSt1c)

It can be concluded that for this loading case the skin laminate should have a larger inplane stiffness (F_2A) than the stiffener laminate

4.3.1 Four-Point Bending tests
A four point bending test set up was used to load the specimens with a constant bending moment over the width of the skin-stiffener interface The dimensions of the test set up can be seen in figure no.8. The tests were performed with a velocity of 1 mm/min. During the tests the applied load and the displacements of the grips were measured

The specimens all showe1 a simular failure behaviour.
When the applied moment increases the specimens show an increasing curvature At a certain load level a crack initiates in the fillet of the bond layer As the bending moment increases the crack propagates. In the specimens with a skin laminate thickness of 1.81 mm the cracks propagate in the bond layer. In the specimens with a skin thickness of 3.62 mm the cracks propagate either in the bond
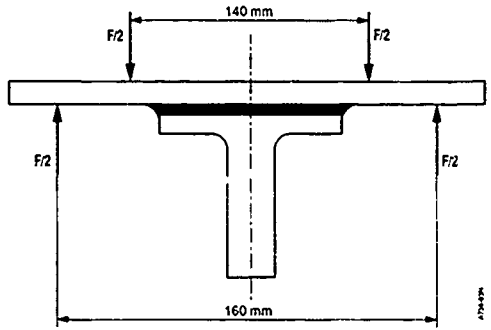
Fig 8 Locations of the applied forces during the four-point bending test

layer or in the top layers of the skin laminate As the crack propagates the specimens still are able to carry more load while the stiffness of the specimens decreases At a certain load level the stiffener is separated from the skin laminate and the applied bending moment drops to a lower level

Failure of the specimens may be caused by the following stress situations:

1) Peel stresses caused by the bending moment.

Bending of the specimen introduces peel stesses in the bond layer which will be maximum at the edge of the stiffener flange (see Fig 9a) (Ref 2)
The peel stresses can be reduced by increasing the ratio between the bending stiffness of the skin laminate and the bending stiffness of the flange of the stiffener A flexible stiffener will attract less load and therefore the peel stresses will be reduced (see Fig. 9b).

a) High peel stresses at the edge of the stiffener flange

b) Reduced peel stresses at the edge of the stiffener flange
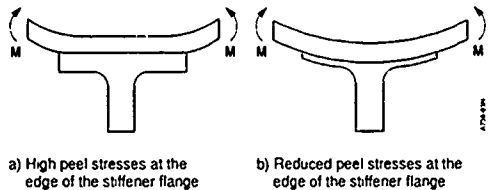
Fig 9 Peel stresses caused by a bending moment M

2) Shear stresses caused by the bending moment

Bending of the skin and stiffener flange will introduce shear in the bond layer This shear stress will, again, be maximum at the edge of the stiffener flange (Ref 2)

3) Stresses caused by an anticlastic curvature of the skin laminate

when the skin laminate is loaded in pure bending the longitudinal curvature in the x_2-x_3 plane is positive whereas the transverse curvature in the x_1 - x_3 plane is negative (see Fig 10) As a result the top surface of the skin laminate becomes saddle shaped. This will lead to stresses (peel and shear stresses) in the bond layer. This anticlastic curvature was only visible in the specimens with a skin laminate thickness of 3.62 mm.
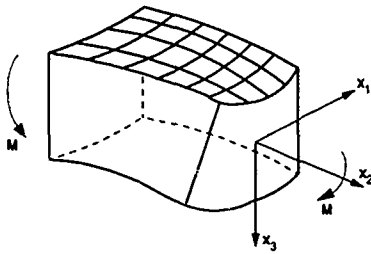
Fig 10 Anticlastic curvature of a beam in pure bending

Fig 11 Pull off tests

4.3.2 Four-Point bending test results

In the following table the test results of the four point bending tests can be seen The bending moments in this table are the bending moments when a crack propagated from the fillet into the bond layer or into the top layers of the skin laminate, since the specimens were considered then to be failed.

	E_2A_{skin} / E_2A_{stiff}	D_{22skin} / $D_{22stiff}$	Width of flange (mm)	$M_{cracking}$ (N mm)
Sk1aSt1a	0 52	1 48	44 0	5635
Sk1aSt1b	0 52	1 48	44 095	5597
Sk1aSt2a	0 48	1 16	50 0	5499
Sk1aSt2b	0 48	1 16	51 81	5348
Sk1bSt1a	0 71	1 07	44 0	5041
Sk1bSt1b	0 71	1 07	44 095	4696
Sk1bSt2a	0 66	0 84	50 0	4829
Sk1bSt2b	0 66	0 84	51 81	4677
Sk2aSt1a	1 04	11 5	44 0	30762
Sk2aSt1c	1 04	11 90	45 81	27025
Sk2aSt3a	0 76	3 50	44 0	25013
Sk2aSt3b	0 76	3 50	56 0	25971
St2bSt1a	1 33	7 90	44 0	28079
St2bSt1c	1 33	7 90	45 81	27744
St2bSt3a	0 97	2 36	44 0	23767
St2bSt3b	0 97	2 36	56 0	25204

From these test result_ the following conclusions can be drawn.

The width of the stiffener flange has hardly any influence on the strength of the specimens (compare St2bSt3a with St2bSt3b and Sk2aSt3a with Sk2aSt3b)

The strength of the specimens is pre-dominantly determined by the bending stiffnesses of the skin and stiffener laminates. When the ratio between the D_{22skin} and $D_{22stiffener}$ increases the strength of the specimen increases (compare Sk2aSt1a with Sk2aSt3a and Sk2bSt1a with Sk2bSt3a).

It can be concluded that for this loading case the skin laminate should have a larger bending stiffness (D_{22}) than the laminate in the flange of the stiffener

4.4.1 Pull-off tests

In the third test series the specimens were tested by pulling off the stiffeners (see Fig. 11) The pull off tests were executed with a velocity of 4 mm/min. During the tests the applied load and the displacement of the stiffener blade were measured. For these tests different failure modes could be distinguised These failure modes were
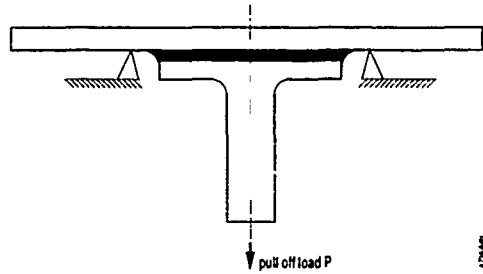
a) Failure in specimens with a skin laminate thickness of 1.81 mm

Failure in these specimens starts with a crack in the fillet of the bond layer. This small crack does not lead to a load drop When the applied load reaches a critical value the crack in the fillet expands and starts to grow in the bond layer or in the top layers of the skin laminate This leads to a load drop and the stiffener is pulled off

b) Failure in specimens with a skin laminate thickness of 3.62 mm.

Failure starts with a crack in the fillet of the bond layer. As in the 1.81 mm specimens this small crack does not lead to a load drop When the applied load reaches a critical value a crack starts in the skin laminate under the edge of the stiffener flange (see Fig. 12) or a crack starts in the interface between the filler and the blade of the stiffener (see Fig 13) The load drops and the stiffener is pulled off
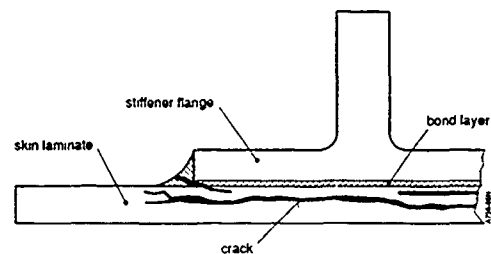
Fig 12 Cracks in the skin laminate under the edge of the stiffener flange
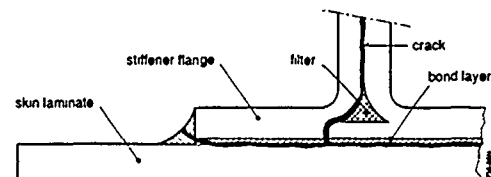
Fig. 13 Cracks in the interface between the filler and the blade of the stiffener

Failure of the specimens may be caused by the following stress conditions:

1) Shear stresses caused by a bending moment

Because a transverse load is applied to the skin laminate a bending moment is built up in the skin and stiffener laminates. This bending moment causes shear stresses in the bond layer.

2) Peel stresses caused by the applied transverse force.

The transverse force will result in a bending of the skin and stiffener At the locations were the transverce force and its reactions are applied, peek peel stresses will occur because of a mismatch in vertical displacements between the stiffener flange and the skin laminate. Peek peel stresses will therefore occur under the stiffener blade and at the edge of the stiffener flange (Ref 2)
The peel stresses at the edge of the stiffener flange can be reduced by increasing the ratio between the bending stiffness of the skin laminate and the stiffener laminate (see Fig 14)
The influence of the peel stresses under the stiffener blade increases as the peel stresses at the edge of the stiffener flange are limited As mentioned above the peel stresses at the edge of the stiffener flange reduce when the ratio between the bending stiffness of the skin and stiffener flange increases This may explane the occurance of cracks near the filler of the specimens with a skin laminate thickness of 3 62 mm.

	E_2A_{skin} / E_2A_{stiff}	D_{22skin} / $D_{22stiff}$	Width of flange L (mm)	$P_{transver}$ (N)
Sk1aSt1a	0 52	1 48	44 0	1155
Sk1aSt1b	0 52	1 48	44 095	975
Sk1aSt2a	0 48	1 16	50 0	828
Sk1aSt2b	0 48	1 16	51 81	838
Sk1bSt1a	0 71	1 07	44 0	1368
Sk1bSt1b	0 71	1 07	44 095	1213
Sk1bSt2a	0 66	0 84	50 0	685
Sk1bSt2b	0 66	0 84	51 81	858
Sk2aSt1a	1 04	11 90	44 0	2875
Sk2aSt1c	1 04	11 90	45 81	3565
Sk2aSt3a	0 76	3 50	44 0	3112
Sk2aSt3b	0 76	3 50	56 0	2030
St2bSt1a	1 33	7 90	44 0	3030
St2bSt1c	1 33	7 90	45 81	3825
St2bSt3a	0 97	2 36	44 0	3348
St2bSt3b	0 97	2 36	56 0	2753

a) High peel stresses at the edge of the stiffener flange

b) Reduced peel stresses at the edge of the stiffener flange

Fig 14 Reducing the peel stresses at the edge of the stiffener flange by increasing the ratio between the bending stiffness of the skin and stiffener flange

4.4.2 Pull off test results
In the following table the test results of the pull off tests can be seen In this table the transverse force is the maximum force reached during the tests.

The pull off tests showed a large amount of scatter. However, two important conclusions can be made.

When the width of the stiffener flange increases the strength of the specimens decrease (compare Sk2aSt3a with Sk2aSt3b and Sk2bSt3a with Sk2bSt3b).

When the ratio between the bending stiffnesses of the skin laminate and the stiffener flange increases, the strength of the specimens increase (compare for example Sk1aSt1a with Sk2aSt1a).

It can be concluded that for this loading condition the skin laminate should have a larger bending stiffness (D_{22}) than the flange of the stiffener The width of the stiffener flange should be limited.

5. ANALYSIS OF THE TEST RESULTS WITH BONDST

5.1 Introduction
The test results have been further analysed with the program BONDST. With this program the stress distribution in a specimen can be calculated in a simplified way. It is investigated whether it is possible to establish a failure criterion based on the stresses calculated with BONDST

5.2 The program BONDST
In the program BONDST the skin stiffener combination is simplified to a two dimensional model with unit length that represents the skin, the stiffener flange and a discrete bond layer (Ref 6) A cross section of the model is presented in figure 15. The stiffener blade is neglected, except that its influence is imposed through the clamped boundary conditions at one end of the model. The model can be loaded at the other end by inplane forces and bending moments (see Fig 16)
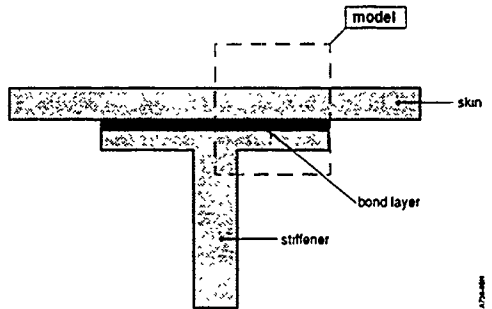
Fig 15 Cross section of the model
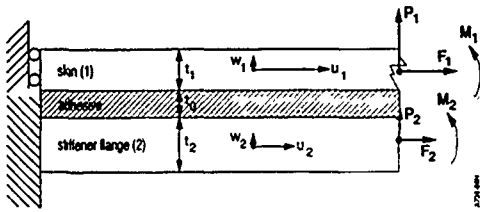
Fig 16 The displacements, the loads and the boundary conditions

	E_2A_{skin}/E_2A_{stiff}	Width L (mm)	t_{skin} (cm)	F_{BONDST} (kN)	σ_{peel} max (MPa)	τ_{max} (MPa)
Sk1aSt1(a,b)	0 57	44 0	1 81	11 9	27 8	91 8
Sk1bSt1(a b)	0 78	44 0	1 81	16 5	23 3	92 2
Sk1aSt2(a,b)	0 63	50 0	1 81	11 6	24 4	87 8
Sk1bSt2(a b)	0 86	50 0	1 81	14 6	16 7	80 0
Sk2aSt1(a,c)	0 57	44 0	3 62	24 2	91 4	114 3
Sk2bSt1(a,c)	0 73	44 0	3 62	28 4	90 0	100 0
Sk2aSt3a	0 57	44 0	3 62	24 3	58 2	130 0
Sk2bSt3a	0 73	44 0	3 62	31 0	41 1	123 0
Sk2aSt3b	0 57	56 0	3 62	24 2	59 9	126 6
Sk2bSt3b	0 73	56 0	3 62	31 7	43 3	125 5

The skin and stiffener flange are represented by beams with extensional and bending stiffness The bond layer has transverse shearing stiffness and extensional stiffness The extensional stiffness of the bond layer is taken into acount in the z-direction only The kinematics of the model are illustrated in figure 17. The program can calculate the deformations in the x-direction and the z-direction of the skin and stiffener blade, the axial stresses in the skin and stiffener blade and the shear and peel stresses in the bond layer. The model is based on several assumptions, which impose limitations on its use. For instance, the shear stress in the bond layer at the free end is not zero. Also, the skin and stiffener flange are modelled as beams, with infinite transverse shear stiffness The transverse shear modulus G_{xz} of these constituents, however, if made of layered composite material is ofthe same order of magnitude as the transverse shear modulus of the bond layer Due to the limitations listed here the results obtained with the model might have at most a qualitative significance.

The purpose of the calculations is to derive a failure criterion for a discreet skin-stiffener combination under different loading conditions. To achieve this the failure loads which were measured during the tests were used as input for the calculations These calculations may lead to a design stress level at which a skin stiffener interface will fale

Fig 17 The kinematics of the model

Stresses in the bond layer caused by a lateral force F1 = 11,600 N
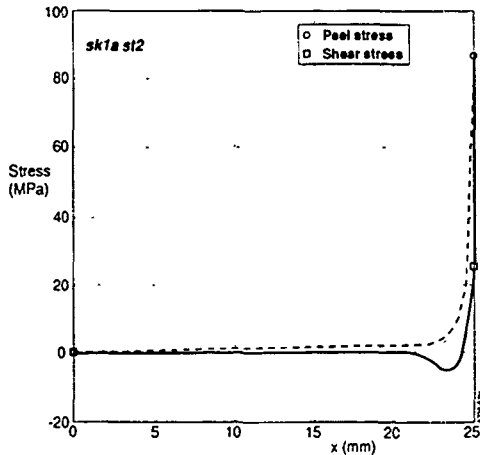
Fig 18 Typical peel and shear stress distributions in the bond layer caused by a lateral force F_1

the stiffener which causes secondary bending when the skin is loaded in tension This bending causes compressive peel stresses in the bond layer BONDST cannot calculate this secondary bending moment, and therefore cannot calculate the resulting peel stresses.

5.3 Lateral tension test results vs. calculated stress levels

Figure 18 shows a typical peel and shear stress distribution in the bond layer caused by a lateral force Maximum peel and shear stresses occur at the edge of the stiffener flange. In the following table the calculated stresses in the bond layer are presented. In the table F_{BONDST} represents the failure load which was measured during the lateral tension tests

The calculations show that large differences occur in the calculated maximum stress levels between the specimens with a skin thickness of 1.81 mm and 3 62 mm. This may be caused by the eccentric position of

5.4 Four-Point test results vs calculated stress levels

Figure 19 shows a typical shear and peel stress distribution in the bond layer caused by a constant bending moment. The figure shows that a bending moment leads to peel stresses at the edge of the stiffener flange The positive peel stresses are followed by negative peel stresses to provide the necessary vertical equilibrium in the bond layer The calculations showed that at a certain distance from the edge of the stiffener flange, the skin and stiffener flange show the same vertical deformations and therefore no peel stresses occur in the bond layer.

Stresses in the bond layer caused by a bending moment M1 = 5,424 N mm
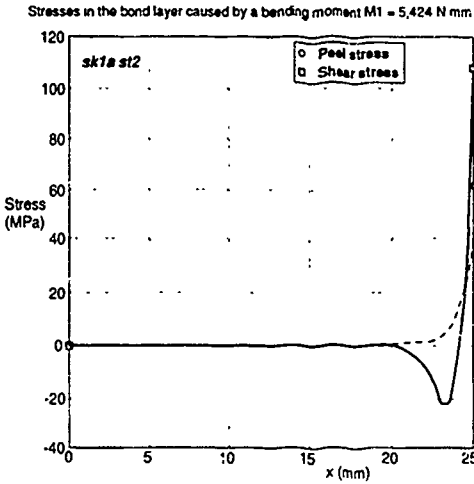
Fig. 19 Typical peel and shear stress distributions in the bond layer caused by a bending moment M_1

A negative bending moment leads to negative shear stresses at the edge of the stiffener flange. The maximum shear stress level keeps below the maximum peel stress level. After the peak the shear stress drops to zero.

In the following table the calculated stresses in the bond layer are presented. In the table M_{BONDST} represents the failure bending moment which was measured during the four point bending tests

	$D_{22skin}/$ $D_{22stiff}$	Width L (mm)	t_{skin} (mm)	M_{BONDST} (N m)	σ_{peel} max (MPa)	τ_{max} (MPa)
Sk1aSt1(a,b)	1 48	44 0	1 81	5616	109 2	66 2
Sk1bSt1(a,b)	1 07	44 0	1 81	4869	110 8	73 9
Sk1aSt2(a,b)	1 16	50 0	1 81	5424	107 7	63 1
Sk1bSt2(a,b)	0 48	50 0	1 81	4753	110 8	70 8
Sk2aSt1(a,c)	11 90	44 0	3 62	28894	171 4	109 5
Sk2bSt1(a,c)	7 90	44 0	3 62	27912	131 1	144 4
Sk2aSt3a	3 70	44 0	3 62	25013	158 0	102 0
Sk2bSt3a	2 36	44 0	3 62	25971	200 0	148.0
Sk2aSt3b	3 50	56 0	3 62	23767	150 0	98 0
Sk2bSt3b	2 36	56 0	3 62	25204	195 5	142 9

The calculations show that the specimens with a skin thickness of 1.81 mm all reach nearly the same maximum stress level (a peel stress of 110 MPa and a shear stress of 70 MPa).
Specimens with a skin thickness of 3.62 mm show large differences in the calculate maximum stress levels. This may be caused by the stresses introduced by the anti clastic curvature of the skin laminate, which BONDST cannot calculate Again the specimens with a skin thickness of 3 62 mm reach higher stress levels than the specimens with a skin thickness of 1.81 mm.

5.5 Pull-Off tests vs. calculated stress levels
Calculations with BONDST showed different stress distributions in the bond layer depending on the bending stiffness ratio of the skin and stiffener flange.

Figure 20 shows the peel and shear stresses in the bond layer caused by a transverse load, in a specimen with a small ratio of the bending stiffness of the skin and stiffener flange High peel stresses occur at the edge of the stiffener flange and under the stiffener blade Because of the large stiffness of the stiffener flange the

Stresses in the bond layer caused by a transverse force P1 = 833 N
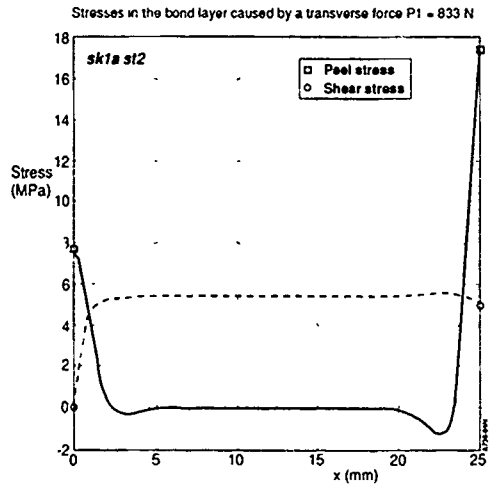
Fig 20 Peel and shear stresses caused by a transverse force P_1 for a specimen with a small ratio between the bending stiffness of the skin and stiffener flange

Stresses in the bond layer caused by a transverse force P1 = 3 220 N
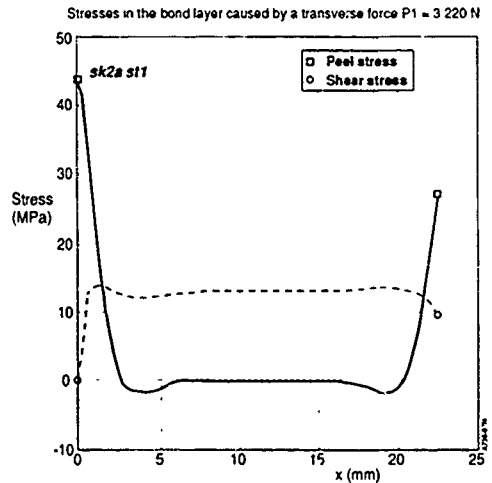
Fig 21 Peel and shear stresses caused by a transverse force P_1 for a specimen with a large ratio between the bending stiffness of the skin and stiffener flange

peel stresses at the edge of the stiffener flange are larger than the peel stresses under the stiffener blade.

The transverse force causes a lineair increasing bending moment, which results in a shear stress which is nearly constant over the complete width of the stiffener flange.

Figure 21 shows the peel and shear stresses when the ratio of the bending stiffness of the skin and stiffener flange is large. The flexible stiffener flange will attract less load and therefore the peak peel stresses are reduced at the edge of the stiffener flange This causes higher peel stresses under the stiffener blade than at the edge of the stiffener flange.

The lineair increasing bending moment again causes a nearly constant shear stress distribution

In the following table the calculated stresses in the bond layer are presented In the table P_{BONDST} represents the maximum load which was measured during the pull off tests The peel stress at $x = 0$ represents the peel stress under the stiffener blade. The peel stress at $x = L/2$ represents the peel stress at the edge of the stiffener

	$D_{22skin}/D_{22stiff}$	Width L (mm)	t_{skin} (mm)	P_{BONDST} (N)	σ_{peel} x = 0 (MPa)	σ_{peel} x=L/2 (MPa)	τ (MPa)
Sk1St 1(a,b)	1.48	44.0	1.81	1065	11.1	21.0	6.8
Sk1bSt 1(a,b)	1.07	44.0	1.81	1291	13.6	30.0	9.6
Sk1aSt 2(a,b)	1.18	50.0	1.81	833	7.8	17.4	5.3
Sk1bSt 2(a,b)	0.48	50.0	1.81	772	7.1	17.8	5.4
Sk2aSt 1(a,c)	11.90	44.0	3.62	3220	4.0	27.1	13.0
Sk2bSt 1(a,c)	7.90	44.0	3.62	3428	45.3	35.3	16.5
Sk2aSt 3a	3.50	44.0	3.62	3112	28.8	30.8	12.3
Sk2bSt 3a	2.36	44.0	3.62	3348	30.0	38.2	14.8
Sk2aSt 3b	3.50	56.0	3.62	2030	18.8	20.0	7.9
Sk2bSt 3b	2.38	56.0	3.62	2753	24.6	31.3	12.3

The tests showed a large amount of scatter. It is therefore difficult to formulate a design criterion for the pull-off tests.

6. CONCLUSIONS

A study of the influence of several design parameters on the strength of a skin-stiffener combination was conducted Test specimens which consisted of a blade-type stiffener secondarily bonded to a skin laminate were fabricated These specimens were tested for three different loading conditions. lateral tension tests, four-point bending tests and pull of tests

The tests showed that failure mainly occurs at the edge of the stiffener flange due to peak stresses at that location The tests provided the following design guides:

1) The lateral inplane stiffness of the skin laminate should be larger than the lateral inplane stiffness of the stiffener flange
2) The skin laminate should have a larger lateral bending stiffness than the stiffener flange
3) The width of the stiffener flange should be limited.

Calculations made with BONDST showed that no failure criterium for the strength of a skin-stiffener interface could be found

7. REFERENCES

1) John N. Dickson and Sherill B Biggers, Lockheed - Georgia Company Marietta, Georgia 30063 and James H. Starnes, Jr NASA Langly Research Center Hampton, Virginia 23665 "Stiffener attachment concepts for graphite-epoxy panels designed for post buckling strength".

2) Dr Ram C Madan "Compposite transport wing technology development" Nasa-cr-178409 N89-26842 February 1988

3) R. van Es EDSC/MSC "Finite element analysis of bonded composite structures" Report no S-182 Fokker Aircraft, Amsterdam, Holland May 1991

4) T W. Anderson Lockheed-California Company Burbank, California "Composite wing fuel containment and damage tolerance-technology demonstration' ACEE Composite Structures Technology Conference, Third special oral review, August 13-16, 1984

5) R C. Madan and A V. Hawley, Douglas Aircraft Company, McDonnell Douglas Corporation Long Beach, California "Subcomponent tests for composite fuselage technology readiness" 21st International SAMPE technical conference, September 25-28 1989

6) J.F M. Wiggenraad, National Aerospace Laboratory NLR The Netherlands "Bond stress calculations for a discreet skin/stiffener interface" NLR CR 92019 C 1992

Defect Analysis using Advanced Interpretation
of the Reflected Wave during Ultrasonic Scanning

L. Schillemans, D. Van Hemelrijck, F. De Roey, W.P. De Wilde, A.H. Cardon
Composite Systems and Adhesion Research Group of the Free University of Brussels
COSARGUB - VUB - Fac. TW - Building Kb - Pleinlaan 2 - 1050 Brussels - Belgium

A.A. Anastassopoulos
University of Patras - Applied Mechanics Laboratory - Dept. of Mechanical Engineering
PO Box 1134 - Greece 261 10 Patras

1. SUMMARY

The paper reports recent developments in the field of the interpretation of the form of the reflected wave during ultrasonic scanning of laminated plates Defect analysis in laminated plates can be achieved by installing a threshold value on the amplitude of the reflected ultrasonic wave If this threshold value has not been achieved, one considers that a defect is causing scatter and the location is registered as such. This is the most elementary form of measuring technique, although it does not provide more detailed information about the depth location of the defect Nevertheless, it already provides some information, although rather "binary" On the used USIP 12 equipment (Krautkramer) a depth-measurement module was added allowing to establish the location of wave scatter through the thickness of the laminated structure. Recently, it has been suggested that the form of the reflected wave could yield some additional information on the types of defects. In particular, the frequency content of the reflected wave could be analysed and be compared for different sorts of defects, thus allowing for a more accurate diagnostic of the defect and its significance Advanced signal processing and pattern recognition techniques are therefore applied Two Carbon/Epoxy laminated plates with several embedded defects have been manufactured and tested Representative results will be given.

2. INTRODUCTION

2.1 General Introduction

One of the methods most widely used in non-destructive testing of materials is the ultrasonic method (ref. [1], [2]). However, in many applications the result is treated as a binary value (good or bad) regardless of the enormous amount of information contained in an ultrasonic A-scan. A small number of users can go beyond this binary threshold by identifying the defect basing themselves on years of practical experience. As it is mentioned in ref. [3], the use of advanced data acquisition boards, depth measurement module and computer software, result into colored C-scan plots as well as three-dimensional plots. Therefore the capabilities of the ultrasonic method is extended by identifying completely the defects location.

However, no information is available about the nature of the defects making the decision for their criticality very difficult. Advanced signal processing and pattern recognition techniques are therefore applied on the ultrasonic signals and proved the ability of defect identification with much lower error rates compared with the statistical expexted when no prior information is available. Thus providing a non-binary result by high level expertise of the signal.

At first, the time domain signal (A-scan) is digitized and stored. Based on this data, numerical algorithms return frequency, autocorrelation, crosscorrelation, convolution and deconvolution domain data. In order to reduce the number of data without loosing any useful information, descriptors are defined and calculated in each domain (i e. number of peaks above a certain level, peak amplitudes, peak position, peak area, inter-peak distance and many others)

Identification of defects is done by classifying the signal under investigation in one of the predefined categories (classes) to distinguish. Before classification is possible, the system has to be "learned" by a given set of signals of which the class is known a priori. Depending on these classes, only a small number of descriptors will be sensitive, meaning that the variability of a descriptor must be minimal in its own class compared with its variability between classes. This is known as being the Wilk's lambda criterion Choosing the most sensitive descriptors defines the features which are going to be used for further classification.

Classification of unknown signals in comparison with the known signals based on these features can be done by different classification schemes. The ones used in this application are the k-nearest neighbour classifier, the modified nearest neighbour classifier, the potential function classifier, the linear classifier and the F-machine.

Practical results will show classification success on laminated carbon epoxy specimens with embedded foreign bodies like aluminum and teflon as defects. Discussion will be made on different values of this success rate using different features and different classification schemes.

2.2 Pattern Recognition

Pattern recognition and classification is a numerical technique which can be applied to quite different domains of applications A few examples of these are tabulated in table 1. Standard commercial packages like ICEPAK (Tektrend) (ref. [4]) and PARECO (Nestor Inc.) (ref. [5], [6] and [7]) provide general numerical algorithm routines which can be used in this variety of domains. However, because of the fact that this principle is now being applied to ultrasonic investigation and examined in more depth in this area, the basic principles of

this technique are integrated in a newly developed program called SPPR (ref. [8]) which stands for Signal Processing and Pattern Recognition at the Free University of Brussels.

Domain	Examples
Engineering	Non-Destructive Testing Quality Control Process Control Geophysics (Seismic exploration)
Military	Communications security Radar and Sonar interpretation
Medical	Electroencephalogram interpretation Electrocardiogram interpretation Diagnosis
Scientific Investigations	

Table 1. Examples of Pattern Recognition Applications

Pattern recognition, which is a branch of artificial intelligence, is used for interpretation and diagnosis It simulates advanced human functions and interfaces man and machine to combine their best capabilities It also automates the routine interpretation carried out by human analysts and therefore captures human expertise and experience in machine form

In general, pattern classification routines can be quite different depending on the amount of information which is known a priori from the phenomena under investigation For instance the Bayes decision theory is based on the assumption that the decision problem is posed in probabilistic terms and that all of the probabilistic values are known Mathematical derivations of this theory applied on multivariate normal densities are extensively described in literature If some of the probabilistic values are unknown, this theory is extended to parameter estimation based on supervised learning which means that the system is "taught" by a number of signals of which the class is a priori known. However, most of the time and especially in the domain of non-destructive testing, little or no probabilistic information is known a priori Supervised learning can then still be applied and this technique is called the nonparametric technique. For the time being, this technique is primarily described in this paper and is applied to the ultrasonic investigation of laminated composite plates Future developments will be made in the domain of unsupervised learning and clustering analysis which means that the classifiers are self-learning without prior probabilistic or class information of the signals under investigation It is clear that this is the supreme solution, if possible, but can nevertheless only be realized when a great number of signals are available which most of the time is not the case.

In practice, the different stages in the classification scheme can be roughly subdivided into 1) signal preprocessing 2) descriptor generation 3) feature definition 4) clustering analysis and 5) signal classification Signal preprocessing involves both the signal acquisition and the conversion of this data to different domains of interest like for instance the time domain, the frequency domain (amplitude and phase), the deconvolution domain and others Descriptor generation is concerned about data reduction by extracting only what is beleived to be vital information in the different domains Feature definition is done by withholding those descriptors which are highly sensitive to a change of class (classes defined by the user) Signal classification can be seen as

"subdividing" the descriptor space for optimum performance, meaning a minimum classification error rate Clustering analysis is an unsupervised method (no class information) of classification

3. SIGNAL PREPROCESSING

3.1 General Information
The ultrasonic signals are generated and received by the USIP 12 (ref [9]) ultrasonic device manufactured by Krautkramer This pulser-receiver is a device which can readily operate transducers in broad-band in a range of 1 to 20 MHz and in narrow-band in the range of 0.5 to 15 MHz A depth measurement module DTM12 is also installed which has a resolution of 1 nsec or 0 01 mm. The data processing and storage is done on a Hewlett-Packard Vectra 80386SX 16 MHz personal computer equipped with an analog to digital convertor board Sonotek STR 825 with a performance of 100 MSamples per second.

3.2 The Time Domain Signal
A subprogram of SPPR, called SCOPE displays 16384 data points for the total time domain signal (fig 1) As most of the time domain signal is zero, it is sufficient to extract portions of 4096 points and send those to file. Each time domain signal can then be considered as three files consisting of 1) the initiating pulse or base pulse, 2) the plate reflected information (fig 2, 3 and 4) and 3) the glass-plate echo or backwall echo in pulse-echo mode For convenience, these are tabulated in table 2

Figures one to four present representative time domain signals Figure 1 shows part of the entire signal of 16384 points but the plate reflected information and the glass-plate echo are well defined. Figures 2, 3 and 4 shows respectively the test plate echo of non defected area, of an area with embedded teflon and of an area with embedded aluminum

	Time Domain signal
1	The base pulse (initiating pulse)
2	The plate echo (plate reflected ultrasonic signal)
3	The backwall echo (glass plate echo)

Table 2 Different Time Domain signals

Conversions to the following domains can be done on either of these time domain signals.

3.3 The Frequency domain
The term frequency domain denotes a mathematical transformation of a time domain signal and is also known as the power domain signal. Time domain signals are now described by their spectral components The transformation in the software package SPPR is based on the Fast Fourier Transform (FFT) algorithm. The FFT of N points needs $O(N\log_2 N)$ operations and is much faster compared to the ordinary Discrete Fourier Transform which needs $O(N^2)$ operations. The result of the FFT is a complex number having a real and imaginary part which is immediately converted to a magnitude (root of the sum of the squared parts) and a phase (arc tan of imaginary over real part) component in providing a more physical understandable background for the result. Frequency transformations of different time domain signals corresponding to different defects, have shown substantial differences in spectrum with a high level of repeatability. Figures 4, 5 and 6 shows the result respectively of the FFT
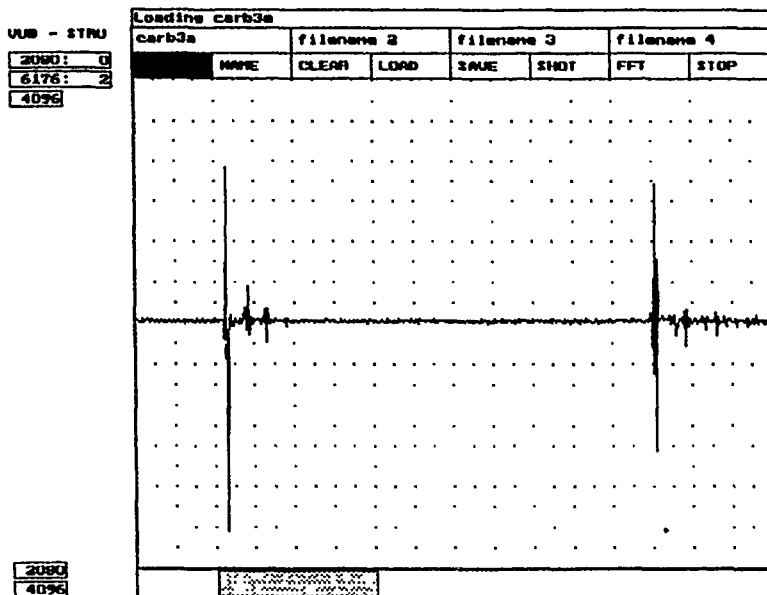
Entire A-Scan Signal

Fig. 1
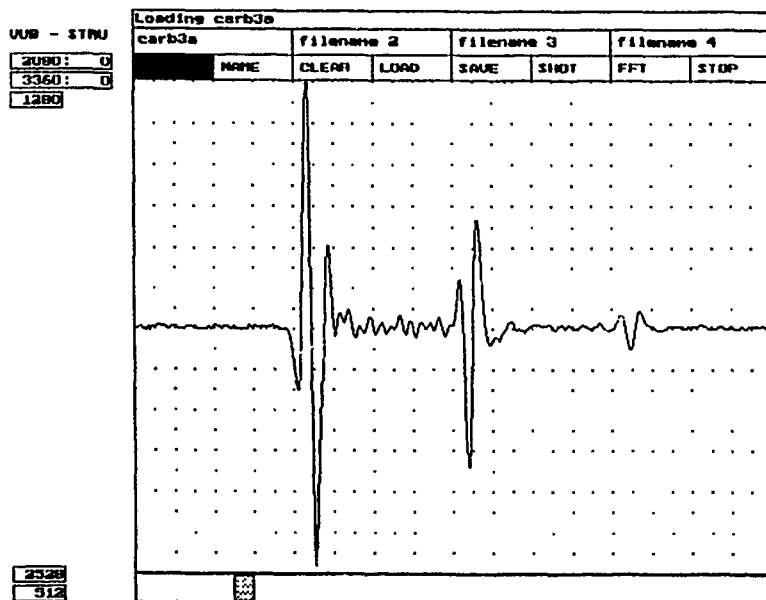
A-Scan Signal from undefected area

Fig. 2
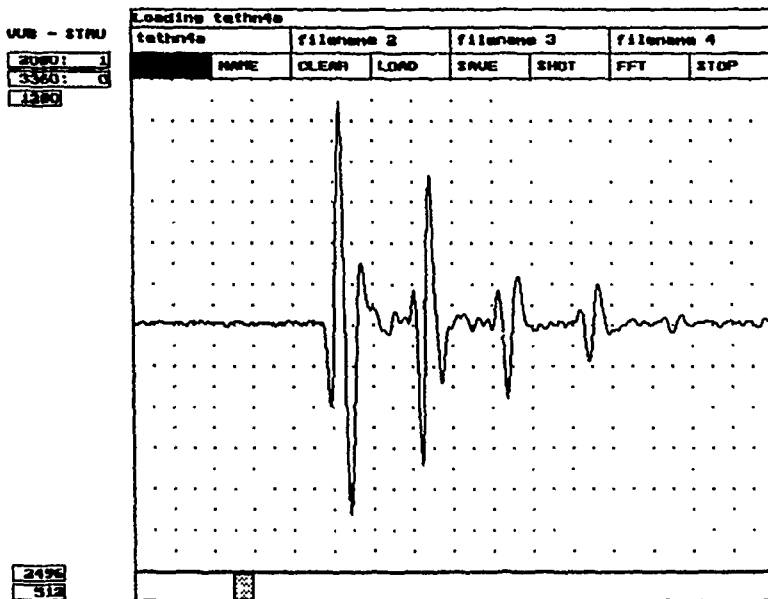
A-Scan Signal from defected area (embedded Teflon)

Fig. 3
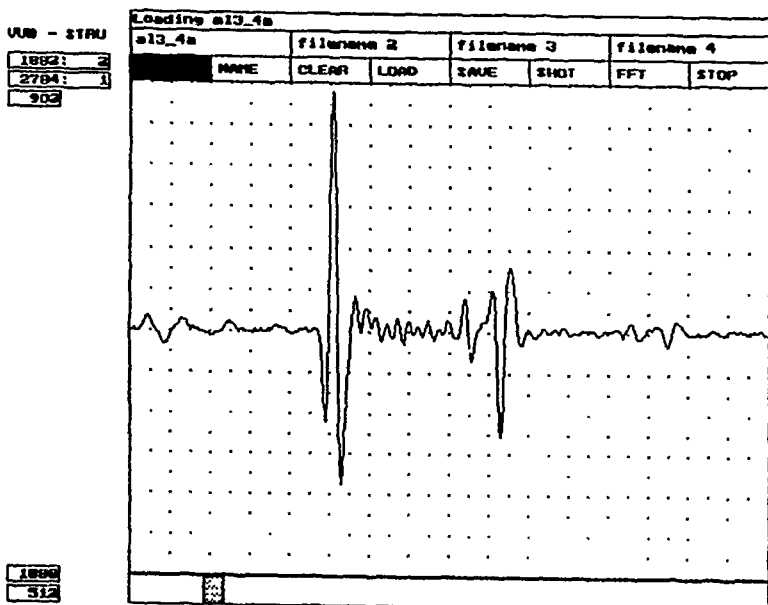
A-Scan Signal from defected area (embedded Aluminium)

Fig. 4

applied to the signals presented in figures 2, 3 and 4. Information extracted out of the frequency domain is therefore thought to be very useful in classifying different defects.

3.4 The Correlation Domain

A time domain signal will sometimes consist of repetitive basic signal parts. This gives the impression that this basic signal part interacts with the medium under investigation. If the time domain signal is compared with this basic part at various time positions, perhaps the locations of maximum correspondence can be found and thus a more pronounced image of the medium can be obtained. This process is known as correlation and one speaks of autocorrelation when this computation is performed with the total signal itself. A correlation of two time domain signals can be calculated in the frequency domain as the multiplication of the corresponding frequency values for the first and the complex conjugate values for the second. Figures 8 and 9 presents respectively the cross-correlation of the signal shown in figure 2 (undefected area) and figure 4 (embedded aluminum area). Finally, figure 10 shows the result of autocorrelation of figure 3 (embedded teflon area).

3.5 The Convolution and Deconvolution Domain

The reasoning applied in section 2.4 on the correlation domain provides the same basic idea applied in the convolution transform. It is now computed in the frequency domain as the multiplication of both the complex frequency component of the original time domain signals. The effect of convolution is to smear out the original time function s(t) in time according to the recipe provided by the response function r(t), for both continuous and discrete case. When knowing a convolution result and knowing a given time function s(t), the problem is to find the response function r(t). This is known to be the deconvolution process. The algorithm is used on ultrasonic signals, they are deconvoluted with the originating base pulse from the transducer to obtain a more pronounced description of the medium under investigation.

4. DESCRIPTOR GENERATION

4.1 Introduction

Assuming that the time domain consists of 4096 points as well as the other domains, for instance the frequency, the autocorrelation and the deconvolution domain. Then a total number of 16384 numbers describes the original signal. It is easily understood that much of this data is redundant. A transformation of this data to a set of other data (descriptors) is made to reduce considerable the amount of data without losing any information. The following descriptors are defined, used and believed to provide no loss of information. Descriptor extraction can be performed in each domain defined above.

4.2 The Descriptors

4.2.1 Statistical descriptors

Several well known statistical parameters are also used as a descriptor. The following are provided in the software package SPPR, see table 3.

4.2.2 The number of peaks above a threshold

The threshold will be expressed as the per cent value of the maximum signal amplitude. The base line is defined as having the minimum signal amplitude value. By counting the number of peaks above the base

line and 10%, 20%, ... up until 90% of maximum signal amplitude, ten descriptors are computed. These descriptors represent a measure for the "activity level" in the signal, considering the time domain.

4.2.3 The peak shape descriptors

For each peak encountered in the signal in each domain, the following number of descriptors are believed to describe this peak sufficiently: peak amplitude, peak position, peak area, peak rise time, peak fall time, peak full width and peak half width. The reasoning is done in the time domain. The amplitude of a peak enables us to gauge the intensity of a physical process. There is no better example then the basic functional priciple of A-scan and/or C-scan to judge an occurrence by the signal amplitude. The peak position returns information on the physical location of disturbances (ref. [13]). The area of a peak gives a measure for the energy content of this peak. This item is particularly useful in the frequency domain. The other peak descriptors describe the shape of the peak related to the kind of defect encountered. These peak shape descriptors are calculated for the five highest peaks in each domain, thus disregarding the background noise.

4.2.4 Inter peak distances

The distance from first to second, from first to third and from second to third highest peak are also computed. They provide information on the signal propagation time and delays within a given medium. As an example, consider the technique to locate the depth of a defect in a specimen by measuring the "time of flight".

4.2.5 Partial areas and total area

The domain under observation is equally subdivided into eight segments. The area covered by the signal is computed in each segment as well as the total area. This information gives a global measurement of energy together with a rough indication of energy spread in the domain.

Descriptor	Interpretation
Mean value	estimates the value around which central clustering can occur
Variance	characterizes the spread of values around the mean value
Standard deviation	known as the square root of variance gives no new information
Skewness	a measure for asymmetry of the distribution alongside the mean value
Kurtosis	represents the amount of "peakness" or "flatness" of a distribution

Table 3. Statistical descriptors

4.3 Domain dependant descriptors

In SPPR the descriptors computation is automated for each domain, discussed in paragraph 2, separately. Not all of the descriptors are calculated in each domain because they do not provide any valuable information or are very sensitive to background noise. The six domains available are the time domain, the squared time domain, the frequency domain, the autocorrelation domain, the cross-correlation domain and the deconvolution domain. For the first four domains an automatic calculation of the descriptors is possible, providing
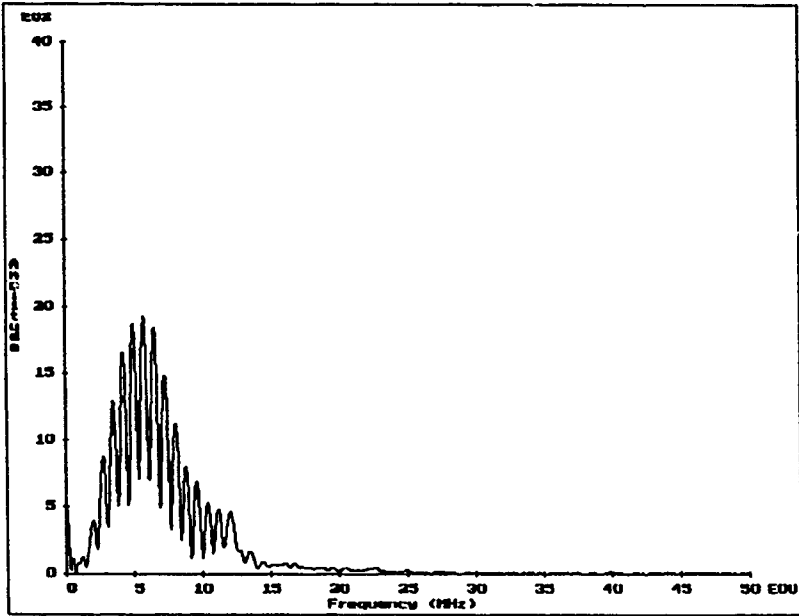
FFT applied on the signal of fig.2

Fig. 5
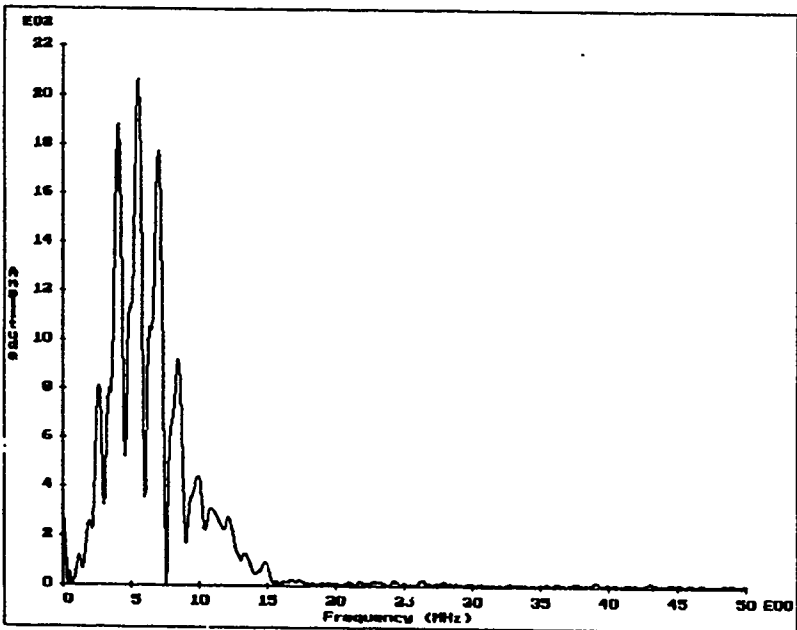
FFT applied on the signal of fig 3

Fig. 6
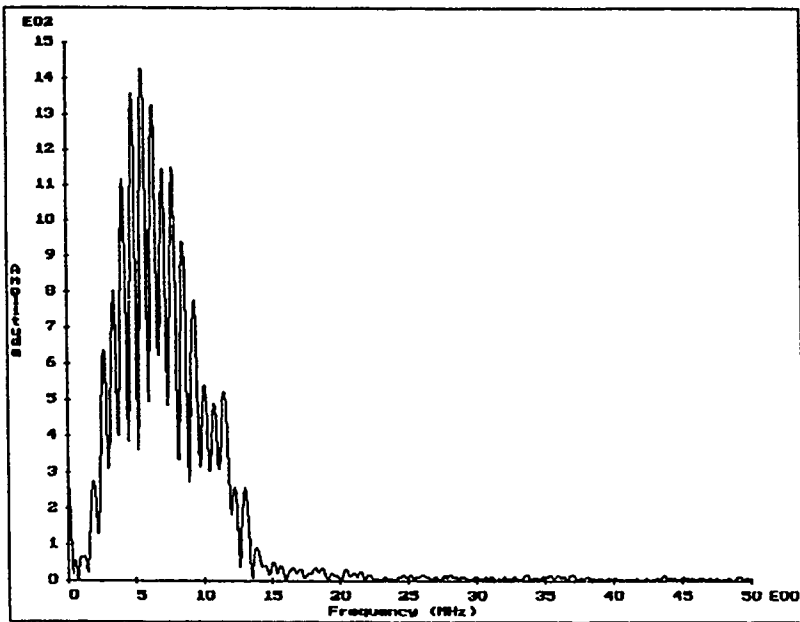
FFT applied on the signal of fig. 4

Fig. 7
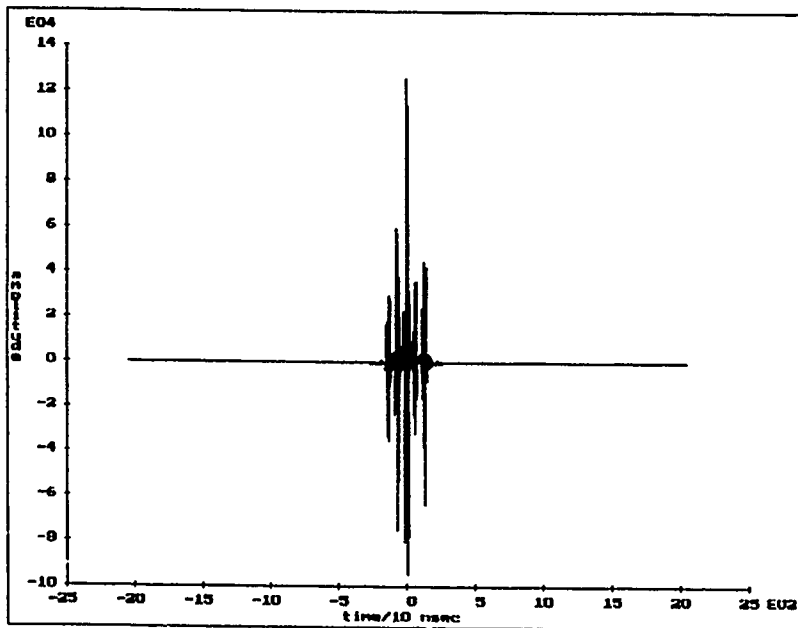
Cross-Correlation of signals of fig. 2 and 3

Fig. 8
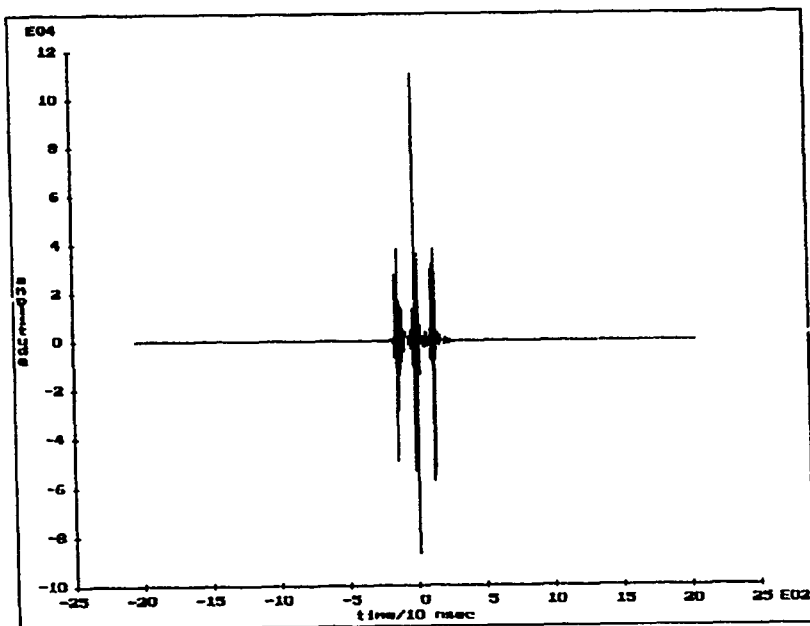
Cross-Correlation of signals of fig. 2 and 4

Fig. 9
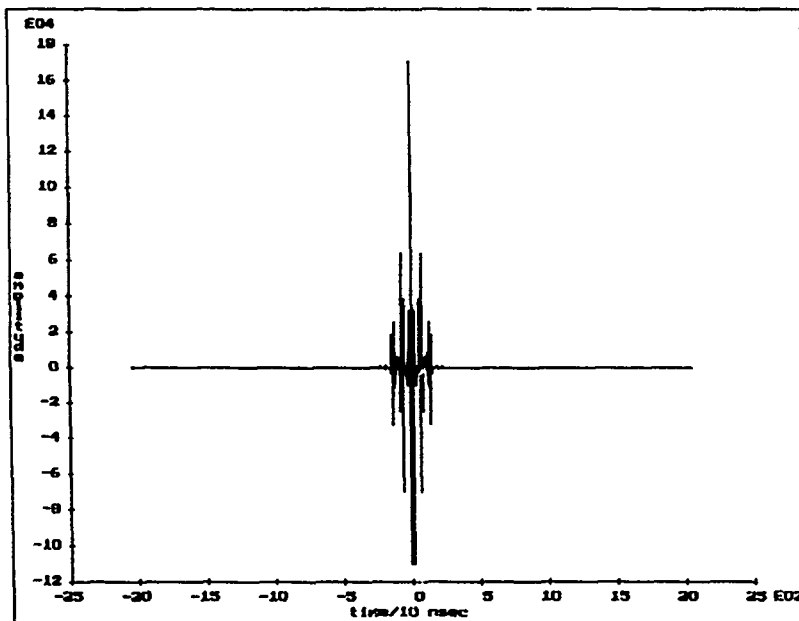
AutoCorrelation of signal of fig. 3

Fig. 10

143 descriptors. This means that the original 16384 number are reduced to 143, a data reduction by a factor of 114.

5. FEATURES DEFINITION

A pattern vector containing more then ten descriptors is in practice not of much use because the dimensionality of the feature space is such that the amount of computation is to high. Practical experience has proven also that the classification error rate most of the time increases when the dimensionality goes beyond a certain level. Thus, out of the descriptors defined before, one extracts a certain number of features which are going to be used in the classification process, these are called the features However, there are no general rules concerning the choice between descriptors. Human intelligence, experience and knowledge about the specific application will be of the utmost importance in this choice which will also determine the success of classification (ref. [14] and [15]).

Some aid can be given by calculating the discriminating power of each descriptor separately. This is done by comparing the variability of a descriptor within it's class with the variability between classes. Furthermore, since two descriptors can hold the same information, they also have the same variability in and between classes The choice of using both of these descriptors would not increase the success rate of the classifier. Therefore, the discriminating power of sets of descriptors must also be examined A method of doing so is based on using the Wilk's Lambda. It consists of maximizing the between-class spread relative to the within-class spread The values of lambda are in the range [0,1]. The lower the values of lambda, the higher the discriminating ability of the descriptor subset. This technique does not change the value of the features. Other techniques to define features are based on reducing an original d-dimensional descriptor space into a (c-1)-dimensional feature space (c being the number of classes) by use of the Fisher's linear discriminant The transformation is done by multiplying the descriptor vectors with a matrix W of which the elements of W are chosen as to produce a feature space with maximum discriminating power.

6. CLASSIFIERS

6.1 Introduction

In some casses, different classes can be separated by a set of hyperplanes in the feature space. The classification can then be performed by a linear classifier Unfortunately, not all of the classification problems are linear. At this point the choice of features is critical since for a given set of features the problem may not be linearly separable while for another set of features it may well be. Several classification theories have been derived, which may produce different decision surfaces. In this paper, five classifiers are discussed, detailed in table 4.

	Classifier
1	The K-Nearest Neighbour Classifier (K-NNC)
2	The Modified K-Nearest Neighbour Classifier
3	The Potential Function Classifier
4	The Linear Classifier
5	The F-Machine Classifier

Table 4. Classifiers used in the present study

In the first three classifiers, decision is made based on direct distance measurements in the feature space The two remaining classifiers base their decision on generalized discriminating functions. In the case of a linear classifier it can be proven that the generalized discriminating function is nothing more than a weighted distance. A very different classifier, to be studied in future work, is based on the estimation of the probability distribution function and is called the Bayes classifier (further reading in ref. [15] and [16]).

6.2 Classifier Design

By applying pattern recognition techniques, an effort is being made to pass some of the human intelligence to the computer. Like a well known face in a crowd is easily recognized by a human, so will a computer easily recognize an input pattern if it is supplied with previously known patterns. Those patterns will be used to design, or teach, the classifier. At this point, a distinction has to be made between two general classifier design methodologies: a) supervised learning and b) unsupervised learning. In the first, the training samples used to design a classifier are labelled to show their category membership. In the latter, unlabeled samples are used. In the present case, supervised learning is studied Thus, a well defined training sample set is a prerequisite to proceed in classification. Before proceeding in the classifier design, questions like how big must the training set be, which are the representative points for each class and how can they be identified need a clear answer Two general methods can be applied. a) The store all method and b) Clustering analysis In the first method, all the available data is used to design the classifier. In the second one, the central points of each class is determined and used for classifier design Until now, the store all method is investigated. During the classifier design process, the training points may be relocated in feature space in order to reinforce or to weaken a particular event and change the decision surface. The term locates will denote these representative points whose initial values are the entire training set (store all method) or are the clusters (clustering analysis) which do not remain unchanged during the design process In other words, the training set, or a part of it, is substituted by the locates During the learning process, the locates are modified whilst the initial training set remains unchanged. The locates will be denoted by B1, B2, ... and will be allocated to the classes in the following way: B1, B2, .. , B(n1) for class 1, B(n1+1), B(n1+2), . . , B(n2) for class 2, B(n2+1), B(n2+2), ... , B(n3) for class 3, etc.

6.3 The Linear Classifier

The decision surface of a linear classifier is a hyperplane in the feature space The discriminant function is a linear combination of the components of the pattern vector X and is written as follows:

$$g(X) = W^T X + W_0 \qquad (1)$$

where W is the so called weight vector and W_0 is the threshold weight. A two-category linear classifier implements the following decision rule "Decide w_1 if g(X) > 0 and decide w_2 if g(X) < 0". If g(X) = 0, the pattern vector can be assigned to either class. The equation g(X) = 0 defines the decision surface that separates points assigned to w_1 from points assigned to w_2.

In order to be able to classify the unknown patterns, then the classifier has to be taught first. For instance, the weight values have to be calculated using the available training data. The discrimination function is rewritten in the form:

$$g(X) = a^T Y \qquad (5)$$

where $\qquad Y = [\,1\; x_1 \ldots x_n\,]^T = [\,1\; X\,]^T$

and $\qquad a = [\,W_0\; w_1 \ldots w_n\,]^T = [\,W_0\; W\,]^T \qquad (6)$

Then a sample Y_i which is labelled w_i is classified correctly if $a^T Y_i > 0$ and misclassified if $a^T Y_i < 0$. In the latter case, it is observed that Y_i is classified correctly if $a^T(-Y_i) > 0$. Thus, by replacing all the samples labelled w_2 by their negatives, the labels can be disregarded and a weight vector can be constructed satisfying $a^T Y_i > 0$ for all the samples. The approach to follow in order to find a solution to the set of linear inequalities $a^T Y_i > 0$ will be to define a criterion function $J(a)$ which is minimized if "a" is a solution vector. Starting with some arbitrarely chosen weight vector a_1, the gradient vector $grad(J(a_1))$ is computed. The next value a_2 is obtained by moving some distance from a_1 along the negative of this gradient. In general $a_{k+1} = a_k - r_k\, J(a_k)$. The selection of $J(a) = sum(-a^T Y)$ leads to the correction learning rule:

$$a_{k+1} = a_k + r_k\, sum(Y) \qquad (7)$$

where the summation is made over all of the misclassified samples. It has been proven that the above procedure always converges if a linear solution exists. A modification to the above algortihm is to consider the samples in a sequence and modify the weight vector whenever it misclassifies a sample. The above equation becomes then: $a_{k+1} = a_k + Y$, where Y is the misclassified sample. There are several ways to generalize the above described theory for the multicategory case. For instance, one might reduce the problem from c classes to c-1 two-class problems, where the i-th problem is solved by a linear discriminant function that separates points assigned to w_i from those not assigned to w_i. A more extravagant approach would be to use $c(c-1)/2$ linear discriminant functions, one for every pair of classes. Another approach is to define c linear discriminant functions:

$$g_i(X) = W_i^T X + W_{0i} \qquad i = 1 .. c$$
$$g_i(Y) = a_i^T Y \qquad i = 1 .. c \qquad (8)$$

and assign X_n to w_i if $g_i(X) > g_j(X)$ for all j not equal to i. This expression can also be written in the form $(g_i(X) - g_j(X)) > 0$ showing the correspondence with the two-category case. The boundary between the classes i and j is defined by the equation $g_i(X) = g_j(X)$. Finally, the error correction learning procedure for the two categories case can be generalized for the multicategory case. The multicategory error correction rule is the following: assume that the pattern vector X is a member of class i and it has incorrectly been assigned to class j due to the proximity of weight W_j. Then the weights are modified as follows:

$$W_j = W_j - X \quad \text{and} \quad W_i = W_i + X \qquad (9)$$

while all the other weights remain unchanged. More explanations about this algorithm and the convergence proof can be found in the references.

6.4 The F-Machine

The F-Machine is based on the same principles and is designed in the same way as the linear classifier. It can be viewed as a combination of a linear classifier and a descriptor preprocessor which generates new descriptors by transforming the original set to a new set by a non-linear transformation. This non-linear transformation can be quadratic, cubic or even higher order. The decision surface generated by the classifier is then no more linear in the original descriptor space. A hypersurface is constructed.

The F-Machine is more complicated than the linear classifier and does not offer any advantage if the classes are linearly separable. The main advantage lies in the fact that non-linear decision surfaces and/or hypersurfaces can be generated using this classifier. Thus a non-linear problem is solved by a linear algorithm in higher dimensionality feature space.

6.5 The Distances

As previously noted, certain classifiers base their decision on distance measurements. Three different types of distance measurements were programmed and evaluated, listed in table 5. The sum and the maximum are taken over each ordinate i in the feature space of q dimensionality.

Distance Type	Formulation
Euclidean distance	$sqrt(sum(B_i - X_i)^2)$
City Block distance	$sum(B_i - X_i)$
Square distance	$max(B_i - X_i)$

Table 5. Different types of distance measurements

6.6 The k-Nearest Neighbour Classifier (k-NNC)

Let $X_1, X_2, .. , X_n$ be a set of N labelled samples, and let X_m be the sample nearest to the unknown sample X. Then the nearest neighbour rule for classifying X is to assign it the label associated with X_m. Let D_{ij} denote the distance of the unknown pattern vector X from the j-locate of the i-class. Then the decision of the NNC is given by: X belongs to w_i if $min(D_{ij}) < min(D_{ki})$ for all the i different from k. The previously described NNC classifier is a special case of the k-NNC. The k-NNC classifies the unknown pattern vector X by assigning it to the label most frequently occurring among the k nearest samples. In other words, the basic nearest neighbour classifier is applied k times and the decision is made by examining the k nearest neighbours and take a vote. The decision surface produced by the NNC and the k-NNC is a combination of hyperplanes.

6.7 The Modified Nearest Classifier

By adding weights to the NNC, the modified NNC is established. Let $W_1, W_2, ...$ denote the weights which are allocated to the classes in the following way (the same as the locates): $W_1, ... , W_{N1}$ for class 1, $W_{N1+1}, ... , W_{N2}$ for class 2, $W_{N2+1}, ... , W_{N3}$ for class 3, etc. Let D_{ij} represent the distance of the unknown pattern vector X from the j-th locate of the i-class. Then the decision of the NNC is given by: X belongs to w_i if $min(W_j D_{ij}) < min(W_1 D_{ki})$ for all the i different from k. The learning process of the modified NNC will be discussed together with the learning process of the potential function classifier PFC.

6.8 The Potential Function Classifier (PFC)

Let P(D) be defined as a monotonically decreasing function of D (e.g. $P(D) = 1/D^2$). The the decision rule of the potential function classifier is given by: X belongs to w_i if $max(W_j P(D_{ij})) > max(W_1 P(K_{k1}))$ for all the i different from k. In the above described decision rule the same terminology is used as in the modified NNC.

6.9 Learning in a multi-category NNC or PFC

Learning can roughly be subdivided in Error Correction Learning and Reinforcement Learning (ref. [16]). Both principles can also be applied at the same time.

a) Error Correction Learning: Assume that the pattern vector X is a member of class 1 (Teacher's label T=1), but that it has incorrectly been attributed to class 3 (classifier decision M=3) due to the proximity of locate B_i and weight W_i. Let B_j be that locate in class 1 which is the closest (measured in terms of weighted distance) to X. The the locates and weights are modified as follows:

$$B_j = B_j - k\,(B_j - X) \quad \text{and} \quad B_i = B_i + k\,(B_i - X)$$
$$W_j = W_j - 1 \quad \text{and} \quad W_i = W_i + 1 \tag{10}$$

where k and 1 are the interaction parameters which control the magnitude of locate movement and the increments of weights respectively. All other locates and weights remain unchanged.

b) Reinforcement Learning: Assume that X was correctly assigned to class 3 by the proximity of B_h. This locate and its corresponding weight are then modified as follows:

$$B_h = B_h - k_r\,(B_h - X)$$
$$W_h = W_h - 1_r \tag{11}$$

where k_r and 1_r are the interaction parameters which control the magnitude of locate movement and the increment of weights respectively.

While using both techniques of learning, growing and pruning scores can be calculated. These are techniques which remove or add locates in the classifier design stage. This is not yet applied in the SPPR package, so the entire set training set is always used in the design process.

7. EXPERIMENTAL PROCEDURE

Two Carbon Epoxy 16 layers laminated plates have been prepared and several kinds of defects were embedded in both plates. The plates were manufactured from Ciba-Geigy T300/914 prepreg while the defects used were polyester, paper, polyimide, aluminium, vacuum bag, copper, siliconrubber, polypropyleen, peelply, teflon and glass fiber The defects were located at different depths. The defects embedded in the first plate are shown in fig 11, while quite similar although not identical are the defect positions in the second plate. C-scan plots of the first plate are given in fig. 13 (plate defect echo). A focused shock-wave probe of 10 MHz and a near field length of 15 mm was used. By the use of the depth measurement module, a three-dimensional graph can be produced as it is shown in fig. 14. As it can be found from the aforementioned figures, one may describe only the shape and the depth of the defects and not their nature.

The purpose of Pattern Recognition applied on Ultrasonic Data is to analyse further the C-scan images Thus for each embedded defect (the location previously found by C-scan), 16 A-scan shots were taken at different locations (some of them already presented in fig 1 to 4). The shots taken from one plate were used to teach the classifier, the shots taken from the other plate were used for classification. For each of the shots, descriptors were calculated in four domains (time, square time, frequency and autocorrelation domain).

Sensitivity calculations, based on Wilk's Lambda, were also performed. Then a selection of features and classifier was made and the classification error rate was calculated. This practical error rate was then compared with the theoretical one which is obtained when classifying the signals at random without prior information. This is the upper limit for the classification error rate.

8. RESULTS

Results are supplied on seperate pages inserted at the back of this paper.

9. DISCUSSION

Comparison of the time domain signals (fig. 2, 3 and 4) with the corresponding frequency domain (fig. 5, 6 and 7) as well as with cross-correlation results (fig 8 and 9) indicates that in the time domain representation the presence of the defect is more easily to identify and to explain physically On the other hand frequency and cross-correlation domain representation seem more useful for the interpretation of the nature of the defect. Further research on information presented in domains different from the time domain is necessary.

In table 6, already a vast number of classification cases are reported. The Wilk's Lambda, the classification method and the classification error rate are reported as well As it can be derived from this table, the error rate in most cases ranges between 17 and 27% In the cases that classification returns a high error rate (except the cases where the potential function classifier was used), this was due to the presence of one defect which is difficult to classify, i e plastic (PLP) It appeared to be very difficult to distinguish the defect signals obtain. J from polyamide (PIM) and paper (PAP) Tgis even occurs when the Lambda value is low.

The potential function classifier always returns a higher error rate compared with the theoretical one when classifying the signals at random A possible explanation is that instability occurs in the case of a distance coming to close to zero In that case, although the potential function reaches infinity, a finite value is substituted for practical reasons A solution is to remove the locates which causes this problem. In any case, it very well demonstrates a peculiar effect demanding further investigation.

Comparing lines 1, 2 and 4 from table 6 shows that the 1-NNC, the 3-NNC and the M-NNC produce exactly the same error rate (27%) the same error rate resulted from the classification problems mentioned in lines 5 and 6 as well as from the problems in lines 23, 24 and 25 It shows that the results seem to be independant from the classifier selection Actually, it indicates that the discriminating power of a classifier is at first determined by the quality of the feature set which has been given Other reasons contributing to the above described phenomenon is that first all these classifiers are different versions of the basic distance classification method and second the training and the test set are quite small in numbers. Better results are to be expected when the number of the training samples increases.

To conclude, by considering that the feature set was arbitrarely chosen (so not the best possible), and considering that the training set was not optimized (the store all method was used), the results can be viewed as encouraging for further investigation.

10. CONCLUSIONS

Browsing over the results, one can conclude that in all cases the classification error rate is much lower then the one obtained when classifying at random. Therefore, pattern recognition techniques applied on ultrasonic data has proven to have great potential, especially when the choice of features and classifier can be refined in future after continuous research.

Pattern recognition techniques couples with expert systems and applied on ultrasonic A-scan signals as well as on other non-destructive testing methods, acoustic emisssion or acousto ultrasonic, is beleived to increase dramatically the capabilities of these methods.

11. ACKNOWLEDGEMENTS

12. REFERENCES

[1] R D. Adams, P. Cawley, "A review of defect types and nondestructive testing techniques for composites and bonded joints", NDT International, Vol 21 Number 4, August 88.

[2] A. Vary, "The acousto-ultrasonic approach", Acousto electronics, ed J C. Duke, Plenum Press.

[3] D. Van Hemelrijck, H. Sol, W P. De Wilde, A H Cardon, F. De Roey, L. Schillemans, F. Boulpaep, "Automation of C-scan data acquisition"

[4] Nondestructive testing handbook, Speedtronics Ltd

[5] C.H. Chen, "High resolution spectral analysis NDE techniques for flaw characterization, prediction and discrimination", NATO ASI Series, Vol F44, Signal Processing and Pattern Recognition in NDE, Springer-Verlag Berlin Heidelberg 88

[6] IUNDE 2 0, User's manual, Information Research Laboratory Inc

[7] A.R. Baker, C G Windsor, "The classification of defects from ultrasonic data using neural networks. the Hopfield method", NDT International, Vol 22, No 2, April 1989

[8] A.A. Anastassopoulos, "Signal Processing and Pattern Recognition of Ultrasonic Data", Internal Report at the Free University of Brussels, Dept. of Structural Analysis, September 1991.

[9] Krautkramer, Operating manual USIP 12 and DTM 12

[10] E. Oran Brigham, "The Fast Fourier Transform", Prentice Hall Inc.

[11] D E. Newland, "An introduction to random vibrations and spectral analysis", Longman Press.

[12] W H. Press, B.P. Flannery, S.A. Teukolsky, W T. Vetterling, "Numerical Recipes in C", Cambridge University Press 1989.

[13] T E. Preuss, G. Clark, "Use of Time of flight C-scanning for assessment of impact damage of composites", Composites, Vol 19, nr 2, 1988.

[14] C. Roy, A. Maslouhi, D. Gaucher, Z Piasta, "Classification of acoustic emission sources in CFRP assisted by pattern recognition analysis", Can Aero. Sp. J. Vol 34 No 4, pp 224-232, 1988.

[15] R.O. Duda, P E. Hart, "Pattern classification and scene analysis", John Wiley & Sons Inc, 1973.

[16] B C. Batchelor, "Practical approach to pattern recognition", Plenum Press, 1974.

[17] P. Dickstein, Y Segal, E Segal, A.N Sinclair, "Statistical pattern recognition techniques a sample problem of ultrasonic determination of interfacial weakness in adhesive joints", Journal of nondestructive evaluation.

[18] C Roy, J. Allard, A. Maslouhi, Z. Piasta, "Pattern recognition characterization of microfailures in composites via analytical quantitative acoustic emission".

[19] C. Roy, A Maslouhi, M El Ghorba, "Study of failure processes in fiber reinforced composites using acoustic emission techniques", Agard, No 462, 1990.

[20] P.A. Dickstein, S Girshovich, Y. Sternberg, A.N. Sinclair, H. Leibovitch, "Ultrasonic feature-based classification of the interfacial condition in composite adhesive joints", Res. Nondestr. Eval. 2, pp 207-224, 1990.

[21] P.A. Dickstein, S. Girshovich, Y. Sternberg, A.N. Sinclair, H Leibovitch, A. Notea, "Non linear correlation between statistically sensitive ultrasonic features and strength of composite adhesive joints", Progress in quantitative NDE, Vol 10, Plenum-Press

[22] P.W. Becker, "An introduction to the design of pattern recognition devices", International Centre for Mechanical Sciences CISM, Udine, Springer-verlag Wien New-York, July 1971.

[23] G. Longo, B. Picinbono, "Time and frequency representation of signals and systems", International Centre for Mechanical Sciences CISM, Udine, Springer-verlag Wien New-York, 1989.
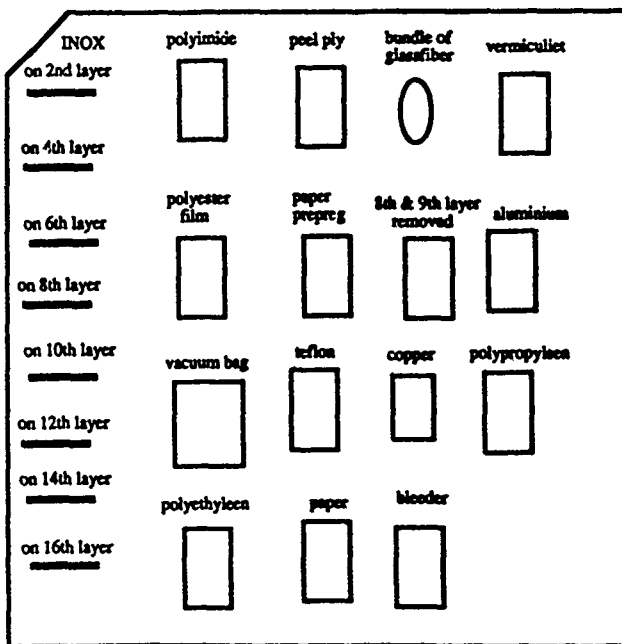
Figure 11 : Location of Defects
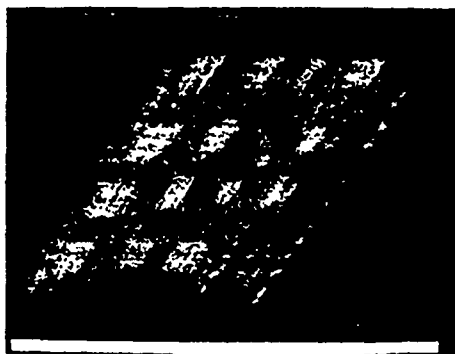
Figure 14 : 3D location of defects
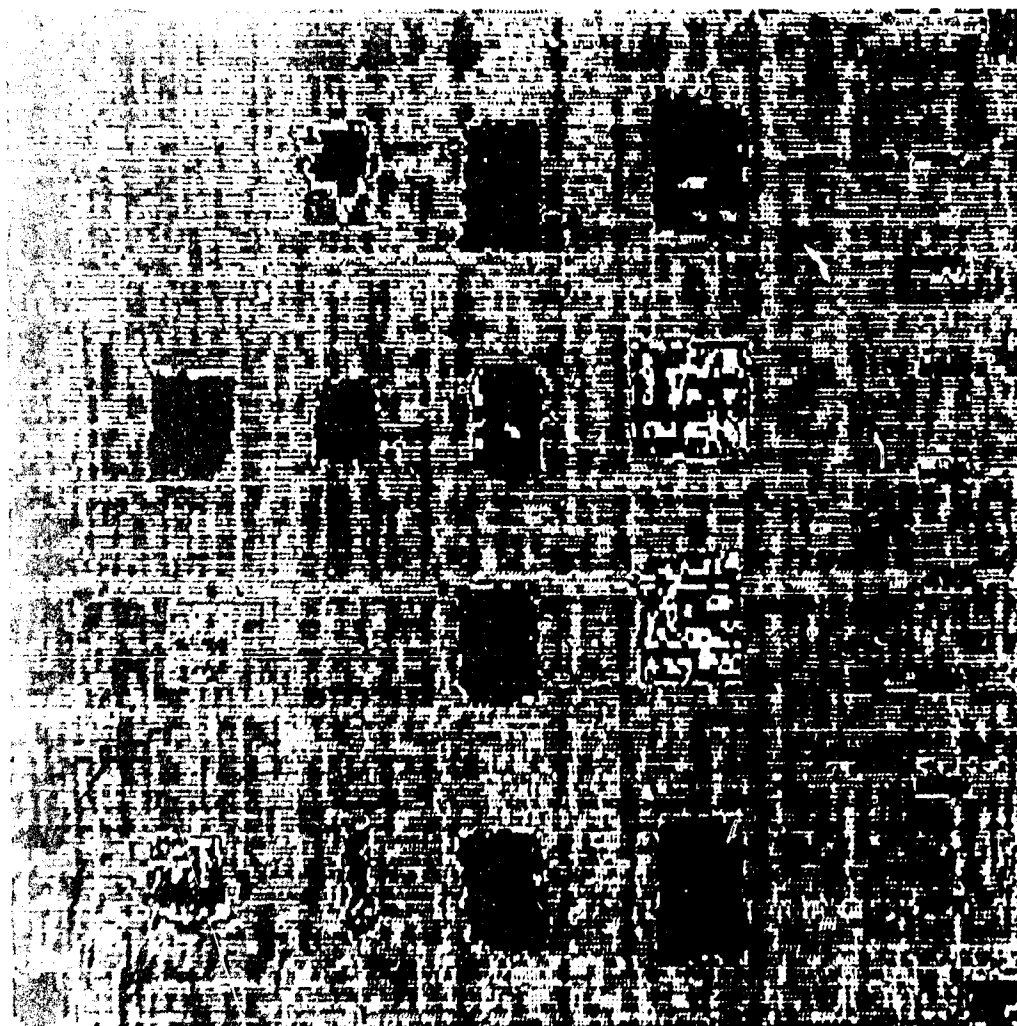
Figure 13 : Defect echo.

8. RESULTS part a

Nr.	Classes	Features	Lambda	Classifier	Error Rate Theory [%]	Error rate Practice [%]
1	0, 1, 2	8, 12, 15, 18, 19, 69, 74, 77, 98	0.0077	1-NNC	67	27
2	0, 1, 2	8, 12, 15, 18, 19, 69, 74, 77, 98	0.0077	3-NNC	67	27
3	0, 1, 2	8, 12, 15, 18, 19, 69, 74, 77, 98	0.0077	PFC	67	86
4	0, 1, 2	8, 12, 15, 18, 19, 69, 74, 77, 98	0.0077	M-NNC	67	27
5	1, 2, 3	8, 12, 15, 18, 19, 69, 74, 77, 98	0.0190	1-NNC	67	17
6	1, 2, 3	8, 12, 15, 18, 19, 69, 74, 77, 98	0.0190	M-NNC	67	17
7	2, 3, 4	8, 12, 15, 18, 19, 69, 74, 77, 98	0.0909	1-NNC	67	46
8	1, 2, 3, 4	8, 12, 15, 18, 19, 69, 74, 77, 98	0.0151	1-NNC	75	46
9	0, 1, 2, 3	8, 12, 15, 18, 19, 69, 74, 77, 98	0.0065	1-NNC	75	25
10	0, 1, 2, 3	8, 12, 15, 18, 19, 69, 74, 77, 98	0.0066	M-NNC	75	25
11	0, 1, 2, 3, 4	8, 12, 15, 18, 19, 69, 74, 77, 98	0.0053	1-NNC	80	42
12	0, 1, 2, 3, 4	8, 12, 15, 18, 19, 69, 74, 77, 98	0.0906	PFC	80	100
13	5, 6	13, 27, 31, 69, 73, 77, 80, 96, 116	0.3710	1-NNC	50	50
14	5, 6	58, 71, 74, 77, 80, 81, 83, 98, 117	0.2550	1-NNC	50	19
15	5, 6	5, 12, 27, 71, 77, 80, 81, 83, 117	0.1124	1-NNC	50	20
16	5, 6, 7	6, 12, 15, 18, 27, 39, 43, 71, 80	0.0682	1-NNC	67	41
17	5, 6, 7	6, 12, 15, 18, 27, 39, 43, 71, 80	0.0682	Lin Class	67	52
18	5, 6, 7	6, 12, 15, 18, 27, 39, 43, 71, 80	0.0682	M-NNC	67	39
19	5, 7	6, 12, 15, 18, 27, 39, 43, 71, 80	0.3319	1-NNC	50	-
20	5, 7	12, 15, 18, 22, 25, 70, 98, 99, 100	0.2762	1-NNC	50	63
21	8, 9	5, 12, 15, 18, 25, 70, 98, 99, 100	0.1294	1-NNC	50	26
22	7, 8, 9	5, 12, 15, 18, 25, 70, 98, 99, 100	0.0619	1-NNC	67	39
23	6, 8, 9	5, 12, 15, 18, 25, 70, 98, 99, 100	0.0607	1-NNC	67	54
24	6, 8, 9	5, 12, 15, 18, 25, 70, 98, 99, 100	0.0607	Lin Class	67	54
25	6, 8, 9	5, 12, 15, 18, 25, 70, 98, 99, 100	0.0607	PFC	67	81
26	7, 8, 9	5, 12, 15, 18, 25, 70, 98, 100	0.0247	1-NNC	67	30
27	8, 10, 11	6, 11, 14, 17, 27, 39, 43, 56, 74	0.3210	NNC	67	27
28	8, 10, 11	6, 11, 14, 17, 27, 39, 43, 56, 74	0.3210	M-NNC	67	27
29	8, 10, 11	6, 11, 14, 17, 27, 39, 43, 56, 74	0.3210	Lin Class	67	27
30	12, 13	1, 4, 5, 6, 26, 27, 28, 29, 33	0.0149	1-NNC	50	6
31	12, 13	4, 5, 6, 7, 26, 27, 28, 31, 35	0.0000	1-NNC	50	25
32	12, 13	1, 4, 5, 6, 26, 27, 28, 29, 33	0.0149	Lin Class	50	6
33	12, 13	1, 4, 5, 6, 26, 27, 28, 29, 33	0.0149	PFC	50	50
34	5, 12, 14	6, 27, 28, 29, 69, 71, 89, 90, 91	0.0000	1-NNC	67	13
35	5, 12, 14	6, 27, 28, 29, 69, 71, 89, 90, 91	0.0000	M-NNC	67	13
36	5, 12, 14	6, 27, 28, 29, 69, 71, 89, 90, 91	0.0000	PFC	67	63
37	5, 12, 14, 15	6, 27, 28, 29, 69, 71, 89, 90, 91	0.0000	1-NNC	75	17
38	5, 12, 13, 14	6, 27, 28, 29, 69, 71, 89, 90, 91	0.0000	1-NNC	75	38
39	9, 14, 15	6, 27, 28, 29, 69, 71, 89, 90, 91	0.0000	1-NNC	75	8
40	13, 15, 16	6, 27, 28, 29, 69, 71, 89, 90, 91	0.0000	1-NNC	75	38
41	5, 6	27, 28, 29, 69, 71, 89, 90, 91, 98	0.1140	1-NNC	50	31
42	5, 6, 7	27, 28, 29, 69, 71, 89, 90, 91, 98	0.0831	1-NNC	67	59
43	8, 9	4, 27, 28, 29, 69, 71, 89, 90, 91	0.0640	1-NNC	50	25
44	8, 9, 11	4, 27, 28, 29, 69, 71, 89, 90, 91	0.0469	1-NNC	67	50
45	9, 12, 15	9, 10, 22, 26, 27, 28, 40, 42, 43	0.0893	1-NNC	67	17
46	12, 13	3, 4, 8, 9, 17, 19, 23, 33, 39	0.0422	1-NNC	50	31
47	12, 13	3, 4, 8, 9, 17, 19, 23, 33, 39	0.0422	1-NNC	50	17
48	5, 6	11, 14, 17, 32, 34, 36, 45, 108, 119	0.1369	1-NNC	50	38
49	5, 6	11, 14, 17, 34, 36	0.1543	1-NNC	50	50
50	5, 7	11, 14, 17, 23, 24, 80, 119, 125, 128	0.1033	1-NNC	50	0

Table 6a Results of Classification

Classes: 0: Copper CU, 1: Siliconrubber SIL, 2: Polypropyleen PPR, 3: Peelply PEP, 4: Plastic PLP, 5: Paper PAP, 6. Polyester PES, 7.
Polyimide PIM, 8: Aluminium AL, 9. Vacuumbag VAP, 10: Teflon TEF, 11: No defect CAR, 12 Teflon Coated Glassfiber
TCG, 13: Glassfiber GLA, 14 Teflon d=0.22mm TE2, 15: Teflon d=0.05mm TE1, 16: Paper Prepreg PAG

Features: Numbering is taken as shown in Appendix A.

Classifier:

|	
k-NNC	k-nearest neighbour classifier
M-NNC	modified nearest neighbour classifier
PFC	potential function classifier
Lin Class	linear classifier

8. RESULTS part b

Nr.	Classes	Features	Lambda	Classifier	Error Rate Theory [%]	Error rate Practice [%]
51	6, 8	2, 3, 11, 14, 17, 23, 24, 95, 96	0.0000	1-NNC	50	0
52	6, 8	2, 3, 11, 14, 17, 23, 24, 95, 96	0.0000	PFC	50	100
53	6, 9	1, 11, 14, 17, 23, 63, 120, 126, 133	0.0479	1-NNC	50	6
54	6, 9	1, 11, 14, 17, 23, 63, 120, 126, 133	0.0479	PFC	50	31
55	5, 8	1, 2, 3, 18, 22, 23, 43, 95, 96	0.0000	1-NNC	50	0
56	5, 7	11, 14, 17, 22, 23, 47, 76 77, 80	0 1211	1-NNC	50	31
57	5, 7	11, 14, 17, 22, 23, 47, 76, 77, 80	0.1211	M-NNC	50	37
58	5, 8	1, 2, 3, 18, 22, 23, 43, 95, 96	0 0000	PFC	50	63
59	5, 9	11, 14, 16, 33, 39, 45, 64, 117, 132	0.1112	1-NNC	50	31
60	5, 9	16, 33, 45, 64, 14, 11, 39, 132, 117	0.1113	PFC	50	50
61	7, 8	3, 2, 43, 18, 1, 26, 27, 16, 95	0.0000	1-NNC	50	6
62	7, 8	3, 2, 43, 18, 1, 26, 27, 16, 95	0 0000	PFC	50	63
63	7, 9	125,119,16, 24, 15, 108, 33, 101, 80	0.0218	PFC	50	69
65	7, 9	125,119,16, 24, 15, 108, 33, 101, 80	0.0218	1-NNC	50	13
66	8, 9	1, 2, 95, 96, 45, 24, 27, 26, 15	0.0084	1-NNC	50	13
67	8, 9	1, 2, 95, 96, 45, 24, 27, 26, 15	0 0084	PFC	50	69
69	5, 6, 7	11, 14, 23, 17, 80, 119, 125, 24, 128	0.1883	1-NNC	67	25
70	5, 6, 7	11, 14, 23, 17, 80, 119, 125, 24, 128	0.1883	PFC	67	67
71	5, 6, 8	3, 17, 23, 11, 14, 96, 95, 43, 2	0.1634	1-NNC	67	17
72	5, 6, 8	3, 17, 23, 11, 14, 96, 95, 43, 2	0 1634	PFC	67	100
73	5, 6, 9	11, 14, 23, 17, 45, 16, 33, 63, 108	0 0286	1-NNC	67	13
74	5, 6, 9	11, 14, 23, 17, 45, 16, 33, 63, 108	0 0286	PFC	67	84
75	6, 7, 8	3, 23, 11, 17, 14, 24, 43, 1, 96	0 0000	1-NNC	67	8
76	6, 7, 8	3, 23, 11, 17, 14, 24, 43, 1, 96	0 0000	PFC	67	96
77	6, 7, 9	11, 14, 23, 17, 119, 125, 24, 1, 108	0 0000	1-NNC	67	29
78	6, 7, 9	11, 14, 23, 17, 119, 125, 24, 1, 108	0 0000	PFC	67	83
79	6, 8, 9	23, 1, 11, 14, 17, 96, 95, 3, 45	0 0018	1-NNC	67	25
80	6, 8, 9	23, 1, 11, 14, 17, 96, 95, 3, 45	0 0018	PFC	67	96
81	5, 7, 8	3, 43, 18, 2, 96, 1, 95, 23, 11	0 0000	1-NNC	67	29
82	5, 7, 8	3, 43, 18, 2, 96, 1, 95, 23, 11	0 0000	PFC	67	75
83	5, 7, 9	16, 22, 44, 18, 26, 92, 27, 11, 14	0 1288	1-NNC	67	46
84	5, 7, 9	16, 22, 44, 18, 26, 92, 27, 11, 14	0 1288	PFC	67	58
85	5, 8, 9	1, 2, 95, 96, 45, 24, 27, 15, 26	0 0117	1-NNC	67	46
86	5, 8, 9	1, 2, 95, 96, 45, 24, 27, 15, 26	0.0117	PFC	67	83
87	7, 8, 9	1, 2, 24, 3, 95, 96, 43, 27, 26	0 0099	1-NNC	67	29
88	7, 8, 9	1, 2, 24, 3, 95, 96, 43, 27, 26	0 0099	PFC	67	75
89	5, 6, 7	3, 11, 23, 14, 17, 96, 43, 95, 24	0 0000	1-NNC	67	8
90	5, 6, 7, 8	3, 11, 23, 14, 17, 96, 43, 95, 24	0 0000	M-NNC	75	13
91	5, 6, 7, 9	11, 14, 23, 17, 119, 125, 16, 33, 80	0.0043	1-NNC	75	29
92	5, 6, 7, 9	11, 14, 23, 17, 119, 125, 16, 33, 80	0.0043	M-NNC	75	29
93	6, 7, 8, 9	23, 11, 14, 17, 1, 3, 24, 95, 96	0 0019	1-NNC	75	54
94	6, 7, 8, 9	23, 11, 14, 17, 1, 3, 24, 95, 96	0 0019	M-NNC	75	54
95	5, 7, 8, 9	3, 1, 2, 96, 95, 16, 43, 24, 22	0 0636	1-NNC	75	33
96	5, 7, 8, 9	3, 1, 2, 96, 95, 16, 43, 24, 22	0 0636	M-NNC	75	33
97	5, 6, 8, 9	11, 14, 23, 17, 3, 1, 96, 95, 2	0.0000	1-NNC	75	42
98	5, 6, 8, 9	11, 14, 23, 17, 3, 1, 96, 95, 2	0 0000	M-NNC	75	42
99	5, 6, 7, 8, 9	11, 14, 23, 17, 3, 1, 96, 95, 24	0 0030	1-NNC	80	50
100	5, 6, 7, 8	11, 14, 23, 17, 3, 1, 96, 95, 24	0 0030	M-NNC	80	50

Table 6b. Results of Classification

Classes 0. Copper CU, 1: Siliconrubber SIL, 2: Polypropyleen PPR, 3. Peelply PEP, 4: Plastic PLP, 5 Paper PAP, 6· Polyester PES, 7: Polyimude PIM, 8: Aluminium AL, 9: Vacuumbag VAP, 10. Teflon TEF, 11: No defect CAR, 12: Teflon Coated Glassfiber TCG, 13: Glassfiber GLA, 14: Teflon d=0.22mm TE2, 15: Teflon d=0 035mm TE1, 16: Paper Prepreg PAG

Features: Numbening is taken as shown in Appendix A.

Classifier:
k-NNC	k-nearest neighbour classifier
M-NNC	modified nearest neighbour classifier
PFC	potential function classifier
Lin Class	linear classifier

Appendix A : Numbering of Descriptors (Automatic generation in 4 domains)

TD = Time Domain ; MD = Square Time Domain ; FR = Frequency Domain ; AC = Autocorrelation Domain

Features Numbering	TD	MD	FR	AC
# of peaks above signal base line	1		64	107
# of peaks above 10% maximum peak amplitude	2		65	108
# of peaks above 20% maximum peak amplitude	3		66	109
# of peaks above 30% maximum peak amplitude	4		67	110
# of peaks above 40% maximum peak amplitude	5		68	111
# of peaks above 50% maximum peak amplitude	6		69	112
# of peaks above 60% maximum peak amplitude	7		70	113
# of peaks above 70% maximum peak amplitude	8		71	114
# of peaks above 80% maximum peak amplitude	9		72	115
# of peaks above 90% maximum peak amplitude	10		73	116
1st greatest peak amplitude	11		74	117
1st greatest peak position	12		75	118
1st greatest peak area	13		76	119
2nd greatest peak amplitude	14		77	120
2nd greatest peak position	15		78	121
2nd greatest peak area	16		79	122
3rd greatest peak amplitude	17		80	123
3rd greatest peak position	18		81	124
3rd greatest peak area	19		82	125
4th greatest peak amplitude	20		83	126
4th greatest peak position	21		84	127
4th greatest peak area	22		85	128
5th greatest peak amplitude	23		86	129
5th greatest peak position	24		87	130
5th greatest peak area	25		88	131
Inter peak distance 1st and 2nd peak	26		89	132
Inter peak distance 1st and 3rd peak	27		90	133
Inter peak distance 2nd and 3rd peak	28		91	134
Mean value	29		92	
Variance	30		93	
Standard deviation	31		94	
Average deviation	32		95	
Skewness	33		96	
Kurtosis	34		97	
1st greatest peak rise time	35			
1st greatest peak fall time	36			
1st greatest peak full width	37			
1st greatest peak half width	38			
2nd greatest peak rise time	39			
2nd greatest peak fall time	40			
2nd greatest peak full width	41			
2nd greatest peak half width	42			
3rd greatest peak rise time	43			
3rd greatest peak fall time	44			
3rd greatest peak full width	45			
3rd greatest peak half width	46			
4th greatest peak rise time	47			
4th greatest peak fall time	48			
4th greatest peak full width	49			
4th greatest peak half width	50			
5th greatest peak rise time	51			
5th greatest peak fall time	52			
5th greatest peak full width	53			
5th greatest peak half width	54			
Total area		55	98	135
Partial area of band 1		56	99	136
Partial area of band 2		57	100	137
Partial area of band 3		58	101	138
Partial area of band 4		59	102	139
Partial area of band 5		60	103	140
Partial area of band 6		61	104	141
Partial area of band 7		62	105	142
Partial area of band 8		63	106	143

DAMAGE DETECTION BY ACOUSTO-ULTRASONIC LOCATION (AUL)

Z. P. Marioli-Riga, A. N. Karanika
R&D Department
Advanced Materials, Processes and Mfg Lab
Hellenic Aerospace Industry

T. P. Philippidis, S. A. Paipetis
Department of Mechanical Engineering
University of Patras
Patras 260 01, Greece

Abstract

Damage detection in aircraft structures in-situ is important, especially with not visible defects in composite components for a variety of reasons. In the present paper a new technique based on the Acousto-Ultrasonic (AU) concept is introduced, but instead of extracting information from the externally generated pulsed wave, as with AU, the characteristics of waves reflected from defects are measured. In this way it was possible to identify and locate defected areas in honeycomb panels and thermoplastic carbon fibre laminates The results were correlated with ultrasonic C-scans, and satisfactory agreement was obtained. The present is part of a major project aiming at the development of fast inspection method for aircraft components during routine maintenance cycles.

1. Introduction

Damage detection in aircraft structures under *in-situ* conditions and within the limitations of hangar facilities is of great importance and the relevant NDI techniques certainly play a decisive role.

In recent years adhesives were increasingly used both in structural as well as in nonstructural applications. Easily applicable, reliable and fast non-destructive inspection is most welcome with adhesively bonded joints, e.g. helicopter honeycomb structures and helicopter rotor blades. Furthermore, the effect of environmental conditions or of service-induced damage on the performance of bonded joints during service life, such as impact, requires additional reassurance of bond quality. Consequently, there is a need for NDE techniques capable of characterizing the structural performance of bonded joints reliably both after fabrication and during service life.

Debonding and delamination damage was observed in honeycomb panels (skins) on several occasions after a number of flights as a result of vibrations and complex stress states.

By the standard coin tapping test debonding can be detected, however, the results strongly depend on inspector's experience to perceive acoustic differences by the ear. Besides, by means of portable pulse-echo ultrasonics unbonds can be detected, but the efficiency of the method on weakbonds is questionable. Although ultrasonic C-Scan may produce reliable results, the application of the method has considerable limitations, since the aircraft components concerned must be disassembled.

For an *in-situ* inspection, Acoustic Emission (AE) techniques have also limitations since load application is necessary, while Acousto-Ultrasonics (AU), introduced by Vary [1], is a relatively new technique under development. Recent studies [2-4], however, have demonstrated that AU methods can be used to provide quantitative information of the mechanical performance of bonded joints by correlating the AU stress wave propagation characteristics and joint strength.

From the practical point of view, the AU method offers some advantages. The technique requires access to one side of the structure only and is potentially suitable for use on existing structures where two-side accessability and the structure must not be disassembled [5].

In the present paper, an AU location (AUL) technique is proposed, tested on various aircraft composite components, either carbon fibre reinforced laminates (CFRP) or honeycomb panels and gave promising results. The method consists in capturing reflections of externally generated ultrasonic low frequency waves from existing defects. The reflected waves are detected by a network of AE sensors and defect location is performed by measuring differences in arrival times at the nodes of the network.

Results from representative aircraft composite components were correlated with ultrasonic C-scan recordings to verify the validity of the method and are encouraging.

2. Materials and Experimental Procedure

The present experimental study was mainly concerned with the assessment of the capability of the AUL technique in detecting debonding in adhesively bonded structures and delaminations in CFRP panels. To this end, a helicopter panel assembly made of Al-alloy 2024-T4 skins and honeycomb Al-Al 5052 core adhesively bonded in a sandwich construction was tested. Besides, panels made of carbon reinforced thermoplastic (PEEK) laminates were produced in a heating press at a moulding cycle of 370°C and 10 bars for 7 min. The stacking sequence was [45/90/-45/0]2s and artificial defects were induced by inserting teflon film tabs at the 2nd, 8th and 15th layer interfaces. The helicopter panel assembly was damaged in flight with debonding developed between Al skin and core. The major debonded area was approximately 12 cm^2.

In the first place panels were C-scanned to evaluate structural integrity and assess the validity of AUL results In Figs 1 and 2 images taken from through-transmission inspection of a typical sandwich panel and CFRP laminate respectively are shown These plots clearly reveal the exact location and magnitude of defects enabling thus calibration of hardware settings for the AUL technique on unflawed areas.
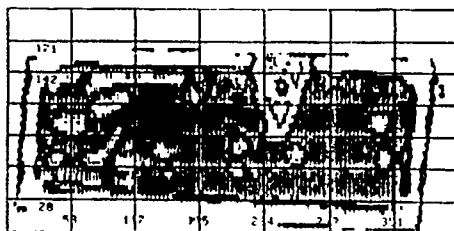

Fig.1 : C-Scan representation of H/P sandwich panel by means of through-transmission ultrasonic inspection
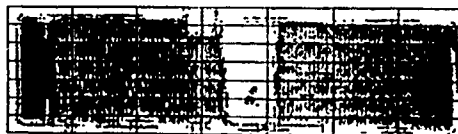
Fig 2 : C-Scan representation of Carbon/Peek [45/90/-45/0]2s laminate by means of through-transmission ultrasonic inspection.

Measurements were carried out by means of LOCAN- and SPAR-TAN-AT AE systems of Physical Acoustics Corporation (PAC), Princeton USA using 150 kHz resonance transducers, type PAC R15 and 40 dB gain preamplifierss, type PAC 1220A. System threshold level was 30 dB. Externally generated waves were pulsed into the test specimens by means of R15 sensors using built-in pulsers of the respective AE system at a repetition rate of 1 Hz, pulse width 1μs and rise time < 100 ns.

Initially, application of an AU technique was attempted - not by performing frequency analysis of the reflected wave after having travelled through the medium. By scanning the whole surface of the specimen with a set of two transducers, a pulser-receiver pair separated by a constant distance of 60 mm, it was hoped that a 3D plot of certain descriptors of the burst waves detected by the AE sensor would reveal defect areas. Although some encouraging results were initially produced, it was eventually decided to abandon the technique, mainly due to the lack of repeatability in the measured descriptors values, probably a result of different coupling conditions.

The only parameter of the detected wave not seriously affected by the coupling efficiency between probes and specimens was the travelling time between pulser and receiver. Then the idea for the new technique AUL was conceived in a straightforward manner. It was decided to perform the classical AE location, by measuring arrival times at the different sensors of a network. However, instead of considering the externally generated wave, the ones occurring from reflections due to defect boundaries were recorded and damage location was obtained.
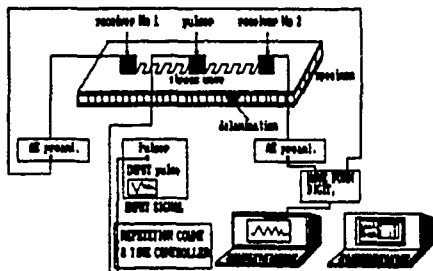
Fig 3 : Schematic diagram of the Acousto-Ultrasonic Location (AUL) set-up.

The AUL experimental set-up used is illustrated in Fig. 3 and measurements were performed as follows: Two AE transducers were used, 185 mm apart for the sandwich panel and 140 mm for the CFRP laminate and the pulser was placed halfway this distance. The latter was selected by measuring wave attenuation. Such a typical attenuation curve for the helicopter sandwich panel of Fig. 1 is shown in Fig. 4.
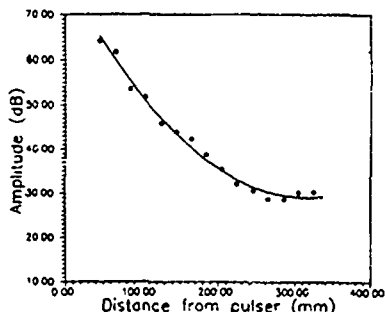
Fig.4 . Wave attenuation characteristic curve for a H/P sandwich panel assy.

The set of the three R15 sensors was moved in parallel to itself by steps of 10 mm to scan the area. Reflected waves from the defect regions were received by the two AE sensors and simple linear location calculations were performed based on the arrival time difference between the two receiving sensors, see Fig. 5.

$$a = \frac{l + v \Delta t}{2}$$

v : stress wave velocity

Δt = t₁ - t₂
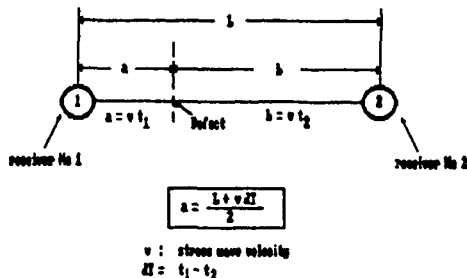
Fig.5 : Linear location principle.

3. Results and Discussion

Typical results of the AUL method applied as above are given in Figs. 6 and 7. According to this new technique the stress wave generated by the pulser is reflected on the defect boundaries and the absolute time values at the moment that the reflected waves are received by the AE sensors are used to locate the defects. Fig. 6 illustrates the results obtained from the helicopter panel and Fig. 7 those of the carbon/PEEK laminate. For correlation purposes the AUL graphs were superimposed on ultrasonic C-scans of the same scale. In these figures the two receiving AE transducers were denoted by triangles while the solid circles indicate the predicted defect location. The C-scan background of Fig. 6 is a magnification of the defect area of Fig. 1 to match the dimensions of the location plot. As confirmed from Figs. 6 and 7, the AUL results are in satisfactory agreement with those of the C-scans proving how promising the present method is

Fig.6 : AU-Location results for the honeycomb panel superimposed on C-Scan graph.

Fig.7 . AU-Location results for the Carbon/Peek laminate superimposed on C-Scan graph.

Further inspection of the results reveals that the AUL technique detects the most critical points of the defect. This observation is also supported by the fact that for the artificial defect of Fig. 7, the location points are vertically ordered, while for the the real debonding in the honeycomb panel, Fig. 6, the locates are quite randomly distributed. However, the bond quality around the critical points is, at least till present, beyond the limits of the method. Currently, further investigation is performed, aiming at the determination of defect dimensions.

The main advantage of the AUL technique over conventional ultrasonic C-scan inspection is the increased scanning speed of large areas. Furthermore, this new NDI method is applicable in-situ during maintenance, thanks to the flexibility of the portable AE instrumentation. By using expandable AE systems supporting a large number of monitoring channels, such as SPARTAN-AT of PAC, it is possible to evaluate the structural integrity of a large aircraft panel right away.

4. Conclusions

A new experimental technique is introduced for the detection and location of defective, i.e. debonded or delaminated, areas in honeycomb panels and composite laminates. The method is based on the AU concept, e.g. on the analysis of acoustic emission signals simulated by ultrasonic waves externally generated by a pulsed source and travelling through the material. Despite similarity with conventional AU techniques, the present method aims primarily at flaw detection and location rather than the investigation of the integrated effect of material damage on the ultrasonic signal characteristics [1]. Furthermore, in the approach so far outlined, the ultrasonic pulsed wave is used to generate reflections from the boundaries of the defective areas, and location is performed by measuring differences of wave arrival times in a network of piezoelectric receivers. Since the method is dealing with the characteristics of reflected waves rather than of the externally generated ultrasonic wave, careful calibration of the AE hardware setup as well as selective positioning of the pulser and the detecting transducers are necessary.

Results from the honeycomb panels and artificially defected carbon/PEEK laminates tested are satisfactory and in agreement with ultrasonic C-scan images. Once the proper calibration of the hardware was successful, the technique proved its reliability and repeatability.

Naturally, several features need further investigation, as for example the effect of the pulser position in-between the two receivers on the exact determination of the defect position, when performing linear location. Furthermore, the effect of the coupling between probes and test specimen on the accuracy of the results must be also be investigated, since during the present work, it was proved that it has a strong influence on the reflected wave descriptors.

In conclusion it can be stated that the results of the present experimental procedure are encouraging and the method can be further developed into a reliable, fast NDE technique for in-situ integrity assessment of aerospace components.

REFERENCES

1. A. Vary, The Acousto-Ultrasonic Approach, in Acousto-Ultrasonics, ed. J.C.Duke, Jr., Plenum Publishing Corp., 1988.
2. A. Vary. Acousto-Ultrasonic Characterization of Fibre Reinforced Composites, Materials Evaluation 40(6), 650-662, (1982).
3. A. F. Vargas, Acoustic Emission Evaluation of Adhesive Bonded Joints on Helicopter Rotor Blades, Physical Acoustics Corp., TR 103-54/1983, Lawrenceville, N.J. USA.
4. J. R. Mitchell, Multi-Parameter, Multi-Frequency Acousto-Ultrasonics for Detecting Impact Damage in Composites, Physical Acoustics Corp., TR 103-72A-7/1987, Lawrenceville, N.J. USA.
5. A. Fahr, S. Tanary, Non Destructive Evaluation of Adhesively Bonded Joints, in Impact of Emerging NDE-NDI Methods on Aircraft Design, Manufacture and Maintenance, AGARD-CP-462, 1989.

PREDICTION OF DELAMINATION IN TAPERED UNIDIRECTIONAL GLASS FIBRE EPOXY WITH DROPPED PLIES UNDER STATIC TENSION AND COMPRESSION

by

Michael R. Wisnom
Department of Aerospace Engineering
University of Bristol
Queen's Building
University Walk
Bristol BS8 1TR
United Kingdom

ABSTRACT

The mechanism of delamination in tapered unidirectional specimens with dropped plies is discussed. Results from six sets of static tests with different numbers of dropped and continuous plies are presented. Specimens with 2 dropped/4 continuous, 2 dropped/8 continuous and 6 dropped/4 continuous plies were tested in tension, and specimens with 2 dropped/16 continuous, 2 dropped/32 continuous and 4 dropped/32 continuous plies were tested in compression. In all cases failure occurred by delamination into the thick section both above and below the dropped plies. Results are compared with predictions from a simple formula based on the strain energy release rate associated with the terminating plies, with the fracture energy determined from tension tests on a unidirectional specimen with cut central plies. Good correlation was found, and this approach is recommended as a design method for predicting delamination in tapered sections.

1. INTRODUCTION

Delamination is a major cause of failure in composite structures and so accurate prediction of the onset of delamination and understanding the fundamental controlling mechanisms are of considerable importance. A tapered section involving the progressive dropping of plies is one of the structural configurations which is prone to delamination. Tapered sections are very commonly used to achieve changes in thickness. A typical example is a helicopter rotor blade, where increased thickness is necessary near the root. Rotor blades are often made predominantly from unidirectional composites since the loading is mainly in the spanwise direction. Glass fibre-epoxy is a frequently used material because of its good strength and damage tolerance. The study of delamination in tapered unidirectional glass fibre-epoxy is therefore directly relevant to the design of composite rotor blades. It also provides a very simple configuration with which to investigate some of the fundamental mechanisms controlling delamination in tapered sections.

Most composite structures are made of laminates with plies of different orientations. Free edge stresses are a major cause of delamination in such configurations. Edge effects make the study of the effect of taper much more difficult and also tend to cause much greater scatter in test results. However these effects are not present in unidirectional composites. Glass fibre-epoxy is a good material with which to study delamination because it is possible to detect the initiation and propagation of delamination visually.

Delamination in composites has been extensively investigated, but there is not yet a concensus on a reliable method to predict accurately its occurrence. A number of authors have investigated the problem of delamination in tapered laminates and attempted to predict failure based on maximum stresses [1,2], averaged stresses [3] and strain energy release rates [4]. However these studies have all concerned quite complex laminates with multiple dropped plies which present difficulties in both test and analysis.

In the present study a more fundamental approach has been adopted by concentrating solely on unidirectional specimens with simple symmetric tapered sections. A design method based on an equation derived from a strain energy release rate analysis is presented, and correlation between predictions and experimental results for both static tension and compression is performed.

2. EXPERIMENTAL

2.1 Tension Tests

Three series of tension tests were carried out on tapered unidirectional glass fibre-epoxy specimens with dropped plies. The material was Ciba Geigy pre-preg with E glass fibres in a 913 epoxy matrix. The configurations tested were all symmetric, with 2 dropped/8 continuous, 2 dropped/4 continuous and 6 dropped/4 continuous plies. Plies were dropped in pairs. The 6 dropped plies were in three groups, with a spacing of 2 mm between the forward pair and the other two pairs. Each specimen had a taper at both ends so that the

gripped ends were both the full thickness. This was done to avoid failures at the tabs. The tapered panels were made in a press-clave between flat plates. The thickness between the plates was kept constant by positioning fill-in plies on the outside of the release cloth in the thin section, as shown in Fig. 1.
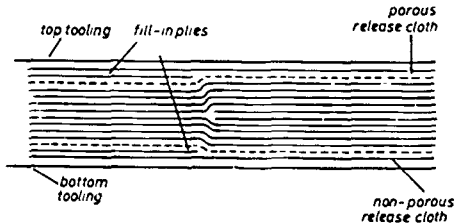

FIG 1 MANUFACTURING METHOD FOR TAPERED SPECIMENS

Specimens 200 x 10 mm with a gauge length of 100 mm and 50 mm aluminium alloy tabs were tested under displacement control at a rate of 0.5 mm/min. The length of the thin section in the middle was 27 mm. Load versus displacement plots were produced using a chart recorder. Back lighting was used in order to detect onset of delamination.

All the specimens behaved very similarly. The lines at the ends of the dropped plies became much more visible at relatively low loads, indicating fracture of the matrix ahead of the dropped plies. Delamination started immediately above and below the end of the dropped plies, and spread stably over a small area before rapidly propagating to the tab. In all cases the location of the delamination corresponded closely to the interface between continuous and discontinuous plies. No significant fibre failure was visible. For the specimens with six dropped plies, the delamination initiated at the forward pair and followed the interface with the continuous plies.

The specimens with 2 dropped plies generally delaminated stably across most of the width of the specimen over a length of several millimetres. The specimens with 6 dropped plies were much more unstable, with no delamination past the start of the outer dropped plies before rapid propagation occurred. In none of the tests was there any delamination into the thin section.

The results are summarised in Table 1. Stresses have been calculated on the basis of the actual average widths but nominal thicknesses using a ply thickness of 0.127 mm and the number of plies in the thick section. This was done in order to avoid discrepancies due to different thicknesses which are normally caused predominantly by variations in the amount of resin. The nominal ply thickness corresponds to a volume fraction of 60%. The stresses are those at which total delamination to the tab occurred, which could be clearly identified by a drop in the load. The stress at onset of delamination was more difficult to determine objectively, but

was quite close to the propagation stress. In all cases the two ends delaminated separately, and the values given are those for the first delamination.

2.2 Compression Tests

Three series of compression tests were carried out on specimens of the same material with 2 dropped/16 continuous, 2 dropped/32 continuous and 4 dropped/32 continuous plies. Much thicker specimens were required than those tested in tension in order to avoid buckling failures. Panels were made up using the same ply fill-in technique as before, but with only a single taper. Specimens 10 mm wide were cut and tabbed as before. The gauge length was 20 mm for the specimens with 32 continuous plies. A reduced length of 15 mm was used for the specimens with only 16 continuous plies. The end of the terminated plies was positioned in the centre of the gauge length. Specimens were tested in an IITRI fixture in an Instron machine under displacement control with a crosshead rate of 0.5 mm/min.

For the specimens with 4 dropped/32 continuous plies, a small amount of delamination occurred stably and then propagated rapidly to the tabs. The specimens then started to bulge outwards, and at this point a small amount of delamination also occurred into the thin end of the specimen, at the mid-plane. With a small further increase in the load, catastrophic compressive failure occurred in the centre of the specimen, at the drop.

For the 2 dropped/16 continuous ply specimens, a small amount of stable delamination into the thick section was also seen, but then catastrophic failure occurred. It is thought that the failure sequence was similar to the thicker specimens, but occurred more rapidly because of the much lower buckling stress.

The 2 dropped/32 continuous ply specimens behaved similarly. Two specimens delaminated back to the tabs before final failure, and two failed catastrophically before significant delamination occurred.

In all cases the main delamination was accompanied by a large drop in load, and the stress at which this occurred was taken as the failure stress. Results are shown in Table 2. As before, stresses are based on actual widths and nominal thicknesses of the thick section.

3. FACTORS AFFECTING FAILURE

Three factors may be important in influencing failure in tapered sections, and these have all been investigated. Firstly there is the stress concentration associated with the terminating plies. Secondly there are interlaminar shear and normal stresses induced by the tapered geometry. Finally there is the effect of the curved fibres adjacent to the ply drop.

The effect of the stress concentration caused by the ply drop has been investigated using straight specimens with the central plies cut across the full width [5]. This produces a similar stress concentration effect as for specimens with dropped plies, but without the geometric effects of the taper. When tested in tension, these specimens delaminated in a very similar manner to the dropped ply specimens. The resin between the ends of the cut plies fractured very early on. Later, delamination initiated above and below the terminating plies on both sides of the cut. After a small amount of delamination at increasing load, the specimens delaminated to the ends at approximately constant load. The delamination stresses were lower than for dropped ply specimens with the same number of continuous and discontinuous plies, and the propagation was generally more stable. In some cases it was possible to unload the specimens during propagation, measure the delaminated area and then reload them. These differences are believed to be due to the effect of through thickness compressive stresses induced in the taper of the dropped ply tension specimens, which inhibit the initiation of delamination. However, once the delamination has spread away from the drop, the through thickness stresses are greatly reduced, and so the delamination propagates rapidly. This explains why in all cases the propagation of delamination for the dropped ply specimens occurred unstably.

Tests on scaled specimens indicated a significant size effect, with the delamination stress decreasing with increasing specimen size. This shows that a simple stress analysis cannot be used to predict failure since the stress distributions in scaled specimens are identical.

Another problem is that linear elastic analysis of these specimens with the resin between the ends of the cut plies already fractured produces a singularity at the cut. There are two approaches to this problem. One is to use the stress at a point or averaged over a distance away from the cut, and the other is to use a fracture mechanics approach. Both these methods have been investigated [6]. It has been found that with the point and average stress criteria the distance parameters are not material constants, but vary significantly with specimen geometry. Use of a strain energy release rate approach gave better results, although it was found that the fracture energy is also not strictly a constant. For an increase in thickness of a factor of 8, the apparent fracture energy increased by 69% [6,7]. Although this is an important effect, over a limited range of size it should still be possible to make useful engineering predictions.

The effect of interlaminar stresses due to the tapered geometry but without the terminated plies was investigated by means of tension specimens waisted through the thickness [8]. These were made by machining straight specimens with a diamond wheel. Relatively severe waisting

was found to be necessary to ensure failure in the tapered section. Panels 4.4 mm thick were waisted down to 1 mm with a radius of 32 mm and to 2 mm with a radius of 64 mm using a diamond wheel. This gave two tapered sections of length approximately 10 and 12 mm respectively on each specimen. For these specimens without a macroscopic singularity it was found that a stress based failure criterion worked satisfactorily. The interlaminar shear stress was found to be the most important component, although there was a significant interaction with stresses in the fibre direction. The effect of this interaction could be accounted for using the Tsai-Wu failure criterion. Testing of scaled specimens indicated no significant effect of size on strength.

The effect of fibre curvature was investigated by means of specimens with an inclusion in the middle [5]. This produced a change in thickness analogous to that caused by dropped plies, but without the stress concentration due to the terminating plies. Tension specimens were fabricated with eight unidirectional composite plies, and two extra "plies" of thin nylon film in the middle over half the length. A similar manufacturing technique was used as for the dropped ply specimens, with nylon film in-fills on the outside of the release cloth. The thickness of the film was similar to the composite ply thickness.

These specimens all failed due to fibre breakage in the tab region. Linear elastic finite element analysis showed that there were interlaminar tensile stresses of up to 128 MPa present at the start of the thin section at the failure load. Despite these high stresses there was no indication of any delamination spreading from the nylon film into the thin section of the composite.

The angle of the plies in the tapered region was estimated from photos to be between about 6 and 7 degrees on either side of the centreline. No fibre damage was observed in this region despite the significant curvature of the plies.

Compression specimens with an inclusion at the middle were also fabricated. In this case 32 continuous composite plies were used, with two layers of film adhesive in the middle. This produced a taper angle of about 3 to 4 degrees. Even with this amount of misalignment and ply curvature these specimens all failed at the tabs with no damage visible in the tapered section.

From this work it was concluded that the critical parameter affecting delamination in tapered unidirectional composites is the strain energy release rate due to the terminating plies. The tapered specimens with inclusions did not delaminate despite high stresses being present locally. In this case it appears that the strain energy release rate was not sufficient to drive the delamination. Neither did premature failure occur as a result of fibre curvature in the tapered region. The machined tapered specimens did

delaminate, but a large thickness change and relatively small radius were required to produce failure. In cases where terminating plies are present, the effect of the stress concentration is likely to be much more significant than the effect of overall interlaminar stresses.

4. PREDICTION OF DELAMINATION

Based on the previous work a method has been proposed to predict delamination of tapered sections. This method is now described and then applied to both the tension and compression tests presented earlier.

Fig. 2 shows the geometry of delamination in a specimen with cut plies. Consider the extension of an existing delamination of length a by an amount δa. The effect of the propagation is to unload a volume δabt, and increase the stress in a volume $\delta ab(h-t)$ from σ to $\sigma h/(h-t)$, where b is the specimen width, h the total thickness, t the thickness of terminated plies and σ the stress based on the total thickness. This gives the following expression for the strain energy release rate:

$$G = \frac{\sigma^2 ht}{4E(h-t)} \qquad (1)$$

Where E is the fibre direction Young's modulus. The effect of the local stress field around the crack tip does not affect the strain energy release rate since this stress field simply moves along the specimen.
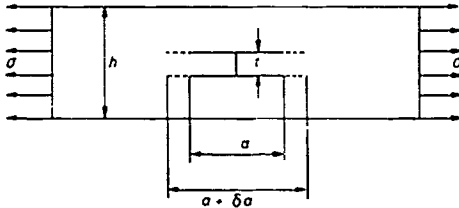

FIG 2 GEOMETRY OF CUT PLY DELAMINATION

The same equation also applies to the dropped ply specimens after they have delaminated some distance. In both cases the initial energy release rate is different from that given by (1), and this can be calculated by finite element analysis. For the cut ply case G was found to be initially slightly higher, whilst for the dropped ply case it was lower [5]. However it has been found that use of this simple equation actually gives better correlation with test results than using initial values of energy release rate calculated by linear elastic finite element analysis. The reason for this is thought to be because a plastic zone arises at the end of the terminating plies, modifying the initial energy release rate [9].

The finite element analysis also confirmed that for both the cut ply and dropped ply tension tests, the delamination is a pure mode II failure.

Rearranging (1) gives the delamination stress as:

$$\sigma = \sqrt{4EG_c(h-t)/ht} \qquad (2)$$

The value of the fracture energy G_c was determined from cut ply tension delamination tests. Specimens with 2 cut and 8 continuous plies were used. As discussed earlier, the fracture energy was found to increase with increasing number of plies. Five of the tapered specimens had plies dropped in pairs, and one had a block of 4 plies dropped together. A specimen with 2 cut plies was therefore considered to be the most appropriate for deducing the fracture energy. The average delamination propagation stress for 6 specimens was 773 MPa, with a coefficient of variation of 2.2%. Using the nominal ply thickness of .127 mm, and Young's modulus of 43.9 GPa, equation (1) gives a value of G_c of 1.08 N/mm.

Using this value of G_c, and equation (2), the delamination stresses for all six cases of dropped ply specimens can be predicted. For the case with 6 dropped plies it was assumed that delamination was controlled by the forward pair of dropped plies. For this case the delamination stress based on the thin section stress was actually the same as for the 2 dropped/4 continuous ply case. Predicted delamination stresses based on the thick section are compared with the average experimental results in Table 3.

5. DISCUSSION

The experimental results are very consistent, with low values of coefficient of variation. These therefore provide a good basis for assessing the accuracy of the predictions. The results show that the delamination strength decreases with the number of dropped plies. There is also a trend of increasing strength with increasing number of continuous plies, both in tension and compression.

The correlation between predicted and measured delamination stresses is good, with results being within about 6% in all but one of the six cases. The worst correlation is for the 2 dropped /8 continuous ply specimens, where the predicted strength is about 20% less than measured. These specimens had the same number of plies as the cut ply specimens from which the fracture energy value was deduced. The reason for the higher strength than predicted is believed to be due to the beneficial effect of through thickness compressive stresses generated by the tapered geometry.

At first sight the prediction for this case might be regarded as over conservative. However, if any initial delamination is present in the region of the drop, for example due to impact damage or manufacturing defects, then the point from which delamination propagation would start may be beyond the zone of compressive normal stress. It may therefore be over optimistic to rely on the presence of these beneficial stresses when predicting strength. The proposed method is therefore still considered to be

a good basis for design.

The prediction for the 2 dropped/4 continuous ply tension specimens is less conservative. In this case there are only half as many continuous plies, and so the magnitude of through thickness compressive stresses is reduced.

For the 6 dropped/4 continuous ply case the measured strength is slightly lower than predicted. As stated earlier, the strength is controlled by the forward pair of dropped plies, and so this specimen is initially equivalent to the 2 dropped/4 continuous ply case. The reason that it is relatively weaker is again thought to be due to the effect of through thickness compression. In this case the compressive forces induced by the taper are reacted on the next pairs of dropped plies, and so there is not the same effect of compression induced across the plies where delamination initiates.

For the compression tests, the applicability of the proposed method is less clear. In this case no cracks were observed immediately at the end of the dropped plies as occurred in tension, and as was assumed in deriving the energy release rate equation (1). However, the presence of a resin pocket in front of the dropped plies is believed to have a similar effect to a crack, since the stiffness and yield strength of the resin are both low, and so use of this equation may still be justified.

A further problem in the compression tests is that through thickness tensile stresses arise at the ply drop. It is therefore no longer a pure mode II delamination but mixed mode I and II.

Despite these problems, the correlation between predicted and measured delamination stresses in compression is very good. This may be partly fortuitous. A trend of increasing fracture energy with thickness has been observed [7]. On this basis the compression specimens would be expected to be stronger than predicted since the thickness is greater than that of the cut ply specimens used to measure the fracture energy. On the other hand due to the mixed mode nature of the failure under compression these specimens would be expected to be weaker than predicted since the mode I fracture energy is less than the mode II value. For the unidirectional glass fibre-epoxy specimens tested here, these two effects appear to be cancelling each other out, and so close predictions are obtained.

However, this may not always be the case. For example, preliminary work on carbon fibre-epoxy has suggested that this material may be more susceptible to the effect of through thickness tensile stresses, and so predictions based on the proposed approach may be unconservative. More investigation of this effect is required. A possible way around it could be to measure a value of fracture energy from cut ply specimens in compression as well as in tension, and use the appropriate value depending on the type of loading. This would require a change in the specimen manufacturing method to provide a gap between the ends of the cut plies in order to prevent them butting up under compression.

Preliminary work on specimens with dropped ±45° plies suggests that it should be possible to extend the proposed method to cater for situations where the material is not purely unidirectional.

Fatigue tests have also been carried out which indicate that a similar approach can be used for the design of tapered sections subject to fatigue loading. In this case it is the delamination propagation rate as a function of strain energy release rate which can be used as the basis of predicting life.

6. CONCLUSIONS

The critical parameter affecting delamination in tapered unidirectional composites with dropped plies is the strain energy release rate associated with the terminating plies. Through thickness normal stresses are also important, inhibiting delamination when they are compressive, but decreasing strength when they are tensile.

A method has been presented for predicting the strength of tapered sections based on a simple equation for the strain energy release rate and a value of fracture energy measured from a unidirectional specimen with the central plies cut across the full width. This method has been applied to three sets of tapered tension specimens and three sets of compression specimens. In five of the six cases the predictions are within about 6% of measured delamination strengths, and in the sixth case the prediction is conservative by about 20%.

This approach is recommended as a design method, although some caution is required in applying it to compression loading due to possible adverse effects of through thickness tensile stresses. Further investigation of this effect is being undertaken. The proposed approach looks promising as the basis for a general design methodology for predicting static and fatigue strength of tapered composites.

No. dropped plies	2	2	6
No. continuous plies	4	8	4
Delamination Stress (MPa) Thick Section	721 751 752 724	968 953 970 976	406 403 413 410
Average Stress (MPa) Thick Section	737	967	408
C.v. (%)	2.3	1.0	1.1
Average Stress (MPa) Thin Section	1106	1209	1020

Table 1: Experimental Results for Dropped Ply Specimens in Tension

No. dropped plies	2	2	4
No. continuous plies	16	32	32
Delamination Stress (MPa) Thick Section	775 762 732 801	920 862 875 892	549 572 581 560
Average Stress (MPa) Thick Section	767	887	565
C.v. (%)	3.7	2.8	2.5
Average Stress (MPa) Thin Section	863	942	636

Table 2: Experimental Results for Dropped Ply Specimens in Compression

No. dropped plies	2	2	6	2	2	4
No. continuous plies	4	8	4	16	32	32
Tension or compression	T	T	T	C	C	C
Measured delamination Stress (MPa)	737	967	408	767	887	565
Predicted delamination Stress (MPa)	706	773	424	815	838	576
Difference (%)	-4.2	-20.1	+3.9	+6.3	-5.5	+1.9

Table 3: Correlation of Predicted and Measured Delamination Stresses

References

1. Kemp, B.L., and Johnson, E.R., "Response and Failure Analysis of a Graphite-Epoxy Laminate Containing Terminating Internal Plies", Paper no AIAA 85-0608, Proc. of AIAA/ ASME/ASCE/AHS 26th Structures, Structural Dynamics and Materials Conf., Orlando, 1985, pp 13-24.

2. Curry, J.M., Johnson, E.R., and Starnes, J.H., "Effect of Dropped Plies on the Strength of Graphite-Epoxy Laminates", Paper no. AIAA 87-0874, Proc. of AIAA IASME/ASCE/AHS 28th Structures, Structural Dynamics and Materials Conf., Monterey, 1987, pp 737-747.

3. Fish, J.C. and Lee, S.W., "Delamination of Tapered Composite Structures", Engineering Fracture Mechanics, 34, No. 1, 1989, pp 43-54.

4. Salpekar, S.A., Raju, I.S., and O'Brien, T.K., "Strain Energy Release Rate Analysis of Delamination in a Tapered Laminate Subjected to Tension Load", Proc. American Soc. for Composites 3rd Tech. Conf., Seattle, 1988, pp 642-654.

5. Wisnom, M. R., "Delamination in Tapered Unidirectional Glass Fibre-Epoxy Under Static Tension Loading", Proc. AIAA Structures, Structural Dynamics and Materials Conference, Baltimore, April 1991, pp 1162-1172.

6. Cui, W.C., Wisnom, M.R. and Jones, M, "A Comparison of Fracture Criteria for Unidirectional Glass Fibre-Epoxy Specimens with Cut Central Plies", 5th Int. Conf. on Fibre Reinforced Composites, Newcastle, March 1992.

7. Wisnom, M.R., "On the Increase in Fracture Energy with Thickness in Delamination of Unidirectional Glass Fibre-Epoxy with Cut Central Plies", Journal of Reinforced Plastics and Composites, in press.

8. Cui, W.C., Wisnom, M.R., and Jones, M., "A Comparison of Failure Criteria for Delamination of Unidirectional Glass Fibre-Epoxy Specimens Waisted Through the Thickness", Composites, in press.

9. Wisnom, M.R., "The Application of Fracture Mechanics to Predict Delamination in Composites", 2nd Int. Conf. on Composite Structures & Materials, Beijing, August 1992.

ALLOWABLE COMPRESSION STRENGTH FOR CFRP-COMPONENTS OF FIGHTER AIRCRAFT DETERMINED BY CAI-TEST

by

J. Bauer
G. Günther
R. Neumeier

Deutsche Aerospace
MESSERSCHMITT-BÖLKOW-BLOHM AG.
Unternehmensbereich Flugzeuge
P.O. Box 801160, 8000 Munich 80
Germany

Introduction

One of the basic properties of carbon fibre reinforced plastic laminates is to react on impacts with a matrix failure mainly in the interfaces of the plies In principle multiple delamintions occur between the plies extending over a certain area.

These impact damages have two detrimental effects First they create a significant compression strength reduction and second it cannot be expected that all of them are visible The second effect is enlarged by the application of the modern toughened resin systems and leads to the conclusion that unknown strength reducing damages may be present in the structure which therefore did not cause any maintenance or repair action

To overcome this problem and to provide the complete structural integrity, Damage Tolerance requirements were defined against low velocity impacts. These have been determined investigating the scenarios, which the aircraft will experience during its service life (see Fig 1) Impact energy levels have been determined and specified for dedicated structural regions I e the outer surface of the aircraft is separated into various regions and to these are assigned certain impact energy levels. For reference test purposes the shape of the impactor was specified to be 1 inch hemispherical and such do not risk to create visible damages due to sharpness

For the A/C manufacturer these Damage Tolerance requirements let arise the problem how to make sure that the structure achieves the specified level. The most common approach to solve this problem is to introduce the Damage Tolerance aspect into the sizing criteria during structural layout, i e the method to determine the required thicknesses and lay-ups

A simple and practicable criteria is the limitation of the fibre strains in the laminate These may be loaded up to certain strain values in tension and in compression. Providing fibres in all 4 directions (0°, + 45°, -45°, 90°) any loading condition is controlled comprehensively. Applying this sizing criteria the establishment of Design llowables is reduced to the derivation of two limiting strain allowables

Since an impact does not reduce the tension strength to a considerable extend the limiting tension strain cannot be based on an "after impact" criteria More severe is the require-

ment of repairability since the original material tension strength can hardly be restored whatever repair method is under consideration.

The allowable compression strain is therefore the design value which must ensure the required level of Damage Tolerance against low velocity impacts and which must cover the strength critical influences as well.

Since the understanding of the compression after impact behaviour has not yet settled, a comprehensive test programme was conducted investigating coupons and ply drop off specimens the prepreg system Narmco 5245C/T800. The test results data base was evaluated and used for the derivation of the limiting strain allowables in compression This procedure is a significant step within the Damage Tolerance qualification route as detailed in Fig. 2

COMPRESSION AFTER IMPACT TEST PROCEDURES

A well-known test procedure for compression after impact (CAI) is the so-called "Boeing Test". This test set-up requires specimens with the dimensions of 100 x 150 mm and a thickness of about 4 mm. The test fixture was not designed for the test of larger specimen sizes and a scaling up of the specimen dimensions is not possible due to buckling reasons. Regarding the worst case damage sizes, which have to be assumed in A/C structures, the restriction of a specimen width of 100 mm cannot be accepted Varying the damage sizes while keeping the specimen width constant, an influence from of specimen width to damage size (W/D) cannot be excluded and not demonstrated as well. Doubts arised if the "Boeing Test" set-up is feasible to create a satisfactoring knowledge about "compression after impact" effects which is sufficient to take it as a basis for the derivation of Design Allowables These doubts could not be eliminated and it was decided to develop another test set-up which allows to test a wider range of specimen dimensions Especially a flexibility in the thickness and the width dimensions was seen to be of great interest.

It is the nature of compression tests that the load introduction and the anti-buckling device require special attention and efforts Additionally the effort increases with the specimen dimensions since higher loads are involved and only little misa-

lignement create easily large bending moments .

The test set-up was designed for the following specimen geometry:

Length (constant)	l	= 300 mm
Max Width	w	= 250 mm
Thicknesses	t	= 4 - 8 mm

Fig. 3 details the assembly drawing. The main features are the upper and lower load introduction devices providing a constant load distribution of the specimen by a moment-free load transfer through the upper and lower bearing bolt. These two bearing bolts have centric guides to ensure the lateral centricity. The centric installation of the upper and lower devices is of essential importance and can be easily guaranteed, adjusting the alignement of the lower to the upper bearing block by using one of the bolts. The specimen itself is laterally clamped by two stiff angles in order to prevent brushing-up of the load introduction frontal areas.

The manufacturing tolerances for the parts were relatively tight to guarantee the centric installation of the specimen

Fig. 4 details the drawing for the anti-buckling device. Two thick Aluminium plates assembled with steel masks to carry 18 pillows are clamping the specimen in between with a defined force This is adjustable by cup springs under disks The anti-buckling guide restricts the minimum specimen width to 100 mm which represents the width dimension of the "Boeing Test"

TESTING

The new test set-up was applied to investigate plain coupons and Ply Drop Offs mainly keeping the ratio of width to damage size constant, i.e. W/D = 4. This required a special procedure for specimen preparation

1 Manufacturing of a base plate from which the specimen will be cut off (E g. l = 2 m and w = 300 mm)

2 Application of the impacts.

3 Determination of the impact damage sizes by Ultrasonic Inspection

4. Cut out the specimens with the required widthes (W/D = 4') from the base plate.

5 Static test at RT or elevated temperature

During an initial test phase of the "wide specimen test set-up" intensive checks on instrumented damaged and undamaged specimen have been undertaken to collect experience and to settle the test procedure This exercise approved that reproducable compression after impact values are generated but naturally, the method is not applicable, to measure the undamaged strength

The aim of the test program was to identify important parameters which are of interest for the derivation of Design Allowables

- Different delamination sizes have been created applying different impact energies. The support conditions during impact have been a 200 x 200 mm frame and the experience has shown that 3 impact energy levels, 15 J, 30 J and 60 J, are sufficient to find out the residual strength (strain) versus damage size characteristic.

- The width to damage size characteristic was investigated in the range from W/D = 2 up to W/D = 8

- Three thicknesses have been tested: t = 4, 6 and 8 mm

TEST RESULTS CONCLUSIONS

The evaluation of the test results allowed some basic conclusions which are valid for the investigated material Narmco 5245C/T800.

1. There is no significant difference in residual strength between RT/AR and h/w tests.

2. The ratio of specimen width to delamination diameter has no influence in the range of W/D = 2 up to 8.

3. The damage threshold is dependent on the thickness. With increasing thickness the damage threshold is rising to higher impact energies. But once the damage threshold is exceeded the occuring damage is comparably larger in thick laminates

4. The residual strength after impact is dependent on the laminate thickness. Considering the damage size effect thick laminates are less susceptible to impact damages than thin ones

5. Small damages being generated with impact energies at or below the damage threshold do not affect the original laminate strength.

6. In Ply Drop Off regions the occuring impact damages are considerably larger in comparison to plain laminates.

7   The characteristic of residual strain versus damage size from Ply Drop Offs correspond well to the results of the plain coupons.

Fig. 5 is providing an overview of the characteristics which have been discovered.

From fracture toughness measurements with the 5245C/T800 material and a comparison to values from untoughened resin systems a certain performance in compression after impact strength was expected. The test programme did not confirm these expectations This may indicate that fracture toughness is not a reliable parameter to correlate with the Damage Tolerance performance of a material.

LIMITING STRAIN ALLOWABLES IN COMPRESSION

The experience with the compression after impact tests indicated that the ratio of width to delamination size is of no influence but the thickness dependency should not be neglected during the establishment of the limiting strain allowable in compression Test Data for very thin laminates have been taken into account from H/C sandwich data tested in CAI Such a data file could be assembled covering laminate thicknesses starting at 0.75 mm and ending up with 8 mm

Combining the Damage Tolerance requirements of the fighter aircraft structure with the allocated structural thicknesses and the B-basis CAI test values, the limiting strain allowables given in Fig 6 have been derived Obviously the overall level of the allowable compression strain is rather small and the question is allowed whether these values are too pressimistic In this context the correlation between coupon tests and real structures is often questional. This objection can be rejected based on test results from 4-point bending boxes which allowed to compare coupons with a structural feature. These boxes failed

consistently through the impact damages at strain levels which fit into the coupon data.

In a wider range another confirmation of the derived Design Allowables can be seen in the qualification tests for the fighter aircraft structure.

Representative full scale structural boxes with CFC skins are impacted according to the referring requirement and afterwards in Fatigue cycled. The impacts were throughout the test monitored for damage growth control and up to now no implications have been experienced. This remains valid as well for the final residual strength tests.

SUMMARY AND CONCLUSION

A test set-up has been developed for CAI tests allowing coupon sizes from 300 x 100 up to 300 x 250 mm and thicknesses from 4 to 8 mm. The test set-up approved to measure the residual compression strength after impact in accordance with other test methods e.g. the "Boeing Test" and 4-point bending boxes. The test set-up is applicable for the investigation of all relevant test parameters and provides in addition to current test procedures the possibility to vary the geometric dimensions, width and thickness, in a wide comfortable range. This performance emphasizes its application for data collection and subsequent Design Allowables derivation.

The experience with the Damage Tolerance aspects during the development of a fighter aircraft demonstrates that it is possible to introduce and consider impact requirements in the structural design phase

Low Energy Impact Risks of a Fighter Aircraft

- Hail (horizontal and vertical component)
- Runway stones
- Droping light weight tools
  Refuelling by gravity
- Installation and maintenance of the ejection seat
- Assembly and disassembly of the pre-cooler or the fin
- Working platforms
- Installation and dismount of external stores
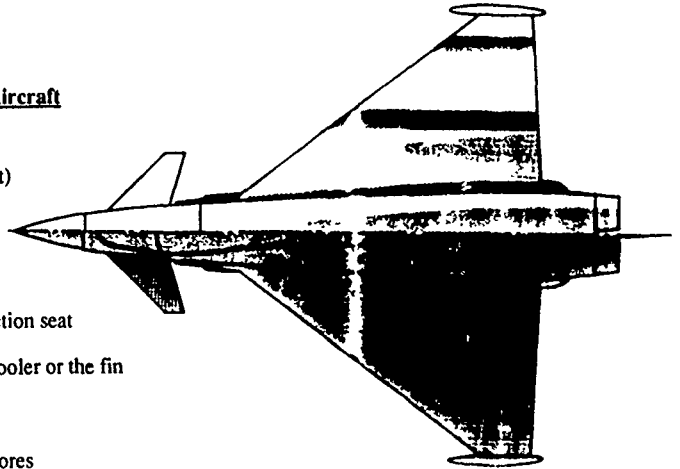
FIG. 1   IMPACT RISKS OF FIGHTER AIRCRAFT
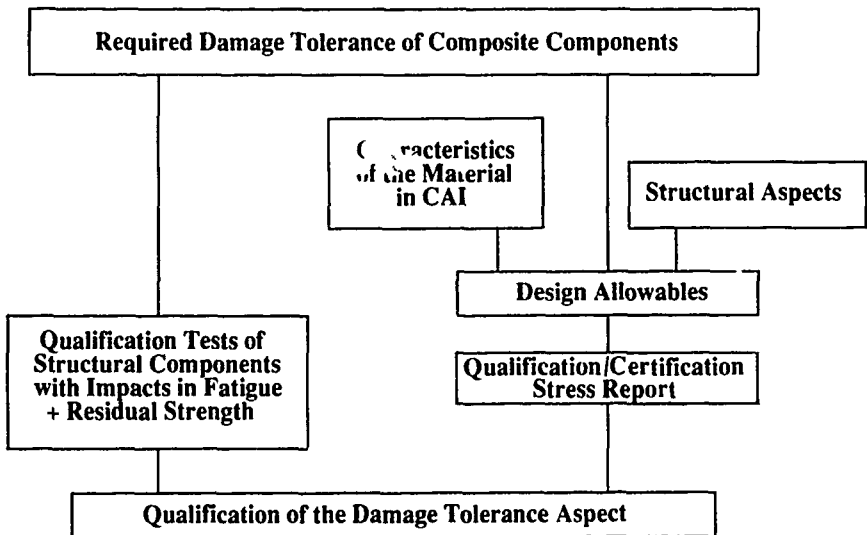
FIG. 2   CFC DAMAGE TOLERANCE QUALIFICATION

FIG. 3   WIDE SPECIMEN TEST SET-UP

FIG. 4   ANTI BUCKLING GUIDE

RESIDUAL
COMPRESSION
STRAIN
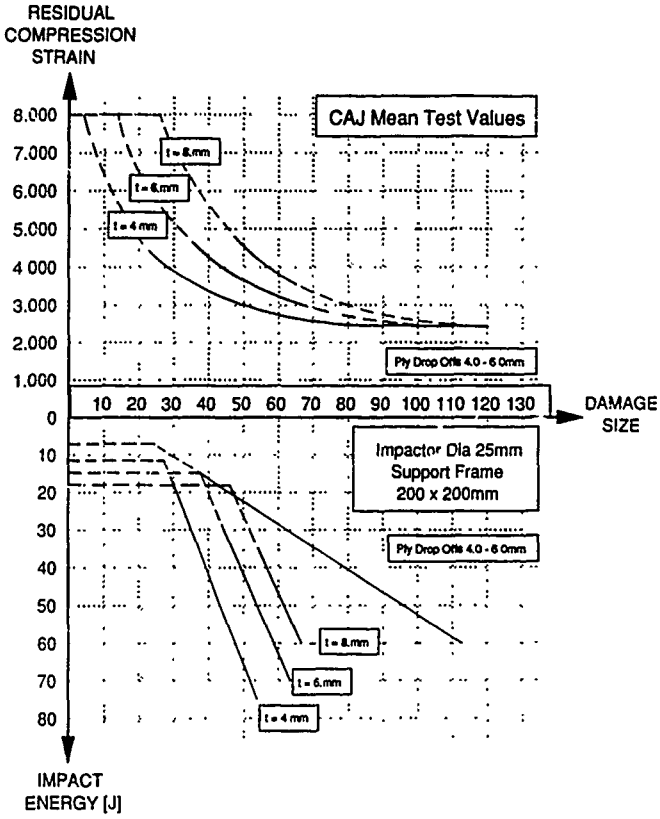
Fig. 5 COMPRESSION AFTER IMPACT CHARACTERISTIC

In-Plane Compression Strain vs Thickness
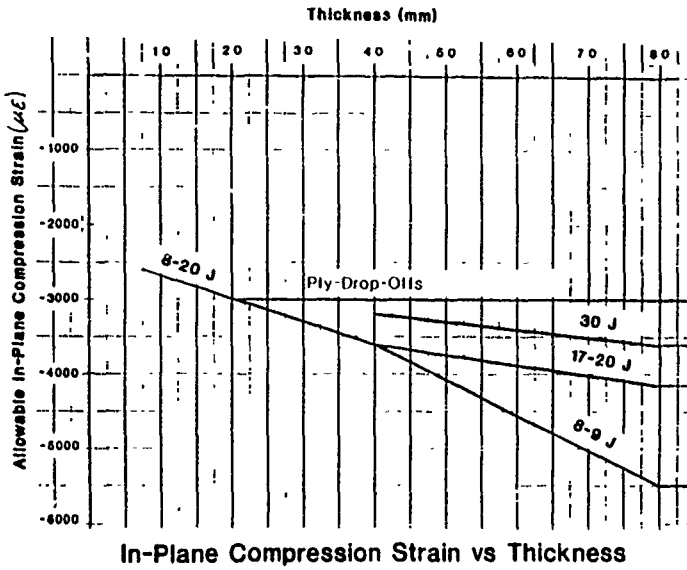
FIG. 6   IN PLANE COMPRESSION STRAIN VERSUS THICKNESS

Repairing Delaminations with Low Viscosity Epoxy Resins

A.J. Russell and C.P. Bowers*

Defence Research Establishment Pacific
F.M.O. Victoria, B.C., Canada
V0S 1B0

1. SUMMARY
Although resin injection is the procedure most often specified for repairing delaminations, field experience as well as numerous experimental investigations have shown it to be unreliable and in many cases ineffective. This paper identifies some of the reasons for this and then goes on to describe the successful development of an epoxy resin specially formulated for delamination repair. The ability of this resin to fully restore the out of-plane properties of delaminated carbon/epoxy laminates is demonstrated and some of the more practical aspects of repairing delaminations both on and off aircraft are discussed.

2. INTRODUCTION
The Achilles' heel of most laminated organic matrix composite materials currently utilized in advanced fighter aircraft and helicopters is their poor interlaminar properties. Both during assembly and in-service this weakness can lead to the formation of delaminations from a number of different causes including hole drilling, fastener installation, pry damage, impact damage, free edge stresses and lightning strikes. While considerable research and development activity has been directed towards characterizing the interlaminar fracture and fatigue properties of these materials and to assessing the structural significance of delaminations, much less effort has gone into developing effective repair procedures. Most of the repair options that have been considered involve one of the following:

(i) removal of the delaminated material and installation of a patch;

(ii) stabilization of the delaminated plies with mechanical fasteners; or

(iii) injection of an adhesive into the delaminations.

The suitability of each of these procedures depends on the loading conditions, the thickness of the part and the nature of the material. For example, impact damage of lightweight honeycomb sandwich structure, will normally require the removal of the delaminated skin material to gain access to the damaged core. On the other hand, for laminates thicker than 5 mm, bonded scarf patches become excessively large and the use of bolted patches may be limited by weight restrictions and airflow perturbation considerations. Under these circumstances, options (ii) and (iii) are clearly preferable. For monolithic carbon/epoxy structure containing fastener holes it has been demonstrated that by using blind fasteners to "clamp-up" impact damage induced delaminations it is possible to fully restore the design ultimate compression strength [1]. However, in regions of high interlaminar shear stress or in bonded structures which experience design strains in excess of 4000 micro-strain it is unlikely that this approach would be satisfactory. Under these conditions, resin injection would appear to be the most promising method for repairing delaminations in as far as it produces no significant stress concentration, results in a negligible increase in weight and has the potential to fully restore all of the interlaminar properties. Unfortunately, most reported attempts to develop and qualify resin injection repairs have been unsuccessful [1-3]. These findings are supported by our own experience with resin injection repairs of delaminations on the CF-18, which is that the qualified adhesive and procedure specified in the structural repair manual seldom work satisfactorily.

This paper reviews the results of a research program aimed at improving our ability to repair delaminations in the carbon/epoxy structure of the CF-18 aircraft. The origins and nature of these delaminations is discussed and tests carried out to quantify and model the flow of resin into some typical delaminations are described. The rheological, thermal and mechanical properties of a specially formulated epoxy resin are characterized and its ability to completely infiltrate and rebond delaminations is evaluated. Tests to determine to what extent it is possible to restore the compression strength, damage tolerance and the ability of the laminate to support high interlaminar shear stresses are described. Finally, some specific delamination repair procedures for use both on-aircraft and in an autoclave are suggested and the influence of contaminants entering the delaminations prior to repair investigated. A more detailed description of some of this work can be found in references 4-7.

3. CF-18 SERVICE EXPERIENCE
Generally speaking, the carbon/epoxy composite structure on the CF-18 has proven to be relatively damage resistant. Most of the damage requiring repair has been caused by mishandling or by foreign object damage either in flight or on take-off and landing and has been limited by and large to the lightweight honeycomb sandwich structure found on the flight control surfaces and numerous doors and access covers. See Figure 1. The monolithic carbon/epoxy structure, which is mostly between 5 and 15 mm in thickness and limited to the wing skins and vertical stabilizer, has a higher impact energy threshold and is

* DAS Eng, NDHQ, Ottawa, ONT , Canada.
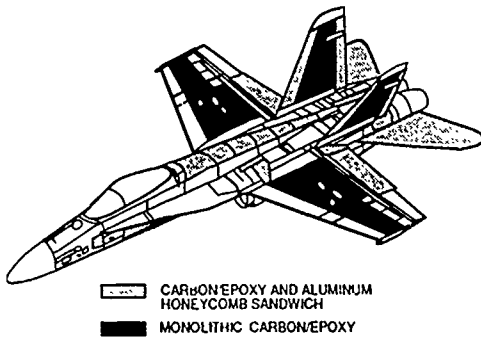
Figure 1   Usage of carbon/epoxy on the CF-1.8.

also less likely to show visible signs of damage. Since no routine non-destructive examinations are carried out, the existence and distribution of delaminations is largely unknown. However, some of the trailing edge wing panels were partially inspected ultrasonically in 1989 following the discovery of a manufacturing related problem associated with the mechanical attachment of the skins to the underlying substructure. An unexpected sensitivity to fit-up tolerances at rib/spar joints, as shown in Figure 2, had produced delaminations adjacent to fastener holes in some trailing edge panels. Out of approximately 30 fastener
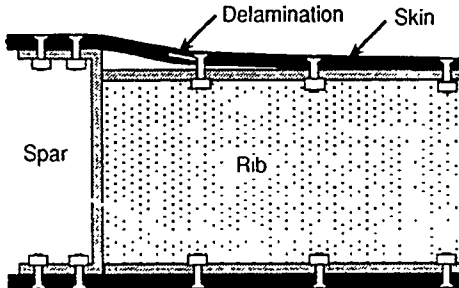
Figure 2 . Localized bending and delamination caused by poor fit-up.

holes that were inspected on each trailing edge panel on 15 different aircraft an average of one delamination per aircraft was found. In most instances the delaminations were less than 25 mm in diameter, although in some cases the manual inspections indicated delaminated areas as large as 50 x 80mm. Based on recent C-scanning of some of the delaminations, it has been concluded that inspections with hand held transducers tend to over-estimate the size and degree of connectivity of the delaminations. In addition to the type of delaminations described above it is also likely that wing-skin delaminations resulting from impact damage could occur from time to time, although as mentioned before this has not been a problem to date. It was therefore the goal of this program to develop resin injection repairs for both fit-up and impact induced delaminations.

4. RESIN INFILTRATION TESTS

Figure 3 shows the geometry used to model the flow of resin into a delamination.   The resin enters the delamination under pressure P_1 through a hole of radius R_1 and is assumed to flow radially outwards within the delamination cavity of opening h. For a resin
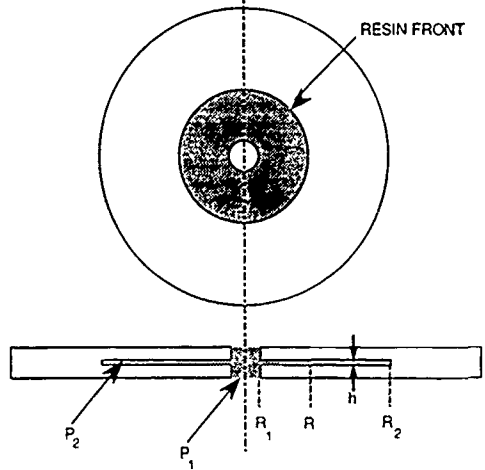
Figure 3 . Resin flow model geometry.

of viscosity η the time taken to reach a radius R is given by [4]:

$$t = \frac{3\eta[\ R^2\ (2\ \ln(R/R_1)\ \text{-}1) + R_1^2\ ]}{(P_1\text{-}P_2)\,h^2} \qquad (1)$$

where P_2 is the pressure ahead of the resin front   In order to verify the applicability of this model to real delaminations, and to determine typical values for h, a series of infiltration tests were carried out. The holed plate shear (HPS) test specimen shown in Figure 4 reproduces the fastener hole and shear loading of the fit-up problem described above while maintaining the concentric geometry of the resin flow model.
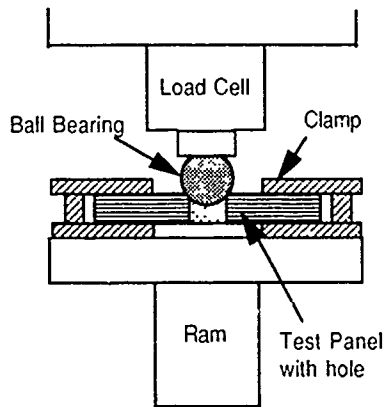
Figure 4   Holed plate shear test loading arrangement.

Delaminations are created by applying a load to the fastener hole while supporting the specimen on a ring of the desired diameter. Initial tests were carried out on the same material and stacking sequence as the CF-18 trailing edge panels (48 plies of Hercules' AS4/3501-6 carbon/epoxy comprising 8% 0s, 84% ±45s and 8% 0s). In later tests the thickness was varied but the ply orientation percentages were kept the same.

Resin infiltration was carried out in an ultrasonic C-scan tank so that the resin front position could be determined as a function of time. A low viscosity epoxy resin without curing agent was forced into the fastener hole under pressure after pre-evacuating the delaminations. Details as to how this was accomplished are given in Reference 4. Figure 5 shows one set of C-scan images recorded during the infiltration of a 48 ply specimen containing 76 mm diameter delaminations.
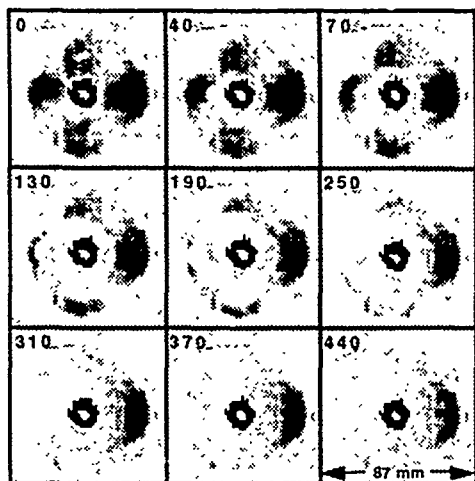
Figure 5 . A series of C-scan images showing resin infiltration as a function of time (minutes).

The resin front position in each of the 4 quadrants of the delaminated area was measured from each image and plotted as a function of time. Equation 1 was then least squares fitted to each data set using h as the fitting parameter. Figure 6 shows the data fits corresponding to the images shown in Figure 5. In most cases the
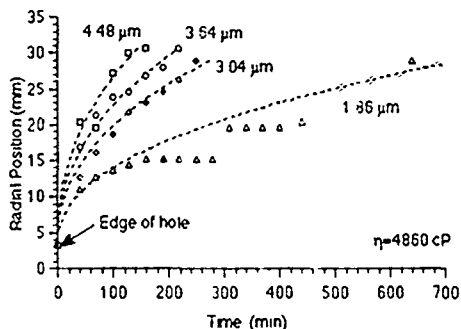
Figure 6 . Resin front position versus time

agreement with the model was quite good, with values of h ranging from 1 to 10 μm The fitted values of h will be referred to as h_{eff} since they represent the effective delamination opening for resin flow and appear to be somewhat lower than the actual openings observed microscopically on polished cross sections (see figure 16 for example). As might be anticipated, there was considerable scatter in the h_{eff} values from quadrant to quadrant and from one specimen to another. Nevertheless, the results showed a strong dependence of h_{eff} on both delamination size and laminate thickness as shown in Figures 7 and 8. While it is evident that the
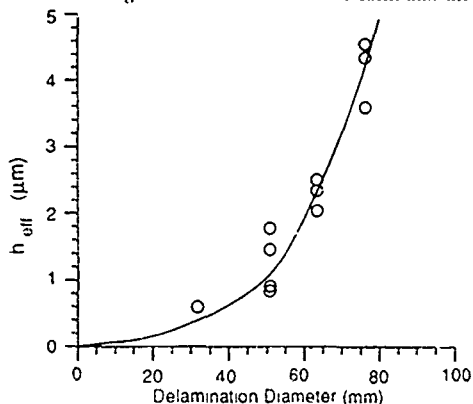
Figure 7 . Effect of delamination size on delamination opening.
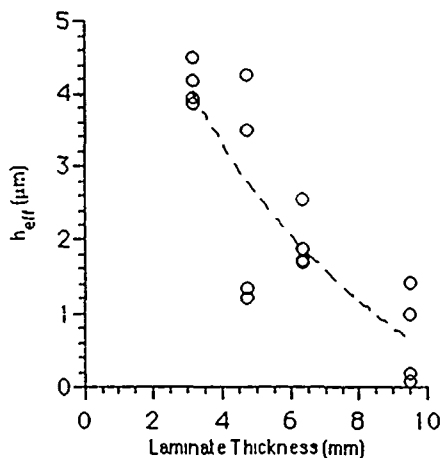
Figure 7 . Effect of laminate thickness on delamination opening

higher h_{eff} values correspond to greater thru-thickness compliances, no increase in h_{eff} was observed as the injection pressure was raised. It is hypothesised that the delaminations open momentarily following the initiation of delamination growth and that fracture debris limits the extent to which they subsequently close up. The thinner HPS specimens and those supported on the larger diameter clamps are less restrained from opening and therefore end up with larger values of h_{eff}

From the flow model and the measured values of h_{eff} it is possible to predict the amount of resin flow required to successfully repair some typical delaminations. First, however, it is necessary to recognize that the resin viscosity is a function of both time and temperature. By modifying Equation 1, the total flow potential of the resin from the time of mixing to the time of cure can be compared with the flow requirement to completely fill an area of radius R_2:

$$\int_{t_0}^{t_{cure}} \frac{1}{\eta} dt \geq \frac{3[\, R_2^2 \,(2\,\ln(R_2/R_1)\,-1) + R_1^2\,]}{(P_1 - P_2)\, h_{eff}^2} \qquad (2)$$

Table 1 gives the value of the quantity on the right hand side of Equation 2 for some representative delamination

Table 1   Resin flow requirements for some typical repair conditions. Laminate thickness = 6mm.

Delamination Size		Resin Flow Requirement (Pa^{-1})	
Diameter (mm)	h_{eff} (μ m)	350 kPa on- aircraft repair	700 kPa autoclave repair with vacuum
30	0 4	52680	26310
50	1.4	14400	7200
75	3 9	4740	2370

sizes and injection parameters These data reveal that small delaminations provide greater flow resistance to resin infiltration than larger delaminations and indicate that a viable delamination repair resin should have a flow potential of the order of 50,000 Pa ^{1} In comparison, the epoxy adhesive currently specified for delamination repair on the F-18 was found to have a flow potential of only 800 Pa ^{1} and because of the short pot life not all of this is realized in practice. Although other commercially available epoxy adhesives having superior flow properties were identified none of these approached the desired 50,000 Pa ^{1} Consequently, the development of a resin system designed specifically for repairing delaminations was undertaken in house

5. RESIN DEVELOPMENT

5.1 Adhesive Formulation

In addition to the aforementioned flow requirement, an adhesive for repairing delaminations must also possess a number of other properties These include the ability to effectively rebond the delaminated surfaces together and an adequate resistance to the moisture and temperature regimes encountered by the component being repaired as well as a cure temperature that is compatible with on-aircraft repair Thus, while viscosity is clearly an important consideration it should not be the over-riding factor in formulating a resin system. For example, a low viscosity bi-functional epoxy was chosen rather than a lower viscosity mono-functional epoxy because of the low glass transition temperature, T_g, and poor mechanical properties resulting from the latter's inability to cross link Likewise, very low viscosity amines were avoided as curing agents because their high volatility can cause them to "boil off" during cure, producing a porous bond

line. Latency of cure, as determined by differential scanning calorimetry, was the key parameter in selecting a curing agent.   Other factors which influenced the resin formulation were surface wetting characteristics, and the ability to withstand a post-cure at 177°C , which might arise if the same component required a full autoclave repair at some later date.

The delamination repair epoxy that was ultimately developed will be referred to in this paper simply as the DREp resin. Unless otherwise stated, the cure cycle used consisted of a 0.5°C/min ramp to 140°C followed by a 2 hour hold and a cool-down cycle which lasted a minimum of 45 minutes This gave a glass transition temperature of close to 140°C which dropped to 120°C upon saturation with moisture   Cure temperatures down to 110°C also gave satisfactory results but with lower T_gs At higher temperatures, the T_g followed the cure temperature up to 160°C with little improvement beyond this point.

5.2 Flow Properties

Figure 9 shows the reciprocal viscosity of the DREp resin as a function of time for four different infiltration cycles At 25°C the initial viscosity was 650 centi-Poise
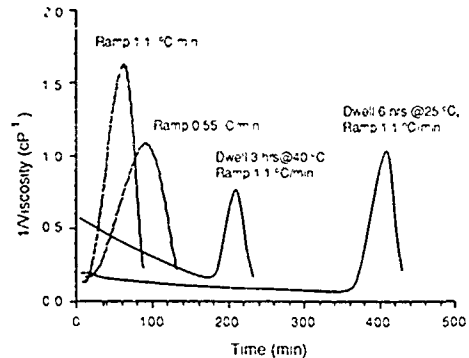
Figure 9 . Plots of 1/viscosity versus time for four different infiltration/curing cycles.

(cP), increasing to 1725 cP after 6 hours On heating freshly mixed resin at 1 1°C/min the viscosity fell to a minimum of 60 cP after 1 hour and then increased rapidly as the resin cured The areas under the curves in Figure 9 represent the total flow potential as defined by the left hand side of Equation 2. These areas, which are plotted as a function of time in Figure 10 are relatively unaffected by the heating rate. What is important to note, however, is that for repair procedures where the resin is injected at low or ambient temperature and then cured without further application of pressure only a fraction of the total flow potential is realized In some cases this may be as little as 50%.

5.3 Mechanical Properties

Tests were carried out to measure the interlaminar shear properties of delaminated ply interfaces rebonded with the DREp resin.   Unidirectional laminates, containing 24 plies of AS4/3501-6 carbon/epoxy pre-preg and containing non-adhesive inserts on the mid-plane were fabricated and cut into 20 mm x 150 mm end notched flexure (ENF) specimens [8] Delaminations were grown in shear from the ends of the inserts to within 20mm of the ends of the specimens   The delaminations were then opened slightly, filled with resin, clamped shut and cured for 2
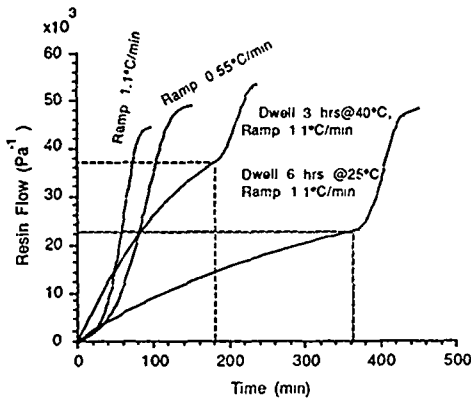
Figure 10 . Flow of the DREp resin as a function of time for four different infiltration/curing cycles.

hours at 140°C. The middle 75 mm of some of the rebonded specimens were cut up into short beam shear specimens while the others were used for mode II interlaminar fracture and fatigue tests. The results of the short beam shear tests, plotted in Figures 11 and 12 indicate that the rebonded strength was close to that of
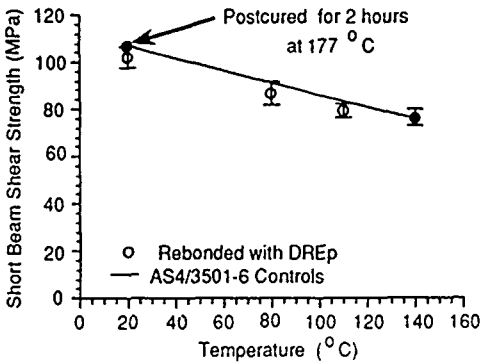
Figure 11 . Short beam shear strength - dry.
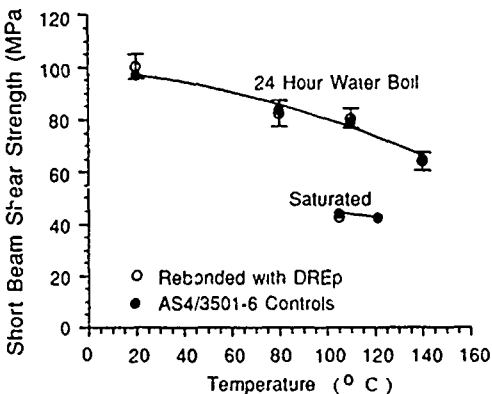
Figure 12 . Short beam shear strength - wet

the controls under all conditions tested. However, there were more mid-plane failures in the rebonded specimens particularly at elevated temperatures and after moisture conditioning. The mode II interlaminar fracture toughness, G_{IIc} as measured by the ENF test, was found to be 40 to 50% higher in the rebonded specimens than in the controls. See Table 2 . While

Table 2 . Mode II interlaminar fracture toughness.

Temperature (^{0} C)	G_{IIc} (J/m^2)	Control Values (J/m^2)
20	940, 1011, 904, 927	630
100	785, 740, 758	530

some of this increase can probably be attributed to the greater toughness of the DREp resin compared to the composite matrix, part of it undoubtedly originates from the greater thickness of the interlaminar matrix layer present in the rebonded specimens and the beneficial effect that this has on G_{IIc} [9] Figure 13 compares the interlaminar fatigue crack growth rates under shear loading of rebonded specimens with those of the controls While no change is apparent at low values of ΔG_{II} the greater fatigue resistance at higher values is consistent with the observed improvement in G_{IIc}.
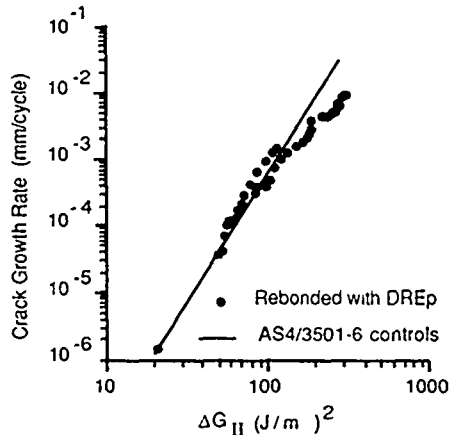
Figure 13 . Interlaminar fatigue crack growth rate.

6. REPAIR OF HPS SPECIMENS
As well as providing information pertaining to resin flow, the HPS specimens proved to be suitable for evaluating resin infiltration procedures and also as a mechanical test for assessing the reparability of delaminations in regions of high interlaminar shear stress.

6.1 Resin Infiltration
Resin injection repairs to delaminated holed plate shear specimens were carried out in a two stage process as shown in Figure 14. First, the plate was placed in a transparent plastic box, the air evacuated and DREp resin injected into the fastener hole. Next the specimen

(a) EVACUATION AND RESIN INJECTION

(b) PRESSURE INFILTRATION AND CURE
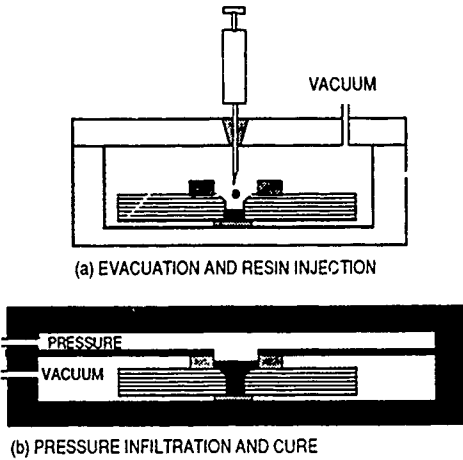
Figure 14 . Repair procedure for HPS specimens.

BEFORE REPAIR   AFTER REPAIR

Figure 15 .   Ultrasonic C-scan images taken before and after repair

was transferred to a steel box which was then placed between the platens of a hot press. Initially the whole of the interior of the box was pressurized (125-500 kPa) as the temperature was raised but success with this procedure was inconsistent. By pressurizing ti fastener hole while the specimen was immersec in water it was discovered that there was a leakage ou.h from the delaminations out to the specimen ed ·ͻ in some of the specimens. Not only did this result in a loss of vacuum but it allowed air to enter the delaminations and stop the flow of resin. This problem was eliminated by either sealing the edges of the specimen or by maintaining the vacuum throughout the cure cycle using an arrangement such as that shown in Figure 14b. When this latter procedure was adopted, resin wetted areas could often be observed on the edges of the specimens following repair   A metallographic examination of these areas revealed that the resin had leaked out via matrix cracks running transversely through the six 45° plies located at the mid-plane of the laminate.

The extent of resin infiltration was determined by ultrasonic nspection and by metallographic techniques. Figure 15 shows amplitude C-scan images of a well repaired (a, and a poorly repaired (b) HPS specimen taken before and after repair. The success of the DREp resin in filling all of the crevices and surface features on the fracture surface as well as the presence or absence of any bondline porosity was ascertained by sectioning some of the repaired plates, sanding and polishing the cut edges and examining them at high magnification with an optical microscope. In general, any plates which appeared from the ultrasonic C-scan to have been successfully repaired, exhibited void-free bondlines with no evidence of poor surface wetting. A section through a well repaired delamination showing the typical "hackle" features characteristic of mode II interlaminar fracture can be seen in Figure 16

6.2 Post-Repair Failure Loads

The mechanical effectiveness of the repairs was investigated by re-loading the HPS specimens and comparing the post-repair failure loads with the initial damage loads.   The load-displacement curves, an example of which is shown in Figure   were linear to
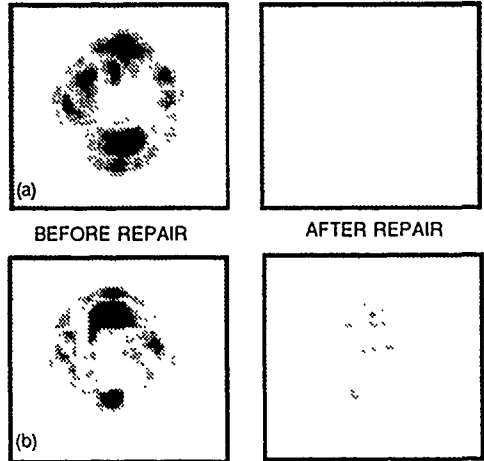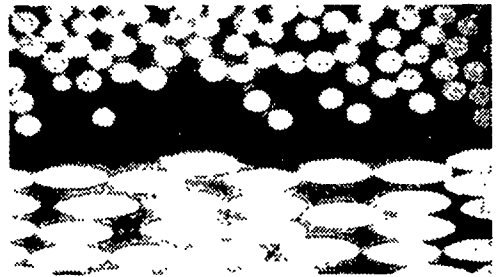
Figure 16 . Section through a rebonded delamination
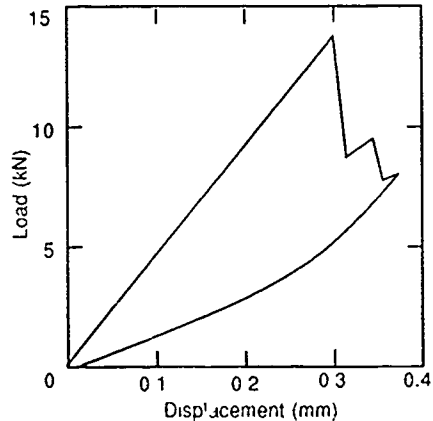
Figure 1 .   Example of a load-displacement curve for a holed plate shear test.

failure and the maximum load was found to be quite reproducible from specimen to specimen. Preliminary tests revealed that it was necessary to repair the initial hole drilling damage prior to the first loading in order to obtain a valid comparison [5] Figure 18 shows that at
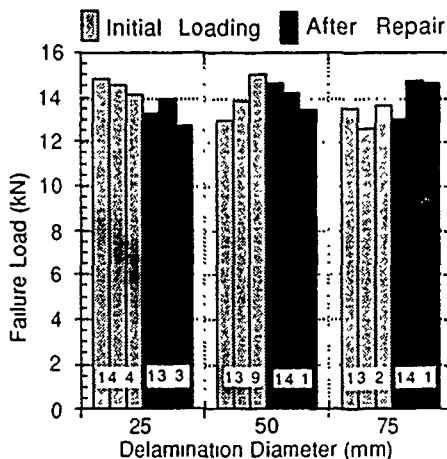
Figure 18 . Restoration of HPS failure load as a function of delamination size.

Figure 20 . Representative C-scan images of the CAI specimens for each impact energy

ambient temperature all of the post-repair failure loads were within 10% of the initial values The loading compliances were also restored but these were found, in general, to be a less sensitive measure of the quality of the repair At elevated temperatures, Figure 19 , the effectiveness of the repairs gradually decreases reflecting the lower T_g of the DREp resin compared to that of the matrix.

Figure 19   Effect of temperature on the restoration of the HPS specimen failure loads

7. IMPACT DAMAGE REPAIR

7.1 Restoration of Compression Strength
A series of tests were carried out to assess the effectiveness of resin injection repairs at restoring the compression strength after impact (CAI) Quasi-isotropic laminates of AS4/3501-6 carbon/epoxy, 40 plies thick, were machined into 100 mm x 150 mm CAI specimens Low velocity impacts of approximately, 10, 20, 30, 40 and 55 joules produced a range of delamination sizes as shown in Figure 20 At the three lower energies back-surface damage was either absent

or limited to longitudinal splitting of the outer ply However, at 40 and 55 joules damage was clearly visible with up to 6 plies protruding beyond the back surface directly beneath the point-of-impact. For each impact energy, 2 specimens were loaded in compression as damaged while 2 were first repaired with the DREp resin. The repair procedure was essentially the same as that described for the HPS specimens except that the resin was forced into the delaminations either through the back surface damage or via 3 or 4 small (<1 mmø) holes drilled into the laminate. The test results, plotted in Figure 21, indicate that almost all of the compression strength can be restored for impact energies below 30J and that even when back surface damage is present, acceptable failure strains can still be attained
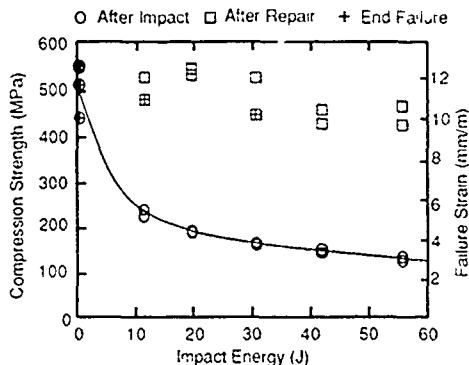
Figure 21 . Restoration of compression after impact strength

7.2 Restoration of Damage Tolerance
A second set of CAI tests were run in order to determine how effective the injection repairs were in restoring the ability of the laminate to sustain further impact damage As before, 4 plates were impacted at each of five energies, however, only one was tested as damaged, two were repaired and then re-impacted with the same energy as before and one was impacted a second time without repair Ultrasonic C-scans taken after each impact revealed, Figure 22, that the sizes of the delaminations produced in the repaired plates were significantly smaller than in the as-fabricated specimens This finding was supported by the compression test data, Figure 23, which indicated that the CAI strengths were greater in the repaired specimens, particularly those impacted at the higher impact energies Metallographic examination of some of the impacted plates also revealed that the bondline thickness was greater in the plates impacted at the higher energies

■ After Repair   □ No Repair
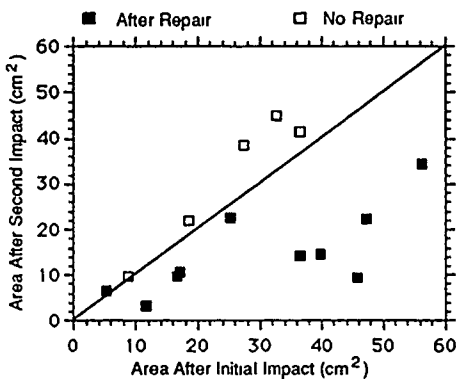
Figure 22 . Change in delamination size following second impact.
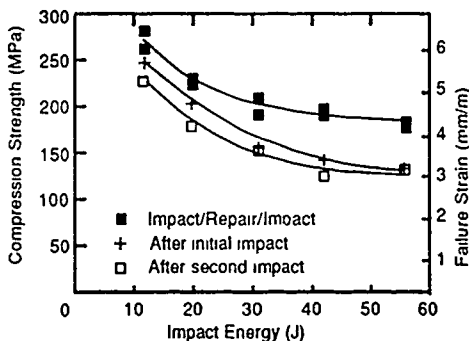
Figure 23 . Compression strength after impact of repaired CAI specimens.

8. CONTAMINATION EFFECTS

Unlike most other repair situations involving adhesive bonding, the inaccessibility of the delamination fracture surfaces precludes the use of any normal type of surface preparation prior to resin injection. Consequently, the possibility of one or more of the numerous contaminants, commonly encountered around aircraft, entering into the delaminations prior to repair is of concern. Although, no attempt was made to determine the likelihood of contaminant ingress, some tests were carried out to investigate what effect some typical aircraft fluids might have on the repair strength if they were present inside the delaminations. Five glass beakers, each containing three delaminated HPS specimens were placed in turn in an evacuated chamber and filled with one of the following contaminants, JP-4 jet fuel, H-537 hydraulic fluid, detergent, seawater and "Ultragel" (an ultrasonic couplant). After the specimens were completely covered, the vacuum was vented allowing atmospheric pressure to gradually force the contaminants into the delaminations over a period of 2 months. Upon removal, the specimens were dried for 4 hours at 121°C, repaired as described in section 6.1 and finally re-loaded to failure. Ultrasonic C-scans were taken to confirm that the delaminations had been completely infiltrated by the contaminants and also to inspect the repairs

The test results are shown in Figure 24. The specimens that had been immersed in JP-4 regained most of their initial load bearing capacity, indicating that little or no residue remained after drying. None of the hydraulic
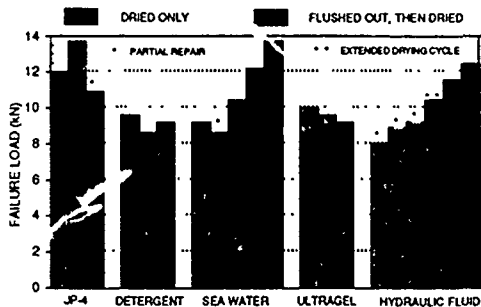
Figure 24 . Effect of prior contamination on HPS post-repair failure loads.

fluid contaminated specimens was properly repaired, the C-scans indicating that only the region closest to the fastener hole had been rebonded. Since this suggested that not all of the H-537 had evaporated prior to repair an additional test was run using an extended drying time of 2 days. This specimen did produce a defect-free C-scan but the failure load was still only 80% of the initial value. One further attempt to remove all traces of hydraulic fluid was made by flushing JP-4 through the delaminations of two more specimens, in through the fastener hole and out via 4 small holes drilled around the periphery. This procedure was successful in restoring approximately 90% of the original strength, Figure 24. C-scan images with no defect indications were obtained for all three of the water based fluids but the mean failure loads were all low, between 9.1 and 9.6 kN. In view of the residues left behind when these fluids evaporate as well as the similarities in both the failure loads and loading compliances it is reasonable to assume that these loads represent the maximum attainable by purely mechanical interlocking without any effective adhesion. An attempt was made at removing seawater by flushing distilled water through the delaminations in the same manner as was done with JP-4 for the hydraulic fluid contaminated specimens. The 2 specimens repaired in this manner had failure loads close to the 13kN of the uncontaminated control specimens indicating that most of the seawater had been removed.

9 REPAIR PROCEDURES

9.1 Autoclave repairs

Any components that can be readily removed from the aircraft, can in principle be repaired in an autoclave in a similar manner to the test specimens. Figure 25 illustrates one way that this could be done in practice. Another option would be to limit heating to the repair area alone by means of a heating blanket and to use the autoclave solely for the application of pressure.

9.2 On-Aircraft repairs

For fixed components such as the wing skins of the CF-18 where removal is both time consuming and expensive it is preferable to repair delaminations and impact damage on the aircraft. However, with access limited to only one side of each skin, it is no longer possible to assume that a vacuum can be maintained

(1) EVACUATE DELAMINATION

(2) INJECT RESIN

(3) MAINTAIN VACUUM AND PRESSURE DURING INFILTRATION AND CURE IN AUTOCLAVE
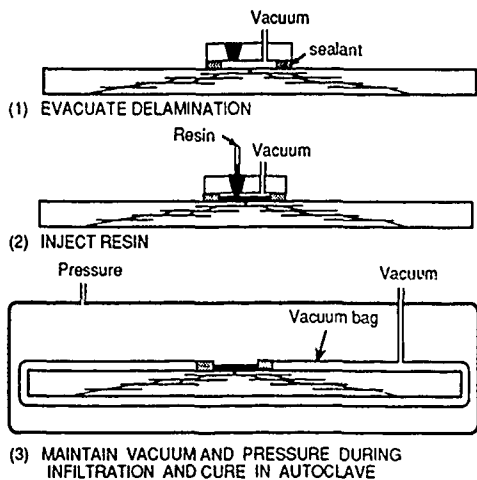
Figure 25 . Autoclave delamination repair procedure.

ahead of the advancing resin front. Consequently, it would seem likely that pockets of air would be trapped within the delaminations both as porosity in the bondline as well as in the form of larger unwetted areas. In order to investigate this further 3 HPS specimens were repaired without vacuum by a flow-through procedure in which the resin was forced in through the fastener hole and air allowed to escape via 4 equi-spaced holes drilled into the periphery of the delaminations. A "resin dam" was taped over each hole to prevent excess loss of resin and to reduce the pressure gradient within the delamination cavity. Rather surprisingly these repairs were just as successful as those carried out using a vacuum, there being no C-scan indications, no bondline porosity and similar post-repair failure loads [6].

One possible arrangement for carrying out this type of on-aircraft flow-through repair is shown in Figure 26.
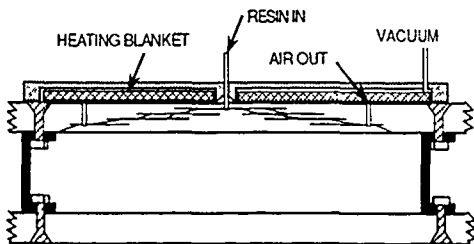
Figure 26 . Arrangement for on-aircraft delamination repair.

Here, the vacuum, which is used only to clamp the injection point and heating blanket to the skin, is isolated from the vent holes. Injection pressures in excess of 350 kPa (50 psi) have been consistently achieved with a prototype device of this sort. The major limitation to repairing delaminations in this manner is the presence of sufficient back-surface damage that the resin leaks through the laminate rather than entering the delaminations

10. CONCLUDING REMARKS

This investigation has clearly demonstrated that when complete infiltration is achieved, resin injection repairs can fully restore the structural integrity of delaminated carbon/epoxy components. Our findings reveal that small delaminations and particularly those in thick laminates are more difficult to infiltrate and have lower than optimum bondline thicknesses Fortunately, these types of delaminations are much less likely to lead to compression failures and in many instances may not need to be repaired at all. Our results also indicate that repaired delaminations can sustain the same interlaminar shear loadings as the original laminate This should make it possible to extend delamination repair zones to include locations adjacent to splice plates, ply drop-offs or other sources of interlaminar shear stresses.

Based on our experience, ultrasonic C scanning, in which the amplitude of any reflections originating from between the front and back surfaces is recorded, should provide an acceptable means of verifying the quality of a repair Time-of-flight C-scans are useful for determining delamination depths prior to repair but are of limited value in assessing the degree of resin infiltration For critical repairs where it is suspected that contaminants are present it may also be necessary to flush a suitable solvent through the delaminations and carry out a chemical analysis of the effluent.

From a mechanistic viewpoint, it may appear somewhat surprising that some of the out-of-plane mechanical properties improve following repair since the original chemically cross-linked ply interfaces have been replaced with bonded interfaces relying on adhesion and mechanical interlocking for strength. Evidently, any loss in strength is more than compensated for by the reduction in interlaminar stresses which results from the increased separation of the plies and by the improvement in mode II interlaminar fracture toughness. This is particularly true as the bondline thickness increases ie. in the larger diameter HPS specimens and in the CAI specimens impacted at the higher energies. In a sense, injection repairs can be regarded as being analogous to interleaved composites where the addition of a layer of toughened epoxy between the plies has been proven to substantially improve the damage tolerance [10].

This investigation into the repairability of delaminations by resin injection was carried out in response to a specific requirement, i e. the need to be able to repair CF-18 wing skin delaminations caused by either fit-up stresses or by impact damage Thus, while much of this work may be applicable to other material systems and loading conditions, different circumstances may make it necessary to address other concerns. For example, not only would delaminations grown under predominantly mode I conditions have smoother fracture surfaces but the effectiveness of mechanical interlocking at supporting opening stresses is likely to be considerably less than in shear Under these conditions, repair validation tests dominated by opening mode stresses would be more appropriate Also, in instances where delaminations have a tendency to recur, such as at a free edge, it would be preferable if the resistance to delamination could be substantially improved rather than merely restored While this could probably be achieved by adding a rubber toughening additive to the adhesive, the benefits of this would have to be weighed against the loss in resin flow. On the other hand, for delaminations that are only a few plies

deep, resin flow will be less important but it may be necessary to reduce the injection pressure and devise a means of clamping down the surface plies during infiltration and cure.

11. REFERENCES

1. J.D. Labor, G.M. Button and N.M. Bhatia "Depot Level Repairs for Composite Structures, Development and Validation - Volume 1", NADC report 79172-60 Vol 1, 1979

2. R.B. Ostrom, R.H. Stone, L.O Fogg and L.W. Smith "Field Level Repair for Composite Structures" NADC report 79174-60, 1985.

3 S.H. Myhre, "Advanced Composite Repair - Recent Developments and Some Problems", in Composite Repairs, SAMPE monograph No 1, pp 14-25, 1981

4. A.J. Russell and C.P Bowers, "Resin Requirements for Successful Repair of Delaminations", in Proceedings of the 36th International SAMPE Symposium, Edited by Stinson, Adsit and Gordaninejad, pp. 2279-2290, 1991.

5. A.J. Russell, C.P. Bowers and A J. Moss, "Repair of Delaminations and Impact Damage in Composite Aircraft Structures", in Composite Structures 6 pp 145-159, Elsevier Applied Science, London, 1991.

6. A J Russell and C. P. Bowers, "Injection Repair of Interlaminar Damage in Graphite/Epoxy Composites", in the proceedings of the First Canadian International Composites Conference and Exhibition, Montreal PQ, 4-6 September 1991.

7. K.I. McRae, A G. McCray, A.J. Russell and C.P Bowers, "Ultrasonic Imaging of Pre/Post Repair Delamination Damage Around Fastener Holes in Graphite/ Epoxy Composite Material," in Damage Detection and Quality Assurance in Composite Materials, ASTM STP , 1992..

8 A J. Russell and K N. Street, "Moisture and Temperature Effects on the Mixed-Mode Delamination Fracture of Unidirectional Graphite/Epoxy", in Delamination and Debonding, ASTM STP 876 pp 349-370, 1985.,

9. A.J. Russell, "Micromechanisms of Interlaminar Fracture and Fatigue", Polymer Composites, Vol 8, pp. 342-351, 1987.

10. R E Evans and J E Masters, "A New Generation of Epoxy Composites for Primary Structural Applications", in Toughened Composites, ASTM STP 937, pp. 413-436, 1987.

NUMERICAL DETERMINATION OF THE RESIDUAL STRENGTH
OF BATTLE DAMAGED COMPOSITE PLATES

T. Schneider, J. Möws, M. Rother
Dornier Luftfahrt GmbH
P.O Box 13 03
7990 Friednchshafen 1
Germany

SUMMARY
High energy impact damage by projectiles is a permanent thread to all aircraft or helicopters in combat situations Besides the actual damage extent, caused by the incident, and its effect on airworthiness, the question of the residual strength of the damaged structure arises Based on the experimental findings on the damage extent in shot-affected APC2/AS4 composite plates, a theoretical prediction of the residual compressive strength is given in terms of strength, stability and fracture mechanics principles. These predictions are compared with test results from four specimens, which have been cut out from the original plates It will be shown, that the delaminations, caused by the high energy impact, triggered the final compressive failure of the specimens with the start of an unstable delamination growth and that this event can be correctly predicted by a numerical analysis, if local out-of-plane deformations are taken into account

1. INTRODUCTION
One of the limiting factors for the application of Continuous Fibre Reinforced Plastics (CFRP) in primary aircraft structures is the uncertainty, felt by development engineers and operator staff, with respect to evolution and growth of damages within structural components Even if the damage event is obvious, as it is the case with high energy impact damage (HEID), the full extent of structural damage is still unknown and must be determined with non-destructive testing (NDT) equipment Another question, which arises after the occurence of damage, is the capability of the remaining structure to carry loads

Current state-of-the-art for dealing with these problems is the experimental verification Large aircraft components are predamaged by impact loads, artificial delaminations or other supposed manufacturing defects and subsequently submitted to static or dynamic loads until final failure occurs or a predefined number of cycles has been reached without further damage growth (for examples, see ref [1]) This procedure is very costly and time-consuming, especially, if other environmental conditions than room temperature and normal moisture content must be reproduced Therefore, considerable efforts are made by aircraft manufacturers as well as research institutes to provide analytical or numerical procedures for the prediction of the structural behaviour of damaged CFRP components.

The application of Linear-Elastic Fracture Mechanics (LEFM) principles seems to be a promising way to deal with delamination problems. Sun and Manoharan [2,3] pointed out, that the total energy release rate G is constant during delamination growth, although its components G_I and G_{II} do not converge to definite values as the assumed crack extension Δa becomes very small. Numerous other investigators reported successful applications of the energy release rate criterion to delamination

problems for static or dynamic loading, e g ref. [4] and [5].

The aim of the current study was to see, whether LEFM methods in combination with a finite element analysis can predict the onset of delamination growth and subsequently the residual strength of composite plates, which had been subjected to high energy impact loads by projectiles

2. HIGH-ENERGY IMPACT APPLICATION
2.1. Specimen definition
Geometry and lay up
For the impact tests, 240 x 240 mm plates from unidirectional APC2/AS4 prepreg had been manufactured They consisted of 34 layers, each 0 124 mm thick, giving a total plate thickness of 4 2 mm The stacking sequence was identical for all APC2/ AS4 plates·

$$(-45/+45/0/-45/+45/0/-45/+45/90/-45/+45/0/-45/+45/0/-45/+45/_{sym})$$

Material properties
Stiffness and strength properties for unidirectional APC2/AS4 prepreg (room temperature, moisture content as received) are listed in table 1.

UD-Properties APC2/AS4 RT/as received		
E_{xx}	109 8	GPa
E_{yy}	10 1	GPa
E_{zz}	10 1	GPa
$G_{xy} = G_{zx}$	3 7	GPa
G_{yz}	1 3	GPa
$v_{xy} = v_{zx}$	0 3	-
v_{yz}	0 42	-
$\sigma_{xx,T}$	2050	MPa
$\sigma_{xx,C}$	1200	MPa
$\sigma_{yy\,T}$	87	MPa
$\sigma_{yy\,C}$	230	MPa
τ_{xy}	185	MPa

T Tension   C Compression

Table 1. Material properties

2 2. High energy Impact application
The four plates, which have been used in this study, had been part of an extensive test program to investigate the damage extent in various structural concepts after high energy impact [6] Two plates had been used as the forward and rear wall in a

Fig 1 Plate S-19672R after high-energy impact application

box type structure Cubic steel projectiles were fired with a velocity of appr 1660 m/s from a short distance on the center of the face plate

The visual damage was nearly the same for all four plates Fig 1 shows the visual damage in an APC2/AS4 plate after the impact of a 7 5 g cubic steel mass with a velocity of 1603 m/s The projectiles perforated both plates, leaving an open hole with extensive laminate splitting along the hole edges Both the top and bottom surface layers separated as a narrow, diagonal strip nearly over the whole plate width

For the residual strength tests, the plates were cut to dimensions

Penetration hole diameter   30 mm
Delamination diameter   60 mm
Laminate thickness   4,2 mm
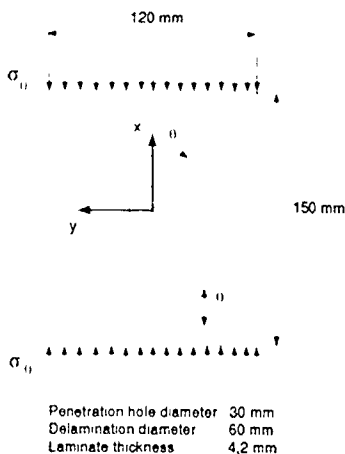
Fig 2 Plate geometry for residual strength tests

of 150 x 120 mm with the penetration hole in the centre of the specimens, fig 2

2.3 NDT results

Ultrasonic C-scan inspection had been performed directly after the impact tests They revealed internal delaminations with a round shape and a diameter of approximately twice the diameter of the open hole [6] However, C-scan pictures give no information about the position of the delamination in the laminate thickness direction

As this additional information is vital for numerical strength predictions on a fracture mechanics basis, the plates were inspected once again by ultrasonic D-scan after machine contouring The D-scan method is based on the measurement of the time interval between the emission of the ultrasonic signal and the arrival of the echo reflected by the delamination This time interval can be directly related to the position of the delamination within the laminate

A major disadvantage of this method is, that only the delamination, which lies nearest to the laminate surface, can be recorded If additional delaminations occur below this first damage, it remains undetected as long as its area is smaller than the shadow of the outer delamination

The results of the D-scan inspections are shown in fig 3 Although different in details, the relevant findings are similar for all four plates Around the penetration hole the impact caused a nearly circular delaminated area with a diameter of 50 - 60 mm in a depth of appr 50 % of the laminate thickness Also clearly visible is the shape of the separated strips of the surface layers The curved black lines and some shaded areas around its ends are caused by the strain gauge wiring and the silicon coating

Fig. 3: D-scans of APC2/AS4 plates after high-energy impact application

3. NUMERICAL INVESTIGATIONS

3.1. Calculation of Energy Release Rates

The main point of interest of this study was the prediction of the residual strength of battle damaged plates and its comparison with experimental results. Three different failure modes had to be considered.

☐ in-plane compression failure
☐ global plate buckling
☐ delamination growth with or without local buckling of sub-laminates

While the first two criteria represent standard problems, which can be solved with nearly all commercially available finite element programs, the latter involves the application of fracture mechanics principles in conjunction with a three-dimensional linear-elastic finite element analysis. For this purpose, a post-processor for Dornier's finite element code COSA-DEMEL called SAM3D has been developed [7]. Based on the virtual crack extension method, as it has been described by Parks [8] and Hellen [9], this processor calculates local energy release rates along the crack front of an embedded crack or a surface flaw in three-dimensional structures


Mode I   Mode II   Mode III
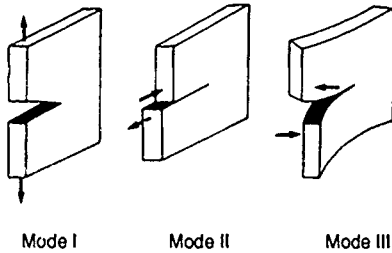
Fig 4: Definition of fracture modes

Due to the orthotropic material properties, delaminations between plies with different fiber orientations generally produce a mixed mode problem, where all three modes of fracture (fig 4) are present at the tip of the delamination. As the critical energy release rate of composite materials is different for mode I, II and III, it is necessary to split the total energy release rate G_{total}, calculated by the virtual crack extension method, into the contributions of each single mode

$$G_{total} = G_I + G_{II} + G_{III} \tag{1}$$

Similar to the virtual crack closure method by Rybicki and Kanninen [10], the relative displacements of the nodal points A and B on the crack surfaces next to the crack tip (fig 5) are used to estimate the contributions of the single modes G_I, G_{II} and G_{III} to the total energy release rate For orthotropic materials, the relations between the energy release rates and the near-tip crack surface displacements u', v' and w' read [11,12]:

$$G_I \sim F_1 \, \Delta w'^2 \tag{2a}$$
$$G_{II} \sim F_2 \, \Delta u'^2 \tag{2b}$$
$$G_{III} \sim F_3 \, \Delta v'^2 \tag{2c}$$

with

$$F_1 = \sqrt{\chi + \lambda} / (2\sqrt{2} \sqrt{a_{11} a_{22}} \, (\chi + \lambda)) \tag{3a}$$

$$F_2 = \sqrt{\chi + \lambda} / (2\sqrt{2} \, a_{11} \, (\chi + \lambda)) \tag{3b}$$

$$F_3 = 1/2 \, \sqrt{(a_{55}/a_{44})} \, (\chi + \sqrt{\chi^2 - \lambda^2})/a_{44} \tag{3c}$$

and

$$\chi = (2a_{12} + a_{66})/2a_{11}, \tag{4}$$
$$\lambda^2 = a_{22} / a_{11} \tag{5}$$

where a_{ij} is the compliance matrix of the layers above and below the delamination plane and u', v', w' the deformations with respect to the local coordinate system, as defined in fig. 5.
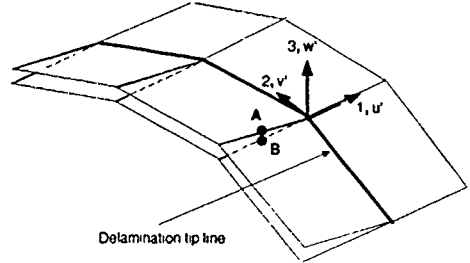

Fig 5: Definition of the local coordinate system at the delamination front

3.2. Finite Element Models

For the numerical strength prediction two different finite element models were created The strength prediction according to the classical laminate theory (CLT) was performed with a two-dimensional model with only one element in the laminate thickness direction, fig 6 Due to symmetry conditions, only one quarter of the plate was modelled Laminate properties for the given lay-up are listed in table 2. The single ply analysis is
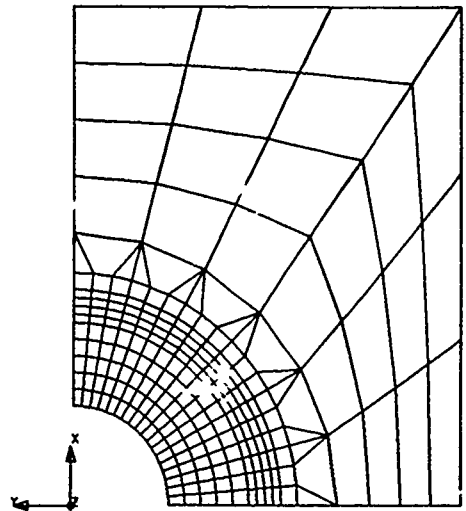

Fig. 6: Two dimensional finite element model
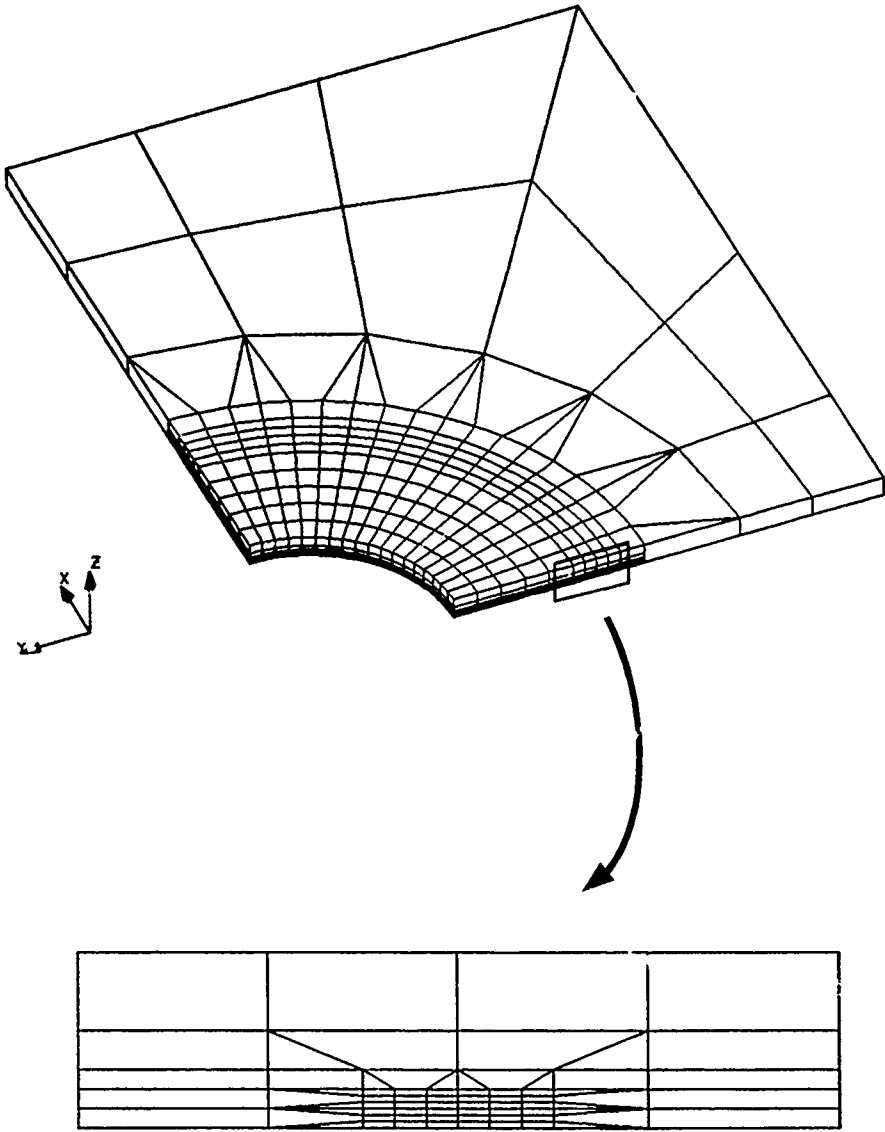
Fig 7   Three-dimensional finite element model with mesh refinement around the delamination front

28-6

done on the element level, with ply stresses and margins of safety for matrix and fibre failure as output. The delaminations are not taken into account in this analysis

The determination of energy release rates along the delamination tip requires the calculation of the three-dimensional stress and strain state in the vicinity of the crack front. For this purpose, the two-dimensional model, as depicted in fig 6, was extended in the z-direction. Additionally, a considerable mesh refinement was necessary in the layers above and below the suspected delamination plane, fig 7

conditions along the assumed symmetry planes" on the ply level. A comparison of the laminate displacements along x = 0 and y = 0 between the two- and the three-dimensional model nevertheless revealed a good correlation and therefore the influence of this local errors on the remaining model was judged to be minor

The full 3D model consisted of 1782 brick elements, each with 26 nodes, 264 wedge-shaped elements with 18 nodes and a total of 16248 nodes with 45167 degrees of freedom. The circular delamination was modelled between the 16th and 17th ply of the laminate (see 3 5 1)

Laminate Properties for (24/70/6)-Lay-up APC2/AS4		
E_{xx}	39540 MPa	
E_{yy}	25780 MPa	
G_{xy}	21198 MPa	
υ_{xy}	0 61	-

Table 2: Laminate properties

Due to limitations in available computer storage space, the three-dimensional model had to be restricted to one quarter of the plate and to one half of the laminate thickness. Although this is correct on the laminate level (symmetric and balanced lay-up, delamination not considered), it leads to incorrect

3.3. Strength Prediction by CLT

As expected the linear-elastic 2D-analysis gave the highest stresses and strains at the penetration hole edge at x=0. First ply failure is predicted to occur in the 0°-plies at a total load F = 56,3 kN by matrix cracking, followed by a compressive fibre failure of the same plies at F = 68,1 kN. This is considered to be the ultimate laminate strength

3.4. Determination of the Theoretical Buckling Load

COSA-DEMEL currently offers no buckling analysis solution. Therefore the special purpose program COSA-FEST [13] was used to predict the overall buckling load for the plates. As this program uses special plate elements with a quintic displacement function, a relative coarse mesh was sufficient for this analysis. The delamination was assumed to be in the mid-plane of
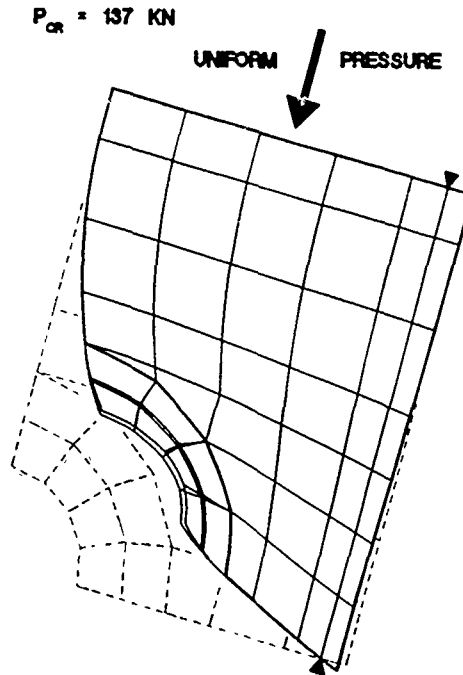

Fig. 8. Global buckling mode shape

the laminate, creating two sub-laminates with identical thickness. Fig 8 shows the undeformed mesh together with the shape of the first buckling mode. Instability is predicted for a total load of F = 137 kN. This is far beyond the strength limit from CLT and therefore global buckling could be excluded.

3.5. Fracture Mechanics Calculations

3.5.1. Energy Release Rates for In Plane Loading

The calculation of energy release rates requires the knowledge of the delamination position within the laminate lay-up. NDT results from D-scan-measurements revealed a delamination depth of approximately 2.1 mm, with a resolution of about 3 or 4 plies.

As ply-angle variations of 90° between neighbouring layers are known to produce high interlaminar stresses, the most probable location for the delamination plane was between the 16th and 17th layer of the laminate, i.e. the -45°- and +45°-plies. In order to verify this assumption, a second analysis run was performed, in which the orientations of the 15th and 16th plies were exchanged, but the position of the delamination remained between the 16th and 17th ply. With this minor deviation from the given stacking sequence, G-values for a -45/0-interface delamination could be calculated without any modelling effort.

Although the finite element model was restricted to one quarter of the plate, energy release rates are given for $0° \leq \theta \leq 180°$. This was achieved by simply exchanging the orientations of the ±45°-plies in the model and rerunning the analysis, fig 9. Again, the compatibility conditions at $\theta=0°$ and $\theta=90°$ on the ply level can not be met by this model, but if the G-values at
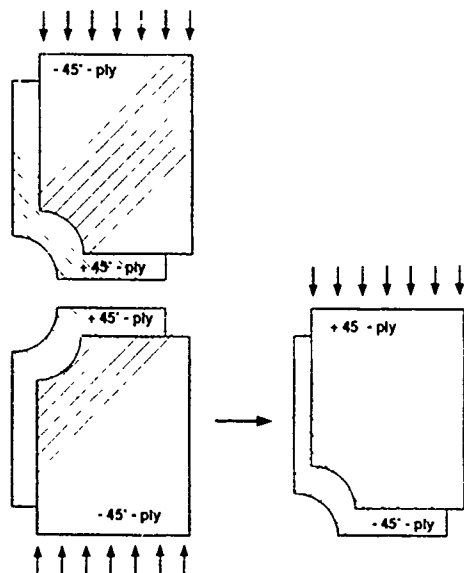

Fig. 9: Fibre directions relative to penetration hole edge in the -45/+45-interface

this locations are dropped, the analysis will give useful results for the rest of the structure.

Non-dimensionalized total energy release rates G_{total}/G_{Ref} are compared for the -45/+45- and -45/0- interface in fig 10, with

$$G_{Ref} = \varepsilon_x^2 E_x t \qquad (6)$$

where E_x is the laminate modulus in x-direction, t the total laminate thickness and ε_x given by

$$\varepsilon_x = \sigma_x/E_x = F_x/(b\, t\, E_x) \qquad (7)$$

(b = laminate width)

For both interfaces, the highest energy release rate is found between $80° \leq \theta \leq 100°$ with nearly identical peak values. The shape of the G-distribution in this range had to be approximated due to the inaccuracy of the G-calculations at the assumed symmetry line. For $\theta < 40°$ and $\theta > 140°$ the energy release rate is negligible. The contributions of the individual crack modes to the total energy release rate is shown in figs 11 and 12 for the +45/-45- and -45/0-interface.

According to LEFM principles, delamination growth in a structure will occur, if

$$G = G_c \qquad (8)$$

where G_c is the critical energy release rate or fracture toughness of the material. If the toughness is not identical for all crack modes, as it is the case with CFRP, critical energy release rates for each single mode G_{Ic}, G_{IIc} and G_{IIIc} must be determined. The general failure criterion then reads

$$(G_I/G_{Ic})^m + (G_{II}/G_{IIc})^n + (G_{III}/G_{IIIc})^p = 1 \qquad (9)$$

Investigations by Johnson and Mangalgiri [14] have shown, that for several resin systems m = n = 1 provides the best fit to experimental data (Mode III was not considered in this mixed mode problem) and therefore was selected for this study. Several authors reported critical energy release rates G_{Ic} and G_{IIc} for APC2/AS4, usually determined with the double cantilever beam (DCB) and the end notched flexure (ENF) specimen for Mode I and II respectively. These values are given in table 3.

Values for G_{IIIc} have not been found in the published literature due to the current lack of a specimen type, which produces

Reference	G_{Ic} [N/mm]	G_{IIc} [N/mm]
Kim, Dharan [15]	1,34	1,77
Prel, Davies [16]	1,46	1,11 - 1,86[*]
Gillespie, Carlsson [17]	1,75	-
Hashemi et al [18]	1,60	1,65
Russell, Street [19]	1,33	1,76

[*] Range of G_{IIc} values determined with three different specimen types

Table 3. Critical energy release rates for APC2/AS4
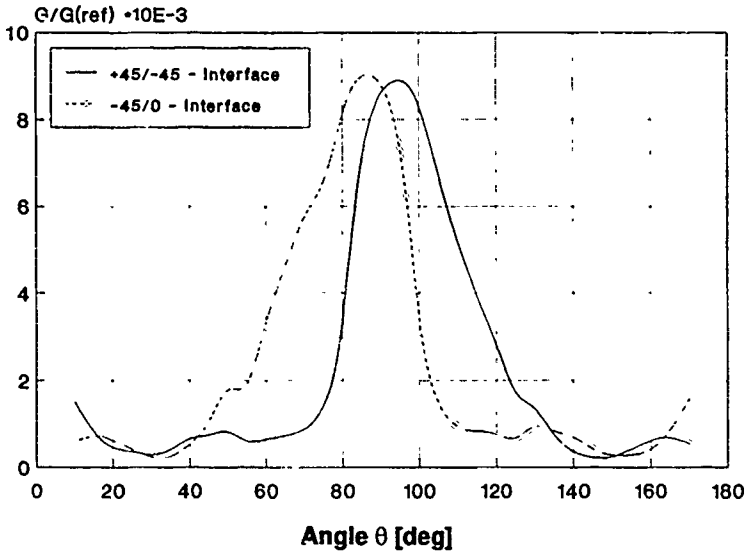
Fig. 10: Total energy release rates for the -45/+45- and -45/0-interfaces
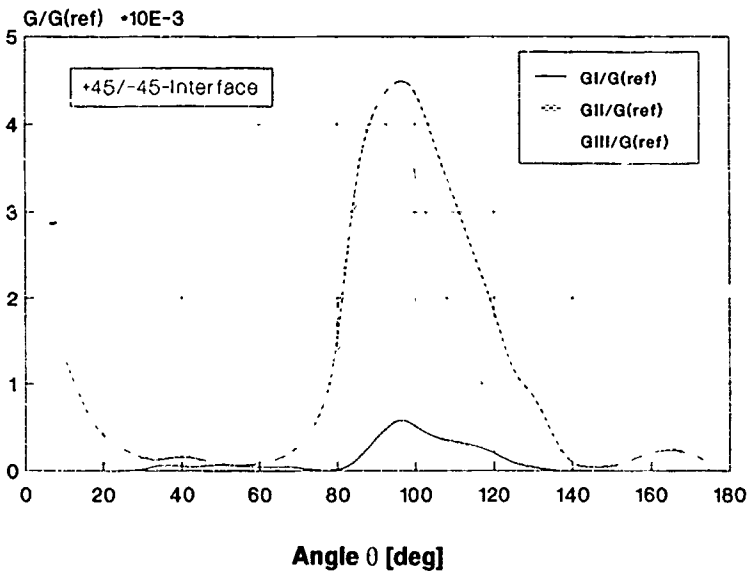
Fig 11: Energy release rates for individual fracture modes for the -45/+45-interface

G/G(ref) •10E-3
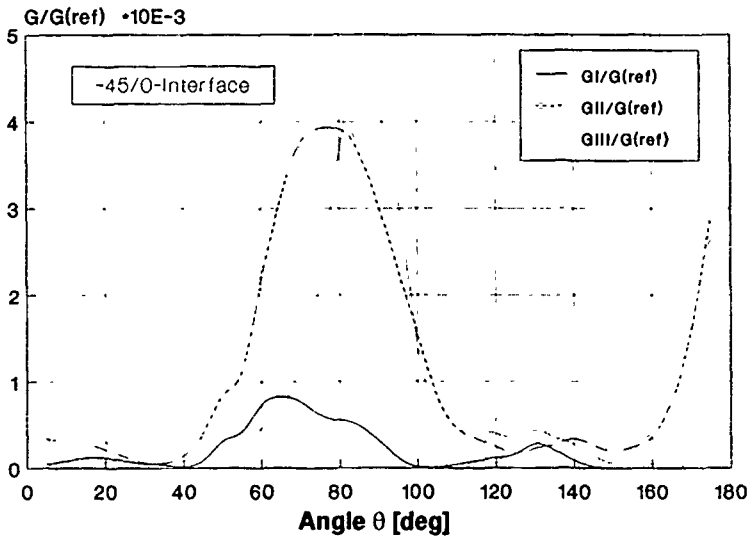
Fig. 12: Energy release rates for individual fracture modes for the -45/0-interface

pure Mode III conditions along the delamination tip [20] As an approximation, $G_{IIc} = G_{IIIc}$ and p = 1 have been used throughout this study

From eq (9) the critical load for delamination growth initiation can be calculated by inserting G_I-, G_{II}- and G_{III}-values for $\theta = 90°$ from figs 11 and 12 in the mixed-mode failure criterion As critical material properties, the values determined by Russell and Street (see tab 3) have been used Maximum compressive loads for the onset of delamination growth are

$$F_{onset} = 654 \text{ kN} \quad \text{for the } +45/-45\text{-interface}$$
$$F_{onset} = 662 \text{ kN} \quad \text{for the } -45/0\text{-interface}$$

Both critical load levels are much higher than the strength and stability limit of the plates and therefore delamination growth onset under pure in-plane loads could be excluded

3.5.2 Energy Release Rates for Local Out of Plane Deformations

Although the buckling analysis gave no indication of instability related failure, the possiblity of local out-of-plane deformations in the high-loaded area at $\theta = 90°$ have also been considered For this purpose a prescribed z-deformation of the outer sublaminate perpendicular to the plate along the y-axis has been applied. It must be emphasized, that this procedure does not represent a real post-buckling analysis, but only can give qualitative hints of the structural behaviour in the presence of out-of-plane deformations
For this analysis, the nodal points of the sub-laminate along y=0 from the tip of the delamination to the edge of the penetration hole have been deflected according to

$$w = w_{max} (1 - (r^2/a^2))^2 \qquad (10)$$

with w, r and a as defined in fig 13 and $w_{max} = 1$ mm

The results of the G-analysis for this case are given in fig 14 for $0 \leq \theta \leq 90°$ Compared to G-values for pure in-plane loads the total non-dimensionalized energy release rate is now two orders of magnitude higher with mode I as the dominating contribution.
Compared to the critical energy release rates, the ratio of G_I to G_{Ic} is now larger than 1 and therefore it can be concluded, that, if any substantial out-of-plane deformation takes places (either from local buckling or any other local damage event), delamination growth would occur. However, a critical load can not be given for this case, as the relation between z-deformations and load level can only be established by a post-buckling analysis, which couldn't be performed within this work.

4. EXPERIMENTAL STRENGTH EVALUATION
4.1. Test setup
The residual strength tests were performed in a standard compression-after-impact (CAI) testing device Free edges of the plates have been simply supported, fig 15 The compression load was applied uniformly along the upper plate edge with a constant rate of 2mm/min
At predefined load levels or after the occurance of audible damage propagation the tests were interrupted and the specimens were removed from the testing device in order to estab-
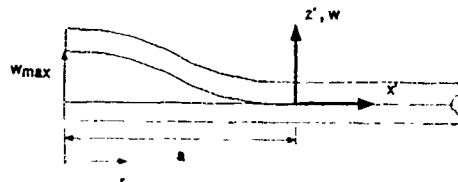

Fig 13 Prescribed out-of-plane deformation at x=0
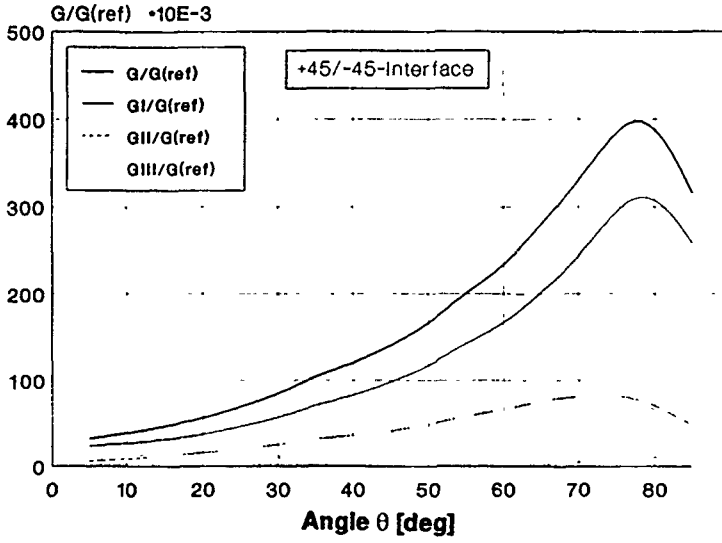
Fig. 14: Energy release rates for simulated out-of-plane deformation of the outer sub-laminate
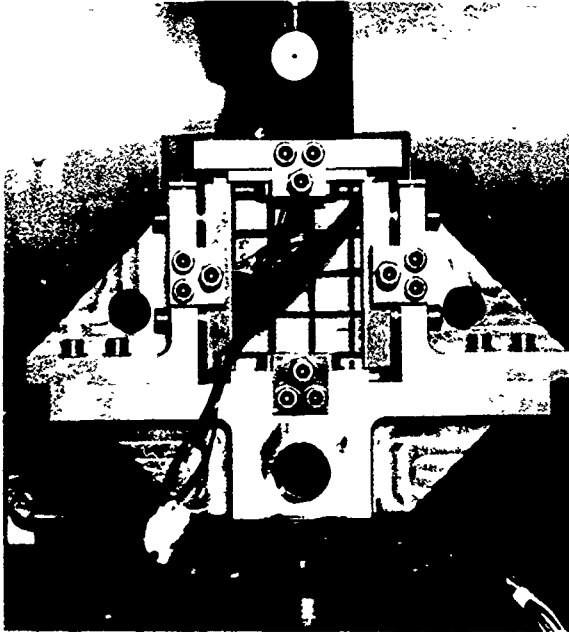
Fig. 15: Specimen fixture for residual compressive strength evaluation

lish the damage extent by D-scanning This procedure was repeated until final fracture occured.

4.2. Test results

The final fracture loads of all four plates are listed in table 4. Two of them (No S-19672V and S-19679V) failed without any detectable delamination growth before final fracture For the others (No S-19672R and S-19679R) delamination growth perpendicular to the loading direction prior to total failure was determined. The D-scans of these specimens are depicted in figs 17 and 18 at three different damage states (before the test, after delamination growth and after final fracture)

The delamination growth occured at load levels of 81,3 kN (S-19672R) and 92,0 kN (S-19679R), together with a sudden drop of the compression load to 70 and 83,3 kN, respectively. When the specimens were reloaded after NDT, final fracture took place at 72 kN (S-19672R) and 89,5 kN (S-19679R) For both plates, the load at delamination growth onset was therefore defined as the compressive strength and compared to the theoretical predictions, fig. 16

4.3. Fractography

Visible inspection of the plates after the test showed two different failure mechanisms The first one is a typical compressive failure with laminate splitting and crushing, fig. 19. Only minor delaminations are found around this fracture zone (see also fig 17).

In the other case a delamination can be found across the plate width, accompagnied by a compressive failure of the sublaminates at the opposite ends of the delamination along the edge of the plate, fig 20

Plate No.	Failure load [kN]	
	experimental	2D-FE-Analysis
S-19672V	99 6	}
S-19672R	81.3	} 68 1
S-19679V	107 0	}
S-19679R	92 0	}

Table 4: Residual strength test results

After the visual inspection, sections of one of the plates, taken 5 mm away from the edges, were examined by microscope, fig 21. They illustrate once more the different appearances of both failure mechanisms.

From these findings the following failure sequence may be deducted First fibre failure took place at $\theta = 90°$ on one or both sides of the penetration hole, accompanied by local out-of-plane deformations of the broken plies These deformations, together with the load redistribution, led to a sharp rise of the mode I energy release rate and subsequently to an unstable growth of the delamination across the plate width This event was immediately followed by the compression failure of the sub-laminates

5. CONCLUSIONS

The aim of the study was the numerical determination of the residual strength of battle damaged composite plates and the experimental validation of these predictions Three different
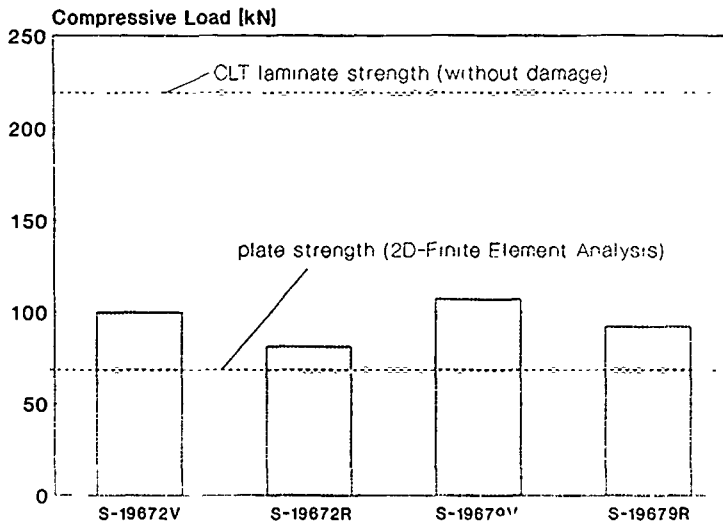

Fig. 16: Comparison of theoretical and experime   pressive strength after HEID

a) test start

b) after delamination
   growth

c) after final
   failure

Delamination
depth in [%]
of laminate
thickness

↑ Side view see fig 19

Fig 17: D-scan pictures of delamination growth and final fracture of plate no. S-19672R

a) test start

Delamination
depth in [%]
of laminate
thickness

b) after delamination
growth

c) after final
failure

↑ Side view see fig 20

Fig 18   D-scan pictures of delamination growth and final fracture of plate no S-19679R

Fig. 19. Side view of plate no S-19672R after fracture

FIG. 20 Side view of plate no S-19679R after fracture

types of failure were examined, i e strength failure according to CLT, global buckling and delamination growth onset From these calculations and the comparison with the test results, the following conclusions can be drawn

⊓ The strength predictions according to CLT are conservative (between 19 and 57%)

⊓ The compressive strength reduction of the battle damaged plates ranges from 51 to 63 % compared to the analytical strength of the undamaged laminate

⊓ Numerical energy release rate calculations predicted no delamination growth for pure in-plane loading Any out-of-plane deformation, however, would increase the energy release rate by two orders of magnitude and hence would lead to mode-I driven delamination growth onset

⊓ Post-failure analysis of the specimens revealed two different failure mechanisms Besides a pure compressive failure mode with no substantial extent of delaminations around the fracture path a second failure mode was identified, which was interpreted as an interaction between compressive failure and delamination growth due to out-oi plane deformations

One of the main goals of this study was the validation of the fracture mechanics approach for numerical strength predictions of delaminated structures Although the numerical analyses were correct in predicting no delamination growth, the intended validation remains incomplete, because strength failure preceded any eventual delamination growth onset However, it can be concluded from these results, that delaminations under pure static in-plane loads are uncritical as long as no out-of-

plane deformation of the sub-laminates occur In the latter case, a detailed post-buckling analysis is necessary in order to predict load level and location of delamination growth onset

6. ACKNOWLEDGEMENT

7. REFERENCES

[1]   Brocker W , Worthe K , 'Fatigue Behaviour of Composite Structures", in 'Fatigue Management , AGARD CP 506, May 1991, Paper 6

[2]   Manoharan M G , Sun C T , Strain Energy Release Rates of an Interfacial Crack between Two Anisotropic Solids under Uniform Axial Strain , Comp Science and Technology, Vol 39 (1990), pp 99-116

[3]   Sun C T , Manoharan M G , Strain Energy Release Rates of an Interfacial Crack Between Two Orthotropic Solids", J of Comp Materials, Vol 23, May 1989

[4]   Murri G B , Salpekar S A , O'Brien T K , Fatigue Delamination Onset Prediction in Unidirectional Tapered Laminates , in 'Composite Materials Fatigue and Fracture, Third Volume, ASTM STP 1110 , T K O'Brien (ed), American Society for Testing and Materials,

Philadelphia, 1991

[5] Martin R.H , Jackson W C , "Damage Prediction in Cross-Plied Curved Composite Laminates", NASA Techn Memorandum 104089, July 1991

[6] Benz A , "Damage Tolerance CFK-Strukturen II· Minimierung des Faserausreißens und der Beschadigung von ebenen FVK-Platten bei Beschuß", Report No SY30-409/90, Dornier Luftfahrt GmbH *(in German)*

[7] Schneider T., "Untersuchung zur Ermittlung der Restfestigkeit von durch Hochgeschwindigkeitsimpact geschadigten Faserverbundplatten", Report No SC20-A-019/92, Dornier Luftfahrt GmbH *(in German)*

[8] Parks D M , "A Stiffness Derivative Finite Element Technique for Determination of Crack Tip Stress Intensity Factors", Int J of Fracture, Vol 10, 1974

[9] Hellen T K ,'On the Method of Virtual Crack Extension", Int J for Numerical Methods in Engineering, Vol. 9, 1975

[10] Rybicki E., Kanninen M , "A Finite Element Calculation of Stress Intensity Factors by a Modified Crack Closure Integral", Eng. Fract Mech , Vol 9 (1977), pp 931-938

[11] Friedrich K (ed.), "Application of Fracture Mechanics to Composite Materials", Composite Materials Series Volume 6, Elsevier Science Publishers B V , Amsterdam, 1989, ISBN 0-444-87286-8

[12] Tada H , Paris P , Irwin G , "The Stress Analysis of Crack Handbook", 2nd edition, Del Research Corporation, St Louis, Missouri, 1985

[13] Fix A , "Berechnung der Stabilitat von Strukturen nach der Finite Elemente Methode", Report No. BMVg-FBWT 82-8,Dornier Luftfahrt GmbH, Friedrichshafen, Germany, *(in German)*

[14] Johnson W S , Mangalgiri P.D , "Influence of the Resin on Interlaminar Mixed-Mode Fracture", Toughened Composites, ASTM STP 937, N.J Johnston (ed), American Society for Testing and Materials, Philadelphia, 1987

[15] Kim W C , Dharan K H , "A Fracture Control Plan For Composite Structures", Eng Fracture Mechanics, Vol. 34, No 2

[16] Prel Y.J et al , "Mode I and Mode II Delamination of Thermosetting and Thermoplastic Composites", 2nd ASTM Symposium on Comp Materials Fatigue and Fracture, Cincinnati, Ohio, 1987

[17] Gillespie J W , Carlsson L A , Smily A J , "Rate Dependent Mode I Interlaminar Crack Growth Mechanisms in Graphite/Epoxy and Graphite/PEEK", Comp Science and Technology, Vol 28, No 1

[18] Hashemi S , Kinloch A.J., Williams G , "Mixed-Mode Fracture in Fiber-Polymer Composite Laminates", in "Composite Materials· Fatigue and Fracture, Third Volume, ASTM STP 1110", T.K O'Brien (ed), American Society for Testing And Materials, Philadelphia, 1991

[19] Russell A J , Street K N., "The Effect of Matrix Toughness on Delamination· Static and Fatigue Fracture Under Mode II Shear Loading of Graphite Fiber Composites", in "Toughened Composites", ASTM STP 937, N J Johnston (ed), American Society for Testing and Materials, Philadelphia, 1987

[20] Martin R H , "Interlaminar Fracture Characterization A Current Review", NASA Contractor Report 187573, NASA Langley Research Center, Hampton, Virginia, July 1991

3 mm

Plate No. S-19672R

Plate No. S-19679R

3 mm
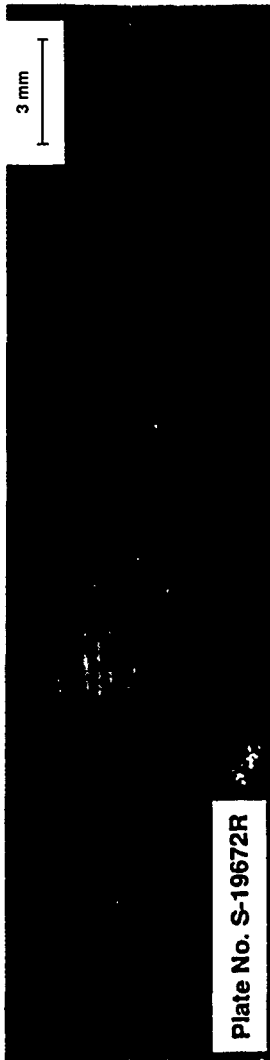
Fig 21 Micrographs of failed sections

Effect of impacts on CFRP Structures,
Results of a Comprehensive Test Program for Practical Use

I Kröber
Deutsche Airbus GmᵇH
P.O. Box 107845
D-2800 Bremen 1, Germany

SUMMARY

An experimental investigation was performed to establish the influence of impacts on the medium-tough CFRP material Ciba 6376/HTA. The results of this program enable a designer to dimension CFRP components. The compressive strain during impact was determined as a function of impact and impact energy Slight increases of this compressive strain above a certain threshould resulted in catastrophic failure. Furthermore the influence of the thickness on residual strength and visible damage thrushold is given It was found, that the allowable strain limit not only depends on the impact energy but also on the laminate lay-up, especially the proportion of 0°-plies Drop weight impacts show lower C-Scan damage areas compared with air gun impacts However, the residual strain is the same in both cases As opposed to coupons, stringer stiffened panels result in a scale-up effect of 15% concerning the allowable strain limit However, this effect might change for different geometries

1. INTRODUCTION

Fiber composite structures are being used to an increasing extent in modern aircraft The most important group of materials used for this purpose being carbon fiber-reinforced epoxy resins (CFRP) This paper deals only with this material group

In order to demonstrate adequate airworthiness, all possible loads and failure criteria of a component have to be considered. Contrary to metals, an important load type for CFRP is the damage resulting from mechanical impacts Impacts can occur in service (on the ground or in flight), during maintenance and even in the production line (shop floor impacts) Whereas, in the first case, the component may already be under load during the impact this does not apply in the latter two cases.

The measure for the intensity of an impact is the energy of the impactor Naturally, the shape and consistency of the impactor also play a role since the damage caused by sharp hard objects will differ from that caused by round soft ones The latter fact was not the object of the tests described here since, with only some exceptions, a steel ball with a diameter of 20 mm was used as impactor for the tests

From a certain energy onwards, impacts cause a steep reduction in strength of the CFRP laminate, more strongly so in the case of compression than in the case of tension. Consequently, related tests are performed mainly with compressive loads,

as in the case in question The same applies to stress risers resulting from holes and openings in structures, but to a lesser degree /1 – 5/.

Important influence factors for the degradation of a component as a result of impact are the material as such, the ratio of mass to speed of the impactor, the laminate thickness and – very important – the laminate lay-up.

All the test specimens described in this paper were manufactured from unidirectional tapes of Ciba 6376/ HTA.

If not other mentioned the impacts were produced with an air gun system. This system is a development of the test department of Deutsche Airbus

2. INFLUENCE OF THE MATERIAL

The toughness of the resin plays the most important role where the material is concerned, although the type of fiber and its diameter as well as the fiber-matrix adhesion are also significant Fig. 1 shows the residual strength after an impact with the standardized Boeing Impact Test versus the fracture toughness The impact tests were carried out at the central laboratory of MBB The test will not be described in detail further here since the graph merely serves to classify the materials


Figure 1. Fracture toughness of materials

Three material groups are evident, these can be referred to as brittle, medium-tough and tough The first group includes the already classic systems such as 913C/T300, F550/T300 as well as some newer materials The medium-tough materials

are currently being used for newer projects at Deutsche Air-bus since they offer the best compromise between impact resistance, the other important material characteristics and, last but not least, the price. Moreover, a point to note is that tough systems often reveal weakness under compressive loads in a moist hot condition and/or an intolerable reduction in the softening temperature after moisture absorption

3. FAILURE THRESHOLD AS A FUNCTION OF PRE-STRAIN AND ENERGY

A test series were carried out to find the pre-strain under which a specimen fails abruptly as a result of an impact with a given energy. Those tests were already done in 1978 for brittle materials /1/.

The specimens with the dimensions 250 x 110 x 5 25 mm (length, width, thickness) consisted of 42 plies with a laminate lay-up of 28 6% 0^0 plies, 57% $\pm 45^0$ plies and 14.3% 90^0 plies (28 6/57/14.3) and a stacking of (+ 45,0,-45,90,-45,0, + 45)$_6$ The load was applied by means of a pressure on the upper specimen surface. All edges were simply supported during the test.

The tests were carried out by trial and error for a constant energy level. The specimens under different compressive pre-strains either withstood the impact or failed By repetition of the series for other energies, a "line of catastrophic failure" was obtained for the pre-strain as a function of the impact energy

Fig 2 shows the results of such a test series It is evident that a component can be subjected to a compressive strain of 0 3% and 0 25% at an impact energy of 32 J and 50 J, respectively

Figure 2   Effect of energy and pre-strain on catastrophic failure

As expected, residual strength tests with the specimens which had not failed indicated failure strains above the failure threshold This therefore confirmed that components under load are more strongly damaged by impacts than components which are not under load In three cases, the damage due to an impact of less than 11 J was so small that the rupture did not occur in the damaged cross-section at the center of the specimen but near the load application point (Fig. 3)

It is remarkable that none of the specimens which were intact showed any visible damage on the front side, not even at 66 J and preload.

Figure 3   Residual strain after impact with pre-strain

After the impact, some of the specimens were fatigue tested in a compression-compression constant amplitude test (R = 10) with a maximum compression strain of 0 31% Despite this very high load with compare to the failure curve, three specimens reached 10^6 load cycles Their residual strength is also distinctly above the failure threshold (except for the mentioned failure in the area of the load application in one case) Only 10540 load cycles were reached at 50 J impact which is hardly surprising since the maximum strain in the fatigue test is higher than that of the failure threshold at this point of the curve At 32 J, these two strains are identical so that the related specimen reached 275634 load cycles This specimen had a strain of 0 18% during the impact The greater damage as a result of the pre-strain has had an effect here since the specimen without pre-strain reached 10^6 load cycles under otherwise identical conditions (Fig 4)

Figure 4   Residual strain after impact with pre-strain and cycling

This test series permits the following conclusions In civil aircraft design, the limit load is defined to be this load, that occurs with a probability of 10^{-9}. The coincidence of limit load with a 50 J impact reduces this probability considerably. Hence it is sufficient to combine a 50 J impact with the so-called "Get Home Loads"

4. INFLUENCE OF THICKNESS

It is clear that the thickness has a decisive influence on the sensitivity of a laminate to impacts In a further test series, tne thickness of the specimens was therefore systematically varied whilst retaining the same dimensions as in the foregoing section.

Laminate lay-up (+ 45, 0, -45, 90, -45, 0, + 45) n

where n = 2, 3, 4, 6

Fig 5 shows the residual strength as a function of the thickness after subjecting the specimens to 32 J and 48 ᵀ respectively
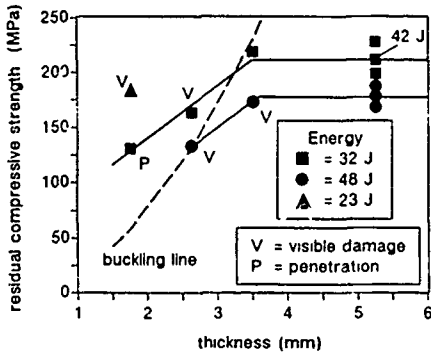

*Figure 5   Influence of thickness on residual compressive
strength after impact*

The strength increases initially and then reaches a constant maximum value The question of whether this would still apply to even thicker specimens would have to be the subject of further investigations

A point to note when assessing these results is that the residual strength of the thin specimens is above their buckling stress However, buckling cannot be the cause of the failure since it would then have to occur at the same stress level, irrespective of the intensity of the impact, which is not the case

5. VISIBLE DAMAGE THRESHOLD

The visible damage threshold is important for demonstration of adequate safety.

Yet, damage visibility is initially subjective, depending on the point of view For example, English literature refers to visible and barely visible damage (VID, BVID), a definition which is not satisfactory In the tests described here, the following objective definition was therefore chosen for the visibility of a damage on the front side.

visible damage. fiber delamination and/or
fiber cracks visible
dent diameter > 9 mm

great damage: fiber delamination and/or
fiber cracks visible
dent diameter > 15 mm

A dent of 9 mm diameter produced in fully plastic material by a 20 mm ball would cause a dent depth of 1 1 mm However, in reality the dent depth is considerably lower There are two possible explanations for this:

The material springs back elastically after the ball impact; however, the surface discolorations produced on the larger diameter due to micro-cracks remain,
or
the cracks propagate like a bow wave to a diameter larger than that of the dent.

Fig 6 shows an attempt to find the visible damage threshold, giving the impact energy as a function of the specimen thickness The lines drawn show the visible damage threshold for the case in question with some scatter
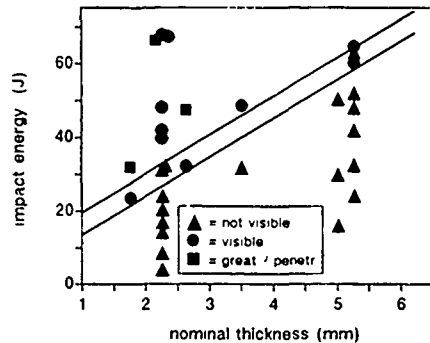

*Figure 6   Visible damage threshold as function of energy and
thickness*

However, an important fact to be borne in mind in connection with the general problem of visible damage thresholds is that an object with edges and corners will produce dents at far lower energies than the 20 mm ball considered here Furthermore, the hardness of the impactor also plays a role. The effect of hailstone will differ from that of a stone or rubber part

6. INFLUENCE OF LAMINATE LAY-UP

From the theory of elasticity, it follows that the stress increase due to holes or cracks depends in orthotropic materials on their elastic constants /6, 7/ The higher the modulus of elasticity in load direction compared to that transverse to it, the higher is the stress intensity factor /8/

It is therefore all the more surprising that this aspect has hardly been given consideration in literature and discussions on the extent of allowable strains for CFRP components which are endangered by impacts

To clarify this situation, a test series was conducted with laminates of the following lay-ups

x% 0⁰ / (90-x)% ± 45" / 10% 90⁰

where x = 10, 30, 50, 70

In addition to that the quasi-isotropic laminate 25/50/25 was used for comparison as this is mostly referred to in the literature

The specimen dimensions were 250 x 110 x 5 mm

6.1 Impacts With Air Gun

Fig 7 confirms the above expectations very impressively. It shows the normalized residual compressive strength versus the impact energy. The theoretical strength of the laminates is taken as reference The test results of the undamaged reference specimens with 10, 25 and 30% 0^0-plies show good agreement with the theoretical values However, the test values for the 0^0 dominant laminates 50/40/10 and 70/20/10 were clearly below the theoretical values. This relates to the difficulty of introducing the required high specific loads properly into the laminate.

The reciprocal value of the curves shown in Fig 7 is the stress intensity factor This has to be considered for dimensioning for CFRP components which are endangered by impact
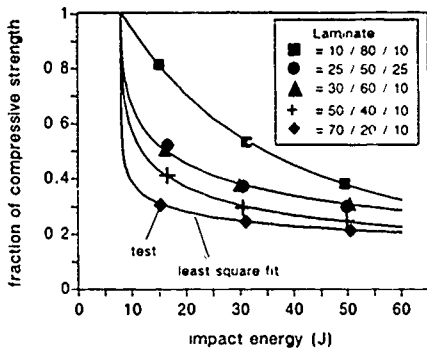

Figure 7 Strength reduction due to impact

It is convenient to take the strain as a design criterion for CFRP components Fig 8 shows the strain reached versus the 0^0-ply share of the laminates for the three different energies used It is evident that strains between 0 3% and 0 5% can be used as a design limit at an impact of 50 J, depending on the 0^0-ply share of the laminates in question
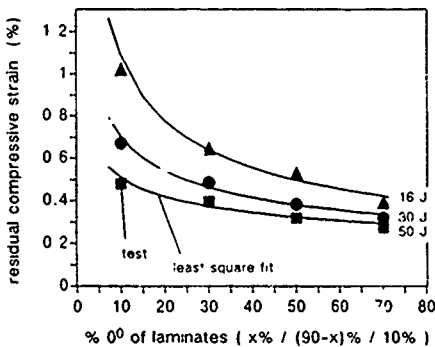

Figure 8 Residual compressive strain after impact

Now, the reader might object that the specimens here are very narrow and that the behavior may be very different in real components However, the scale-up effect is not very big as pointed out below.

Although the allowable strain decreases with increasing 0^0-ply share, these laminates nevertheless bear higher loads due to their higher stiffness (Fig 9)
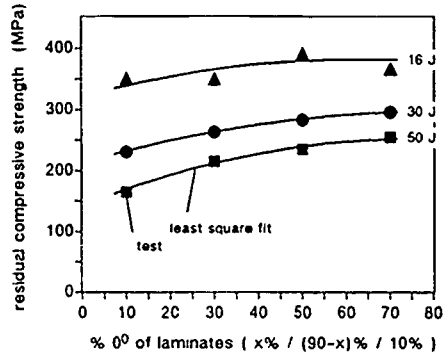

Figure 9 Residual compressive strength after impact

6.2 Damage Due To Open Hole

Although not directly related to the subject but very useful for comparison, Fig 10 and 11 - analogous to Fig 7 and 8 - show reduced laminate damage as a result of unloaded open holes compared with impacts The specimens with a central hole had the same dimensions as the impact specimens Naturally, the dependence of the stress intensity factor on the laminate lay-up was again confirmed

To obtain uniform conditions, the test results have been converted to the infinite plate using the correction function in accordance with /9, 10/ However, this practically only affects the 25 mm hole with 6%
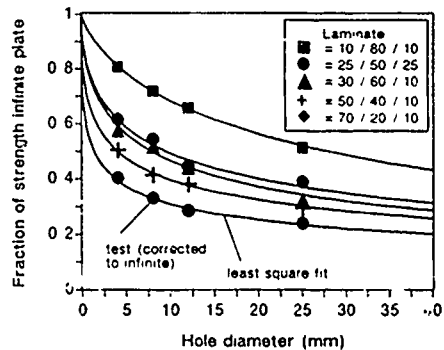

*Figure 10 Strength reduction due to open hole*
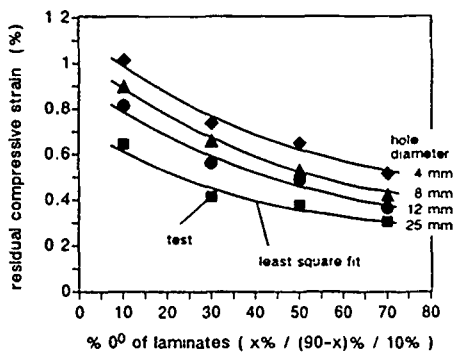
Figure 11 Residual compressive strain due to open hole

6.3 Impacts With Drop Weight

One specimen each per laminate type was subjected to an impact of 32 J and 48 J with a drop weight. The specimens were held in the same fixture, turned by 90°, as in the comparable tests with the air gun system The impactor had a mass of 4 08 kg and a semi-spherical tip of 20 mm diameter so that it corresponded to the ball of identical diameter used in the other tests Fig 12 documents that there is practically no verifiable difference in the strength behavior, irrespective of the impact method used
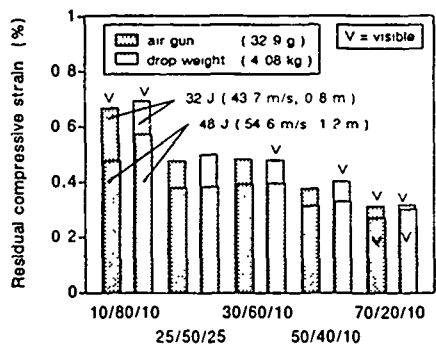

Figure 12.Residual compressive strain after impact, comparison of drop weight with air gun impacts

The result was surprising since the drop weight-induced C-Scan damage was smaller Depending on the laminate, the damage only reached approx. 75 - 92% at 32 J and 55 - 62 % at 48 J of the values reached with the air gun system

Tests conducted with large stringer stiffened panels produced the same result Conversely, this therefore means that the damage size of a component does not necessarily permit conclusions as to the residual strength Obviously the intensity of the damage and not the size of it is responsible for the rupture

Nevertheless, further investigations will have to be conducted into this since in another related test series not only smaller

damage sizes but also higher loads were reached with the drop weight compared to the air gun system

6.4 Stringer Stiffened Panels

The technology program for a planned CFRP wing at Deutsche Airbus also includes tests on stringer stiffened panels Although a description of the parts is not the subject of this paper, an attempt will nonetheless be made to quantify the mentioned scale-up effect between small specimens (coupons) and a real structure

The panels consisted of a plane skin measuring 1500 x 650 x 4 25 mm and the laminates 29/58/12 and 50/40/10 Adhesive film was used to bond five identical pre-fabricated T-stringers onto the skin over its entire length with a pitch of 140 mm. The stringers had a flange of 70 x 1.875 mm and a web of 52 x 7 875 mm made from 52/38/10 laminate. The buckling length was limited to 700 mm by two ribs which were attached by bonding The ribs were milled out at the positions of the stringer webs Supports at the ribs hold the panel against lateral displacement

Fig 13 shows the known strain curves plotted versus the 0°-ply share for the 50 J impact and the 25 mm hole. The graph also shows the strains reached in some of the panel tests The values are related to the overall C G of the skin/stringer cross-section
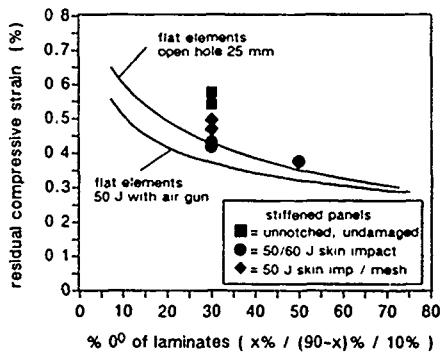

Figure 13.Residual compressive strain after impact, comparison of stiffened panels with coupons

The panel tests have again confirmed the dependence of the achievable strain level on the 0°-ply share of the laminate. However, this does not infer a reduction in the failure load since all panels showed a failure load of 1400 kN at 50 J impact

The strain curve of the coupons with 25 mm hole agrees surprisingly well with the strains reached in the panel tests, thus providing a good means of comparison for consideration of the effect of a 50 J impact

Panels with damage other than skin impact damage reached higher strains and thus also higher failure loads. This increased strain level was also observed at the panels with 50 J skin impact which, for reasons of lightning protection, had been provided with an additional metallic mesh (exterior) and

a layer of glass fabric (interior), each 0 1 mm thick. These layers of fabric seem to dampen the impact, thereby decreasing the intensity of the damage.

The plotted values for the undamaged panels show that a 50 J impact causes a strength reduction of approx. 23%.

An investigation of the scale-up effect between coupons and stiffened panels shows, that there is a 15% increase of residual strain in favour of the panels This is a relative low value compared with a ten times higher cross section of the panel

It was therefore demonstrated that tests with flat coupons are well suited for investigations into the effects of impacts on CFRP laminates

7. CONCLUSION

Depending on the energy, impacts cause a reduction in the strength of CFRP laminates The reduction is increased further if the laminates are subjected to a compressive load during the impact

The energy of an impact required to produce visible damage is difficult to define in an objective manner. It is, however, clearly dependent on the thickness

Open holes of the size common for riveted connections damage the laminates less than impacts of the intensity to be demonstrated for certification

C-Scan measurements have shown that impacts produced with high mass but low speed cause smaller damage than impacts produced with low mass but high speed However, this did not lead to higher residual strengths in one test series Tests carried out with stringer stiffened panels produced the same results This therefore indicates that the intensity of a damage does not depend on its size By contrast, in another test series with flat coupons, the strength after impacts with a drop weight was higher than in the case of the air gun system

The most important conclusion to be drawn from these tests is that the allowable strain for the dimensioning of CFRP components depends not only on the impact energy but also on the 0^0-ply share of the laminate

A comparison between the results obtained with coupons and with stringer stiffened panels shows that the coupons are well suited for investigating the effects of impacts on CFRP laminates The determined scale-up effect in favour of the panels was approx 15% for the geometries considered

If this effect is taken into account then a 0 42% strain for compressive loads can be used for CFRP structures having 30% of 0^0-plies. This value decreases linearly to 0 35% if there is 50% of 0^0-plies

This reduction of the allowable strain with the increasing amount of 0^0-plies does not necessarily imply heavier components since the weight depends on the product of strain and modulus of elasticity. Laminates having a high proportion of 0^0-plies are just as good as those with a smaller amount of such plies.

Nevertheless, the trend for design will be in favour of a panel with damage-tolerant skin (small proportion of 0^0-plies) and stiffer stringers with mainly 0^0-plies because primarily the skin is endangered by impact.

REFERENCES

/1/ Starnes, J H ; Rhodes, M D., Williams, J.G., "The Effect of Impact Damage and Circular Holes on the Compressive Strength of a Graphite Epoxy Laminate", NASA-TM-78796. Oktober 1978

/2/ Williams, J G , Anderson, M S , Rhodes, M D , Starnes, J H and Stroud, W D , "Recent Developments in the Design, Testing and Impact Tolerance of Stiffened Composite Panels", NASA-TM-80077, April 1979

/3/ Card, M F and Rhodes, M D , "Graphite-Epoxy Panel Compression Strength Reduction Due to Local Impact", AGARD 50th Meeting, Athens, Greece April 13-18, 1980

/4/ Williams, J G and Rhodes, M D , "The Effect of Resin on the Impact Damage Tolerance of Graphite-Epoxy Laminates", NASA-TM-83213, Oktober 1981

/5/ Starnes, J H and Williams, J G , "Failure Characteristics of Graphite-Epoxy Structural Components Loaded in Compression", NASA-TM-84552, September 1982

/6/ Sawin, G N , " Spannungserhöhung am Rande von Löchern", VEB Verlag Technik, Berlin, Germany, 1956

/7/ Lekhnitskii, S G , Anisotropic Plates", Gordon and Breach, London, U K , 1968

/8/ Garbo, S P and Ogonowski, J M , "Strength prediction of composite laminates with unloaded fastener holes", in AIAA Journal, 18, 5, May 1980

/9/ Awerbuch, J , "Fracture Behaviour and Notch Sensitivity of Composite Materials", Workshop on Failure Mechanisms in Composites, DFVLR Braunschweig, Germany, July 1982

/10/ Sendeckyj, G P, "Fracture Mechanics of Composites", ASTM, stp 593, 1975, Card No 75-26425, Page 131

MODE I INTERLAMINAR FRACTURE OF A CONTINUOUS ECR GLASS FIBRE-POLYAMIDE 12-COMPOSITE AS A FUNCTION OF THERMAL TREATMENT

G.C. Christopoulos
G.C. Papanicolaou
K. Friedrich [+]
Mechanical Engineering Department, University of Patras
261 10 Patras, Greece
+ Institute for Composite Materials Ltd.
University of Kaiserslautern
6750 Kaiserslautern, Germany

SUMMARY
The interlaminar fracture behavior of a composite made of continuous environmental corrosion resistant glass fibres (ECR-GF) in Polyamide 12 (PA12) matrix has been investigated. On special interest was how different thermal cycles during the production of the laminates affect the semicrystalline nature of this thermoplastic composite material, and thus the mode I - interlaminar fracture toughness.

1 INTRODUCTION
Failure of composite materials may often occur as a result of local defects. Interlaminar separation or delamination is one of the most important and life limiting failure mechanisms in composite structures. These kinds of defects may develop during the manufacturing process due to insufficient consolidation or non optimum curing cycles, or from the existance of foreign particles. It may also result from three dimensional interlaminar stresses, which develop at free edges or discontinuities (Ref. 1)

In order to achieve higher values of interlaminar fracture toughness the use of composite materials with thermoplastic matrices is possible (Ref. 2). On the other hand it is well recognized that the microstructure, such as crystallinity and morphology, of semicrystalline thermoplastic composites highly depends on the processing conditions employed during the manufacturing of laminates. Taking into account that large parts processing requires heavy tools with high thermal inertia, the effects of cooling rate on crystallinity, morphology and mechanical properties are of increasing interest in research (Ref. 3-5).

In order to study these effects with respect to the relation between interlaminar fracture toughness and thermal history, Enviromental Corrosion Resistant (ECR) Glass Fibres (GF) in a Polyamide 12 (PA12) matrix system was selected for the present investigation. Different morphologies in the matrix can be achieved by controlling the thermal treatment during the processing of the laminates.

2 MATERIALS AND PREPARATIONS
The material used in this study was an ECR-GF/PA12 tape, 30mm in width and 0.55mm in thickness, supplied by Baycomp Co, Canada. Laminates were manufactured within a steel mold and the use of a heat press. Prior to manufacturing it was found out by using a DSC testing device, that the melting temperature of the tape material was about 175°C. Each laminate contained six layers of ECR GF/PA12, and the final thickness of the plates was 3.4 mm. A thin steel foil, 30μm thick, coated with release agent, was

included in the middle of the laminate during the moulding operation, in order to obtain a starter crack

Three different thermal cycles were adopted during the manufacturing of the laminates, Fig 1. Material subjected to the first type of treatment was heated within 15 min from room temperature (RT) up to 220°C, under 0 3MPa of pressure, and then held at 220°C under 1.6MPa of pressure for 5 min. For specimens made under the second type of thermal cycle, heating took place from RT to 220°C within 10 min under 0.3MPa of pressure, then for 10 min at 220°C under 1 1MPa of pressure, and at the end for 5 min at 220°C under 1.6MPa of pressure During the third type of heat treatment, specimens were heated first from RT to 220°C under 0 16MPa of pressure within 5 min, then held at 220°C under 1.6MPa of pressure for 15 min. After each heat treatment specimens were cooled down from 220°C to RT with a cooling rate of 4°C/min.

After manufacturing of the laminates, some of the specimens from each thermal cycle were annealed by heating from room temperature, RT, to 150°C and held at this temperature for 5 hours. The cooling rate in the annealing cycle was the same as in the manufacturing process, i e. 4°C/min.

3 MICROSCOPY AND CALORIMETRY
Specimens were cut by using of a diamont wheel in dimensions of 150mm long by 20mm wide By using of reflected light microscopy technique, after polishing cross section of the specimens, the fiber arrangement within the volume of the specimens was investigated

The interlaminar fracture surfaces of the tested specimens were studied by using a Jeol scanning electron microscope (JEM-5400 SEM) All specimens were coated with a thin layer of gold in a sputtering chamber.

Measurements of the degree of crystallinity in the unidirectional laminates were performed with the technology of differential scanning calorimetry. A Du Pont DSC system, model 910, was used for all the experiments with a heating rate of 10°C/min The weight of the samples, which were cut from the laminates plates previously subjected to the different thermal and annealing cycles, was about 10 milligrams The calculation of the degree of crystallinity, X_C, was made from the following equation

$$X_c = \frac{\Delta H}{\Delta H_f (1 - W_f)} \qquad (1)$$

where ΔH_f is the heat of fusion of fully crystalline PA12, taken as 210J/g, W_f is the weight fraction of fibers in the sample (equal to 0.64 for the present case) and ΔH is the heat of fusion of the samples as determined for the differently heat treated laminate plates The results of the degree of crystallinity for each thermal treatment of ECR-GF/PA12 are listed in Table I.

4 INTERLAMINAR FRACTURE TESTS AND DATA REDUCTION METHODS
The most commonly used test for interlaminar fracture toughness in mode I, Fig 2, is the Double Cantilever Beam (DCB) test (Ref. 6). The specimens, after the different thermal treatments, were loaded continuously at room temperature (22°C), with a crosshead speed of 1mm/min Crack length a, load P, and crack opening displacement δ, were measured every 5mm during crack propagation To avoid errors due to large displacements the ratio of crack opening displacement to crack length, δ/a, was kept below 0 4; thus the overestimation of G_{IC} was kept less than 5% (Ref 7-8).
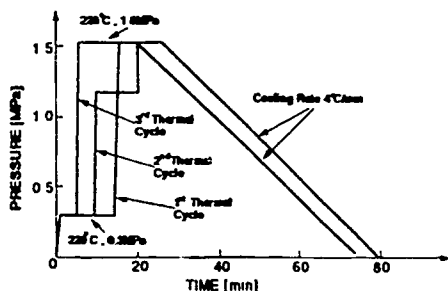

Figure 1: Thermal cycles
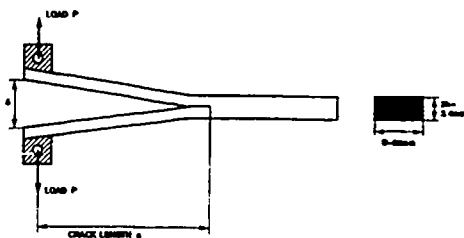
Figure 2. Mode-I DCB test specimen

In this paper three different data reduction methods have been used. The beam theory (BT), the corrected beam theory (CBT), and the experimental compliance method (ECM)

The simple beam theory expression for G_{IC} of a perfectly built-in DCB specimen is as follows :

$$G_{IC} = \frac{3P\delta}{2Ba} \qquad (2)$$

In practise the above expression underestimates the compliance as the beam is not perfectly built-in. A means of correction for this effect is to treat the beam as containing a slightly longer crack $(a+\Delta)$. Δ may be found experimentally as the deviation from the origin, by plotting the cube root of the compliance C, where $C = \delta/P$, as a function of crack length a. G_{IC} is then given by:

$$G_{IC} = \frac{3P\delta}{2B(a + \Delta)} \qquad (3)$$

An alternative approach is to plot the compliance C, versus crack length a, on a log-log plot. The slope of this plot, n, can then be used to give G_{IC} as follows:

$$C = ma^n \qquad (4)$$

from which follows·

$$G_{IC} = \frac{nP\delta}{2Ba} \qquad (5)$$

5 EXPERIMENTAL RESULTS
The experimental results from mode I interlaminar fracture tests are listed below in Table I. Each value is the average of three or four test specimens. The initiation values of fracture toughness $G_{IC(INIT)}$ were taken when starting the test from the end of the foil. Propagation values of toughness, $G_{IC(PROP)}$, are an average of data taken from longer crack lengths and have been corrected for large displacements wherever this was necessary

TABLE I

Thermal treatment of ECR GF/PA12	Degree of crystallinity X_c [%]	Initiation G_{IC} [kJ/m^2]	Propagation G_{IC} [kJ/m^2]
Prepreg tape	30	---	---
First Thermal Cycle Not Annealed	35	0.39	1.86
First Thermal Cycle Annealed 5h at 150 °C	38	0.50	1.25
Second Thermal Cycle Not Annealed	34	0.17	1.51
Second Thermal Cycle Annealed 5h at 150 °C	37	0.40	1.11
Third Thermal Cycle Not Annealed	37	0.29	2.12
Third Thermal Cycle Annealed 5h at 150 °C	42	0.45	1.29

6 RESULTS AND DISCUSSION
The DSC thermographs showed that the melting temperature Tm, remains constant, independent of the processing history. However, in all cases, melting curves possessed a double endothermic peak, less or more pronounced, which was attributed to variations of the crystalline form and size.

It is clear from the results tabulated in Table I that, when the crystallized samples undergo a further heat treatment such as annealing, a post-crystallization process occurs and a higher degree of crystallinity is observed (Fig. 3). Experimental results show that the fracture parameters are very sensitive to the different thermal treatments. More precisesly $G_{IC(PROP)}$ decreases with the annealing treatment while the opposite effect is observed with $G_{IC(INIT)}$ (Fig. 4). In order to explain the above behavior it is important to note that except from the degree of crystallinity, other important parameters can exist which affect the fracture process as well, e.g. the size of crystallites created in the matrix material, the spherulitic morphology and weak boundaries between the spherulites. As the latter factors have not been characterized so far in this study, a detailed description about the effects of the different thermal treatments on these parameters can not be presented at the moment.
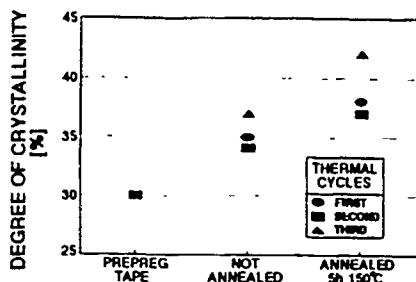

Figure 3: Degree of crystallinity versus thermal treatment
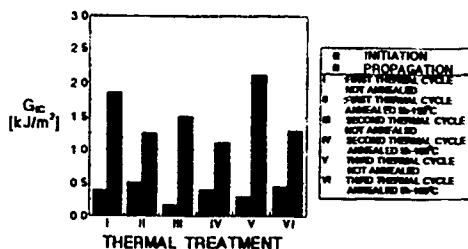
Figure 4: G_{IC} versus thermal treatment

Nevertheless the combination of the above mentioned parameters, which all depend on the processing history, is responsible for the finally observed fracture behavior of the composite. In our case as the degree of crystallinity increases, an enhanced resistance to the initiation process of crack propagation is observed, due to the high strength of crystallites and hence a greater $G_{IC(INIT)}$ is obtained As the crack propagates, specimens with higher degree of crystallinity show a decrease in $G_{IC(PROP)}$ due to the enhanced brittleness of the crystallized material.

7 OBSERVATIONS DURING TESTING AND MICROSCOPY INVESTIGATIONS
The non-annealed specimens resulted in a quasi stable crack growth behavior with the occurance of a smooth stick-slip crack growth A big amount of fibers bridged the crack tip up to 20-30 mm and an extensive formation of crack branching and jumping

took place In the case of the annealed specimens, a small amount of fibers bridged the crack tip up to only 10 mm behind it, also the formation of crack branching and jumping was less pronounced, while crack propagation was more stable than in the former case (Fig. 5).
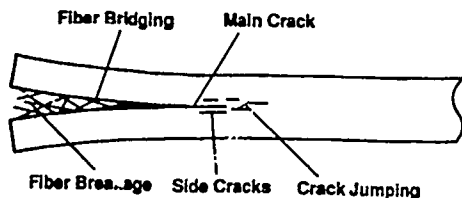

Figure 5: Observed failure mechanisms

First thermal cycle
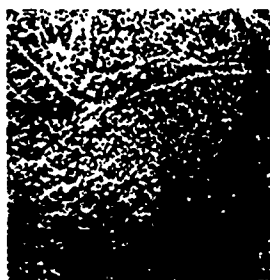
Second thermal cycle


Third thermal cycle

Figure 6. Polished cross sections

From reflected light microscopy it was observed that the best fiber/matrix arrangement in the volume of the laminate plates, was achieved during the third thermal cycle because the molten material was subjected to the highest pressure level for a longer time, compared to the other two thermal cycles. The worst fiber/matrix arrangement was observed in the second thermal cycle, with layers of matrix rich areas, while after the first thermal cycle a non uniform fibers distribution with the occurance of areas with high or low fibers arrangement was visible (Fig. 6)

Micrographs of the fracture surfaces are given in Fig 7 Crack propagation direction, is always from the lower left corner to the upper right corner of the pictures. It is obvious that bonding between fibers and matrix was not so good for both annealed and non-annealed specimens. In the case of annealed specimens a higher brittleness of the matrix appeared on the fractured surfaces, due to the higher degree of crystallinity.
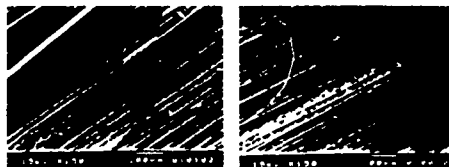
Not annealed
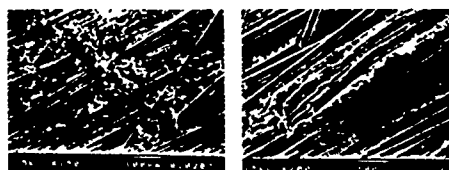
Annealed

Figure 7: Micrographs of fracture surfaces

8 CONCLUSIONS

The effects of thermal treatment on the mode 1 interlaminar fracture toughness of ECR GF/PA12 were demonstrated The used material as subjected to different thermal cycles by changing pressure levels and time duration in each step of pressure Longer time under higher pressure results in higher propagation values of interlaminar fracture toughness, $G_{IC(PROP)}$, due to better consolidation and fiber/matrix arrangement.

Subsequent annealing of specimens from all thermal cycles resulted in an increase in the degree of crystallinity This effect caused higher values of initiation interlaminar fracture toughness, $G_{IC(INIT)}$, due to the higher strength of crystalline matrix, but smaller values of propagation interlaminar fracture toughness, because of the enhanced brittleness of the post-crystallized material

In conlusion manufacturing process and thermal treatment of composites with a semi-crystalline thermoplastic matrix such as PA12, play a very important role in their interlaminar fracture toughness, therefore they are very important if one wants to obtain optimum structure- properties relationships

REFERENCES

[1] Fnedrich, K., (ed.), "Application of Fracture Mechanics to Composite Materials", Elsevier Sci. Publ., Amsterdam, 1989.

[2] Chang I.Y., Lee J.K., "Recent Development in Thermoplastic Composites· A Review of Matrix Systems and Processing Methods", J.Thermoplastic Composite Materials, 1, 1988, pp 277-295.

[3] Blundell, D J , Crick, R.A., Fife, B., Peacock, J., Keller, A , Waddon, A., "Spherulitic Morphology of the Matrix of Thermoplastic PEEK/Carbon Fibre Aromatic Polymer Composites", J.Materials Science, 24, 1989, pp 2057-2064.

[4] Talbott, M.F , Springer, G S., Berglund, L.A., "The Effects of Crystallinity on the Mechanical Properties of PEEK Polymer and Graphite Fiber Reinforced PEEK", J.Composite Materials, 21, November 1987, pp 1056-1081.

[5] Lee, W I , Talbott, M.F , Springer, G S , Berglund, L A., "Effects of Cooling Rate on the Crystallinity and Mechanical Properties of Thermoplastic Composites", J.Reinforced Plastics and Composites, 6, January 1987, pp 2-12

[6] Sela, N , Ishai, O., "Interlaminar Fracture Toughness And Toughening of Laminated Composite Materials: a Review", J.Composites, 20, 5, 1989, pp 423-435.

[7] Williams, J G., "Large Displacement and End Block Effects in the DCB Interlaminar Test in Mode I and II", J Composite Materials, 21, 1987, pp 330-347.

[8] Davies, P "Interlaminar Fracture Testing of Composites, Protocol for Joint Round Robin", ESIS, April 1990.

RECORDER'S REPORT OF FINAL ROUND-TABLE DISCUSSION

by

Steven L. Donaldson, USAF Materials Directorate,
Wright-Patterson AFB, Ohio USA

Christof Kindervater, German Aerospace Research Establishment,
DLR, Stuttgart, Germany

The final round-table discussion provided an open forum where invited panel members gave their comments on several topics related to the delamination and debonding of composites. In addition, all audience participants were solicited for their comments.

The following subjects were proposed by the session chairman as topics for discussion:

1. State of analysis of debonding and delamination
2. State of detection
3. State of repair methods
4. Innovative designs to minimize debonding
5. Environmental effects
6. Suggestions for follow-up activities
7. Other topics

The following is a brief summary of the discussion:

1. Current State of Analysis of Debonding and Delamination

a. The question still remains, are we selecting the correct damage to model?

- Models to predict damage geometry from design requirements (e.g., impact energy) are becoming more available. However, this step is still mostly empirical. We impact a part, examine the damage, then model a simplification of that damage in the structure.

- The laminate geometry and damage type modeled in the literature are often unrealistic.

b. Can we model the damage correctly?

- Methods (mostly finite element modeling, FEM) to model single delaminations are successful and well developed.

- Real parts may have many cracks which interact. There are no generalized methods to account for this at the structural level. What price do we pay for simplification to a single crack?

- Simple models (like strain to failure) are terribly inadequate. They do not account for specific design details which can strongly effect such things as crack stability.

- Different finite element codes can produce very different results. Two well-used codes run on the same model gave results which varied by 300%.

c. To what level of detail should we model the damage?

- Delamination analysis now seems successful, but only for specific structural details (e.g., stiffener to skin attachment). Industry feels they don't have the resources to go into this level of detail for the entire structure. Each problem requires a new model.

- It was felt by some that FEM packages and computing power are now becoming simple enough to use and cheap enough that industry can and must go into modeling at the detail level.

d. Other comments:

- The scale-up of analytical models and coupon results to full-size structures is still largely unsuccessful. We will always ultimately have to run large-scale tests. However, up-front analytical design studies will help designers get control of the many variables involved and lead to a more optimized design.

- In aircraft design, a factor of 1.5 is used for ultimate, plus there is a B-basis factor (a factor used to account for the statistical variation in material strength), as well as a reserve factor. We are utilizing typically less than 65% of the ultimate strength of a composite. The effects of delamination/debonding appear at 70-80% of ultimate. Therefore, it may appear that delamination is not a problem in aircraft structures. Anything that might be a problem would be confirmed by tests. Service experience has shown, however, some delaminations in actual flight structures.

- More work needs to be done to answer practical problems, such as:

- Blocking Plies
- Ply Drop-offs
- Free Edge Effects
- Bolted Joints

- It is not clear how to account for delamination growth. Due to the high growth exponents in, for example, da/dN vs ΔG data, should we design to threshold values of toughness?

e. Suggestions for follow-up activities:

- A strong consensus was that a group should be formed to study design criteria for damage tolerance. The group would summarize currently available analytical methods and design criteria used. They would ultimately make recommendations and propose standards for design. The group may wish to use a round-robin approach. We cannot attain, nor do we require perfect criteria, but any guidelines in this direction would be very useful to industry.

- A discussion of failure criteria for composites is necessary. This includes those used for the basic material, as well as bolted/bonded joints, cut-outs, and other details

- 3-D failure criteria must be established.

- A discussion of scaleability is necessary. How large do specimens need to be to get data realistic for use in structural designs?

- We need to discuss the real flight service experience with composites. What are the real problems encountered thus far?

- We need benchmarks so that analytical results can be compared. The current UK effort could serve as a starting point for FEM comparisons.

2. Current State of Detection of Delamination and Debonding

a. In general, most were impressed with the progress made to detect delamination and debonding.

b. Standards for "barely visible impact damage" do not exist. BVID depends on material, lighting, dent depth, paint, damage location (T-tail vs landing gear door), etc. An arbitrary single-valued standard is not appropriate.

c. Optical fibers for real-time damage detection (for health monitoring systems) show much promise.

d. Some areas still have needs:

- Detection of matrix degradation
- Detection of interphase degradation

- Detection of contamination in adhesive joints
- Detection of internal delaminations which are shadowed by others
- Improved NDT techniques for bonded joints
- Detection of damage from a "stand-off" distance

3. Current State of Repair Methods

a. Repair methods for epoxy matrix composites seem to be well in-hand. If damage can be detected, it can most likely be repaired

b. Repair of thermoplastics may not be as easy as first thought (the thinking was that to repair delaminations just re-heat and re-press), because in actual structures we won't be able to support the back surface. In addition, resin injected may not bond to crack surfaces.

c. Suggestions for follow-up activities:

- General discussion of optimal repair methods including design for repairability.

4. Innovative Designs to Minimize Debonding

a. Must consider during initial design phase.

b. Cannot use simple rules with these complex materials. The challenge is to have sophisticated analysis tools in quick, easy-to-use form for designers.

c. Toughened resins are now in common use.

d. Advanced 3D design concepts, such as weaving and braiding, hold promise. Complex manufacturing and high costs must be addressed.

5. Environmental Effects

a. At what level should we run our tests to make predictions about the effects of environment on structural performance? Most of the data exists, yet still needs to be synthesized correctly.

b. Composites are seeing more space applications. UV, atomic oxygen, and vacuum exposure degrade the material. The method currently used to avoid this degradation is to apply protective coatings. The long-term need is for resistant materials, especially resin systems, which do not require coatings.

Note that the discussion of follow-up activities (item 6) has been included under the subject headings. Finally, no "other topics" (item 7) were discussed.

REPORT DOCUMENTATION PAGE

1. Recipient's Reference	2. Originator's Reference	3. Further Reference	4. Security Classification of Document
	AGARD-CP-530	ISBN 92-835-0696-0	UNCLASSIFIED

5. Originator	Advisory Group for Aerospace Research and Development North Atlantic Treaty Organization 7 Rue Ancelle, 92200 Neuilly sur Seine, France

6. Title	DEBONDING/DELAMINATION OF COMPOSITES

7. Presented at	the 74th Meeting of the AGARD Structures and Materials Panel, held in Patras, Greece 24th—29th May 1992.

8. Author(s)/Editor(s)	9. Date
Various	December 1992

10. Author's/Editor's Address	11. Pages
Various	302

12. Distribution Statement	This document is distributed in accordance with AGARD policies and regulations, which are outlined on the back covers of all AGARD publications.

13. Keywords/Descriptors	
Composite laminates	Impact damage
Debonding	Damage tolerance
Delamination	Edge delamination
CFRP materials	

14. Abstract

Composite laminate components are prone to debonding/delamination when subjected to high interlaminar stress or when under impact. While delamination failure in itself is not usually catastrophic, its weakening influence on a component may lead to subsequent failure modes. Hence debonding or delamination may significantly reduce the strength of an aircraft or its fatigue life.

In bringing together the various experiences of air forces, governments, industry and universities, the meeting has helped to identify the key issues related to the debonding/delamination problem.

AGARD Conference Proceedings 530 Advisory Group for Aerospace Research and Development, NATO DEBONDING/DELAMINATION OF COMPOSITES Published December 1992 302 pages Composite laminate components are prone to debonding/ delamination when subjected to high interlaminar stress or when under impact. While delamination failure in itself is not usually catastrophic, its weakening influence on a component may lead to subsequent failure modes Hence debonding or delamination may significantly reduce the strength of an aircraft or its fatigue life. In bringing together the various experiences of air forces, governments, industry and universities, the meeting has P.T.O.	AGARD-CP-530 Composite laminates Debonding Delamination CFRP materials Impact damage Damage tolerance Edge delamination
AGARD Conference Proceedings 530 Advisory Group for Aerospace Research and Development, NATO DEBONDING/DELAMINATION OF COMPOSITES Published December 1992 302 pages Composite laminate components are prone to debonding/ delamination when subjected to high interlaminar stress or when under impact. While delamination failure in itself is not usually catastrophic, its weakening influence on a component may lead to subsequent failure modes Hence debonding or delamination may significantly reduce the strength of an aircraft or its fatigue life In bringing together the various experiences of air forces, governments, industry and universities, the meeting has P.T.O.	AGARD-CP-530 Composite laminates Debonding Delamination CFRP materials Impact damage Damage tolerance Edge delamination
AGARD Conference Proceedings 530 Advisory Group for Aerospace Research and Development, NATO DEBONDING/DELAMINATION OF COMPOSITES Published December 1992 302 pages Composite laminate components are prone to debonding/ delamination when subjected to high interlaminar stress or when under impact. While delamination failure in itself is not usually catastrophic, its weakening influence on a component may lead to subsequent failure modes Hence debonding or delamination may significantly reduce the strength of an aircraft or its fatigue life. In bringing together the various experiences of air forces, governments, industry and universities, the meeting has P.T.O.	AGARD-CP-530 Composite laminates Debonding Delamination CFRP materials Impact damage Damage tolerance Edge delamination
AGARD Conference Proceedings 530 Advisory Group for Aerospace Research and Development, NATO DEBONDING/DELAMINATION OF COMPOSITES Published December 1992 302 pages Composite laminate components are prone to debonding/ delamination when subjected to high interlaminar stress or when under impact. While delamination failure in itself is not usually catastrophic, its weakening influence on a component may lead to subsequent failure modes Hence debonding or delamination may significantly reduce the strength of an aircraft or its fatigue life In bringing together the various experiences of air forces, governments, industry and universities, the meeting has P.T.O.	AGARD-CP-530 Composite laminates Debonding Delamination CFRP materials Impact damage Damage tolerance Edge delamination

helped to identify the key issues related to the debonding/delamination problem

Papers presented at the 74th Meeting of the Structures and Materials Panel of AGARD held in Patras, Greece, 24th-29th May 1992.

ISBN 92-835-0696-0

AGARD

NATO ⊕ OTAN

7 RUE ANCELLE · 92200 NEUILLY-SUR-SEINE

FRANCE

Telephone (1)47 38 57 00   Telex 610 176
Telecopie (1)47 38 57 99

L AGARD ne detient pas de stocks de ses publications, dans un but de distribution generale a l adresse ci-dessus. La diffusion initiale des publications de l AGARD est effectuee aupres des pays membres de cette organisation par l intermediaire des Centres Nationaux de Distribution suivants A l exception des Etats-Unis, ces centres disposent parfois d exemplaires additionnels, dans les cas contraire, on peut se procurer ces exemplaires sous forme de microfiches ou de microcopies aupres des Agences de Vente dont la liste suite

CENTRES DE DIFFUSION NATIONAUX

ALLEMAGNE
Fachinformationszentrum,
Karlsruhe
D-7514 Eggenstein-Leopoldshafen 2

BELGIQUE
Coordonnateur AGARD-VSL
Etat-Major de la Force Aerienne
Quartier Reine Elisabeth
Rue d'Evere, 1140 Bruxelles

CANADA
Directeur du Service des Renseignements Scientifiques
Ministere de la Defense Nationale
Ottawa, Ontario K1A 0K2

DANEMARK
Danish Defence Research Board
Ved Idraetsparken 4
2100 Copenhagen O

ESPAGNE
INTA (AGARD Publications)
Pintor Rosales 34
28008 Madrid

ETATS-UNIS
National Aeronautics and Space Administration
Langley Research Center
M S 180
Hampton, Virginia 23665

FRANCE
O N E R A (Direction)
29, Avenue de la Division Leclerc
92322 Chatillon Cedex

GRECE
Hellenic Air Force
Air War College
Scientific and Technical Library
Dekelia Air Force Base
Dekelia, Athens TGA 1010

ISLANDE
Director of Aviation
c o Flugrad
Reykjavik

ITALIE
Aeronautica Militare
Ufficio del Delegato Nazionale all AGARD
Aeroporto Pratica di Mare
00040 Pomezia (Roma)

LUXEMBOURG
Voir Belgique

NORVEGE
Norwegian Defence Research Establishment
Attn Biblioteket
P O Box 25
N-2007 Kjeller

PAYS-BAS
Netherlands Delegation to AGARD
National Aerospace Laboratory NLR
Kluyverweg 1
2629 HS Delft

PORTUGAL
Portuguese National Coordinator to AGARD
Gabinete de Estudos e Programas
CLAFA
Base de Alfragide
Alfragide
2700 Amadora

ROYAUME UNI
Defence Research Information Centre
Kentigern House
65 Brown Street
Glasgow G2 8EX

TURQUIE
Milli Savunma Başkanlığı (MSB)
ARGE Daire Başkanlığı (ARGE)
Ankara

LE CENTRE NATIONAL DE DISTRIBUTION DES ETATS-UNIS (NASA) NE DETIENT PAS DE STOCKS
DES PUBLICATIONS AGARD ET LES DEMANDES D'EXEMPLAIRES DOIVENT ETRE ADRESSEES DIRECTEMENT
AU SERVICE NATIONAL TECHNIQUE DE L INFORMATION (NTIS) DONT L ADRESSE SUIT

AGENCES DE VENTE

National Technical Information Service
(NTIS)
5285 Port Royal Road
Springfield, Virginia 22161
Etats-Unis

ESA Information Retrieval Service
European Space Agency
10, rue Mario Nikis
75015 Paris
France

The British Library
Document Supply Division
Boston Spa, Wetherby
West Yorkshire LS23 7BQ
Royaume Uni

Les demandes de microfiches ou de photocopies de documents AGARD (y compris les demandes faites aupres du NTIS) doivent comporter la denomination AGARD, ainsi que le numero de serie de l AGARD (par exemple AGARD-AG-315) Des informations analogues, telles que le titre et la date de publication sont souhaitables Veuiller noter qu il y a lieu de specifier AGARD-R-nnn et AGARD-AR-nnn lors de la commande de rapports AGARD et les rapports consultatifs AGARD respectivement Des references bibliographiques completes ainsi que des resumes des publications AGARD figurent dans les journaux suivants

Scientifique and Technical Aerospace Reports (STAR)
publie par la NASA Scientific and Technical
Information Division
NASA Headquarters (NTT)
Washington D C 20546
Etats-Unis

Government Reports Announcements and Index (GRA&I)
publie par le National Technical Information Service
Springfield
Virginia 22161
Etats-Unis

(accessible egalement en mode interactif dans la base de
donnees bibliographiques en ligne du NTIS, et sur CD-ROM)

AGARD

NATO ⊕ OTAN

7 RUE ANCELLE · 92200 NEUILLY-SUR-SEINE

FRANCE

Telephone (1)47.38 57 00 · Telex 610 176
Telefax (1)47 38 57 99

**DISTRIBUTION OF UNCLASSIFIED
AGARD PUBLICATIONS**

AGARD does NOT hold stocks of AGARD publications at the above address for general distribution. Initial distribution of AGARD publications is made to AGARD Member Nations through the following National Distribution Centres. Further copies are sometimes available from these Centres (except in the United States), but if not may be purchased in Microfiche or Photocopy form from the Sales Agencies listed below.

NATIONAL DISTRIBUTION CENTRES

BELGIUM
Coordonnateur AGARD — VSL
Etat-Major de la Force Aérienne
Quartier Reine Elisabeth
Rue d'Evere, 1140 Bruxelles

CANADA
Director Scientific Information Services
Dept of National Defence
Ottawa, Ontario K1A 0K2

DENMARK
Danish Defence Research Board
Ved Idraetsparken 4
2100 Copenhagen Ø

FRANCE
O N E R.A (Direction)
29 Avenue de la Division Leclerc
92322 Châtillon Cedex

GERMANY
Fachinformationszentrum
Karlsruhe
D-7514 Eggenstein-Leopoldshafen 2

GREECE
Hellenic Air Force
Air War College
Scientific and Technical Library
Dekelia Air Force Base
Dekelia, Athens TGA 1010

ICELAND
Director of Aviation
c/o Flugrad
Reykjavik

ITALY
Aeronautica Militare
Ufficio del Delegato Nazionale all'AGARD
Aeroporto Pratica di Mare
00040 Pomezia (Roma)

LUXEMBOURG
See Belgium

NETHERLANDS
Netherlands Delegation to AGARD
National Aerospace Laboratory, NLR
Kluyverweg 1
2629 HS Delft

NORWAY
Norwegian Defence Research Establishment
Attn Biblioteket
P.O. Box 25
N-2007 Kjeller

PORTUGAL
Portuguese National Coordinator to AGARD
Gabinete de Estudos e Programas
CLAFA
Base de Alfragide
Alfragide
2700 Amadora

SPAIN
INTA (AGARD Publications)
Pintor Rosales 34
28008 Madrid

TURKEY
Millı Savunma Başkanlığı (MSB)
ARGE Daire Başkanlığı (ARGE)
Ankara

UNITED KINGDOM
Defence Research Information Centre
Kentigern House
65 Brown Street
Glasgow G2 8EX

UNITED STATES
National Aeronautics and Space Administration (NASA)
Langley Research Center
M/S 180
Hampton, Virginia 23665

THE UNITED STATES NATIONAL DISTRIBUTION CENTRE (NASA) DOES NOT HOLD
STOCKS OF AGARD PUBLICATIONS, AND APPLICATIONS FOR COPIES SHOULD BE MADE
DIRECT TO THE NATIONAL TECHNICAL INFORMATION SERVICE (NTIS) AT THE ADDRESS BELOW

SALES AGENCIES

National Technical
Information Service (NTIS)
5285 Port Royal Road
Springfield, Virginia 22161
United States

ESA/Information Retrieval Service
European Space Agency
10, rue Mario Nikis
75015 Paris
France

The British Library
Document Supply Centre
Boston Spa, Wetherby
West Yorkshire LS23 7BQ
United Kingdom

Requests for microfiches or photocopies of AGARD documents (including requests to NTIS) should include the word 'AGARD' and the AGARD serial number (for example AGARD-AG-315) Collateral information such as title and publication date is desirable Note that AGARD Reports and Advisory Reports should be specified as AGARD-R-nnn and AGARD-AR-nnn, respectively Full bibliographical references and abstracts of AGARD publications are given in the following journals

Scientific and Technical Aerospace Reports (STAR)
published by NASA Scientific and Technical
Information Division
NASA Headquarters (NTT)
Washington D.C. 20546
United States

Government Reports Announcements and Index (GRA&I)
published by the National Technical Information Service
Springfield
Virginia 22161
United States

(also available online in the NTIS Bibliographic
Database or on CD-ROM)